issn 0424-7116
An open-access journal by
the German Quaternary Association
Editor-in-chief: Christopher Lüthgens

E&G

Quaternary Science Journal

Eiszeitalter und Gegenwart

Special issue

Quaternary research from and inspired by the first virtual DEUQUA conference

Guest editors: Julia Meister, Hans von Suchodoletz, and Christian Zeeden

Copernicus Publications
The Innovative Open Access Publisher

E&G Quaternary Science Journal

An open-access journal of the German Quaternary Association

E&G Quaternary Science Journal (EGQSJ) is an interdisciplinary open-access journal published by the German Quaternary Association (DEUQUA) since 1951, and it is one of the longest-running journals related to Quaternary research. EGQSJ publishes peer-reviewed articles and express reports, as well as thesis abstracts related to Quaternary geology, paleo-environments, paleo-ecology, soil science, paleo-climatology, geomorphology, geochronology, archaeology, and geoarchaeology focussing on, but not limited to, research from central Europe.

Copernicus Publications
The Innovative Open Access Publisher

Copernicus Publications
Bahnhofsallee 1e
37081 Göttingen
Germany

Phone: +49 551 90 03 39 0
Fax: +49 551 90 03 39 70

publications@copernicus.org
https://publications.copernicus.org

Printed in Germany.
Schaltungsdienst Lange o.H.G.

ISSN 0424-7116

Published by Copernicus GmbH (Copernicus Publications) on behalf of the
German Quaternary Association (DEUQUA).

Image credit:
Scientific drilling at the "Schwalbenberg" site in the Lower Middle Rhine Valley in western central Germany (Vinnepand et al., this special issue) in 2014. Photo by Andreas Vött (2014).

https://www.eg-quaternary-science-journal.net/

E&G
Quaternary Science Journal
An open-access journal of the German Quaternary Association
https://www.eg-quaternary-science-journal.net/

Editor-in-chief

Christopher Lüthgens
University of Natural Resources and
Life Sciences, Vienna
Institute of Applied Geology
Peter-Jordan-Str. 82
1190 Vienna
Austria
christopher.luethgens@boku.ac.at

Managing editors

Daniela Sauer
University of Goettingen
Institute of Geography
Physical Geography
Goldschmidtstr. 5
37077 Goettingen
Germany
daniela.sauer@geo.uni-goettingen.de

Michael Zech
Technical University of Dresden
Institute of Geography
Heisenberg Chair of Physical Geography with
focus on paleoenvironmental research
Helmholtzstr. 10
01069 Dresden
Germany
michael.zech@tu-dresden.de

Associate editors

Becky Briant
Birkbeck, University of London
Department of Geography
Malet Street
London WC1E 7HX
United Kingdom

Eleanor Brown
Natural England
Chief Scientist Directorate
Mail Hub Natural England, County Hall,
Spetchley Road
Worcester, Worcestershire WR5 2NP
United Kingdom

Elisabeth Dietze
University of Goettingen
Institute of Geography,
Physical Geography
Goldschmidtstr. 5
37077 Goettingen
Germany

Markus Fuchs
Justus-Liebig-University Giessen
Department of Geography
Senckenbergstrasse 1
35390 Giessen
Germany

Sven Lukas
University of Lund
Department of Geology
Sölvegatan 12
22362 Lund
Sweden

Jan-Hendrik May
University of Melbourne
School of Geography
221 Bouverie St
Carlton 3053
Australia

Julia Meister
University of Wuerzburg
Institute of Geography and Geology
Geoarchaeology and Quaternary Science
Am Hubland
97074 Wuerzburg
Germany

Tony Reimann
University of Cologne
Geomorphology and Geochronology
Zülpicher Str. 45
50674 Köln
Germany

Gilles Rixhon
Université de Strasbourg
Ecole Nationale du Génie de l’Eau et de
l’Environnement Strasbourg
Laboratoire LIVE
Rue de l’Argonne 3
67000 Strasbourg
France

Zsófia Ruszkiczay-Rüdiger
Research Centre for Astronomy and Earth
Sciences
Institute for Geological and Geochemical
Research
Budaörsi út 45
1112 Budapest
Hungary

Bernhard Salcher
Salzburg University
Department of Geography and Geology
Hellbrunner Strasse 34
5020 Salzburg
Austria

E&G
Quaternary Science Journal
An open-access journal of the German Quaternary Association
https://www.eg-quaternary-science-journal.net/

Associate editors

Tobias Sprafke
Kompetenzzentrum Boden
(Center of Competence for Soils)
BFH-HAFL
Länggasse 85
3052 Zollikofen
Switzerland

Ingmar Unkel
Heidelberg University
Faculty of Chemistry and Earth Sciences
Institute of Geography, Geomorphology
and Soil Geography
Im Neuenheimer Feld 348
69120 Heidelberg
Germany

Hans von Suchodoletz
Leipzig University
Institute of Geography
Johannisallee 19a
04103 Leipzig
Germany

Christian Zeeden
LIAG,
Leibniz Institute for Applied Geophysics S5
Stilleweg 2
30655 Hannover
Germany

Guest editors

Special Issue:
"Quaternary research from and inspired by the first virtual DEUQUA conference"

Julia Meister
University of Wuerzburg
Institute of Geography and Geology
Geoarchaeology and Quaternary Science
Am Hubland
97074 Wuerzburg
Germany

Hans von Suchodoletz
Leipzig University
Institute of Geography
Johannisallee 19a
04103 Leipzig
Germany

Christian Zeeden
LIAG,
Leibniz Institute for Applied Geophysics S5
Stilleweg 2
30655 Hannover
Germany

Advisory board

Flavio Anselmetti
Institute of Geological Sciences and Oeschger
Centre for Climate Change Research
University of Bern
Baltzerstrasse 1+3
3012 Bern
Switzerland

Pierre Antoine
UMR 8591 CNRS / Univ. Paris I & UPEC
Laboratoire de Géographie Physique
Environnements Quaternaires et actuels
1 Place A. Briand
92 195 Meudon
France

Margot Böse
Freie Universität Berlin
Institute of Geographical Sciences
Physical Geography
Malteserstr. 74-100
12249 Berlin
Germany

Chris Clark
University of Sheffield
Department of Geography
Winter Street
Sheffield S10 2TN
United Kingdom

Philip Gibbard
University of Cambridge
Scott Polar Research Institute
Lensfield Road
Cambridge CB2 1ER
United Kingdom

Susan Ivy-Ochs
ETH Zürich
Ion Beam Physics and Earth Science
Department
Otto-Stern-Weg 5
8093 Zürich
Switzerland

E&G
Quaternary Science Journal
An open-access journal of the German Quaternary Association
https://www.eg-quaternary-science-journal.net/

Copernicus Publications
The Innovative Open Access Publisher

Editorial Support

Natascha Töpfer
editorial@copernicus.org

Publication Production

Sarah Schneemann
production@copernicus.org

E&G Quaternary Sci. J., 72, 185–187, 2023
https://doi.org/10.5194/egqsj-72-185-2023

Open Access E&G Quaternary Science Journal

Preface

Preface: Quaternary research from and inspired by the first virtual DEUQUA conference

Julia Meister[1], **Hans von Suchodoletz**[2], **and Christian Zeeden**[3]

[1]Institute of Geography and Geology, University of Würzburg, 97074 Würzburg, Germany
[2]Institute of Geography, University of Leipzig, 04103 Leipzig, Germany
[3]Rock Physics and Borehole Geophysics, Leibniz Institute for Applied Geophysics, 30655 Hanover, Germany

Correspondence: Julia Meister (julia.meister@uni-wuerzburg.de)

Relevant dates: Published: 9 August 2023

How to cite: Meister, J., von Suchodoletz, H., and Zeeden, C.: Preface: Quaternary research from and inspired by the first virtual DEUQUA conference, E&G Quaternary Sci. J., 72, 185–187, https://doi.org/10.5194/egqsj-72-185-2023, 2023.

1 The vDEUQUA2021 online conference

The global Covid-19 pandemic, which began in 2020 and did not abate until 2022, had not only a major impact on the lives of millions of people, but also a noticeable impact on science (Jack and Glover, 2021; Schadeberg et al., 2022). In this context, as with numerous other conferences, the regular meeting of the German Quaternary Association (DEUQUA) had to be postponed from 2020 to 2022, so in early 2021 the following question arose: “do we want to live for 4 years without intensive exchange on Quaternary science issues?” To fill this gap, a team of eight Quaternary scientists at different career stages from different research institutions organized the virtual “vDEUQUA2021” meeting from 29 to 30 September 2021. Supported by DEUQUA and the scientific platform Sciencesconf as well as the University of Würzburg, it was possible to organize this meeting via the online platforms Gather and Zoom. The online format limited classical face-to-face exchange but at the same time enabled an unprecedented international DEUQUA conference with more than 180 participants from 21 countries, with a share of more than 50 % early-career scientists. This led to intensive exchange and networking within a much broader Quaternary community than at previous on-site DEUQUA meetings.

The very interdisciplinary conference program and the high number of contributions impressively demonstrated the strong interest in Quaternary science and the high demand for scientific exchange despite – or especially because of – the exceptional pandemic situation. This may be explained by (i) the key role that Quaternary science plays in determining the pre-industrial background of the dramatic current climatic, geomorphological and geoecological changes due to strongly increased human activity (“the past is the key to the future”; Woodroffe and Murray-Wallace, 2012; McCaroll, 2015) and (ii) the rapid methodical developments within this field that are permanently expanding the possibilities of approaching climate and environmental archives in novel ways, as well as of addressing new research questions, requiring intensive and rapid scientific exchange and feedback (Banerji et al., 2022; Britton et al., 2022). Accordingly, these recent developments are also reflected in the 12 articles of this conference volume, which deal with pre-industrial climatic, geomorphological and geoecological changes as well as with methodological developments.

2 The contributions to this volume

Vinnepand et al. (2023) study paleoenvironmental changes at the Schwalbenberg RP1 loess–paleosol sequence in the Middle Rhine Valley in Germany between $\sim$40 and 22 ka using a multi-method approach. Their results confirm the assumption of synsedimentary soil formation during interstadials, show loess provenance changes with overall dominating local to regional dust sources and confirm the close temporal linkages of their proxies to those in other paleoclimate archives in the North Atlantic region.

Tinapp et al. (2023) report on valley development of the Elbe Valley near Dresden during the last ~ 15 kyr. Their study links sedimentation, soil formation and archeology in the area. Sedimentologically, they find that a Preboreal clayey sedimentation phase is followed by two fine sandy sedimentation phases before Holocene clayey sedimentation occurs. Of particular interest is the finding that during a longer period between the Atlantic and Subboreal the Lower Weichsel Terrace was used for settlement by the Linear Pottery culture. Thereafter flooding led to sparser (Bronze Age) or absent settlements on the lower terrace.

Pötter et al. (2023) reconstruct a wetland environment for a late Middle to Upper Pleniglacial (approx. 30–20 ka) loess sequence in western Germany. They find that the investigated section was influenced by periodical flooding, leading to marshy conditions and a stressed ecosystem. Overall, the results show that the landscape of the study area was much more fragmented during this time than previously thought.

Hardt et al. (2023) investigate the geomorphological and geological characteristics of the archeological sites Hawelti–Melazo and their surroundings in northern Ethiopia by performing sedimentological analyses, as well as direct (luminescence) and indirect (radiocarbon) sediment dating. They were able to reconstruct the paleoenvironmental conditions in the late Quaternary, which they integrated into the wider context of Tigray.

Schwahn et al. (2023) investigate the loess sequence of Köndringen in the Upper Rhine Graben using a multi-method approach including the measurement of color, grain size, organic matter and carbonate content. The analyses reveal that the sequence comprises several fossil soils and layers of reworked soil material. According to luminescence dating, it reaches back more than 500 000 years.

Ullmann et al. (2022) highlight the application of a freely available tool for Google Earth Engine. The software allows cloud-free satellite images to be processed. They show processing examples for the Nile Delta (Egypt) and how remote sensing images are used to find indications of buried landforms, such as former river branches of the Nile.

Liu et al. (2022) present an isotope geochemical study on mammoth tooth enamel from the Upper Rhine Graben. Their work is both methodological and applied. While methodological aspects of obtaining ideal samples are discussed, their study also reports high-resolution paleoenvironmental records of likely sub-seasonal resolution.

Engel et al. (2022) investigate the late-glacial Bergstraßenneckar, a former course of the Neckar River in the Upper Rhine Graben in southwest Germany, by sediment cores and geophysical measurements. They were able to reconstruct the shift from a running river to silting-up meanders that took place about 11 000 to 10 500 years ago.

Abdulkarim et al. (2022) analyze the patterns and provenance of paleochannels in the French Upper Rhine alluvial plain. They find at least five paleochannel groups which can be distinguished. Assessing their timing and sedimentology will shed further light on the paleochannel evolution of the area.

Schulze et al. (2022) study a Late Weichselian loess–paleosol sequence in the southern Upper Rhine Graben in southwestern Germany using a multi-method approach. They found drier conditions in the southern compared with the northern Upper Rhine Graben, and they confirm an earlier start of massive loess accumulation compared with the arrival of glaciers in the foreland of the Alps.

Kirchner et al. (2022) evaluate recent soil agro-potential and search for evidence of prehistoric and historic land use by applying a pedo-geomorphological approach in the surroundings of Munigua, a small Roman city in the ancient province of Hispania Baetica (SW Spain). The available evidence of Roman agricultural use in the Munigua area suggests that the city's economy was by no means solely focused on mining.

Labahn et al. (2022) measure δ^{18}O of plant-derived lipids in a loess–paleosol sequence in Serbia over the last glacial–interglacial cycle, a method that was recently proposed as a paleoclimatic/paleohydrologic proxy. They obtained enough bulk lipids for analysis, demonstrating the general applicability of this method to loess–paleosol sequences. Furthermore, systematically higher values in paleosols compared with loess layers were observed. However, short-term climatic fluctuations could not be recognized, which requires further research.

Acknowledgements. We warmly thank all the authors and reviewers who contributed to or supported this special issue during the challenging Covid-19 period. We are very grateful to Chief Editor Christopher Lüthgens for his assistance in creating this special issue.

Financial support. This open-access publication was funded by Julius-Maximilians-Universität Würzburg.

References

Abdulkarim, M., Chapkanski, S., Ertlen, D., Mahmood, H., Obioha, E., Preusser, F., Rambeau, C., Salomon, F., Schiemann, M., and Schmitt, L.: Morpho-sedimentary characteristics of Holocene paleochannels in the Upper Rhine alluvial plain, France, E&G Quaternary Sci. J., 71, 191–212, https://doi.org/10.5194/egqsj-71-191-2022, 2022.

Banerji, U. S., Goswami, V., and Joshi, K. B.: Quaternary dating and instrumental development: An overview, J. Asian Earth Sci., X 7, 100091, https://doi.org/10.1016/j.jaesx.2022.100091, 2022.

Britton, K., Crowley, B. E., Bataille, C. P., Miller, J. H., and Wooller, M. J.: Editorial: A Golden Age for Strontium Isotope Research? Current Advances in Paleoecological and Archaeological Research, Front. Ecol. Evolut., 9, 820295, https://doi.org/10.3389/fevo.2021.820295, 2022.

Engel, M., Henselowsky, F., Roth, F., Kadereit, A., Herzog, M., Hecht, S., Lindauer, S., Bubenzer, O., and Schukraft, G.: Fluvial activity of the late-glacial to Holocene "Bergstraßenneckar" in the Upper Rhine Graben near Heidelberg, Germany – first results, E&G Quaternary Sci. J., 71, 213–226, https://doi.org/10.5194/egqsj-71-213-2022, 2022.

Hardt, J., Nir, N., Lüthgens, C., Menn, T. M., and Schütt, B.: Palaeoenvironmental research at Hawelti–Melazo (Tigray, northern Ethiopia) – insights from sedimentological and geomorphological analyses, E&G Quaternary Sci. J., 72, 37–55, https://doi.org/10.5194/egqsj-72-37-2023, 2023.

Jack, T., and Glover, A.: Online conferencing in the midst of COVID-19: an "already existing experiment" in academic internationalization without air travel, Sustainability: Science, Practice and Policy, 17, 292–304, https://doi.org/10.1080/15487733.2021.1946297, 2021.

Kirchner, A., Herrmann, N., Matras, P., Müller, I., Meister, J., and Schattner, T. G.: A pedo-geomorphological view on land use and its potential in the surroundings of the ancient Hispano-Roman city Munigua (Seville, SW Spain), E&G Quaternary Sci. J., 71, 123–143, https://doi.org/10.5194/egqsj-71-123-2022, 2022.

Labahn, J., Bittner, L., Hirschmann, P., Roettig, C.-B., Burghardt, D., Glaser, B., Marković, S. B., and Zech, M.: ^{18}O analyses of bulk lipids as novel paleoclimate tool in loess research – a pilot study, E&G Quaternary Sci. J., 71, 83–90, https://doi.org/10.5194/egqsj-71-83-2022, 2022.

Liu, Z., Prendergast, A., Drysdale, R., and May, J.-H.: Comparison of bulk and sequential sampling methodologies on mammoth tooth enamel and their implications in paleoenvironmental reconstructions, E&G Quaternary Sci. J., 71, 227–241, https://doi.org/10.5194/egqsj-71-227-2022, 2022.

McCaroll, D.: 'Study the past, if you would divine the future': a retrospective on measuring and understanding Quaternary climate change, J. Quaternary Sci., 30, 154–187, https://doi.org/10.1002/jqs.2775, 2015.

Pötter, S., Seeger, K., Richter, C., Brill, D., Knaak, M., Lehmkuhl, F., and Schulte, P.: Pleniglacial dynamics in an oceanic central European loess landscape, E&G Quaternary Sci. J., 72, 77–94, https://doi.org/10.5194/egqsj-72-77-2023, 2023.

Schadeberg, A., Ford, E., Wieczorek, A.M., Gammage, L.C., López-Acosta, M., Buselic, I., Turk Dermastia, T., Fontela, M., Galobart, C., Llopis Monferrer, N., Lubósny, M., Piarulli, S., and Suaria, G.: Productivity, pressure, and new perspectives: impacts of the COVID-19 pandemic on marine early-career researchers, ICES J. Mar. Sci., 79, 2298–2310, https://doi.org/10.1093/icesjms/fsac167, 2022.

Schulze, T., Schwahn, L., Fülling, A., Zeeden, C., Preusser, F., and Sprafke, T.: Investigating the loess–palaeosol sequence of Bahlingen-Schönenberg (Kaiserstuhl), southwestern Germany, using a multi-methodological approach, E&G Quaternary Sci. J., 71, 145–162, https://doi.org/10.5194/egqsj-71-145-2022, 2022.

Schwahn, L., Schulze, T., Fülling, A., Zeeden, C., Preusser, F., and Sprafke, T.: Multi-method study of the Middle Pleistocene loess–palaeosol sequence of Köndringen, SW Germany, E&G Quaternary Sci. J., 72, 1–21, https://doi.org/10.5194/egqsj-72-1-2023, 2023.

Tinapp, C., Selzer, J., Döhlert-Albani, N., Fischer, B., Heinrich, S., Herbig, C., Kreienbrink, F., Lauer, T., Schneider, B., and Stäuble, H.: Late Weichselian–Holocene valley development of the Elbe valley near Dresden – linking sedimentation, soil formation and archaeology, E&G Quaternary Sci. J., 72, 95–111, https://doi.org/10.5194/egqsj-72-95-2023, 2023.

Ullmann, T., Möller, E., Baumhauer, R., Lange-Athinodorou, E., and Meister, J.: A new Google Earth Engine tool for spaceborne detection of buried palaeogeographical features – examples from the Nile Delta (Egypt), E&G Quaternary Sci. J., 71, 243–247, https://doi.org/10.5194/egqsj-71-243-2022, 2022.

Vinnepand, M., Fischer, P., Hambach, U., Jöris, O., Craig, C.-A., Zeeden, C., Thornton, B., Tütken, T., Prud'homme, C., Schulte, P., Moine, O., Fitzsimmons, K. E., Laag, C., Lehmkuhl, F., Schirmer, W., and Vött, A.: What do dust sinks tell us about their sources and past environmental dynamics? A case study for oxygen isotope stages 3–2 in the Middle Rhine Valley, Germany, E&G Quaternary Sci. J., 72, 163–184, https://doi.org/10.5194/egqsj-72-163-2023, 2023.

Woodroffe, C. D. and Murray-Wallace, C. V.: Sea-level rise and coastal change: the past as a guide to the future, Quaternary Sci. Rev., 54, 4–11, https://doi.org/10.1016/j.quascirev.2012.05.009, 2012.

E&G Quaternary Sci. J., 72, 163–184, 2023
https://doi.org/10.5194/egqsj-72-163-2023

Open Access E&G Quaternary Science Journal

Research article

What do dust sinks tell us about their sources and past environmental dynamics? A case study for oxygen isotope stages 3–2 in the Middle Rhine Valley, Germany

Mathias Vinnepand[1], **Peter Fischer**[1], **Ulrich Hambach**[2,3], **Olaf Jöris**[4], **Carol-Ann Craig**[5], **Christian Zeeden**[6], **Barry Thornton**[5], **Thomas Tütken**[7], **Charlotte Prud'homme**[8], **Philipp Schulte**[9], **Olivier Moine**[10], **Kathryn E. Fitzsimmons**[11], **Christian Laag**[12,13], **Frank Lehmkuhl**[9], **Wolfgang Schirmer**[14], **and Andreas Vött**[1]

[1]Natural Hazard Research and Geoarchaeology, Institute for Geography,
Johannes Gutenberg-Universität Mainz, 55099 Mainz, Germany
[2]BayCEER and Chair of Geomorphology, University of Bayreuth, 95440 Bayreuth, Germany
[3]Emil Racovita Institute of Speleology (ERIS), Romanian Academy, Cluj-Napoca branch,
Clinicilor 5, 400006 Cluj-Napoca, Romania
[4]MONREPOS Archaeological Research Centre and Museum for Human Behavioural Evolution,
Leibniz-Zentrum für Archäologie, 56567 Neuwied, Germany
[5]Environmental and Biogeochemical Sciences Group, The James Hutton Institute, Aberdeen, AB15 8QH, Scotland, UK
[6]Rock Physics and Borehole Geophysics, LIAG – Leibniz Institute for Applied Geophysics, 30655 Hanover, Germany
[7]Applied and Analytical Paleontology, Institute of Geosciences, Johannes
Gutenberg-Universität Mainz, 55099 Mainz, Germany
[8]Institute of Earth Surface Dynamics, University of Lausanne, 1015 Lausanne, Switzerland
[9]Chair in Physical Geography and Geoecology, Department of Geography, RWTH Aachen, 52056 Aachen, Germany
[10]Laboratoire de Géographie Physique, UMR 8591 CNRS Université Paris 1 UPEC, Thiais 94320, France
[11]Department of Geosciences, University of Tübingen, 72076 Tübingen, Germany
[12]Department of Research and Development, Nolte Geoservices GmbH, 48301 Nottuln, Germany
[13]Institut de Physique du Globe de Paris, CNRS, Université Paris Cité, 75238 Paris, France
[14]independent researcher: Wolkenstein 24, 91320 Wolkenstein, Germany

Correspondence: Mathias Vinnepand (mavinnep@uni-mainz.de) and Peter Fischer (p.fischer@geo.uni-mainz.de)

Relevant dates: Received: 24 May 2022 – Revised: 13 June 2023 – Accepted: 20 June 2023 –
Published: 4 August 2023

How to cite: Vinnepand, M., Fischer, P., Hambach, U., Jöris, O., Craig, C.-A., Zeeden, C., Thornton, B., Tütken, T., Prud'homme, C., Schulte, P., Moine, O., Fitzsimmons, K. E., Laag, C., Lehmkuhl, F., Schirmer, W., and Vött, A.: What do dust sinks tell us about their sources and past environmental dynamics? A case study for oxygen isotope stages 3–2 in the Middle Rhine Valley, Germany, E&G Quaternary Sci. J., 72, 163–184, https://doi.org/10.5194/egqsj-72-163-2023, 2023.

Abstract: The study of geological archives of dust is of great relevance as they are directly linked to past atmospheric circulation and bear the potential to reconstruct dust provenance and flux relative to climate changes. Among the dust sinks, loess–palaeosol sequences (LPSs) represent the only continental and non-aquatic archives that are predominantly built up by dust deposits close to source areas, providing detailed information on Quaternary climatic and terrestrial environmental changes. Upper Pleistocene LPSs of western central Europe have been investigated in great detail showing their linkage to millennial-scale northern hemispheric climate oscillations, but comprehensive data on dust composition and potential source–sink relationships as well as inferred past atmospheric circulation patterns for this region are still fragmentary.

Here, we present an integrative approach that systematically combines sedimentological, rock magnetic, and bulk geochemical data, as well as information on Sr and Nd isotope composition, enabling a synthetic interpretation of LPS formation. We focus on the Schwalbenberg RP1 profile in the Middle Rhine Valley in Germany and integrate our data into a robust age model that has recently been established based on high-resolution radiocarbon dating of earthworm calcite granules. We show that Schwalbenberg RP1 is subdivided into a lower section corresponding to late oxygen isotope stage 3 (OIS; $\sim$ 40–30 ka) and an upper section dating into the Last Glacial Maximum (LGM; $\sim$ 24–22 ka), separated by a major stratigraphic unconformity. Sedimentological proxies of wind dynamics (U ratio) and pedogenesis (finest clay) of the lower section attest to comparable and largely synchronous patterns of northern hemispheric climatic changes supporting the overall synchronicity of climatic changes in and around the North Atlantic region. The anisotropy of magnetic susceptibility (AMS) reveals a clear correlation between finer grain size and increasing AMS foliation within interstadials, possibly owing to continuous accumulation of dust during pedogenic phases. Such a clear negative correlation has so far not been described for any LPS on stadial–interstadial scales.

Distinct shifts in several proxy data supported by changes in isotope composition (^{87}Sr/^{86}Sr and εNd) within the lower section are interpreted as changes in provenance and decreasing weathering simultaneously with an overall cooling and aridification towards the end of OIS 3 (after $\sim$ 35 ka) and enhanced wind activity with significant input of coarse-grained material recycled from local sources related to increased landscape instability (after $\sim$ 31.5 ka). We find that environmental conditions within the upper section, most likely dominated by local to regional environmental signals, significantly differ from those in the lower section. In addition, AMS-based reconstructions of near-surface wind trends may indicate the influence of north-easterly winds beside the overall dominance of westerlies. The integrative approach contributes to a more comprehensive understanding of LPS formation including changes in dust composition and associated circulation patterns during Quaternary climate changes.

Kurzfassung:

Die Untersuchung geologischer Staubarchive ist von großer Bedeutung, da diese unmittelbar mit der atmosphärischen Zirkulation verknüpft sind und somit das Potenzial besitzen, sowohl Änderungen in der Staub-Herkunft als auch im Staubfluss in Verbindung mit Klimaänderungen zu rekonstruieren. Löss-Paläosol-Sequenzen (LPS) stellen in diesem Zusammenhang die einzigen kontinentalen nicht-aquatischen Archive dar, die sich aus Staubablagerungen bilden, die in relativer Nähe ihrer Liefergebiete liegen. Sie liefern zudem detaillierte Informationen über klimatische und terrestrische Umweltveränderungen im Quartär, die sich in Proxy-Daten der Staubzusammensetzung und der syn- und postsedimentären Veränderung widerspiegeln. Zwar belegen detaillierte Untersuchungen von LPS im westlichen Mitteleuropa direkte Verknüpfungen mit den jungpleistozänen Klimaschwankungen der nördlichen Hemisphäre, jedoch sind umfassende Daten zur Staubzusammensetzung und zur Kopplung von Staubquellen und -senken sowie zu den abgeleiteten atmosphärischen Zirkulationsmustern in der Region immer noch lückenhaft.

Unter Anwendung eines integrativen Ansatzes, der systematisch sedimentologische, gesteinsmagnetische und geochemische Daten kombiniert und durch Daten zur Isotopenzusammensetzung ergänzt wird, ist eine synthetische Interpretation der Bildung von LPS, hier am Beispiel des Profils RP1 am Schwalbenberg im Mittelrheintal, möglich. Wir verbinden unsere Daten mit einem detaillierten und robusten Altersmodell, das kürzlich auf der Grundlage hochauflösender Radiokohlenstoffdatierungen an Regenwurmkalziten (sog. Earthworm Calcite Granules, ECG) publiziert wurde. Auf Basis dieses Altersmodells kann gezeigt werden, dass das Profil RP1 in zwei Abschnitte, die durch eine deutliche Diskordanz getrennt sind, gegliedert wird. Der liegende Abschnitt entspricht dabei dem späten Sauerstoff-Isotopenstadium (OIS) 3 ($\sim$ 40–30 ka), während der hangende Abschnitt in das Letztglaziale Maximum (LGM) datiert ($\sim$ 24–22 ka). Für den liegenden Abschnitt zeigen die sedimentologischen Proxy-Daten (U Ratio, feinster Ton) vergleichbare und weitgehend synchrone Muster zwischen dem Schwalbenberg und Daten aus grönländischen Eisbohrkernen (NGRIP) und unterstützten somit die Annahme einer Synchronität von Klimaänderungen in und um den Nordatlantik.

Die Anisotropie der Magnetischen Suszeptibilität (AMS) zeigt in Interstadialen eine klare Korrelation kleinerer Korngrößen mit zunehmender AMS-Foliation, die möglicherweise auf kontinuierliche Staubakkumulation während der Pedogenese zurückzuführen ist. Ein solch klarer Zusammenhang wurde für LPS mit stadial–interstadialer Auflösung bisher nicht beschrieben.

Im liegenden Abschnitt von Profil RP1 am Schwalbenberg wird eine Abkühlung und Aridifizierung im späten OIS 3 (nach ∼ 35 ka) durch signifikante Änderungen in verschiedenen Proxy-Daten und der Isotopenzusammensetzung (^{87}Sr/^{86}Sr und εNd) deutlich, die auf unterschiedliche Staubquellen und abnehmende Verwitterung hindeuten. Zusätzlich führt eine erhöhte Instabilität der Landschaft in Richtung des LGM (nach ∼ 31,5 ka) zu verstärkter Windaktivität und dem Eintrag grobkörnigen Materials, das aus lokalen Quellen recycelt wurde.

Die Proxy-Daten des hangenden Abschnitts deuten auf Umweltbedingungen hin, die sich signifikant von jenen des Liegenden unterscheiden und vermutlich durch lokale bis regionale Einflüsse dominiert werden. AMS-basierte Rekonstruktionen der oberflächennahen Windtrends lassen neben der Dominanz von Westwinden auf einen phasenweisen Einfluss von Winden aus nordöstlicher Richtung schließen. Insgesamt sehen wir den vorgestellten integrativen Ansatz als einen wichtigen Beitrag zum besseren Verständnis der Bildung von LPS, welche die Veränderungen der Staubzusammensetzung und damit verbundener Zirkulationsmuster im Zuge quartärer Klimaänderungen besser beleuchtet.

1 Introduction

The production of mineral dust, its aeolian transport, and its deposition are important processes of the Earth–atmosphere system affecting the global radiative balance, changing the hydroclimate, and providing nutrients to both terrestrial and marine ecosystems (Muhs, 2013; Knippertz and Stuut, 2014; Marx et al., 2018). In order to understand potential links between dust flux and climate changes during the Quaternary, the study of geological archives of dust is of great relevance, as these are directly linked to past atmospheric circulation (Schaffernicht et al., 2020). As such they bear the potential to reconstruct dust provenance and dust flux relative to Quaternary climate changes whose proxies are frequently recorded in some of these archives (e.g. Mahowald et al., 2006; Újvári et al., 2016).

While ice, marine, and lake records are prominent Quaternary palaeoenvironmental and palaeoclimatic archives also tracing variations in atmospheric dustiness (e.g. Rasmussen et al., 2014; Sirocko et al., 2016; Kämpf et al., 2022), loess–palaeosol sequences (LPSs) represent the only continental and non-aquatic archive that is predominantly built up by dust deposits close to source areas (Muhs, 2013). They are thus providing detailed information on terrestrial palaeoenvironmental and palaeoclimatic change including dust composition and post-sedimentary alteration (e.g. Újvári et al., 2012; Schaetzl et al., 2018).

In western and central Europe, enhanced dust deposition during Upper Pleistocene stadial periods has been largely ascribed to increased fine particle production through glacial grinding activity, frost shattering, and entrainment of silty material from alluvial plains; glacial outwash plains; endorheic basins; and exposed continental shelves (Frechen et al., 2003; Antoine et al., 2009; Smalley et al., 2009; Lehmkuhl et al., 2021; Pötter et al., 2021). In combination with gustier winds related to steepened meridional temperature gradients during stadial periods (McGee et al., 2010), the increased dustiness is reflected in peak dust accumulation especially during oxygen isotope stage (OIS) 2 along the western European loess belt (e.g. Frechen et al., 2003; Újvári et al., 2017; Fischer et al., 2021; Schmidt et al., 2021). This pattern is also observed in regional aquatic archives, such as maar lakes (e.g. Seelos et al., 2009; Fuhrmann et al., 2021) and supra-regional archives, such as Greenland ice cores (e.g. Rasmussen et al., 2014; Újvári et al., 2022).

In recent times, Upper Pleistocene key LPSs in western Europe have been investigated in great detail showing their linkage to northern hemispheric glacial–interglacial and millennial-timescale climate oscillations (e.g. Rousseau et al., 2007; Moine et al., 2017; Fischer et al., 2021; Prud'homme et al., 2022), but comprehensive data on dust composition and potential source–sink relationships as well as inferred palaeo-wind directions for this region are still scarce (e.g. Taylor et al., 2014; Schatz et al., 2015).

With this study we aim to contribute to a better understanding of dust provenance and past environmental dynamics using different methodological tools to investigate dust composition and to discuss potential source–sink relationships during late OIS 3 (∼ 40–30 ka) and parts of OIS 2 (∼ 24–22 ka) in western central Europe. Over the last few years, we were able to show that the Schwalbenberg LPSs in the Middle Rhine Valley in Germany resolve the last glacial cycle in exceptional temporal detail (Fischer et al., 2021; Vinnepand et al., 2022), proving previous studies that suggested a linkage with the last glacial millennial-scale climate oscillations recorded in Greenland ice cores (Schirmer, 2000, 2011). Here, we focus on the 5.6 m deep section RP1, exposed at the southern edge of the Schwalbenberg. The RP1 profile was studied in detail by Fischer et al. (2021). Beside quantitative climate reconstructions based on the study of oxygen and carbon isotopes of earthworm calcite granules (ECGs), Bayesian age modelling based on radiocarbon dating of ECGs was used to establish a robust and reliable age model of the Schwalbenberg RP1 LPS (Prud'homme et al., 2022). Here, we use high-resolution sedimentological, rock magnetic, and bulk geochemical data to characterize dust composition along the stratigraphy. In addition, isotope geochemical measurements (^{143}Nd/^{144}Nd and ^{87}Sr/^{86}Sr) were conducted at lower resolution.

The *U* ratio, defined as the ratio of coarse versus medium plus fine silt, is employed to reconstruct wind dynamics and potential processes of sediment reworking (Vandenberghe et al., 1985; Vandenberghe, 2013). In addition, the finest clay content mostly reflects pedogenically formed clay (Schulte and Lehmkuhl, 2018) but potentially also dust components that have travelled longer distances (e.g. Muhs, 2013).

Beside such sedimentological data, the magnetic susceptibility evolved to an essential stratigraphic tool in the investigation of LPSs. As shown for many sites in Eurasia, magnetic susceptibility increases in palaeosols (magnetic enhancement), while relatively unaltered loess shows lower values. In contrast, lower magnetic susceptibility in palaeosols compared to loess is explained by the wind-vigour model (e.g. Evans and Heller, 2001); by waterlogging causing dissolution of iron minerals, which is mainly observed in loess affected by periglacial conditions (e.g. Taylor et al., 2014; Fischer et al., 2019); or by high amounts of primary magnetically enhanced sediments and their weathering products (von Suchodoletz et al., 2009; Obreht et al., 2016). In addition to low field bulk magnetic susceptibility (hereafter MS) the frequency-dependent magnetic susceptibility (hereafter MS_{fd}) is a qualitative parameter that allows us to determine the relative amount of newly formed ultrafine magnetic particles in the course of (incipient) pedogenesis (e.g. Buggle et al., 2014; Bradák et al., 2021). In the context of the reconstruction of past circulation patterns, the anisotropy of magnetic susceptibility (AMS) can additionally be utilized, which potentially reflects near-surface wind directions, if the primary magnetic fabric is preserved (Hrouda, 2007; Zhang et al., 2010; Taylor and Lagroix, 2015; Zeeden and Hambach, 2021).

In addition to these physical parameters, the bulk element composition is frequently employed to identify potential provenance shifts and sediment recycling as well as weathering intensity (cf. Buggle et al., 2011; Klasen et al., 2015; Profe et al., 2016; Vinnepand et al., 2022). In combination with Sr and Nd isotope geochemistry, which is a common tool in provenance studies (Grousset and Biscaye, 1989, 2005), potential changes in dust sources as well as secondary alteration of isotope signals may be detected in LPSs. While ^{143}Nd/^{144}Nd is a well-established provenance proxy that is strongly resistant to surface processes (e.g. weathering) (Goldstein and Jacobsen, 1988; Meyer et al., 2009; Grousset and Biscaye, 2005), ^{87}Sr/^{86}Sr might be prone to grain size effects (Feng et al., 2009) and to alteration through weathering (e.g. Clauer and Chaudhuri, 1995), potentially limiting a straightforward interpretation in terms of changing dust sources.

The systematic combination of these physical and geochemical proxy data opens the perspective for a comprehensive interpretation of LPS formation in the Middle Rhine Valley in Germany. Employing such an integrative approach, we aim to detect significant shifts in dust composition and discuss potential causes against the background of palaeoenvironmental and palaeoclimatic oscillations during the time period investigated.

2 Regional setting and stratigraphy

The Schwalbenberg site in the Middle Rhine Valley is located in the centre of the Rhenish Massif (Germany; 50.562378° N, 7.240425° E; ∼90–135 m a.s.l. – above sea level; Fig. 1). Up to 30 m thick Upper Pleistocene LPSs drape the lower middle terrace 1 (LMT 1) of the penultimate glaciation (cf. Boenigk and Frechen, 2006) and at least two further, older terrace levels of the Rhine, overall resolving Atlantic-driven Upper Pleistocene climate oscillations in more detail than any other terrestrial archive in the region described so far (Fischer et al., 2021). Nowadays, the area is characterized rather by a maritime climate influence (mean annual temperature: 10.2 °C; mean annual precipitation: 643 mm; Deutscher Wetterdienst, 2023), with low-air-pressure systems predominantly entering the area from the Atlantic to the west (Prud'homme et al., 2022).

During the Upper Pleistocene the site was situated between the glaciated Alps in the south; the Fennoscandian (FIS) and British–Irish ice sheets (BIIS) in the north, which reached their maximum extents during the Last Glacial Maximum (LGM) (e.g. Lambeck et al., 2014); and the – at this time – dried out plains of the English Channel westward and north-westward (Fig. 1), all of which are considered important dust-producing and dust source areas for LPSs in western and central European periglacial realms (Antoine et al., 2009; Lehmkuhl et al., 2021; Baykal et al., 2022). In addition, the alluvial plains of – over long periods – braided river systems, here the Rhine and its tributaries, are assumed to represent major regional dust sources during stadial phases (e.g. Schatz et al., 2015; Rousseau et al., 2018).

Furthermore, the Rhenish Massif itself experienced intensive frost-weathering in the most severe cold periods of the Pleistocene and intensive sediment relocation under cold and humid conditions, forming Pleistocene periglacial slope deposits (PPSDs) (Sauer and Felix-Henningsen, 2006), rep-

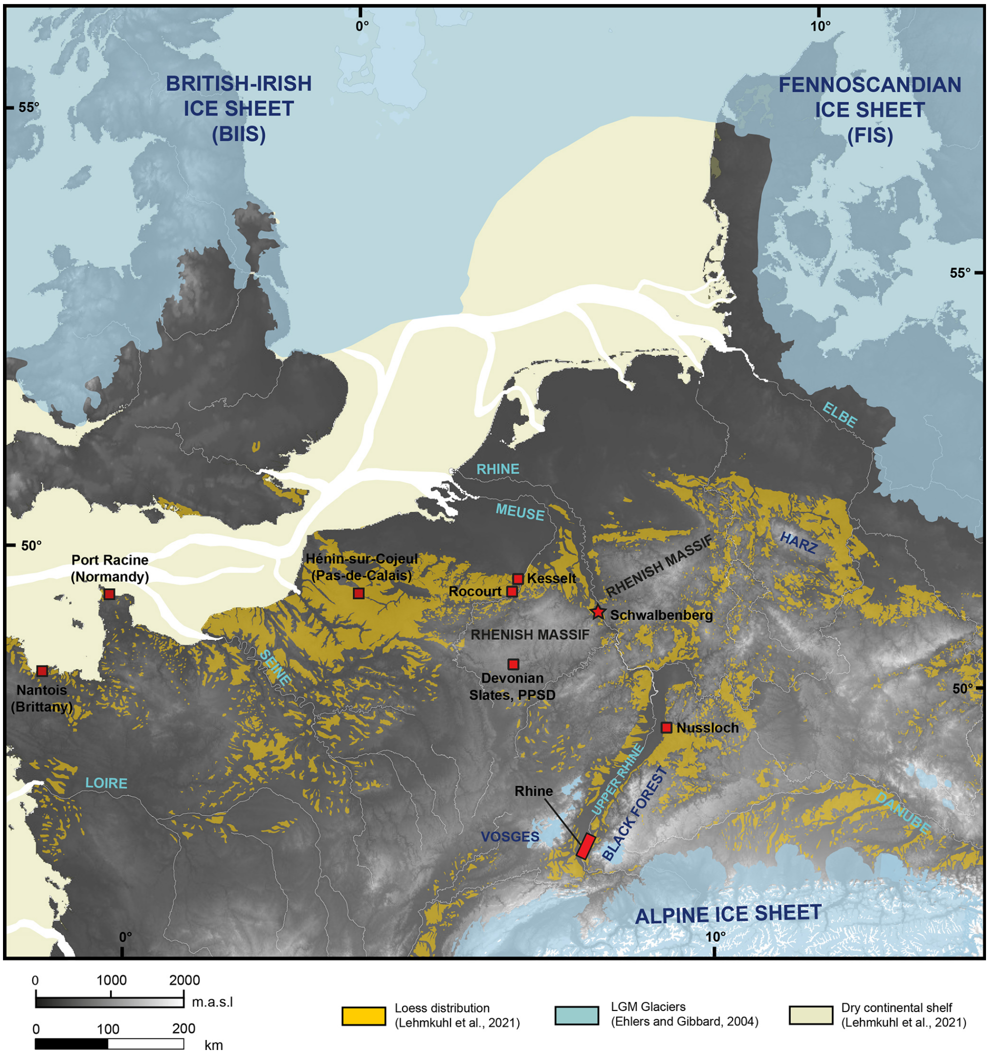

Figure 1. Map based on the digital elevation model (GLOBE 1.0) showing western central Europe during the Last Glacial Maximum (LGM, centred at ∼ 22 ka); the location of the Schwalbenberg site in the Middle Rhine Valley, Germany; and selected key sites (see text for explanation). The Schwalbenberg site is located between the Alpine ice sheet in the south and the Fennoscandian and British–Irish ice sheets in the north.

resenting potential subordinated local dust sources (Janus, 1988; Römer et al., 2016).

During the Upper Pleistocene, the Schwalbenberg site was located close to the alluvial plains of the braided systems of the rivers Ahr and Rhine, reflecting possible sources of mineral dust of local to regional origin. The comparably small Ahr River catchment (6.63 $\mathrm{m^3\,s^{-1}}$ mean annual discharge; Ministry for Environment RLP, 2021) is located in the northern parts of the Eifel area where Devonian rocks (mostly schistose clayey silt- and sandstones and subordinated limestones) are predominant (Meschede, 2018; Fig. 2). In contrast, the Rhine catchment until the mouth of the Ahr (2010 $\mathrm{m^3\,s^{-1}}$ mean annual discharge ∼ 20 km south of Schwalbenberg; International commission for the hydrology of the Rhine basin, 2021) includes the north-western Alps and the Upper Rhine Graben (with small tributaries draining parts of the Vosges, Black Forest, and Odenwald), as well as its main tributaries with the rivers Neckar (draining parts of the Swabian Alb, Triassic Keuperbergland (Keuper Uplands), Black Forest, and Odenwald), Main (draining the Fichtel Mountains, Franconian Alb, and several other Franconian uplands), Lahn (draining the Rhenish Massif), Nahe (draining predominantly the Saar–Nahe basin), and Mosel (draining parts of the Vosges, the easternmost Paris Basin, and the Rhenish Massif) (Meyer and Stets, 1996; Fig. 2).

In this study, we focus on the 5.60 m thick RP1 profile located at the southern fringe of the Schwalbenberg facing the Ahr valley (Figs. 3, 4). The profile was described and subdivided into 21 stratigraphic units (SUs), correlated to superordinate stratigraphic units (SSUs) D, E, and F within the gen-

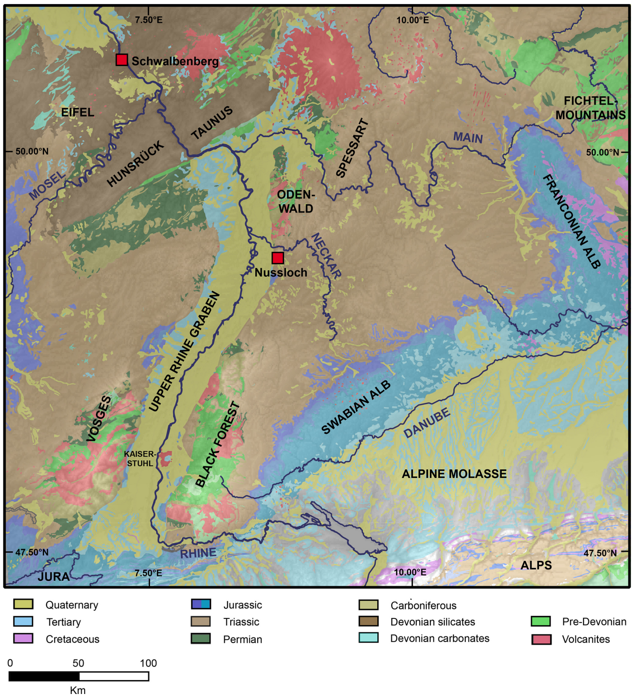

Figure 2. Geological map showing the main geological units of the Rhine catchment up to the Lower Rhine Embayment (Federal Institute for Geosciences and Natural Resources Germany, 2022). Calcareous rocks and sediments dominate the Rhine catchment in the northern Alps and the Molasse basin. The flanks of the Upper Rhine Graben include volcanites and metamorphic pre-Devonian rocks as well as Triassic siliciclastics and carbonates. The Rhenish Massif is dominated by Devonian slates and sandstones, and subordinated Devonian limestones occur.

eral Schwalbenberg stratigraphic model (Fischer et al., 2021; see Table 1). The SSUs were defined by lithology and by the classification of palaeosols according to the IUSS Working Group WRB (Schad et al., 2015).

High-resolution radiocarbon dating on ECGs confirm that the lower section of the sequence covers late OIS 3, which is characterized by the formation of Calcaric Cambisols at Schwalbenberg correlated to Greenland Interstadials (GIs) 8–6 (cf. Fischer et al., 2021; Prud'homme et al., 2022). The Calcaric Cambisols of SUs 2–6 build a soil complex, whilst the uppermost Calcaric Cambisol (SU 8), correlated to GI 6, is clearly separated from the previous one by a loess layer (SU 7).

Based on the RP1 age model (Prud'homme et al., 2022), the Gelic Gleysol of SU 11 covers the transition from GI 5.2 to Greenland Stadial (GS) 5.2. A formation during milder climate conditions during GI 5.2 is likely. The next loess layer of SU 12 is truncated due to erosion prior to accumulation of the upper section represented by SSU F.

SSU F above the unconformity (base of SU 13) contains reworked loess, loess, and weakly developed Gelic Gleysols correlated to OIS 2 between ∼ 24 000 and 21 900 cal BP (see Sect. 3.5).

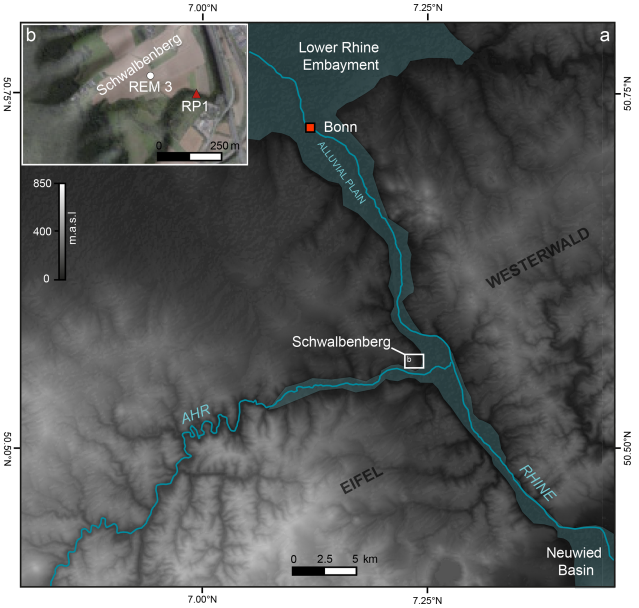

Figure 3. **(a)** Map of the Lower Middle Rhine Valley in western central Germany based on the digital elevation model (DEM based on SRTM 30 data by USGS (2022). The Schwalbenberg site is located north-west of the confluence of the Rhine and the Ahr. These river systems are the most important source areas of mineral dust. **(b)** The inset map (BingMaps, 2021) shows the position of the REM 3 key LPSs and the RP1 section (cf. Fischer et al., 2021; Prud'homme et al., 2022).

3 Materials and methods

Continuous sampling in 2 cm intervals was performed for grain size, bulk geochemical, and rock magnetic analyses including the determination of the anisotropy of magnetic susceptibility (AMS). However, the latter was conducted for every second sample (see Sect. 3.3). In addition, we collected 30 samples with 5 cm sampling width for Sr and Nd isotope analyses according to stratigraphy (see Fig. 4 for sample distribution, sampling intervals are given in Table S2).

3.1 Laser granulometry

We analysed the grain size of samples from the Schwalbenberg RP1 profile to calculate the *U* ratio and finest clay proportion. The *U* ratio is defined as the ratio of coarse versus medium and fine silt (Vandenberghe et al., 1985; Újvári et al., 2016) and is used to discriminate between sediments that were transported by dynamic and relatively strong winds (high *U* ratio) and those transported by weaker winds (low *U* ratio) (Vandenberghe et al., 1997). The finest clay proportion (fCl $< 0.2\,\mu$m) mainly reflects post-depositional

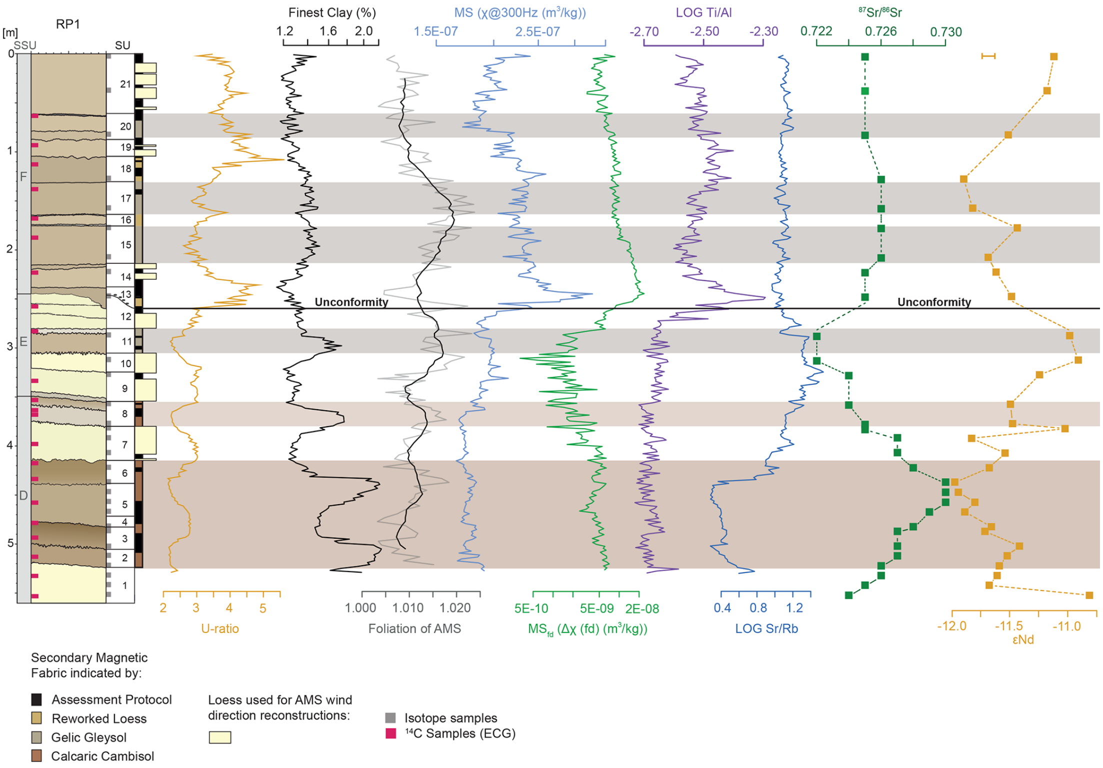

Figure 4. From left to right: stratigraphic log of profile RP1 and positions of ECG samples used for radiocarbon dating (modified after Prud'homme et al., 2022; radiocarbon ages are given in Table 1). SSUs and SUs are given according to Fischer et al. (2021); log depicting secondary magnetic fabric and loess layers used for AMS-based reconstruction of near-surface wind directions following the statistical assessment (see Supplement for details); grain size data: U ratio and finest clay; magnetic fabric and environmental magnetism: foliation of the AMS, MS (χ @300 Hz), and $\mathrm{MS_{fd}}$ ($\Delta\chi$(fd)); geochemical data: log Ti/Al and log Sr/Rb; isotope geochemistry: $^{87}\mathrm{Sr}/^{86}\mathrm{Sr}$ and εNd. Sr and Nd isotope sampling positions are indicated by grey squares next to the stratigraphic log of SUs, and 2σ for internal basalt standard measurements (reproducibility) is below the size of the sample symbols for $^{87}\mathrm{Sr}/^{86}\mathrm{Sr}$ but exceeds these for εNd (see scale in the data plot). For the calculation, statistics and uncertainty of AMS data, and details on sample reproducibility of isotope measurements, we refer the reader to the Supplement.

grain size reduction by chemical weathering (Schulte and Lehmkuhl, 2018).

We undertook granulometry using a laser diffraction particle size analyser (LS 13 320 PIDS, Beckman Coulter) to analyse non-decalcified samples (cf. Schulte et al., 2016). Sample pre-treatment involved removal of organic carbon by 0.70 mL 20 % H_2O_2 and dispersion with 25 mL of $Na_4P_2O_7$ at 0.1 mol L^{-1} for 12 h (Jones, 2003; Blott et al., 2004). Quadrupole measurements using two different concentrations ensured high precision. Through data processing, we applied the Mie theory (fluid RI: 1.33; sample RI: 1.55; imaginary RI: 0.1; Jones, 2003; Ozer et al., 2010).

3.2 Bulk geochemistry

We integrated the Ti/Al ratio as a provenance indicator, as both elements are relatively immobile and their ratio is not significantly affected by weathering or pedogenesis (e.g. Zech et al., 2008; Sheldon and Tabor, 2009). In addition, we complementarily use the Sr/Rb ratio as an indicator of weathering intensity based on the assumption that Sr shows an analogous behaviour to Ca being easily soluble and mobile in the course of weathering, while Rb behaves relatively immobile under moderate weathering conditions due to strong adsorption to clay minerals (e.g. Buggle et al., 2011). We are aware of the fact that the initial Sr/Rb ratio is maybe partly masked by the dynamics of carbonate-bound Sr in the course of secondary carbonate precipitation (e.g. Buggle et al., 2011; Profe et al., 2016), the latter effect being detailed by Vinnepand et al. (2020) for the Schwalbenberg LPS.

We determined element composition with a polarization energy dispersive X-ray fluorescence (EDP-XRF) spectrometer (Spectro Xepos, Spectro) onto pressed sample pellets (bulk sediments < 2 mm) (see Vinnepand et al., 2022). Measurements were performed in duplicates to ensure data quality (measurements were excluded in the case when duplicates exceeded 3σ). We used the decadic logarithm (log ratios) of element ratios for data symmetry and to overcome the closed sum constraint (Weltje et al., 2015; Profe et al., 2016). For

Table 1. Subdivision of the RP1 profile into superordinate stratigraphic units (SSUs) F, E, and D (lower (older) SSUs are not exposed at RP1) and stratigraphic units (SUs) and their corresponding lithological and pedological interpretation (see Fischer et al., 2021, for further details). The ages were published by Prud'homme et al. (2022) based on radiocarbon dating applied to 22 ECG samples, and the calibration was based on IntCal20 (Reimer et al., 2020). The Greenland events are shown according to the INTIMATE event stratigraphy (Rasmussen et al., 2014). The radiocarbon ages have been integrated into Bayesian age modelling (Prud'homme et al., 2022) using the Bacon software (Blaauw and Christeny, 2011). The age model is integrated into Fig. 6 in the Discussion section.

Profile RP1	SSU	SU	Lithology/pedology	Age (cal BP) min–max (2σ)	Greenland events
Upper section	F	21	Loess	–	
	F	20	Gelic Gleysol	21 426–22 150	GS 2.1a
	F	19	Loess	22 327–22 500	GS 2.1a
	F	18	Reworked loess	22 424–22 652	GS 2.1a
	F	17	Gelic Gleysol	22 557–22 846	GS 2.1a
	F	16	Reworked loess	22 793–23 073	GS 2.1a
	F	15	Gelic Gleysol	23 079–23 663	GI 2.2
	F	14	Loess	23 863–24 619	GS 3
Unconformity (base of SU 13)	F	13	Reworked loess	–	–
Lower section	E	12	Loess	30 199–30 970	GS 5.2/GI 5.1
	E	11	Gelic Gleysol	31 128–32 018	GI 5.2/GS 5.2
	E	10	Loess	–	GI 5.2/GS 5.2
	E	9	Loess (partly laminated)	31 862–33 931	GS 6/GI 5.2
	E	9	Loess (partly laminated)	32 562–33 412	GI 6/GS 6
	E	9	Loess (partly laminated)	32 922–33 614	GI 6/GS 6
	D	8	Calcaric Cambisol	33 077–33 703	GI 6
	D	7	Loess	33 728–34 310	GS 7
		6		34 749–34 153	GI 7/GS 7
	D	6	Soil complex (Calcaric Cambisols, SU 2–6)	35 134–34 453	GI 7/GS 7
	D	5		34 879–35 675	GI 7
	D	4		35 298–36 380	GS 8
	D	3		36 406–37 473	GI 8
	D	2		36 826–38 129	GI 8
	D	1	Loess	37 374–38 873	GS 9
	D	1	Loess	38 162–39 963	GS 9

integrating the element concentrations of Sr and Nd in the context of mixing equations (cf. Faure and Mensing, 2005), we applied XRF measurements to the same samples used for isotopic measurements (see Sect. 3.4).

3.3 Magnetic susceptibility and anisotropy of magnetic susceptibility

Since the 1980s environmental magnetic parameters have been recognized as fundamental palaeoclimate proxies for Eurasian LPSs, and low field magnetic susceptibility (MS) was established as a stratigraphic tool, facilitating correlations between terrestrial deposits and the marine record. The latter is based on stratigraphic oxygen isotope data for oceanic foraminifera, which in turn is a proxy for global ice volume (e.g. Evans and Heller, 2003; Liu et al., 2012). The frequency dependency of magnetic susceptibility ($\mathrm{MS}_{\mathrm{fd}}$), also expressed as the absolute difference of χ @300 Hz and χ @3000 (Hz χ @300 Hz–χ @3000 Hz $= \Delta\chi$), provides information on magnetic grain size spectra and may allow for the assignment of magnetic enhancement to soil formation processes to wind vigour effects and depletion due to hydromorphy in comparison to the low field MS (Forster et al., 1994; Bradák et al., 2021).

Furthermore, MS in LPS deposits has one additional application. Directional measurements of MS on oriented samples are used for fabric analyses. The AMS (anisotropy of magnetic susceptibility) method is an established structural indicator even in unconsolidated geological materials (Bradák et al., 2020). Magnetic fabric can be correctly approximated by a second-order symmetric tensor and fabric magnitude (i.e. degree of anisotropy) and fabric shape (i.e. prolate or oblate). Additionally, the orientation of principal axes of AMS ellipsoids (K_{MAX}, K_{INT}, K_{MIN}) can be used for fabric characterization and quantification (Hrouda, 2007).

In order to study the natural physical properties of the undisturbed sedimentological fabric, we collected oriented samples (cube edge lengths 2 cm, hence 8 cm^3 sample volume) exhibiting a ∼ 2.1 cm vertical spacing of their centres (Zeeden et al., 2015; Zeeden and Hambach, 2021). The volume MS was measured using a susceptibility bridge (VFSM; Magnon, Germany) at AC fields of 300 A m^{-1} at 300 and 3000 Hz, respectively. Subsequently, the resulting values were mass normalized and given as mass-specific MS (χ) (cf. Buggle et al., 2014; Zeeden et al., 2018). Every second sample (∼ 4.2 cm stratigraphic resolution) was subject to AMS measurements using a MFK1-FA kappabridge (AGICO) in a 400 A m^{-1} and 976 Hz alternating field and a rotator. We visualized the results of AMS measurements as a magnetic susceptibility ellipsoid with three orthogonal principal axes: the maximum axis (K_{MAX}), the intermediate axis (K_{INT}), and the minimal axis (K_{MIN}) by using the Anisoft v. 5.0.18 software supplied by AGICO. The magnetic susceptibility ellipsoid defines the overall magnetic fabric of a rock sample, reflecting the statistically preferred orientation of mineral grains. In this study, we employed the most common anisotropy parameters that are used to investigate the nature of magnetic fabrics in LPS, i.e. lineation (L) and foliation (F) describing the shaped and oblateness of an AMS ellipsoid, respectively. The data are presented in rose diagrams of K_{MAX} and stereoplots displaying the full spatial orientation of K_{MAX}, K_{INT}, and K_{MIN}. The applied assessment protocol (see Fig. 4) and associated statistical analyses are detailed in the Supplement.

3.4 Strontium and neodymium isotope geochemistry

The original Sr and Nd isotope compositions of igneous rocks represent fingerprints for their petrogenesis (e.g. preferential partitioning of incompatible Nd and Rb into the melt and compatible Sm and Sr into the solid residue during magmatic differentiation) and age (radioactive decay of ^{87}Rb to ^{87}Sr and ^{147}Sm to ^{143}Nd) (DePaolo and Wasserburg, 1976; Goldstein et al., 1984; Grousset and Biscaye, 1989). This leads to characteristic $^{143}\mathrm{Nd}/^{144}\mathrm{Nd}$ (εNd) and $^{87}\mathrm{Sr}/^{86}\mathrm{Sr}$ isotope signatures in crustal and mantle rocks, with felsic rocks having high $^{87}\mathrm{Sr}/^{86}\mathrm{Sr}$ and low $^{143}\mathrm{Nd}/^{144}\mathrm{Nd}$ (εNd) and the inverse for mafic (mantle-derived) rocks (εNd represents the original measured $^{143}\mathrm{Nd}/^{144}\mathrm{Nd}$ normalized to the chondritic uniform reservoir 0.512638 (CHUR, $t = 0$) (Faure and Mensing, 2005) following the equation

$$\varepsilon\mathrm{Nd} = \left(^{144/143\mathrm{Nd}}\mathrm{sample}/^{144/143\mathrm{Nd}}\mathrm{CHUR} - 1\right) \times 10\,000. \quad (1)$$

Older rocks of similar mineralogical composition have more radiogenic $^{87}\mathrm{Sr}/^{86}\mathrm{Sr}$ and εNd due to prolonged radioactive decay. Sediments forming through physical weathering of crustal rocks inherit the isotope composition of their bedrock (Goldstein and Jacobsen, 1988, 1987). The Sr isotope composition in a dust sink may differ from the source due to mineral sorting e.g. during (aeolian) transport (Újvári et al., 2012), and selective depletion of Sr-bearing minerals during chemical weathering (e.g. Drouet et al., 2007). Hence, more soluble Sr-rich minerals such as carbonates may change the original $^{87}\mathrm{Sr}/^{86}\mathrm{Sr}$ bulk sediment composition. In contrast, εNd is strongly resistant to surface weathering and grain size sorting effects (Meyer et al., 2009; Újvári et al., 2012; Wang et al., 2007; Zhu et al., 2021), still reflecting the original or rather unchanged source rock composition. Prior to sample digestion, we dissolved pedogenic calcites while preserving clay minerals (0.5 M acetic acid) (Újvári et al., 2012). For sample digestion, we used 6 mL of 48 % HF (AR grade) and 1 mL of trace grade 68 % $\mathrm{HNO_3}$ and heated the mixture at 150 °C in Teflon bombs. Purified Sr and Nd fractions were used to determine $^{143}\mathrm{Nd}/^{144}\mathrm{Nd}$ and $^{87}\mathrm{Sr}/^{86}\mathrm{Sr}$ using an Isotopix Phoenix TIMS (thermal ionization mass spectrometer) device through multi-dynamic analyses. For quality control, we ran the NIST SRM 987 reference material ($^{87}\mathrm{Sr}/^{86}\mathrm{Sr} = 0.710255 \pm 0.000013$ at 2σ, $n = 5$) for Sr and the JNdi-1 reference material ($^{143}\mathrm{Nd}/^{144}\mathrm{Nd} = 0.512103 \pm 0.000004$ at 2σ, $n = 7$) for Nd. The average standard error for 100 ratios of data for each of the samples is 0.000011 for $^{87}\mathrm{Sr}//^{86}\mathrm{Sr}$ and 0.000002 ± 2 SE for $^{143}\mathrm{Nd}/^{144}\mathrm{Nd}$ (for more information on sample preparation, purification, and quality control, please see Supplement).

3.5 Age modelling

Prud'homme et al. (2022) constrained the time span of a distinct unconformity at the base of SU 13 as a ∼ 5–6 kyr hiatus spanning 30 970–30 199 to 24 619–23 863 cal BP, based on the closest radiocarbon ages below and above the unconformity, respectively (see Table 1). Quantitative climate reconstructions and the age model presented in Prud'homme et al. (2022) were related to the stratigraphical positions of the ECG samples chosen for either stable isotope analyses or radiocarbon dating, whereof no samples were taken from SU 13 and the lower part of SU 14 (both SUs located above the unconformity). Here, we performed continuous sampling in 2 cm intervals for grain size, bulk geochemical, and rock magnetic analyses. Thus, we produced a continuous analytical data set along a discontinuous age model. To account for this, we also integrated the stratigraphic information as described by Fischer et al. (2021). Based on their litho- and pedostratigraphic model, the erosional phase causing the hiatus in section RP1 must have taken place with or shortly after the deposition of the Eltville tephra. This tephra, whose average age is around 24.3 ka (Zens et al., 2017; Förster et al., 2020), is an important stratigraphic marker found in many western European LPSs (e.g. Meijs et al., 1983). We then re-calculated the age model with 2 cm intervals using the Bacon software (Blaauw and Christeny, 2011) and the IntCal20 calibration curve (Reimer et al., 2020). For the profile section from 260 cm (base of SU 13 = unconformity) to 222 cm below surface (position of the first radiocarbon sample above the unconformity), we assume a continuous age decrease with depth, ranging from 24 300 to 23 945 cal BP.

With regard to our interpretation of the proxy data plotted against the age model (Fig. 6), we are aware that age uncer-

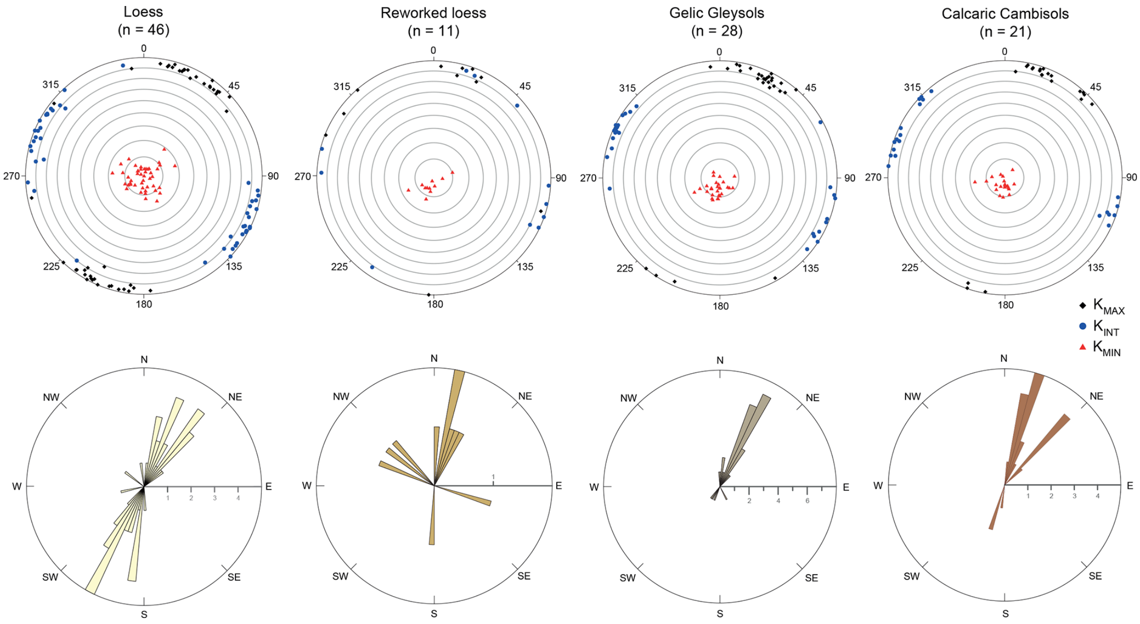

Figure 5. Stereoplots showing the full spatial orientation of K_{MAX}, K_{INT}, and K_{MIN} and rose diagrams of the lineations for all samples that passed the criteria as outlined (Fig. 4 and Sect. S1 in the Supplement) and the subsets for loess, reworked loess, Gelic Gleysols, and Calcaric Cambisols. See Figs. S1 and S2 for a comparison of all samples for each sediment type.

tainties occur both in the radiocarbon-based age model and in the INTIMATE (INTegration of Ice-core, MArine and TErrestrial records) event stratigraphy. In the latter, for instance, the maximal counting error for GI 5.2 is 1024 years (Rasmussen et al., 2014) and thus in a similar range as the errors in the underlying Bacon age model.

4 Results

4.1 Down-profile variation in selected proxy data

A clear subdivision of the RP1 profile is visible in all selected proxies. Based on significant sedimentological changes in the stratigraphical succession, a lower section (SUs 1–12) reaching to the unconformity and an upper section above the unconformity (SUs 13–21) are distinguished (Fig. 4). The *U* ratio shows maxima in the loess layers (SUs 7, 9, 10, 12) and in the middle of the basal soil complex (SUs 1–6), while the finest clay shows an inverse behaviour with distinct maxima in all well-developed palaeosols. Above the unconformity, the variations in clay content are significantly lower, showing a minimum at the transition from SU 13 to 14 and weak maxima in the Gelic Gleysols of SUs 15 and 17. In contrast, the *U* ratio shows higher and significant variations with absolute maxima in SUs 13 and 18 and weak minima in the Gelic Gleysols (SUs 15 and 17). Throughout the profile and especially below the unconformity, minima in the *U* ratio and maxima in the finest clay correspond to increased foliation values.

The MS shows low variations in the entire lower part, with a slight decrease from the base to the midst of SU 8, followed by slight increases towards the midst of SU 11 from where it slightly decreases again. Obviously, palaeosols and loess layers are not clearly differentiated. The $\mathrm{MS_{fd}}$ shows an overall decrease from the base to SU 11, with increased amplitudes above SU 6 and an inverse trend compared to the MS from the top of SU 8 to SU 11. In the top part of SU 11, the values significantly increase towards the unconformity. In SU 13 both MS and $\mathrm{MS_{fd}}$ reach maximum values, whereof the MS forms a distinct peak. Above, the MS shows minima in SUs 15, 17, and 20, where intensive hydromorphic staining has been observed. Another maximum is observed at the base of the reworked loess of SU 18, while the $\mathrm{MS_{fd}}$ is continuously decreasing towards the top of the sequence. Log Ti/Al shows minor variations throughout the lower section, with slightly increasing values on top of the Calcaric Cambisol of SU 8. As described for the MS and $\mathrm{MS_{fd}}$, also log Ti/Al increases towards the unconformity and above, again forming a distinct maximum in SU 13. Generally lowered values are observed until the top of SU 17 and above SU 19, with higher values in between. Log Sr/Rb shows the lowest values in the well-developed palaeosols of the basal soil complex. From the top of SU 5 the values increase, before they newly decrease from the top of SU 11 towards the unconformity. Remarkably, the MS and log Sr/Rb show a high correlation from SU 7 to SU 11. Above the unconformity, log Sr/Rb shows no significant variations. Both the $^{87}\mathrm{Sr}/^{86}\mathrm{Sr}$ ratio and εNd cover a relative restricted range from 0.722 to 0.730 and from −10.77 to −11.98, respectively. The ^{87}Sr/^{86}Sr ratio increases from the base until SU 6. In contrast, apart from the lowermost sample εNd follows this trend until SU 3 but turns into the opposite trend thereafter, reaching the absolute minimum at the base of SU 6, accompanied by the absolute maximum of ^{87}Sr/^{86}Sr. Towards the unconformity, both ^{87}Sr/^{86}Sr and εNd show an inverse behaviour with decreasing ^{87}Sr/^{86}Sr and increasing εNd values. Above the unconformity, throughout the upper section only minor variations in ^{87}Sr/^{86}Sr occur. In contrast, εNd overall decreases towards the base of SU 18, apart from one peak at the top of SU 16. From the base of SU 18 it increases again until the top of the sequence, thus being decoupled from ^{87}Sr/^{86}Sr in the upper part of the sequence.

To sum up, all proxy records indicate not only significantly differing characteristics below and above the unconformity but also a clear change starting in the upper part of the Gelic Gleysol of SU 11.

4.2 Magnetic fabric

Overall, the preferential direction of the lineation of all samples that passed the assessment protocol (see Fig. 4, Sect. S1) is SSW to NNE (Fig. 5). This is also true for datasets comprising all samples (Figs. S1, 2). All stereoplots show a horizontal plain defined by K_{MAX}, K_{INT}, and K_{MIN} plotting perpendicular to this plain and close to the vertical axis. It should be noted that the principal axes of the AMS ellipsoids and the resulting lineations are linears and not vectors, as they do not indicate a distinct direction but only an alignment. For example, an NE-pointing trend in the rose diagrams is equivalent to a SW trend and vice versa, as the diagram is to be read point-symmetrically. In the rose diagrams of lineation and stereoplots, the loess units indicate clear populations (∼ 15 to ∼ 45° and ∼ 195 to ∼ 225°) aligned ∼ NE-SW. However, reworked loess exhibits a second subordinate direction perpendicular to the main direction (∼ NNE–SSW), possibly reflecting multiple water-runoff and sediment reworking effects (cf. Tarling and Hrouda, 1993). The Gelic Gleysols show a clear dominance of NNE–SSW lineations, and the Calcaric Cambisols show a preferential trend of lineations scattering between NNE–NE and SSW–SW. Further information on the AMS results is given in the Supplement.

5 Discussion

5.1 Stratigraphic interpretation of proxy data

In order to comprehensively discuss our results, all Schwalbenberg RP1 proxy data were plotted against the radiocarbon-derived Bayesian age model (Fig. 6) accomplished by sedimentation rate and precipitation quantification (Prud'homme et al., 2022). Schwalbenberg RP1 is subdivided into a lower section that covers the period from the end of GS 9 until the end of GS 5.2 (∼ 39 200–30 800 cal BP) and an upper section covering the last third of GS 3 until GS 2.1 (∼ 24 300–21 900 cal BP). In the lower section, well-developed palaeosols and loess layers particularly resolve the period from GIs 8–5.2 and corresponding GSs, respectively. Ranging between 2 and 3, the *U* ratio shows values typical for central European LPSs, with lower values during interstadials related to reduced wind activity and higher values during stadials indicating gustier winds (e.g. Vandenberghe, 2013; Kämpf et al., 2022).

The basal soil complex (SUs 2–6) contains well-developed Calcaric Cambisol horizons depicted by two distinct clay peaks and lowest Sr/Rb values, attesting intensive weathering and pedogenesis. In this context, the increase in ^{87}Sr/^{86}Sr is unlikely to predominantly reflect provenance changes due to its susceptibility to weathering impacts (cf. Clauer and Chauduri, 1995), while the distinct shift in εNd might be related to a dust source signal (see Sect. S4).

The first clay maximum is followed by an increase in the *U* ratio and a distinct peak in the sedimentation rate, corresponding to the second half of GI 8. After a short decline, the Schwalbenberg sedimentation rate increases in tandem with elevated dust probabilities in the nearby Eifel maar lakes (Eifel Laminated Sediment Archive, ELSA, dust probability; Seelos et al., 2009), indicating continuous dust input until the beginning of GI 5.2. This pattern diverges from the trend recorded in the North Greenland Ice Core Project (NGRIP), where high Ca^{2+} values relate to GSs and distinct minima to GIs. This difference supports the idea of an accretionary character of the Schwalbenberg LPSs in general and the palaeosols in particular, as described by Vinnepand et al. (2020) and Fischer et al. (2021).

After GI 7, clay contents in RP1generally decrease but still peak within the palaeosols of GI 6 (Calcaric Cambisol) and GI 5.2 (Gelic Gleysol). The *U* ratio follows exactly the opposite trend, showing overall coarsening. Hence, this indicates enhanced wind activity from GS 7 onwards, with clear maxima during GSs and reduction during GIs, respectively.

The MS_{fd} shows overall decreasing values from SU 1 up to the base of SU 11, indicating a continuous reduction in fine magnetic particles. As MS is contemporaneously increasing (Fig. 4), we assume that this opposite trend is related to a domination of wind vigour over pedogenesis (e.g. Evans and Heller, 2001). This is also supported by high *U* ratio values especially in loess layers (SUs 9 and 10) and a strong increase in log Sr/Rb, indicating reduced weathering and input of primary carbonates at the same time (see Vinnepand et al., 2020; Fischer et al., 2021).

Log Ti/Al, which is interpreted to relate to provenance (Zech et al., 2008; Profe et al., 2016), shows only minor fluctuations in the entire lower section until SU 12. In contrast, significant decreases in ^{87}Sr/^{86}Sr and increases in εNd are observed within GS 7 (top of SU 6 and SU 7) towards GI 6 (SU 8) and GS 6 (on top of SU 8) towards GI 5.2 (SU 11), respectively.

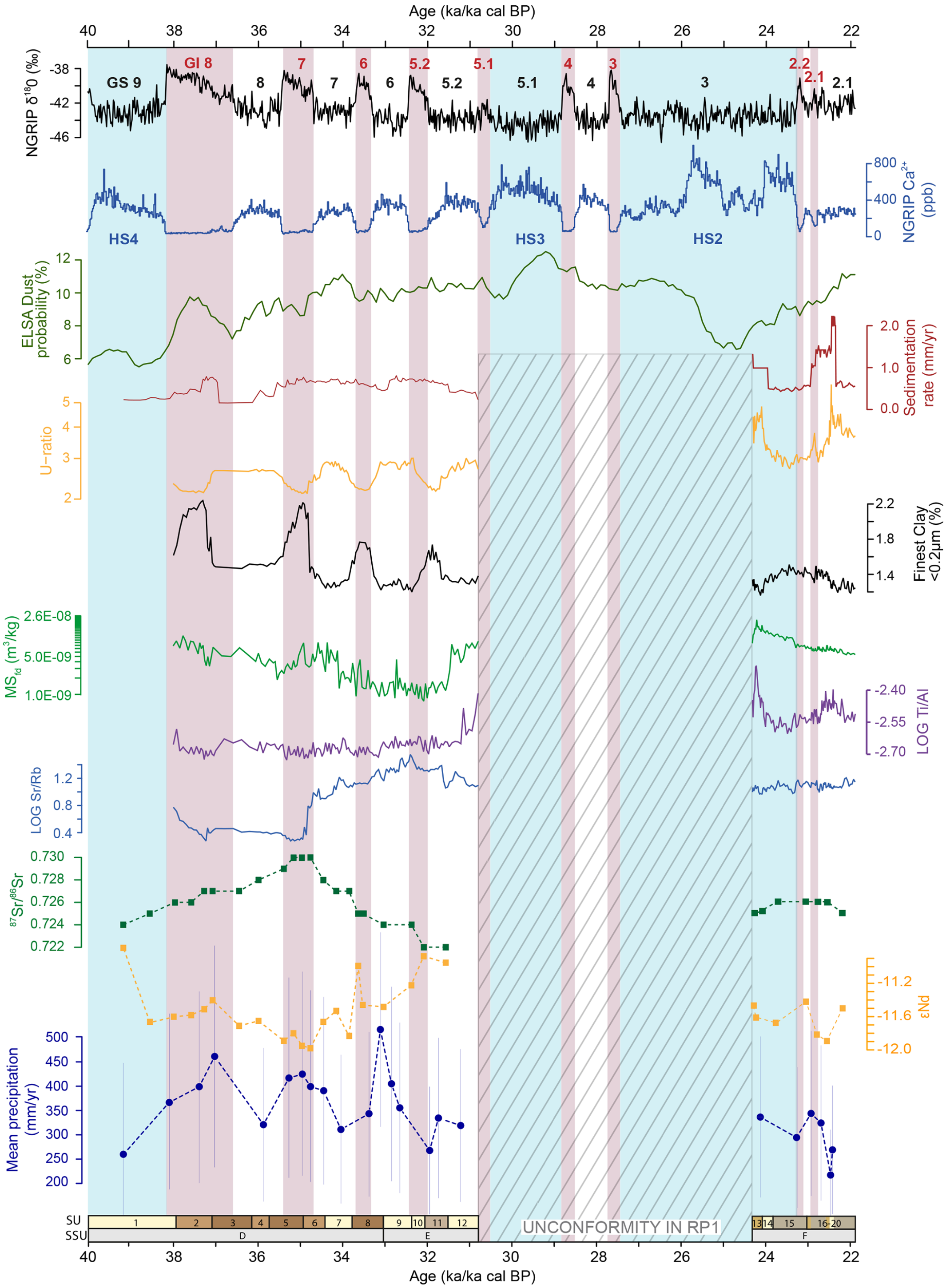

Figure 6. Comparison of selected proxy data from Schwalbenberg RP1, compared with the NGRIP event stratigraphy, with δ^{18}O and Ca^{2+} according to Rasmussen et al. (2014), and ELSA dust probability according to Seelos et al. (2009). Greenland Interstadials (GIs 8 to 2.1) are numbered in red and Greenland Stadials (GSs) in black, and Heinrich Stadials (HS4 to HS2) according to Reutenauer et al. (2015) are highlighted in light blue. Originally given as ages in years before 2000, the chronological scale has been shifted by 50 years to allow for direct comparisons with the calibrated radiocarbon scale given in calibrated years before CE 1950 (cal BP). Chronostratigraphy and sedimentation rates from Schwalbenberg are based on Bayesian age–depth modelling of the radiocarbon dated sequence using IntCal20 (cf. Prud'homme et al., 2022). U ratio, finest clay, frequency dependence of magnetic susceptibility MS$_{\mathrm{fd}}$ ($\Delta\chi$(fd)), log Ti/Al, and log SR/Rb are based on a continuous 2 cm sampling interval. ^{87}Sr/^{86}Sr and εNd are based on 35 samples along the profile (see Fig. 4). Mean annual precipitation estimates are based on the δ^{13}C values of ECGs (Prud'homme et al., 2022). SUs and SSUs according to Fischer et al. (2021). All data are given in Tables ST1 and ST2 in the Supplement.

These trends are likely to be related to a provenance change (see Sect. 5.2) that was contemporary with a strong decrease in reconstructed precipitation values.

During the following GS 5.2 a significant shift occurred. This was characterized by increased input of fine magnetic particles in accordance with a distinct increase in log Ti/Al and enhanced wind dynamics as indicated by the U ratio. In combination with the observed isotopic signals, this indicates severe changes in palaeoenvironmental conditions (see Sect. 5.3).

Above the unconformity, which we constrain to a hiatus of up to 6.5 kyr (between 30 800 and 24 300 cal BP), completely different characteristics are observed in both the stratigraphic record and the proxy data. We interpret the maxima in the U ratio, MS, and $\mathrm{MS_{fd}}$ as well as in log Ti/Al in SU 13 as the result of sediment relocation and recycling involving re-deposition of the Eltville tephra. The latter contains detrital volcanogenic magnetic Ti–Fe oxides which show frequently an oxidized rim of maghemite resulting from low-temperature oxidation upon incorporation into sediment. This oxidation process leads to particle-internal fining causing increasing superparamagnetic behaviour similar to pedogenic neo-formation. Here, it is limited to the maghemized shell consisting of ultrafine domains in the superparamagnetic single-domain (SD) range and therefore significantly increases the MS (e.g. Liu et al., 2012; Zhang et al., 2021). The highest sedimentation rates are in accordance with input of coarser material as indicated by the highest U ratio values. ELSA dust probability is also indicating increased dustiness, which is – for this time interval – not observed in NGRIP $\mathrm{Ca^{2+}}$. The finest clay at RP1 is slightly increased where the U ratio forms a minimum related to the weakly developed Gelic Gleysols. After the distinct maximum, the $\mathrm{MS_{fd}}$ shows a continuous decrease. While log Sr/Rb and $^{87}\mathrm{Sr}/^{86}\mathrm{Sr}$ show almost no variations, log Ti/Al is increasing contemporarily with fluctuating εNd during GS 2, for which the lowest precipitation value is reconstructed. Overall, the stratigraphy and related proxy data and the comparison to NGRIP indicate that above the unconformity the dominance of local to regional effects caused the major changes.

5.2 Isotope geochemistry and AMS-derived near-surface wind trends: identification of dust source–sink relationships?

Potential shifts in dust provenance from the OIS 3 to OIS 2 transition have been reported based on bulk geochemistry and luminescence sensitivity for different Schwalbenberg LPSs (Klasen et al., 2015; Profe et al., 2016; Fitzsimmons et al., 2021; Vinnepand et al., 2022). These studies indicate that sediment recycling within local source areas as well as changes in wind direction may have caused the different signals. Here, we add information on isotopic composition and AMS-derived near-surface wind trends for Schwalbenberg RP1. We compare Sr and Nd isotope data from different potential dust source areas in western Europe (Fig. 7a). As stated before (see Sects. 4.1, 5.1), the variations in εNd are restricted to a narrow range, and significant shifts in $^{87}\mathrm{Sr}/^{86}\mathrm{Sr}$ in the lower section of the sequence may be related to enhanced in situ weathering. Against this background, caution is required in interpreting the presented data, but, nevertheless, our combination of proxies allows for some substantial contributions to the discussion of dust source-to-sink relationships. This is especially true as data on dust provenance based on precisely dated LPSs are still rather scarce, with Schwalbenberg RP1 representing one of the best dated LPSs of the wider region (Prud'homme et al., 2022).

Overall, the relatively coarse character of the silt and the regional geographic setting of the Schwalbenberg at the confluence of the rivers Ahr and Rhine in the centre of the Rhenish Massif (Fig. 1) suggest dominating local to regional dust components in most parts of the RP1 profile. Figure 7 shows that the Schwalbenberg Sr and Nd isotope data generally plot along a gradient between the recent suspended sediment load of the Upper Rhine (Tricca et al., 1999) and Devonian slates from the Rhenish Massif (Moragues-Quiroga et al., 2017). Hence, both the Rhine catchment and the Rhenish Massif can be assumed as potential silt source areas. In addition, both mixing hyperbolas between Eifel volcanites and the Devonian slates and the Siebengebirge and Westerwald volcanites and the Devonian slates indicate a certain amount of these volcanites to the Schwalbenberg LPSs. This might also be reflected in the relatively high Nd concentrations at Schwalbenberg (mean: 68.48 ppm; $n = 30$) in comparison to the Rhine suspended sediment load (11.1 ppm; Tricca et al., 1999), the Devonian slates of the Rhenish Massif (mean: 44.39 ppm; $n = 5$; Moragues-Quiroga et al., 2017), and regional Pleistocene periglacial slope deposits (mean = 44.64 ppm; $n = 3$; Moragues-Quiroga et al., 2017). As reference, leucite basalt and phonolite andesites typically have high Nd concentrations around 81 ppm (Faure and Mensing, 2005).

In contrast to Schwalbenberg, the LPS key sections of Nussloch (Figs. 1, 7), located approx. 200 km south-southeast on the eastern bank of the Upper Rhine, appear to be dominated by dust input from the alluvial plain of the Rhine River and other local sources (Schatz et al., 2015).

For other LPSs like Kesselt and Rocourt, both situated in Belgium at the north-western edge of the Rhenish Massif (Fig. 1), Sr and Nd isotope values of sediments that were deposited within the LGM (Gallet et al., 1998) indicate an important role of the Rhenish Massif as an additional local dust source besides the Rhine system. Similar findings were also reported for OIS 2 loess within the southern part of the Lower Rhine Embayment and the north-western edge of the Rhenish Massif (northern edge of the Eifel area) by Janus (1988). In that study a systematic increase in heavy minerals indicative of short-distance transport from the Eifel and Rhenish Massif sediment source towards LPSs located north-west of Schwalbenberg was observed, next to heavy minerals indica-

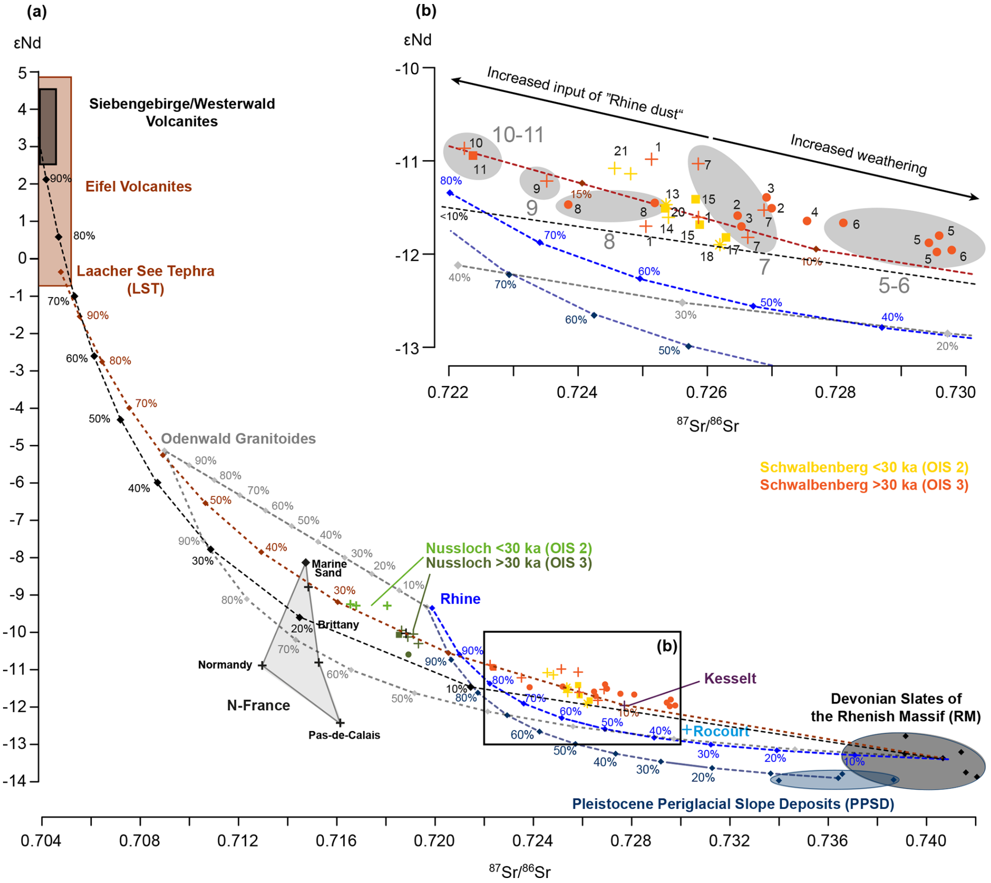

Figure 7. **(a)** εNd and $^{87}Sr/^{86}Sr$ of reference samples from different sites in western central Europe in comparison to Schwalbenberg RP1. Mixing hyperbolas indicate the possible mixing of two endmembers (in percentage) considering their Sr and Nd element concentrations and their respective isotope values (cf. Faure and Mensing, 2005; all data are presented in Table ST3 in the Supplement) and were calculated for mixtures between different endmembers (Devonian slate saprolite of the Rhenish Massif as continental crust endmember (grey; Moragues-Quiroga et al., 2017), Rhine suspended sediment load (blue; Tricca et al., 1999), Odenwald granitoids (light grey; Siebel et al., 2012), Siebengebirge and Westerwald volcanites (black; Schubert et al., 2015), Laacher See tephra and Eifel volcanites (red, as mantle-representing endmember; Wörner et al., 1985; note that Förster et al. (2020) showed that the Eltville tephra found at Schwalbenberg originated from an earlier eruption of the Laacher See volcano at 24.3 ka), northern France (Gallet et al., 1998), and Pleistocene periglacial slope deposits (PPSDs) in the Rhenish Massif (Moragues-Quiroga et al., 2017)). Our plot suggests that the Schwalbenberg LPSs are dominated by sediments from the Rhine valley as also described for Nussloch (Schatz et al., 2015). Compared to the latter, the isotope composition of the Kesselt and Rocourt LPSs (Gallet et al., 1998) (see Fig. 1) and the Schwalbenberg LPSs indicate a higher amount of dust originating from Devonian slates of the Rhenish Massif and/or PPSDs overlying the Devonian rocks. In addition, mantle-derived material from the Eifel and from the Siebengebirge and Westerwald potentially contributes to the dust deposited at Schwalbenberg. Odenwald granitoids may reflect a contribution via small Rhine tributaries. **(b)** Detail of plot **(a)** (see inset): the grey numbers refer to SUs, and the grey ellipses highlight that the samples above SU 7 up to SU 11 may reflect an enhanced contribution of sediments from the Rhine towards the end of OIS 3. In contrast, SUs below SU 7 down to SU 5, correlating to matured Calcaric Cambisols from the basal soil complex of the RP1 profile, plot offsite towards more radiogenic Sr isotope values, indicating enhanced weathering. Symbology: loess (+), reworked loess (∗), Gelic Gleysols (■), and Calcaric Cambisols (•).

tive of Rhine terraces and small Eifel riverbeds dissecting the Rhine terraces as the main source areas.

Although the data shown in Fig. 7 indicate general differences in dust provenance, we have to keep in mind that (i) the variations in Schwalbenberg RP1 Sr isotope composition are certainly also influenced by in situ pedogenesis (see Fig. 7b, especially within SUs 5 and 6 where the strongest weathering is observed); (ii) the reference data for the suspended sediment load from the southernmost part of the Upper Rhine River (south of the Kaiserstuhl; see Fig. 1) mainly reflect material originating from Miocene marine sediments of the Alpine Molasse (Buhl et al., 1991), thus not including important Rhine tributaries located further north (e.g. the rivers Main, Nahe, Lahn, and Mosel); (iii) also non-alpine provenance spectra contribute considerably to the Pleistocene and recent sediment budged of the Upper Rhine (Preusser et al., 2021; Hülscher et al., 2018); and (iv) sediments from the Rhine catchment most likely experienced several cycles of grain size reduction, sorting, and mixing within the alluvial plain and fluvial transport prior to its deposition at the Schwalbenberg LPSs. Such processes occurring in the alluvial plains of river systems have recently been discussed by Pötter et al. (2021) for LPSs from the Lower Danube and by Baykal et al. (2022) for LPSs from the northern fringe of the European loess belt in the context of dust provenance.

Despite the given limitations a clear change in isotope composition after GI 7 (top of SU 6 and SU 7) and after GI 6 (SU 8) up to GS 5.2 (top SU 11) is indicated by slightly increasing εNd and decreasing ^{87}Sr/^{86}Sr values, pointing to enhanced input of dust being more comparable to the Rhine suspended load (see Fig. 7b). This trend is accompanied by a reduction of fine magnetic particles (decreasing MS$_{\mathrm{fd}}$), reduced weathering (increasing log Sr/Rb), and gustier winds indicated by a dominance of wind vigour (inverse behaviour of MS and MS$_{\mathrm{fd}}$) and high U ratio values (see Sect. 5.1).

Throughout the upper section of RP1 both isotope ratios do not show typical inverse trends (Fig. 6). This may be due to sediment sorting and reworking as observed within the RP1 upper section, which may have biased the Sr isotope composition. Nevertheless, slightly varying εNd values in combination with significant variations in log Ti/Al might reflect increased dust input from local to regional sources of the Rhenish Massif. In combination with the AMS-based reconstruction of SSW–NNE near-surface wind trends (Figs. 4, 8), we assume that the alluvial plains of the rivers Rhine and Ahr most likely are the dominating local sediment sources for the investigated part of the Schwalbenberg LPS.

Based on our AMS data, however, we cannot decide whether the near-surface winds came from SSW or NNE, but wind regime statistics for the Schwalbenberg site in the valley setting indicate an overall dominance of westerly and south-westerly winds during the LGM and recent times (Prud'homme et al., 2022).

In addition to these large alluvial sources, exposed fine-grained rocks (e.g. in the incised upper Ahr valley), alluvial plains of small creeks, abandoned river terraces, and widespread Pleistocene periglacial slope deposits (PPSDs) may also have played an important role in silt production. Furthermore, recycling of loess deposits may have contributed an additional dust component into the LPS (cf. Mroczek, 2013).

Overall, the obtained data on dust provenance and near-surface wind trends point to dominating local dust sources that were associated with gustier winds with predominant SSW–NNE wind directions in stadial phases, while interstadials may have been characterized by a significant dust component from more distant sources. In this context, we found a significant negative relationship between the AMS foliation (F) and the U ratio in SUs 5, 7, and 8 (see Fig. S4), whereof SU 5 correlates to GI 7 and SU 8 to GI 6 (Fig. 6). This may indicate that fine to medium silt particles establish the AMS signal within these interstadials, possibly owing to the continuous accumulation of dust during soil formation resulting in accretionary palaeosols (Fischer et al., 2021; Vinnepand et al., 2022). To our knowledge, such a clear correlation between finer grain sizes and increasing foliation has been so far not described in any LPS on stadial–interstadial scales (cf. Bradák et al., 2021). However, Zhang et al. (2010) proposed a model in which more frequent summer precipitation during relative mild climatic periods (interglacials and interstadials) led to an improved settling of anisotropic grains (e.g. micas and clay minerals), causing the overall increased AMS foliation. In contrast, most loess units throughout RP1 and weakly developed Gelic Gleysols in the upper section (SUs 15, 17, 20) show a positive linear relationship between F and the U ratio, indicating that coarse silt particles play a major role for the AMS signal in these units that were related to gustier winds and input of short-travelled dust.

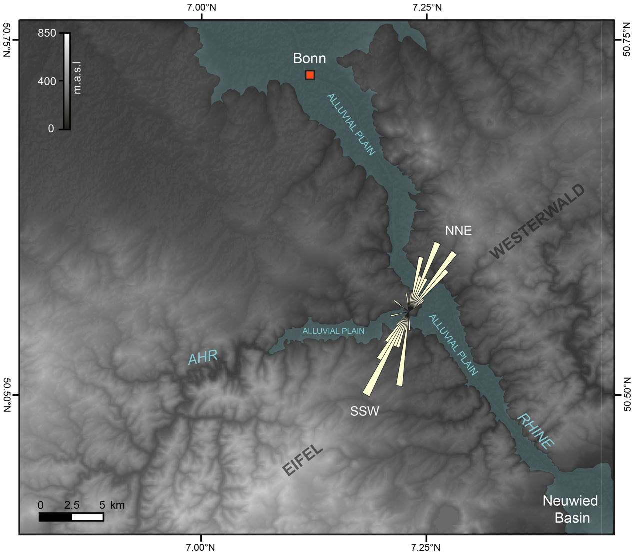

Figure 8. DEM-based map (SRTM 30; USGS 2022) showing reconstructed near-surface wind trends for the Schwalbenberg site and possible short distance entrainment areas for mineral dust. The SSW–NNE wind trend estimates are only based on AMS measurements of loess samples (beige rose diagram), which passed the assessment protocol for primary magnetic fabric (see Fig. 4) that is described in Sects. 3.3 and S1. For AMS stereoplots and rose diagrams please see Fig. 5.

5.3 Palaeoenvironmental and palaeoclimatic implications

Millennial- to centennial-scale synchronicity between the Schwalbenberg LPSs and the NGRIP δ^{18}O record was proposed based on litho- and pedostratigraphic evidence combined with organic carbon contents (Fischer et al., 2021), further attested by radiocarbon dating and a quantitative climate reconstruction based on the investigation of ECGs (Prud'homme et al., 2022). Here we observe very largely synchronous patterns between NGRIP δ^{18}O and Ca^{2+} and the Schwalbenberg sedimentological proxies (U ratio, finest clay), further supporting the close synchronicity of western European and North Atlantic climate changes. In addition, we present proxy data allowing for further characterization of the dust deposited within the Schwalbenberg LPSs and comprehensive palaeoenvironmental reconstructions based on magnetic fabric, environmental magnetism, bulk geochemistry, and isotope composition.

The lower section of the Schwalbenberg RP1 profile covers in high resolution the period from the end of GS 9 (contemporary with Heinrich Stadial 4) to the end of GS 5.2 (Fig. 6). In the wider region this period is characterized by a distinct opening of the landscape as suggested by a landscape evolution model of the Eifel area that is based on multi-method approaches applied to ELSA (Sirocko et al., 2016). This model documents the transition from boreal forested environments (landscape evolution zone (LEZ) 7, onset ∼ 49 years b2k) to steppe-like open environments (LEZ 6, ∼ 36.4–28.45 years b2k), which is interpreted as the environmental reaction due to a longer cooling trend accompanied by increased aridity in the Rhenish Massif at roughly the time of the OIS 3 to OIS 2 transition. At Schwalbenberg this cooling trend is, on the one hand, reflected in decreasing intensities of soil formation from the lower soil complex (SUs 2–6, covering GI 8 and 7) towards the Calcaric Cambisol correlated to GI 6 (SU 8) and the Gelic Gleysol correlated to GI 5 (SU 11) (cf. Vinnepand et al., 2020; Fischer et al., 2021). On the other hand, overall increasing U ratio values and the reduction of fine magnetic particles as indicated by decreasing MS_{fd} values point towards an enhancement of wind activity and increasing dryness simultaneously with reduced sediment recycling until mid-GS 5.2 at ∼ 31 500 cal BP. The latter is also supported by reduced weathering intensity following GI 7, as evidenced in a slightly increasing log Sr/Rb ratio accompanied by a distinct decrease in $^{87}Sr/^{86}Sr$ and an increase in εNd. This can be interpreted in terms of an enhanced input of dust that carries an isotope signal comparable to that of the Rhine's suspended load (Fig. 7b). This trend coincides with distinct aridification, climate cooling, and grain coarsening observed in some LPSs along the Rhine during late OIS 3 (Prud'homme et al., 2018; Vinnepand et al., 2020) and might be related to intensified periglacial conditions in the local silt sources and enhanced glacial grinding activity and sediment availability in front of the advancing Alpine ice sheet and the Rhine Glacier in particular (Ivy-Ochs et al., 2008).

For the interstadial periods we are able to reconstruct reduced but still pronounced dust deposition at the Schwalbenberg LPSs (Fischer et al., 2021; Prud'homme et al., 2022). Vegetation cover and moister conditions as suggested by Prud'homme et al. (2022) especially for GIs 8–6 for Schwalbenberg favour (reduced) dust deposition rather than its entrainment (see Újvári et al., 2016). In addition, intensified syn-sedimentary soil formation in interstadials, especially during GI 8 and GI 7, leads to the production of clay minerals in the course of silicate weathering, hampering the entrainment of particles due to strong cohesion and adhesion forces (cf. Újvári et al., 2016). As discussed before, we observed an inverse correlation of the U ratio and the AMS foliation but a positive correlation of the finest clay and the foliation within the Calcaric Cambisols of the lower section of RP1 (see Sect. S1). This could point, beside secondary grain size reduction in the course of pedogenesis, to an input of finer-grained (potentially long-distant) aeolian material during interstadials, which might be also visible in described shifts in εNd (see Sect. 5.2).

At Schwalbenberg we observe a further distinct shift around 31 500 cal BP associated with increased wind activity and in particular significantly enhanced sediment recycling reflected by a distinct shift in MS_{fd} and a potential provenance shift indicated by log Ti/Al (Fig. 6). On a regional scale, the same period is characterized by increased flood activity in the Eifel area (Sirocko et al., 2016) possibly related to enhanced seasonal landscape instability caused by a reduced vegetation cover and associated sediment relocation. On a supra-regional scale, the advancing Fennoscandian (FIS) and British–Irish ice sheets (BIIS) correlating with the onset of the LGM (Lambeck et al., 2014), with some moderate ice marginal retreats during HS3 (Toucanne et al., 2015), and the further advancing Rhine Glacier (Ivy-Ochs et al., 2008) played an important role in dust production and circulation patterns in western, central, and eastern Europe (Schaffernicht et al., 2020). Simultaneously, a significant increase in the sedimentation rate occurred at Nussloch (Prud'homme et al., 2022), whereas in northern France the first genuine loess unit originates only from the following stadial GS 5.1 (Antoine et al., 2014). Associated with overall cooler and drier conditions over western and central Europe during the LGM, evidence is provided for cyclones that were capable of triggering enhanced dustiness related to higher wind speeds (Pinto and Ludwig, 2020). This is in agreement with the assumption of strong NW winds especially between 34 and 17 ka, resulting in local input of coarse aeolian material, high sedimentation rates, and the SE-trending "greda" morphology at Nussloch (Antoine et al., 2009).

At Schwalbenberg RP1, however, on top of the distinct unconformity that is related to local channel formation and sediment relocation, which may have reworked and included the Eltville tephra (Fischer et al., 2021), different proxies pinpoint environmental conditions that were significantly different from the preceding ones that were most likely dominated by local to regional signals.

Sediment relocation reflected within SU 13 was followed by reduced wind activity, input of finer-grained sediments, and reduced sedimentation rates until ∼ 22 900 cal BP, roughly coinciding with the later part of LEZ 5 in the Eifel area that represents the transition from steppe to tundra-like environments (Sirocko et al., 2016).

After 22 900 cal BP, the sedimentation rate and *U* ratio reach the highest values throughout the entire RP1 profile, indicating increased dustiness but also potential sediment reworking processes. Enhanced dustiness is, however, also reflected in the REM 3 LPS (cf. Fischer et al., 2021; Fig. 3) and the ELSA dust probability (Fig. 6) associated with the development of the polar desert of LEZ 4 in the Eifel area (Sirocko et al., 2016) but is decoupled from NGRIP Ca^{2+}, which shows a clear minimum after 23 300 BP.

Further evidence for local to regional dust transport is provided by heavy mineral analyses of the Dehner Maar, where increased dust activity and a shift from predominantly westerly to strong easterly winds is reported for the period from 23 until 20 ka (Römer et al., 2016). In this context, the AMS-based reconstruction of near-surface wind trends at Schwalbenberg RP1 may point to periods with significant north-easterly winds during overall dominating western wind directions (Prud'homme et al., 2022). This would be in agreement with dust-cycle simulations for the LGM, showing that beside westerlies and embedded cyclones persistent easterlies associated with anticyclonic flow may have also played a significant role for dust deposition. These would have resulted in westward-running dust plumes and associated high dust accumulation rates in the North German plain including adjacent regions (Pinto and Ludwig, 2020; Schaffernicht et al., 2020).

6 Conclusions

We present an integrative approach that systematically combines physical and geochemical proxies, enabling a synthetic interpretation of LPS formation in western central Europe. We focus on the Schwalbenberg RP1 LPS that is exposed north-west of the confluence of the Ahr and Rhine rivers in the centre of the Rhenish Massif. We integrate our data into a robust and reliable age model that has been established based on high-resolution dating of ECGs. We show that Schwalbenberg RP1 is subdivided into a lower section and an upper section that are separated by a major stratigraphic unconformity. Whereas the lower section corresponds to late OIS 3 ($\sim$ 39 200–30 800 cal BP; end of GS 9 until GS 5.2), the upper section dates into the LGM ($\sim$ 24 300–21 900 cal BP; end of GS 3 until GS 2.1).

In general, we could confirm the assumption of syn-sedimentary soil formation during interstadials, give evidence for provenance changes with overall dominating local to regional dust sources, and confirm the close temporal linkages to other climate archives in the North Atlantic region, which we have highlighted in earlier studies.

Based on our synthetic approach we can draw the following, more specific conclusions:

- In combination with the established age model, the sedimentological proxies of the lower section at Schwalbenberg RP1 attest to – to a certain degree – similar and largely synchronous patterns of northern hemispheric climatic changes as evidenced in NGRIP $\delta^{18}O$ and Ca^{2+}, supporting the overall synchronicity of climatic changes in and around the North Atlantic region.

- A significant negative relationship between the AMS foliation and the *U* ratio found in interstadial palaeosols and intercalated stadial loess layers, respectively, may indicate that fine to medium silt particles increase the foliation. This could possibly reflect the continuous accumulation of fine dust during soil formation and the simultaneous increase in precipitation, causing improved alignment of sediment grains into the bedding plain. To our knowledge, such a clear correlation between finer grain size and increasing foliation has so far not been described for any LPS for stadial–interstadial cycles, i.e. on millennial to centennial timescales.

- A distinct shift towards increased input of "Rhine dust" and reduced weathering intensity occurs simultaneously with an overall cooling and aridification trend in Europe towards the end of OIS 3.

- A further distinct shift visible in all proxy data around 31 500 cal BP, interpreted in terms of enhanced wind activity with significant input of coarse-grained material recycled from local sources, is possibly related to increased landscape instability when tundra-like conditions – probably associated with deep seasonal or even permafrost – developed towards the LGM.

- The proxies within the upper section pinpoint environmental conditions that were significantly different from those in the lower section, which were most likely dominated by more local to regional signals and high sedimentation rates.

- AMS-based reconstructions of near-surface wind trends may indicate the influence of north-easterly winds beside the overall dominance of westerlies and embedded cyclones, causing high dust accumulation rates.

Overall, by integrating our approach in the study of LPSs over a broader geographic area, we see the opportunity for a more comprehensive understanding of LPS formation including changes in dust composition and associated circulation patterns during Quaternary climate changes.

Data availability. All raw data are available in the tables of the Supplement with this publication.

Supplement. The supplement related to this article is available online at: https://doi.org/10.5194/egqsj-72-163-2023-supplement.

Author contributions. This study was designed by PF, UH, MV, and CZ. Fieldwork and sampling was done by PF, UH, OM, MV, and the TerraClime team. Granulometric and bulk geochemical analyses were performed by FL and PS at RWTH Aachen University. The Sr and Nd isotope analyses were conducted by CC at the James Hutton Institute in Aberdeen, Scotland. Interpretation and manuscript writing were executed by MV and PF, with the contribution of all other authors. Research funds were raised by KF, PF, and AV (see below).

Competing interests. At least one of the (co-)authors is a member of the editorial board of *E&G Quaternary Science Journal*. The peer-review process was guided by an independent editor, and the authors do not have any other competing interests to declare.

Special issue statement. This article is part of the special issue "Quaternary research from and inspired by the first virtual DEUQUA conference". It is a result of the vDEUQUA2021 online conference in September/October 2021.

Acknowledgements. This articles contributes to the TerraClime project (project number 337232800) funded by the German Research Foundation (DFG). We greatly appreciate the extensive fieldwork conducted by the whole TerraClime Team and associates, namely Kristina Reetz (JGU Mainz), Alexandra Nimmrichter (JGU Mainz), and Aileen Klinger (JGU Mainz). We would like to thank the two reviewers for constructive comments that helped to significantly improve the manuscript.

Financial support. This research has been supported by the Deutsche Forschungsgemeinschaft (grant no. 337232800).

This open-access publication was funded
by Johannes Gutenberg University Mainz.

Review statement. This paper was edited by Hans von Suchodoletz and reviewed by two anonymous referees.

References

Antoine, P., Rousseau, D.-D., Moine, O., Kunesch, S., Hatté, C., Lang, A., Tissoux, H., and Zöller, L.: Rapid and cyclic aeolian deposition during the Last Glacial in European loess: a high-resolution record from Nussloch, Germany, Quaternary Sci. Rev., 28, 2955–2973, https://doi.org/10.1016/j.quascirev.2009.08.001, 2009.

Antoine, P., Goval, E., Jamet, G., Coutard, S., Moine, O., Hérisson, D., Auguste, P., Guérin, G., Lagroix, F., Schmidt, E., Robert, V., Debenham, N., Meszner, S., and Bahain, J. J.: The upper pleistocene loess sequences of havrincourt (Pas-de-Calais, France). Stratigraphy, palaeoenvironments, geochronology and human occupations, Quaternaire, 25, 321–368, https://doi.org/10.4000/quaternaire.7278, 2014.

Baykal, Y., Stevens, T., Bateman, M. D., Pfaff, K., Sechi, D., Banak, A., Šuica, S., Zhang, H., and Nie, J.: Eurasian Ice Sheet derived meltwater pulses and their role in driving atmospheric dust activity: Late Quaternary loess sources in SE England, Quaternary Sci. Rev., 296, 107804, https://doi.org/10.1016/j.quascirev.2022.107804, 2022.

Blaauw, M. and Christeny, J. A.: Flexible paleoclimate age-depth models using an autoregressive gamma process, Bayesian Anal., 6, 457–474, https://doi.org/10.1214/11-BA618, 2011.

Blott, S. J., Croft, D. J., Pye, K., Saye, S. E., and Wilson, H. E.: Particle size analysis by laser diffraction, Geological Society, London, Special Publications, 232, 63–73, https://doi.org/10.1144/GSL.SP.2004.232.01.08, 2004.

Boenigk, W. and Frechen, M.: The Pliocene and Quaternary fluvial archives of the Rhine system, Quaternary Sci. Rev., 25, 550–574, https://doi.org/10.1016/j.quascirev.2005.01.018, 2006.

Bradák, B., Seto, Y., Chadima, M., Kovács, J., Tanos, P., Újvári, G., and Hyodo, M.: Magnetic fabric of loess and its significance in Pleistocene environment reconstructions, Earth-Sci. Rev., 210, 103385, https://doi.org/10.1016/j.earscirev.2020.103385, 2020.

Bradák, B., Seto, Y., Stevens, T., Újvári, G., Fehér, K., and Költringer, C.: Magnetic susceptibility in the European Loess Belt: New and existing models of magnetic enhancement in loess, Palaeogeogr. Palaeocl., 569, 110329, https://doi.org/10.1016/j.palaeo.2021.110329, 2021.

Buggle, B., Glaser, B., Hambach, U., Gerasimenko, N., and Marković, S.: An evaluation of geochemical weathering indices in loess-paleosol studies, Quaternary Int., 240, 12–21, https://doi.org/10.1016/j.quaint.2010.07.019, 2011.

Buggle, B., Hambach, U., Müller, K., Zöller, L., Marković, S. B., and Glaser, B.: Iron mineralogical proxies and quaternary climate change in SE-european loess-paleosol sequences, Catena, 117, 4–22, https://doi.org/10.1016/j.catena.2013.06.012, 2014.

Buhl, D., Neuser, R. D., Richter, D. K., Riedel, D., Roberts, B., Strauss, H., and Veizer, J.: Nature and nurture: Environmental isotope story of the River Rhine, Naturwissenschaften, 78, 337–346, https://doi.org/10.1007/BF01131605, 1991.

Clauer, N. and Chaudhuri, S.: Clays in Crustal Environments, Springer, Berlin, Heidelberg, https://doi.org/10.1007/978-3-642-79085-0, 1995.

DePaolo, D. J. and Wasserburg, G. J.: Nd isotopic variations and petrogenetic models, Geophys. Res. Lett., 3, 249–252, https://doi.org/10.1029/GL003i005p00249, 1976.

Deutscher Wetterdienst: Deutscher Wetterdienst (German Meteorological Service): https://www.dwd.de/DE/leistungen/klimadatendeutschland/klimadatendeutschland.html, (last access: 2 March 2022), 2023.

Drouet, Th., Herbauts, J., Gruber, W., and Demaiffe, D.: Natural strontium isotope composition as a tracer of weathering patterns and of exchangeable calcium sources in acid leached soils developed on loess of central Belgium, Eur. J. Soil Sci., 58, 302–319, https://doi.org/10.1111/j.1365-2389.2006.00840.x, 2007.

Evans, M. E. and Heller, F.: Magnetism of loess/palaeosol sequences: recent developments, Earth-Sci. Rev., 54, 129–144, https://doi.org/10.1016/S0012-8252(01)00044-7, 2001.

Evans, M. E. and Heller, F.: Environmental Magnetism: Principles and Applications of Enviromagnetics, Elsevier, Amsterdam, 318 pp., ISBN 978-0-122-43851-6, 2003.

Faure, G. and Mensing, T. M.: Principles and applications, John Wiley & Sons, Inc, New York, ISBN 978-0-471-38437-3, 2005.

Federal Institute for Geosciences and Natural Resources Germany: Federal Institute for Geosciences and Natural Resources Germany, https://www.bgr.bund.de/DE/Home/homepage_node.html, last access: 23 March 2022.

Feng, J.-L., Zhu, L.-P., Zhen, X.-L., and Hu, Z.-G.: Grain size effect on Sr and Nd isotopic compositions in eolian dust: implications for tracing dust provenance and Nd model age, Geochem. J., 43, 123–131, https://doi.org/10.2343/geochemj.1.0007, 2009.

Fischer, P., Hambach, U., Klasen, N., Schulte, P., Zeeden, C., Steininger, F., Lehmkuhl, F., Gerlach, R., and Radtke, U.: Landscape instability at the end of MIS 3 in western Central Europe: evidence from a multi proxy study on a Loess-Palaeosol-Sequence from the eastern Lower Rhine Embayment, Germany, Quaternary Int., 502, 119–136, https://doi.org/10.1016/j.quaint.2017.09.008, 2019.

Fischer, P., Jöris, O., Fitzsimmons, K. E., Vinnepand, M., Prud'homme, C., Schulte, P., Hatté, C., Hambach, U., Lindauer, S., Zeeden, C., Peric, Z., Lehmkuhl, F., Wunderlich, T., Wilken, D., Schirmer, W., and Vött, A.: Millennial-scale terrestrial ecosystem responses to Upper Pleistocene climatic changes: 4D-reconstruction of the Schwalbenberg Loess-Palaeosol-Sequence (Middle Rhine Valley, Germany), CATENA, 196, 104913, https://doi.org/10.1016/j.catena.2020.104913, 2021.

Fitzsimmons, K. E., Perić, Z., Nowatzki, M., Lindauer, S., Vinnepand, M., Prud'homme, C., Dave, A. K., Vött, A., and Fischer, P.: Luminescence Sensitivity of Rhine Valley Loess: Indicators of Source Variability?, Quaternary, 5, 1, https://doi.org/10.3390/quat5010001, 2021.

Förster, M. W., Zemlitskaya, A., Otter, L. M., Buhre, S., and Sirocko, F.: Late Pleistocene Eifel eruptions: insights from clinopyroxene and glass geochemistry of tephra layers from Eifel Laminated Sediment Archive sediment cores, J. Quaternary Sci., 35, 186–198, https://doi.org/10.1002/jqs.3134, 2020.

Forster, Th., Evans, M. E., and Heller, F.: The frequency dependence of low field susceptibility in loess sediments, Geophys. J. Int., 118, 636–642, https://doi.org/10.1111/j.1365-246X.1994.tb03990.x, 1994.

Frechen, M., Oches, E., and Kohlfeld, K.: Loess in Europe – mass accumulation rates during the Last Glacial Period, Quaternary Sci. Rev., 22, 1835–1857, https://doi.org/10.1016/S0277-3791(03)00183-5, 2003.

Fuhrmann, F., Seelos, K., and Sirocko, F.: Eolian sedimentation in central European Auel dry maar from 60 to 13 ka, Quaternary Res., 101, 4-12, https://doi.org/10.1017/qua.2020.81, 2021.

Gallet, S., Jahn, B., Van Vliet Lanoë, B., Dia, A., and Rossello, E.: Loess geochemistry and its implications for particle origin and composition of the upper continental crust, Earth Planet. Sci. Lett., 156, 157–172, https://doi.org/10.1016/S0012-821X(97)00218-5, 1998.

Goldstein, S. J. and Jacobsen, S. B.: The Nd and Sr isotopic systematics of river-water dissolved material: Implications for the sources of Nd and Sr in seawater, Chem. Geol.: Isotope Geoscience section, 66, 245–272, https://doi.org/10.1016/0168-9622(87)90045-5, 1987.

Goldstein, S. J. and Jacobsen, S. B.: Nd and Sr isotopic systematics of river water suspended material: implications for crustal evolution, Earth Planet. Sci. Lett., 87, 249–265, https://doi.org/10.1016/0012-821X(88)90013-1, 1988.

Goldstein, S. L., O'Nions, R. K., and Hamilton, P. J.: A Sm-Nd isotopic study of atmospheric dusts and particulates from major river systems, Earth Planet. Sci. Lett., 70, 221–236, https://doi.org/10.1016/0012-821X(84)90007-4, 1984.

Grousset, F. E. and Biscaye, P. E.: Nd and Sr Isotopes as Tracers of Wind Transport: Atlantic Aerosols and Surface Sediments, in: Paleoclimatology and Paleometeorology: Modern and Past Patterns of Global Atmospheric Transport, edited by: Leinen, M. and Sarnthein, M., Springer Netherlands, Dordrecht, 385–400, https://doi.org/10.1007/978-94-009-0995-3_16, 1989.

Grousset, F. E. and Biscaye, P. E.: Tracing dust sources and transport patterns using Sr, Nd and Pb isotopes, Chem. Geol., 222, 149–167, https://doi.org/10.1016/J.CHEMGEO.2005.05.006, 2005.

Hrouda, F.: Anisotropy of magnetic susceptibility of rocks in the Rayleigh Law region: Modelling errors arising from linear fit to non-linear data, Studia Geophyssica et Geodaetica, 51, 423–438, https://doi.org/10.1007/s11200-007-0024-5, 2007.

Hülscher, J., Bahlburg, H., and Pfänder, J.: New geochemical results indicate a non-alpine provenance for the Alpine Spectrum (epidote, garnet, hornblende) in quaternary Upper Rhine sediment, Sediment. Geol., 375, 134–144, https://doi.org/10.1016/j.sedgeo.2018.02.010, 2018.

Ivy-Ochs, S., Kerschner, H., Reuther, A., Preusser, F., Heine, K., Maisch, M., Kubik, P. W., and Schlüchter, C.: Chronology of the last glacial cycle in the European Alps, J. Quaternary Sci., 23, 559–573, https://doi.org/10.1002/jqs.1202, 2008.

Janus, U.: Löss der südlichen niederrheinischen Bucht, Kölner Geographische Arbeiten, 49, ISSN 0454-1294. 1988.

Jones, R. M.: Particle size analysis by laser diffraction: ISO 13320, standard operating procedures, and Mie theory, American Laboratory, Corpus ID 221270121, 2003.

Kämpf, L., Rius, D., Duprat-Oualid, F., Crouzet, C., and Millet, L.: Evidence for wind patterns and associated landscape response in Western Europe between 46 and 16 ka cal. BP, Quaternary Sci. Rev., 298, 107846, https://doi.org/10.1016/j.quascirev.2022.107846, 2022.

Klasen, N., Fischer, P., Lehmkuhl, F., and Hilgers, A.: Luminescence dating of loess deposits from the Remagen-Schwalbenberg site, Western Germany, Geochronometria, 42, 67–77, https://doi.org/10.1515/geochr-2015-0008, 2015.

Knippertz, P. and Stuut, J.-B. W. (Eds.): Mineral Dust, Springer Netherlands, Dordrecht, https://doi.org/10.1007/978-94-017-8978-3, 2014.

Lambeck, K., Rouby, H., Purcell, A., Sun, Y., and Sambridge, M.: Sea level and global ice volumes from the Last Glacial Maximum to the Holocene, P. Natl. Acad. Sci. USA, 111, 15296–15303, https://doi.org/10.1073/pnas.1411762111, 2014.

Lehmkuhl, F., Nett, J. J., Pötter, S., Schulte, P., Sprafke, T., Jary, Z., Antoine, P., Wacha, L., Wolf, D., Zerboni, A., Hošek, J., Marković, S. B., Obreht, I., Sümegi, P., Veres, D., Zeeden, C., Boemke, B., Schaubert, V., Viehweger, J., and Hambach, U.: Loess landscapes of Europe – Mapping, geomorphology, and zonal differentiation, Earth-Sci. Rev., 215, 103496, https://doi.org/10.1016/j.earscirev.2020.103496, 2021.

Liu, Q., Roberts, A. P., Larrasoaña, J. C., Banerjee, S. K., Guyodo, Y., Tauxe, L., and Oldfield, F.: Environmental magnetism: Principles and applications, Rev. Geophys., 50, RG4002, https://doi.org/10.1029/2012RG000393, 2012.

Mahowald, N. M., Muhs, D. R., Levis, S., Rasch, P. J., Yoshioka, M., Zender, C. S., and Luo, C.: Change in atmospheric mineral aerosols in response to climate: Last glacial period, preindustrial, modern, and doubled carbon dioxide climates, J. Geophys. Res.-Atmos., 111, D10202, https://doi.org/10.1029/2005JD006653, 2006.

Marx, S. K., Kamber, B. S., McGowan, H. A., Petherick, L. M., McTainsh, G. H., Stromsoe, N., Hooper, J. N., and May, J.-H.: Palaeo-dust records: A window to understanding past environments, Global Planet. Change, 165, 13–43, https://doi.org/10.1016/j.gloplacha.2018.03.001, 2018.

McGee, D., Broecker, W. S., and Winckler, G.: Gustiness: The driver of glacial dustiness?, Quaternary Sci. Rev., 29, 2340–2350, https://doi.org/10.1016/j.quascirev.2010.06.009, 2010.

Meijs, E., Mücher, H., Ouwerkerk, G., Romein, A., and Stoltenberg, H.: Evidence of Presence of the Eltville Tuff Layer in Dutsch and Belgian Limbourg and the Consequences for the Loess Stratigraphy, E&G Quaternary Sci. J., 33, 59–78, https://doi.org/10.3285/eg.33.1.06, 1983.

Meschede, M.: Geologie Deutschlands: ein prozessorientierter Ansatz, Springer Spektrum, Berlin, 252 pp., ISBN 978-3662452974, 2018.

Meyer, R., Nicoll, G. R., Hertogen, J., Troll, V. R., Ellam, R. M., and Emeleus, C. H.: Trace element and isotope constraints on crustal anatexis by upwelling mantle melts in the North Atlantic Igneous Province: an example from the Isle of Rum, NW Scotland, Geol. Magazine, 146, 382–399, https://doi.org/10.1017/S0016756809006244, 2009.

Meyer, W. and Stets, J.: Das Rheintal zwischen Bingen und Bonn, Borntraeger, Berlin, 386 pp., ISBN 978-3-443-15069-3, 1996.

Moine, O., Antoine, P., Hatté, C., Landais, A., Mathieu, J., Prud'homme, C., and Rousseau, D. D.: The impact of Last Glacial climate variability in west-European loess revealed by radiocarbon dating of fossil earthworm granules, P. Natl. Acad. Sci. USA, 114, 209–214, https://doi.org/10.1073/pnas.1614751114, 2017.

Moragues-Quiroga, C., Juilleret, J., Gourdol, L., Pelt, E., Perrone, T., Aubert, A., Morvan, G., Chabaux, F., Legout, A., Stille, P., and Hissler, C.: Genesis and evolution of regoliths: Evidence from trace and major elements and Sr-Nd-Pb-U isotopes, CATENA, 149, 185–198, https://doi.org/10.1016/j.catena.2016.09.015, 2017.

Mroczek, P.: Recycled loesses – A micromorphological approach to the determination of local source areas of Weichselian loess, Quaternary Int., 296, 241–250, https://doi.org/10.1016/j.quaint.2013.02.040, 2013.

Muhs, D. R.: The geologic records of dust in the quaternary, Aeolian Res., 9, 3–48, https://doi.org/10.1016/j.aeolia.2012.08.001, 2013.

Obreht, I., Zeeden, C., Hambach, U., Veres, D., Marković, S. B., Bösken, J., Svirčev, Z., Bačević, N., Gavrilov, M. B., and Lehmkuhl, F.: Tracing the influence of Mediterranean climate on Southeastern Europe during the past 350,000 years, Sci. Rep., 6, 36334, https://doi.org/10.1038/srep36334, 2016.

Ozer, M., Orhan, M., and Isik, N. S.: Effect of Particle Optical Properties on Size Distribution of Soils Obtained by Laser Diffraction, Environ. Eng. Geosci., 16, 163–173, https://doi.org/10.2113/gseegeosci.16.2.163, 2010.

Pinto, J. G. and Ludwig, P.: Extratropical cyclones over the North Atlantic and western Europe during the Last Glacial Maximum and implications for proxy interpretation, Clim. Past, 16, 611–626, https://doi.org/10.5194/cp-16-611-2020, 2020.

Pötter, S., Veres, D., Baykal, Y., Nett, J. J., Schulte, P., Hambach, U., and Lehmkuhl, F.: Disentangling Sedimentary Pathways for the Pleniglacial Lower Danube Loess Based on Geochemical Signatures, Front. Earth Sci., 9, 600010, https://doi.org/10.3389/feart.2021.600010, 2021.

Preusser, F., Büschelberger, M., Kemna, H. A., Miocic, J., Mueller, D., and May, J.-H.: Exploring possible links between Quaternary aggradation in the Upper Rhine Graben and the glaciation history of northern Switzerland, Int. J. Earth Sci. (Geol. Rundsch), 110, 1827–1846, https://doi.org/10.1007/s00531-021-02043-7, 2021.

Profe, J., Zolitschka, B., Schirmer, W., Frechen, M., and Ohlendorf, C.: Geochemistry unravels MIS 3/2 paleoenvironmental dynamics at the loess–paleosol sequence Schwalbenberg II, Germany, Palaeogeogr. Palaeoclim. Palaeoecol., 459, 537–551, https://doi.org/10.1016/j.palaeo.2016.07.022, 2016.

Prud'homme, C., Lécuyer, C., Antoine, P., Hatté, C., Moine, O., Fourel, F., Amiot, R., Martineau, F., and Rousseau, D.-D.: δ 13 C signal of earthworm calcite granules: A new proxy for palaeoprecipitation reconstructions during the Last Glacial in western Europe, Quaternary Sci. Rev., 179, 158–166, https://doi.org/10.1016/j.quascirev.2017.11.017, 2018.

Prud'homme, C., Fischer, P., Jöris, O., Gromov, S., Vinnepand, M., Hatté, C., Vonhof, H., Moine, O., Vött, A., and Fitzsimmons, K. E.: Millennial-timescale quantitative estimates of climate dynamics in central Europe from earthworm calcite granules in loess deposits, Commun. Earth Environ., 3, 1–14, https://doi.org/10.1038/s43247-022-00595-3, 2022.

Rasmussen, S. O., Bigler, M., Blockley, S. P., Blunier, T., Buchardt, S. L., Clausen, H. B., Cvijanovic, I., Dahl-Jensen, D., Johnsen, S. J., Fischer, H., Gkinis, V., Guillevic, M., Hoek, W. Z., Lowe, J. J., Pedro, J. B., Popp, T., Seierstad, I. K., Steffensen, J. P., Svensson, A. M., Vallelonga, P., Vinther, B. M., Walker, M. J. C., Wheatley, J. J., and Winstrup, M.: A stratigraphic framework for abrupt climatic changes during the Last Glacial period based on three synchronized Greenland ice-core records: refining and extending the INTIMATE event stratigraphy, Quaternary Sci. Rev., 106, 14–28, https://doi.org/10.1016/j.quascirev.2014.09.007, 2014.

Reimer, P. J., Austin, W. E. N., Bard, E., Bayliss, A., Blackwell, P. G., Bronk Ramsey, C., Butzin, M., Cheng, H., Edwards, R. L., Friedrich, M., Grootes, P. M., Guilderson, T. P., Hajdas, I., Heaton, T. J., Hogg, A. G., Hughen, K. A., Kromer, B., Manning, S. W., Muscheler, R., Palmer, J. G., Pearson, C., Van Der Plicht, J., Reimer, R. W., Richards, D. A., Scott, E. M., Southon, J. R., Turney, C. S. M., Wacker, L., Adolphi, F., Büntgen, U., Capano, M., Fahrni, S. M., Fogtmann-Schulz, A., Friedrich, R., Köhler, P., Kudsk, S., Miyake, F., Olsen, J., Reinig, F., Sakamoto, M., Sookdeo, A., and Talamo, S.: The IntCal20 Northern Hemisphere Radiocarbon Age Calibration Curve (0–55 cal kBP), Radiocarbon, 62, 725–757, https://doi.org/10.1017/RDC.2020.41, 2020.

Reutenauer, C., Landais, A., Blunier, T., Bréant, C., Kageyama, M., Woillez, M.-N., Risi, C., Mariotti, V., and Braconnot, P.: Quantifying molecular oxygen isotope variations during a Heinrich stadial, Clim. Past, 11, 1527–1551, https://doi.org/10.5194/cp-11-1527-2015, 2015.

Römer, W., Lehmkuhl, F., and Sirocko, F.: Late Pleistocene aeolian dust provenances and wind direction changes reconstructed by heavy mineral analysis of the sediments of the Dehner dry maar (Eifel, Germany), Global Planet. Change, 147, 25–39, https://doi.org/10.1016/j.gloplacha.2016.10.012, 2016.

Rousseau, D. D., Sima, A., Antoine, P., Hatté, C., Lang, A., and Zöller, L.: Link between European and North Atlantic abrupt climate changes over the last glaciation, Geophys. Res. Lett., 34, L22713, https://doi.org/10.1029/2007GL031716, 2007.

Rousseau, D.-D., Derbyshire, E., Antoine, P., and Hatté, C.: European Loess Records, Reference Module in Earth Systems and Environmental Sciences, Elsevier, Amsterdam, https://doi.org/10.1016/b978-0-12-409548-9.11136-4, 2018.

Sauer, D. and Felix-Henningsen, P.: Saprolite, soils, and sediments in the Rhenish Massif as records of climate and landscape history, Quaternary Int., 156–157, 4–12, https://doi.org/10.1016/j.quaint.2006.05.001, 2006.

Schad, P., Van Huyssteen, M., Anjos, L., Gaistordo, C., Deckers, J., Dondeyne, S., Eberhardt, E., Gerasimova, M., Harms, B., Jones, A., Krasilnikov, P., Reinsch, T., Vargas, T., and Zhang, G.: World reference base for soil resources 2014 International soil classification system for naming soils and creating legends for soil maps, 3rd Ed., edited by: Peter Schad, Cornie van Huyssteen, Erika Micheli, FAO, Rome (Italy), ISBN 978-92-5-108369-7, 2015.

Schaetzl, R. J., Bettis, E. A., Crouvi, O., Fitzsimmons, K. E., Grimley, D. A., Hambach, U., Lehmkuhl, F., Marković, S. B., Mason, J. A., Owczarek, P., Roberts, H. M., Rousseau, D.-D., Stevens, T., Vandenberghe, J., Zárate, M., Veres, D., Yang, S., Zech, M., Conroy, J. L., Dave, A. K., Faust, D., Hao, Q., Obreht, I., Prud'homme, C., Smalley, I., Tripaldi, A., Zeeden, C., and Zech, R.: Approaches and challenges to the study of loess – Introduction to the LoessFest Special Issue, Quaternary Res., 89, 563–618, https://doi.org/10.1017/qua.2018.15, 2018.

Schaffernicht, E. J., Ludwig, P., and Shao, Y.: Linkage between dust cycle and loess of the Last Glacial Maximum in Europe, Atmos. Chem. Phys., 20, 4969–4986, https://doi.org/10.5194/acp-20-4969-2020, 2020.

Schatz, A.-K., Qi, Y., Siebel, W., Wu, J., and Zöller, L.: Tracking potential source areas of Central European loess: examples from Tokaj (HU), Nussloch (D) and Grub (AT), Open Geosci., 7, 678–7, https://doi.org/10.1515/geo-2015-0048, 2015.

Schirmer, W.: Eine Klimakurve des Oberpleistozäns aus dem rheinischen Löss, E&G Quaternary Sci. J., 50, 25–49, https://doi.org/10.3285/eg.50.1.02, 2000.

Schirmer, W.: Rhine loess at Schwalbenberg II — MIS 4 and 3, E&G Quaternary Sci. J., 61, 32–47, https://doi.org/10.3285/eg.61.1.03, 2011.

Schmidt, C., Zeeden, C., Krauß, L., Lehmkuhl, F., and Zöller, L.: A chronological and palaeoenvironmental re-evaluation of two loess-palaeosol records in the northern Harz foreland, Germany, based on innovative modelling tools, Boreas, 50, 746–763, https://doi.org/10.1111/bor.12510, 2021.

Schubert, S., Jung, S., Pfänder, J. A., Hauff, F., and Garbe-Schönberg, D.: Petrogenesis of Tertiary continental intraplate lavas between Siebengebirge and Westerwald, Germany: Constraints from trace element systematics and Nd, Sr and Pb isotopes, J. Volcanol. Geotherm. Res., 305, 84–99, https://doi.org/10.1016/J.JVOLGEORES.2015.08.023, 2015.

Schulte, P. and Lehmkuhl, F.: The difference of two laser diffraction patterns as an indicator for post-depositional grain size reduction in loess-paleosol sequences, Palaeogeogr. Palaeoclim. Palaeoecol., 509, 126–136, https://doi.org/10.1016/j.palaeo.2017.02.022, 2018.

Schulte, P., Lehmkuhl, F., Steininger, F., Loibl, D., Lockot, G., Protze, J., Fischer, P., and Stauch, G.: Influence of HCl pretreatment and organo-mineral complexes on laser diffraction measurement of loess–paleosol-sequences, CATENA, 137, 392–405, https://doi.org/10.1016/j.catena.2015.10.015, 2016.

Seelos, K., Sirocko, F., and Dietrich, S.: A continuous high-resolution dust record for the reconstruction of wind systems in central Europe (Eifel, Western Germany) over the past 133 ka, Geophys. Res. Lett., 36, L2072, https://doi.org/10.1029/2009GL039716, 2009.

Sheldon, N. D. and Tabor, N. J.: Quantitative paleoenvironmental and paleoclimatic reconstruction using paleosols, Earth-Sci. Rev., 95, 1–52, https://doi.org/10.1016/j.earscirev.2009.03.004, 2009.

Siebel, W., Eroğlu, S., Shang, C. K., and Rohrmüller, J.: Zircon geochronology, elemental and Sr-Nd isotope geochemistry of two Variscan granitoids from the Odenwald-Spessart crystalline complex (mid-German crystalline rise), Mineral. Petrol., 105, 187–200, https://doi.org/10.1007/s00710-012-0200-3, 2012.

Sirocko, F., Knapp, H., Dreher, F., Förster, M. W., Albert, J., Brunck, H., Veres, D., Dietrich, S., Zech, M., Hambach, U., Röhner, M., Rudert, S., Schwibus, K., Adams, C., and Sigl, P.: The ELSA-Vegetation-Stack: Reconstruction of Landscape Evolution Zones (LEZ) from laminated Eifel maar sediments of the last 60,000 years, Global Planet. Change, 142, 108–135, https://doi.org/10.1016/j.gloplacha.2016.03.005, 2016.

Smalley, I., O'Hara-Dhand, K., Wint, J., Machalett, B., Jary, Z., and Jefferson, I.: Rivers and loess: The significance of long river transportation in the complex event-sequence approach to loess deposit formation, Quaternary Int., 198, 7–18, https://doi.org/10.1016/j.quaint.2008.06.009, 2009.

Tarling, D. H. and Hrouda, F.: The Magnetic Anisotropy of Rocks, Chapman & Hall, London, 1993.

Taylor, S. N. and Lagroix, F.: Magnetic anisotropy reveals the depositional and postdepositional history of a loess-paleosol sequence at Nussloch (Germany): AMS of the Nussloch Loess-Paleosol Sequence, J. Geophys. Res.-Solid Earth, 120, 2859–2876, https://doi.org/10.1002/2014JB011803, 2015.

Taylor, S. N., Lagroix, F., Rousseau, D. D., and Antoine, P.: Mineral magnetic characterization of the upper pleniglacial nussloch loess sequence (Germany): An insight into local environmental processes, Geophys. J. Int., 199, 1463–1480, https://doi.org/10.1093/gji/ggu331, 2014.

Toucanne, S., Soulet, G., Freslon, N., Jacinto, R. S., Dennielou, B., Zaragosi, S., Eynaud, F., Bourillet, J.-F., and Bayon, G.: Millennial-scale fluctuations of the European Ice Sheet at the end of the last glacial, and their potential impact on global climate, Quaternary Sci. Rev., 123, 113–133, 2015.

Tricca, A., Stille, P., Steinmann, M., Kiefel, B., Samuel, J., and Eikenberg, J.: Rare earth elements and Sr and Nd isotopic compositions of dissolved and suspended loads from small river systems in the Vosges mountains (France), the river Rhine and groundwater, Chem. Geol., 160, 139–158, https://doi.org/10.1016/S0009-2541(99)00065-0, 1999.

Újvári, G., Varga, A., Ramos, F. C., Kovács, J., Németh, T., and Stevens, T.: Evaluating the use of clay mineralogy, Sr–Nd isotopes and zircon U–Pb ages in tracking dust provenance: An example from loess of the Carpathian Basin, Chem. Geol., 304–305, 83–96, https://doi.org/10.1016/j.chemgeo.2012.02.007, 2012.

Újvári, G., Kok, J. F., Varga, G., and Kovács, J.: The physics of wind-blown loess: Implications for grain size proxy interpretations in Quaternary paleoclimate studies, Earth-Sci. Rev., 154, 247–278, https://doi.org/10.1016/j.earscirev.2016.01.006, 2016.

Újvári, G., Stevens, T., Molnár, M., Demény, A., Lambert, F., Varga, G., Jull, A. J. T., Páll-Gergely, B., Buylaert, J.-P., and Kovács, J.: Coupled European and Greenland last glacial dust activity driven by North Atlantic climate, P. Natl. Acad. Sci. USA, 114, E10632–E10638, https://doi.org/10.1073/pnas.1712651114, 2017.

Újvári, G., Klötzli, U., Stevens, T., Svensson, A., Ludwig, P., Vennemann, T., Gier, S., Horschinegg, M., Palcsu, L., Hippler, D., Kovács, J., Di Biagio, C., and Formenti, P.: Greenland Ice Core Record of Last Glacial Dust Sources and Atmospheric Circulation, J. Geophys. Res.-Atmos., 127, e2022JD036597, https://doi.org/10.1029/2022JD036597, 2022.

Vandenberghe, J.: Grain size of fine-grained windblown sediment: A powerful proxy for process identification, Earth-Sci. Rev., 121, 18–30, https://doi.org/10.1016/j.earscirev.2013.03.001, 2013.

Vandenberghe, J., Mücher, H., Roebroeks, W., and Gemke, D.: Lithostratigraphy and palaeoenvironment of the Pleistocene deposits at Maastricht-Belvédère, southern Limburg, the Netherlands, Analecta Praehistorica Leidensia 18-Maastricht-Belvédère: Stratigraphy, palaeoenvironment and archaeology of the middle and late pleistocene deposits, Analecta Praehist. Leiden, 18, 7–18, 1985.

Vandenberghe, J., Zhisheng, A., Nugteren, G., Huayu, L., and Van Huissteden, K.: New absolute time scale for the Quaternary climate in the Chinese Loess region by grain-size analysis, Geology, 25, 35–38, https://doi.org/10.1130/0091-7613(1997)025<0035:NATSFT>2.3.CO;2, 1997.

Vinnepand, M., Fischer, P., Fitzsimmons, K., Thornton, B., Fiedler, S., and Vött, A.: Combining Inorganic and Organic Carbon Stable Isotope Signatures in the Schwalbenberg Loess-Palaeosol-Sequence Near Remagen (Middle Rhine Valley, Germany), Front. Earth Sci., 8, 276, https://doi.org/10.3389/feart.2020.00276, 2020.

Vinnepand, M., Fischer, P., Jöris, O., Hambach, U., Zeeden, C., Schulte, P., Fitzsimmons, K. E., Prud'homme, C., Perić, Z., Schirmer, W., Lehmkuhl, F., Fiedler, S., and Vött, A., Decoding geochemical signals of the Schwalbenberg Loess-Palaeosol-Sequences – A key to Upper Pleistocene ecosystem responses to climate changes in western Central Europe, Catena, 212, 106076, https://doi.org/10.1016/j.catena.2022.106076, 2022.

von Suchodoletz, H., Kühn, P., Hambach, U., Dietze, M., Zöller, L., and Faust, D.: Loess-like and palaeosol sediments from Lanzarote (Canary Islands/Spain) – Indicators of palaeoenvironmental change during the Late Quaternary, Palaeogeogr. Palaeoclimatol. Palaeoecol., 278, 71–87, https://doi.org/10.1016/j.palaeo.2009.03.019, 2009.

Wang, Y.-X., Yang, J.-D., Chen, J., Zhang, K.-J., and Rao, W.-B.: The Sr and Nd isotopic variations of the Chinese Loess Plateau during the past 7 Ma: Implications for the East Asian winter monsoon and source areas of loess, Palaeogeogr. Palaeoclimatol. Palaeoecol., 249, 351–361, https://doi.org/10.1016/j.palaeo.2007.02.010, 2007.

Weltje, G. J., Bloemsma, M. R., Tjallingii, R., Heslop, D., Röhl, U., and Croudace, I. W.: Prediction of Geochemical Composition from XRF Core Scanner Data: A New Multivariate Approach Including Automatic Selection of Calibration Samples and Quantification of Uncertainties, in: Micro-XRF Studies of Sediment Cores: Applications of a non-destructive tool for the environmental sciences, edited by: Croudace, I. W. and Rothwell, R. G., Springer Netherlands, Dordrecht, 507–534, https://doi.org/10.1007/978-94-017-9849-5_21, 2015.

Wörner, G., Staudigel, H., and Zindler, A.: Isotopic constraints on open system evolution of the Laacher See magma chamber (Eifel, West Germany), Earth Planet. Sci. Lett., 75, 37–49, https://doi.org/10.1016/0012-821X(85)90048-2, 1985.

Zech, M., Zech, R., Zech, W., Glaser, B., Brodowski, S., and Amelung, W.: Characterisation and palaeoclimate of a loess-like permafrost palaeosol sequence in NE Siberia, Geoderma, 143, 281–295, https://doi.org/10.1016/j.geoderma.2007.11.012, 2008.

Zeeden, C. and Hambach, U.: Magnetic Susceptibility Properties of Loess From the Willendorf Archaeological Site: Implications for the Syn/Post-Depositional Interpretation of Magnetic Fabric, Front. Earth Sci., 8, 599491, https://doi.org/10.3389/feart.2020.599491, 2021.

Zeeden, C., Hambach, U., and Händel, M.: Loess magnetic fabric of the Krems-Wachtberg archaeological site, Quaternary Int., 372, 188–194, https://doi.org/10.1016/j.quaint.2014.11.001, 2015.

Zeeden, C., Hambach, U., Obreht, I., Hao, Q., Abels, H. A., Veres, D., Lehmkuhl, F., Gavrilov, M. B., and Marković, S. B.: Patterns and timing of loess-paleosol transitions in Eurasia: Constraints for paleoclimate studies, Global Planet. Change, 162, 1-7, https://doi.org/10.1016/j.gloplacha.2017.12.021, 2018.

Zens, J., Zeeden, C., Römer, W., Fuchs, M., Klasen, N., and Lehmkuhl, F.: The Eltville Tephra (Western Europe) age revised: Integrating stratigraphic and dating information from different Last Glacial loess localities, Palaeogeogr. Palaeoclimatol. Palaeoecol., 466, 240–251, https://doi.org/10.1016/j.palaeo.2016.11.033, 2017.

Zhang, Q., Appel, E., Stanjek, H., Byrne, J. M., Berthold, C., Sorwat, J., Rösler, W., and Seemann, T.: Humidity related magnetite alteration in an experimental setup, Geophys. J. Int., 224, 69–85, https://doi.org/10.1093/gji/ggaa394, 2021.

Zhang, R., Kravchinsky, V. A., Zhu, R., and Yue, L.: Paleomonsoon route reconstruction along a W–E transect in the Chinese Loess Plateau using the anisotropy of magnetic susceptibility: Summer monsoon model, Earth Planet. Sci. Lett., 299, 436–446, https://doi.org/10.1016/j.epsl.2010.09.026, 2010.

Zhu, X., Liu, L., Wang, X., and Ji, J.: The Sr-Nd isotope geochemical tracing of Xiashu Loess and its implications for the material transport mechanism of the Yangtze River, CATENA, 203, 105335, https://doi.org/10.1016/j.catena.2021.105335, 2021.

E&G Quaternary Sci. J., 72, 95–111, 2023
https://doi.org/10.5194/egqsj-72-95-2023

Open Access E&G Quaternary Science Journal

Research article

Late Weichselian–Holocene valley development of the Elbe valley near Dresden – linking sedimentation, soil formation and archaeology

Christian Tinapp[1,2], **Johannes Selzer**[2], **Norman Döhlert-Albani**[1], **Birgit Fischer**[1], **Susann Heinrich**[3], **Christoph Herbig**[4], **Frauke Kreienbrink**[1], **Tobias Lauer**[3,5], **Birgit Schneider**[2], and **Harald Stäuble**[1]

[1]Saxonian Archaeological Heritage Office, Zur Wetterwarte 7, 01109 Dresden, Germany
[2]Institute of Geography, Leipzig University, Johannisallee 19a, 04103 Leipzig, Germany
[3]Max Planck Institute for Evolutionary Anthropology, Deutscher Platz 6, 04103 Leipzig, Germany
[4]independent researcher: Am Dorf 12, 63517 Rodenbach, Germany
[5]Department of Geosciences, University of Tübingen, Schnarrenbergerstrasse 94–96, 72076 Tübingen, Germany

Correspondence: Christian Tinapp (christian.tinapp@lfa.sachsen.de) and Johannes Selzer (johannes.selzer@bodengeo.de)

Relevant dates: Received: 21 July 2022 – Revised: 13 March 2023 – Accepted: 22 March 2023 – Published: 16 May 2023

How to cite: Tinapp, C., Selzer, J., Döhlert-Albani, N., Fischer, B., Heinrich, S., Herbig, C., Kreienbrink, F., Lauer, T., Schneider, B., and Stäuble, H.: Late Weichselian–Holocene valley development of the Elbe valley near Dresden – linking sedimentation, soil formation and archaeology, E&G Quaternary Sci. J., 72, 95–111, https://doi.org/10.5194/egqsj-72-95-2023, 2023.

Abstract: Valley infills are essential for understanding changes in hydrology and landscape. Anthropogenic activities are proven by prehistoric settlement remains, which mark distinct sediments and soils as usable land during certain time periods. In 2009 and 2018/19, excavations by the Saxonian Archaeological Heritage Office were conducted in the Elbe valley between Meißen and Dresden, preceding the construction of two natural gas pipelines. As a result, two important multicultural prehistoric sites were discovered on the Lower Weichselian Terrace (LWT) in different sediments and on varying stratigraphic levels.

During this study sediments and soils at the excavation sites and throughout the pipe trench have been documented. Micromorphological, sedimentological and geochemical investigations and analyses of archaeobotanical and archaeological finds, complemented by ^{14}C and optically stimulated luminescence (OSL) dating, enabled deciphering the structure of sediments and soils. Two major sites were the focus. At the Clieben site, an early Neolithic settlement and former topsoil, developed in a Weichselian valley loam above gravels and sands, are covered by younger overbank fines. At the Brockwitz site, shallow incision channels in the LWT were filled with clayey overbank fines during the Preboreal. An overprinting humic soil horizon was later anthropogenically overprinted during the early and middle Neolithic period. An omnipresent layer of Subboreal or younger overbank fines, covering the majority of the LWT in combination with the spatially confined Preboreal overbank fines, mirrors the ever-growing risk of flooding in a formerly attractive settlement area.

Published by Copernicus Publications on behalf of the Deutsche Quartärvereinigung (DEUQUA) e.V.

Kurzfassung: Talsedimente erlauben wichtige Einblicke in Veränderungen der Landschaft und der Hydrologie. Prähistorische anthropogene Aktivitäten hinterlassen Spuren in Sediment und Boden, die für bestimmte Phasen die Nutzbarkeit belegen. In den Jahren 2009 und 2018/19 führte der Bau von zwei Erdgasleitungen zu Ausgrabungen des Landesamtes für Archäologie Sachsen im Elbetal zwischen Meißen und Dresden. Zwei mehrphasige Siedlungsplätze wurden auf der Tieferen Niederterrasse (Lower Weichselian Terrace, LWT) entdeckt. Die Funde lagen in unterschiedlichen Sedimenten auf verschiedenen stratigraphischen Niveaus. Im Rahmen der Arbeiten wurden Sedimente und Böden im Bereich der Ausgrabungsplätze und im Bereich des Rohrgrabens aufgenommen. Mikromorphologische, sedimentologische, geochemische Untersuchungen, archäobotanische und archäologische Funde sowie ^{14}C- und OSL-Datierungen ermöglichen die zeitliche Einordnung der Sedimente und Böden. Dabei stehen zwei größere Areale im Fokus. Im Cliebener Untersuchungsareal liegen frühneolithische Siedlungsreste im Bereich eines begrabenen Bodens aus weichselzeitlichem Tallehm über Kiesen und Sanden, die von jüngeren Auenlehmen überdeckt werden. Im Brockwitzer Untersuchungsareal befinden sich flach eingeschnittene Rinnen in der LWT, die bereits im Präboreal mit tonigem Lehm verfüllt wurden. Ein in diesen Sedimenten entstandener humoser Oberbodenhorizont wurde durch anthropogene Aktivitäten während des Früh- und Mittelneolithikums überprägt. Nahezu die gesamte LWT wird von jüngeren Auenlehmen überdeckt, die seit dem Subboreal abgelagert wurden. Dies belegt die zunehmende Gefahr von Überschwemmungen auf einer ehemals siedlungsgünstigen Terrassenfläche.

1 Introduction

Archaeological sites in river valleys are important sources to reconstruct the Late Pleistocene–Holocene landscape development. This is due to the fact that prehistoric settlements or activities on the surfaces of different sediment and soil types demonstrate their accessibility for at least temporal site usage and that this accessibility strongly interacted with the river dynamics controlled by different external factors – tectonic activity, climate change, base level change and anthropogenic activity (Kaiser et al., 2012; Houben et al., 2013; Notebaert et al., 2018; Tinapp et al., 2019; Khoravichenar et al., 2020; von Suchodoletz et al., 2018, 2022).

The Elbe is the largest river in northeastern Germany. However, compared with other important central European river systems, such as the Rhine (Schirmer 1995), Vistula (Starkel et al., 2006) or Danube (Schellmann, 2018), late Weichselian–Holocene river and valley development is only fragmentarily understood (Kaiser et al., 2012). This is also caused by the fact that many archaeological sites within the Elbe valley still lack precise allocations to distinct sedimentary units (Ullrich and Ender, 2014; Conrad and Ender, 2016; Meller and Friederich, 2018). During the last years two pipeline construction projects have facilitated valuable transects across the sediments of the upper Elbe valley between the cities of Dresden and Meißen, allowing for studying the late Weichselian–Holocene evolution.

In the course of the archaeological excavations during the construction of the OPAL (Ostsee-Pipeline-Anbindungsleitung) natural gas pipeline in 2009, performed by the Saxonian Archaeological Heritage Office, an early Neolithic, middle Neolithic, late Bronze Age and medieval Slavic settlement were discovered (Steinmann, 2010). Later on, the construction of the EUGAL (Europäische Gas-Anbindungsleitung) pipeline parallel to the OPAL in 2019 allowed for further excavations, resulting in the expansion of already known and the discovery of new archaeological sites such as an early Mesolithic camp site and a middle Neolithic palisade/ditch enclosure (Kreienbrink et al., 2020; Döhlert-Albani et al., 2022; Stäuble et al., 2022).

Nearly all those archaeological sites were subsequently covered by overbank fines, whereas their archaeological features cut different older sediment units mostly belonging to the Lower Weichselian Terrace (LWT; “Tiefere weichselzeitliche Niederterrasse”) of the Elbe River. Former geologic references indicate the sediments of the LWT to be sand and gravels with a younger cover of sandy loam or loamy sand called “valley loam” (*Tallehm*; Alexowsky, 2005). However, the discovery of not yet described clayey sediments with an overprinting palaeosol covering the LWT at the Brockwitz study site made further studies necessary.

Hence, this study aims to reconstruct the late Weichselian–Holocene evolution of the Elbe valley between the cities of Dresden and Meißen. This will allow for valid conclusions about former human occupation and its geomorphic–palaeoenvironmental context in the river valley and a comparison with the fluvial histories of other central European river systems. During our study we applied a comprehensive geoarchaeological approach that closely combined geoscientific methods with the archaeological excavations, an approach that is necessary to precisely study human–environmental interactions but that has been not very often systematically applied so far (von Suchodoletz et al., 2020). Our geoscientific set of methods encompassed stratigraph-

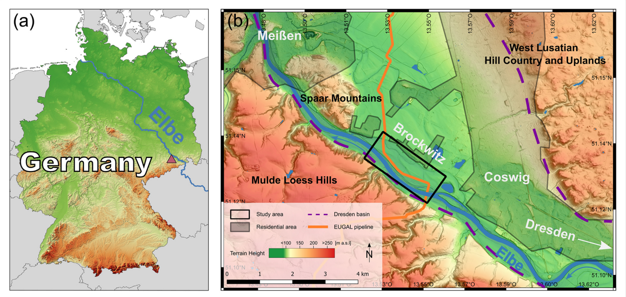

Figure 1. **(a)** The location of the study site with the Elbe River course and **(b)** the EUGAL pipeline in the Elbe valley with the study site (© GeoBasis-DE/BKG 2020, DGM1-GeoSN, OpenStreetMap contributors 2020 under the Open Data Commons Open Database License (ODbL) v1.0).

ical, micromorphological, sedimentological–geochemical and archaeobotanical methods as well as radiocarbon and luminescence dating and enabled the analysis of the formerly and newly detected fluvial sediments and palaeosols and their precise relations with former human activities.

2 Regional setting

The study area is situated in the northwestern Dresden basin ("Dresdner Elbtalweitung"), between the cities of Coswig and Meißen on the right Elbe banks (Figs. 1 and 2). Here, the about 3–8 km wide Dresden basin is framed by the West Lusatian Hill Country and Uplands ("Westlausitzer Hügel- und Bergland") granite massif to the east and northeast, the Mulde Loess Hills ("Mulde-Lösshügelland") to the west and the hilly "Großenhainer Pflege" to the north (Mannsfeld and Bernhardt, 2008; Tinapp, 2022).

Being one of central Europe's largest rivers (river length of 1094 km, catchment of 148 000 km^2) (Pusch et al., 2009), the Elbe originates from the southern Giant Mountains ("Krkonoše") in the Czech Republic at 1386 m a.s.l. From there, the upper Elbe flows in an arc through Bohemia, heads north and after crossing the German border passes over into the middle Elbe valley when entering the North German Plain north of the city of Meißen. Finally, the river meets the North Sea west of Hamburg (Hantke, 1993; Pusch et al., 2009).

Between the cities of Dresden and Meißen the Elbe valley's course has been predefined by the Variscan Elbe Fault System (EFS), one of the major crustal shear zones in Europe (Scheck et al., 2002). Up to 650 m of Cretaceous shallow marine and alluvial sand- and limestone reflect a manifold landscape history in and around this sedimentary basin (Tröger 2008). Simultaneously to the formation of the North Atlantic, the EFS shear zone reactivated during a late Cretaceous–early Cenozoic compression phase, when western Lusatia was moved southwestwards and thrusted over the EFS and its Cretaceous sediments (Krentz, 2008).

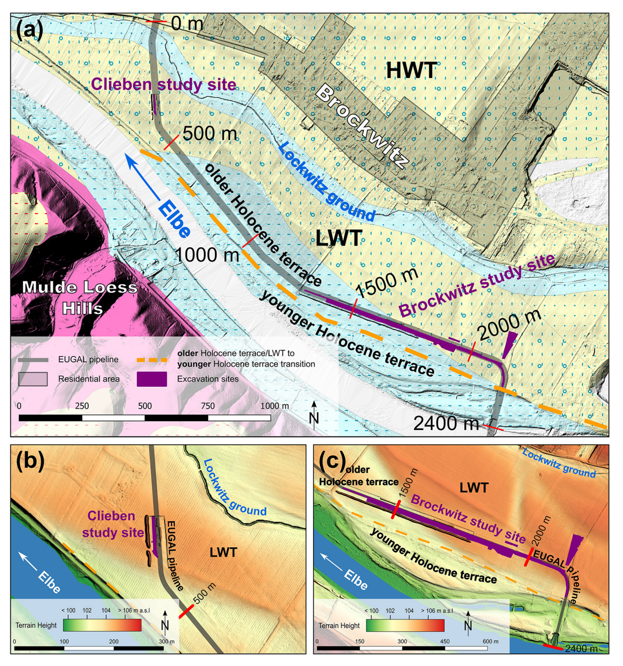

Figure 2. **(a)** Detailed view of the study area around the EUGAL pipeline with close-ups on the **(b)** Clieben and **(c)** Brockwitz study sites (© DGM1-GeoSN, OpenStreetMap contributors 2020 under the Open Data Commons Open Database License (ODbL) v1.0: Geologische Karte der eiszeitlich bedeckten Gebiete Sachsen 1 : 50 000 – LfULG Sachsen).

Until the Pliocene, a levelled landscape with shallow river valleys and a higher altitude than the current highlands had established. Throughout the Quaternary strong fluvial incision took place, resulting in the formation of multiple sets of river terraces (Wolf et al., 2008). In the study area, the current Elbe valley was initially used by several smaller streams, and only strong meltwater erosion caused by a lowered erosional base following the Elster 2 glaciation enabled the Elbe River to flow along its quasi-current course in the Dresden basin.

During the Drenthe stage of the Saalian glaciation the glaciers maximally advanced just south of the city of Meißen (Eissmann, 2002). Subsequently, up to 20 m thick sands were deposited in the Elbe valley by melting water. During the following Warthe stage strong river erosion occurred, forming several deep channels southeast of the Spaar Mountains, which represent the Quaternary base in this part of the Elbe valley (Huhle, 2015) (Fig. 1b).

During the Weichselian glaciation, a gravely Higher Weichselian Terrace (HWT) and Lower Weichselian Terrace (LWT) were aggraded under periglacial conditions (Wolf et al., 1994; Eissmann, 2002). Most likely during the Last Glacial Maximum were the gravely LWT sediments subsequently covered by a so-called valley loam (Tallehm; Alexowsky, 2005). Due to erosional processes during the Weichselian deglaciation, full LWT sequences including the covering valley loam are only rarely preserved (Eissmann, 1997).

During the Late Pleistocene and Holocene two additional fluvial terraces were aggraded (Wolf et al., 2008). The older and morphologically higher terrace is dated from the Late Pleistocene to Middle Holocene (Wolf et al., 1994, 2008), and the younger one had formed since the late Subboreal (Wolf et al., 2008; Lange et al., 2016). Holocene overbank fines cover both Holocene terraces and the LWT.

The Elbe valley between the cities of Dresden and Meißen has been occupied by sedentary humans for the last ca. 7500 years (Brestrich, 1998; Stäuble, 2010, 2016). Accordingly, during archaeological excavations in 2009 and 2018/19 at our Clieben study site, features of an early Neolithic village were discovered within the valley loam in the uppermost part of the LWT fines that was covered by younger overbank fines (Fig. 4; Steinmann, 2010; Kreienbrink et al., 2020; Kreienbrink, 2022). Here, about 10 LPC (Linear Pottery culture) houses were detected, and a large-scale geophysical survey gave evidence that these belong to a major early Neolithic settlement. Also a few late Bronze Age features were found between the early Neolithic pits on the same stratigraphical level (Kreienbrink, 2022).

Further to the south, at our Brockwitz study site, early Mesolithic, early and middle Neolithic, early and late Bronze Age, Iron Age, and medieval Slavic archaeological remains have been uncovered at different levels within different deposits during archaeological excavations in 2009 and 2018/19 (Steinmann, 2010; Kreienbrink et al., 2020; Döhlert-Albani et al., 2022). Most sites were situated on the LWT, and only early medieval Slavic features were predominantly situated on the older Holocene terrace (Tinapp et al., 2022).

3 Methods

3.1 Fieldwork

Parallel to the EUGAL pipeline construction in 2019, a 2400 m long stretch of the pipe trench with a depth of about 3 m, locally 6 m, has been examined. As a result, 42 profiles were logged, and the strata's courses were recorded and paralleled. The distinct strata were characterized in the field for grain size; sediment/soil colour; humus and moisture content; and pedogenetic and further features such as archaeological finds, plant material, sediment features or anomalies. Furthermore, plant and/or wood material was taken for radiocarbon dating.

At the Clieben and Brockwitz study sites profiles have been recorded in detail during the excavations. Their description followed the FAO (Food and Agriculture Organization of the United Nations) classification (IUSS Working Group WRB, 2014; soil colour was determined using the Munsell soil colour chart). Furthermore, samples were taken for sedimentological, micromorphological and palaeoecological analyses, as well as for optically stimulated luminescence (OSL) dating.

3.2 Sedimentological analyses

- First, bulk sediment samples were air-dried and sieved to obtain the fine fraction of < 2 mm that was used for the analyses. A portion of this material was subsequently ground in a planetary ball mill (PM 200) for 10 min to obtain a grain size of < 30 µm that is needed for X-ray fluorescence (XRF) and elemental analysis (CNS). Grain-size analyses were conducted on organic-free (pretreated with 35 % H_2O_2) material. The sand fraction was analysed by sieve analysis, and the clay silt fraction was analysed by X-ray granulometry (XRG; Micromeritics SediGraph III 5120).

- pH values were measured in a 0.01 M $CaCl_2$ suspension following DIN ISO 10390 with a ratio of 1 : 2.5 (soil / water).

- Carbonate contents were measured with the volumetric method referring to Scheibler by using an Eijkelkamp calcimeter.

- Total organic carbon (TOC) was determined by measuring C_{total} with a vario EL cube elemental analyser (Elementar) and subsequently subtracting inorganic carbon (taken from the carbonate measurements) from C_{total}. Total nitrogen and sulfur contents were measured with the vario EL cube elemental analyser in parallel with C_{total}.

- Element concentrations were measured using non-destructive X-ray fluorescence spectrometry (XRF). For this purpose, bulk samples were mixed with a wax binder (CEREOX Licowax) and pressed into 32 mm pellets. The measurements were performed with an energy-dispersive polarization XRF (EDPXRF) SPECTRO XEPOS (SPECTRO Analytical Instruments Ltd.) analyser in a helium gas atmosphere. All elements from Na to U were determined simultaneously and adjusted to the sample weight.

Pedogenesis depends not only on the properties of the parent material, the climatic conditions and human activity but also significantly on time. Weathering indices are multicomponent ratios of lithogeochemical compositional element and are commonly used to estimate weathering intensity, since they depict structural and mineralogical changes of the sediments during weathering. Over the past decades, very different indices and element ratios have been developed for different sediments in various climates (Pandarinath, 2022). Generally, the applied ratios usually expressed as oxidic proportions in moles determined by means of XRF are included in the calculation. Ideally, the applied ratios should only have been altered by pedogenetic processes.

During weathering, soluble cations with a low ion potential of < 3 (e.g. K^+, Na^+, Ca^{2+}, Mg^{2+}) are washed out relatively easily, whereas e.g. Al^{3+} with a high ion potential of 5.9 is bound in clay minerals and forms relatively insoluble hydroxides between a pH value of 4 and 10. Thus, the Al_2O_3 content changes very little during weathering and can hence be assumed to be constant (Bowen, 1979; Kausch, 2009). Consequently we selected the weathering index (VWI, visual weathering index) of Birkeland (1999), whereof low ratios indicate intensive weathering:

$$\mathrm{VWI} = (\mathrm{K_2O} + \mathrm{Na_2O} + \mathrm{CaO} + \mathrm{MgO})/\mathrm{Al}_{2\mathrm{O}_3}.$$

In general, ion mobility decreases and the tendency of adsorption to fine-grain sediment or soil particles increases with a rising ion radius (Smykatz-Kloss et al., 2004). Hence, the larger Rb^+ ion is better adsorbed compared with the smaller K^+ ion so that the K_2O/Rb_2O ratio normally decreases during in situ soil formation. However, it is also assumed that high values in loess/palaeosol sequences could also reflect secondary potassium enrichment, possibly caused by clay accumulation due to the input of preweathered material (Fischer et al., 2012).

Also the ratios Rb/Sr and K_2O/Na_2O can be interpreted using differences in ionic radii. The respective smaller ions in the denominator ($Sr^{2''+}$ and Na^+) are more easily discharged as a result of weathering than the larger ions in the numerator (Rb^+ and K^+). Hence, high ratios represent strong weathering (Smykatz-Kloss, 2003; Reitner and Ottner, 2011).

3.3 Numerical dating

Luminescence (OSL) dating

Six luminescence samples were taken at the Brockwitz study site using light-tight steel tubes, which were hammered into the freshly cleaned outcrop walls (for sampling positions, see Fig. 7).

Preparation of the coarse-grain quartz fraction (180–250 µm) was done under subdued red light in the Department of Human Evolution, Max Planck Institute for Evolutionary Anthropology (Leipzig). Sample preparation started with drying and sieving, and subsequent chemical preparation included a treatment with 10 % HCl and 30 % H_2O_2 to remove carbonates and organic material, respectively. Following this, quartz was separated from the other mineral fractions by density separation using sodium polytungstate solutions (2.62 and 2.70 $\mathrm{g\,cm^{-3}}$). Finally, the quartz-rich material was etched with 40 % hydrofluoric acid (HF) for 60 min and subsequently resieved.

Equivalent dose (De) measurements using a single-grain regeneration (SAR) approach (Murray and Wintle, 2003) were performed on a Risø TL/OSL (thermoluminescence) DA-20 reader equipped with blue and IR-emitting diodes. The blue stimulated quartz signal was measured at 125 °C for 40 s, and the 340 nm emission was filtered through a Hoya U340 filter. Irradiation was conducted with a calibrated $^{90}Sr/^{90}Y$ beta source (dose rate of 0.1 $\mathrm{Gy\,s^{-1}}$). The preheat and cutheat temperatures were set to 170 °C, respectively, as this combination yielded satisfying results of the dose recovery test with a ratio of the measured to the given dose of 1.08 ± 0.09.

Between 24 and 48 aliquots with 2 mm size were measured of each sample. This aliquot size was chosen to obtain a sufficient high signal-to-noise ratio. The dose response curve was built with four regenerative doses, and for a quality check IR depletion and recycling ratios were determined. For final De estimation, only aliquots with deviations of $< 20\,\%$ from unity (IR depletion and recycling ratio) were accepted.

Material for dosimetry was taken from the sampling spots and their nearby surroundings. Concentrations of the radioactive elements U, Th and K were determined using high-resolution gamma spectrometry at the Felsenkeller laboratory (VKTA) in Dresden, Germany, using a N-type detector.

Radiocarbon dating

Five radiocarbon samples were analysed in the Curt-Engelhorn-Zentrum Archäometrie in Mannheim (CEZ) using accelerator mass spectrometry (AMS) radiocarbon dating and were calibrated using IntCal20 and SwissCal 1.0.

3.4 Micromorphology

Micromorphological samples were taken from the Brockwitz study site in 2018 to characterize the different sediment layers and soil horizons. Thin sections were prepared from oriented and undisturbed blocks that were impregnated with resin. The thin sections were analysed using a petrographic microscope under plane-polarized light (ppl), cross-polarized light (xpl) and oblique incident light (oil). The microscopic description mainly followed the terminology after Bullock et al. (1985) and Stoops (2003).

3.5 Palaeobotanical analyses

Plant macroremains were extracted by flotation and wet sieving (mesh widths of 2, 0.5 and 0.25 mm) and determined under magnification from 6.3× to 40× using standard literature (e.g. Cappers et al., 2012) and the reference collection at the Laboratory of Archaeobotany, Institute of Prehistoric Archaeology, Goethe University. Attribution of the taxa to ecological units followed Oberdorfer (2001).

4 Results

The pipe trench and especially the uncovered sediments and soils at the two study sites during the excavations (Clieben and Brockwitz) allowed for detailed examinations of the late Weichselian and Holocene deposits in the Elbe valley.

Table 1. Stratigraphical positions (also see Fig. 7), dosimetric data, equivalent doses (De) and quartz OSL ages of the luminescence samples taken from profile 17 at the Brockwitz study site. The De values are based on the weighted mean of all accepted single De’s.

Sample ID (L-Eva)	Unit	U [ppm]	Th [ppm]	K [%]	Cosmic Dose [mGy a^{-1}]	Total dose rate [mGy a^{-1}]	De (weighted mean) [Gy]	Age [ka]
1867	Overbank fines	3.9 ± 0.4	13.3 ± 0.8	1.87 ± 0.1	0.21 ± 0.02	3.09 ± 0.2	13.1 ± 3.7	4.24 ± 1.23
1868	Neolithic ditch	5.4 ± 0.6	14.6 ± 1.0	2.0 ± 0.1	0.19 ± 0.02	3.49 ± 0.2	28.2 ± 1.4	8.07 ± 0.64
1869	Clayey loam	4.1 ± 0.5	13.4 ± 0.9	1.92 ± 0.1	0.18 ± 0.02	3.15 ± 0.2	32.3 ± 3.7	10.27 ± 1.36
1870	Neolithic ditch	5.5 ± 0.6	14.4 ± 0.9	1.97 ± 0.1	0.18 ± 0.02	3.47 ± 0.2	27.2 ± 1.1	7.84 ± 0.58
1871	LWT sands	1.07 ± 0.2	2.98 ± 0.2	1.36 ± 0.1	0.17 ± 0.02	1.60 ± 0.2	25.1 ± 1.9	15.65 ± 2.15
1872	LWT sands	0.77 ± 0.2	2.32 ± 0.2	1.42 ± 0.1	0.16 ± 0.02	1.56 ± 0.2	22.9 ± 3.0	14.72 ± 2.60

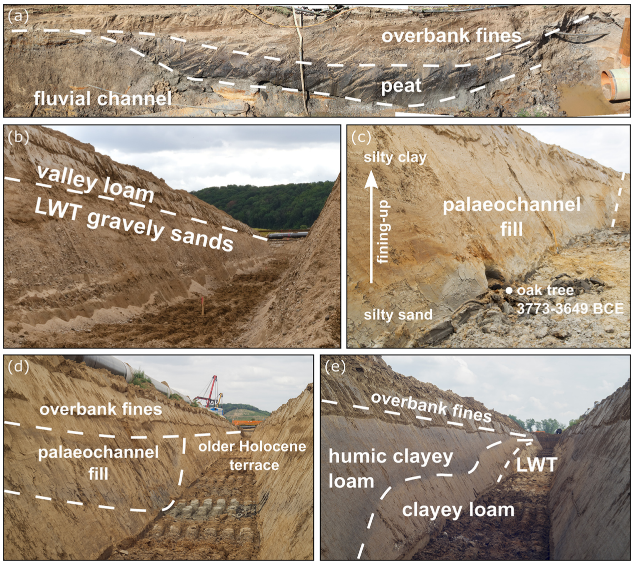

Figure 3. Several locations along the pipeline trench. **(a)** West-oriented profile in the Lockwitz ground, exposing peat covered by overbank fines surrounded by fluvial channel sediments (at 35 m). **(b)** South-oriented profile exposing LWT gravels with valley loam and Holocene overbank fines (at 350 m). **(c)** West-oriented profile south of the Clieben study site, exposing a palaeochannel at the transition of the LWT to the older Holocene terrace (at 430 m). **(d)** Southeast-oriented profile showing sediments of the older Holocene terrace with a palaeochannel and overlying overbank fines (at 870 m). **(e)** Southeast-oriented profile exposing clayey loam with a humic topsoil and arising LWT sediments in the background (at 1780 m).

4.1 Trench

Based on the examination of about 2.4 km of the EUGAL pipeline trench, several distinct sedimentary units could be identified. However, due to time and security constraints during pipeline construction, sediment description and sampling could not always be carried out at the same qualitative level along the trench.

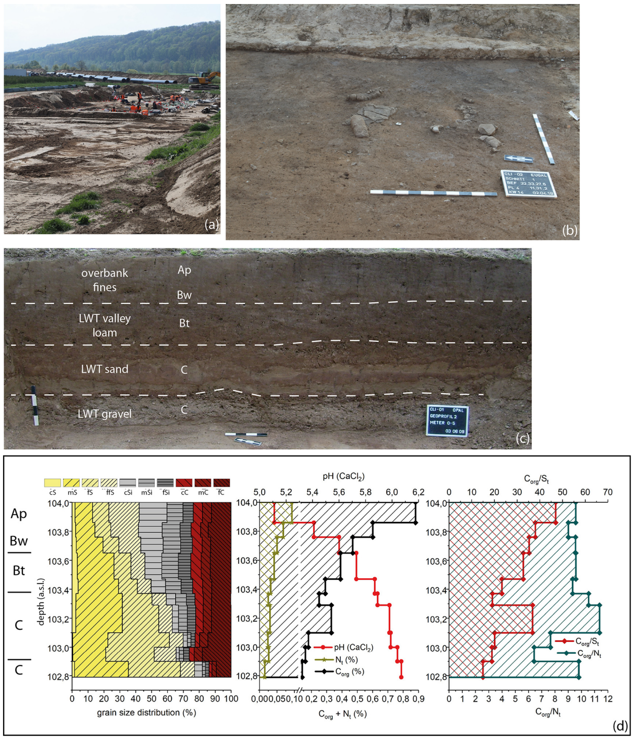

Figure 4. Clieben study site. **(a)** Overview of the archaeological excavations in 2019. **(b)** A section of the Neolithic surface with a broken rubbing stone. **(c)** Photo of profile 2 documented in 2008: the uppermost part of the LWT is formed by a valley loam that is covered by younger Holocene overbank fines. **(d)** Analytical values of profile 2 with particle size distribution and pH values, as well as organic carbon, sulfur and nitrogen contents and ratios.

4.1.1 LWT

LWT sediments were mainly found in two areas along the trench: in the northwestern part of the Clieben study site (Fig. 2, 150–420 m) and the southeastern part of the Brockwitz study site (Fig. 2, 2075–2175 m). LWT sandy gravels were superimposed by valley loam, which was covered by Holocene overbank fines (Fig. 3b). Remains of an early Neolithic settlement and linked archaeological findings at the Clieben study site stratigraphically reach from the surface of the valley loam into the underlying gravels and sands (Fig. 4). The terrain rises to > 104 m a.s.l. in the former settlement area at the Clieben study site (at 340 m), roughly 1 m higher compared with the surroundings (Fig. 2b). Similarly, in the southeastern part of the Brockwitz study site, a terrain height of 105 m a.s.l. (at ∼ 2125 m) after a steady ascent to the southeast marks a local maximum that surpasses its surrounding terrain height by ca. 1 m (Fig. 2c).

4.1.2 LWT and clayey loam

Along approximately 500 m of the pipe trench (1575–2075 m), i.e. a major part of the Brockwitz study site, a sequence of basal LWT gravely sands were cropped out. Upwards, these concordantly pass over into a 1–2 m thick layer of clayey loam that is overlain by Holocene overbank fines (Fig. 3e). OSL dating indicates a late Weichselian formation of the upper LWT deposits around 15 ka (Table 1, Fig. 7). In agreement with the OSL ages, an early Mesolithic camp site (at 1870 m) at the base of the clayey loam indicates a predominantly early Holocene deposition of the clayey loam. To the southeastern part of the Brockwitz study site, the clayey loam crosses out in gradually arising LWT sediments (at 2075 m).

One distinct palaeochannel was discovered in this part of the pipe trench (at 1950 m), cutting the clayey loam and the underlying LWT sands and gravels. The channel filling was similar to the clayey loam. These sediments are covered by older and younger Holocene overbank fines that are separated from each other by another palaeosol.

4.1.3 Holocene sediments

Gravely and sandy sediments of the older Holocene terrace with overlying overbank fines dominated the pipe trench for approximately 1.1 km between the Clieben and Brockwitz study sites (Fig. 3d, 420–1525 m). The base of the older Holocene terrace was formed by an about 1 m thick layer of gravely sands with some loamy strata showing a general decrease in gravels upwards. These were covered by ca. 2.5 m sandy overbank fines with a fining-upward trend. Here, strata thicknesses vary widely along the trench. Repeatedly, the base of the overbank fines reached deeper than the pipe trench, implying a vertical extension of > 4 m at these sections. Wood samples were taken from an oak tree that was found at the transition from the terrace gravels to the overlying overbank fines (635 m), which were 4.3 m thick at this particular location. Radiocarbon dating of this material gave a terminus post quem for the onset of the fine overbank sedimentation between 3962 and 3802 BCE (MAMS-45651, Table 2). Partly observed palaeosols divide the overbank into an older and younger sedimentation phase.

South of the Brockwitz study site (at 2240 m) the transition of the LWT with its covering overbank fines towards the current Elbe floodplain is marked by a ca. 2 m drop in terrain height. Within the latter the stratigraphy is dominated by sands and gravels of the younger Holocene terrace with covering younger Holocene overbank fines. With closer proximity to the river, the overbank fines' thickness gradually decreases. Additionally, a former river island with a thick gravel body, surpassing its vicinity by ca. 1 m, was observed close to the current bank of the Elbe River between 2300 and 2350 m (Fig. 2).

4.1.4 Holocene channels

The northwesternmost section of the pipe trench was dominated by non-LWT gravely sands. These stretched for approximately 150 m southward along the trench and subsequently thinned out into LWT sediments north of the Clieben study site around 150 m. Within these non-LWT gravely sands, an up to 3.3 m thick trough-shaped layer of dark-brown organic sediments with plant remains such as roots and stalks was embedded, showing a maximum lateral extent of ca. 25 m (Fig. 3a). Archaeobotanical analyses of the excavated organic material from the profile base classified these as sedge peat derived from a large variety of plant taxa, giving insight into the former local vegetation during the Boreal. The sedge peat/reed is represented by *Carex* spp., *Alisma plantago-aquatica* agg., *Lycopus europaeus*, *Scirpus lacustris*, *Typha* or *Oenanthe aquatica*, and several taxa suggest nutrient-rich conditions with a herbaceous vegetation in some parts of the banks (*Rumex maritimus*, *Ranunculus sceleratus*, *Polygonum lapathifolium*, *Polygonum minus* and *Chenopodium polyspermum*). Remains of *Betula pendula*, *Quercus*, *Polygonum dumetorum*, *Thalictrum flavum* and *Urtica dioica* mirror the adjacent alluvial forest, whereas aquatic plants such as *Nymphaea alba* or *Ceratophyllum demersum* show a standing waterbody without strong currents or waves.

The archaeobotanical analyses of the overlying layers dating to the Atlantic period merely confirmed the Boreal taxa spectrum with only minor alterations. The more abundant annuals *Atriplex* and *Chenopodium album* could have been distributed along the riverbanks or hint to nearby human activities. Especially seeds of the bladder cherry *Physalis alkekengi* are of special interest, since its natural distribution is on riverbanks in southeastern Europe. Hence, it must have been brought to the study area most probably with LPC settlers as a cultivated plant (Herbig 2012, p. 153).

The radiocarbon ages of three peat samples were 7776–7595 BCE (MAMS-44467), 6742–6573 BCE (MAMS-47072) and 3961–3800 BCE (MAMS-47071) (see Table 2). Hence, peat formation extended from the Boreal until the Atlantic period. Subsequently, the peat was covered by about 3 m thick overbank fines (loamy sands), into which the bed of the "Lockwitzbach" current creek is embedded.

Within an eastward bend of the trench south of the Clieben study site (Fig. 3c), the terrain height suddenly drops by about 1 m. Here, a diagonal, ca. 25 m wide palaeochannel marks the transition between the LWT to the north and the

Table 2. Results of the ^{14}C analyses.

MAMS	Unit	Material	^{14}C age [years]	±	δ^{13}C [‰]	Cal 1σ cal BCE [years]	Cal 2σ cal BCE [years]	C [%]
44 467	Peat, Lockwitz ground	Wood	8693	30	−27.9	7720–7613	7780–7600	57.8
44 468	Older Holocene terrace	Wood	4943	25	−27.5	3761–3664	3773–3657	50.1
45 651	Older Holocene terrace	Wood	5093	22	−28.4	3955–3813	3962–3802	53.4
47 071	Peat, Lockwitz ground	Seed	5090	23	−23.6	3953–3809	3961–3800	54.8
47 072	Peat, Lockwitz ground	Seed	7817	28	−26.7	6683–6600	6739–6576	46.9

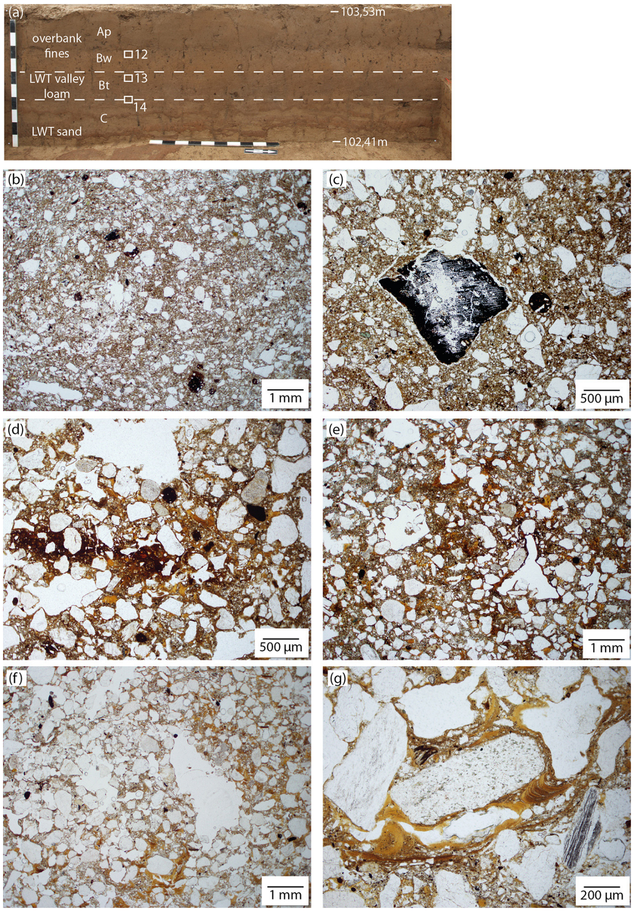

Figure 5. Clieben study site. **(a)** Photo of profile 3 which was studied in 2019 with locations of the thin-section samples (12: overbank fines, 13: LWT valley loam, 14: transition LWT valley loam to LWT sands). Microphotos of the thin sections (all in ppl): **(b)** sandy and silty overbank fines with disorthic iron oxide nodules, **(c)** overbank fines with charcoal pieces, **(d)** valley loam with disorthic iron oxide nodules and matrix impregnation, **(e)** valley loam with clay infillings and coatings of voids, **(f)** sandy material of the LWT, and **(g)** LWT material with clay infillings and coating of a void.

older Holocene terrace to the south and southeast (Fig. 2a). At the trench base at ca. 3 m depth, the channel is filled with organic-rich loamy sands, which contained one oak tree trunk. This oak tree has been radiocarbon-dated to 3773–3649 BCE (MAMS-44468, Table 2), i.e. to the late Atlantic period. The loamy sands are superimposed by grey sands, then followed by a fining-upward loam layer with a thickness of ca. 1 m that contained small proportions of sand and charcoal. The top of the profile was formed by 1.9 m thick clayey overbank fines (Fig. 3c). In addition to this a palaeochannel, three further palaeochannels with equal or smaller dimensions and similar sedimentary fillings were observed that were also incised into the sediments of the older Holocene terrace.

4.2 Clieben study site

Post holes and pits found between 0.5 and 1 m below the surface after removal of the covering overbank fines prove an early Neolithic settlement on the LWT (Fig. 4a and b; Steinmann, 2010; Kreienbrink, 2022). Furthermore also some features originating from the late Bronze Age were recorded on the same level. The northern boundary of the settlement is represented by the remnants of an old channel used by a small creek (Lockwitzbach) in recent times (Figs. 2 and 3a). In the south, the LWT is limited by the older Holocene terrace.

In the central part of the early Neolithic settlement the stratigraphical base is formed by LWT sands that merge upwards into the valley loam without clear boundaries (Fig. 4c). Soil development – weathering and lessivage – overprinted these Weichselian sediments. The Neolithic surface is found at an altitude of 103.6 m a.s.l. on the topographically highest part of the valley loam, and the LWT including the archaeological surface is covered by younger Holocene overbank fines. The latter consist of brown loamy sands that contain charcoal, fired clay and younger potsherds.

According to the analytical values of profile 2, the valley loam contains ∼ 0.3 % organic carbon, and the highest values of 0.9 % are found in the recent plough horizon (Ap) at the top of the overbank fines. However, the Neolithic surface with archaeological features and findings (upper part of the Bt horizon) does not show a peak of organic carbon. This is consistent with nearly the same colour of the valley loam and the Holocene overbank fines (dark yellowish brown, 10YR4/4).

The micromorphological analyses of samples taken from profile 3 prove that the upper overbank fines contain dis-

Figure 6. Brockwitz study site. **(a)** Aerial photo of the archaeological excavation with the Neolithic palisade in 2018 (1850–1940 m). **(b)** The early Mesolithic chipping floor during excavations. **(c)** Microliths (at 1870 m).

orthic (reworked) iron oxide nodules and charcoal pieces (Fig. 5b, c).

Pedogenic transformation of the Holocene overbank fines is rather weak, as only few small clay infillings and coatings of voids could be detected. Also the underlying Weichselian valley loam contains reworked iron oxides (disorthic nodules). In addition, in situ formed ferruginous matrix impregnations and an increasing number of clay coatings and infillings (Fig. 5d, e) are detectable in the valley loam. The latter features are undisturbed, indicating a stable period of postsedimentary soil formation during the late Weichselian to Holocene. The transition to the underlying LWT sands is clear, and these show downwards decreasing features of soil formation with the exception of clay illuviation features like infillings and coatings of voids that were even found in greater profile depth (Fig. 5f, g).

4.3 Brockwitz study site

The geological structure at the Brockwitz study site is less homogeneous compared to Clieben. A small area in the southeastern part belongs to the topographically highest peaks of the LWT, showing heights around 105 m a.s.l. (2075–2175 m). Here, some late Bronze Age features were dug into the valley loam and the underlying gravels and sands, and overbank fines are missing here. Compared to the elevated terrain in the southeast, the height of the remaining LWT surface is 1–3 m lower in most other parts of the study site. However, nowadays this altitudinal difference is levelled by Holocene overbank fines. Several sediment profiles were recorded here, and a combined sampling approach was applied to the sediments, soils and Neolithic features of profile 17 (Figs. 6, 7).

The base of that profile is formed by LWT sands that were dated by OSL to around 15 ka (Table 1, Fig. 7) and show only minor pedogenetic features. Thin sections show that parts of the sands are free of finer components, while clay illuviation, bridging the individual grains, is visible in other parts (Fig. 8e, f). Upwards the sands merge into clayey loam with up to 1 m thickness. Soil development overprinted parts of the latter material, and a 0.4 m thick Ahb horizon had established at its surface. The OSL date from the lowest part of the clayey loam shows an early Holocene age of 10.27 ± 1.36 ka (Table 1). In this layer clay percentages reach > 40 %, while sand remains around 20 %. Micromorphological samples were taken from both the undisturbed clayey loam and a Neolithic ditch filled with relocated clayey loam. The infilling is dark greyish brown and thus seems to be rich in organic matter and contains numerous undisturbed clay infillings and coatings of voids (Fig. 8b–d). Charcoal pieces prove anthropogenic activities (Fig. 8c). Deep cracks in the Ahb horizon caused by shrinking of the clayey material were filled with brown-coloured, younger overbank fines. Also macroscopic analysis shows strong aggregation features, while under the microscope vertic properties such as slickensides are absent. Despite the dark colour of the Ahb horizon (very dark greyish brown, 10YR3/2) organic carbon values reach only 0.6 % (Fig. 7).

The small VWI ratios in the upper, clay-rich C horizon show obvious preweathering of the substrate (Fig. 9). This tendency becomes even clearer in the K_2O/Rb_2O ratios. In the clay-rich Ahb and C horizons (103.4–102.55 m a.s.l.), the K_2O/Rb_2O ratio is < 400 and clearly demarcated from the other horizons, indicating in situ soil formation. Despite very high clay contents, it cannot be assumed that preweathered material was introduced.

The commonly used Rb/Sr ratio is based on different ion radii, since the much smaller Sr^{2+} ion is more easily leached during weathering, whereas Rb is fixed to clay (McLennan et al., 1993; Reitner and Ottner, 2011). Hence, high Rb/Sr ratios indicate intense weathering.

Similarly, due to partial adsorption of K^+ on clay minerals and organic substances, less K^+ is removed compared with the smaller Na^+ ion during chemical weathering so that increasing K_2O/Na_2O ratios indicate chemical weathering (Smykatz-Kloss, 2003). When comparing the soluble alkali cations K^+ and Na^+, a clear enrichment of the larger and therefore less mobile K^+ compared to the Na^+ ion can be detected during soil formation. Although both cations are dissolved during chemical weathering, some of the K^+ ions (radius of 138 pm) can subsequently be adsorbed again by fine-grain particles such as clay minerals or organic matter and thus be partially retained in the soil, while the smaller Na^+ ion (102 pm) is discharged into the soil solution. Given

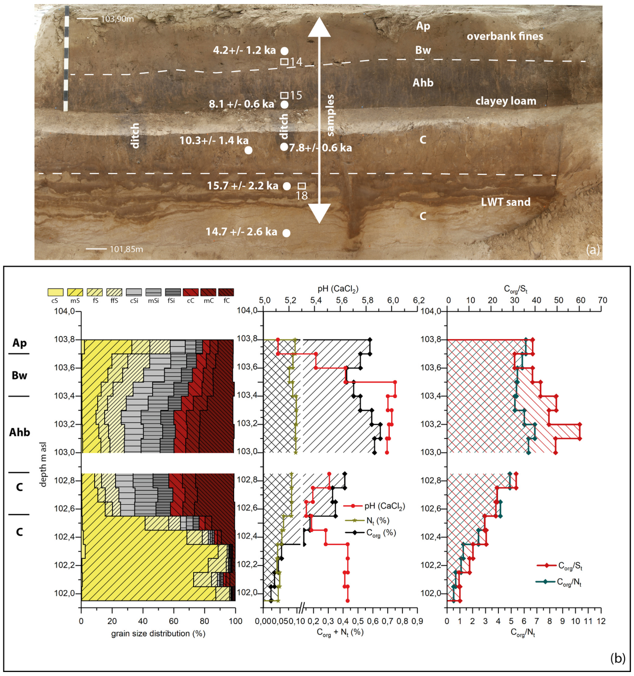

Figure 7. Brockwitz study site. **(a)** Photo of profile 17 (at 1860 m) that was studied in 2018 with two ditches from the Neolithic palisade, OSL ages and the positions of micromorphological samples (14: overbank fines, 15: clayey loam/Neolithic ditch, 18: LWT sands). **(b)** Analytical values of this profile with the particle size distribution and pH values, as well as organic carbon, sulfur and nitrogen contents and ratios.

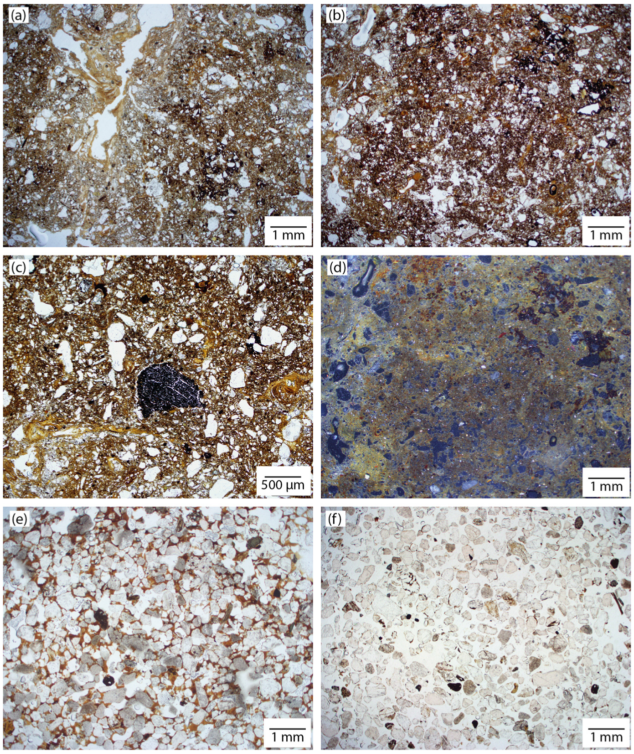

Figure 8. Brockwitz study site. Microphotos of profile 17 (A–C and E–F in ppl, D in oil). Sample 14 (overbank fines): **(a)** loamy cover sediment with iron oxides and clay coating of a void. Sample 15 (clayey loam from Neolithic ditch): **(b)** clayey loam rich in clay infillings and coatings of voids, **(c)** clayey loam with charcoal pieces, and **(d)** dark greyish brown of the clayey loam due to organic matter. Sample 18 (LWT sands): **(e)** sandy material of the LWT with clay bridging the sand grains and **(f)** sandy material of the LWT without fines.

that both the Rb/Sr and K_2O/Na_2O ratio are increased in the Ahb and C horizon, this clearly indicates their intensive weathering.

Just a few centimetres above the base of the clayey loam, an early Mesolithic campsite for hafting and retooling was discovered and excavated near profile 17 (Fig. 6). It consists of silex artefacts, destroyed by fire; quartzite pebbles; and pieces of burnt animal bone (Fischer in Döhlert-Albani et al., 2022). This demonstrates short human activity during the middle Preboreal causing the accumulation of a great number of artefacts and leftovers from meals (Fig. 6). Afterwards, clay-rich overbank sedimentation covered these artefacts relatively contemporaneously largely without replacing them, since > 50 % of the silex inventory are chips of < 1 cm in length. The next verified human activities took place during the early and middle Neolithic leaving many pits, with up to six parallel ditches belonging to former palisades (Figs. 6, 7). Two OSL samples taken from the archaeosediments in one of these ditches gave early Neolithic ages of 7.8 ± 0.6 and 8.1 ± 0.6 ka (Table 1). Despite these numerical ages, a younger age (middle Neolithic: 6.4–4.8 ka; Miera et al., 2022) is assumed here for archaeological reasons; i.e. the luminescence ages must be overestimated (Stäuble et al., 2022). Later, these archaeosediments and the overprinting Ahb soil horizon were covered by younger overbank fines. The latter deposition started at the end of the Neolithic or the beginning of the Bronze Age during the Subboreal period, which is proved by the OSL age of 4.2 ± 1.2 ka and archaeological features of the late Bronze Age, which were partly dug into these younger overbank fines.

The younger overbank fines covering the clayey loam are more sandy and less clayey compared with the latter. Similar to the overbank fines in Clieben, their colour is dark yellowish brown (10YR4/4) and they contain charcoal pieces and reworked iron oxides (Fig. 8a).

5 Discussion

5.1 Late Weichselian–Holocene transition

During the late Weichselian cold period, the LWT showed a surface with a diverse morphology (Fig. 10): around 15 ka older gravels, supposedly deposited between the Denekamp Interstadial and the Last Glacial Maximum (LGM) (30 000–20 000 ka) (Alexowsky, 2005; Litt et al., 2007), nearly

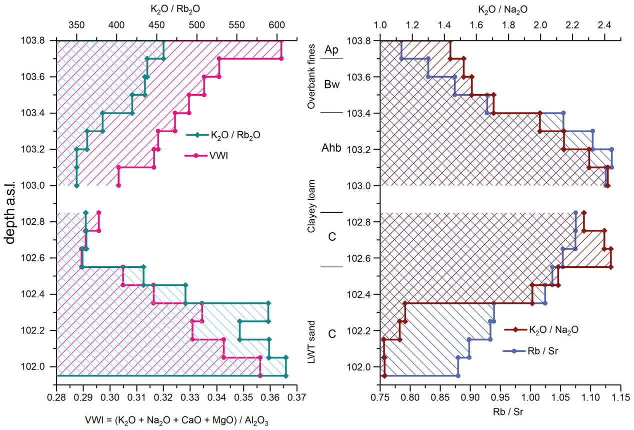

Figure 9. Brockwitz study site. Profile 17 with the alteration index (VWI) and the element ratios of K_2O, Rb_2O / Sr and K_2O / Na_2O.

reached an altitude of 105 m a.s.l., while sands were deposited in a 3 m deep channel at the Brockwitz study site. During that time the large gravel plain of the LWT, belonging to the braided Elbe River system (Kaiser et al., 2012), was dissected by several shallowly incised channels. Subsequently, fluvial sands were deposited during the initial warmer phases of the final glacial period. The channels on the LWT had been preserved and remained visible until the transition to the Holocene, quite similar to other late Weichselian terraces of the Rhine River or Danube River systems (Schirmer, 1995; Schellmann, 2018).

Sedimentation and erosion in the study area and especially during the formation of the LWT were closely connected to the larger-scale development of the Elbe River system. Seemingly, intense incision occurred in the central European river systems during the Early Holocene. However, in the Elbe valley this switch apparently occurred later (Brose and Präger, 1983) compared with other central European river systems (Kaiser et al., 2012). Here, a late Weichselian–Early Holocene anastomosing channel pattern is assumed. During that time the “Lockwitz ground” at the northern valley margin of our study area also formed part of the Elbe floodplain (Figs. 2, 3a). According to our ^{14}C dates, this channel was abandoned only after a middle–late Preboreal incision phase of the Elbe system, and its organic sediments demonstrate boggy conditions from the Boreal until the Atlantic period. Here, the location of the channel near the transition to the HWT intensified water influx, supporting organic-rich sedimentation regardless of the deep incision of the main Elbe channel. Hence, the location of the Lockwitz ground at the transition from the LWT towards the HWT defines it as a seam channel (*Nahtrinne*). This channel type marks the border between different terraces and hence aids as their distinction and was described e.g. at the Rhine, Main and Danube terraces (Schirmer, 1995; Schellmann, 2018).

The clayey loam was deposited in abandoned channels on the LWT during the Early Holocene. Whereas the covering younger Late Holocene overbank sediments were explained by increasing river discharge caused by anthropogenic impact on the catchment, the cause of the deposition of these Early Holocene deposits has not been addressed so far. Similar observations were reported from the lower Weser valley (Schellmann, 1994; Schirmer, 1995). It is located in the low mountain ranges of southern northern Germany, i.e. some kilometres south of the North German Plain. There, a dark soil (*Feuchtschwarzerde*) had developed in overbank fines, which were deposited in palaeochannels (*Aurinnen*) incised in Weichselian gravels. According to Schellmann (1994) these soils had developed in the Allerød period as well as in the Early Holocene. Similar conditions are also found for the Elbe valley between Dresden and Riesa. Here the valley bottom still consists of Palaeozoic rocks, whereas in the North German Plain near Riesa some kilometres to the north, glacial sediments dominate the valley bottom. Hence, we suggest that gravel accumulation in the narrow parts of the valley, especially upstream of the Spaar Mountains, decelerated the Early Holocene incision (Fig. 2). Consequently the lower parts of the LWT were submerged during Early Holocene flood events so that the clayey loam could be deposited. After the middle–late Preboreal incision, floods no longer reached the LWT, so clayey loam deposition ended. This scenario is also reflected by the early Mesolithic camp site. The microliths were embedded in the basal clayey loam and remained predominately undisturbed as a result of ongoing sedimentation during the early Preboreal. After deposition ended, a humic A horizon developed during the late Preboreal and the Boreal, which did not reach the level of the early Mesolithic finds.

Different weathering indices and element ratios gave clear evidence for soil formation in the course of chemical weathering within the clay-rich Ahb and C horizon (Fig. 9). It can be clearly seen that the lowest VWI values could be detected at the sediment base of the clayey loam between 102.6 and 102.8 m a.s.l. This is clear evidence of weathering and thus soil formation, which is also validated by the K_2O/Rb_2O ratio because there is greater retention and thus slower release of heavier alkali metal ions (Rb^+) from clay minerals compared to the lighter alkali metal ion (K^+) (Bosq et al., 2020; Matys Grygar et al., 2020). In comparison to Na and Ca, a possible resorption of K to clay minerals and its stronger binding through sorptive complexes in the soil are considered to be more likely. These conditions can lead to K enrichment when weathering processes are weak or, conversely, K depletion under stronger weathering conditions (Buggle et al., 2011). Although the highest organic carbon values only reach 0.6 %, the low values for VWI are an indication of soil formation that has taken place within these deposits. Additionally, also the Rb/Sr ratio proved to be very meaningful in investigations of the intensity of weathering of loess palaeosols (Reitner and Ottner, 2011). Accordingly, at our study site the highest Rb/Sr ratios were found in the clay-rich Ahb and C horizon, proving their high weathering intensity.

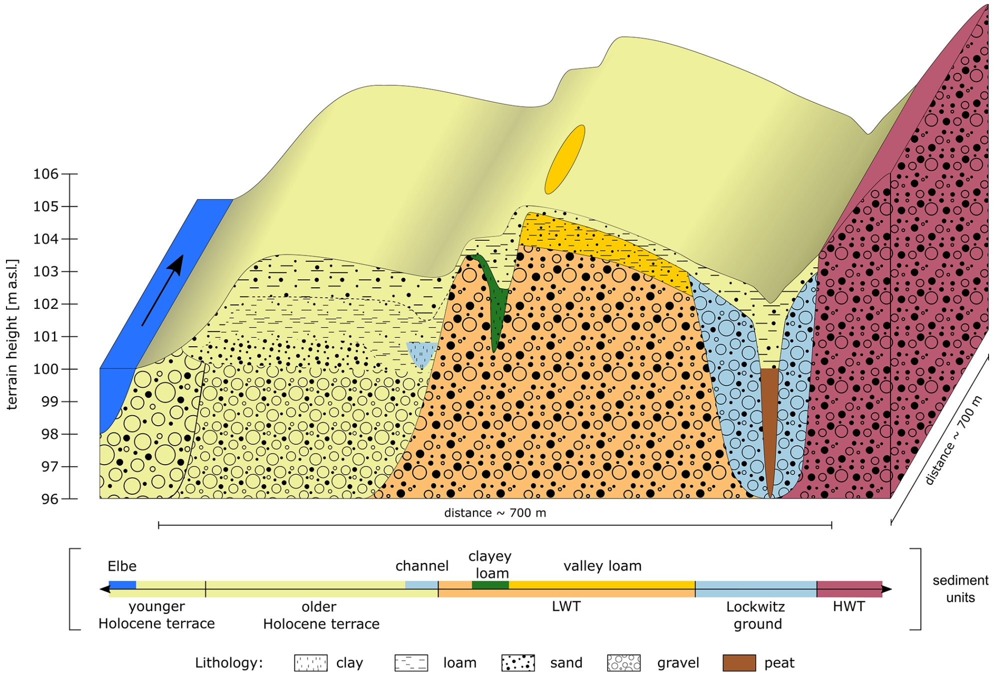

Figure 10. Schematic transect through the right bank of the Elbe valley in the study area in the northwestern Dresden basin between the Spaar Mountains and the city of Coswig, south of Meißen (see Fig. 1b for the location). HWT: Higher Weichselian Terrace, LWT: Lower Weichselian Terrace.

Most of the oldest detected Holocene floodplain sediments in several central European river systems are peats (Hiller et al., 1991; Tinapp, 2002; Notebaert et al., 2018; Tinapp et al., 2019). These were usually covered by humic fine-grain material with relatively constant vertical contents of organic matter, and its formation is suggested to have occurred during long-lasting periods with high groundwater levels and reduced composition of organic material. This material was referred to as "black floodplain soil" in the Ohm (Rittweger, 2000) or "black clay" in the Pleiße River (Tinapp et al., 2019) and was dated to between the Boreal and Atlantic periods. Similar formations were also described from various other river systems in central Europe (Schirmer, 1983; Bork, 1983; Brosche, 1984; Pretzsch, 1994; Schellmann, 1994; Hilgart, 1995; Bos et al., 2008; Brown et al., 2018; von Suchodoletz et al., 2022). Their stratigraphical position and properties, however, differ greatly from those of the Early Holocene clayey loam on the Elbe LWT. In the latter, the low content of organic carbon of 0.6 % (Fig. 7), mainly derived from in situ soil formation, slightly decreases downwards to 0.2 % (Fig. 7) in the lower part just above the LWT sands and gravels. This indicates only minor input of organic material during sedimentation. Furthermore, the sand content of the clayey loam reaches $> 20\,\%$, indicating the temporal influence of flowing water during its deposition. In contrast, low sand values of $< 2\,\%$ in the black floodplain soil (Rittweger, 2000) and the black clay (Tinapp et al., 2019) demonstrate different sedimentation conditions for these layers.

Consequently, given that there are no signs of long-lasting periods with high groundwater and reduced decomposition of organic material, as well as higher sand contents, despite visual similarities with the black-coloured fine-grain Holocene sediments known from many other central European river valleys, the fine-grain Early Holocene material on the LWT in Brockwitz must have had a different genesis.

During the early Holocene, early Mesolithic hunters and gatherers occupied a former LWT river channel for several days and left their remains in the basal clayey loam. Hence, sedimentation of the latter had apparently started before. After this short human occupation, nearly 0.8 m of clayey loam has been deposited. Its low content of organic carbon, originating from soil development, suggests a merely sparse vegetation cover. Therefore, a relatively short sedimentation process at the transition from the Younger Dryas to the Preboreal is assumed, when the vegetation cover on the LWT was thinner than during subsequent periods. Afterwards, long-lasting development of the overprinting dark-coloured humic topsoil horizon began.

5.2 Holocene overbank deposits

The first human settlers appeared in the study area around 7500 BCE, colonized the LWT surface, and left their traces in the form of pits that were dug into the upper sediments and the overprinting topsoil. The lack of overbank sediments in the prehistoric pits at both the Clieben and Brockwitz study sites evidences that floods did not reach these locations during the Atlantic period.

Later, during the end of the Subboreal, floods must have reached the higher parts of the LWT surface again, since overbank fines were deposited at both study sites, Clieben and Brockwitz. Accordingly, parts of the late Bronze Age settlement are situated around the topographically highest part of the LWT, which is not reached by floods even today. Furthermore, in topographically lower positions of the settlement, some archaeological features were found within the younger overbank fines that are connected to a scattered intercalated humic horizon (Tinapp et al., 2022). Also, medieval Slavic features were found in the same stratigraphic position. Therefore, the younger Holocene overbank fines can be divided into a lower Bronze Age–medieval period and an overlying younger part.

The early Neolithic archaeological finds and features represent the best parameters to distinguish between the valley loam and the overlying younger Holocene overbank fines, since these finds are found at the surface and in the upper part of the former. In contrast, the sedimentological proxies are rather diffuse to some extent so that neither organic carbon nor the particle size distribution could help to differentiate both units from each other (Figs. 4, 5). Accordingly, also the assumed former topsoil horizon of the Atlantic period, overprinting the Weichselian valley loam, could not properly be detected by these proxies. The archaeological finds in the upper part of the valley loam are distributed over the whole excavated area, regardless of whether archaeological features were documented below those finds. This find distribution, as well as some special find situations (Fig. 4b) and the mostly remarkably deeply preserved postholes and pits, clearly evidences only minor erosion processes after settlement abandonment, leading to the predominant preservation of the occupation layer of the settlement. Some of the archaeological finds were used at the surface of the settlement (rubbing stones; Fig. 4b). According to observations, pottery fragments within the occupation layer are generally heavily fragmented and weathered and their edges are rounded. This suggests their long-term atmospheric exposition and possibly also human activity at or near the surface, before they were covered by younger floodplain fines.

Large sections of the pipe trench in the current floodplain were cut through the older Holocene terrace. A buried oak tree from > 6 ka at the transition of the lower sandy gravels to the overlying overbank fines confirms that coarse fluvial sedimentation stopped at the end of the Atlantic period and that since then only younger overbank fines have been deposited (Wolf et al., 2008). In contrast to other central European river valleys (Schirmer, 1995), there is no evidence for more than two Holocene terraces in the Elbe valley between Dresden and Meißen.

5.3 Valley development and prehistory

Many studies demonstrate the spatial link between fluvial terraces and (pre)historic sites (Torke, 2012; Brown et al., 2018; Tinapp et al., 2020), since fertile land facilitating settlement founding was available in close vicinity to rivers. Accordingly, also in the Elbe valley many prehistoric settlements were formerly detected (Brestrich, 1998; Torke, 2012; Ullrich and Ender, 2014; Conrad and Ender, 2016; Meller and Friederich, 2018). Whereas late Bronze Age–medieval archaeological features were regularly found within the current floodplains (Hiller et al., 1991), older prehistoric sites were often found on fluvial terraces below a cover of younger overbank fines (Tinapp et al., 2020). Hitherto, most LPC settlements between Dresden and Meißen have been discovered on the left banks of the Elbe River (Brestrich, 1998; Stäuble, 2010). Hence, given its location on the right riverbank, the geographic location of the early Neolithic village at the Clieben study site was under discussion in archaeology after its discovery in 2008 (Steinmann, 2010). Given that the channel at the Lockwitz ground had been abandoned already during the Preboreal and subsequently developed into a peat swamp, its active phase is much older than the LPC settlement. Hence, an active Elbe channel north of the Clieben study site can clearly be excluded for that time, confirming that the LPC settlement must actually have been located on the right bank of the Elbe River. This forms an important finding with respect to the reconstruction of the spread of the initial LPC in central Europe (Brestrich, 1998; Stäuble, 2010).

Generally, data about the late Weichselian–Holocene development of the Elbe River system are still rather patchy (Kaiser et al., 2012). This also leads to difficulties in linking the fluvial sediments and hence the local geomorphic–palaeoenvironmental conditions – strongly influencing human behaviour – of the upper with those of the middle Elbe valley. Accordingly, also our detailed geoarchaeological approach applied to a rather unstudied area in the northern Dresden basin strongly stresses the need for further research regarding the late Weichselian–Holocene Elbe valley development to better understand former regional patterns of human settlement.

6 Conclusions

Our geoarchaeological investigations during the OPAL and the EUGAL pipeline constructions in the northern Dresden basin between Meißen and Dresden gave new insights into the fluvial sediments that were deposited since 15 ka in this part of the Elbe valley. Overall, one phase of clayey sedimentation during the Early Holocene and two subsequent periods of fine overbank sedimentation have been deciphered on the LWT, separated from each other by a long-lasting period without fluvial sedimentation during the Atlantic period. Preboreal clayey sedimentation on the LWT is quite unique in central Europe, suggesting a later incision of the Elbe River compared with other central European rivers.

Sedimentation processes and soil development in this part of the Elbe valley were connected to former human occupation. While the palaeochannels on the LWT were temporarily reached by floods during the Preboreal, only allowing a short occupation by Mesolithic humans, the early Neolithic findings were found below the following fine-grain younger Holocene overbanks. Hence, during a longer period between the Atlantic and Subboreal, the LWT was no longer flooded, allowing for LPC settlements on the LWT. The following late Bronze Age features were mainly concentrated around the topographic peaks of the LWT, and subsequent temporary flooding of most parts of the LWT obviously stopped the intensive anthropogenic occupation.

Only multidisciplinary approaches allow for reconstructing the interdependence between humans and nature in fluvial environments, since accurately recorded archaeological excavations have to be combined with geoarchaeological investigations to identify distinct sediment units and soils and their relation with human finds.

Data availability. The archaeological data in the "Results" section can be found in Döhlert-Albani et al. (2022) (Sect. 4.1 and 4.3), Kreienbrink et al. (2022) (Sect. 4.1 and 4.2) and Stäuble et al. (2022) (Sect. 4.1 and 4.3). The palaeobotanical data can be found in Tinapp et al. (2022) (Sect. 4.1).

Supplement. The supplement related to this article is available online at: https://doi.org/10.5194/egqsj-72-95-2023-supplement.

Author contributions. HS, FK and CT organized the project. CT, JS, FK, NDA and TL carried out the fieldwork. The concept and structure of the paper were organized by CT and JS. The laboratory work was done by CH (plant macro remains), BS (geochemistry, particle size distribution) and TL (OSL). Thin-section analysis was carried out by SH. Archaeological investigations were performed by FK, NDA and BF. CT and JS took the lead in writing the manuscript, with input from BF, SH, CH, BS, TL, FK, NDA and HS. All authors discussed the results and contributed to the final manuscript.

Competing interests. The contact author has declared that none of the authors has any competing interests.

Special issue statement. This article is part of the special issue "Quaternary research from and inspired by the first virtual DEUQUA conference". It is a result of the vDEUQUA2021 online conference in September/October 2021.

Review statement. This paper was edited by Christian Zeeden and reviewed by Philipp Schulte and two anonymous referees.

References

Alexowsky, W.: Geologische Karte des Freistaates Sachsen, Erläuterungen zu Blatt 4947 Wilsdruff, Dresden, ISBN 3896793985, 2005.

Birkeland, P. W.: Soils and Geomorphology. Oxford University Press, New York, Oxford, ISBN 9780195078862, 448 pp., 1999.

Bork, H.-R.: Die holozäne Relief- und Bodenentwicklung in Lössgebieten, Catena, supplementary volume, 1–93, ISBN 3923381026, 1983.

Bosq, M., Bertranan, P., Degeai, J.-P., Queffelec, A., and Moine, O.: Geochemical signature of sources, recycling and weathering in the Last Glacial loess from the Rhône Valley (southeast France) and comparison with other European regions, Aeolia Res., 42, 100561, https://doi.org/10.1016/j.aeolia.2019.100561, 2020.

Bowen, H. J. M.: Environmental Chemistry of the Elements, London, ISBN 978-0121204501, 333 pp., 1979.

Brestrich, W.: Gedanken zur archäologischen Kulturlandschaft des oberen Elbtals, in: Archäologische Forschungen in frühgeschichtlichen Siedlungslandschaften, Festschrift für Georg Kossack zum 75. Geburtstag, edited by: Küster, H., Lang, A., and Schauer, P., Regensburger Beitr. Prähist. Arch. 5, Regensburg, 67–91, ISBN 3930480247, 1998.

Brosche, K. H.: Zur jungpleistozänen und holozänen Entwicklung des Werratales zwischen Hannoversch Münden und Phillipsthal (östl. Bad Hersfeld), Eiszeitalter u. Gegenwart, 34, 105–129, https://doi.org/10.3285/eg.34.1.06, 1984.

Brose, F. and Präger, F.: Regionale Zusammenhänge und Differenzierungen der holozänen Flussgenese im nordmitteleuropäischen Vergletscherungsgebiet, in: Das Jungquartär und seine Nutzung im Küsten- und Binnentiefland der DDR und der VR Polen, Vorträge und Erörterungen von der 4. Bilateralen Arbeitstagung 1979 in Greifswald, edited by: Kliewe, H., Galon, R., Jäger, K.-D., and Niewiarowski, Petermanns Geogr. Mitt. supplementary issue, 282, Gotha, 164–175, 1983.

Brown, A. G., Lespez, L., Sear, D. A., Macaire, J.-J., Houben, P., Klimek, K., Brazier, R. E., Van Oost, K., and Pears, B.: Natural vs anthropogenic streams in Europe: History, ecology and implications for restoration, river-rewilding and riverine ecosystem services, Earth-Sci. Rev., 180, 185–205, https://doi.org/10.1016/j.earscirev.2018.02.001, 2018.

Buggle, B., Glaser, B., Hambach, U., Gerasimenko, N., and Marković, S.: An evaluation of geochemical weathering indices in loess–paleosol studies, Quaternart Int., 240, 12–21, https://doi.org/10.1016/j.quaint.2010.07.019, 2011.

Bullock, P., Fedoroff, N., Jongerius, A., Stoops, G., and Tursina, T. (Eds.): Handbook for soil thin section description, Waine Research Publications, Albrighton, Wolverhampton, 152 pp., ISBN 9780905184098, 152 pp., 1985.

Cappers, R. T. J., Bekker, R. M., and Jans, J. E. A.: Digitale zadenatlas van Nederland – Digital seed atlas of the Netherlands. Groningen Archaeological Studies 4, 2nd Edn., Barkhuis Publishing, Eelde, ISBN 9077922113, 2012.

Conrad, S. and Ender, W.: Ein Tell bei Rosenfeld. Siedlungsspuren des Früh- und Mittelneolithikums, der vorrömischen Eisen- und Römischen Kaiserzeit sowie des Mittelalters am Elbufer nördlich von Torgau, in: Ausgrabungen in Sachsen 5, edited by: Smolnik, R., Arbeits- und Forschungsberichte zur sächsischen. Bodendenkmalpflege, supplement, 31, Dresden, 217-232, ISBN 9783943770261, 2016.

Döhlert-Albani, N., Conrad, M., Fischer, B., Kreienbrink, F., Oehlert, M., and Stäuble, H.: Ein polykultureller Siedlungsplatz bei Brockwitz an der Elbe, in: Steinzeitjägerin trifft auf Bergknappen. Trassenarchäologie an EUGAL und OPAL in Sachsen, edited by: Smolnik, R., Arbeits- und Forschungsberichte zur sächsischen Bodendenkmalpflege, supplement, 35, Dresden, 231–303, ISBN 9783943770759, 2022.

Eissmann, L.: Das quartäre Eiszeitalter in Sachsen und Nordostthüringen, Altenburger Naturwiss. Forsch. 8, Altenburg, 98 pp., ISSN 02325381, 1997.

Eissmann, L.: Quaternary geology of eastern Germany (Saxony, Saxon-Anhalt, South Brandenburg, Thüringia), type area of the Elsterian and Saalian stages in Europe, Quaternary Sci. Rev., 21, 1275–1346, https://doi.org/10.1016/S0277-3791(01)00075-0, 2002.

Fischer, P., Hilgers, A., Protze, J., Kels, H., Lehmkuhl, F., and Gerlach, R.: Formation and geochronology of Last Interglacial to Lower Weichselian loess/palaeosol sequences – case studies from the Lower Rhine Embayment, Germany, E&G – Quaternary Sci. J., 61, 48–63, https://doi.org/10.3285/eg.61.1.04, 2012.

Hantke, R.: Flußgeschichte Mitteleuropas: Skizzen zu einer Erd-, Vegetations-, und Klimageschichte der letzten 40 Millionen Jahre, Ferdinand Enke Verlag, Stuttgart, ISBN 3432997817, 459 pp., 1993.

Herbig, C.: Unkraut oder in Gärten kultivierte Heilpflanze? Die Rolle des Schwarzen Bilsenkrauts (Hyoscyamus niger L.) im Neolithikum. Neue archäobotanische Nachweise in linienbandkeramischen Brunnenbefunden in Sachsen, in: Verzweigungen. Eine Würdigung für A.J. Kalis u. J. Meurers-Balke, edited by: Stobbe, A. and Tegtmeier, U., Frankfurter Archäol. Schr. 18, Bonn, 147–157, ISBN 9783774937680, 2012.

Hilgart, M.: Die geomorphologische Entwicklung des Altmühl- und Donautales im Raum Dietfurt-Kelheim-Regensburg im jüngeren Quartär, Forschungen zur deutschen Landeskunde, 242, Trier, ISBN 9783881430548, 336pp., 1995.

Hiller, A., Litt, T., and Eissmann, L.: Zur Entwicklung der jungquartären Tieflandstäler im Elbe-Saale-Gebiet unter besonderer Berücksichtigung von 14C-Daten, Eiszeitalter u. Gegenwart, 41, 26–46, https://doi.org/10.3285/eg.41.1.03, 1991.

Houben, P., Schmidt, M., Mauz, B., Stobbe, A., and Lang, A.: Asynchronous Holocene colluvial and alluvial aggradation: A matter of hydrosedimentary connectivity, Holocene, 23, 544–555, https://doi.org/10.1177/0959683612463105, 2013.

Huhle, K.: Lithostratigrafie einiger Bohrungen in der Dresdner Elbtalwanne, Geologica Saxonica, 60, 461–488, ISBN 9783910005651, 2015.

IUSS Working Group WRB: World Reference Base for Soil Resources 2014, in: World Soil Resources Reports No. 106 FAO, Rome, 192, ISBN 9789251083697, 2014.

Kaiser, K., Lorenz, S., Germer, S., Juschus, O., Küster, M., Libra, J., Bens, O., and Hüttl, R. F.: Late Quaternary evolution of rivers, lakes and peatlands in northeast Germany reflecting past climatic and human impact – an overview, Quaternary Sci. J., 61, 103–132, https://doi.org/10.3285/eg.61.2.01, 2012.

Kausch, B.: Geoarchäologische Untersuchungen an Schwemmfächern als korrelate Sedimentkörper holozäner Bodenerosion zur Erfassung morphodynamischer Prozessphasen in der Region Trier, Geographische Gesellschaft Trier, ISBN 978-3-921599-61-7, 272 pp., 2009.

Khoravichenar, A., Fattahi, M., Amini, H., and von Suchodoletz, H.: The potential of small mountain river systems for paleoenvironmental reconstructions in drylands – an example from the Binaloud Mountains in northeastern Iran, Geosciences, 10, 448, https://doi.org/10.3390/geosciences10110448, 2020.

Kreienbrink, F.: Eine linienbandkeramische Siedlung bei Clieben in der nordwestlichen Dresdner Elbtalweitung, in: Steinzeitjägerin trifft auf Bergknappen. Trassenarchäologie an EUGAL und OPAL in Sachsen, edited by: Smolnik, R., Arbeits- und Forschungsberichte zur sächsischen Bodendenkmalpflege, supplement, 35, Dresden, 217–230, ISBN 9783943770759, 2022.

Kreienbrink, F., Döhlert-Albani, N., Conrad, M., Herbig, C., Martin, I., Schuber, M., Tinapp, C., Hößler, R., Johl, S., Krämer, U., Mauksch, K., Priske, C., and Stäuble, H.: Von der Großenhainer Pflege übers Elbetal ins Erzgebirge. Die Ausgrabungen an der EUGAL, in: Ausgrabungen in Sachsen 7, edited by: Smolnik, R., Arbeits- und Forschungsberichte zur sächsischen Bodendenkmalpflege, supplement, 34, 134–149, ISBN 9783943770537, 2020.

Krentz, O.: Postvariszische tektonische Entwicklung. in: Geologie von Sachsen, edited by: Pälchen, W. and Walter, H., E. Schweizerbart'sche Verlagsbuchhandlung, Stuttgart, 472–478, ISBN 9783510652709, 2008.

Lange, J.-M., Alexowsky, W., and Haubold, F.: Die Entwicklung der Elbe und ihr Einfluss auf die quartäre Landschaftsformung in der Umgebung von Dresden, in: Erkundungen in Sachsen und Schlesien. Quartäre Sedimente im landschaftsgenetischen Kontext, edited by: Faust, D. and Heller, K., conference volume, 25–30 September 2016, Dresden, Berlin, 13–30, https://doi.org/10.3285/g.00015, 2016.

Litt, T., Behre, K.-E., Meyer, K.-D., Stephan, H.-J., und Wansa, S.: Stratigraphical terms for the Quaternary of the North German Glaciation Area, E & G – Quaternary Sci. J., 56, 1–2, 7–65, 2007.

Mannsfeld, K. and Bernhardt, A.: Dresdner Elbtalweitung, in: Naturräume in Sachsen. Forschungen zur deutschen Landeskunde, edited by: Mannsfeld, K. and Syrbe, R.-U., Deutsche Akademie für Landeskunde, Leipzig, 148–154, ISBN 9783881430784, 2008.

Matys Grygar, T., Mach, K., Hron, K., Fačevicová, K., Martinez, M., Zeeden, C., and Schnabl, P.: Lithological correction of chemical weathering proxies based on K, Rb, and Mg contents for isolation of orbital signals in clastic sedimentary archives, Sediment. Geol., 406, 105758, https://doi.org/10.1016/j.sedgeo.2020.105717, 2020.

McLennan, S. M., Hemming, S., McDaniel, D. K., and Hanson, G. N.: Geochemical approaches to sedimentation, provenance and tectonics, Geological Society of America, Special Papers, 285, 21–40, 1993.

Meller, H. and Friederich, S. (Eds.): Archäologie in der Flussaue – 20 Jahre Hochwasserschutz und Ortsumgehung Eutzsch, Archäologie in Sachsen-Anhalt, 27, Halle, ISBN 9783944507804, 2018.

Miera, J. J., Schmidt, K., von Suchodoletz, H., Ulrich, M., Werther, L., Zielhofer, C., Ettel, P., and Veit, U.: Large-scale investigations on Neolithic settlement dynamics in Central Germany based on machine learning analysis: a case study from the Weiße Elster river catchment, PLoS ONE 17, e0265835, https://doi.org/10.1371/journal.pone.0265835, 2022.

Murray, A. S. and Wintle, A. G.: The single aliquot regenerative dose protocol: Potential for improvements in reliability, Radiat. Meas., 37, 377–381, https://doi.org/10.1016/S1350-4487(03)00053-2, 2003.

Notebaert, B., Broothaerts, N., and Verstraeten, G.: Evidence of anthropogenic tipping points in fluvial dynamics in Europe, Global Planet. Change, 164, 27–38, https://doi.org/10.1016/S1350-4487(03)00053-2, 2018.

Oberdorfer, E.: Pflanzensoziologische Exkursionsflora, Ulmer, Stuttgart, ISBN 9783800131310, 2001.

Pandarinath, K.: Application potential of chemical weathering indices in the identification of hydrothermally altered surface volcanic rocks from geothermal fields, Geosci. J., 26, 415–442 https://doi.org/10.1007/s12303-021-0042-2, 2022.

Pretzsch, K.: Spätpleistozäne und holozäne Ablagerungen als Indikatoren der fluvialen Morphodynamik im Bereich der mittleren Leine, Göttinger Geogr. Abh., 99, Göttingen, ISBN 9783884520994, 105 pp., 1994.

Pusch, M., Behrendt, H., Gancarczyk, A., Kronvang, B., Sandin, L., Stendera, S., Wolter, C., Andersen, H. E., Fischer, H., Hoffmann, C. C., Nowacki, F., Schöll, F., Svendsen, L. M., Bäthe, J., Friberg, N., Hachol, J., Pedersen, M. L., Scholten, M., and Wnuk-Glawdel, E.: Rivers of the Central European Highlands and Plains, in: Rivers of Europe, edited by: Tockner, K., Uehlinger, U., and Robinson, C. T., London, 525–576, ISBN 9780123694492, 2009.

Reitner, J. M. and Ottner, F.: Geochemische Charakterisierung der Verwitterungsintensität der Löss-Paläoboden-Sequenz von Wels/Aschet, in: Die Löss-Sequenz Wels/Aschet (ehemalige Lehmgrube Würzburger), Mitteilungen der Kommission für Quartärforschung der Österreichischen Akademie der Wissenschaften 19, edited by: Van Husen, D. and Reitner, J. M., Verlag der Österreichischen Akademie der Wissenschaften, Wien, ISBN 978-3-7001-6992-5, 2011.

Rittweger, H.: The Black Floodplain Soil“ in the Amöneburger Becken, Germany: a lower Holocene marker horizon and indicator of an upper Atlantic to Subboreal dry period in Central Europe?, Catena, 41, 143–164, https://doi.org/10.1016/S0341-8162(00)00113-2, 2000.

Scheck, M., Bayer, U., Otto, V., Lamarche, J., Banka, D., and Pharaoh, T.: The Elbe Fault System in North Central Europe – a basement controlled zone of crustal weakness, Tectonophysics, 360, 281–299, https://doi.org/10.1016/S0040-1951(02)00357-8, 2002.

Schellmann, G.: Die Talentwicklung der unteren Oberweser im jüngeren Quartär, Düsseldorfer Geographische Schriften, 34, 11–43, 1994.

Schellmann, G.: Quartärgeologische Karte 1:25.000 des Donautals auf Blatt 7039 Mintraching mit Erläuterungen. Kartierungsergebnisse aus den Jahren 2008 und 2009, Bamberger Geographische Schriften, SF 14, 105–162, 2018.

Schirmer, W.: Die Talentwicklung an Main und Regnitz seit dem Hochwürm, Geol. Jahrb., A 71, 11–43, 1983.

Schirmer, W.: Valley bottoms in the Late Quaternary, Z. für Geomorphologie N.F., Suppl.-Bd, 100, 27–51, 1995.

Smykatz-Kloss, B.: Die Lößvorkommen des Pleiser Hügellandes bei Bonn und von Neustadt/Wied sowie der Picardie: Mineralogisch-geochemische und geomorphologische Charakterisierung, Verwitterungs-Beeinflussung und Herkunft der Lösse. Dissertation Universität Bonn, Bonn, 343 pp., http://hss.ulb.uni-bonn.de:90/2003/0308/0308.htm (last access: 2 March 2023), 2003.

Smykatz-Kloss, W., Smykatz-Kloss, B., Naguib, N., and Zöller, L.: The reconstruction of paleoclimatological changes from mineralogical and geochemical compositions of loess and alluvial loess profiles, edited by: Smykatz-Kloss, W. and Felix-Henningsen, P., Palaeoecology of Quaternary Drylands. Lecture Notes in Earth Sciences, 102, Springer-Verlag, Heidelberg, 101–118, ISBN 3540403450, 2004.

Starkel, L., Soja, R., and Michczynska, D. J.: Past hydrological events reflected in Holocene history of Polish rivers, Catena, 66, 24–33, 2006.

Stäuble, H.: Linienband- und Stichbandkeramische Kulturen, in: Ur- und Frühgeschichte Sachsens. Atlas zur Geschichte und Landeskunde von Sachsen. supplement map B I 1.1–1.5, edited by: Heynowski, R. and Reiß, R., Leipzig, Dresden, 24–42, ISBN 9783896799234, 2010.

Stäuble, H.: Neues zur Bandkeramik in Sachsen: Die letzten 25 Jahre, in: Centenary of Jaroslav Palliardi's Neolithic and Aeneolithic relative chronology (1914–2014), edited by: Kovárník, J., Ústí nad Orlicí, 67–106, ISBN 9788074053962, 2016.

Stäuble, H., Döhlert-Albani, N., and Kreienbrink, F.: Eine neolithische Palisaden-/Grabenanlage mit Elbblick, in: Steinzeitjägerin trifft auf Bergknappen. Trassenarchäologie an EUGAL und OPAL in Sachsen, edited by: Smolnik, R., Arbeits- und Forschungsberichte zur sächsischen Bodendenkmalpflege, supplement, 35, Dresden, 245–266, ISBN 9783943770759, 2022.

Steinmann, C.: Die OPAL-Trasse als archäologisches Großprojekt, in: Ausgrabungen in Sachsen 2, edited by: Smolnik, R., Arbeits- und Forschungsberichte zur sächsischen Bodendenkmalpflege, supplement 21, Dresden, 227–230, ISBN 9783910008915, 2010.

Stoops, G.: Guidelines for analysis and description of soil and regolith thin sections, Soil Science Society of America, Inc., Madison, ISBN 9780891188421, 2003.

Tinapp, C.: Geoarchäologische Untersuchungen zur holozänen Landschaftsentwicklung der südlichen Leipziger Tieflandsbucht, Trierer Geographische Studien, 26, Trier, 275 pp., ISBN 3921599377, 2002.

Tinapp, C.: Geoarchäologische Untersuchungen an der OPAL- und EUGAL-Trasse, in: Steinzeitjägerin trifft auf Bergknappen. Trassenarchäologie an EUGAL und OPAL in Sachsen, edited by: Smolnik, R., Arbeits- und Forschungsberichte zur sächsischen Bodendenkmalpflege, supplement, 35, Dresden, 21–29, ISBN 9783943770759, 2022.

Tinapp, C., Heinrich, S., Herbig, C., Schneider, B., Stäuble, H., Miera, J., and von Suchodoletz, H.: Holocene floodplain evolution in a Central European loess landscape – Geoarchaeological investigations of the lower Pleiße valley in NW-Saxony, E & G – Quaternary Sci. J., 68, 95–105, https://doi.org/10.5194/egqsj-68-95-2019, 2019.

Tinapp, C., Heine, Y., Heinrich, S., Herbig, C., Schneider, B., Stäuble, H., and von Suchodoletz, H.: Die Pleißeaue südlich von Leipzig. Geoarchäologische Erkenntnisse zur stratigraphischen Position archäologischer Fundstellen im unteren Pleißetal, in: Ausgrabungen in Sachsen 7, edited by: Smolnik, R., Arbeits- und Forschungsberichte zur sächsischen Bodendenkmalpflege, supplement, 34, Dresden, 7–19, ISBN 9783943770537, 2020.

Tinapp, C., Selzer, J., Heinrich, S., Herbig, C., Lauer, T., and Schneider, B.: Das Elbtal bei Coswig. Geoarchäologische Erkenntnisse zur holozänen Entwicklung eines früh besiedelten Landschaftsraums, in: Steinzeitjägerin trifft auf Bergknappen. Trassenarchäologie an EUGAL und OPAL in Sachsen, edited by: Smolnik, R., Arbeits- und Forschungsberichte zur sächsischen Bodendenkmalpflege, supplement, 35, Dresden, 193–206, ISBN 9783943770759, 2022.

Torke, M.: Siedeln am Strom: Risiko oder Chance? Zu Urrelief, präurbaner Topographie und Hochwasserexposition Pirnas vor der Stadtwerdung, edited by Smolnik, R., Arbeits- und Forschungsberichte zur sächsischen Bodendenkmalpflege 53/54, Dresden, 359-410, ISBN 9783943770056, 2012.

Tröger, K.-A.: Kreide – Oberkreide, in: Geologie von Sachsen, edited by: Pälchen, W. and Walter, H., E. Schweizerbart'sche Verlagsbuchandlung, Stuttgart, 311–358, ISBN 9783510652709, 2008.

Ullrich, O. and Ender, W.: Siedlungsbefunde und ein Brunnen aus der Elbaue im Kieswerk Liebersee (Gem. Staritz, Lkr. Nordsachsen, in: Ausgrabungen in Sachsen 4, edited by: Smolnik, R., Arbeits- und Forschungsberichte zur sächsischen Bodendenkmalpflege, supplement 27, Dresden, 160–170, ISBN 9783943770131, 2014.

von Suchodoletz, H., Gärtner, A., Zielhofer, C., and Faust, D.: Eemian and post-Eemian fluvial dynamics in the Lesser Caucasus, Quaternary Sci. Rev. 191, 189–203, https://doi.org/10.1016/j.quascirev.2018.05.012, 2018.

von Suchodoletz, H., Berg, S., Eckmeier, E., Werther, L., and Zielhofer, C.: Preface: Special Issue "Geoarchaeology and past human–environment interactions", E & G – Quaternary Sci. J., 68, 237–240, https://doi.org/10.5194/egqsj-68-237-2020, 2020.

von Suchodoletz, H., Pohle, M., Khosravichenar, A., Ulrich, M., Hein, M., Tinapp, C., Schultz, J., Ballasus, H., Veit, U., Ettel, P., Werther, L., Zielhofer, C., and Werban, U.: The fluvial architecture of buried floodplain sediments of the Weiße Elster River (Germany) revealed by a novel method combination of drill cores with two-dimensional and spatially resolved geophysical measurements, Earth Surf. Process. Landf., 47, 955–976, https://doi.org/10.1002/esp.5296, 2022.

Wolf, L., Alexowsky, W., Dietze, W., Hiller, A., Krbetschek, M., Lange, J.-M., Seifert, M., Tröger, K.-A., Voigt, T., and Walther, H.: Fluviatile und glaziäre Ablagerungen am äußersten Rand der Elster- und Saale-Vereisung; die spättertiäre und quartäre Geschichte des sächsischen Elbegebietes (Exkursion A2), in: Das Quartär Mitteldeutschlands, edited by: Eissmann, L. and Litt, T., Altenburger naturwissenschaftliche Forschungen, Altenburg, 190–232, ISSN 02325381, 1994.

Wolf, L., Alexowsky, W., Heilmann, H. and Symanngk, R.: Quartär, in: Geologie von Sachsen, edited by: Pälchen, W. and Walter, H., E. Schweizerbart'sche Verlagsbuchandlung, Stuttgart, 419–472, ISBN 9783510652709, 2008.

E&G Quaternary Sci. J., 72, 77–94, 2023
https://doi.org/10.5194/egqsj-72-77-2023

Open Access E&G Quaternary Science Journal

Research article

Pleniglacial dynamics in an oceanic central European loess landscape

Stephan Pötter[1,2], **Katharina Seeger**[3], **Christiane Richter**[4], **Dominik Brill**[3], **Mathias Knaak**[5], **Frank Lehmkuhl**[1], **and Philipp Schulte**[1]

[1]Department of Geography, RWTH Aachen University, 52062 Aachen, Germany
[2]Chair of Geography, University of Koblenz-Landau, 56070 Koblenz, Germany
[3]Institute of Geography, University of Cologne, 50923 Cologne, Germany
[4]Institute of Geography, Technical University Dresden, 01069 Dresden, Germany
[5]Division Applied Geosciences, Geological Survey of North Rhine-Westphalia, 47803 Krefeld, Germany

Correspondence: Stephan Pötter (stephan.poetter@geo.rwth-aachen.de)

Relevant dates: Received: 13 May 2022 – Revised: 21 December 2022 – Accepted: 23 February 2023 – Published: 24 April 2023

How to cite: Pötter, S., Seeger, K., Richter, C., Brill, D., Knaak, M., Lehmkuhl, F., and Schulte, P.: Pleniglacial dynamics in an oceanic central European loess landscape, E&G Quaternary Sci. J., 72, 77–94, https://doi.org/10.5194/egqsj-72-77-2023, 2023.

Abstract: Loess–palaeosol sequences (LPSs) of the oceanic-influenced European loess belt underwent frequent post-depositional processes induced by surface runoff or periglacial processes. The interpretation of such atypical LPSs is not straightforward, and they cannot be easily used for regional to continental correlations. Within the last few years, however, such sequences gained increased attention, as they are valuable archives for regional landscape dynamics. In this study, the Siersdorf LPS was analysed using a multi-proxy approach using sedimentological, geochemical, and spectrophotometric methods combined with luminescence dating and tentative malacological tests to unravel Pleniglacial dynamics of the Lower Rhine Embayment. A marshy wetland environment for the late Middle Pleniglacial to the early Upper Pleniglacial was shown by colour reflectance and grain size distribution. Age inversions from luminescence dating paired with geochemical and sedimentological data reveal long-lasting erosional processes during the early Upper Pleniglacial, which were constrained to a relatively small catchment with short transport ranges. The upper sequence shows typical marker horizons for the study area and indicate harsh, cold-arid conditions for the late Upper Pleniglacial. In comparison with other terrestrial archives, the Siersdorf LPS shows that the Lower Rhine Embayment was more diverse than previously assumed, regarding not only its geomorphological settings and related processes but also its ecosystems and environments.

Kurzfassung: Die Lössprofile des ozeanisch beeinflussten europäischen Lössgürtels wurden häufig durch Oberflächenabfluss oder periglaziale Prozesse umgelagert. Die Interpretation solcher atypischen LPS ist nicht einfach und sie können nicht ohne weiteres für regionale bis kontinentale Korrelationen verwendet werden. In den letzten Jahren haben solche Sequenzen jedoch zunehmend an Bedeutung gewonnen, da sie wertvolle Archive für die regionale Landschaftsdynamik darstellen. In dieser Studie wurde das Lössprofil Siersdorf mit Hilfe eines Multi-Proxy-Ansatzes analysiert, der sedimentologische, geochemische und spektrophotometrische Methoden mit Lumineszenzdatierungen und versuchsweisen malakologischen Untersuchungen kombiniert, um die pleniglaziale Dynamik der Niederrheinischen Bucht zu entschlüsseln. Die Farbadaten und die Korngrößenverteilungen zeigen, dass das Profil vom späten Mittelpleniglazial bis zum frühen Oberpleniglazial in einem sumpfigen Feuchtgebiet lag. Altersinversionen aus Lumineszenzdatierungen gepaart mit geochemischen und sedimentologischen Daten lassen auf lang anhaltende Erosionsprozesse während des frühen Oberen Pleniglazials schließen, die auf ein relativ kleines Einzugsgebiet mit kurzen Transportstrecken beschränkt waren. Die obere Abfolge zeigt typische Markerhorizonte für das Untersuchungsgebiet und weist auf raue, kalt-trockene Bedingungen für das späte Obere Pleniglazial hin. Im Vergleich zu anderen terrestrischen Archiven zeigt das Siersdorfer LPS, dass die Niederrheinische Bucht vielfältiger war als bisher angenommen, nicht nur in Bezug auf ihre geomorphologischen Gegebenheiten und die damit verbundenen Prozesse, sondern auch in Bezug auf ihre Ökosysteme und Lebensräume.

1 Introduction

Throughout the last few decades, loess–palaeosol sequences (LPSs) have been frequently analysed to reconstruct palaeoclimatic and palaeoenvironmental conditions of the terrestrial realms (Hatté et al., 2001, 2013; Marković et al., 2005; Kukla et al., 1988; Zech et al., 2013; Torre et al., 2020; Varga et al., 2011). Therefore, sequences are investigated, which are as complete and undisturbed as possible to allow interregional correlations (Marković et al., 2018; Lehmkuhl et al., 2016) or direct reconstructions of atmospheric conditions (Obreht et al., 2017; Rousseau and Hatté, 2021; Bokhorst et al., 2011). These aeolian LPSs were formed out of mineral dust, which was deposited on topographic barriers (Lehmkuhl et al., 2016; Antoine et al., 2016), biological crusts (Svirčev et al., 2013), or vegetation, typically grasses (Zech et al., 2013, 2011). The deposited dust undergoes quasi-pedogenic processes called loessification processes (Sprafke and Obreht, 2016), leading to its unique characteristics, such as its silty texture and porosity (Pécsi and Richter, 1996; Koch and Neumeister, 2005). Due to these properties, loess is prone to post-depositional reworking and erosion, especially by water (Meszner et al., 2013, p. 201), and in regions affected by permafrost, by periglacial activities and slope processes (Lehmkuhl et al., 2021, 2016). This proneness can lead to hiatuses in the stratigraphy (Obreht et al., 2015; Steup and Fuchs, 2017) or the reworking of sediments. Additionally, weathering and soil formation processes, such as decalcification, feldspar weathering, or lessivation of clay, can transform the pristine sediments on various scales and can give valuable hints on past environmental conditions (Fenn et al., 2020, 2021; Marković et al., 2018; Lehmkuhl et al., 2016).

The European loess belt (ELB; loess domain II sensu; Lehmkuhl et al., 2021), stretches from the shores of the English Channel (Antoine et al., 2003; Stevens et al., 2020) throughout Belgium (Haesaerts et al., 2016), Germany (Lehmkuhl et al., 2018), and Poland (Jary and Ciszek, 2013) towards Ukraine (Veres et al., 2018). Especially the western ELB (subdomain IIa sensu; Lehmkuhl et al., 2021), which is characterised by a humid, oceanic climate, was prone to erosional processes such as slope wash or solifluction (Lehmkuhl et al., 2016). These conditions led to frequent reorganisation processes of landscape systems due to widespread erosion throughout the ELB (Meszner et al., 2013), partially leading to relief reversals (Fischer et al., 2012; Kels, 2007; Lehmkuhl et al., 2015). The continental ice sheets to the north and the periglacially shaped central European uplands to the south dominated the Pleistocene palaeogeography of the ELB, acting as potential dust sources of Pleistocene loess deposits due to high production rates of detrital material (Baykal et al., 2021; Skurzyński et al., 2019, 2020; Vinnepand et al., 2022). Additionally, the climatic conditions and vicinity to continental and Alpine ice sheets induced periglacial conditions, especially during glacial and stadial phases (Jary, 2009; Lehmkuhl et al., 2021; Vandenberghe et al., 2014; Stadelmaier et al., 2021).

The results of these processes are, compared to other European loess regions like the Danube Basin (Marković et al., 2015), complex stratigraphic records with unconformities and polygenetic pedocomplexes in the western ELB. Therefore, complete Late Pleistocene LPSs, without any hiatuses or discordances, are scarce (Schirmer, 2002; Zens et al., 2018). Within the last few years, however, considerable attention was given to non-typical LPSs, which were either strongly reworked (Klinge et al., 2017; Steup and Fuchs, 2017; Meszner et al., 2014) or which were characterised by changing depositional milieus (Mayr et al., 2017; Sümegi et al., 2015; Hošek et al., 2017). These archives allow a detailed view of the interplay of climate, landscape development, and environment and are, therefore, a crucial addition to the vast set of Pleistocene sediment archives.

Here, we present geochronological and proxy data for a new LPS in the Lower Rhine Embayment (North Rhine-Westphalia, Germany). The Siersdorf (SID) LPS developed in a channel incised into an older Pleistocene terrace of the Meuse. It represents a high-resolution record of the transition from the late Middle (MPG) to the Upper Pleniglacial (UPG). Unlike typical LPSs from the area, the Middle Pleniglacial stadial conditions are not imprinted as a series of phases of differently intense soil formation processes but as a uniform unit of greyish-brownish silt, most likely linked to semi-terrestrial marshy conditions. In this study, we analyse the sedimentological, geochemical, and spectrophotometric data to unravel the genesis of this atypical sedimentary succession. The geomorphological and palaeoenvironmental ramifications are discussed in the framework of loess research in the Rhine catchment. The Siersdorf LPS is a crucial addition to the framework of Pleniglacial landscape reconstruction, as it is so far the first reported LPS from the Lower Rhine Embayment which records semi-terrestrial conditions during the late Middle Pleniglacial to Upper Pleniglacial. This reconstruction shows that the Pleniglacial Lower Rhine Embayment was more diverse than previously assumed, regarding not only its geomorphological settings and related processes but also its ecosystems and environments.

2 Research area and study site

2.1 The Lower Rhine Embayment

The Lower Rhine Embayment (LRE) is part of the European rift system and covers the southernmost part of the Lower Rhine catchment. It is situated on the transition of the central European uplands, namely the Rhenish Massif, and the northern German lowlands (Böse et al., 2022). As a loess region, the LRE is part of the western European maritime (Atlantic) loess subdomain of the ELB sensu (Lehmkuhl et al., 2021). This part of the ELB was dominated by North Atlantic climate conditions during the Late Pleistocene (Antoine et al., 2001, 2009; Fischer et al., 2021). Due to the oceanic climate and the accompanied high landscape dynamics (Fischer et al., 2017), the distribution and characteristics of loess deposits in the LRE are strongly site-specific, depending on geomorphological settings and related processes.

Four main geomorphological positions for LPSs can be summarised (Lehmkuhl et al., 2016). LPSs in plateau situations are often affected by erosion, both by surface runoff and by deflation (Schirmer, 2016; Antoine et al., 2016). Additionally, chemical processes such as (carbonate) solution and leaching may affect these sequences. Slope positions in the LRE are especially prone to erosional processes. Truncation, e.g. related to phases of widespread erosion, may remove previously formed LPSs in their entirety (Schirmer, 2016). Similar conditions have been reported from adjacent regions of the ELB (Meszner et al., 2013; Antoine et al., 2016). Besides fluvial relocation, processes such as solifluction play a major role in slope positions (Lehmkuhl et al., 2016). Under periglacial conditions, a slope gradient of 2° is sufficient to initiate reworking by solifluction (Lehmkuhl, 2016). Relocated material is transported downslope and deposited on the slope toe. These positions act not only as sediment traps during loess formation (Antoine et al., 2016) but also as sinks of soil sediments and other relocated material (Kappler et al., 2018; Kühn et al., 2017). This also applies to depressions and erosional channels. Within these topographic sinks, detrital material of various origins, i.e. aeolian, colluvial, or other slope sediments, accumulates, leading to complex stratigraphical archives. As the geomorphological setting and sedimentological processes are crucial in the formation of sediment sequences, their discussion is essential to understand the evolution of LPSs and for their correlation with other environmental archives (Marković et al., 2018; Lehmkuhl et al., 2016; Fischer et al., 2017).

The LRE builds the easternmost part of this maritime loess domain, which shows comparable stratigraphic records for the Late Pleistocene from northern France towards the study area (Haesaerts et al., 2011; Meijs, 2002; Schirmer, 2016; Antoine et al., 2014): the oldest sequence builds the last interglacial, i.e. Eemian, palaeosol, a truncated brown-leached soil complex. The Weichselian glacial succession starts with an early glacial (115–72 ka) complex, consisting of a grey forest soil and a steppe-like soil. The Lower Pleniglacial (LPG; 70–58 ka) is the phase with the first reported (and preserved) loess formation in central Europe (Frechen et al., 2003), accompanied by periglacial conditions. The Middle Pleniglacial (MPG; 58–32 ka) was characterised by reduced dust accumulation (Antoine et al., 2001), frequent relocation of older sediments and soils (Meszner et al., 2013), and phases of soil formation (Fischer et al., 2021; Schirmer et al., 2012). However, MPG sequences are often only preserved in geomorphologically favourable settings. The Upper Pleniglacial (UPG; 32–15 ka) was characterised by enhanced dust accretion and harsh, periglacial conditions (Lehmkuhl et al., 2021). Typical features for these periods are Gelic Gleysols (tundra gleys) and ice-wedge casts (Antoine et al., 2016). In the LRE, the UPG deposits show a typical succession encompassing inter alia the so-called Eben Zone (Schirmer, 2003).

The study site is located within the so-called Aldenhoven loess plateau as part of the Börde region of Jülich (Knaak et al., 2021). This plateau, situated between the Wurm, Inde, and Rur rivers in the foreland of the northern Eifel Mountains (Fig. 1), is slightly inclined towards the northeast (170–75 m a.s.l.). Vast loess blankets cover the palaeorelief, which is characterised by small dendritic river systems. These blankets mainly formed during the Late Pleistocene as dust was entrained from the Middle Pleistocene terraces of the Rhine, Meuse, and Rur rivers. Steps in the landscape, where loess thicknesses vary considerably within a few metres, are indicative of recent differential tectonic processes. Late Pleistocene to Holocene features approx. 1 km northwest of the studied sequence, such as solifluction layers or other stratigraphic markers, show tectonically induced offsets of approx. 1 m, indicating younger tectonic movements (Fig. S1 in the Supplement). Additionally, tectonics shaped the hydrological system, as river deflections are abundant in the study area.

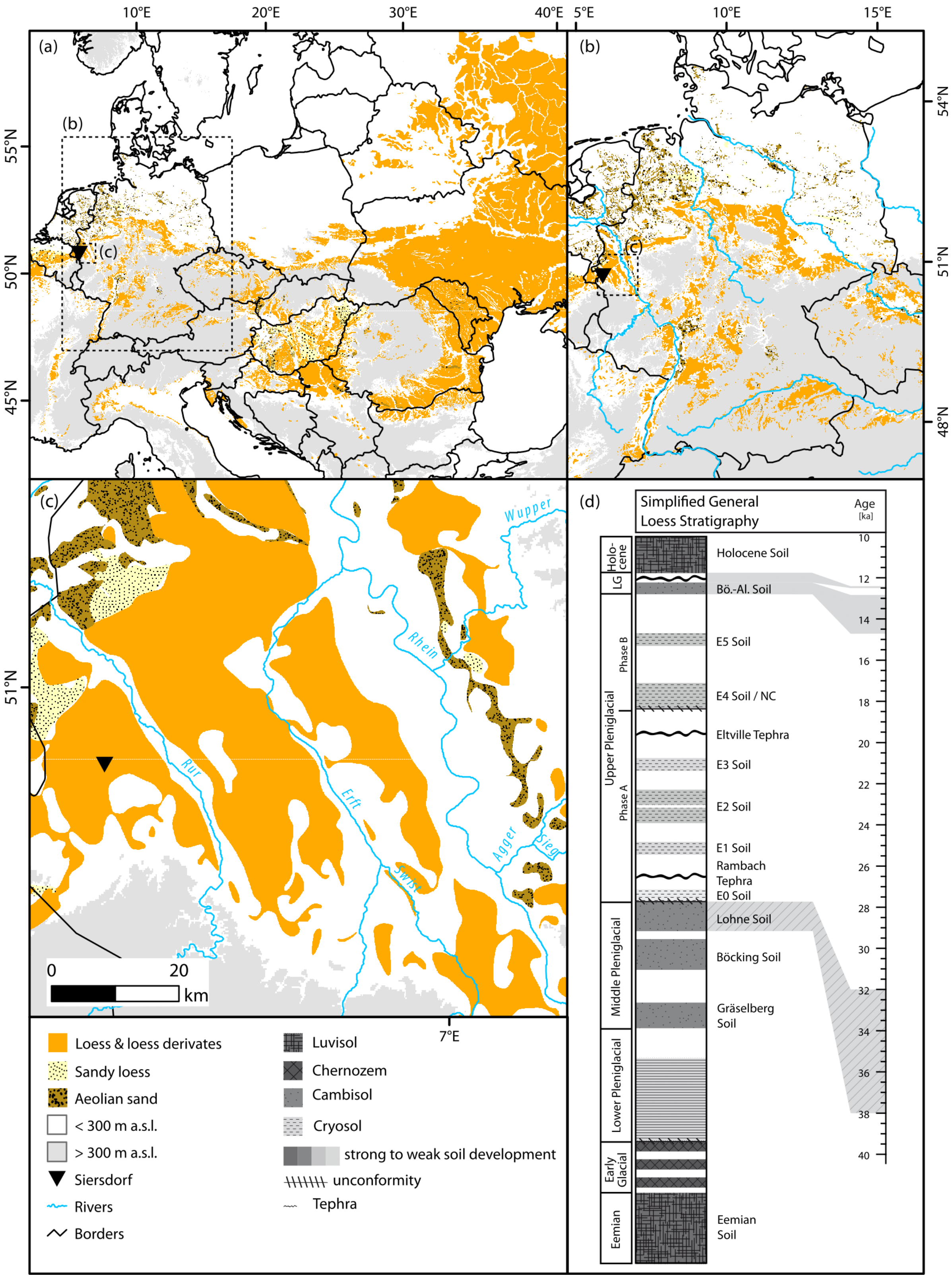

Figure 1. Location of the Siersdorf LPS (black triangle) **(a)** within the European loess belt, **(b)** in Germany, and **(c)** within the Lower Rhine Embayment. Distribution of aeolian sediment according to Lehmkuhl et al. (2021). **(d)** Simplified and generalised loess stratigraphy for central Europe, adapted from Zens et al. (2018).

2.2 The Siersdorf loess–palaeosol sequence

The Siersdorf (SID) LPS was exposed during construction works of the Zeelink natural gas pipeline in the central part of the Aldenhoven loess plateau (Fig. 1). The investigated sequence is 6 m thick (Fig. 2) and developed within a channel of a presumably Middle Pleistocene terrace of the Meuse. The deposits of the Meuse covered large parts of the central LRE during the Pleistocene (Boenigk and Frechen, 2006). The incised channel acted as a sediment trap throughout the Late Pleistocene and Holocene. Based on field observations, the sequence can be subdivided into five main units: the base, unit I, is characterised by greyish-dark-brownish silts, which change colour during drying to grey. Nearby core drillings indicate strong hydromorphic overprinting of these layers (Fig. S2). The upper part of this layer shows a high abundance of mollusc shells and shell fragments. The overlying loess (unit II) is laminated and partially characterised by cryoturbation features. At the base of this relocated loess, a thin, blackish layer occurs. The laminated layer stretches from 4.8 to 3.5 m below surface. Small ice-wedge pseudomorphs frequently disturb the layering, which shows varying contents of silt and sand. On top of the layered loess adjoins an orange, wavy layer (unit III). Greyish-brownish palaeosol layers, which show characteristics of Gelic Gleysols, built the uppermost part of unit III. Above this complex, the sequence consists of relatively unaltered loess (unit IV). This loess is also the fill material for massive ice-wedge pseudomorphs approx. 3 m left of the sampled section, which pierces the below-lying units until the top of the lowermost layer (Fig. 2). A humic, finely layered colluvial unit covers the loess (unit V). This reworked sediment contains small pebbles and charcoal flitters. The uppermost 90 cm of the sequence is anthropogenically disturbed.

3 Methods

3.1 Field work and sampling

The SID LPS was sampled in May 2021 after exposure during construction works of the Zeelink natural gas pipeline. Prior to description and sampling, several decimetres of exposed sediments were removed to avoid contamination with weathered and relocated material. The sequence was described in detail from the bottom to the top. Samples for sedimentological, geochemical, and colorimetric analyses were taken in a continuous sampling trench. Sampling was conducted using freshly cleaned tools and sterile plastic bags. The anthropogenically disturbed uppermost 90 cm was not sampled. The colluvial unit (0.9–1.7 m) was sampled in 10 cm increments, whereas the rest of the sequence was sampled every 5 cm.

For luminescence dating, six samples were taken horizontally with steel cylinders from selected units (for position of samples, see Fig. 2). Subsequently, the sediment within a 30 cm distance to the cylinders was sampled for dose rate determination.

3.2 Sedimentological, geochemical, and spectrophotometric analyses

The samples were dried at 35 °C, sieved to the fraction < 2 mm, and two subsamples of each sample (0.1 and 0.3 g) were pre-treated with 0.7 mL H_2O_2 (30 %) at 70 °C for 12 h. This process was repeated until bleaching of the material was visible (Allen and Thornley, 2004) but not longer than 3 d. To keep the particles dispersed during analysis, the samples were treated with 1.25 mL $Na_4P_2O_7 \cdot 10H_2O$ in an overhead shaker for 12 h. The grain size was determined with a Beckman Coulter LS 13 320 laser diffractometer using Mie theory (fluid refractive index (RI): 1.33, sample RI: 1.55, imaginary RI: 0.1) (Özer et al., 2010; Nottebaum et al., 2015; Schulte et al., 2016). Grain size distributions were calculated and visualised as distribution heatmaps according to Schulte and Lehmkuhl (2018, Fig. 3). To detect (neo-)formations of clay minerals, the differences between the two optical models of Mie theory and the Fraunhofer approximation were calculated and centred log transformed (Schulte and Lehmkuhl, 2018). The results are visualised as heatmaps as well (Fig. 4).

Inorganic geochemistry was analysed using energy dispersive x-ray fluorescence (EDPXRF) using a SPECTRO XEPOS. This device detects 50 elements from sodium (Na) to uranium (U), excluding erbium and ytterbium. The samples were sieved to the silt fraction (< 63 µm) and dried at 105 °C for 12 h. A subsample of 8 g for each sample was mixed with 2 g FLUXANA CEREOX wax, homogenised in a shaker. The sample was pressed to a pellet with a pressure of 19.2 MPa for 120 s. The measurements were conducted by means of a pre-calibrated method. Each sample was measured in duplicate, and the pellets were rotated by 90° between measurements to avoid matrix effects. Conspicuous samples, where the difference of both measurements was striking, were measured again in duplicate to avoid analytical artefacts. Geochemical data are visualised as depth plots and in the form of the A–CN–K ternary diagram according to Nesbitt and Young (1984). The carbonate content was defined volumetrically using a SCHEIBLER apparatus (ISO 20693, 1995; Schaller, 2000).

Spectrophotometric analysis was conducted using a Konica Minolta CM-5 spectrophotometer, following previously published methodologies (Eckmeier and Gerlach, 2012; Vlaminck et al., 2016). This device uses the diffused reflected light from a standardised source (2° Standard Observer, Illuminant C) to obtain the colour spectra of the visible light (360 to 740 nm). The results were converted to the CIELAB colour space ($L^*a^*b^*$) using the SpectraMagic NX software (Konica Minolta). The dried and homogenised samples were measured in duplicate and averaged.

Figure 2. **(a)** Simplified stratigraphic sketch of the Siersdorf loess–palaeosol sequence. **(b)** Short description of main stratigraphic units. **(c)** Photo of the sequence after sampling (photo: Stephan Pötter). **(d)** Laminated loess package and basal palaeosol (photo: Philipp Schulte). **(e)** Ice-wedge cast, approx. 3 m left of the sampled sequence, piercing the underlying layers for more than 2 m (photo: Stephan Pötter).

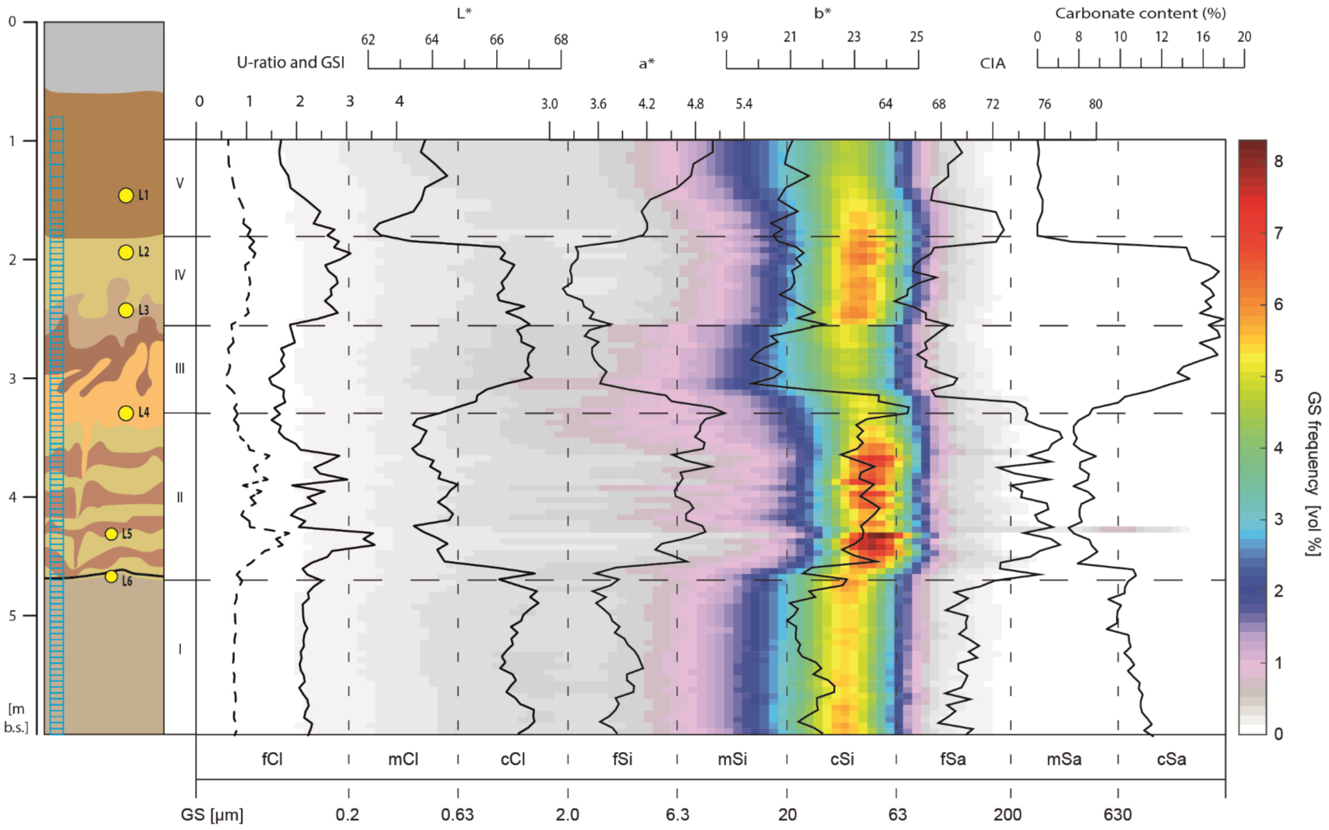

Figure 3. Heatmap visualisation of grain size distribution displayed with various sedimentological, geochemical, and spectrophotometric proxies of the Siersdorf LPS. Stratigraphic units (I–V) are shown for orientation.

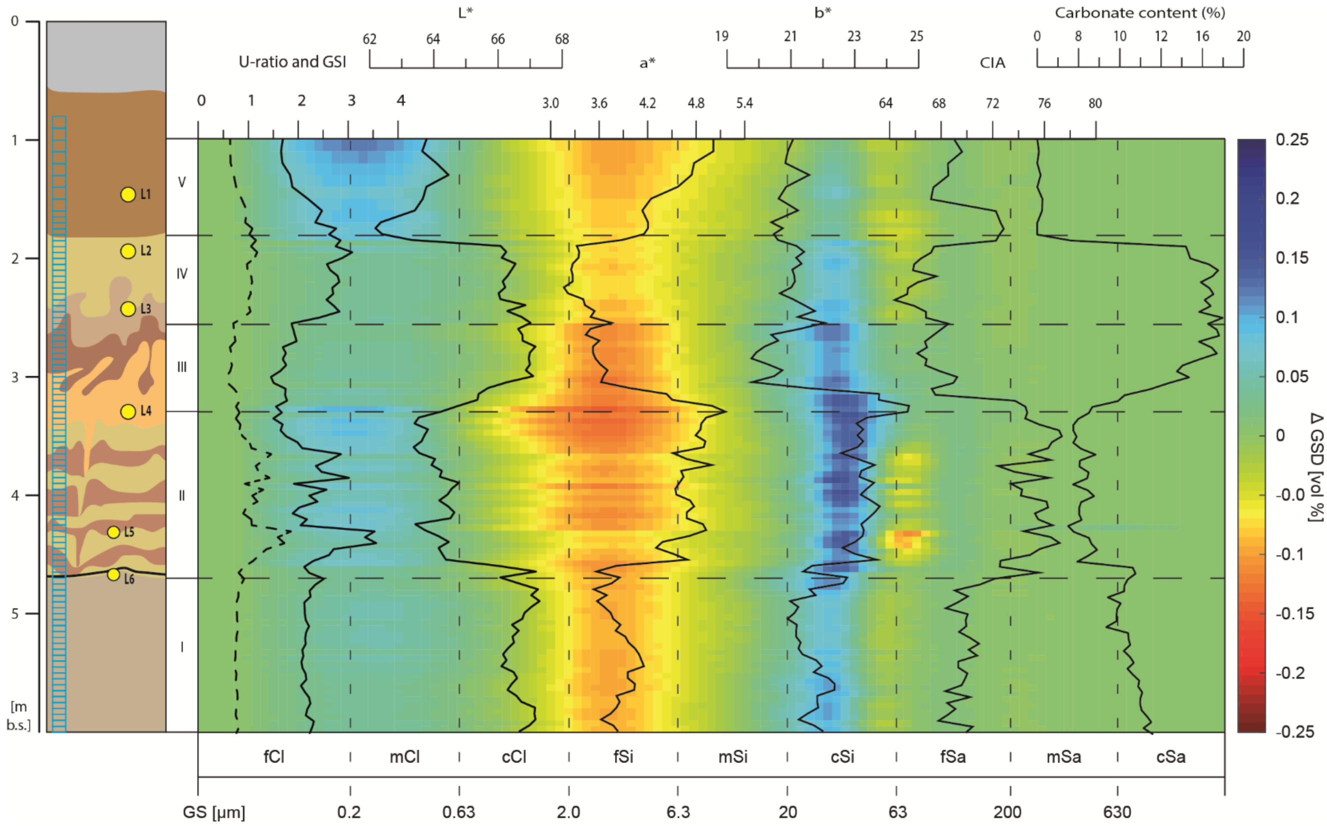

Figure 4. Heatmap visualisation of the difference between two optical models (ΔGSD) displayed with various sedimentological, geochemical, and spectrophotometric proxies of the Siersdorf LPS. Stratigraphic units (I–V) are shown for orientation.

3.3 Luminescence dating

Sample preparation and measurements were conducted in the Cologne Luminescence Laboratory (Cologne, Germany) and included pre-processing under red light conditions. Standard procedures of fine-grain preparation included chemical treatment with HCl (10 %), H_2O_2 (10 %), and $Na_2C_2O_4$ (0.01 N) to remove carbonates, organic components, and aggregates. The 4–11 µm fraction was then separated by settling due to gravitation and centrifugation following Frechen et al. (1996). To derive pure quartz, the 4–11 µm fraction was etched with HF (37 %) and finally washed with HCl (10 %).

Equivalent dose measurements were performed on an automated Risø TL/OSL DA-15 reader (DTU Nutech, Roskilde, Denmark) equipped with a calibrated ^{90}Sr / ^{90}Y beta source. Discs were prepared by pipetting a suspension of 1 mg sediment and 0.2 mL deionised water and drying them afterwards. Polymineralic fine-grain samples were stimulated for 200 s by using infrared diodes (870 nm, FWHM = 40) and detected through an interference filter (410 nm). To obtain a feldspar signal not (or not significantly) affected by anomalous fading, a post-infrared infrared (pIRIR) stimulated luminescence protocol was applied with a second stimulation temperature of 290 °C ($pIRIR_{290}$) following Thiel et al. (2011). For quartz fine-grain samples, signals were stimulated with blue LEDs and detected through a U340 filter. Measurements followed a conventional single aliquot regenerative dose (SAR) protocol (Murray and Wintle, 2000).

The suitability of both measurement protocols for the samples of this study was tested based on preheat plateau (only for quartz samples) and dose recovery tests (for all samples). Furthermore, laboratory residual doses after solar simulator bleaching for 24 h and laboratory fading following Auclair et al. (2003) were determined for $pIRIR_{290}$ signals. For each sample, the palaeodose was calculated based on 5–12 accepted aliquots. Aliquots outside a 2σ range were excluded from further calculations. Since scatter in dose distributions of fine-grain samples is completely absent (reflected by overdispersions of around zero for all samples), the arithmetic mean plus standard deviation was chosen to calculate burial doses.

Dose rates were determined by measuring uranium, thorium, and potassium contents using high-resolution gamma spectrometry (Ortec PROFILE M-Series GEM P-type Coaxial HPGe Gamma-Ray Detector). Dosimetry and age calculation were conducted in the DRAC environment (version 1.2; Durcan et al., 2015) using typical water contents of European loess (i.e. 15 ± 5 %; Pécsi, 1990; Klasen et al., 2015) instead of in situ measured ones, as these likely underestimate the hydromorphic conditions at the SID site. Further details on the measurement procedure of dose rate and equivalent dose determination are given in the Supplement.

4 Results

4.1 Sedimentological, geochemical, and spectrophotometric analyses

The grain size distributions (GSDs) of SID show typical patterns for central European loess deposits. Figure S3 shows the distribution curves for all main units identified during fieldwork. The lowermost unit I shows a unimodal GSD with a mode in the middle-coarse silt fraction. The contents of fine particles, especially fine silt and clay, are elevated. The laminated loess unit shows high variations in GSDs. The overlying cryoturbated loess layers show less variations, with strong modes in coarse silt and varying clay and sand contents. The GSD of the brownish-greyish palaeosol also shows a unimodal shape with a mode in coarse silt. Since other fractions, especially clay, are increased, this mode does not show as high values as the other layers. The uppermost loess layer shows a strong coarse silt mode, whereas the colluvial unit is relatively clay rich.

The geochemical results (Figs. 3–5) were utilised to calculate the Chemical Index of Alteration (CIA; Nesbitt and Young, 1982) to determine phases of enhanced chemical weathering. The basal complex does not show any variations in the CIA with all values being lower than 70. The laminated loess package shows higher values of > 70, as does the orange cryoturbated layer. The uppermost loess layer again shows decreased values, with a peak on the base of the overlying colluvial unit. The A–CN–K ternary diagram shows a distribution broadly parallel to the CN join, which can be broadly divided into two clusters (Fig. 5). The lower cluster is uniformly parallel, whereas the upper cluster shows some tendencies towards a more vertical distribution. A similar pattern is reflected by spectrophotometric analyses. The lower unit shows slight variations in the L^*, a^*, and b^* values. The layered unit shows rapidly decreased L^* and increased a^* and b^* values. The orange cryoturbated layer shows the maximum values for a^* and b^*, whereas the upper loess shows decreased redness and yellowness values. The colluvial unit is characterised by dark (low L^*) and brown colours (high a^*).

4.2 Luminescence dating

The results of the luminescence experiments are presented in the Supplement. All parameters relevant for age calculation and calculated ages for the six luminescence samples are presented in Table 1. Palaeodoses were calculated based on De measurements of 5–10 aliquots that were all accepted for data analysis (the very low scatter between De values did not require a larger number of aliquots). Given the absence of significant over-dispersion (Figs. S11 and S12), the arithmetic mean was chosen as the appropriate age model.

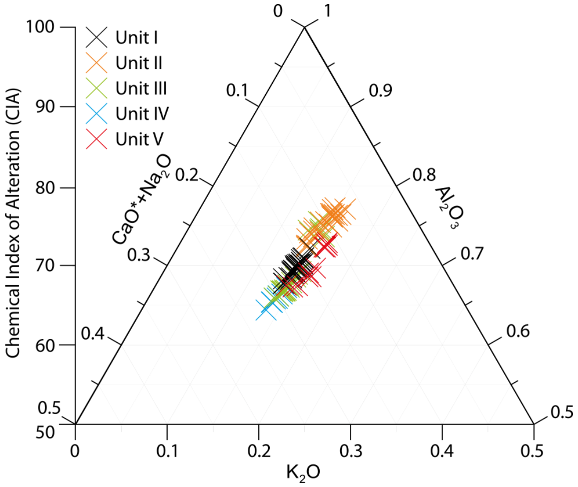

Figure 5. A–CN–K ternary diagram according to Nesbitt and Young (1984) for the Siersdorf LPS. The Chemical Index of Alteration is displayed on the *y* axis.

For polymineralic samples, burial doses range from 77 ± 1 Gyr (SID L1) to 177 ± 5 Gyr (SID L4). For the uppermost five samples, resulting ages are in stratigraphic order (Fig. 6). In contrast, the quartz ages are in line with the whole sedimentary sequence except for SID L1. Here, the quartz age of 34 ka significantly overestimates the feldspar age of 16 ka. Since it causes an inversion compared to the layers dated below, the quartz age of SID L1 should not be trusted. We have no explanation for this overestimation (since the pIRIR ages are significantly younger, this cannot be a bleaching issue), but this unit must be younger than at least 20 ka (SID L2). For SID L2 and L3, both quartz and feldspar ages are identical and yield ages of 18 to 23 ka. The quartz and pIRIR$_{290}$ ages calculated for samples SID L4 and L5 overlap within their uncertainties. The quartz and pIRIR$_{290}$ ages for SID L6 show an age inversion to the samples above and are therefore not stratigraphically consistent.

5 Discussion

5.1 Formation processes of an atypical loess sequence in the Lower Rhine Embayment

The Siersdorf LPS is a valuable archive for Weichselian Pleniglacial landscape dynamics. Combined sedimentological, geochemical, and spectrophotometric methods reveal distinct changes of environmental conditions and associated geomorphic processes during the formation of the investigated LPS, indicating a more heterogeneous environment in the LRE than previously assumed.

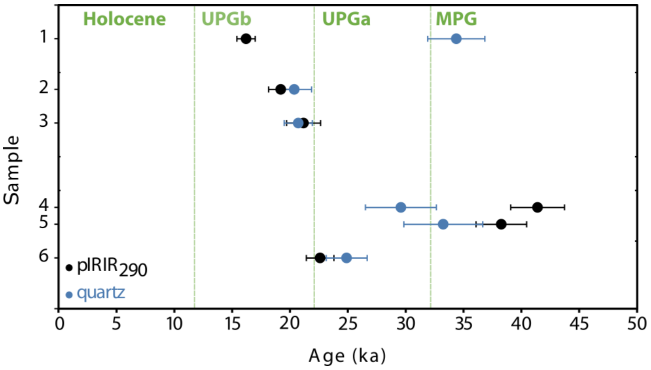

Figure 6. Age depth plot with feldspar ages and quartz ages. Age estimates for the Middle Pleniglacial (MPG), early Upper Pleniglacial (UPGa), late Upper Pleniglacial (UPGb), and the Holocene according to Zens et al. (2018).

5.1.1 Unit I

Unit I shows uniform patterns in most of the analysed proxy data. Especially the GSD and ΔGSD show almost no variations within this unit (Figs. 3 and 4). The low, uniform ΔGSD excludes this unit as a palaeosol, as pedogenic processes would favour the formation of clay minerals (Schulte and Lehmkuhl, 2018), which was observed for LPSs in the Rhine–Meuse catchment (Zens et al., 2018). The lack of large quantities of sand, as well as the uniform GSD of the unit, excludes large-scale relocation processes, pointing to an in situ formation of this unit. In-field measurements of the magnetic susceptibility in SID revealed low values for the respective lithological unit (Knaak et al., 2021), precluding biogenic formation of iron oxides. The proxy data, e.g. the low and uniform ΔGSD, indicate that unit I does not represent a typical interstadial palaeosol.

The unit's bright-greyish hues, shown by high L^* and low a^* and b^* values (Fig. 3), indicate a reductive milieu during or after deposition of the medium-coarse silt. The uniform sedimentology together with these grey shades point to a depositional milieu differing from the typical dust traps such as topographic barriers (Antoine et al., 2016; Lehmkuhl et al., 2016) or vegetation. A possible explanation for these prevailing reductive conditions would be a dust deposition in a semi-terrestrial environment. Such an environment was reported from the Bobingen LPS (BOB) in southern Germany (Mayr et al., 2017). The site was covered by a lake during the MPG, which is reflected by highly reduced blueish-greyish sediments and lacustrine faunal remains. During the late MPG, the lake silted up, and typical subaerial loess formation began. A similar situation was reported from the Ringen LPS (RGE) in the Middle Rhine Valley, where a gyttja was correlated to the MPG based on palynological evidence (Henze, 1998). This unit shows blueish-greyish hues and a silty-clayey texture and is approx. 2 m thick (Fig. S4). The colour and texture change towards the top, as the top is more oxidised and contains coarser grains. This succession reveals that the gyttja at the Ringen LPS, as a trap for both moisture and mineral dust, was continually covered by increased input of aeolian detrital material during the MPG–UPG transition, silting up the marshy environment. Similar conditions have been reported from the Bína LPS in Slovakia, although these were correlated to the Lower Pleniglacial (marine isotope stage (MIS) 4) (Hošek et al., 2017).

Besides macroscopic similarities between the two units of SID and RGE, the respective sedimentological evidence also points to similar environmental conditions. Both LPSs show unimodal GSDs, dominated by medium-coarse silt with slightly elevated clay contents (Fig. S3). These distributions indicate input of aeolian dust. Increased sand contents indicate additional but considerably less input by surface runoff. The water-saturated conditions are imprinted not only in greyish colours and sedimentology but also in wavy, flaky structures reported from field observations, indicating a micro-layering in a quiescent depositional environment. In RGE and BOB, the sediment is completely bleached and shows signs of intense reduction of ferruginous compounds, namely blueish-greyish hues. In SID, however, the lower intensity of reduction processes indicates shorter phases of semi-terrestrial conditions compared to the former sites. However, another plausible explanation is that the unit did not develop under proper lacustrine conditions comparable to BOB or RGE but in a marshy wetland situation, presumably with seasonal drying phenomena.

Within around 10 %, the carbonate content within unit I allowed the preservation of a high number of mollusc shells and shell fragments. Although no samples according to proper malacological protocols were taken, some cautious interpretation of malacofauna is feasible, always against the backdrop of the methodological issues. For this rough screening, bulk sediment samples from unit I were wet sieved (2 mm mesh) to separate the molluscs from the sediment. The tentative analyses show a poor species community with only two species comprising a high number (> 2000 individuals) of *Trochulus hispidus* and a smaller number (< 30 individuals) of *Succinella oblonga*. Both are euryoecious species, tolerating a wide range of conditions. The high number of shells that stood out visually in this layer is an indication that there was more vegetation and thus food supply and shelter compared to the rest of the sequence. However, *Trochulus hispidus* as well as *Succinella oblonga* are typical representatives of the poor snail communities found under extreme environmental conditions within Pleistocene loess ecosystems (e.g. Moine, 2008), as they are highly adaptable and able to tolerate both drought as well as temporary flooding. Their mere presence might indicate frequent wet-to-waterlogged ground conditions due to a depressed relief, permafrost-caused impermeable subsoil, and enhanced precipitation. Although caution is required due to methodological deficits, the low biodiversity and imbalance in the distribution of individuals among species equally indicate a highly stressed ecosystem and harsh conditions. Better conditions e.g. due to better-drained grounds and longer vegetation periods usually relate to a higher biodiversity within the snail communities (see Moine, 2008). For a more reliable interpretation, however, a detailed examination of the gastropod fauna is necessary, including an adequate sampling technique and analyses of the complete sequence.

From a geomorphogenetic point of view, the position of SID in an incised channel favours both sediment accumulation and moisture availability (Lehmkuhl et al., 2016). Especially during times with waterlogging, e.g. induced by permafrost conditions, moisture became concentrated in such depressions. These conditions led to the formation of wetlands, with temporary flooding within the channel caused by increased precipitation. As the Late Pleistocene was characterised by several phases of relatively enhanced dust fluxes (Zens et al., 2018; Fischer et al., 2021), and the SID site is located near potential dust sources, mainly the Pleistocene braided systems of the Meuse and the Rhine, as well as their tributaries (Lehmkuhl et al., 2018), these ponds were subjected to periodical inputs of aeolian dust. Although unit I partially shows slightly elevated sand contents (Fig. 3), the generally fine and particular unimodal GSD indicates input of aeolian dust into this marshy environment as the major sedimentological process.

5.1.2 Unit II

After the marshy environment was covered with aeolian dust, formation of unit II began. This unit's main characteristics are a distinct layering with alternating dark brown and ochre-beige bands as well as small ice-wedge pseudomorphs permeating the layers. Generally, the transition from unit I to unit II shows sharp decreases or increases in most analysed proxies (Figs. 3 and 4). Especially the GSD from a medium-coarse silt mode to a mode bordering the fine-sand fraction may indicate erosional processes during this transitional period. Layered units in LPSs are well known from the ELB (Lehmkuhl et al., 2021; Antoine et al., 2016, 2001, 2013). They are usually correlated to the Upper Pleniglacial Hesbaye loess (Haesaerts et al., 2016; Schirmer, 2016) and are explained by a shift towards colder, more humid climatic conditions, including extensive snow covers during winter. Dust sedimentation on snow covers leads to a fine lamination, which is most likely due to micro-sorting processes during snowmelt. These laminations are usually a few millimetres thick with sandy bases fining-up upwards (Antoine et al., 2001). The laminations in SID, however, are partly several centimetres thick and show distinct differences in both colour and grain size. These differences show up by the reflectance data and the grain size patterns: generally, unit II is coarser than unit I. Additionally, it shows larger GSD variations with sandier bands. These sandier bands usually show higher a^* values and a higher CIA, indicating soil sediment eroded from higher topographic positions deposited in the channel. The GSD, especially with the high fluctuations of sand contents, excludes in situ soil-forming processes in this unit, although the ΔGSD is elevated in the clay fraction compared to unit I. Usually, this proxy is an indicator for in situ soil formation, as it reflects the neo-formation of clay minerals (Schulte and Lehmkuhl, 2018). In the case of unit II, however, the high ΔGSD together with other granulometric and sedimentological features rather point to a short-range transport of eroded soil material, where clay agglomerates were not destroyed during transport, and clay particles were not removed by further outwash. The stratigraphic inconsistencies of the luminescence ages (see Fig. 6 and Sect. 4.2) also indicate relocation by surface runoff, hindering complete bleaching of the material. Relatively low contents of carbonate within unit II also point to soil sediments, as carbonates were removed by leaching prior relocation. The lighter bands are associated with higher grain size index (GSI) and U-ratio values due to increased aeolian input of mineral dust or rather increased deposition of relocated loess (Fig. 4). The slightly vertical point distribution within the upper cluster of the A–CN–K ternary diagram, a feature which indicates hydraulic sorting (Pötter et al., 2021; Ohta, 2004), also points to reworking. Unit II was frequently overprinted by harsh, periglacial conditions, as indicated by a multitude of small, centimetre-scale ice-wedge casts permeating several layers of the package. The sedimentological features of the unit are the results of fluctuating environmental conditions during the formation phase of unit II.

5.1.3 Unit III

Unit III of the SID LPS shows a characteristic succession of an orange layer and two distinct palaeosol layers (Fig. 2). The sediments of unit III generally have finer GSD modes compared to unit II, paired with a slightly decreased U ratio and GSI. The entire unit shows evidence of heavy reworking by cryoturbation, especially wavy-layer contacts and low ΔGSD values for the clay fraction. This succession strongly resembles the so-called Eben Zone (see Sect. 5.2), which is an important UPG marker horizon for the oceanic ELB (Lehmkuhl et al., 2021; Schirmer, 2003). This zone is reflected in the proxy data, e.g. by enhanced clay contents and low GSI and U-ratio values between 3 and 2.5 m depth. The reworking of the soil material is expressed in the absence of very fine particles, shown in the ΔGSD ratios (Fig. 4). Generally, unit III shows fewer signs of intensive soil formation processes and less evidence for reworking by surface runoff than the layers of unit II. The carbonate contents and L^* values are increased as opposed to the decreased CIA and a^* values (Fig. 3).

5.1.4 Unit IV

Unit IV is composed of relatively unaltered loess. The unit is well sorted and is characterised by a typical GSD for central European loess deposits, showing a strong mode in the coarse silt fraction (Fig. S3). The high carbonate contents of approx. 20 % and $L*$ values of approx. 66 show characteristic values for pristine Late Pleistocene deposits of the western ELB. Unit IV was, therefore, formed by the deposition of aeolian dust and subsequent loessification processes. The sharp contact to the above-lying unit V, however, both observed in the field and in proxy data (Figs. 3 and 4), points to a phase of erosion after unit IV was formed.

5.1.5 Unit V

The uppermost unit V shows a combination of no carbonate, high $a*$ values, and reflectance ($L*$). Macroscopic features, such as the fine layering and the high abundance of charcoal flitters, together with lack of carbonate and relatively uniform GSD, point to a colluvial origin of this layer. During colluviation, (soil) sediment eroded from higher positions was transported to and deposited at the site. Additionally, the layer was influenced by post-depositional alterations, such as decalcification.

5.2 Reconstruction of Pleniglacial dynamics

In combination with the luminescence dating results (see Sect. 3.2), the formation processes of the Siersdorf LPS draw a detailed picture of regional imprints of the late MPG–UPG transition in the western ELB. The Pleniglacial dynamics of the SID site are summarised in the following conceptual model (see also Fig. 7). The correlation of unit I to the MPG–UPG transition (Fig. 7a and b) is based on one sample (SID L6) near the upper boundary of the unit. Luminescence analyses yield ages of 24.9 ± 1.8 ka (Q) and 22.6 ± 1.2 ka (KF, potassium feldspar) respectively. These ages indicate that the marshy environment at SID prevailed at least until the Upper Pleniglacial phase a (UPGa) sensu (Zens et al., 2018). Nearby core drillings, however, show that this unit is in total approx. 2 m thick, reaching a depth of around 7 m (Fig. S2). Therefore, the waterlogged environment in the incised terrace channel occurred during large parts of the UPGa and most likely also during the MPG–UPG transition. This interpretation, however, is based on the SID L6 sample and stratigraphic evidence. Further and more detailed reconstructions of fluctuations within the MPG require a denser chronological framework, e.g. by radiocarbon dating of mollusc shells. Nonetheless, the here-presented data allow a tentative correlation of unit I to the MPG–UPG transition.

The MPG, closely correlated with the MIS 3, was a phase of severe environmental fluctuations in the ELB. Periods of climatic ameliorations and pedogenesis, due to higher moisture availability (Fischer et al., 2021; Antoine et al., 2013; Schirmer et al., 2012; Hošek et al., 2017; Vinnepand et al., 2020), alternated with periods of erosion and (re-)deposition of soils and sediment (Meszner et al., 2011, 2013). Phases of soil formations can be traced in proxy data, as the ΔGSD signals (Zens et al., 2018), organic carbon contents (Fischer et al., 2021), or the $a*$ values increase in palaeosols (Krauß et al., 2016), whereas relocation can be reconstructed e.g. using grain size data (Meszner et al., 2014). In SID, the late MPG and early UPG are characterised by marshy conditions (see Sect. 5.1). These conditions were favoured by waterlogging

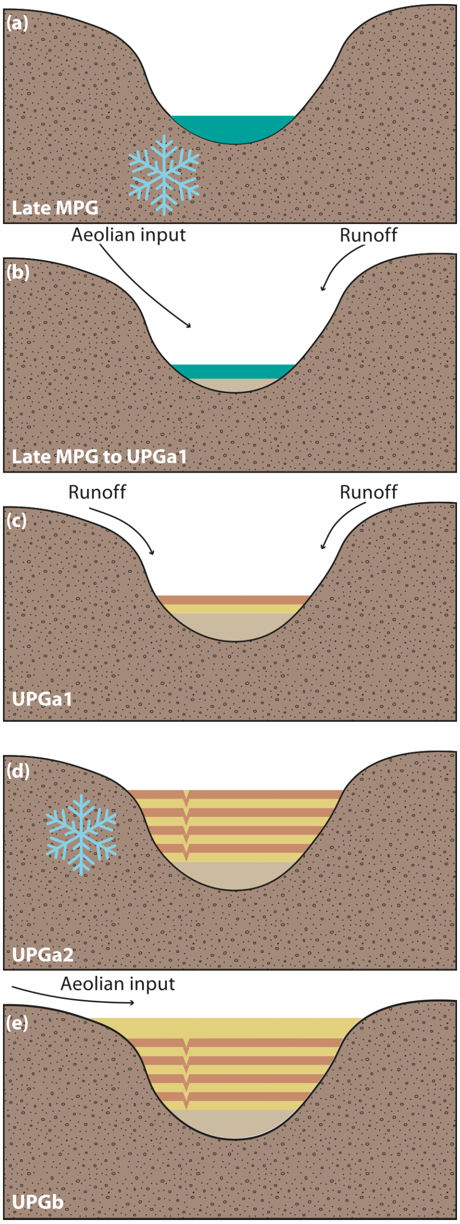

Figure 7. Schematic model of the Middle and early Upper Pleniglacial site formation of the Siersdorf LPS. **(a)** Marshy wetland conditions during the late MPG. **(b)** Silting up by aeolian input and surface runoff during the late MPG to early UPG. **(c)** Formation of layered unit by relocation of silty and sandy material by surface runoff in the early UPG (UPGa$_1$). **(d)** Periglacial overprinting and deformation of the layered unit during the LGM (UPGa$_2$). **(e)** Typical, subaerial loess formation during the UPGb.

due to permafrost (Fig. 7a), which was observed for other regions of the ELB (Sedov et al., 2016). These conditions are also reflected in the tentative malacological results, which show a potentially wet environment where the faunal assemblages were subjected to environmental stress.

The silting up of the marshy environment lasted during the MPG–UPG transitions until the early UPG (UPGa sensu; Zens et al., 2018). This phase of rapid climatic deterioration is in European loess landscapes coupled with a strong increase in dust production and subsequent loess formation (Meszner et al., 2013; Meyer-Heintze et al., 2018; Lehmkuhl et al., 2016; Antoine et al., 2013, 2009). This period is considered the phase with the highest dust accumulation rates in Europe (Zens et al., 2018; Frechen et al., 2003). In the LRE and other oceanic-influenced loess regions, the loess deposits of the beginning UPG, the so-called UPGa (Lehmkuhl et al., 2016; Zens et al., 2018, 2017), are named Hesbaye loess, (Schirmer, 2016) after the Belgian loess region (Haesaerts et al., 1997, 1981). The layered Hesbaye loess is often characterised by fluvial reworking or by dust deposition and loess formation under snow-influenced conditions. This feature is typical for the ELB and can be found from France towards the East European Plain (Antoine et al., 2009; Zens et al., 2018; Lehmkuhl et al., 2021). In SID, the layered unit II is dated by the quartz ages of samples SID L4 and L5 to 36.7–26.5 ka (Fig. 6). These calculated ages are stratigraphically inconsistent compared to SID L6, indicating deposition of older material after the formation of unit I. The inherited older ages of L4 and L5 as well as slightly older feldspar ages point to incomplete bleaching due to the relocation of the sediment, which points to a short transport range during sediment transport by surface runoff. The erosional processes during the MPG–UPG transition and the early UPG are widespread phenomena within the ELB (Meszner et al., 2013), often removing large parts or even entire MPG successions. The proxy data of unit II, in combination with the luminescence properties, allow for a reconstruction of short-scale transport of Middle Pleniglacial soil material during the UPGa, particularly to the steppe phase (Zens et al., 2018; Sirocko et al., 2016). The relocated material was frequently subjected to harsh, periglacial conditions, as indicated by a multitude of small ice-wedge casts (Fig. 2). Based on these geomorphological features, the periglacial overprinting is correlated to the tundra stage of the UPGa (Zens et al., 2018; Sirocko et al., 2016) where cold, dry conditions prevailed.

The later UPG succession (UPGb; Lehmkuhl et al., 2016; Zens et al., 2018, 2017) is also known as the Brabant member in the regional stratigraphy and mostly reflects loess formation during fully glacial conditions (Schirmer, 2016, 2000). Samples L4 and L3 bracket the orange and brownish-greyish complex of unit III, with ages between 30 and 21 ka. The ages, especially derived from quartz minerals (L4: 29.6 ± 3.1 ka; L3: 20.7 ± 1.2 ka), as well as the characteristics of this unit, allow a correlation with the so-called Eben Zone, composed of the orange Kesselt layer and the brownish-greyish Belmen and Elfgen soils (Schirmer, 2003). The high overlap of quartz- and feldspar-derived luminescence ages can be explained by the aeolian origin of this layer, which was indeed overprinted by periglacial processes but not by relocation. This characteristic zone is restricted to the Lower Rhine area and is a key marker layer for the UPG (Zens et al., 2018; Lehmkuhl et al., 2016, 2021). Samples L3 and L2 reflect the MIS 2 age of the Brabant loess. Their partial overlap within uncertainties allows a tentative, semi-quantitative reconstruction of accumulation rates, which were the highest during the LGM. This is in accordance with the general aeolian setting of the ELB (Rousseau et al., 2021). The typical subaerial characteristics of the upper units of SID indicate drier conditions compared to unit I, which can be related to the ongoing filling of the channel and lower moisture availability.

As the geomorphological setting is crucial not only for dust accumulation but also for preservation of LPSs especially (Lehmkuhl et al., 2016; Antoine et al., 2016; Marković et al., 2018), the favourable position of SID in a channel incised into an old Meuse River terrace led to a relatively thick accumulation of most likely Middle but especially Upper Pleniglacial sediments. Although LPSs in other extraordinary geomorphological situations such as loess dunes, so-called *gredas* (Antoine et al., 2001, 2009), or near watersheds (Henze, 1998; Zens et al., 2018) allow even thicker Pleniglacial loess deposits, the UPG record of SID exceeds those of many other regions in adjacent areas (Krauß et al., 2021; Antoine et al., 2016; Rahimzadeh et al., 2021; Krauß et al., 2016). Unit IV preserved 1 m of unaltered loess. Although loess formation generally continued throughout the late glacial in the Rhenish loess realm (Zens et al., 2018; Fischer et al., 2021), the SID sequence does not show any signs of late MIS 2 loess formation. The uppermost sample SID L2 within the Brabant loess yields quartz ages of 20.4 ± 1.5 ka (feldspar: 19.2 ± 1.1 ka), indicating late UPG ages for loess formation of the youngest preserved loess. Late glacial loess formation cannot be excluded for SID. However, these deposits were most likely eroded during the Pleistocene–Holocene transition. Extremely harsh and cold periglacial conditions during the UPG have influenced the sequence, as a large approx. 2 m deep ice-wedge pseudomorph pierced almost the entire sequence 3 m from the sampling spot (Fig. 2). As this cast is filled with material very similar to unit IV and pierces all underlying units, the age can be constrained to the UPG, although no direct timing was possible.

The LRE was strongly affected by anthropogenically induced soil erosion since the Early to Middle Holocene (Gerlach, 2006; Gerlach et al., 2006; Protze, 2014; Schulz, 2007; Gerz, 2017). However, the feldspar age calculated from the sample SID L1, taken from the base of the colluvial unit, yields a late glacial age (16.2 ± 0.8 ka). The quartz age (34.4 ± 2.5 ka) was excluded from the discussion, as it cannot be explained e.g. by partial bleaching possibly during extreme precipitation events. As the widespread and intensive colluviation in the area only occurred in the Middle to Late Holocene (Schulz, 2007; Protze, 2014), it appears that the material was not fully bleached during relocation. Therefore, an exact timing of these erosional processes is not possible. Stratigraphical evidence of nearby exposures, however, indicates tectonic activities during the Late Pleistocene and Holocene, as features such as the decalcification boundary were affected by tectonic displacement. Therefore, the colluviation in SID could be the result of a landscape reorganisation due to tectonic movements in a highly active region (Fernández-Steeger et al., 2011; Reicherter et al., 2011; Grützner et al., 2016).

The sedimentary sequence of SID shows a complex interplay of various depositional milieus together with proposed active tectonic setting. It is a valuable archive for landscape dynamics in the LRE and suggests that the area was highly diverse during the Late Pleistocene. The high-resolution sedimentological, geochemical, and spectrophotometric analyses reveal a change from wetter conditions with ephemeral ponds and wetlands to a silting up of these wetlands and highly erosive conditions towards typical subaerial loess formation. The SID sequence, therefore, is a crucial addition to the framework of the landscape analyses of the Pleniglacial western ELB.

6 Conclusions

The Siersdorf LPS is an important site for Late Pleistocene dynamics of the Lower Rhine Embayment, indicating changing depositional environments during the period covered. The combination of sedimentological, geochemical, and spectrophotometric data with luminescence dating and tentative malacological tests shows that the sequence was under the influence of a marshy wetland environment during the late MPG and early UPGa, a unique feature for the LRE. Observed permafrost-induced conditions show the strong influence of the geomorphological setting and related processes on characteristics of sedimentary sequences. The UPGb was influenced by long-lasting erosional processes, which, however, were constrained to short-range transport mechanisms. The typical subaerial formation processes of the upper part of the sequence correlated to the UPGa, with typical regional marker horizons such as the Eben Zone, point to cold-arid conditions during this time, as observed for large parts of the European loess belt. Overall, this study stresses the importance of the geomorphological setting and related sedimentological and post-depositional processes in relation to the formation, preservation, and resulting characteristics of LPSs. Our results show not only that the LRE was subjected to fluctuating climate during the Pleniglacial but also that the area was more fragmented than previously thought, especially regarding the environmental setting.

Data availability. Data are available upon request to the corresponding author.

Supplement. The supplement related to this article is available online at: https://doi.org/10.5194/egqsj-72-77-2023-supplement.

Author contributions. SP designed the study together with FL and PS. PS, MK, FL, and SP took the analysed samples during two separate fieldwork campaigns in 2020. KS and DB performed luminescence dating and laboratory tests and compiled and discussed the results within the scientific framework. CR analysed the mollusc shells and fragments, which were provided by MK, and discussed their interpretability. SP wrote the initial draft of the manuscript with helpful comments and suggestions from the other authors. All authors discussed the data and participated in its interpretation.

Competing interests. The contact author has declared that none of the authors has any competing interests.

Special issue statement. This article is part of the special issue "Quaternary research from and inspired by the first virtual DEUQUA conference". It is a result of the vDEUQUA2021 online conference in September/October 2021.

Acknowledgements. We thank Marianne Dohms, Renate Erdweg, and their team for the laboratory framework and Klaus Reicherter for his helpful comments on the tectonic evolution of the Lower Rhine Embayment in the field. We also thank the three anonymous reviewers for their constructive comments and remarks, which substantially improved this manuscript, and the editorial team for the uncomplicated handling of the manuscript.

Financial support. The investigations were carried out in the frame of the CRC 806 Our way to Europe – funded by the Deutsche Forschungsgemeinschaft (DFG, German Research Foundation, grant no. 57444011-SFB 806).

This open-access publication was funded
by the RWTH Aachen University.

Review statement. This paper was edited by Julia Meister and reviewed by three anonymous referees.

References

Allen, J. R. L. and Thornley, D. M.: Laser granulometry of Holocene estuarine silts: effects of hydrogen peroxide treatment, Holocene, 14, 290–295, https://doi.org/10.1191/0959683604hl681rr, 2004.

Antoine, P., Rousseau, D.-D., Zöller, L., Lang, A., Munaut, A.-V., Hatté, C., and Fontugne, M.: High-resolution record of the last Interglacial–glacial cycle in the Nussloch loess–palaeosol sequences, Upper Rhine Area, Germany, Quatern. Int., 76–77, 211–229, https://doi.org/10.1016/S1040-6182(00)00104-X, 2001.

Antoine, P., Catt, J., Lautridou, J.-P., and Sommé, J.: The loess and coversands of northern France and southern England, J. Quaternary Sci., 18, 309–318, https://doi.org/10.1002/jqs.750, 2003.

Antoine, P., Rousseau, D.-D., Moine, O., Kunesch, S., Hatté, C., Lang, A., Tissoux, H., and Zöller, L.: Rapid and cyclic aeolian deposition during the Last Glacial in European loess: a high-resolution record from Nussloch, Germany, Quaternary Sci. Rev., 28, 2955–2973, https://doi.org/10.1016/j.quascirev.2009.08.001, 2009.

Antoine, P., Rousseau, D.-D., Degeai, J.-P., Moine, O., Lagroix, F., Kreutzer, S., Fuchs, M., Hatté, C., Gauthier, C., Svoboda, J., and Lisá, L.: High-resolution record of the environmental response to climatic variations during the Last Interglacial–Glacial cycle in Central Europe: the loess-palaeosol sequence of Dolní Věstonice (Czech Republic), Quaternary Sci. Rev., 67, 17–38, https://doi.org/10.1016/j.quascirev.2013.01.014, 2013.

Antoine, P., Goval, E., Jamet, G., Coutard, S., Moine, O., Hérisson, D., Auguste, P., Guérin, G., Lagroix, F., Schmidt, E., Robert, V., Debenham, N., Meszner, S., and Bahain, J.-J.: Les séquences loessiques pléistocène supérieur d'Havrincourt (Pas-de-Calais, France): stratigraphie, paléoenvironnements, géochronologie et occupations paléolithiques, Quaternaire, 25, 321–368, https://doi.org/10.4000/quaternaire.7278, 2014.

Antoine, P., Coutard, S., Guerin, G., Deschodt, L., Goval, E., Locht, J.-L., and Paris, C.: Upper Pleistocene loess-palaeosol records from Northern France in the European context: Environmental background and dating of the Middle Palaeolithic, Quatern. Int., 411, 4–24, https://doi.org/10.1016/j.quaint.2015.11.036, 2016.

Auclair, M., Lamothe, M., and Huot, S.: Measurement of anomalous fading for feldspar IRSL using SAR, Radiat. Meas., 37, 487–492, https://doi.org/10.1016/S1350-4487(03)00018-0, 2003.

Baykal, Y., Stevens, T., Engström-Johansson, A., Skurzyński, J., Zhang, H., He, J., Lu, H., Adamiec, G., Költringer, C., and Jary, Z.: Detrital zircon U–Pb age analysis of last glacial loess sources and proglacial sediment dynamics in the Northern European Plain, Quaternary Sci. Rev., 274, 107265, https://doi.org/10.1016/j.quascirev.2021.107265, 2021.

Boenigk, W. and Frechen, M.: The Pliocene and Quaternary fluvial archives of the Rhine system, Quaternary Sci. Rev., 25, 550–574, https://doi.org/10.1016/j.quascirev.2005.01.018, 2006.

Bokhorst, M. P., Vandenberghe, J., Sümegi, P., Łanczont, M., Gerasimenko, N. P., Matviishina, Z. N., Marković, S. B., and Frechen, M.: Atmospheric circulation patterns in central and eastern Europe during the Weichselian Pleniglacial inferred from loess grain-size records, Quatern. Int., 234, 62–74, https://doi.org/10.1016/j.quaint.2010.07.018, 2011.

Böse, M., Ehlers, J., and Lehmkuhl, F.: Der Mittelgebirgsrand, in: Deutschlands Norden, Springer, Berlin, Heidelberg, 63–87, https://doi.org/10.1007/978-3-662-64361-7_4, 2022.

Durcan, J. A., King, G., and Duller, G. A. T.: DRAC: Dose Rate and Age Calculator for trapped charge dating, Quat. Geochronol., 28, 54–61, https://doi.org/10.1016/j.quageo.2015.03.012, 2015.

Eckmeier, E. and Gerlach, R.: Characterization of Archaeological Soils and Sediments Using VIS Spectroscopy, eTopoi – Journal for Ancient Studies, 3, 285–290, https://doi.org/10.17169/refubium-21739, 2012.

Fenn, K., Durcan, J. A., Thomas, D. S. G., Millar, I. L., and Marković, S. B.: Re-analysis of late Quaternary dust mass accumulation rates in Serbia using new luminescence chronology for loess–palaeosol sequence at Surduk, Boreas, 49, 634–652, https://doi.org/10.1111/bor.12445, 2020.

Fenn, K., Thomas, D. S. G., Durcan, J. A., Millar, I. L., Veres, D., Piermattei, A., and Lane, C. S.: A tale of two signals: Global and local influences on the Late Pleistocene loess sequences in Bulgarian Lower Danube, Quaternary Sci. Rev., 274, 107264, https://doi.org/10.1016/j.quascirev.2021.107264, 2021.

Fernández-Steeger, T., Grützner, C., Reicherter, K., and Schaub, A.: Aquisgrani terrae motus factus est (part 1): The Aachen cathedral (Germany) built on weak ground?, Quatern. Int., 242, 138–148, https://doi.org/10.1016/j.quaint.2011.05.004, 2011.

Fischer, P., Hilgers, A., Protze, J., Kels, H., Lehmkuhl, F., and Gerlach, R.: Formation and geochronology of Last Interglacial to Lower Weichselian loess/palaeosol sequences – case studies from the Lower Rhine Embayment, Germany, E&G Quaternary Sci. J., 61, 48–63, https://doi.org/10.3285/eg.61.1.04, 2012.

Fischer, P., Hambach, U., Klasen, N., Schulte, P., Zeeden, C., Steininger, F., Lehmkuhl, F., Gerlach, R., and Radtke, U.: Landscape instability at the end of MIS 3 in western Central Europe: evidence from a multi proxy study on a Loess-Palaeosol-Sequence from the eastern Lower Rhine Embayment, Germany, Quatern. Int., 502, 119–136, https://doi.org/10.1016/j.quaint.2017.09.008, 2017.

Fischer, P., Jöris, O., Fitzsimmons, K. E., Vinnepand, M., Prud'homme, C., Schulte, P., Hatté, C., Hambach, U., Lindauer, S., Zeeden, C., Peric, Z., Lehmkuhl, F., Wunderlich, T., Wilken, D., Schirmer, W., and Vött, A.: Millennial-scale terrestrial ecosystem responses to Upper Pleistocene climatic changes: 4D-reconstruction of the Schwalbenberg Loess-Palaeosol-Sequence (Middle Rhine Valley, Germany), CATENA, 196, 104913, https://doi.org/10.1016/j.catena.2020.104913, 2021.

Frechen, M., Schweitzer, U., and Zander, A.: Improvements in sample preparation for the fine grain technique, Anc. TL, 14, 15–17, 1996.

Frechen, M., Oches, E. A., and Kohfeld, K. E.: Loess in Europe – mass accumulation rates during the Last Glacial Period, Quaternary Sci. Rev., 22, 1835–1857, https://doi.org/10.1016/S0277-3791(03)00183-5, 2003.

Gerlach, R.: Holozän: Die Umgestaltung der Landschaft durch den Menschen seit dem Neolithikum, in: Urgeschichte im Rheinland, edited by: Kunow, J. and Wegner, H., Verlag des Rheinischen Vereins für Denkmalpflege und Landschaftsschutz, Köln, 87–98, ISBN 9783880948143, 2006.

Gerlach, R., Baumewerd-Schmidt, H., van den Borg, K., Eckmeier, E., and Schmidt, M. W. I.: Prehistoric alteration of soil in the Lower Rhine Basin, Northwest Germany – archaeological, 14C and geochemical evidence, Geoderma, 136, 38–50, https://doi.org/10.1016/j.geoderma.2006.01.011, 2006.

Gerz, J.: Prähistorische Mensch-Umwelt-Interaktionen im Spiegel von Kolluvien und Befundböden in zwei Löss-Altsiedellandschaften mit unterschiedlicher Boden- und Kulturgeschichte (Schwarzerderegion bei Halle/Saale und Parabraunerderegion Niederrheinische Bucht), Universitäts- und Stadtbibliothek Köln, Köln, URN urn:nbn:de:hbz:38-75297, 2017.

Grützner, C., Fischer, P., and Reicherter, K.: Holocene surface ruptures of the Rurrand Fault, Germany – insights from palaeoseismology, remote sensing and shallow geophysics, Geophys. J. Int., 204, 1662–1677, https://doi.org/10.1093/gji/ggv558, 2016.

Haesaerts, P., Juvigne, E., Kuyl, O., Mucher, H., and Roebroeks, W.: An account of the excursion of June, 13, 1981 in the Hesbaye area and to Dutch Limbourg, devoted to the chronostratigraphy of Upper Pleistocene loess, Ann.-Soc. Geol. Belg., 104, 223–240, 1981.

Haesaerts, P., Mestdagh, H., and Bosquet, D.: La séquence loessique de Remicourt (Hesbaye, Belgique), Notae Praehistoricae, 17, 45–52, 1997.

Haesaerts, P., Pirson, S., and Meijs, E.: Revised Lithostratigraphy of the aeolian loess deposits. Addendum to F. Gullentops et al. 2001. “Quaternary lithostratigraphic units (Belgium)”, Geol. Belg., 4, 153–164, 2011.

Haesaerts, P., Damblon, F., Gerasimenko, N., Spagna, P., and Pirson, S.: The Late Pleistocene loess-palaeosol sequence of Middle Belgium, Quatern. Int., 411, 25–43, https://doi.org/10.1016/j.quaint.2016.02.012, 2016.

Hatté, C., Antoine, P., Fontugne, M., Lang, A., Rousseau, D.-D., and Zöller, L.: δ^{13}C of Loess Organic Matter as a Potential Proxy for Paleoprecipitation, Quaternary Res., 55, 33–38, https://doi.org/10.1006/qres.2000.2191, 2001.

Hatté, C., Gauthier, C., Rousseau, D.-D., Antoine, P., Fuchs, M., Lagroix, F., Marković, S. B., Moine, O., and Sima, A.: Excursions to C4 vegetation recorded in the Upper Pleistocene loess of Surduk (Northern Serbia): an organic isotope geochemistry study, Clim. Past, 9, 1001–1014, https://doi.org/10.5194/cp-9-1001-2013, 2013.

Henze, N.: Kennzeichnung des Oberwürmlösses der Niederrheinischen Bucht, Geologisches Institut der Universität zu Köln, Dissertation, Köln, 212 pp., ISBN 978-3-934027-00-8, 1998.

Hošek, J., Lisá, L., Hambach, U., Petr, L., Vejrostová, L., Bajer, A., Grygar, T. M., Moska, P., Gottvald, Z., and Horsák, M.: Middle Pleniglacial pedogenesis on the northwestern edge of the Carpathian basin: A multidisciplinary investigation of the Bíňa pedo-sedimentary section, SW Slovakia, Palaeogeogr. Palaeoclimatol. Palaeoecol., 487, 321–339, https://doi.org/10.1016/j.palaeo.2017.09.017, 2017.

ISO 20693: Soil quality – Determination of carbonate content – Volumetric method, International Organization for Standardization, Geneva, 1995.

Jary, Z.: Periglacial markers within the Late Pleistocene loess–palaeosol sequences in Poland and Western Ukraine, Quatern. Int., 198, 124–135, https://doi.org/10.1016/j.quaint.2008.01.008, 2009.

Jary, Z. and Ciszek, D.: Late Pleistocene loess–palaeosol sequences in Poland and western Ukraine, Quatern. Int., 296, 37–50, https://doi.org/10.1016/j.quaint.2012.07.009, 2013.

Kappler, C., Kaiser, K., Tanski, P., Klos, F., Fülling, A., Mrotzek, A., Sommer, M., and Bens, O.: Stratigraphy and age of colluvial deposits indicating Late Holocene soil erosion in northeastern Germany, CATENA, 170, 224–245, https://doi.org/10.1016/j.catena.2018.06.010, 2018.

Kels, H.: Bau und Bilanzierung der Lössdecke am westlichen Niederrhein, Heinrich-Heine-Universität Düsseldorf, URN urn:nbn:de:hbz:061-20070220-084835-4, 2007.

Klasen, N., Fischer, P., Lehmkuhl, F., and Hilgers, A.: Luminescence dating of loess deposits from the Remagen-Schwalbenberg site, Western Germany, Geochronometria, 42, https://doi.org/10.1515/geochr-2015-0008, 2015.

Klinge, M., Lehmkuhl, F., Schulte, P., Hülle, D., and Nottebaum, V.: Implications of (reworked) aeolian sediments and paleosols for Holocene environmental change in Western Mongolia, Geomorphology, 292, 59–71, https://doi.org/10.1016/j.geomorph.2017.04.027, 2017.

Knaak, M., Becker, S., Steffens, W., Mustereit, B., Hartkopf-Fröder, C., Prinz, L., Stichling, S., Schulte, P., and Lehmkuhl, F.: Boden des Jahres 2021 – ein Lössprofil auf der Aldenhovener Lössplatte, in: Archäologie im Rheinland 2020, Nünnerich-Asmus, Oppenheim, ISBN 978-3-96176-162-3, 2021.

Koch, R. and Neumeister, H.: Zur Klassifikation von Lösssedimenten nach genetischen Kriterien (About the classification of loess sediments using genetic criteria), Z. Geomorphol. NF, 49, 183–203, 2005.

Krauß, L., Zens, J., Zeeden, C., Schulte, P., Eckmeier, E., and Lehmkuhl, F.: A multi-proxy analysis of two loess-paleosol sequences in the northern Harz foreland, Germany, Palaeogeogr. Palaeoclimatol. Palaeoecol., 461, 401–417, https://doi.org/10.1016/j.palaeo.2016.09.001, 2016.

Krauß, L., Klasen, N., Schulte, P., and Lehmkuhl, F.: New results concerning the pedo- and chronostratigraphy of the loess–palaeosol sequence Attenfeld (Bavaria, Germany) derived from a multi-methodological approach, J. Quaternary Sci., 36, 1382–1396, https://doi.org/10.1002/jqs.3298, 2021.

Kühn, P., Lehndorff, E., and Fuchs, M.: Lateglacial to Holocene pedogenesis and formation of colluvial deposits in a loess landscape of Central Europe (Wetterau, Germany), CATENA, 154, 118–135, https://doi.org/10.1016/j.catena.2017.02.015, 2017.

Kukla, G., Heller, F., Ming, L. X., Chun, X. T., Sheng, L. T., and Sheng, A. Z.: Pleistocene climates in China dated by magnetic susceptibility, Geology, 16, 811–814, https://doi.org/10.1130/0091-7613(1988)016<0811:PCICDB>2.3.CO;2, 1988.

Lehmkuhl, F.: Modern and past periglacial features in Central Asia and their implication for paleoclimate reconstructions, Prog. Phys. Geogr. Earth Environ., 40, 369–391, https://doi.org/10.1177/0309133315615778, 2016.

Lehmkuhl, F., Wirtz, S., Falk, D., and Kels, H.: Geowissenschaftliche Untersuchungen zur Landschaftsentwicklung im Tagebau Garzweiler – LANU-Projekt 2012–2014, in: Archäologie im Rheinland 2014, edited by: Kunow, J. and Trier, M., Theiss Verlag, Stuttgart, 64–66, ISBN 978-3-8062-3214-1, 2015.

Lehmkuhl, F., Zens, J., Krauß, L., Schulte, P., and Kels, H.: Loess-paleosol sequences at the northern European loess belt in Germany: Distribution, geomorphology and stratigraphy, Quaternary Sci. Rev., 153, 11–30, https://doi.org/10.1016/j.quascirev.2016.10.008, 2016.

Lehmkuhl, F., Pötter, S., Pauligk, A., and Bösken, J.: Loess and other Quaternary sediments in Germany, J. Maps, 14, 330–340, https://doi.org/10.1080/17445647.2018.1473817, 2018.

Lehmkuhl, F., Nett, J. J., Pötter, S., Schulte, P., Sprafke, T., Jary, Z., Antoine, P., Wacha, L., Wolf, D., Zerboni, A., Hošek, J., Marković, S. B., Obreht, I., Sümegi, P., Veres, D., Zeeden, C., Boemke, B. J., Schaubert, V., Viehweger, J., and Hambach, U.: Loess landscapes of Europe – mapping, geomorphology, and zonal differentiation, Earth-Sci. Rev., 215, 103496, https://doi.org/10.1016/j.earscirev.2020.103496, 2021.

Marković, S. B., McCoy, W. D., Oches, E. A., Savic, S., Gaudenyi, T., Jovanovic, M., Stevens, T., Walther, R., Ivanisevic, P., and Galic, Z.: Paleoclimate record in the Upper Pleistocene loess-paleosol sequence at Petrovaradin brickyard (Vojvodina, Serbia), Geol. Carpathica, 56, 545–552, 2005.

Marković, S. B., Stevens, T., Kukla, G. J., Hambach, U., Fitzsimmons, K. E., Gibbard, P., Buggle, B., Zech, M., Guo, Z., Hao, Q., Wu, H., O'Hara Dhand, K., Smalley, I. J., Újvári, G., Sümegi, P., Timar-Gabor, A., Veres, D., Sirocko, F., Vasiljević, D. A., Jary, Z., Svensson, A., Jović, V., Lehmkuhl, F., Kovács, J., and Svirčev, Z.: Danube loess stratigraphy – Towards a pan-European loess stratigraphic model, Earth-Sci. Rev., 148, 228–258, https://doi.org/10.1016/j.earscirev.2015.06.005, 2015.

Marković, S. B., Stevens, T., Mason, J., Vandenberghe, J., Yang, S., Veres, D., Újvári, G., Timar-Gabor, A., Zeeden, C., Guo, Z., Hao, Q., Obreht, I., Hambach, U., Wu, H., Gavrilov, M. B., Rolf, C., Tomić, N., and Lehmkuhl, F.: Loess correlations – Between myth and reality, Palaeogeogr. Palaeoclimatol. Palaeoecol., 509, 4–23, https://doi.org/10.1016/j.palaeo.2018.04.018, 2018.

Mayr, C., Matzke-Karasz, R., Stojakowits, P., Lowick, S. E., Zolitschka, B., Heigl, T., Mollath, R., Theuerkauf, M., Weckend, M.-O., Bäumler, R., and Gregor, H.-J.: Palaeoenvironments during MIS 3 and MIS 2 inferred from lacustrine intercalations in the loess–palaeosol sequence at Bobingen (southern Germany), E&G Quaternary Sci. J., 66, 73–89, https://doi.org/10.5194/egqsj-66-73-2017, 2017.

Meijs, E. P. M.: Loess stratigraphy in Dutch and Belgian Limburg, E&G Quaternary Sci. J., 51, 115–131, https://doi.org/10.3285/eg.51.1.08, 2002.

Meszner, S., Fuchs, M., and Faust, D.: Loess-Palaeosol-Sequences from the loess area of Saxony (Germany), E&G Quaternary Sci. J., 60, 4, https://doi.org/10.3285/eg.60.1.03, 2011.

Meszner, S., Kreutzer, S., Fuchs, M., and Faust, D.: Late Pleistocene landscape dynamics in Saxony, Germany: Paleoenvironmental reconstruction using loess-paleosol sequences, Quatern. Int., 296, 94–107, https://doi.org/10.1016/j.quaint.2012.12.040, 2013.

Meszner, S., Kreutzer, S., Fuchs, M., and Faust, D.: Identifying depositional and pedogenetic controls of Late Pleistocene loess-paleosol sequences (Saxony, Germany) by combined grain size and microscopic analyses, Z. Geomorphol., 58, 63–90, https://doi.org/10.1127/0372-8854/2014/S-00169, 2014.

Meyer-Heintze, S., Sprafke, T., Schulte, P., Terhorst, B., Lomax, J., Fuchs, M., Lehmkuhl, F., Neugebauer-Maresch, C., Einwögerer, T., Händel, M., Simon, U., and Solís Castillo, B.: The MIS 3/2 transition in a new loess profile at Krems-Wachtberg East – A multi-methodological approach, Quatern. Int., 464, 370–385, https://doi.org/10.1016/j.quaint.2017.11.048, 2018.

Moine, O.: West-european malacofauna from loess deposits of the weichselian upper pleniglacial: Compilation and preliminary analysis of the database, Quaternaire, 19, 11–29, https://doi.org/10.4000/quaternaire.1532, 2008.

Murray, A. S. and Wintle, A. G.: Luminescence dating of quartz using an improved single-aliquot regenerative-dose protocol, Radiat. Meas., 32, 57–73, https://doi.org/10.1016/S1350-4487(99)00253-X, 2000.

Nesbitt, H. W. and Young, G. M.: Early Proterozoic climates and plate motions inferred from major element chemistry of lutites, Nature, 299, 715–717, https://doi.org/10.1038/299715a0, 1982.

Nesbitt, H. W. and Young, G. M.: Prediction of some weathering trends of plutonic and volcanic rocks based on thermodynamic and kinetic considerations, Geochim. Cosmochim. Ac., 48, 1523–1534, https://doi.org/10.1016/0016-7037(84)90408-3, 1984.

Nottebaum, V., Stauch, G., Hartmann, K., Zhang, J., and Lehmkuhl, F.: Unmixed loess grain size populations along the northern Qilian Shan (China): Relationships between geomorphologic, sedimentologic and climatic controls, Quatern. Int., 372, 151–166, https://doi.org/10.1016/j.quaint.2014.12.071, 2015.

Obreht, I., Zeeden, C., Schulte, P., Hambach, U., Eckmeier, E., Timar-Gabor, A., and Lehmkuhl, F.: Aeolian dynamics at the Orlovat loess–paleosol sequence, northern Serbia, based on detailed textural and geochemical evidence, Aeolian Res., 18, 69–81, https://doi.org/10.1016/j.aeolia.2015.06.004, 2015.

Obreht, I., Hambach, U., Veres, D., Zeeden, C., Bösken, J., Stevens, T., Marković, S. B., Klasen, N., Brill, D., Burow, C., and Lehmkuhl, F.: Shift of large-scale atmospheric systems over Europe during late MIS 3 and implications for Modern Human dispersal, Sci. Rep., 7, 5848, https://doi.org/10.1038/s41598-017-06285-x, 2017.

Ohta, T.: Geochemistry of Jurassic to earliest Cretaceous deposits in the Nagato Basin, SW Japan: implication of factor analysis to sorting effects and provenance signatures, Sediment. Geol., 171, 159–180, https://doi.org/10.1016/j.sedgeo.2004.05.014, 2004.

Özer, M., Orhan, M., and Işik, N. S.: Effect of particle optical properties on size distribution of soils obtained by laser diffraction, Environ. Eng. Geosci., 16, 163–173, 2010.

Pécsi, M.: Loess is not just the accumulation of dust, Quatern. Int., 7–8, 1–21, https://doi.org/10.1016/1040-6182(90)90034-2, 1990.

Pécsi, M. and Richter, G.: Löß: Herkunft – Gliederung – Landschaften, Borntraeger, Berlin, 391 pp., ISBN 978-3-443-21098-4, 1996.

Pötter, S., Veres, D., Baykal, Y., Nett, J. J., Schulte, P., Hambach, U., and Lehmkuhl, F.: Disentangling sedimentary pathways for the Pleniglacial Lower Danube loess based on geochemical signatures, Front. Earth Sci., 9, 1–25, https://doi.org/10.3389/feart.2021.600010, 2021.

Protze, J.: Eine "Mensch gemachte Landschaft" – Diachrone, geochemische und sedimentologische Untersuchungen an anthropogen beeinflussten Sedimenten und Böden der Niederrheinischen Lössbörde, Hochschulbibliothek der Rheinisch-Westfälischen Technischen Hochschule Aachen, Aachen, URN urn:nbn:de:hbz:82-opus-49066, 2014.

Rahimzadeh, N., Sprafke, T., Thiel, C., Terhorst, B., and Frechen, M.: A comparison of polymineral and K-feldspar post-infrared infrared stimulated luminescence ages of loess from Franconia, southern Germany, E&G Quaternary Sci. J., 70, 53–71, https://doi.org/10.5194/egqsj-70-53-2021, 2021.

Reicherter, K., Schaub, A., Fernández-Steeger, T., Grützner, C., and Kohlberger-Schaub, T.: Aquisgrani terrae motus factus est (part 2): Evidence for medieval earthquake damage in the Aachen Cathedral (Germany), Quatern. Int., 242, 149–157, https://doi.org/10.1016/j.quaint.2011.05.006, 2011.

Rousseau, D.-D. and Hatté, C.: Ground-Air Interface: The Loess Sequences, Markers of Atmospheric Circulation, in: Paleoclimatology, edited by: Ramstein, G., Landais, A., Bouttes, N., Sepulchre, P., and Govin, A., Springer International Publishing, Cham, 157–167, https://doi.org/10.1007/978-3-030-24982-3_13, 2021.

Rousseau, D.-D., Antoine, P., and Sun, Y.: How dusty was the last glacial maximum over Europe?, Quaternary Sci. Rev., 254, 106775, https://doi.org/10.1016/j.quascirev.2020.106775, 2021.

Schaller, K.: Praktikum Zur Bodenkunde Und Pflanzenernährung, 8th edn., Forschungsanstalt Geisenheim, Geisenheim, ISBN 978-3980187213, 2000.

Schirmer, W.: Eine Klimakurve des Oberpleistozäns aus dem rheinischen Löss, E&G Quaternary Sci. J., 50, 25–49, https://doi.org/10.3285/eg.50.1.02, 2000.

Schirmer, W.: Compendium of the Rhein loess sequence, Terra Nostra, 10, 8–23, 2002.

Schirmer, W.: Die Eben-Zone im Oberwürmlöss zwischen Maas und Rhein, in: Landschaftsgeschichte im Europäischen Rheinland, vol. 4, edited by: Schirmer, W., LIT Verlag, Münster, 351–416, ISBN 978-3-825-86009-7, 2003.

Schirmer, W.: Late Pleistocene loess of the Lower Rhine, Quatern. Int., 411, 44–61, https://doi.org/10.1016/j.quaint.2016.01.034, 2016.

Schirmer, W., Ikinger, A., and Nehring, F.: Die terrestrischen Böden im Profil Schwalbenberg/Mittelrhein (Terrestrial soils of the Schwalbenberg profile/Middle Rhine), Mainzer Geowissenschaftliche Mitteilungen, 40, 53–78, 2012.

Schulte, P. and Lehmkuhl, F.: The difference of two laser diffraction patterns as an indicator for post-depositional grain size reduction in loess-paleosol sequences, Palaeogeogr. Palaeoclimatol. Palaeoecol., 509, 126–136, https://doi.org/10.1016/j.palaeo.2017.02.022, 2018.

Schulte, P., Lehmkuhl, F., Steininger, F., Loibl, D., Lockot, G., Protze, J., Fischer, P., and Stauch, G.: Influence of HCl pretreatment and organo-mineral complexes on laser diffraction measurement of loess–paleosol-sequences, CATENA, 137, 392–405, https://doi.org/10.1016/j.catena.2015.10.015, 2016.

Schulz, W.: Die Kolluvien der westlichen Kölner Bucht – Gliederung, Entstehungszeit und geomorphologische Bedeutung, Universitäts- und Stadtbibliothek Köln, Cologne, Germany, URN urn:nbn:de:hbz:38-19656, 2007.

Sedov, S., Rusakov, A., Sheinkman, V., and Korkka, M.: MIS3 paleosols in the center-north of Eastern Europe and Western Siberia: Reductomorphic pedogenesis conditioned by permafrost?, CATENA, 146, 38–47, https://doi.org/10.1016/j.catena.2016.03.022, 2016.

Sirocko, F., Knapp, H., Dreher, F., Förster, M. W., Albert, J., Brunck, H., Veres, D., Dietrich, S., Zech, M., Hambach, U., Röhner, M., Rudert, S., Schwibus, K., Adams, C., and Sigl, P.: The ELSA-Vegetation-Stack: Reconstruction of Landscape Evolution Zones (LEZ) from laminated Eifel maar sediments of the last 60 000 years, Glob. Planet. Change, 142, 108–135, https://doi.org/10.1016/j.gloplacha.2016.03.005, 2016.

Skurzyński, J., Jary, Z., Raczyk, J., Moska, P., Korabiewski, B., Ryzner, K., and Krawczyk, M.: Geochemical characterization of the Late Pleistocene loess-palaeosol sequence in Tyszowce (Sokal Plateau-Ridge, SE Poland), Quatern. Int., 502, 108–118, https://doi.org/10.1016/j.quaint.2018.04.023, 2019.

Skurzyński, J., Jary, Z., Kenis, P., Kubik, R., Moska, P., Raczyk, J., and Seul, C.: Geochemistry and mineralogy of the Late Pleistocene loess-palaeosol sequence in Złota (near Sandomierz, Poland): Implications for weathering, sedimentary recycling and provenance, Geoderma, 375, 114459, https://doi.org/10.1016/j.geoderma.2020.114459, 2020.

Sprafke, T. and Obreht, I.: Loess: Rock, sediment or soil – What is missing for its definition?, Quatern. Int., 399, 198–207, https://doi.org/10.1016/j.quaint.2015.03.033, 2016.

Stadelmaier, K. H., Ludwig, P., Bertran, P., Antoine, P., Shi, X., Lohmann, G., and Pinto, J. G.: A new perspective on permafrost boundaries in France during the Last Glacial Maximum, Clim. Past, 17, 2559–2576, https://doi.org/10.5194/cp-17-2559-2021, 2021.

Steup, R. and Fuchs, M.: The loess sequence at Münzenberg (Wetterau/Germany): A reinterpretation based on new luminescence dating results, Z. Geomorphol., 61, 101–120, https://doi.org/10.1127/zfg_suppl/2016/0408, 2017.

Stevens, T., Sechi, D., Bradák, B., Orbe, R., Baykal, Y., Cossu, G., Tziavaras, C., Andreucci, S., and Pascucci, V.: Abrupt last glacial dust fall over southeast England associated with dynamics of the British-Irish ice sheet, Quaternary Sci. Rev., 250, 106641, https://doi.org/10.1016/j.quascirev.2020.106641, 2020.

Sümegi, P., Náfrádi, K., Molnár, D., and Sávai, S.: Results of paleoecological studies in the loess region of Szeged-Öthalom (SE Hungary), Quatern. Int., 372, 66–78, https://doi.org/10.1016/j.quaint.2014.09.003, 2015.

Svirčev, Z., Marković, S. B., Stevens, T., Codd, G. A., Smalley, I., Simeunović, J., Obreht, I., Dulić, T., Pantelić, D., and Hambach, U.: Importance of biological loess crusts for loess formation in semi-arid environments, Quatern. Int., 296, 206–215, https://doi.org/10.1016/j.quaint.2012.10.048, 2013.

Thiel, C., Buylaert, J.-P., Murray, A., Terhorst, B., Hofer, I., Tsukamoto, S., and Frechen, M.: Luminescence dating of the Stratzing loess profile (Austria) – Testing the potential of an elevated temperature post-IR IRSL protocol, Quatern. Int., 234, 23–31, https://doi.org/10.1016/j.quaint.2010.05.018, 2011.

Torre, G., Gaiero, D. M., Cosentino, N. J., and Coppo, R.: The paleoclimatic message from the polymodal grain-size distribution of late Pleistocene-early Holocene Pampean loess (Argentina), Aeolian Res., 42, 100563, https://doi.org/10.1016/j.aeolia.2019.100563, 2020.

Vandenberghe, J., French, H. M., Gorbunov, A., Marchenko, S., Velichko, A. A., Jin, H., Cui, Z., Zhang, T., and Wan, X.: The Last Permafrost Maximum (LPM) map of the Northern Hemisphere: permafrost extent and mean annual air temperatures, 25–17 ka BP: The Last Permafrost Maximum (LPM) map of the Northern Hemisphere, Boreas, 43, 652–666, https://doi.org/10.1111/bor.12070, 2014.

Varga, A., Újvári, G., and Raucsik, B.: Tectonic versus climatic control on the evolution of a loess–paleosol sequence at Beremend, Hungary: an integrated approach based on paleoecological, clay mineralogical, and geochemical data, Quatern. Int., 240, 71–86, https://doi.org/10.1016/j.quaint.2010.10.032, 2011.

Veres, D., Tecsa, V., Gerasimenko, N., Zeeden, C., Hambach, U., and Timar-Gabor, A.: Short-term soil formation events in last glacial east European loess, evidence from multi-method luminescence dating, Quaternary Sci. Rev., 200, 34–51, https://doi.org/10.1016/j.quascirev.2018.09.037, 2018.

Vinnepand, M., Fischer, P., Fitzsimmons, K., Thornton, B., Fiedler, S., and Vött, A.: Combining Inorganic and Organic Carbon Stable Isotope Signatures in the Schwalbenberg Loess-Palaeosol-Sequence Near Remagen (Middle Rhine Valley, Germany), Front. Earth Sci., 8, 276, https://doi.org/10.3389/feart.2020.00276, 2020.

Vinnepand, M., Fischer, P., Jöris, O., Hambach, U., Zeeden, C., Schulte, P., Fitzsimmons, K. E., Prud'homme, C., Perić, Z., Schirmer, W., Lehmkuhl, F., Fiedler, S., and Vött, A.: Decoding geochemical signals of the Schwalbenberg Loess-Palaeosol-Sequences – A key to Upper Pleistocene ecosystem responses to climate changes in western Central Europe, CATENA, 212, 106076, https://doi.org/10.1016/j.catena.2022.106076, 2022.

Vlaminck, S., Kehl, M., Lauer, T., Shahriari, A., Sharifi, J., Eckmeier, E., Lehndorff, E., Khormali, F., and Frechen, M.: Loess-soil sequence at Toshan (Northern Iran): Insights into late Pleistocene climate change, Quatern. Int., 399, 122–135, https://doi.org/10.1016/j.quaint.2015.04.028, 2016.

Zech, M., Zech, R., Buggle, B., and Zöller, L.: Novel methodological approaches in loess research – interrogating biomarkers and compound-specific stable isotopes, E&G Quaternary Sci. J., 60, 13, https://doi.org/10.3285/eg.60.1.12, 2011.

Zech, R., Zech, M., Marković, S., Hambach, U., and Huang, Y.: Humid glacials, arid interglacials? Critical thoughts on pedogenesis and paleoclimate based on multi-proxy analyses of the loess–paleosol sequence Crvenka, Northern Serbia, Palaeogeogr. Palaeoclimatol. Palaeoecol., 387, 165–175, https://doi.org/10.1016/j.palaeo.2013.07.023, 2013.

Zens, J., Zeeden, C., Römer, W., Fuchs, M., Klasen, N., and Lehmkuhl, F.: The Eltville Tephra (Western Europe) age revised: Integrating stratigraphic and dating information from different Last Glacial loess localities, Palaeogeogr. Palaeoclimatol. Palaeoecol., 466, 240–251, https://doi.org/10.1016/j.palaeo.2016.11.033, 2017.

Zens, J., Schulte, P., Klasen, N., Krauß, L., Pirson, S., Burow, C., Brill, D., Eckmeier, E., Kels, H., Zeeden, C., Spagna, P., and Lehmkuhl, F.: OSL chronologies of paleoenvironmental dynamics recorded by loess-paleosol sequences from Europe: Case studies from the Rhine-Meuse area and the Neckar Basin, Palaeogeogr. Palaeoclimatol. Palaeoecol., 509, 105–125, https://doi.org/10.1016/j.palaeo.2017.07.019, 2018.

E&G Quaternary Sci. J., 72, 37–55, 2023
https://doi.org/10.5194/egqsj-72-37-2023

Open Access E&G Quaternary Science Journal

Research article

Palaeoenvironmental research at Hawelti–Melazo (Tigray, northern Ethiopia) – insights from sedimentological and geomorphological analyses

Jacob Hardt[1], **Nadav Nir**[1], **Christopher Lüthgens**[2], **Thomas M. Menn**[3], **and Brigitta Schütt**[1]

[1]Physical Geography, Department of Earth Sciences, Freie Universität Berlin, Berlin, Germany
[2]Institute for Applied Geology, University of Natural Resources and Life Sciences, Vienna, Austria
[3]freelance archaeologist: Sanaa Branch, Orient Department, German Archaeological Institute (DAI), Berlin, Germany

Correspondence: Jacob Hardt (jacob.hardt@fu-berlin.de)

Relevant dates: Received: 24 June 2022 – Revised: 28 November 2022 – Accepted: 20 December 2022 – Published: 26 January 2023

How to cite: Hardt, J., Nir, N., Lüthgens, C., Menn, T. M., and Schütt, B.: Palaeoenvironmental research at Hawelti–Melazo (Tigray, northern Ethiopia) – insights from sedimentological and geomorphological analyses, E&G Quaternary Sci. J., 72, 37–55, https://doi.org/10.5194/egqsj-72-37-2023, 2023.

Abstract: The sites of Hawelti–Melazo in the Tigray region of the northern Ethiopian Highlands is an archaeological hotspot related to the D'mt kingdom (ca. 800–400 BCE). The existence of several monumental buildings, which have been excavated since the 1950s, underline the importance of this area in the Ethio-Sabaean period. We investigated the geomorphological and geological characteristics of the site and its surroundings and carried out sedimentological analyses, as well as direct (luminescence) and indirect (radiocarbon) sediment dating, to reconstruct the palaeoenvironmental conditions, which we integrated into the wider context of Tigray. Luminescence dating of feldspar grains from the May Agazin catchment indicate enhanced fluvial activity in the late Pleistocene, likely connected to the re-occurring monsoon after the Last Glacial Maximum (LGM). The abundance of trap basalt on the Melazo plateau, which provides the basis for the development of fertile soils, and the presumably higher groundwater level during the Ethio-Sabaean Period, provided favourable settlement conditions. The peninsula-like shape of the Melazo plateau was easily accessible only from the east and northeast, while relatively steep scarps enclose the other edges of the plateau. This adds a possible natural protective function to this site.

Kurzfassung: Die Stätte Hawelti–Melazo in Tigray im nördlichen Hochland von Äthiopien ist ein archäologischer hotspot, der im Zusammenhang mit dem Königreich D'mt steht (ca. 800–400 BCE). Seit den 1950er Jahren wurden dort mehrere Monumentalbauten entdeckt, die die Stellung dieses Gebiets zu äthiosabäischer Zeit unterstreichen. Wir haben die geomorphologischen und geologischen Eigenschaften des Gebiets untersucht, sedimentologische Analysen durchgeführt sowie direkte (Lumineszenz) und indirekte (Radiokohlenstoff) Sedimentdatierungsmethoden angewandt, um die Paläoumweltbedingungen zu rekonstruieren, die wir im weiteren Kontext von Tigray einordnen. Lumineszenzdatierungen an Feldspat-Körnern aus dem Einzugsgebiet des May Agazin deuten auf eine gesteigerte fluviale Aktivität im Spätpleistozän hin, die möglicherweise mit dem wiedereinsetzenden Monsun nach dem LGM in Verbindung steht. Der Trapp-Basalt des Melazo-Plateaus, der die Basis für die Bodenen-

Published by Copernicus Publications on behalf of the Deutsche Quartärvereinigung (DEUQUA) e.V.

twicklung bildet, und die wahrscheinlich höheren Grundwasserstände zur äthio-sabäischen Zeit boten gute Siedlungsbedingungen. Durch die halbinselartige Form des Melazo-Plateaus war es nur vom Osten und Nordosten einfach zugänglich, während die anderen Seiten des Plateaus durch steile Hänge begrenzt werden. Dies gab der Stätte eine zusätzliche natürliche Schutzfunktion.

1 Introduction

Located at the Horn of Africa, the northern highlands of Ethiopia are a region with a diverse and complex geological and archaeological history. The basaltic plateaus and the moderate subtropical climate with annual precipitation exceeding 600 mm at elevations around 2000 m a.s.l. (above sea level) provide the framework for the development of fertile soils and favourable living conditions not only throughout the Holocene. The abundance of natural resources, such as gold, obsidian, gums, incense, and more, led to the integration of this region in the ancient trade network between the Mediterranean and the Indian Ocean (Fattovich, 2012). In terms of archaeology, the area is probably best known for the Kingdom of Aksum (starting in the early first millennium CE), a state polity with the city of Aksum as its centre (French et al., 2009; Harrower et al., 2019). Prior to the Aksumite Period, the archaeological records show that groups related to the foreign Saba kingdom arrived during the first millennium BCE from the Arabian Peninsula (Japp et al., 2011; Fattovich, 2012, 2010). The most prominent remnants of this Ethio-Sabaean culture (ca. 800–400 BCE) in the present-day state of Tigray are several monumental buildings in the South Arabian style in Yeha, Wuqro, and Hawelti–Melazo, which give evidence for a complex hierarchical society and polity, which is named "D'mt" in literature (Fattovich, 2012). All of them are still being investigated or are still being excavated (Japp et al., 2011). D'mt disappears from the archaeological records at ca. 400 BCE, around the time of the decline of the Saba kingdom. The area did soon after witness the rise of the aforementioned, millennium-lasting Kingdom of Aksum (Fattovich, 2010).

Several studies investigated palaeoenvironmental changes and geomorphic activity phases in the northern Ethiopian Highlands (Tigray) and provided data to compare them to cultural epochs or relatively recent political upheavals in the region (Lanckriet et al., 2015; Nyssen et al., 2014, 2004, 2006b; Machado et al., 1998; Pietsch and Machado, 2014).

Here, we focus on the Daragá region of Tigray, which includes the archaeological sites of Hawelti–Melazo (de Contenson, 1961, 1963; Leclant, 1959) and lies within the basaltic Highlands (ca. 2000 m a.s.l.) about 10 km southeast of Aksum. Hawelti–Melazo are important Ethio-Sabaean and Aksumite find places (Menn, 2020). However, their direct surroundings have so far not been in the scope of palaeoenvironmental research. The aim of this study is to understand the late Pleistocene–Holocene environmental conditions of the area, which provided the base for the Ethio-Sabaean and the subsequent Aksumite occupations, using sedimentological analyses, luminescence and radiocarbon sediment dating methods, micromorphological analyses, and geomorphological mapping.

2 Study area

2.1 Archaeological overview

About 10 km southeast of Aksum, the archaeological sites of Hawelti–Melazo are to be found. In simplified terms, the most relevant sites are the hill of Hawelti and the so-called "plateaus" – most importantly Melazo – on the eastern banks of the river May Agazin, about 1.5 km southeast of Hawelti (Fig. 1).

The area first came into scientific consideration in the mid-1950s when a local farmer had accidentally discovered several (Ethio-Sabaean) finds at Goboshila (Melazo). This in turn led to the first excavations in Melazo, bringing to light a temple dedicated to the Sabaean god Almaqah (Leclant, 1959). Excavations continued in 1958 and 1959. On the Melazo plateau (specifically Inda Cherqos), two consecutive churches on top of each other were found, dating to Aksumite and probably medieval times – the older one incorporating spolia of Ethio-Sabaean heritage (de Contenson, 1961). Also, the stelae field on the hill of Hawelti was excavated revealing about 20 stelae, 2 buildings ("temples"), and some 500 finds (de Contenson, 1963). With regard to their dating, the results have to be considered as inconclusive since some of the features and finds are most probably from Ethio-Sabaean times (e.g. the stelae themselves), while others could be later additions. Furthermore, the interpretation of the stelae field's function remains uncertain.

Apart from minor surveys, no further investigations took place in Hawelti–Melazo until the still-ongoing Ethiopian–German cooperation project "Yeha and Hawelti–Melazo" took up work in 2009. Since then, the project has so far delivered one further major excavation site, as well as some 70 more find locations (Japp et al., 2011; Menn, 2020). Mostly, these sites and find locations point to Aksumite and Ethio-Sabaean heritage (Gerlach, 2018). While the former seem to be scattered all over the area, the latter appear to be concentrated on the hill of Hawelti and primarily the plateau of Melazo where also the excavation site is located about 60 m east of the church of Inda Cherqos. Here, a monumental building could be identified. With the construction method

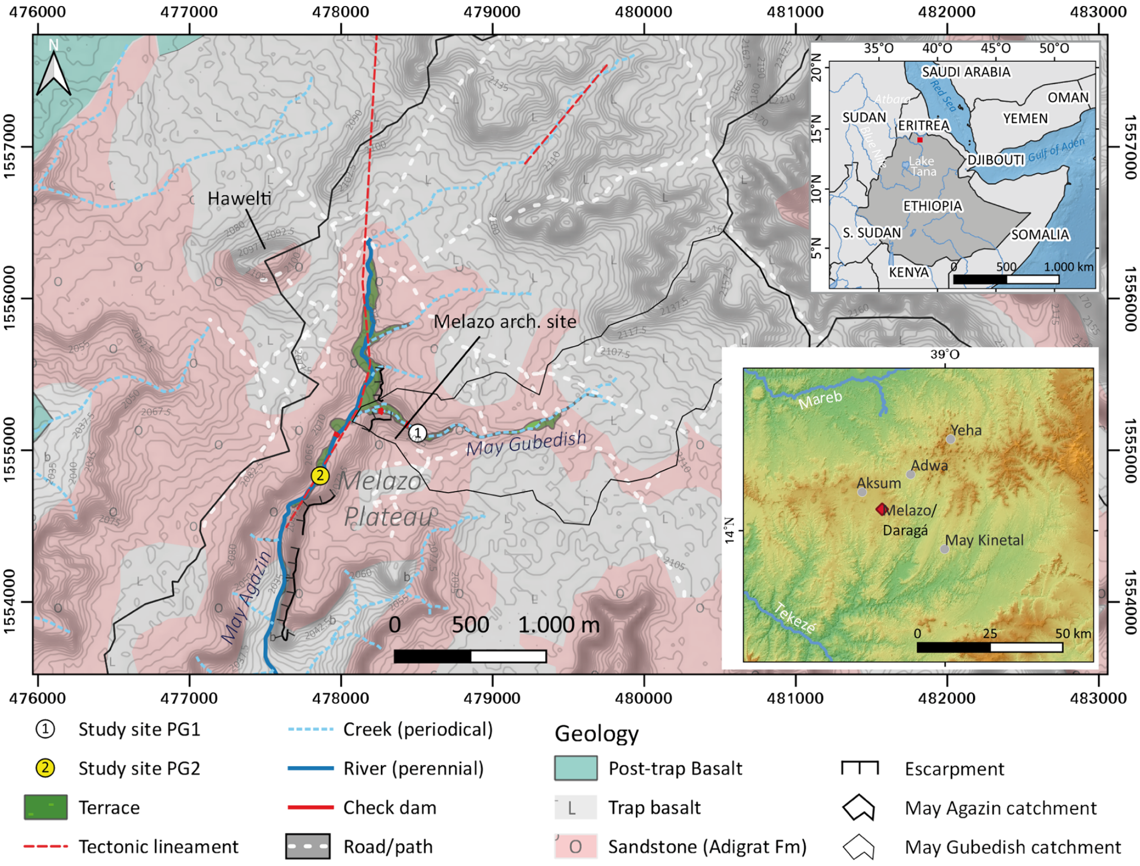

Figure 1. Geological and geomorphological map of the study area, modified from Tadesse (1999) and Hagos et al. (2010). "Melazo arch. site" refers to the location of current excavations. Several other archaeological sites were reported on the Melazo plateau to the south of the current site. Upper inset map shows the position in Ethiopia. Lower inset map shows the position in northern Ethiopia/Tigray.

similar to Yeha's Grat Be'al Gebri (Japp et al., 2011), finds corresponding to those in Yeha, and radiocarbon dating results pointing to the first half of the first millennium BCE, it can be concluded that it is of Ethio-Sabaean origin (Menn, 2020). However, several isolated finds identified during the extensive surveys also indicate the presence and possibly the settlement of people from the lithic period through to the present. Thus, the Hawelti–Melazo area has to be regarded as an archaeological hotspot.

2.2 Climate and palaeoenvironment

The study area lies in the warm and temperate subtropical highland climate zone (*Cwb* after Köppen–Geiger classification). Rainfall is mostly of monsoonal type showing a bimodal annual rainfall distribution with short rains (*belg* in Amharic) in March and long rains (*krempt* in Amharic) in June–August and a total annual precipitation of 600–700 mm (Harrower et al., 2020).

Information on late Pleistocene palaeoenvironmental conditions of the northern Ethiopian Highlands is sparse. According to Lamb et al. (2007b), Lake Tana was desiccated during the Last Glacial Maximum (LGM) due to drought caused by reduced monsoon strength (Lamb et al., 2018). A similar effect – although in a completely different environmental context – is also known for lakes in the now central Sahara (Hoelzmann et al., 2007; Umer et al., 2004). The basin of Lake Tana started to fill again at around 15 ka. In the same sense, Moeyersons et al. (2006) report increasing humidity from ca. 15 ka onwards based on numerical dating of tufa dams near Mekele (Tigray), which indicate a raised groundwater table during the late Pleistocene. Wetter conditions than today prevailed from ca. 15 ka until the mid-Holocene (ca. 5 ka; Armitage et al., 2015), owing to orbitally forced increased monsoon strength (Umer et al., 2004; Williams et al., 2006).

Climatic reconstructions for the area based on palaeopedological findings indicate that precipitation rates might have decreased in the course of the Holocene, which is in agreement with the declining monsoon strength after 5 ka (Armitage et al., 2015). Based on samples obtained close to Yeha, palaeoprecipitation rates of 870 mm a^{-1} were determined for the Early Holocene, which decreased to 780 mm a^{-1} in the first millennium BCE (Pietsch and Machado, 2014). This general trend corresponds to the findings of Dramis et al. (2003), who parallelized stratigraphic sequences in Tigray with lake level records in the Rift Valley.

Machado et al. (1998) describe three "wetter" phases during the last 4000 years with enhanced soil formation, corresponding to so-called stability phases (∼ 2000–1500 BCE, 500 BCE–500 CE, 950–1000 CE), and two "drier" phases, which are represented by an increase in fluvial debris transport (1500–500 BCE, 1500–1000 CE). Lanckriet et al. (2015) compare these phases of varying morphodynamics to palaeoenvironmental studies from Lake Hayk (Lamb et al., 2007a) and Lake Ashenge (Marshall et al., 2009), as well as results from their own study site at May Tsimble (east of Mekele). This comparison confirms the general morphodynamic trends but also emphasizes several additional phases of higher and lower geomorphic activity, triggered by either climatic changes or human impact (Lanckriet et al., 2015). Human impact on the landscape in the form of land use and land cover changes comprises repeated phases of vegetation removal and intensified agriculture or livestock grazing, which have been proven throughout the last 2000–3000 years (Nyssen et al., 2004; Lanckriet et al., 2015, and references therein). Another important human imprint on the landscape are footpaths, which can incise into the land surface (Zgłobicki et al., 2021) and, for example, influence soil properties (Nir et al., 2022) and the gully erosion susceptibility (Busch et al., 2021). A footpath close to the study site was recently investigated by Nir et al. (2022) in terms of soil chemistry and micromorphology.

2.3 Geomorphological setting

The relief of the northern Ethiopian Highlands is largely structurally (tectonically and geologically) determined. Selective erosion of different rock types produced a stepped landscape, which is locally termed *amba* landscape (Coltorti et al., 2007). Several planation surfaces, the oldest being of pre-Ordovician age, once weathered and eroded at low altitudes before Cenozoic uplift of the Ethiopian Highlands, can now be found at altitudes exceeding 2000 m a.s.l. Thus, ongoing erosion not only results in stepped slopes and valleys but also exhumes relatively level palaeosurfaces (Coltorti et al., 2007; Machado, 2015).

The most typical present-day soils of the region are Vertisols and (vertic) Cambisols, which develop predominantly on the basalt surfaces and in the alluvial plains (Ferrari et al., 2015). These soils are characterized by a high content of swelling clays (montmorillonite) (Frankl et al., 2012), black colour, and relatively high fertility (Nyssen et al., 2008). Due to their high swelling potential and the seasonality of the local climate, Vertisols (locally termed *walka*; Nyssen et al., 2008) are prone to soil piping and gully erosion (Frankl et al., 2012; Nyssen et al., 2006b; Busch et al., 2021; Nir et al., 2021). Moreover, the swell-and-shrink cycles of the Vertisols trigger an upward movement of rock fragments originating from the subsurface (argillipedoturbation; Nyssen et al., 2006a).

3 Materials and methods

3.1 Fieldwork and sampling strategy

Two exposures corresponding to sections at eroded channel banks were investigated in the field and sampled for further analysis in February and November 2019. The first site in Daragá (PG1) lies on the southwestern bank of May Gubedish, a small creek flowing in a northwest direction ca. 50 m northeast of the current excavation site of Melazo. The section was chosen due to the proximity to the archaeological site, as it appeared as a potential cultural archive. The second section of Daragá (PG2) was located at the northwestern bank of May Agazin, the receiving stream of May Gubedish, ca. 300 m west of the Melazo temple and 1.5 km south of Hawelti (Table 1).

In terms of chronological control, the silty-clayey PG1 section was sampled for AMS radiocarbon dating (^{14}C), as several charcoal pieces were macroscopically visible during the sampling procedure. Oppositely, organic residue could not be found in the other sections of profile PG2, where suitable layers (sand sized, well sorted) were selected for luminescence dating. Luminescence samples were taken by driving opaque plastic cylinders (25 cm length, 5 cm diameter) into the freshly cleaned sediment, and additional samples from the bulk material were secured for radionuclide analysis.

3.2 Sedimentological analyses

The basic sedimentological analyses were performed at the physical geography laboratory of the Department of Earth Sciences, Freie Universität Berlin.

As a first preparation step, the bulk samples were dried at 105 °C, aggregates were crushed, and particles larger than 2 mm in diameter were removed by sieving. The pH values were measured with a pH meter in a solution of 10 g of dried sediment and 25 mL of 0.01 M KCl. Electrical conductivity was measured in a solution of 10 g of dried sediment in 25 mL of bi-distilled water.

The content of total carbon (TC) was determined with a Leco TruSpec CHN analyser by means of infrared CO_2 detection during sample combustion. The content of total inorganic carbon (TIC) was measured with a Woesthoff Carmhograph C-16. Total organic carbon (TOC) was subsequently calculated by the substraction of the content of TIC from the content of TC. A laser diffractometer (Beckman Coulter LS 13320) was used to determine the grain size distributions of the fractions < 1 mm. Sample preparation for grain size analysis included treatment with HCl for removal of carbonates and dispersion with sodium pyrophosphate ($Na_4P_2O_7$). Sediments from the representative units selected for dating and

Table 1. Sample overview for the studied locations.

	PG1	PG2
Location/coordinates (decimal WGS84)	May Gubedish/14.066703° N, 38.800879° E	May Agazin/14.065173° N, 38.795278° E
Bulk samples for physical and chemical analyses	27	8
Micromorphology samples	5	3
Radiocarbon samples	6 (bulk/charcoal)	/
Luminescence samples	/	2

micromorphological investigation were also mineralogically analysed by X-ray powder diffraction (XRD; Rigaku MiniFlex 600).

3.3 Micromorphological analyses

For micromorphological analyses, five sediment blocks were extracted from different sedimentary units along the profile of the main outcrop (PG1: M1–M5) and three more at sedimentary transition zones from the reference outcrop (PG2: M6_R–M8_R). Blocks were sampled using plastic boxes or jackets of gypsum bandages (plaster of Paris) depending on the sediment type and possible extraction techniques.

The micromorphological samples were dried for 4 d at room temperature (ca. 18 °C) and later heated to 50 °C for 30 h. Following this, sediments were impregnated by a 6 : 4 ($v:v$) mixture of polyester resin and acetone and a small amount of hardener (5–10 mL to 1 L of the above mixture). Due to the heavy saturation and cracking of the clay-enriched sediments, acetone removal was performed, and amounts and ratios were changed according to the reactions and impregnation of the sediments. Sampled blocks were then dried for several weeks at room temperature and cut with a slab saw to ca. 6 × 5 cm "hand-sized" units. These units were sent for 30 µm thick thin section preparation to Quality Thin Section Labs, Arizona. The analysis of the slides was performed applying a Zeiss polarizing microscope following a process performed by common micromorphological studies (Junge et al., 2018; Stoops, 2020; Verrecchia and Trombino, 2021).

3.4 Luminescence dating – sampling, preparation and experimental set-up, and radiocarbon dating

All preparation steps and luminescence measurements were carried out in the Vienna Laboratory for Luminescence Dating (VLL) at the University of Natural Resources and Life Sciences (BOKU) in Vienna, Austria. Sample preparation followed a standardized procedure at the VLL (Lüthgens et al., 2017; Rades et al., 2018), yielding extracts of potassium-rich feldspar and pure quartz. Samples for radionuclide determination were dried and subsequently stored in sealed Petri dishes (∼ 60 g dry weight) for at least a month to re-establish secondary secular radon equilibrium. Details on the radionuclide content and the overall dose rate calculations are provided in Table 3. All luminescence measurements were carried out on Risø TL/OSL DA-20 readers equipped with a $^{90}\mathrm{Sr}/^{90}\mathrm{Y}$ beta source (Bøtter-Jensen et al., 2000, 2003, 2010). Gamma spectrometry measurements for the calculation of the dose rate were performed using a Baltic Scientific Instruments (BSI) high-purity germanium (HPGe) p-type detector (∼ 52 % efficiency). The age calculation was done using the software ADELE (Kulig, 2005). Initial tests revealed very low sensitivity of the quartz in the samples, so all subsequent measurements were conducted using single aliquots of feldspar, which revealed good luminescence qualities in dose recovery experiments using a single aliquot regenerative dose protocol for the dating of feldspar (for details see Table 3). The resulting equivalent dose distributions were not significantly skewed, and average doses were calculated using the central age model (CAM; Galbraith et al., 1999). Unfortunately, only a few aliquots passed the rejection criteria for sample VLL-0492-L (for details see Table 3).

AMS radiocarbon dating was done at the Poznan Radiocarbon Laboratory. The C-14 dates were calibrated with the software OxCal v. 4.2.3 using the IntCal13 atmospheric curve (Reimer et al., 2013).

4 Results

4.1 Geomorphology

The Daragá area is situated at an elevation between 2000 and 2200 m a.s.l. within the Aksum plateau, which consists of the Oligocene trap basalts (Hofmann et al., 1997) and the Mesozoic Adigrat Sandstone (Tadesse, 1999; Hagos et al., 2010). Post-trap tectonic uplift of the region triggered extensive erosion of the flood basalts, resulting in several isolated table mountains (flat-topped mountains, locally named *ambas*) and larger plateau complexes. The plateaus are eroded by inward movement of the surrounding scarps. The inward erosion is promoted by weathering and mass wasting processes (Duszyński et al., 2019), possibly accelerated by human land use (Nyssen et al., 2006a). The archaeological site of Melazo is situated at the southern fringe of the Aksum plateau on a peninsula-like plateau remnant corresponding to an outlier mountain (Fig. 1). The plateau remnant measures ca. 1.6 km in southwest–northeast direction and up to 600 m in the northwest–southeast direction. Its surface is flat-topped at an altitude of 2080 m a.s.l. The surrounding valley bottoms are incised up to 60 m, resulting in steep to cliff-like scarps surrounding the plateau, which expose the various colourful (reddish) facies of the Adigrat formation. To the north, the valley of May Gubedish dissects the plateau. May Gubedish is a tributary to May Agazin, which dissects the plateau on the western side. The valley of May Agazin is up to 400 m wide, and its valley cross profile ranges from an asymmetric V shape to box-like. The valley follows a tectonic lineament (Hagos et al., 2010). Alluvial plains have developed on the wide valley floors; at profile PG2, located ca. 1 km downstream of the confluence of the tributary May Gubedish, these alluvial deposits are exposed. All hydrological regimes of nearby streams are periodical (EMA map sheet 1438 D4) and recent hydraulic constructions such as weirs and check dams were installed to control the runoff (Fig. 2).

Especially to the northeast of the Melazo plateau the soil cover is thin, resulting in frequently outcropping bedrock. The area is rural with sparse settlements; basically the whole plateau is used for arable farming while the alluvial plains of the valley bottoms are used for grazing. Stone bunds separate the fields on the plateau and the slopes, acting as erosion protection measures (Fig. 2). The widespread abundance of rock fragments covering the surface of the plateau areas can be explained by argillipedoturbation, accelerated by the use of ploughs (Nyssen et al., 2002).

The catchment of May Gubedish measures 2.27 km^2. It has a length (east–west) of roughly 3 km and a width (north-northwest–south-southeast) of up to 1 km. Ca. 30 % of the catchment is grounded in Adigrat Sandstone, while the remaining 70 % of the catchment drains trap basalt. The sandstone dominates the lower section of the catchment and is found partly also in its middle reach. The whole headwater area consists exclusively of basaltic bedrock.

While flowing through basaltic bedrock the valley profile of May Gubedish corresponds to a shallow hollow valley. To the north of the Melazo plateau, entering the Adigrat Sandstone, the May Gubedish valley is incised 10 to 20 m with a now box-like valley profile. Thus, the flanks are steeper than in the upper catchment, and slope erosion is more intense. To the northeast and north of Melazo, profile PG1 is exposed at an undercut bank where the channel of May Gubedish today incises ca. 3 m into its own sediments deposited at a local valley widening upstream of a narrow point. Downstream of the narrow point the valley profile gets box-like and is infilled by alluvial deposits. The slopes flanking the channel are covered by numerous loose blocks and stone bunds stabilize the slopes where tillage occurs; gullies can be witnessed on both valley flanks frequently stabilized by check-dams.

4.2 Sedimentology and dating results

The sediment profile PG1, located at the southwestern bank of the May Gubedish creek (Fig. 2), is built of three major lithofacies units: the overlying 160 cm sediments are formed of alternating strata each with a thickness up to 15 cm, summarized as laminated sand, silt, and mud occurring alternatively with horizontally bedded sand facies (Fl/Sh). At 160–310 cm below surface, sedimentary facies are of massive mud and silt (Fm), underlain by clast-supported, horizontally stratified gravel (Gh) 310 cm below surface. The transition between the three lithofacies units takes place gradually. In total, six different sedimentary units occurring in varying thickness and frequency could be observed in the profile (Fig. 3).

Units I and V build the major part of the outcropping sediments. Units II, III, IV, and VI are coarse-grained layers of limited thickness (2–15 cm), which separate units I and V. Unit I has a dark gray-black colour and a clayey-sandy matrix containing sharp-edged gravel. It forms the main sedimentary unit of the Fl/Sh facies of the section and can only be found until a depth of 90 cm. In its uppermost part, at 0–50 cm below surface, unit I is intersected four times by unit II, a poorly sorted stone layer with a sandy-clayey matrix and a thickness of up to 10 cm; the stones have rounded edges and a diameter of 5–10 cm. Unit III is characterized by coarse gravels in a sandy-clayey matrix occurring in thicknesses of 5–10 cm, being recorded five times between 100 and 160 cm below surface. Sedimentary unit IV was recorded in six layers of up to 12 cm thickness between 40 and 90 cm below surface. It corresponds to a red-white-grayish sand layer, occasionally containing cobbles less than 3 cm in diameter. Below 90 cm depth sedimentary unit V appears, becoming the dominating sedimentary unit 160–310 cm below surface (Fm). Unit V is a gray-green massive silty clay, which is heavily compacted. Between 90 and 160 cm below surface gravel layers of unit III are repeatedly embedded into the clayey sediments of unit V. The base of the section (Gh), below 310 cm depth, is characterized by several coarse gravel and stone layers (unit VI) intercalated by unit V. Round-edged stones 15–20 cm in diameter were recorded.

The pH values across most parts of the section are rather heterogeneous and range between pH 5.9 and pH 7.1. The lowest values were measured between 170 and 220 cm below surface (pH 5.2–5.5). The electrical conductivity of the sediments ranges between 0.06 and 0.46 mS cm^{-1}. The uppermost 70 cm of the section show very low conductivity values (0.07–0.09 mS cm^{-1}). Below 70 cm depth, from top to bottom, the electric conductivity values of the sediments increase. The contents in organic (TOC) and inorganic (TIC) carbon are at a generally low level below 0.8 wt % with only minor excursions (Fig. 3).

The radiocarbon dating resulted in ages ranging from 1432 ± 85 BP (DAT4) to 4603 ± 185 BP (DAT5; Table 2). However, the ages are not in a chronostratigraphic order.

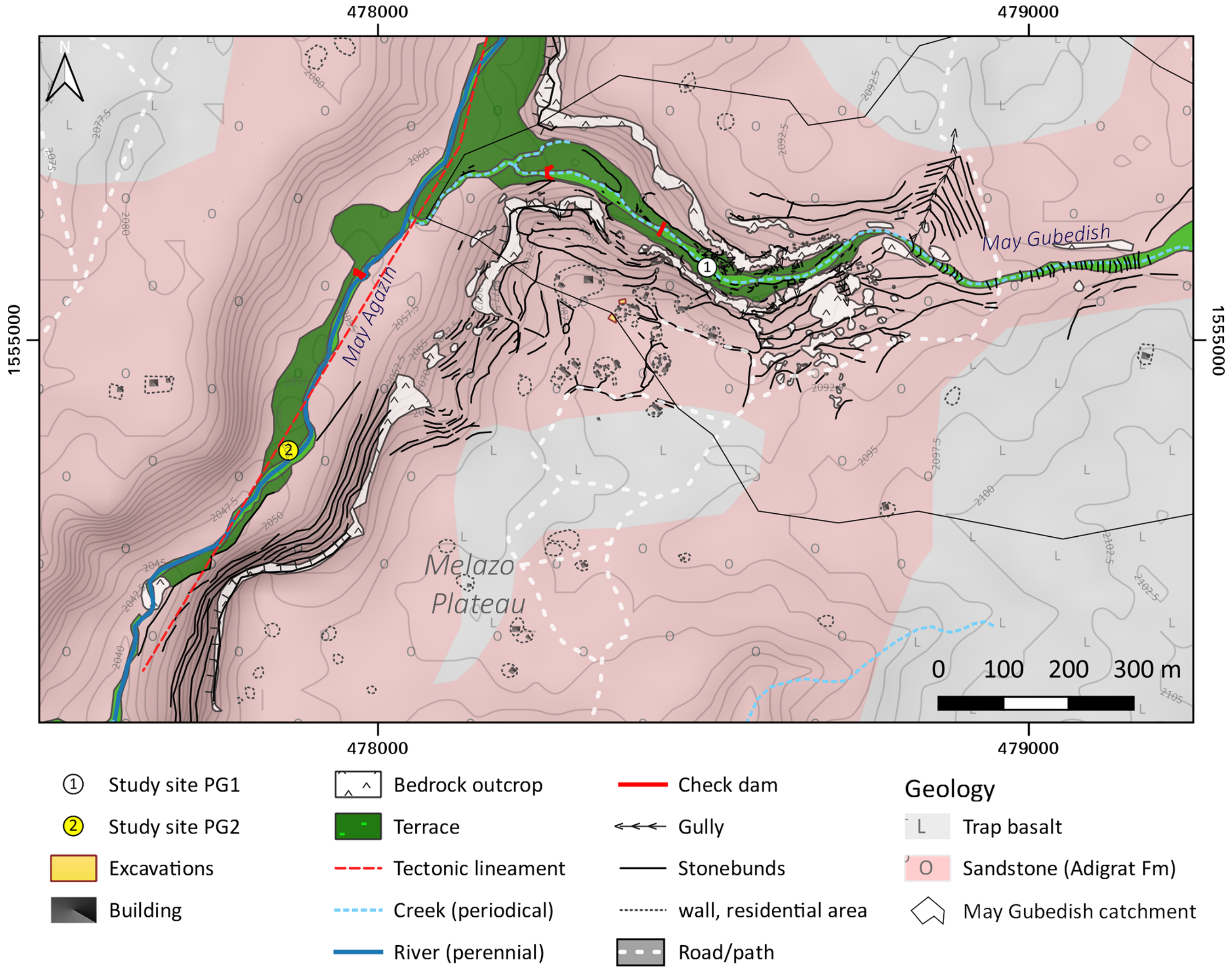

Figure 2. Geomorphological and geological map of the study area. Geology modified from Tadesse (1999) and Hagos et al. (2010). Hillshade and isolines (2.5 m spacing) based on AW3D30 digital elevation model (Jaxa, 2005).

Table 2. Overview of radiocarbon ages. All ages derived from section PG1 at May Gubedish (14.066703° N, 38.800879° E). Calibrated ages calculated using OxCal v. 4.2.3 and the IntCal13 atmospheric curve (Reimer et al., 2013). Values in bold represent the calibrated ages referred to in the text.

Lab code	Field code	Depth (cm)	Raw C-14 age BP	Calibrated age BP
POZ-126495	DAT1	65	1600 ± 30	**1470 ± 65**
POZ-114362	DAT2	70	2840 ± 360	**3021 ± 898**
POZ-123179	DAT3	100	2425 ± 30	**2525 ± 173**
POZ-123180	DAT4	180	1530 ± 30	**1432 ± 85**
POZ-126496	DAT5	365	4045 ± 35	**4603 ± 185**
POZ-122126	DAT6*	30	605 ± 30	**598 ±85**

* Sample DAT6 was taken 5 m downstream from PG1.

Sediment profile PG2, at the northwestern bank of May Agazin (Fig. 2), exposes eight strata, summarized in three different types of lithofacies: laminated sand, silt, and mud (Fl) characterize the overlying strata of the profile (0–260 cm below surface), interrupted by a layer of clast-supported, horizontally stratified gravel (Gh) 30–65 cm below surface. Below 260 cm depth lithofacies of the outcropping sediments correspond to high-energy fluvial deposits of planar-cross-bedded gravel (Gp) and planar-cross-bedded sand (Sp). The top layer (layer 1, 0–30 cm below surface) is of dark brown colour and consists of sandy silt with nested pockets filled with gravels and stones. Layer 2 (30–65 cm below surface) consists of compacted, light brown to gray silty sand with a gravelly matrix, and locally semi-angular stones are horizontally embedded. Underlying layer 3 (65–68 cm below surface) is composed of compacted brown to dark gray silt; its boundaries to the overlying layer 2 and underlying layer 4

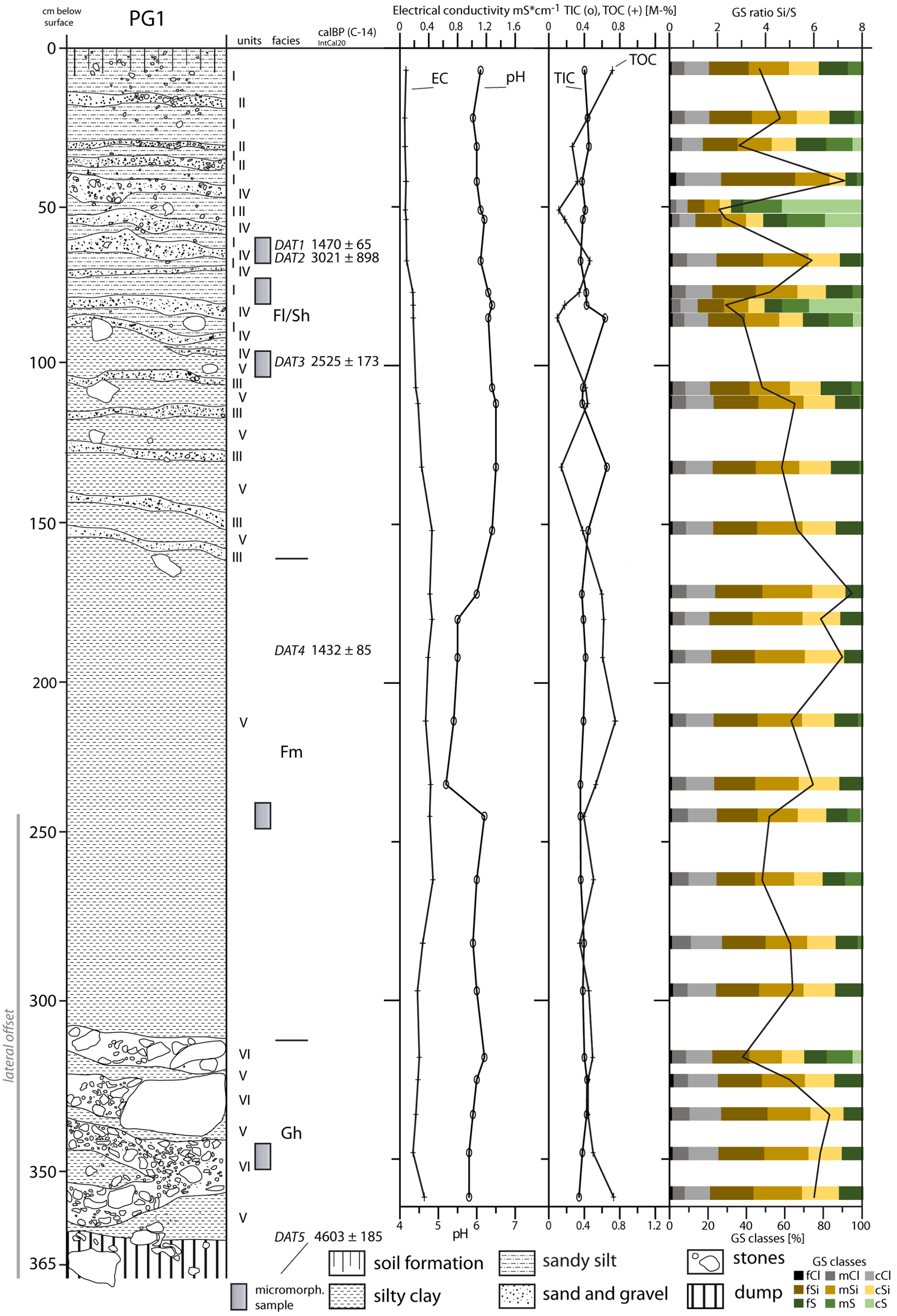

Figure 3. Sediment section PG1. Unit I: gray-black, fine roots, heavily compacted, clayey-sandy matrix with sharp-edged gravel content. Unit II: poorly sorted stone layer, 5 up to max 10 cm in diameter, rounded edges, sandy-clayey matrix. Unit III: coarse gravel layer, sandy-clayey matrix. Unit IV: red-white-grayish sand grains, occasional cobbles less than 3 cm in diameter. Unit V: gray-green massive silty clay, heavily compacted, partially embedded gravel layers (III), vertically elongated rust stains up to 1 cm length. Unit VI: gravel and stone layer. Lithofacies codes according to Miall (1996): Fm – massive mud, silt; Fl – laminated sand, silt, and mud; Sh – horizontally bedded sand; Gh – clast-supported, horizontally stratified gravel. Photographs of section PG1 can be found in the Supplement.

are in sharp contact. Layer 4 (68–74 cm below surface) corresponds to a light brown sandy silt in a gravelly matrix. There are several vertical cracks cutting the whole layer, which are filled with the material of layer 3. These cracks continue throughout the underlying layer 5 (74–87 cm below surface), which has a light brown colour with orange patches and consists of sandy silt with a less gravelly matrix than the above layer. It is connected with a diffuse contact to underlying layer 6 (87–97 cm below surface), a 10 cm thick layer of silt with distinct horizontal rust bands. The aforementioned cracks end in layer 6. Layer 7 (97–152 cm below surface) consists of silt and has a yellowish gray colour. Occasionally there are gravels and stones (2–4 cm in diameter) embedded. Luminescence dating of layer 7 revealed at 120 cm below surface a burial age of 15.9±1.5 ka (fading corrected; see Table 3) for this layer. The exposed basal layer 8 (below 152 cm below surface) is characterized by an intercalation of several sorted sub-layers with various grain sizes; below 220 cm depth the sub-layers become bevelled. Rust and manganese bands occur occasionally. The luminescence measurements for layer 8 (260 cm below surface) yielded a depositional age of 19.5 ± 1.5 ka (fading corrected; see Table 3).

Comparable to section PG1 the pH values of the sediments in section PG2 range between pH 6.7 and pH 7.1. The highest pH value was recognized in layer 2, at a depth of ca. 50 cm. The electrical conductivity increases from ca. 0.2 mS cm^{-1} in layer 1 to the bottom, peaking in layer 4 (0.4 mS cm^{-1}). The TOC content is the highest in layer 1 (1.2 wt %) with two minor peaks in layers 3 (0.3 wt %) and 5 (0.23 wt %). Below 100 cm depth, the TOC decreases to values less than 0.2 wt %.

4.3 Micromorphology

At the May Agazin section (PG1), the groundmass is composed of silty to clayey weakly developed sub-angular blocky peds (Fig. 5a, c, d). The dominating colours are brown-gray-red with reduced grey more present at the bottom part, likely due to changes in groundwater level. Overall pedo-features are mostly in the form of organic and iron impregnations with some pedoturbation and little bioturbation. Little change is evident along the profile with Fe oxides, organic residues, and limpid clays detected along infilled channels. At 65–70 cm below surface (Fig. 5a), disordered interlayerings of coarse sands and gravel-sized grains with finer material are found at times along planar voids or infilled channels. They are mostly layered semi-diagonally at a 45–60° angle. These sub-rounded gravel-sized grains could be a result either of redeposition of fluvial sediments due to sheet erosion from the slopes or of a low-energy fluvial deposition. Sub-rounded sand-sized black metal oxide pseudomorphs are more dominant at this depth. The latter do not seem to be in situ pedofeatures but oxidized and redeposited or pedoturbated within planes. At 110 cm below surface, the grey-gley colour decreases, and a brown-red Fe matrix dominates the micro-

Table 3. Optically stimulated luminescence (OSL): results from radionuclide analysis and luminescence dating. Values in bold represent the fading corrected ages referred to in the text.

Sample lab code	Sample field code	^{238}U (Bq kg^{-1})	^{232}Th (Bq kg^{-1})	^{40}K (Bq kg^{-1})	Depth (m)	Grain size (µm)	Overall dose rate Fs (Gy ka^{-1})[a]	IR50 (n)[b]	IR50 D_e (Gy)[c]	IR50 age (ka) faded[d]	IR50 age (ka) fading corr.[e]
VLL-0491-L	PG-2-OSL5	11.18 ± 1.39	15.25 ± 1.16	200 ± 12	1.2	150–200	1.87 ± 0.15	27	23.43 ± 1.03	12.5 ± 1.1	**15.9 ± 1.5**
VLL-0492-L	PG-2-OSL6	10.80 ± 1.56	12.04 ± 0.95	127 ± 9	2.6	100–300	1.66 ± 0.13	9	25.37 ± 1.51	15.3 ± 1.5	**19.5 ± 1.5**

[a] Cosmic dose rate determined according to Prescott and Stephan (1982; Prescott and Hutton, 1994), calculated with respect to geographical position of the sampling spot (longitude, latitude, and altitude), depth below surface, and average sediment overburden density. Cosmic dose rate assigned with a 10 % error. External and internal dose rate calculated using conversion factors of Adamiec and Aitken (1998) and β attenuation factors of Mejdahl (1979), including an alpha attenuation factor of 0.08 ± 0.01, as well as an internal K content of 12.5 ± 0.5 % (Huntley and Baril, 1997) and an estimated average water content of 15 ± 5 % throughout burial time. Error was propagated to the overall dose rate calculation.

[b] Number of aliquots (4 mm diameter) passing all rejection criteria (20 % recycling ratio, 20 % recuperation in percentage of the natural signal, and 20 % test dose error, all values based on results from dose recovery experiments yielding recovery ratios in agreement with unity within error). A feldspar single-aliquot regenerative-dose (SAR) protocol using a stimulation temperature of 50 °C and a preheat temperature of 250 °C held for 60 s was used for the determination of the equivalent dose (Wallinga et al., 2000). Luminescence signals were detected through a LOT/Oriel D410/30 optical interference filter, selecting the K-feldspar emission at 410 nm (Krbetschek et al., 1997).

[c] Calculated using the CAM (Galbraith et al., 1999).

[d] Calculated using the software ADELE (Kulig, 2005).

[e] Corrected for fading according to the method of Huntley and Lamothe (2001) using the R Luminescence package (Kreutzer et al., 2012). A g value of 2.6 ± 0.3 (average value of 12 aliquots for sample VLL-0491-L) was determined using fading experiments according to Auclair et al. (2003). The fading corrected ages are used for all interpretation in this paper.

mass, indicating either more intense oxidation, most likely due to post-depositional percolation, or the groundwater not reaching up to this level (Fig. 5b). The latter process appears to be more dominant. Voids coated or infilled with limpid clay, sand-sized minerals, and hyper-coated nodules are mostly in association with planes and suggest older plane (crack) formation and therefore several cycles of pedoturbation. This process could occur either near the surface or as result of the total de- and re-hydration of the entire soil column. Some smaller voids are more rounded than the larger ones, and chambers and vesicles are common. These features indicate bioturbation occurred or is preserved over the overlying pedoturbation on the smaller scale (20–100 µm; Fig. 5, Appendix A).

Section PG2, exposing fluvial deposits of May Gubedish, exhibits silicious cementation, as well as vertical Fe oxidized cracking (Fig. 5e, f). The three micromorphological samples taken show sand- to gravel-sized volcanic minerals along with basalt rock fragments (Fig. 5e, f, g). The gravel-sized grains are coated by clay but seem to lack silt, suggesting a surface-related process of mud drying on these grains rather than a post-depositional one. The differences between the layers are related to void sizes (compaction) and to some extent to a dominance of the clayey matrix. The layers, however, exhibit large sub-angular sand- to gravel-sized grains and occasional Fe/Mn pseudomorphs. This suggests a strictly fluvial, medium-energy deposition with very minimal post-depositional activities. At 120 cm below surface (Appendix A) sand-sized grains are deposited sub-horizontally following the inclination of the present-day surface. Iron oxide nodules are mainly ordered vertically along cracks and infilled channels while some of the grains are aggregated. These observations indicate a lower-energy deposition for layer 7 (97–150 cm) than for the lowermost layer (layer 8; Fig. 5g), with some vertical voids indicating roots and/or dehydration cracks (related to the nearby surface above) infilled with oxides. A further decrease in stream energy is evident at 68–74 cm below surface (layer 4, Fig. 4), where the groundmass is compacted, matrix supported, and dominated by clays. A post-depositional silicious cementation has likely replaced biogenic features and post-dates all other features (Fig. 5e, f).

5 Discussion

Both investigated sedimentary sections and the geomorphological mapping provide insights into the late Pleistocene–Holocene palaeoenvironmental development of the Daragá area.

At the May Agazin site (PG2), the outcropping sediments are all of fluvial origin. In the basal layer 8, the sorted sands, gravels, and pebbles indicate fluvial deposition at a point bar close to the channel under varying, but generally rather high, velocities (Pazzaglia, 2013). In the overlying layer 7, laminated sands and fine gravels indicate floodplain deposition possibly related to a shift in the meandering channel in the rather wide May Agazin valley (Hooke, 2022). Accordingly, layers 6, 5, and 4 correspond to cycles fining upwards, indicating decanted floodplain deposits (Dunne and Alto, 2013; Pazzaglia, 2013). In layers 4 and 5, organic carbon contents are slightly increased. While these increased organic carbon contents could relate to redeposited organic material on the floodplain, they might also indicate soil-forming processes in a phase of reduced flood frequency (Kennedy and Woods, 2013). This interpretation agrees with the cracks infilled with fines coated by Fe oxides pervading layers 4, 5, and 6, which are signs of desiccation at the surface (Verrecchia and Trombino, 2021). Also the presence of silicified plant material observed in layer 4 (Fig. 5e) indicates that this layer formed a surface for at least some time and possibly underwent soil-forming processes. We assume that this surface was partly eroded before the accumulation of overlying layer 3 as indicated by the sharp contact between layers 3 and 4. The minor thickness of layer 3 and its sandy character indicate a single smaller flood event (Knox and Daniels, 2002). Also in layer 3, increased organic carbon contents are taken as indicators for post-sedimentary soil development and, thus, indicate a post-sedimentary phase of low flood frequency (Dixon, 2013). In contrast, in the overlying layer 2 the 50 cm thick package of unsorted sand, gravel, and sharp-edged rocks indicates strong flood activities (Benito, 2013) possibly with material contribution from the steep surrounding slopes (Nyssen et al., 2006a). However, as there is no age control for the uppermost metre of the sediment profile, a possible connection between late Holocene human impact such as deforestation (Lanckriet et al., 2015) remains highly speculative.

The deposition of layers 8 (VLL-0492-L; 19.5 ± 1.5 ka) and 7 (VLL-0491-L; 15.9 ± 1.5 ka) falls into the LGM–late Pleistocene glacial–interglacial transition period. Within 1σ error, both ages almost overlap, and within 2σ error, both ages do overlap. Given the poor luminescence properties (dim signals) of both samples, which required 4 mm aliquots each containing several hundreds of grains to be measured, signal averaging may lead to an overestimation of the ages: the luminescence signals from well-bleached grains will be masked by the much brighter luminescence signals from older feldspar grains which were not sufficiently bleached during the last sedimentary cycle (Thrasher et al., 2009; Rhodes, 2011). This is especially true for sample VLL-0492-L, which required measuring in a very broad grain size range from 100–300 µm (compared to a grain size range of only 150–200 µm for sample VLL-0491-L). This increases the averaging effect even more because a higher number of grains is measured per aliquot, which may serve as an explanation of the age offset of the two ages. In addition, the location of the PG2 section lies in the headwater area of the May Agazin catchment, roughly 4 km away from the divide. Thus, the possible transport distances of the feldspar grains

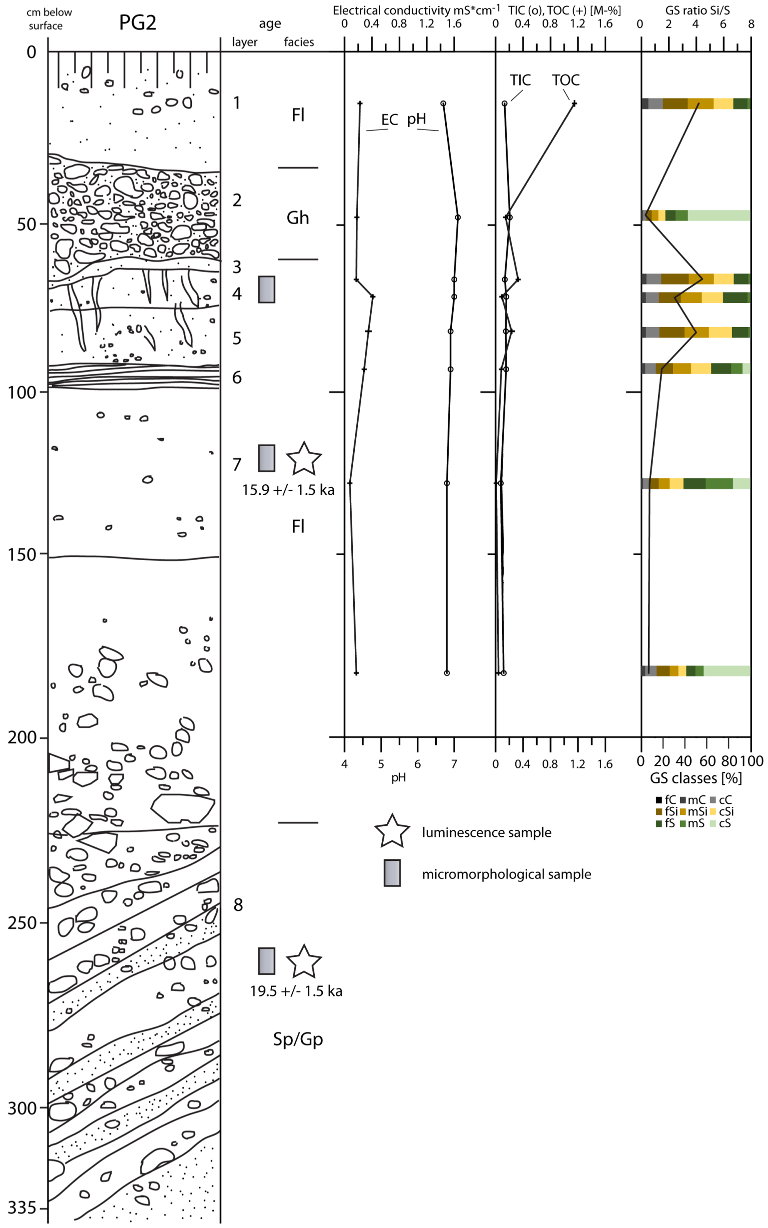

Figure 4. Sediment section PG2 (May Agazin). Layer 1: sandy silt, gravel, and stones, layered in pockets of the matrix, sub-angular small stones. Layer 2: silty sand, matrix more gravelly, rounded and semi-angular stones (2–12 cm), mostly horizontally bedded. Layer 3: sandy silt. Layer 4: sandy silt, gravels part of the matrix, sub-angular small stones. Layer 5: sandy silt with few gravels, very fine. Layer 6: silt. Layer 7: silt, occasional gravels and stones (2–4 cm), unsorted. Layer 8: intercalations of sorted layers, bedded: stones, gravels, sometimes sandy matrix. Lithofacies codes according to Miall (1996): Gp – planar-cross-bedded gravel; Sp – planar-cross-bedded sand; Gh – clast-supported, horizontally stratified gravel; Fl – laminated sand, silt, and mud. A photograph of section PG2 can be found in the Supplement.

are low, reducing the bleaching possibilities owing to only a relatively low rate of possible sedimentary cycles (Mcguire and Rhodes, 2015; Bonnet et al., 2019). Bearing in mind the possible age overestimation owing to methodological issues especially for sample VLL-0491-L, it appears more likely that both luminescence ages should be associated with the younger late Pleistocene and not with the LGM (in the case of unit 8). Consequently, both fluvial sedimentary units relate to the last glacial–interglacial transition and the abrupt onset of the summer monsoon at around ca. 15 ka (Williams et al., 2006; Gasse et al., 2008; Foerster et al., 2012). Being connected to the Nile catchment via the Tekezé and Atbara rivers, this notion is also supported by the increasing contribution of Ethiopian trap basalt components recorded in the Nile delta at the onset of the last African Humid Period (AHP) at ca. 15 ka (Revel et al., 2010; Ménot et al., 2020).

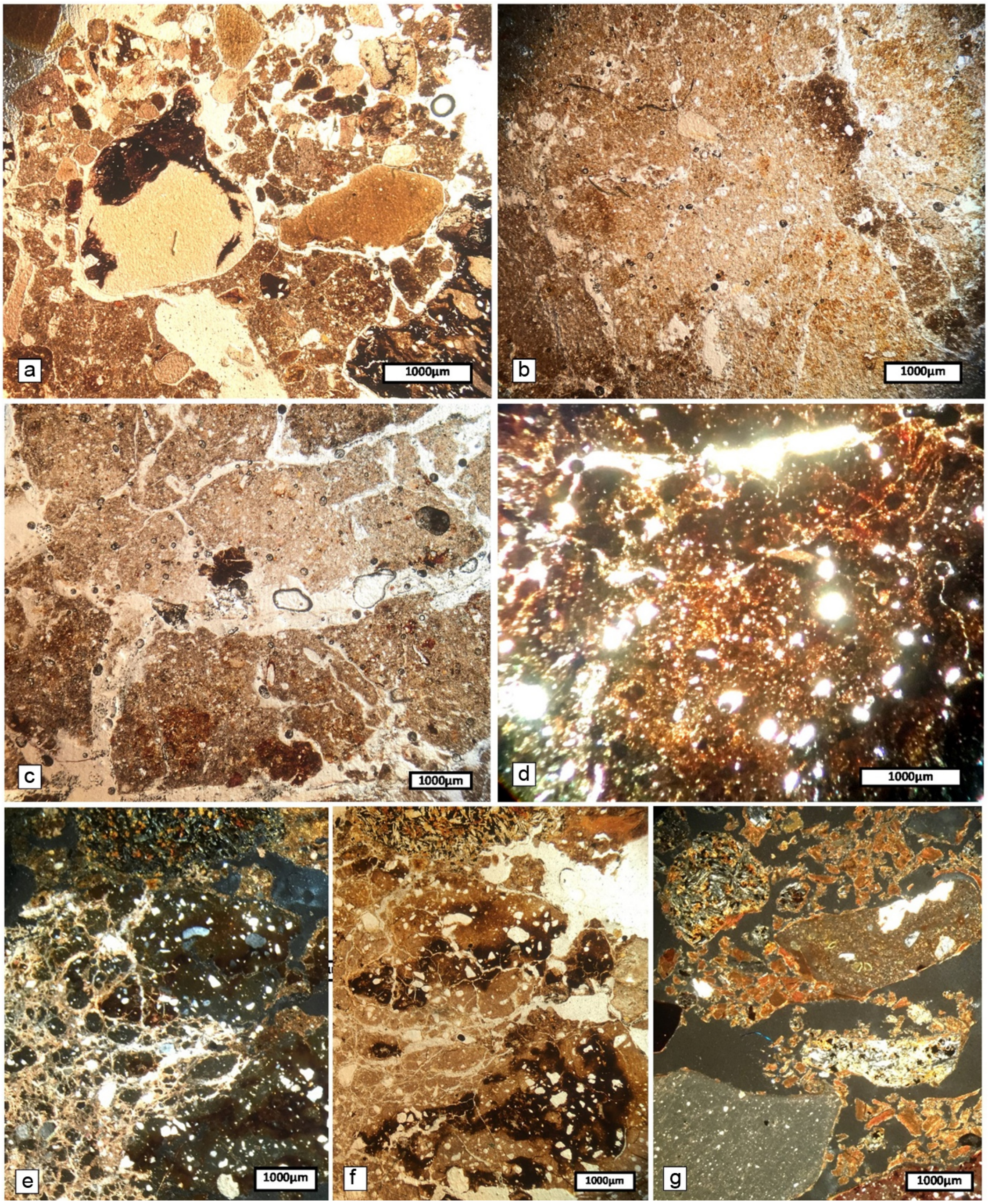

Figure 5. Thin sections of PG1 **(a–d)** and PG2 **(e–g)**. PPL = plane polarized light, and XPL = cross polarized light. **(a)** At 65–70 cm below surface (PPL) notice that the grains undergoing Mn coating are not expressed in the micromass. **(b)** At 100–110 cm below surface (PPL) clay coating and Fe–Mn oxides in a reducing and oxidizing mixed (Fe depletion) groundmass. Notice sub-vertical void along a dark brown groundmass, both typical of the matrix. **(c)** At 245–250 cm (PPL) notice that accommodating and non-accommodating planes, as well as grey and red-brown parts of the micromass, with organic impregnation and Fe–Mn oxides, are more easily differentiated. **(d)** At 365–370 cm (PPL) red-brown colour and non-accommodating planes are both more dominant. **(e)** At PG2 layer 4, 68–74 cm depth (XPL) notice that the (most likely silicious) cement is infilling voids that are cutting through the Mn–Fe oxide micromass, indicating its layer formation. **(f)** At PG2 layer 7, 115–125 cm depth: similar to panel **(e)** in PPL. **(g)** At PG2 layer 8, 255–265 cm depth (XPL) notice the basalt grain in the upper left part and limpid clay coating most of the larger grains and aggregates.

Thus, the lower parts of the PG2 section were deposited due to increased fluvial activity in response to the onset of monsoonal rainfall after a drought period during the LGM. For Lake Ashenge, Marshall et al. (2009) report increasing precipitation due to the returning monsoon already at ca. 16.2 kyr BP, which is in very close agreement with our luminescence data.

The sedimentological record from the riverbank of May Gubedish (PG1), a tributary of May Agazin, indicates completely different fluvial dynamics. The base of this section is formed by a ca. 50 cm thick package of coarse clasts (Gh facies) indicating deposition in the channel under conditions of high stream energy (Pazzaglia, 2013). The whole overlying lithostratigraphic unit (Fm facies) is dominated by silty-clayey deposits, which are in its upper layers horizontally streaked with coarser, sandy-gravelly layers (Fl/Sh facies). Either these deposits are indicative of deposition in a still water body (Reeves, 1968) or they correspond to alluvial deposits on a floodplain under very low stream energy (Pazzaglia, 2013). Deposition in a stagnant water body would require a damming situation downstream of the section, which could have been caused by a local rockfall or landslide along the river banks (Korup, 2013). The outcropping sandstone of the Adigrat Formation along the steep valley flanks and the apparent signs of ongoing gravitational mass movements at the slopes affirm this assumption (Fig. 2). Nyssen et al. (2006a) identified rockfall as an important geomorphic process in the northern Ethiopian highlands, most recently often triggered by livestock trampling. At present, however, no geomorphological evidence of a natural damming situation due to mass movements could be observed along the valley floor. The parent material of the silty-clayey deposits is the weathered trap basalt, which makes up a large part of the May Gubedish catchment (Fig. 2). The repeated occurrence of thin (few centimetres) sand and gravel layers may represent stronger rainfall events triggering slope wash and increased discharge (Cammeraat, 2013). The large clasts, which at times are embedded into the silty-clayey layers, were most likely laterally washed in from the adjacent slopes. Within the silty-clayey parts of the section signs of stratification are lacking due to pedoturbation caused by dry–wet cycles starting from the surface and influenced by a periodically alternating water table level. Consequently, Fe reduction–oxidation cycles, organic decomposition, and clay-bound swell-and-shrink processes were identified in the micromorphological analyses. The process of argillipedoturbation, which causes intense turbation of the material, has been described for Vertisols in Tigray before (Nyssen et al., 2002, 2006a). However, the sand and gravel layers above ca. 160 cm below surface have visibly not been incorporated in the pedoturbation process. Thus, we conclude that pedoturbation has not affected the larger grains and in general has mostly occurred prior to their deposition. Generally, planes and other void types are smaller than the gravels and sands in this unit and are not infilled by organic or Fe oxides as is the case for much of the lower section or even a few of the layers in this unit; i.e. gravel-sized pedomorphic organic features may have been transported within a layer in the unit but not between layers (Fig. 5).

For C-14 dating, bulk soil organic carbon was used and, thus, should be treated with caution, as soil organic carbon can be redeposited several times (e.g. old wood effect) and re-precipitate or move vertically owing to pedo- or bioturbation (Sloss et al., 2013). Our dates therefore should reflect a general time frame for the accumulation of the PG1 profile using different stratigraphic constraints to interpret the accuracy of these dates. A C-14 date from the lower part of this profile (DAT5: 4603 ± 185 BP) reveals that the early accumulation of the coarse, clast-rich Gh facies likely took place during or after the mid-Holocene. From the fines of the Fm facies, one sample was derived (DAT4: 1432 ± 85 BP), and from the layered Fl/Sh facies, three samples for C-14 dating were extracted from gravel layers (DAT1: 1470 ± 65 BP; DAT2: 3021 ± 898 BP; DAT3: 2525 ± 173 BP). Even including an age inversion due to pedoturbation, these dates indicate that sedimentation took place during the first millennium BCE and the first millennium CE; thus, it temporally corresponds to the Ethio-Sabaean and Aksumite material cultures (Phillipson, 2012). An additional date was derived from a sediment sample taken 5 m downstream of the PG 1 profile (DAT6: 598 ± 53 BP) from silty-clayey deposits (Fm facies) at a depth of 30 cm, which represents a younger reaccumulation of the May Gubedish, probably as a lower terrace segment. This age provides a frame for the incision of the May Gubedish river into its infilled valley floor, forming a river terrace that today forms the surface of PG1, which consequently took place after 598 ± 53 BP. This is in agreement with the conclusions of Lanckriet et al. (2015), who report increased channel incision especially in recent and subrecent times due to strongly increased surface runoff as a result of strong deforestation. Two C-14 outliers are likely due to syn- and post-depositional processes. Within the gravel layer DAT2 was dated 500 years older than the 50 cm deeper sample of DAT3 but with the error range of 898 years, overlapping with DAT3. However, one substantial outlier (DAT4) within the well-pedoturbated material at 1 m below this unit falls into the middle of the first millennium CE, still confirming the general age of the deposition to the late Holocene but contradicting the three ages above. This C-14 outlier is likely a result of roots activities or pedoturbation below the horizontal gravel layer. The maximum age for the deposition of the upper 180 cm of the PG1 section falls into the time of or after the decline of the Aksumite Empire (ca. 1400–1000 CE) (Phillipson, 2012), when the geomorphic activity was high due to intensified agriculture and increasing deforestation under comparably drier climatic conditions (Fig. 6; Lanckriet et al., 2015; Darbyshire et al., 2003; Machado et al., 1998).

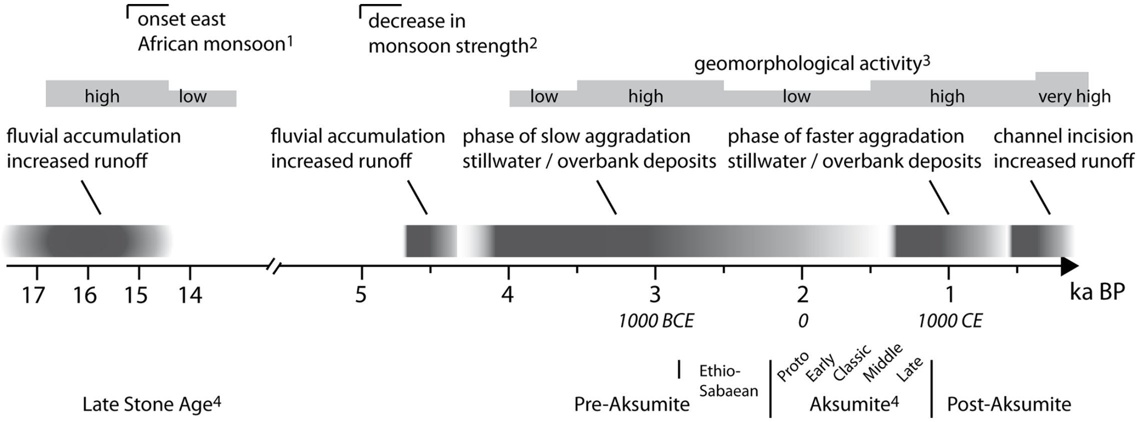

Figure 6. Integration of our results in an environmental and cultural context of northern Ethiopia. 1: Moeyersons et al. (2006), Lamb et al. (2007b), Umer et al. (2004). 2: Armitage et al. (2015). 3: this study and Lanckriet et al. (2015). 4: Bard et al. (2014), Fattovich (2012).

6 Conclusions

The environmental conditions on and around the Melazo plateau were favourable during the time of the Ethio-Sabaean settlement. This is also reflected in the findings of monumental buildings from this period. The landscape of the May Gubedish valley close to the Melazo archaeological site probably looked different during the Ethio-Sabaean period than today. The groundwater level was presumably higher, and water in the valley was probably easier to access than today due to less relief as May Gubedish was flowing at a higher level than today in its own sediments at the valley floor. Also the geological conditions appear favourable: the omnipresent Adigrat Sandstone provides building material, which is also used today for building walls and other structures. The trap basalt, found in the inner part of the Melazo plateau and the surrounding plateaus, provides fertile soils. Beyond, the peninsula-like Melazo plateau has a strong protective function as it is only easily accessible from the east–northeast, while in all other directions steep scarps enclose the plateau. The resulting large viewshed of the Melazo plateau also had tactical advantages as it allowed visitors to be recognized at an early stage. The landscape of the much wider May Agazin valley, however, was probably rather similar to most recent conditions. May Agazin like today was a hindrance for traffic, and during rainy seasons the channel could probably only be crossed at dedicated, and thus easy to control, places.

Our study provides evidence for increased fluvial activity in the May Agazin during the late Pleistocene, which is probably related to the re-occurrence of the monsoonal rainfall after the LGM. In the May Gubedish valley, being a tributary to the valley of May Agazin, coarse fluvial sediments indicating high-energy fluvial dynamics at the base of the channel were deposited around the transition from the middle to late Holocene. During the Ethio-Sabaean and probably early Aksumite period slow aggradation of the valley floor started with most likely increasing depositional rates during the late and post-Aksumite period. Since medieval or subrecent times the channel of May Gubedish incised into its own valley floor sediments – exposing the sediments of PG1 and forming a terrace which today is used for an orchard. These observations generally correlate with other studies on geomorphic activity phases in Tigray.

Appendix A

Table A1. Sedimentary analysis of selected depositional units in the PG1 and PG2 profiles. Grain sizes used are gravel (g), coarse sand (cs), medium sand (ms), fine sand (fs), silt, and clay. Sediment grain size categories are based on laser grain size analysis, while mineral occurrence is interpreted from XRD spectra. Micromass structure, mineral shapes and sizes (for those also visually identified), and pedo-features were obtained through micromorphological observation.

Site	Depth (cm)	Unit	Grain size and structure	Dominant minerals (ordered by abundance)	Pedo-features
PG1	30	Young accumulation	Clay. Weakly developed sub-angular blocky and crumble porous peds	Quartz: sub-angular (ms-fs); kaolinite, muscovite, and chlorite (silt-clay); feldspars (fs-silt); rosenhahnite	Iron mottling. Large accommodating planes and aggregates
	65–70	I/IV	Loam. Weakly developed sub-angular blocky peds, poor sorting, few sub-horizontal grain-supported layers of g-cs-sized grains	Quartz (cs-fs, sub-rounded larger grains to sub-angular smaller grains), kaolinite, muscovite, and chlorite: mostly as coating (fs-clay); plagioclase feldspar (fs); pyroxene: weathered (cs-fs) very rare	Iron mottling, organic impregnation, Mn–Fe pseudomorphs (g-ms), planes
	75–79	I/IV	Loam. Planes – ms sized in width. Moderately developed sub-angular blocky peds, poor sorting	Quartz (g-fs, sub-angular), kaolinite, muscovite, and chlorite: mostly as coating (fs-clay); plagioclase feldspar (fs); pyroxene: weathered (g-cs-fs) very rare	Some planes are infilled by the coarser material including aggregates and pseudomorphs
	95–111	V	Silty clay loam. Sub-angular blocky peds, weakly developed in a massive microstructure	Quartz mostly elliptic shaped (cs-fs); plagioclase feldspar and pyroxene: sub-angular to sub-rounded (fs); kaolinite, muscovite, and chlorite: mostly as coating (silt-clay); rosenhahnite	Iron mottling and organic impregnation, accommodating and non-accommodating planes. Voids are coated and some infilled by limpic clay and Fe–Mn oxides. Cs-sized grains are associated with planes
	345–350	V/VI	Silty loam. Weakly developed peds with poor sorting and open grain-supported structured cs-g grains at the lower part of the groundmass	Quartz: sub-angular (ms-fs), feldspar (fs-silt), kaolinite, muscovite, and chlorite (silt), possible rosenhahnite	Brown micromass with iron mottling and organic impregnation. Bioturbation is slightly more evident from the impregnation of oxides, and limpid clays feature also along infilled channels
PG2	65–68	3	Loamy sand, blocky and moderately developed peds	Quartz: sub-rounded (cs-fs); basalt: sub-angular (g-cs); clinopyroxene: sub-rounded (fs); olivine: (silt) rare; orthopyroxene: (fs) rare	Planar voids coated and filled with clays or larger grains
	68–74	4	Sandy loam, blocky in a poorly to moderately developed peds structure	Quartz: sub-rounded (ms-fs); clinopyroxene: sub-rounded (fs); basalt: sub-angular (cs) rare	Cemented by amorphous silica. Rare (g) size orthopyroxene grains with surrounding constrained minerals (corona texture) – geological feature
	97–152	7	Loamy sand with structural and planar voids. Large grains (cs-g) are crossing sub-horizontally	Basalt: sub-rounded (g-ms); pyroxene: sub-angular to sub-rounded (cs-fs); olivine: (ms-fs) rare; kaolinite, muscovite: coating (clay)	Clay coating on most of the sand-sized grains. Many of the large grains are aggregates. Mn–Fe oxide nodules (pseudomorphs) are also found along vertical lines (cracks)
	152–335	8	Sandy gravel dominant in open grain-supported structure	Quartz: sub-rounded (cs-fs); pyroxene: sub-rounded to sub-angular (ms-fs); basalts: sub-rounded (g-ms)	Three sub-units with g- and s-sized grains: 1. in large voids, 2. dominant clay-coating and 3. combination of (1) and (2) Mn–Fe oxides pseudomorphs (cs-ms) and Fe mottling. Depositional cycles

Data availability. The basic luminescence data are included in this publication. Additional data can be provided by the corresponding author upon request.

Supplement. The supplement related to this article is available online at: https://doi.org/10.5194/egqsj-72-37-2023-supplement.

Author contributions. This study was conceptualized by JH, NN, and BS, who also carried out the field work. JH and NN prepared the original draft of the manuscript. NN carried out the micromorphological analyses. CL conducted the luminescence analyses. TM provided the archaeological background. All authors discussed the results and contributed to various stages in the writing process of this paper, including reviewing and editing.

Competing interests. At least one of the (co-)authors is a member of the editorial board of *E&G Quaternary Science Journal*. The peer-review process was guided by an independent editor, and the authors also have no other competing interests to declare.

Special issue statement. This article is part of the special issue "Quaternary research from and inspired by the first virtual DEUQUA conference". It is a result of the vDEUQUA2021 online conference in September/October 2021.

Acknowledgements. The authors wish to thank Silvan Schmieg and Robert Busch (Freie Universität Berlin) and Kristina Pfeiffer, Victoria Grünberg, Mike Schnelle, Sarah Japp, and Iris Gerlach (German Archaeological Institute (DAI), Sanaa Branch of the Orient Department). Thanks to Mareike Stahlschmidt for guidance in the analysis of the thin sections. We want to thank the two anonymous reviewers for their constructive reviews of this work.

Financial support. This research has been supported by the Deutsche Forschungsgemeinschaft (DFG) within the framework of the SPP 2143 Entangled Africa – Project Routes of Interaction (grant no. 404354728).

We acknowledge support from the Open Access Publication Initiative of Freie Universität Berlin.

Review statement. This paper was edited by Julia Meister and reviewed by two anonymous referees.

References

Adamiec, G. and Aitken, M.: Dose-rate conversion factors: update, Ancient TL, 16, 37–50, 1998.

Armitage, S. J., Bristow, C. S., and Drake, N. A.: West African monsoon dynamics inferred from abrupt fluctuations of Lake Mega-Chad, P. Natl. Acad. Sci. USA, 112, 8543–8548, https://doi.org/10.1073/pnas.1417655112, 2015.

Auclair, M., Lamothe, M., and Huot, S.: Measurement of anomalous fading for feldspar IRSL using SAR, Radiat. Meas., 37, 487–492, https://doi.org/10.1016/S1350-4487(03)00018-0, 2003.

Bard, K. A., Fattovich, R., Manzo, A., and Perlingieri, C.: The chronology of Aksum (Tigrai, Ethiopia): a view from Bieta Giyorgis, Azania, 49, 285–316, https://doi.org/10.1080/0067270X.2014.943484, 2014.

Benito, G.: 13.15 Hazardous Processes: Flooding, in: Treatise on Geomorphology, edited by: Shroder, J. F., Academic Press, San Diego, 243–261, https://doi.org/10.1016/B978-0-12-374739-6.00363-8, 2013.

Bonnet, S., Reimann, T., Wallinga, J., Lague, D., Davy, P., and Lacoste, A.: Landscape dynamics revealed by luminescence signals of feldspars from fluvial terraces, Scientific Reports, 9, 8569, https://doi.org/10.1038/s41598-019-44533-4, 2019.

Bøtter-Jensen, L., Bulur, E., Duller, G. A. T., and Murray, A. S.: Advances in luminescence instrument systems, Radiat. Meas., 32, 523–528, https://doi.org/10.1016/S1350-4487(00)00039-1, 2000.

Bøtter-Jensen, L., McKeever, S. W. S., and Wintle, A. G.: Optically Stimulated Luminescence Dosimetry, Elsevier, 355 pp., https://doi.org/10.1016/B978-0-444-50684-9.X5077-6, 2003.

Bøtter-Jensen, L., Thomsen, K. J., and Jain, M.: Review of optically stimulated luminescence (OSL) instrumental developments for retrospective dosimetry, Radiat. Meas., 45, 253–257, https://doi.org/10.1016/j.radmeas.2009.11.030, 2010.

Busch, R., Hardt, J., Nir, N., and Schütt, B.: Modeling Gully Erosion Susceptibility to Evaluate Human Impact on a Local Landscape System in Tigray, Ethiopia, Remote Sensing, 13, 2009, https://doi.org/10.3390/rs13102009, 2021.

Cammeraat, E. L. H.: 7.33 Semiarid Hillslope Processes, in: Treatise on Geomorphology, edited by: Shroder, J. F., Academic Press, San Diego, 355–362, https://doi.org/10.1016/B978-0-12-374739-6.00184-6, 2013.

Coltorti, M., Dramis, F., and Ollier, C. D.: Planation surfaces in Northern Ethiopia, Geomorphology, 89, 287–296, https://doi.org/10.1016/j.geomorph.2006.12.007, 2007.

de Contenson, H.: Les fouilles à Haoulti-Melazo en 1958, Annales d'Ethiopie, 4, 39–60, 1961.

de Contenson, H.: Les fouilles de Haoulti en 1959 – Rapport préliminaire, Annales d'Ethiopie, 5, 41–86, 1963.

Darbyshire, I., Lamb, H., and Umer, M.: Forest clearance and regrowth in northern Ethiopia during the last 3000 years, Holocene, 13, 537–546, https://doi.org/10.1191/0959683603hl644rp, 2003.

Dixon, J. C.: 4.3 Pedogenesis with Respect to Geomorphology, in: Treatise on Geomorphology, edited by: Shroder, J. F., Academic Press, San Diego, 27–43, https://doi.org/10.1016/B978-0-12-374739-6.00058-0, 2013.

Dramis, F., Umer, M., Calderoni, G., and Haile, M.: Holocene climate phases from buried soils in Tigray (northern

Ethiopia): comparison with lake level fluctuations in the Main Ethiopian Rift, Quaternary Res., 60, 274–283, https://doi.org/10.1016/j.yqres.2003.07.003, 2003.

Dunne, T. and Aalto, R. E.: 9.32 Large River Floodplains, in: Treatise on Geomorphology, edited by: Shroder, J. F., Academic Press, San Diego, 645–678, https://doi.org/10.1016/B978-0-12-374739-6.00258-X, 2013.

Duszyński, F., Migoń, P., and Strzelecki, M.C.: Escarpment retreat in sedimentary tablelands and cuesta landscapes – Landforms, mechanisms and patterns, Earth-Sci. Rev., 196, 102890, https://doi.org/10.1016/j.earscirev.2019.102890, 2019.

Fattovich, R.: The Development of Ancient States in the Northern Horn of Africa, c. 3000 BC–AD 1000: An Archaeological Outline, J. World Prehist., 23, 145–175, https://doi.org/10.1007/s10963-010-9035-1, 2010.

Fattovich, R.: The northern Horn of Africa in the first millennium BCE: local traditions and external connections, Rassegna di Studi Etiopici, 4, 1–60, 2012.

Ferrari, G., Ciampalini, R., Billi, P., and Migoń, P.: Geomorphology of the Archaeological Area of Aksum, in: Landscapes and Landforms of Ethiopia. World Geomorphological Landscapes, edited by: Billi, P., Springer, Dordrecht, 147–161, https://doi.org/10.1007/978-94-017-8026-1_7, 2015.

Foerster, V., Junginger, A., Langkamp, O., Gebru, T., Asrat, A., Umer, M., Lamb, H. F., Wennrich, V., Rethemeyer, J., Nowaczyk, N., Trauth, M. H., and Schaebitz, F.: Climatic change recorded in the sediments of the Chew Bahir basin, southern Ethiopia, during the last 45,000 years, Quatern. Int., 274, 25–37, https://doi.org/10.1016/j.quaint.2012.06.028, 2012.

Frankl, A., Poesen, J., Deckers, J., Haile, M., and Nyssen, J.: Gully head retreat rates in the semi-arid highlands of Northern Ethiopia, Geomorphology, 173–174, 185–195, https://doi.org/10.1016/j.geomorph.2012.06.011, 2012.

French, C., Sulas, F., and Madella, M.: New geoarchaeological investigations of the valley systems in the Aksum area of northern Ethiopia, CATENA, 78, 218–233, https://doi.org/10.1016/j.catena.2009.02.010, 2009.

Galbraith, R. F., Roberts, R. G., Laslett, G. M., Yoshida, H., and Olley, J. M.: Optical dating of single and multiple grains of quartz from Jinmium rock shelter, Northern Australia: Part I, experimental design and statistical models, Archaeometry, 41, 339–364, https://doi.org/10.1111/j.1475-4754.1999.tb00987.x, 1999.

Gasse, F., Chalié, F., Vincens, A., Williams, M. A. J., and Williamson, D.: Climatic patterns in equatorial and southern Africa from 30,000 to 10,000 years ago reconstructed from terrestrial and near-shore proxy data, Quaternary Sci. Rev., 27, 2316–2340, https://doi.org/10.1016/j.quascirev.2008.08.027, 2008.

Gerlach, I.: Zum äthio-sabäischen Kunsthandwerk des frühen 1. Jahrtausends v. Chr., in: Hauptsache Museum – Der alte Orient im Fokus – Festschrift für Ralf-B. Wartke, edited by: Marzahn, J. and Pedde, F., marru – Studien zur Vorderasiatischen Archäologie, 229–252, ISBN 978-3-96327-036-9, 2018.

Hagos, M., Koeberl, C., Kabeto, K., and Koller, F.: Geochemical characteristics of the alkaline basalts and phonolite-trachyte plugs of the Axum area, northern Ethiopia, Austrian J. Earth Sc., 103, 153–170, 2010.

Harrower, M. J., Dumitru, I. A., Perlingieri, C., Nathan, S., Zerue, K., Lamont, J. L., Bausi, A., Swerida, J. L., Bongers, J. L., Woldekiros, H. S., Poolman, L. A., Pohl, C. M., Brandt, S. A., and Peterson, E. A.: Beta Samati: discovery and excavation of an Aksumite town, Antiquity, 93, 1534–1552, https://doi.org/10.15184/aqy.2019.84, 2019.

Harrower, M. J., Nathan, S., Mazzariello, J. C., Zerue, K., Dumitru, I. A., Meresa, Y., Bongers, J. L., Gebreegziabher, G., Zaitchik, B. F., and Anderson, M. C.: Water, Geography, and Aksumite Civilization: The Southern Red Sea Archaeological Histories (SRSAH) Project Survey (2009–2016), Afr. Archaeol. Rev., 37, 51–67, https://doi.org/10.1007/s10437-020-09369-8, 2020.

Hoelzmann, P., Gasse, F., Dupont, L., Salzmann, U., Staubwasser, M., Leuschner, D., and Sirocko, F.: Palaeoenvironmental changes in the arid and sub arid belt (Sahara-Sahel-Arabian Peninsula) from 150 kyr to present, in: Past Climate Variability through Europe and Africa. Developments in Paleoenvironmental Research, edited by: Battarbee, R. W., Gasse, F., and Stickley, C. E., Springer, Dordrecht, 6, 219–256, https://doi.org/10.1007/978-1-4020-2121-3_12, 2007.

Hofmann, C., Courtillot, V., Féraud, G., Rochette, P., Yirgu, G., Ketefo, E., and Pik, R.: Timing of the Ethiopian flood basalt event and implications for plume birth and global change, Nature, 389, 838–841, https://doi.org/10.1038/39853, 1997.

Hooke, J. M.: 6.26 - River Meandering, in: Treatise on Geomorphology (Second Edition), edited by: Shroder, J. F., Academic Press, Oxford, 480–516, https://doi.org/10.1016/B978-0-12-409548-9.12517-5, 2022.

Huntley, D. and Baril, M.: The K content of the K-feldspars being measured in optical and thermoluminescence dating, Ancient TL, 15, 11–13, 1997.

Huntley, D. J. and Lamothe, M.: Ubiquity of anomalous fading in K-feldspars and the measurement and correction for it in optical dating, Can. J. Earth Sci., 38, 1093–1106, https://doi.org/10.1139/e01-013, 2001.

Japp, S., Gerlach, I., Hitgen, H., and Schnelle, M.: Yeha and Hawelti: cultural contacts between Saba' and D´MT – New research by the German Archaeological Institute in Ethiopia, Proc. Sem. Arab. Stud., 41, 145–160, 2011.

JAXA: ALOS Global Digital Surface Model (DSM) ALOS World 3D-30m (AW3D30) Ver. 2.2, JAXA – Japan Aerospace Exploration Agency [data set], https://www.eorc.jaxa.jp/ALOS/en/dataset/aw3d30/aw3d30_e.htm (last access: 17 January 2023), 2005.

Junge, A., Lomax, J., Shahack-Gross, R., Finkelstein, I., and Fuchs, M.: Chronology of an ancient water reservoir and the history of human activity in the Negev Highlands, Israel, Geoarchaeology, 33, 695–707, https://doi.org/10.1002/gea.21682, 2018.

Kennedy, D. M. and Woods, J. L. D.: 14.22 Determining Organic and Carbonate Content in Sediments, in: Treatise on Geomorphology, edited by: Shroder, J. F., Academic Press, San Diego, 262–273, https://doi.org/10.1016/B978-0-12-374739-6.00389-4, 2013.

Knox, J. C. and Daniels, J. M.: Watershed Scale and the Stratigraphic Record of Large Floods, in: Ancient Floods, Modern Hazards, 237–255, https://doi.org/10.1029/WS005p0237, 2002.

Korup, O.: 9.15 Landslides in the Fluvial System, in: Treatise on Geomorphology, edited by: Shroder, J. F., Academic Press, San Diego, 244–259, https://doi.org/10.1016/B978-0-12-374739-6.00240-2, 2013.

Krbetschek, M. R., Götze, J., Dietrich, A., and Trautmann, T.: Spectral information from minerals relevant for luminescence dating, Radiat. Meas., 27, 695–748, https://doi.org/10.1016/S1350-4487(97)00223-0, 1997.

Kreutzer, S., Schmidt, C., Fuchs, M. C., Dietze, M., Fischer, M., and Fuchs, M.: Introducing an R package for luminescence dating analysis, Ancient TL, 30, 1–8, 2012.

Kulig, G.: Erstellung einer Auswertesoftware zur Altersbestimmung mittels Lumineszenzverfahren unter spezieller Berücksichtigung des Einflusses radioaktiver Ungleichgewichte in der 238-U-Zerfallsreihe, Bakkalaureusarbeit Network Computing, TU Freiberg, unpublished thesis, 2005.

Lamb, H. F., Leng, M. J., Telford, R. J., Ayenew, T., and Umer, M.: Oxygen and carbon isotope composition of authigenic carbonate from an Ethiopian lake: a climate record of the last 2000 years, Holocene, 17, 517–526, https://doi.org/10.1177/0959683607076452, 2007a.

Lamb, H. F., Bates, C. R., Coombes, P. V., Marshall, M. H., Umer, M., Davies, S. J., and Dejen, E.: Late Pleistocene desiccation of Lake Tana, source of the Blue Nile, Quaternary Sci. Rev., 26, 287–299, https://doi.org/10.1016/j.quascirev.2006.11.020, 2007b.

Lamb, H. F., Bates, C. R., Bryant, C. L., Davies, S. J., Huws, D. G., Marshall, M. H., Roberts, H. M., and Toland, H.: 150,000-year palaeoclimate record from northern Ethiopia supports early, multiple dispersals of modern humans from Africa, Scientific Reports, 8, 1077, https://doi.org/10.1038/s41598-018-19601-w, 2018.

Lanckriet, S., Schwenninger, J.-L., Frankl, A., and Nyssen, J.: The Late-Holocene geomorphic history of the Ethiopian Highlands: Supportive evidence from May Tsimble, CATENA, 135, 290–303, https://doi.org/10.1016/j.catena.2015.08.011, 2015.

Leclant, J.: Haoulti-Melazo (1955–1956), Annales d'Ethiopie, 3, 43–82, 1959.

Lüthgens, C., Neuhuber, S., Grupe, S., Payer, T., Peresson, M., and Fiebig, M.: Geochronological investigations using a combination of luminescence and cosmogenic nuclide burial dating of drill cores from the Vienna Basin, Z. Dtsch. Ges. Geowiss., 168, 115–140, https://doi.org/10.1127/zdgg/2017/0081, 2017.

Machado, M.: Geomorphology of the Adwa District, in: Landscapes and Landforms of Ethiopia, World Geomorphological Landscapes, edited by: Billi, P., Springer, Dordrecht, 163–178, https://doi.org/10.1007/978-94-017-8026-1_8, 2015.

Machado, M. J., Pérez-González, A., and Benito, G.: Paleoenvironmental Changes during the Last 4000 yr in the Tigray, Northern Ethiopia, Quaternary Res., 49, 312–321, https://doi.org/10.1006/qres.1998.1965, 1998.

Marshall, M., Lamb, H., Davies, S., Leng, M., Bedaso, Z., Umer, M., and Bryant, C.: Climatic change in northern Ethiopia during the past 17,000 years: A diatom and stable isotope record from Lake Ashenge, Palaeogeogr. Palaeocl., 279, 114–127, https://doi.org/10.1016/j.palaeo.2009.05.003, 2009.

McGuire, C. and Rhodes, E. J.: Downstream MET-IRSL single-grain distributions in the Mojave River, southern California: Testing assumptions of a virtual velocity model, Quat. Geochronol., 30, 239–244, https://doi.org/10.1016/j.quageo.2015.02.004, 2015.

Mejdahl, V.: Thermoluminescence dating: beta attenuation in quartz grains, Archaeometry, 21, 61–72, https://doi.org/10.1111/j.1475-4754.1979.tb00241.x, 1979.

Menn, T. M.: Hawelti-Melazo: the French legacy and recent research – In memoriam Henri de Contenson (1926-2019), Annales d'Éthiopie, 33, 155–166, 2020.

Ménot, G., Pivot, S., Bouloubassi, I., Davtian, N., Hennekam, R., Bosch, D., Ducassou, E., Bard, E., Migeon, S., and Revel, M.: Timing and stepwise transitions of the African Humid Period from geochemical proxies in the Nile deep-sea fan sediments, Quaternary Sci. Rev., 228, 106071, https://doi.org/10.1016/j.quascirev.2019.106071, 2020.

Miall, A. D.: The geology of fluvial deposits: sedimentary facies, basin analysis, and petroleum geology, Springer, Berlin [u.a.], XVI, 582 pp., https://doi.org/10.1007/978-3-662-03237-4, 1996.

Moeyersons, J., Nyssen, J., Poesen, J., Deckers, J., and Haile, M.: Age and backfill/overfill stratigraphy of two tufa dams, Tigray Highlands, Ethiopia: Evidence for Late Pleistocene and Holocene wet conditions, Palaeogeogr. Palaeocl., 230, 165–181, https://doi.org/10.1016/j.palaeo.2005.07.013, 2006.

Nir, N., Knitter, D., Hardt, J., and Schütt, B.: Human movement and gully erosion: Investigating feedback mechanisms using Frequency Ratio and Least Cost Path analysis in Tigray, Ethiopia, PLoS ONE, 16, e0245248, https://doi.org/10.1371/journal.pone.0245248, 2021.

Nir, N., Stahlschmidt, M., Busch, R., Lüthgens, C., Schütt, B., and Hardt, J.: Footpaths: Pedogenic and geomorphological long-term effects of human trampling, CATENA, 215, 106312, https://doi.org/10.1016/j.catena.2022.106312, 2022.

Nyssen, J., Moeyersons, J., Poesen, J., Haile, M., and Deckers, J. A.: Argillipedoturbation and the development of rock fragment covers on Vertisols in the Ethiopian Highlands, BELGEO, 2, 183–194, https://doi.org/10.4000/belgeo.16184, 2002.

Nyssen, J., Poesen, J., Moeyersons, J., Deckers, J., Haile, M., and Lang, A.: Human impact on the environment in the Ethiopian and Eritrean highlands – a state of the art, Earth-Sci. Rev., 64, 273–320, https://doi.org/10.1016/S0012-8252(03)00078-3, 2004.

Nyssen, J., Poesen, J., Moeyersons, J., Deckers, J., and Haile, M.: Processes and rates of rock fragment displacement on cliffs and scree slopes in an *amba* landscape, Ethiopia, Geomorphology, 81, 265–275, https://doi.org/10.1016/j.geomorph.2006.04.021, 2006a.

Nyssen, J., Poesen, J., Veyret-Picot, M., Moeyersons, J., Haile, M., Deckers, J., Dewit, J., Naudts, J., Teka, K., and Govers, G.: Assessment of gully erosion rates through interviews and measurements: a case study from northern Ethiopia, Earth Surf. Proc. Land., 31, 167–185, https://doi.org/10.1002/esp.1317, 2006b.

Nyssen, J., Naudts, J., De Geyndt, K., Haile, M., Poesen, J., Moeyersons, J., and Deckers, J.: Soils and land use in the Tigray highlands (Northern Ethiopia), Land Degrad. Dev., 19, 257–274, https://doi.org/10.1002/ldr.840, 2008.

Nyssen, J., Frankl, A., Haile, M., Hurni, H., Descheemaeker, K., Crummey, D., Ritler, A., Portner, B., Nievergelt, B., Moeyersons, J., Munro, N., Deckers, J., Billi, P., and Poesen, J.: Environmental conditions and human drivers for changes to north Ethiopian mountain landscapes over 145 years, Sci. Total Environ., 485-486, 164–179, https://doi.org/10.1016/j.scitotenv.2014.03.052, 2014.

Pazzaglia, F. J.: 9.22 Fluvial Terraces, in: Treatise on Geomorphology, edited by: Shroder, J. F., Academic Press, San Diego, 379–412, https://doi.org/10.1016/B978-0-12-374739-6.00248-7, 2013.

Phillipson, D. W.: Foundations of an African civilisation: Aksum & the Northern Horn, 1000 BC – AD 1300, 1st edn., Eastern Africa series, Currey, Woodbridge, X, 293 pp., ISBN 9781846158735, 2012.

Pietsch, D. and Machado, M. J.: Colluvial deposits – proxies for climate change and cultural chronology. A case study from Tigray, Ethiopia, Z. Geomorphol, 58, 119–136, https://doi.org/10.1127/0372-8854/2012/S-00114, 2014.

Prescott, J. R. and Hutton, J. T.: Cosmic ray contributions to dose rates for luminescence and ESR dating: Large depths and long-term time variations, Radiat. Meas., 23, 497–500, https://doi.org/10.1016/1350-4487(94)90086-8, 1994.

Prescott, J. R. and Stephan, L. G.: The contribution of cosmic radiation to the environmental dose for thermoluminescence dating. Latitude, altitude and depth dependences, PACT, 6, 17–25, 1982.

Rades, E. F., Fiebig, M., and Lüthgens, C.: Luminescence dating of the Rissian type section in southern Germany as a base for correlation, Quatern. Int., 478, 38–50, https://doi.org/10.1016/j.quaint.2016.07.055, 2018.

Reeves, C. C. (Ed.): Chapter 6 Lacustrine Sediments: Clastic, in: Developments in Sedimentology, Elsevier, 77–85, https://doi.org/10.1016/S0070-4571(08)70829-X, 1968.

Reimer, P. J., Bard, E., Bayliss, A., Beck, J. W., Blackwell, P. G., Ramsey, C. B., Buck, C. E., Cheng, H., Edwards, R. L., Friedrich, M., Grootes, P. M., Guilderson, T. P., Haflidason, H., Hajdas, I., Hatte, C., Heaton, T. J., Hoffmann, D. L., Hogg, A. G., Hughen, K. A., Kaiser, K. F., Kromer, B., Manning, S. W., Niu, M., Reimer, R. W., Richards, D. A., Scott, E. M., Southon, J. R., Staff, R. A., Turney, C. S. M., and van der Plicht, J.: Intcal13 and Marine13 Radiocarbon Age Calibration Curves 0–50,000 Years Cal BP, Radiocarbon, 55, 1869–1887, 2013.

Revel, M., Ducassou, E., Grousset, F. E., Bernasconi, S. M., Migeon, S., Revillon, S., Mascle, J., Murat, A., Zaragosi, S., and Bosch, D.: 100,000 Years of African monsoon variability recorded in sediments of the Nile margin, Quaternary Sci. Rev., 29, 1342–1362, https://doi.org/10.1016/j.quascirev.2010.02.006, 2010.

Rhodes, E. J.: Optically Stimulated Luminescence Dating of Sediments over the Past 200,000 Years, Annu. Rev. Earth Pl. Sc., 39, 461–488, https://doi.org/10.1146/annurev-earth-040610-133425, 2011.

Sloss, C. R., Westaway, K. E., Hua, Q., and Murray-Wallace, C. V.: 14.30 An Introduction to Dating Techniques: A Guide for Geomorphologists, in: Treatise on Geomorphology, edited by: Shroder, J. F., Academic Press, San Diego, 346–369, https://doi.org/10.1016/B978-0-12-374739-6.00399-7, 2013.

Stoops, G.: Guidelines for Analysis and Description of Soil and Regolith Thin Sections, 2nd edn., Soil Science Society of America, Inc., https://doi.org/10.1002/9780891189763, 2020.

Tadesse, T.: Geological Map 1:25000 ND 37-6 Axum, Geological Survey of Ethiopia, 1999.

Thrasher, I. M., Mauz, B., Chiverrell, R. C., and Lang, A.: Luminescence dating of glaciofluvial deposits: A review, Earth-Sci. Rev., 97, 133–146, https://doi.org/10.1016/j.earscirev.2009.09.001, 2009.

Umer, M., Legesse, D., Gasse, F., Bonnefille, R., Lamb, H. F., Leng, M. J., and Lamb, A. A.: Late Quaternary climate changes in the Horn of Africa, in: Past Climate Variability through Europe and Africa, edited by: Battarbee, R. W., Gasse, F., and Stickley, C. E., Springer Netherlands, Dordrecht, 159–180, https://doi.org/10.1007/978-1-4020-2121-3_9, 2004.

Verrecchia, E. P. and Trombino, L.: Pedogenic Features, in: A Visual Atlas for Soil Micromorphologists, Springer International Publishing, Cham, 93–133, https://doi.org/10.1007/978-3-030-67806-7_4, 2021.

Wallinga, J., Murray, A., and Wintle, A.: The single-aliquot regenerative-dose (SAR) protocol applied to coarse-grain feldspar, Radiat. Meas., 32, 529–533, https://doi.org/10.1016/S1350-4487(00)00091-3, 2000.

Williams, M., Talbot, M., Aharon, P., Abdl Salaam, Y., Williams, F., and Inge Brendeland, K.: Abrupt return of the summer monsoon 15,000 years ago: new supporting evidence from the lower White Nile valley and Lake Albert, Quaternary Sci. Rev., 25, 2651–2665, https://doi.org/10.1016/j.quascirev.2005.07.019, 2006.

Zgłobicki, W., Poesen, J., De Geeter, S., Boardman, J., Gawrysiak, L., Golosov, V., Ionita, I., Niacsu, L., Rodzik, J., Stankoviansky, M., and Stolz, C.: Sunken lanes – Development and functions in landscapes, Earth-Sci. Rev., 221, 103757, https://doi.org/10.1016/j.earscirev.2021.103757, 2021.

E&G Quaternary Sci. J., 72, 1–21, 2023
https://doi.org/10.5194/egqsj-72-1-2023

Open Access E&G Quaternary Science Journal

Research article

Multi-method study of the Middle Pleistocene loess–palaeosol sequence of Köndringen, SW Germany

Lea Schwahn[1], **Tabea Schulze**[1], **Alexander Fülling**[1], **Christian Zeeden**[2], **Frank Preusser**[1], and **Tobias Sprafke**[3,4]

[1]Institute of Earth and Environmental Sciences, University of Freiburg, Freiburg, Germany
[2]Rock Physics and Borehole Geophysics, Leibniz Institute for Applied Geophysics, Hanover, Germany
[3]Center of Competence for Soils, BFH-HAFL, Zollikofen, Switzerland
[4]Institute of Geography, University of Bern, Bern, Switzerland

Correspondence: Frank Preusser (frank.preusser@geologie.uni-freiburg.de)

Relevant dates: Received: 25 July 2022 – Revised: 8 December 2022 – Accepted: 12 December 2022 – Published: 20 January 2023

How to cite: Schwahn, L., Schulze, T., Fülling, A., Zeeden, C., Preusser, F., and Sprafke, T.: Multi-method study of the Middle Pleistocene loess–palaeosol sequence of Köndringen, SW Germany, E&G Quaternary Sci. J., 72, 1–21, https://doi.org/10.5194/egqsj-72-1-2023, 2023.

Abstract: Loess–palaeosol sequences (LPSs) remain poorly investigated in the southern part of the Upper Rhine Graben but represent an important element to understand the environmental context controlling sediment dynamics in the area. A multi-method approach applied to the LPS at Köndringen reveals that its formation occurred during several glacial–interglacial cycles. Field observations, as well as colour, grain size, magnetic susceptibility, organic carbon, and carbonate content measured in three profiles at 5 cm resolution, provide detailed stratigraphical information. Only minor parts of the LPS are made up of loess sediment, whereas the major parts are polygenetic palaeosols and pedosediments of varying development that are partly intersected, testifying to a complex local geomorphic evolution. The geochronological framework is based on 10 cm resolution infrared-stimulated luminescence (IRSL) screening combined with 18 multi-elevated-temperature post-IR IRSL ages. The luminescence ages indicate that two polygenetic, truncated Luvisols formed during marine isotope stages (MISs) 9(–7?) and MIS 5e, whereas unaltered loess units correspond to the last glacial (MISs 5d–2) and MIS 8. The channel-like structure containing the two truncated Luvisols cuts into >2 m thick pedosediments apparently deposited during MIS 12. At the bottom of the LPS, a horizon with massive carbonate concretions (loess dolls) occurs, which may correspond to at least one older interglacial.

Kurzfassung: Löss-Paläoboden-Sequenzen (LPS) sind im südlichen Teil des Oberrheingrabens bisher nur unzureichend untersucht, obwohl sie ein wichtiges Element für das Verständnis der Umweltbedingungen darstellen, welche die Sedimentdynamik in diesem Gebiet gesteuert haben. Die Anwendung eines Multi-Methoden-Ansatzes auf die LPS in Köndringen enthüllt, dass diese während mehrerer glazial-interglazialer Zyklen entstanden ist. Die Feldansprache dreier Profile und Laboranalysen in 5 cm Auflösung (Farbe, Korngröße, magnetische Suszeptibilität, organischer Kohlenstoff- und Karbonatgehalt), geben detaillierte Informationen über deren stratigraphischen Aufbau. Nur geringe Teile des LPS bestehen aus Löß, der teilweise durch Hangabschwemmungen geschichtet ist, während der größte Teil aus polygenetischen Paläoböden und Pedosedimenten unterschiedlicher Ausprägung besteht, die sich teilweise überschneiden und von einer komplexen lokalen geomorphologischen Entwicklung zeugen. Der geochronologische Rahmen basiert auf Screening mittels Infrarot-Stimulierter Lumineszenz (IRSL) mit einer Auflösung von 10 cm in Kombination mit 18 Altern, die mit dem Multi-Elevated-Temperature post-IR IRSL Verfahren bestimmt wurden. Die Lumineszenzalter deuten darauf hin, dass die beiden polygenetischen, gekappten Luvisole während der marinen Isotopenstadien (MIS) 9(–7?) und MIS 5e entstanden sind, während die Lösseinheiten dem letzten Glazial (MIS 5d-2) und MIS 8 entsprechen. Die rinnenartige Struktur, welche die beiden gekappten Luvisole enthält, schneidet in > 2 m mächtige Pedosedimente ein, die offenbar während MIS 12 abgelagert wurden. An der Basis des LPS findet sich ein Horizont mit großen Karbonatkonkretionen (Lößkindl), die mindestens einem älteren Interglazial entsprechen könnten.

1 Introduction

While the Late Pleistocene climate and environmental history of Central Europe is reasonably well understood (e.g. Preusser, 2004; Heiri et al., 2014; Stephan, 2014; Lehmkuhl et al., 2016; Stojakowits et al., 2021), the timing and extent of Middle Pleistocene glaciations, as well as the number of and the environmental conditions during interglacial and interstadial phases, are controversially discussed (e.g. Kleinmann et al., 2011; Stebich et al., 2020; Tucci et al., 2021). This is mainly related to difficulties in establishing independent and robust chronological frameworks and applies in particular to the northern Alpine foreland (van Husen and Reitner, 2011; Preusser et al., 2011). In fact, Middle Pleistocene pollen records close to the Alps and in the Upper Rhine Graben (URG), a major sink of Alpine debris during the Quaternary, are rare and largely fragmentary (Preusser et al., 2005; Knipping, 2008; Gabriel et al., 2013).

Loess–palaeosol sequences (LPSs) are frequently found in the area between the realms of the Alpine and Scandinavian glaciations, yet most work during the past decades has focussed on the Late Pleistocene (e.g. Meszner et al., 2013; Lehmkuhl et al., 2016; Moine et al., 2017; Zens et al., 2018; Fischer et al., 2021; Rahimzadeh et al., 2021; Zöller et al., 2022; Schulze et al., 2022) with few sites covering the Middle Pleistocene (e.g. Terhorst, 2013; Sprafke, 2016). Some Middle Pleistocene sites have been dated using thermoluminescence (TL; e.g. Zöller et al., 1988; Frechen, 1992); however, this technique does not correspond to the present state of knowledge, and the reliability of the published ages remains uncertain. Relative chronostratigraphy (pedostratigraphy) is based on a priori assumptions and may give biased results. An example is the LPS Wels-Aschet, where Terhorst (2007) suggests a correlation of five fossil palaeosols with marine isotope stages (MISs) 5, 7, 9, 11, and 13–15 (cf. Lisiecki and Raymo, 2005), with the underlying assumption that Luvisols represent interglacial forest ecosystems that have occurred every ca. 100 000 years in Central Europe (Bibus, 2002). While this chronological assignment was apparently supported by palaeomagnetic excursions observed in this LPS (Scholger and Terhorst, 2013), Preusser and Fiebig (2009) discuss a correlation of three of the fossil Luvisols with the three pronounced warm peaks of MIS 7, seemingly supported by infrared-stimulated luminescence (IRSL) dating. This would result in a different correlation with the MIS record as suggested by Terhorst (2007). However, it is unclear if the IRSL ages could be underestimated due to signal instability and saturation effects.

Buylaert et al. (2009) have introduced an approach that allows the dating range of luminescence to be extended, erasing the unstable IRSL component during a first measurement, followed by collecting a more stable signal during subsequent stimulation at an elevated temperature (see review by Zhang and Li, 2020). This post-IR IRSL (pIR) approach was first applied to the LPS from Austria by Thiel et al. (2011a, b, c) and enabled the dating range to be extended back to about 300 ka. Other studies report reliable ages of up to 700 ka (Zander and Hilgers, 2013; Faershtein et al., 2019). A modified version of the pIR approach was suggested by Li and Li (2011) in which IRSL is subsequently stimulated at increasingly higher temperatures with 50 °C increments. The multi-elevated-temperature (MET) pIR (MET-pIR) approach allows signals with increasing stability at higher temperatures to be analysed but at the cost of bleachability of the signal (Kars et al., 2014). Furthermore, higher stimulation temperatures may also induce changes in sensitivity of the signal that may result in incorrect estimates (e.g. Zhang, 2018).

This article is a contribution towards a broader initiative that aims at improving the understanding of the factors controlling deposition in the URG geosystem during the Quaternary. Besides the effects of local tectonics, changes in climate had a major impact on deposition (Weidenfeller and Knipping, 2009; Gabriel et al., 2013; Preusser et al., 2021), in particular linked to the reoccurring glaciations of the Swiss Alps (Preusser et al., 2011), the Black Forest (Hofmann et al., 2020), and the Vosges (Mercier and Jeser, 2004). LPSs reflect changes in past environmental conditions by shifts between loess deposition, soil formation, and phases of erosion and reworking (Sprafke et al., 2014). In the URG, the accumulation of loess is assigned to cold periods (Hädrich, 1975), when the Rhine and its tributaries were braided rivers, with high debris supply due to increased frost weathering and glacial erosion and high transport potential due to meltwater discharge. During periods of a warm and humid climate (as today), the Rhine had an anastomosing to meandering character with limited debris transport and practically absent aeolian sediment activity due to widespread vegetation cover (e.g. Andres et al., 2001; Houben, 2003; Erkens et al., 2009; Kock et al., 2009). These two environmental modes can be termed glacial and temperate conditions (the latter including both interglacials and interstadials). Less well understood are the environmental conditions responsible for the phases of erosion and reworking that are observed in many Central European LPSs (Lehmkuhl et al., 2016; Sprafke, 2016; Zöller et al., 2022). Presumably these are related to the presence of flowing water (e.g. sheet wash), but deflation may also play an important role. In both cases, vegetation cover must be very limited.

Despite the prominent loess cover, LPSs from the southern part of the URG (Fig. 1) have seen very limited attention so far, with the most recent systematic studies reaching back to the 1980s (Bronger, 1969, 1970; Guenther, 1961, 1987; Hädrich, 1980; Hädrich and Lamparski, 1984; Zöller et al., 1988). Parallel to the present study, Schulze et al. (2022) investigated the Late Pleistocene site of Bahlingen-Schönenberg using a similar approach as applied here. The site investigated here is situated in the village of Köndringen at the foothills of the Black Forest (Fig. 1) and comprises a complicated succession of discontinuous units, including partly layered loess sediments (sensu Sprafke and Obreht, 2016), palaeosols, and pedosediments, as well as horizons of large carbonate concretions. These features indicate that several glacial–interglacial cycles are recorded in this outcrop but with a major contribution of slope processes leading to erosion and reworking. As a first step to unravel the complex Middle to Late Pleistocene history of the LPS at Köndringen, we focus on refining tools to derive robust stratigraphies and reliable chronologies in a easily accessible part of the outcrop.

Our multi-method approach combines a qualitative field description of the outcrop with high-resolution (5 cm) sediment and soil analyses (grain size, colour, magnetic susceptibility, organic matter, and carbonate content). A particular focus is on establishing a chronological framework by applying the MET-pIR dating approach. In addition, the potential of high-resolution (10 cm) IRSL screening is tested (e.g. Roberts et al., 2009; May et al., 2018), as this simplified procedure with regard to preparation and measurement may provide quick and low-cost semi-quantitative age information. Based on a discussion of the pedosedimentary evolution within the chronological framework, comparisons are drawn to Central European loess records of the Middle Pleistocene, and persistent gaps of knowledge and possible solutions are identified.

2 Study area

Loess deposits in the southern part of the URG are mainly found in hilly landscapes, mostly superimposing pre-Pleistocene layers with varying thickness (Keßler and Laiber, 1991). The LPS of Köndringen (48.13915° N, 7.813025° E; 220 m above sea level, a.s.l.) is located in the Black Forest foothills (Emmendinger Vorbergzone), which represent fault blocks along the eastern fault system of the URG (Fig. 1). The investigated site is situated next to a small triangular hill (Ottenberg), almost 1 km north-east of the river Elz and about 16 km E of the river Rhine. To the west of the main fault, several minor faults divide the foothills into two parts, the eastern "loess hill zone" mainly underlain by limestone and the western part where sandstone also is present; both regions are covered by loess sediment of varying thickness with up to 10–15 m (Hädrich, 1965; Hädrich and Stahr, 2001). According to heavy mineral analyses the source of the loess must have been the floodplain of the Upper Rhine (Keßler and Laiber, 1991), with the thickest accumulation of loess occurring on the adjacent foothills of the Black Forest and on the nearby Kaiserstuhl (hills of volcanic origin in the centre of the URG).

A comprehensive review of LPS in the study region was provided by Guenther (1987), including a schematic sketch showing the stratigraphic subdivision of key sites that all include several interstadial and interglacial palaeosols. According to this study, the most complex LPSs of the region are located in the wider surroundings of Köndringen and comprise up to seven loess units and six well-developed palaeosols. Unfortunately, the majority of outcrops are not easily accessible anymore. The only study including geochronological methods in the region until recently (Zöller et al., 1988) applied TL dating to eight samples taken from the LPS Riegel (Fig. 1b). While TL dating was at an early stage of development at that time, ages of 153 ± 14 and 183 ± 17 ka for loess from below what was interpreted as the Last Interglacial soil (MIS 5e; 115–130 ka; Lisiecki and Raymo, 2005) agree with the expected time frame. Middle Pleistocene ages of the four older palaeosols at Riegel are confirmed by TL ages of 259 ± 26, 254 ± 24, 273 ± 23, and > 390 ka for lower parts of the sequence. These findings indicate that regional LPSs cover more than four glacial–interglacial cycles, motivating an approach with state-of-the-art methods to the easily accessible but as yet unstudied LPS Köndringen.

3 Materials and methods

3.1 Profile description and sampling

The three investigated profiles are located at the north-eastern end of a 400 m long outcrop along Landecker Weg in Köndringen, where a complex succession of partly layered loess sediments of varying thickness intercalated by partly discontinuous pedocomplexes and loess doll horizons are ex-

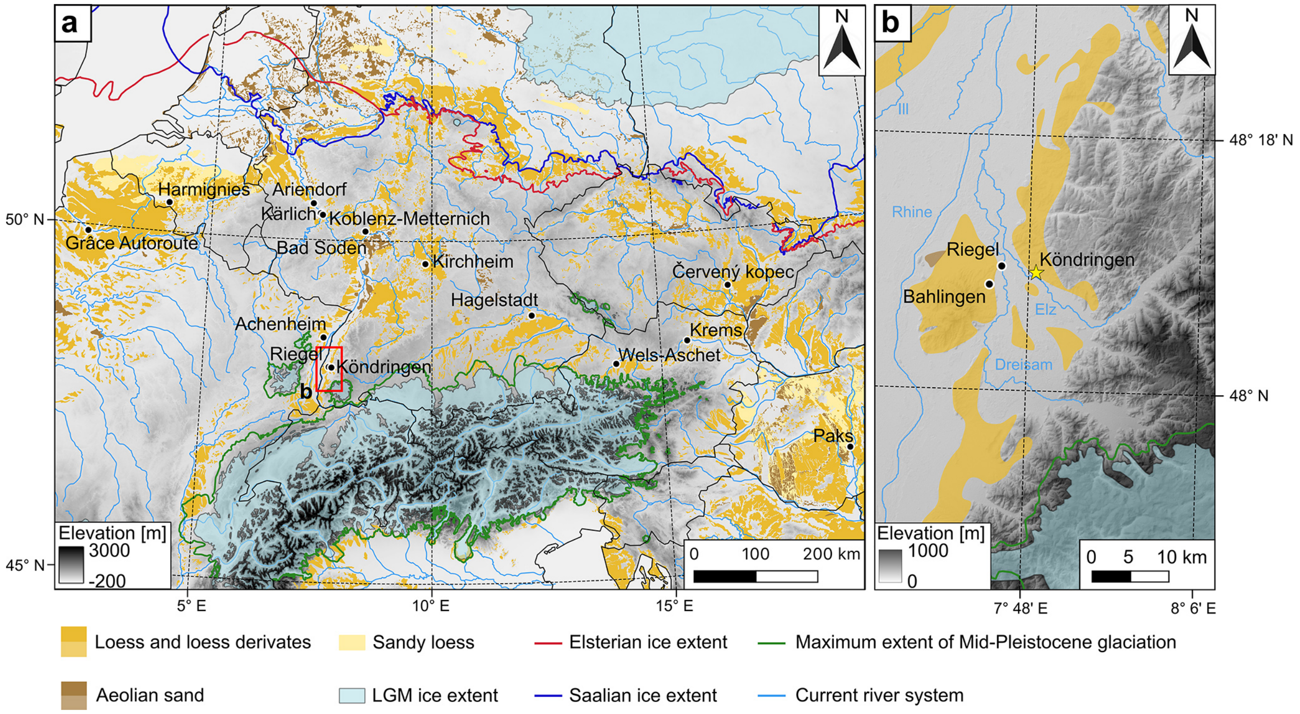

Figure 1. **(a)** Position of the study area in the Central European loess belt with the location of the mainly Middle Pleistocene LPS mentioned in the text: Grâce Autoroute (Antoine et al., 2021), Harmignies (Haesaerts et al., 2019), Ariendorf (Haesaerts et al., 2019), Kärlich (Boenigk and Frechen, 1998), Koblenz-Metternich (Boenigk and Frechen, 2001), Bad Soden (Semmel and Fromm, 1976), Kirchheim (Rösner, 1990), Achenheim (Junkmanns, 1995), Hagelstadt (Strunk, 1990), Wels-Aschet (Terhorst, 2007; Preusser and Fiebig, 2009; Scholger and Terhorst, 2013), Krems shooting range (Sprafke, 2016), Červený kopec (Kukla, 1977), and Paks (Thiel et al., 2014). **(b)** The investigated profile is situated in the foothills of the Black Forest in the village of Köndringen (yellow star). The digital elevation model data were provided by EEA (2016) and processed with QGIS 3.26. Distribution of aeolian sediments after Lehmkuhl et al. (2021), ice extent after Ehlers et al. (2011), river system from http://naturalearthdata.com (last access: 24 October 2022), and country boundary lines from http://landkartenindex.de (last access: 24 October 2022).

posed. The term loess sediments includes both loess and loess-like sediments (Sprafke and Obreht, 2016). Large parts of the outcrop are covered by a patina, vegetation, or debris, and the site remains protected from spring to autumn due to bird colonies nesting in the cliffs. To capture the main elements of stratigraphy in the most accessible part of the outcrop and to keep disturbance to the minimum, three profiles (KÖN-A, KÖN-B, KÖN-C; Fig. 2) of about 70 cm width were prepared by removing ca. 20 cm of surficial material with spades and scratchers. Colour, structural differences, and specific features were documented qualitatively for a general profile description as the basis for the interpretation of the multi-method dataset. From each profile, samples for determining organic matter and carbonate content, magnetic susceptibility, grain size analysis, and colour measurements were taken at 5 cm resolution as a continuous column (Antoine et al., 2009). Pedological horizon designations based on the qualitative field description and laboratory data (mainly colour data) follow FAO (2006) in the way suggested by Sprafke (2016). Samples for IRSL screening were taken every 10 cm using opaque plastic tubes with a length of 5 cm and a diameter of ∼ 3 cm, hammered into the freshly cleaned exposure. For luminescence dating, 18 samples were collected in metal tubes with a length of 10–15 cm, hammered into the cleaned profile.

3.2 Colour measurements

Colour measurements were done with a ColorLite sph850 spectrophotometer at the University of Bern that, which allows wavelengths from 400–700 nm to be measured with a spectral resolution of 3.5 nm (Sprafke, 2016). Samples were air-dried and sieved to fine earth (< 2 mm) and measured in a circular field with a diameter of 3.5 mm. The observer angle was 10°, and the light source (six LEDs) corresponds to D65 light. The measuring head was pushed into the loose sample material until it was completely sealed from daylight. Measurements were done at three different sample positions and the results averaged. After stirring the sample, this procedure was repeated, leading to duplicate results. The spectrophotometer was calibrated using a white standard disc after every 10th measurement. The acquired data (various colour variables, remission spectra) were analysed using Microsoft Ex-

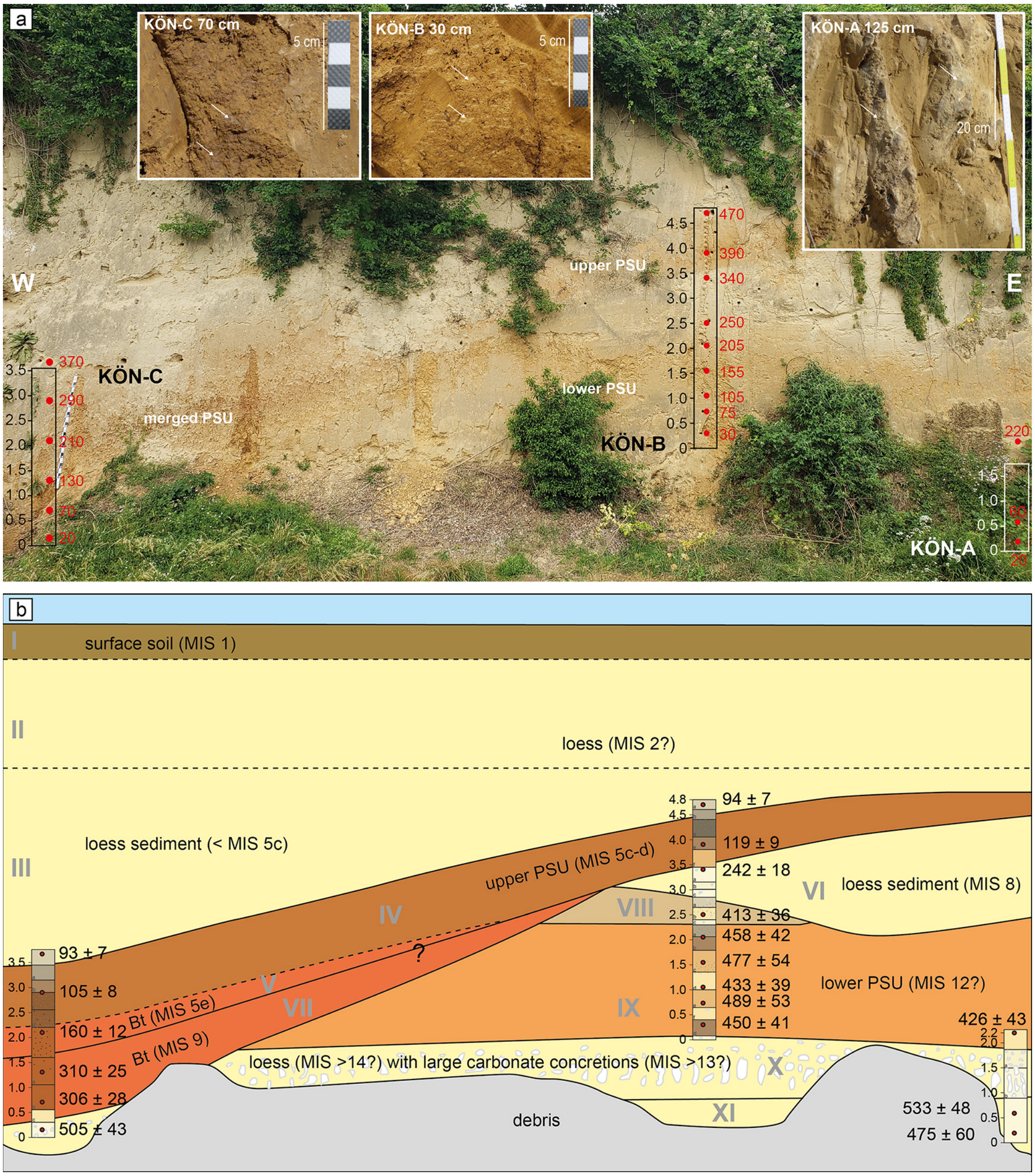

Figure 2. **(a)** Outcrop photo with the two pedosedimentary units (PSUs) merging into one towards the left hand side and location of three studied profiles KÖN-A (overgrown at moment of photography), KÖN-B, and KÖN-C, with the positions of luminescence samples and their numbers (in red). Rectangles mark the position of the sampling columns. The insets show (from left to right, marked with white arrows) clay coatings in a large crack of weakly developed subsoil of profile KÖN-C (at 70 cm), lenticular structure with silt–loam separation as a result of frost action in the lower part of KÖN-B (at 30 cm), and massive carbonate concretions exposed in profile KÖN-A (at 125 cm). **(b)** The stratigraphic units I–XI shown in the outcrop sketch consider chronostratigraphic relations (MIS after Lisiecki and Raymo, 2005) based on luminescence ages (in black, with uncertainties). Detailed profile sketches are given in Fig. 4.

cel© with the software ColorDaTra 1.0.181.5912. Mean values for each sample were calculated and visualised as real colours based on RGB variables, including two-step RGB tuning, useful to determine subtle colour variations in weakly differentiated LPSs (Sprafke et al., 2020). The L^*-value of the CIELAB colour space represents variations in lightness, whereas a^* corresponds to the intensity of red versus green (> 0 or < 0, respectively) and b^* to the intensity of yellow versus blue (> 0 or < 0, respectively) (Viscarra Rossel et al., 2006).

3.3 Sediment and soil analyses

Grain sizes distributions were measured using a Malvern Mastersizer 3000 laser diffraction spectrometry device (Malvern Panalytical). Samples were dried at 105 °C for at least 12 h and sieved through a 1 mm sieve (upper effective limit of the device), and 1–2 g was dispersed for 12 h in 50 mL sodium hexametaphosphate (33 g Na_6 P_6O_{18} and 7 g Na_2CO_3 dissolved in 1 L of distilled water). A similar protocol as used by Abdulkarim et al. (2021) was applied with a particle refractive index of 1.53, a dispersant refractive index of 1.33, an absorption index of 0.01, a stirrer speed of 1660 rpm, and with the ultrasonication off. For every sample five measurements were carried out, and average values were calculated using MATLAB R2021a. The grain size index (GSI: [%20–63 µm] / [% < 20 µm]) was calculated according to Antoine et al. (2009). Clay contents determined by laser diffraction spectrometry for samples from KÖN oscillate around 2 %, which is in disagreement to field-testing trained against classical sedimentation-based methods. Therefore, we assume that the joint clay to fine silt fraction (< 6.3 µm) roughly corresponds to the clay fraction as determined by the classical sieve–pipette analysis. This is in accordance with a large number of studies that confirm a marked difference between the laser diffraction spectrometry device and traditional sedimentation-based methods and suggest the use of alternative boundaries between 4 and 8 µm (mainly depending on soil mineralogy) to translate into "pipette clay" ($clay_p$; e.g. Konert and Vandenberghe, 1997; Antoine et al., 2009).

For the determination of organic matter (C_{org}) and carbonate contents, samples were dried at 105 °C for > 12 h and then pestled with a mortar and sieved to < 2 mm, and about 1 g was used for analyses. In the first cycle, samples were placed in a Nabertherm muffle at 550 °C for 5 h for the determination of organic carbon content (Heiri et al., 2001). Loss on ignition (LOI) was calculated by dividing the dry weight by the weight after the 550 °C burning cycle. However, this value represents double the real organic carbon content (Meyers and Lallier-Verges, 1999), and consequently all values reported have been corrected for this. As C_{org} contents of loess are usually not higher than 0.5 % (Fischer et al., 2021), we must assume that lost interlayer water of clay minerals significantly contributes to the LOI-determined signal. Carbonate contents were subsequently determined using the same material after heating for 3 h at 950 °C (Heiri et al., 2001).

For magnetic susceptibility (weight normalised; χ) measurements, carried out at the Leibniz Institute for Applied Geophysics in Grubenhagen, samples were homogenised and placed in non-magnetic plastic boxes of 6.4 cm^3 so that the material was fixed and could not move. The χ was measured in alternating fields of 505 and 5050 Hz with 400 $A\,m^{-1}$ using a MAGNON VFSM, providing both low-field χ and frequency dependency of the χ. The χ is here given as weight-normalised, taking weights of samples and boxes into account. Temperature-dependent χ was measured following Zeeden et al. (2021) in an argon atmosphere for nine depth intervals (samples: KÖN-A_20–25, KÖN-A_75–80, KÖN-A_140–145, KÖN-B_85–90, KÖN-B_350–355, KÖN-C_75–80, KÖN-C_135–140, KÖN-C_225–230, KÖN-C_280–285) using an AGICO CS3 high-temperature furnace.

3.4 Luminescence screening

In the red-light laboratory, the outer ca. 1 cm of the sample material from the light-contaminated ends of the sampling tubes was discarded. Samples were then dried at 50 °C for at least 24 h and gently pestled in a mortar. Part of the material gained this way was fixed on small steel sample discs that were previously coated with a thin layer of silicon oil (6 mm stamp) so that the sample material would stick to the surface during measurement. For each sample, three subsamples were generated and measured on a Lexsyg Smart device (Freiberg Instruments; Richter et al., 2015) with the detection window centred at 410 nm. The measurement protocol comprised the IRSL stimulation of the natural signal (Ln) and that induced by laboratory irradiation (Tn, ca. 22 Gy), both after heating to 250 °C (preheat) and using a stimulation at 50 °C (Table S1 in the Supplement). The ratio Ln / Tn was calculated based on the IRSL emission recorded during the first 20 s of stimulation after subtracting the last 20 s as background.

3.5 Luminescence dating

The sediment from the outer ends of the aluminium tubes was scraped off and used for determining the activity of dose-rate-relevant elements. The remaining material was dried and subsequently treated with hydrochloric acid (20 %) and hydrogen peroxide (30 %) to remove carbonates and organic matter, respectively, each time, followed by rinsing with deionised water. Due to the low sand content of the sediment, the polymineral fine-grain fraction 4–11 µm was separated for equivalent dose (D_e) determination using Atterberg cylinders and centrifuging. The isolated fine-grain material was placed on stainless steel discs by pipetting from a sediment solution in acetone. For measuring the dose rate, samples were dried, homogenised, and subsequently transferred into flat plastic containers (7.5 × 3 cm). After storage for at least 30 d to allow for the establishment of radioactive equilibrium, the activity of uranium, thorium, and potassium were measured using high-resolution gamma ray spectrometry (Ortec high-purity germanium detector).

Measurements for the determination of D_e were carried out using a Freiberg Instruments Lexsyg Smart device (Richter et al., 2015) with an integrated beta source (max activity 7.1 GBq), delivering ca. 0.645 $Gy\,s^{-1}$ to the sample material in the given geometry (calibration with Freiberg Instruments fine-grain quartz). The MET-pIR protocol originally suggested by Li and Li (2011; see review by Zhang and Li, 2020) was applied using five IRSL steps at progressively higher stimulation temperatures from 50 to 250 °C with a gradual increase of 50 °C (Table S2). The reasoning behind this procedure is that the stability of the signal increases with temperature, through this eliminating the effect of fading that may lead to the underestimation of feldspar IRSL if not corrected for. Li and Li (2011) report stable signals not affected by fading for stimulation temperatures of 200 and 250 °C. However, it is also known that the time to reset pIR signals during sediment transport requires much longer time periods compared to quartz optically stimulated luminescence (OSL). While the exact time depends on factors such as the transport mechanism and prior dose (Smedley et al., 2015), it has been shown for fluvial settings that pIR ages might significantly overestimate the known age of a sediment (Lowick et al., 2012).

Five to six aliquots were measured for each sample, and the integral 0–15 s of signal readout was used for D_e determination after subtracting the last 10 s as background (Fig. 3a). Dose response curves were fitted using the sum of two exponential growth curves (Fig. 3b). Mean D_e was calculated using the Central Age Model (CAM) of Galbraith et al. (1999; Table S3). A dose recovery test was carried out for sample KÖN-A-20, which revealed recovery ratios within 10 % of unity for all stimulation temperatures but 250 °C. For the latter, the recovery ratio was at 150 %. Problems with high-temperature pIR measurements have also been reported by Li et al. (2018) and Preusser et al. (2021) for fluvial samples from the URG, which are likely related to trap-specific changes in electron trapping probability (see Zhang, 2018; Qin et al., 2018). For some of the pIR-250 measurements aliquots had to be rejected due to saturation effects having been reached, similar to observations by Preusser et al. (2021). All other aliquots passed the usual selection criteria (recycling ratio, recuperation, signal intensity; Wintle and Murray, 2006). Dose rates (Table S4) and ages (Table 1) were calculated using ADELEv2017 software (Degering and Degering, 2020), assuming an a-value of 0.08 ± 0.02 (Rees-Jones, 1995) and an internal potassium content of 12.5 ± 0.5 % (Huntley and Baril, 1997). The water content of all samples was measured after sampling, revealing values between 1.5 % and 14 %, with the majority of values above 10 %. However, since the sediment appeared rather dried out near the surface of the exposure, it is expected that these values significantly underestimate the average sediment moisture during burial. For the dose rate calculations, an average water content of 20 ± 5 % was used. Cosmic dose rates were estimated depending on the geographic position (48.13915° N, 7.813025° E), the altitude (216 m a.s.l.), and the sampling depth following Prescott and Hutton (1994). All ages are reported as kiloyears (ka) before the year of sampling and measurement (2021 CE).

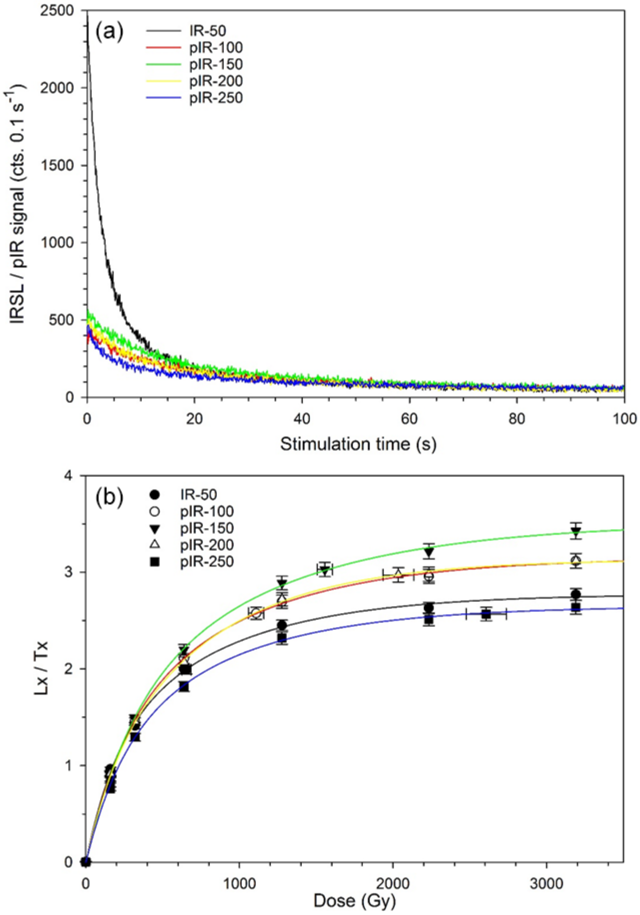

Figure 3. **(a)** Examples of IRSL decay curves (natural signal) and **(b)** dose response curves for different stimulation temperatures (sample KÖN-C-20; see panel **a** for colour codes).

4 Results

4.1 Profile description

The investigated part of the LPS Köndringen consists of loess and two intercalated brownish pedosedimentary units (PSUs). The ca. 1 m thick upper PSU is inclined to the west, cutting into the underlying loess and merging with the horizontally oriented ca. 2 m thick lower PSU (Fig. 2a). The investigated profiles complement each other to a stratigraphy of 11 units (I–XI; Fig. 2b). Designations of the units V to VIII take into account chronostratigraphic relations revealed by luminescence dating (Fig. 4). Profile KÖN-A comprises the lowermost part of the lower PSU (Unit IX) and a ca. 80 cm thick horizon with thick loess dolls (Unit X; Fig. 2), underlain by calcareous loess (Unit XI). The lower PSU (Unit IX) is exposed in KÖN-B and contains weakly aggregated brownish pedosediments, partly with visible layers and frost features (Fig. 2). In the lowermost and the uppermost parts (units IXg and IXa-c) slightly advanced pedogenic aggregation and pigmentation (pale brown) are visi-

Table 1. Ages determined at 50, 100, 150, 200, and 250 °C using the MET-pIR protocol are shown in kiloyears (ka) before the year of sampling and measurement (2021 CE).

Sample	Depth (cm)	IR-50 (ka)	pIR-100 (ka)	pIR-150 (ka)	pIR-200 (ka)	pIR-250 (ka)
KÖN-C-370	330	53 ± 4	72 ± 5	86 ± 6	93 ± 7	97 ± 7
KÖN-C-290	410	64 ± 5	83 ± 6	97 ± 8	105 ± 8	115 ± 9
KÖN-C-210	490	85 ± 6	120 ± 9	147 ± 11	160 ± 12	180 ± 14
KÖN-C-130	570	122 ± 9	206 ± 16	261 ± 20	310 ± 25	441 ± 63
KÖN-C-70	630	131 ± 9	240 ± 24	314 ± 27	306 ± 28	391 ± 56
KÖN-C-20	680	179 ± 13	310 ± 24	430 ± 34	505 ± 43	441 ± 63
KÖN-B-470	230	53 ± 4	69 ± 5	84 ± 6	94 ± 7	97 ± 7
KÖN-B-390	310	69 ± 5	91 ± 8	111 ± 8	119 ± 9	133 ± 10
KÖN-B-340	360	116 ± 8	170 ± 13	215 ± 16	242 ± 18	267 ± 21
KÖN-B-250	450	160 ± 12	265 ± 21	344 ± 28	413 ± 36	469 ± 50
KÖN-B-205	495	166 ± 13	284 ± 22	373 ± 30	458 ± 42	463 ± 50
KÖN-B-155	545	159 ± 12	294 ± 25	431 ± 40	477 ± 54	457 ± 116
KÖN-B-105	595	148 ± 11	263 ± 20	350 ± 28	433 ± 39	476 ± 57
KÖN-B-75	625	162 ± 12	291 ± 25	388 ± 33	489 ± 53	487 ± 69
KÖN-B-30	670	151 ± 11	282 ± 22	394 ± 32	450 ± 41	529 ± 111
KÖN-A-220	580	135 ± 10	293 ± 24	370 ± 30	426 ± 43	603 ± 106
KÖN-A-60	740	186 ± 14	363 ± 34	466 ± 39	533 ± 48	746 ± 87
KÖN-A-20	780	197 ± 15	353 ± 30	452 ± 38	475 ± 60	581 ± 86

ble. Superimposed is brownish loess with a weak pedogenic structure (Unit VIII) and highly calcareous loess (Unit VI). A clear boundary separates Unit VI from Unit IV, which can be subdivided into a weakly aggregated brown lower part (IVf), grading into a weakly to moderately aggregated greyish-brown upper part (IVa), with a gradual transition into overlying loess sediments (Unit III). Profile KÖN-C starts in the lowermost loess with carbonate concretions (Unit X), ends in the uppermost loess (Unit III), and contains the ca. 3 m thick merged PSU, which is well-aggregated and contains clay coatings in most parts. In Unit VII, clay coatings are mainly found along larger aggregate surfaces and in walls of larger pores, whereas the matrix is mainly yellowish-brown (Fig. 2), grading into more intense brown in the upper part (VIIa). By contrast, Unit V is reddish-brown throughout, with numerous clay coatings and some Mn oxides on ped surfaces. Contrary to KÖN-B, Unit IV in KÖN-C is more homogenous, with moderate aggregation and incipient clay coatings in the lower half (IVc–d). The transition into the overlying greyish, partly layered loess (Unit III) is sharp. Units II and I are not investigated due to accessibility problems and correspond to the uppermost, apparently homogenous loess and the present-day surface soil, respectively.

4.2 Colour

Measured colours allow for a rather robust separation of the sequence into subunits (labelled a, b, etc.) shown in Fig. 4. Colour variations in KÖN-A are minimal there is a slight increase in brownish hue in the uppermost part (Unit Xa), indicated by slightly increasing red (a^*) and yellow (b^*) colour components. The lower PSU in KÖN-B is subdivided into light brown to brown units. The incipient palaeosols in the bottom and upper part are darker (lower L^*) and more brownish (higher a^* and b^*), respectively. The uppermost unit (IXa) is again darker, with a less brownish component. From Unit VIII to VI the a^*- and b^*-values strongly decrease, along with an increase in lightness (L^*). Noticeable are a slightly dark (VIIIa) horizon and another slightly more brownish horizon (VIb). The lower half of the upper PSU has high a^*- and b^*-values, whereas in the upper part, the yellowish component decreases rapidly, and darkness stays high, resulting in a greyish-brown colour. In the merged PSU of KÖN-C L^* remains low, whereas a^* and b^* show a comparable (e.g. common increase in the lower part of VII) but partly deviating pattern. We highlight the peak of a^* in Unit V, whereas the peaks of b^* are shifted to the transition into Unit VII. In Unit IV of profile KÖN-C there are little changes in colour, different to profile KÖN-B, the unit of which is two parts.

4.3 Grain size composition

The texture of the LPS Köndringen is largely dominated by medium to coarse silt (Fig. 4). The loess between the two PSUs of KÖN-B (Unit VI) exhibits a clear mode at the medium–coarse silt boundary (20 µm). By contrast, the mode in the merged PSU (units V and VII) oscillates within the medium silt fraction and is less pronounced due to a wider distribution of grain sizes, specifically towards the finer fractions. The upper PSU in KÖN-B has a granulometry quite similar to the underlying loess, whereas the lower PSU has a

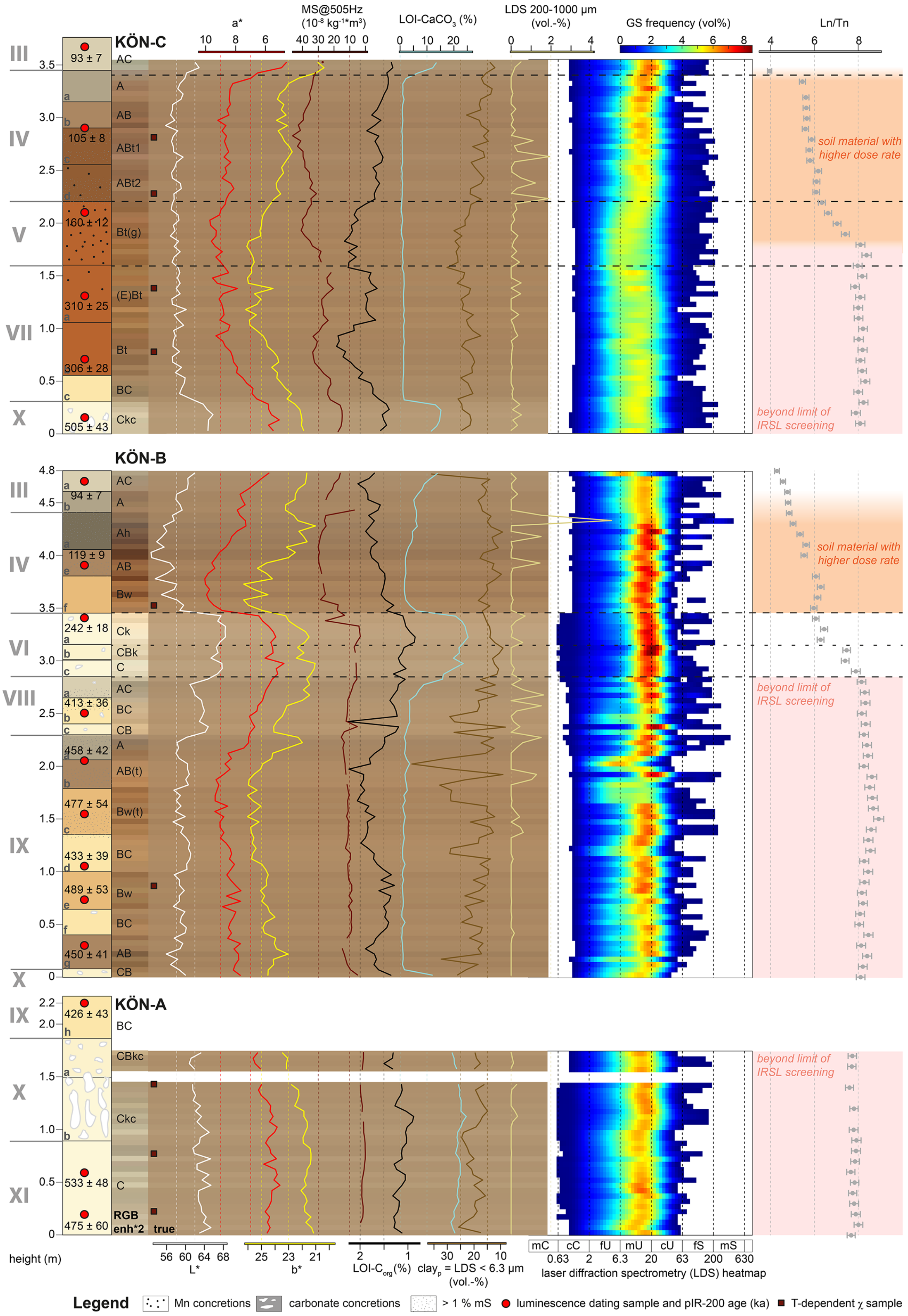

Figure 4. Stratigraphy and laboratory data of the profiles KÖN-A, KÖN-B, and KÖN-C. Real and two-times-enhanced (to the left) RGB colours of each sample are shown as background to the data plots and pedological designations, respectively. Grain size distributions are displayed as heat maps (Schulte and Lehmkuhl, 2018). Ln / Tn ratios are partly beyond the limit of this method (pale red background) or from palaeosols (pale orange background) with a higher dose rate, which is related to the enrichment of clay in such layers. Raw data are available in the Supplement.

variable pattern, with considerable oscillations in the grain size mode, especially in the upper part (VIII and IXa–b). There, more than 1 % medium to coarse sand grains are present; similar peaks are observed in the upper half of the upper PSU (units IVa–b) and the upper half of the merged PSU in KÖN C (units IVc–d).

The loess sediment (Unit VI) between the PSU of KÖN-B contains mostly less than 15 % clay_p, whereas the lowermost loess (Unit X–XI) has 15 %–25 % clay_p. The upper PSU (Unit IV) has only slightly higher clay_p contents compared to the underlying loess (Fig. 4). The lower PSU (Unit IX) exhibits strong oscillations of clay_p contents in the upper half (occasionally larger than 25 %), where we also noted variable grain size modes and the presence of medium to coarse sand. The merged PSU in KÖN-C has clay_p contents of around 25 % in the well-developed palaeosol units V and VII and 15 %–20 % clay_p in the superimposed horizons (IV).

4.4 Carbonate content, organic carbon, and magnetic susceptibility

The loess between the two PSUs in KÖN-B (Unit VI) and the lower loess (units X–XI) mostly have carbonate contents > 15 %, whereas the merged PSU is completely decalcified (Fig. 4). The upper PSU (Unit IV) contains a few percent of carbonate, which constantly increases to > 15 % in the overlying loess (Unit III). As visible in the field, the transition of Unit IV to Unit III is sharp in KÖN-CA. The lower PSU is almost free of carbonate, with minor contents in those parts with a very variable granulometry (units IXa–b and VIII). In Unit VIIIa, there is a constant increase to 15 % towards the upper unit boundary.

LOI C_org contents vary between 1 % in loess and 2 % in the palaeosols and likely represent a mixed signal of organic carbon and clay mineral interlayer water (see Sect. 3.3). Clear peaks in the Bt horizons of the merged PSU (units VIIb and V), high LOI C_org contents in the upper half of Unit IX, and some local peak in IXg, which was interpreted as weak palaeosol (Fig. 4), are present.

Mass-specific χ values vary from 10 to $46 \times 10^{-8}\,\text{m}^3\,\text{kg}^{-1}$. Generally, χ and magnetic enhancement of the frequency dependency is comparable to other loess localities in Eurasia (Fig. 5a–b; e.g. Zeeden et al., 2016; Zeeden and Hambach, 2021). The loess units at the bottom of the sequence (IX and X) and between the two PSUs (Unit VI) show distinctively lower χ, which are in a similar range as the χ from the nearby last glacial LPS Bahlingen-Schönenberg (Schulze et al., 2022). The lower PSU in profile KÖN-B shows slightly enhanced χ, with local maxima in the lowermost and uppermost parts of Unit IX and in Unit VIII. The merged PSU in KÖN-C shows the highest χ and also the highest magnetic enhancement. Distinct peaks in the Bt horizons coincide with those of LOI C_org. The maximum χ values occur in Unit IV and are considerably higher compared to Unit IV in KÖN-B.

The temperature-dependent magnetic susceptibility properties of nine samples are rather complex and vary considerably within the profile. The results cluster in four groups, described by their heating curves (Fig. 5c–f). All samples show an increase in χ at ca. 325 °C and a subsequent decrease towards ca. 500 °C. Furthermore, samples KÖN_A_20–25 and KÖN_A_75–80 (Fig. 5c) show a weak increase until ca. 570 °C before a sharp decrease until 600 °C. Thereafter, χ continues to decrease until ca. 700 °C. The susceptibility reaches values much higher (ca. 9-fold) during cooling than during the heating process. Samples KÖN_B_85–90 and KÖN_C_135–140 (Fig. 5d) show a further decrease in χ during heating with a steep drop at ca. 590 °C. These samples show only slightly higher χ during cooling than during heating. Samples KÖN_A_140–145, KÖN_B_350–355, and KÖN_C_75–80 (Fig. 5e) show a similar pattern as the first group (Fig. 5a) but have a much more pronounced maximum of χ at ca. 570 °C during heating. The susceptibility during cooling is only ca. 3-fold higher than during heating. Samples KÖN_C_225–230 and KÖN_C_280–285 (Fig. 5f) show a rather constant decrease in χ from ca. 300 °C until ca. 600 °C, as well as a clear further decrease in χ until ca. 700 °C.

4.5 IRSL screening

Ln / Tn values in units X and XI of KÖN-C are very consistent with an average of 7.8 ± 0.2 (Fig. 4). In the upper parts of KÖN-B (units X to VIII) and KÖN-C (units X, VIII, VII), average Ln / Tn values of 8.36 ± 0.26 and 8.08 ± 0.24, respectively, are observed. In KÖN-B, the lower part of Unit VI has an average value of 7.59 ± 0.46, whereas the upper part and that continuing into the lower part of Unit IV show a significantly lower value of 6.20 ± 0.35. In the highest part of the sequence investigated here, the mean Ln / Tn value decreases from 6.07 ± 0.14 (380 cm; Unit IVf) to 4.30 ± 0.11 (480 cm; Unit IIIa). In KÖN-C, Unit V shows a gradual decrease in values from ca. 8.14 ± 0.41 (160–180 cm) to 6.16 ± 0.16 (230 cm). These values continue in Unit IVd (mean 6.01 ± 0.26), whereas Unit IVc has a slightly lower mean value of 5.72 ± 0.24. Units IVb and IVa have similar values (mean 5.61 ± 0.10) but the uppermost sample of Unit IVa is slightly lower (5.43 ± 0.14). Significantly lower is the value of the single sample taken from Unit III (3.93 ± 0.11).

4.6 Luminescence dating

The MET-pIR results in five ages per sample (Table 1), which are expected to reflect an increasing stability of the IR-stimulated signal with increasing stimulation temperature. In fact, this trend is clearly observed for the samples investigated here, as shown in Fig. 6a. On average, the pIR-50 ages are at the ratio 0.42 ± 0.09, the pIR-100 ages at 0.69 ± 0.07, and the pIR-150 ages at 0.88 ± 0.06 of the pIR-200 ages that

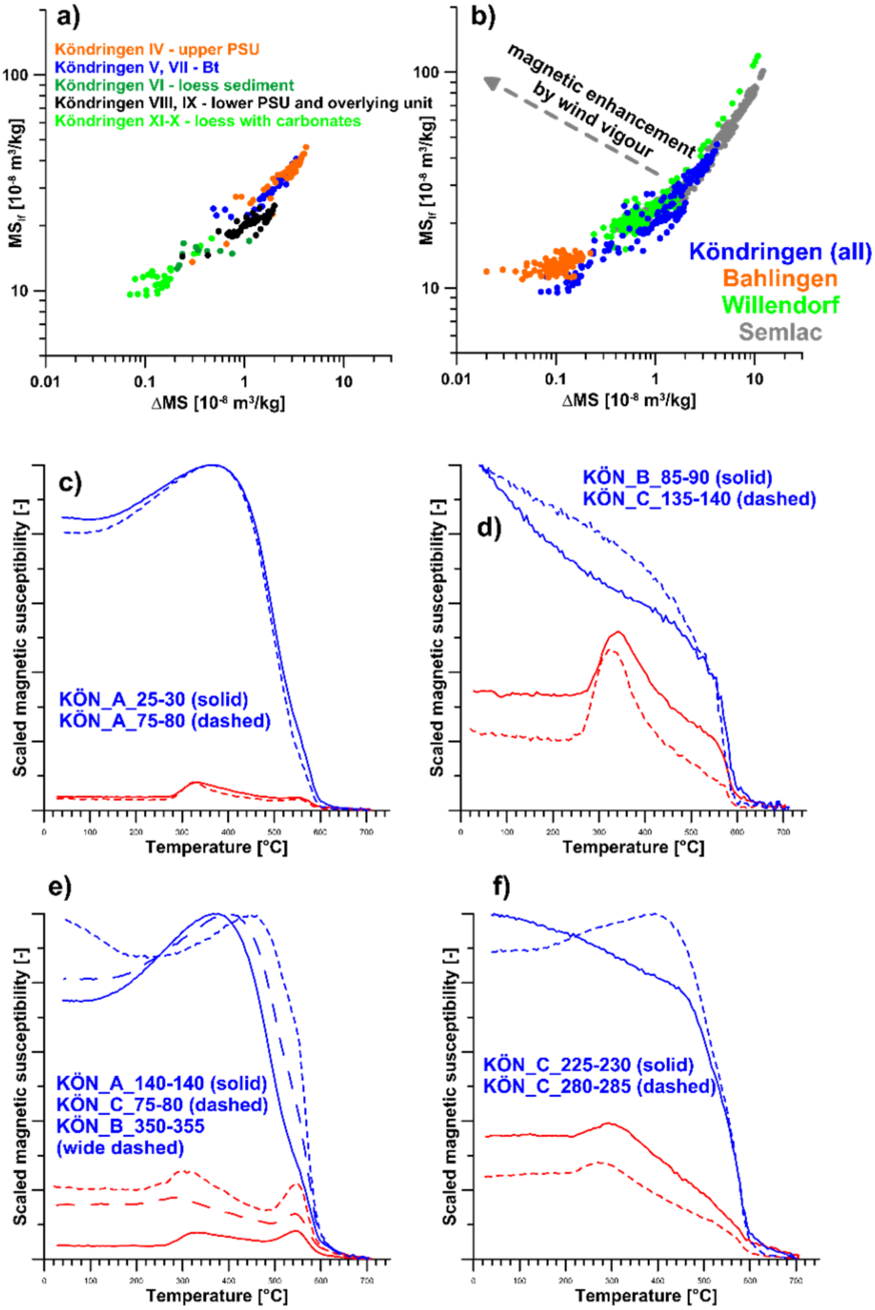

Figure 5. **(a)** Plot of the magnetic susceptibility (ordinate) and its frequency dependency (in %, abscissa) for different stratigraphic units. **(b)** Comparison of the magnetic susceptibility and its frequency dependence on Bahlingen-Schönenberg, Willendorf, and Semlac (Schulze et al., 2022; Zeeden et al., 2016; Zeeden and Hambach, 2021). This shows that the magnetic properties from Köndringen are in line with other available datasets from Eurasia. Strong indications of either wind vigour or dissolution effects are not present. **(c–f)** Temperature-dependent susceptibility during heating (red) and cooling (blue) of the samples indicated in the figure.

are used as reference. The pIR-250 ages are slightly higher (1.14 ± 0.16). The increase in stimulation temperature goes along with an increase in sensitivity change with the single aliquot regenerative dose (SAR) protocol (Fig. 6b), which is in particular strong for pIR-250 and partly leads to poor recycling ratios. Furthermore, there is a clear difference in the shape of dose response curves, with a flatter shape observed for pIR-250. The latter causes a lower saturation dose for pIR-250. In combination with the observation of highly overestimating dose recovery tests, the pIR-250 ages are considered unreliable, and the discussion of the age of the deposits will rely on the pIR-200 ages (Figs. 2 and 4).

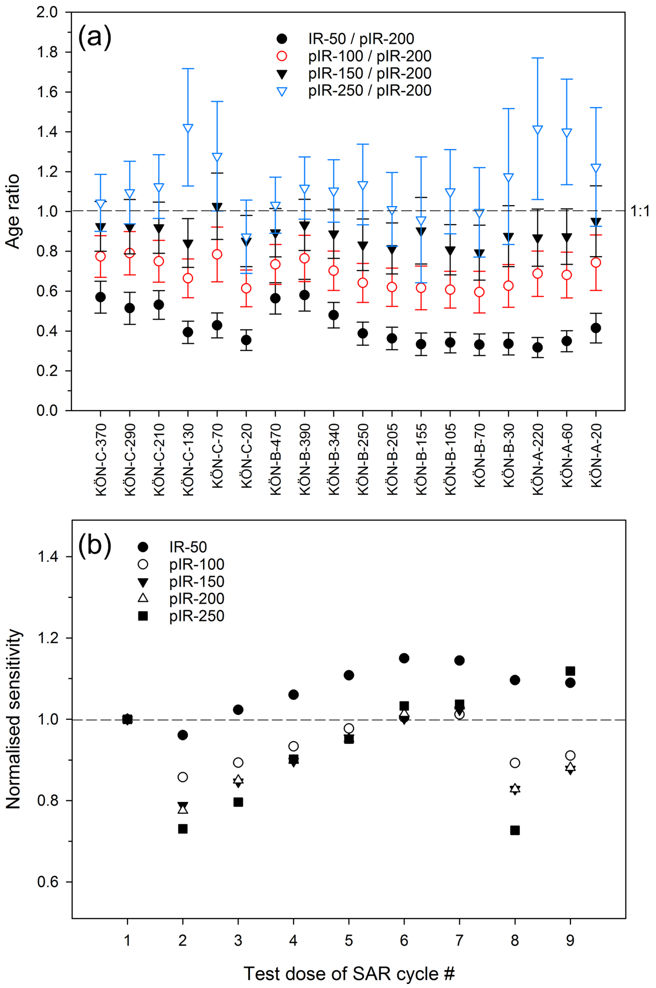

Figure 6. **(a)** The plot of IRSL and pIR ages determined for different stimulation temperatures normalised against the pIR-200 age demonstrates that ages systemically increase with stimulation temperature. **(b)** The test dose sensitivity change during the course of the SAR cycle for different stimulation temperatures normalised to the first measurement (sample KÖN-C-20) is increasingly larger for higher stimulation temperatures.

5 Discussion

5.1 LPS forming processes

The stratigraphically lowest sediment is pale yellow calcareous loess with a carbonate content of around 20 % and a clear texture mode in the medium to coarse silt fraction (ca. 20 µm; Fig. 4). With few exceptions, this mode is present throughout the LPS, which indicates that loess sediments are the parent materials of all palaeosols in the case the latter did not form from pedosediments. The high content of primary carbonate in unaltered loess reinforces earlier notions that sediment brought by the river Rhine, originating from the largely calcareous northern Swiss Alps and the Jura Mountains, must be a major source of the silt (Hädrich, 1975). Compared to last glacial loess of the nearby LPS Bahlingen (Schulze et al., 2022) and other last glacial LPSs from Central Europe, for example, Remagen, Garzweiler, and Krems-Wachtberg (Sprafke et al., 2020), which have grain size modes around 40 µm, the grain size mode at Köndringen is ca. 15–20 µm finer. Regionally distributed data on loess granulometry are not available to clarify if our data reveal deviating silt transport regimes during the Middle Pleistocene or if there is a regional differentiation in grain sizes due to transport distances and topographic barriers between the Rhine and Köndringen; it is planned to investigate this in future studies.

In last glacial LPSs with weak pedogenic differentiation, grain size variations are powerful proxies to reconstruct sedimentation dynamics, resulting from catchment geomorphic processes and wind regimes in reaction to past climate change (Antoine et al., 2009; Vandenberghe, 2013; Schulte et al., 2018; Sprafke et al., 2020). At Köndringen, the three profiles encompass mainly pedosedimentary units and well-developed palaeosols. Here, the wider grain size distribution, including increases in the clay fraction, mainly reflects the effect of post-sedimentary alteration, i.e. pedogenesis (Schulte and Lehmkuhl, 2018). Additionally, the reworking of loess and soil material by slope wash may lead to the admixture of coarse components in the case these are exposed further upslope (Sprafke et al., 2020). As the fraction above 1 mm was not determined quantitatively, we use the fraction 200–1000 µm as proxy for slope wash. Peaks are observed in the upper parts of the PSUs, which reflects a typical phenomenon in Central European LPSs, i.e. landscape degradation and slope processes at the transition of warm and moist to cold and dry environmental conditions (e.g. interglacial to glacial transitions) interrupted by phases of weak to moderate pedogenesis (Semmel, 1968; Bibus, 1974; Terhorst et al., 2002; Sprafke et al., 2014).

Landscape stability results in the alteration of loess and slope deposits by pedogenesis with weathering intensity being mainly a function of duration and humidity. Initial terrestrial (well-aerated) pedogenesis in the presence of sufficient soil moisture leads to organic matter accumulation by humification (darkening) and structural changes by bioturbation, followed by decalcification and oxidation (brownish to reddish pigmentation). In addition to pedogenic structuring (aggregation), pigmentation, and increases in χ, advanced soil development leads to increases in clay content due to silicate weathering of silicates and clay translocation, which mainly takes place in interglacials. Clay translocation in Central European loess may also occur during marked interstadials, usually in the presence of pre-weathered pedosediments (Frechen et al., 2007).

At Köndringen, we observe two major PSUs (Fig. 2; KÖN-B profile) merging into one (KÖN-C profile), with specific properties related to pedogenesis and posterior reworking. All PSUs are largely decalcified, the colours are brown, and clay contents are 5 %–15 % higher than the loess in between (Unit VI), reflecting at least moderate pedogenesis.

Clay coatings on polyhedral ped surfaces in units V and VII indicate long-term pedogenesis, likely under interglacial conditions (Semmel, 1968; Terhorst et al., 2002). The two peaks in LOI C_{org} (Fig. 4) coincide with horizons enriched in illuvial clay, as this method is sensitive to minerals with interlayer water. In the field, illuvial clay of Unit V appears to reach into the upper parts of Unit VII, which itself may be a former eluvial horizon of an older Luvisol. Superimposed on the two well-developed palaeosols is a more humic palaeosol with incipient clay coatings, which may correspond to reactivated illuvial clay from pedosediments (Unit IV). High χ values characterise the merged PSU, with peaks corresponding to the Bt horizons (units V and VII) and maxima in the humic horizons of unit IV. This suggests that χ is sensitive to subsoils of truncated to full interglacial palaeosols but even more to preserved humic topsoils, where biochemical processes occur with high intensity.

The χ values of loess at Köndringen and Bahlingen (Schulze et al., 2022) are rather low; only in units affected by advanced pedogenesis do χ values reach those of other European reference profiles (Fig. 5b). As contents of non-magnetic carbonate are similar (ca. 15 %–25 %) in loess of the URG and the Danube Basin (Sprafke, 2016; Pécsi and Richter, 1996), lower χ values of URG loess are possibly related to a higher share of coarse diamagnetic silicate minerals (e.g. quartz). The basal loess at Köndringen has the lowest χ values due to the additional contribution of (non-magnetic) secondary carbonate visible in the field. The thick carbonate concretions below and the brown colour of the lower PSU (Unit IX) give the impression of long-term pedogenesis. However, χ values of the lower PSU are rather low, indicating a weak to moderate intensity of soil formation or a mix of soil and loess material. Granulometric fluctuations in the upper part and layering, frost features, and the weak pedogenic structure in the lower part of the lower PSU (Fig. 2a) support that it consists mainly of reworked soil material. Some re-established pedogenic structure and slight increases in χ in the lowermost part (IXg) and upper part (IXa–c) of the lower PSU indicate weak to moderate pedogenesis of interstadial intensity. Specifically, Unit IXa may correspond to a humic topsoil formed during this interstadial-type pedogenesis. Unit VIII represents enhanced aeolian sedimentation, with Unit VIIIb likely representing a phase of weak pedogenesis, indicated by lower carbonate contents and a more brownish colour.

We interpret the temperature-dependent susceptibility properties (Fig. 5c–f) as indicative of relevant contributions of magnetite, maghemite, and hematite. For Eurasian loess, the increase in χ at ∼ 300 °C has been related to the alteration of weakly magnetic Fe phases to maghemite or magnetite; the heating curves of the magnetic susceptibility plotted in Fig. 5e are most typical of last (inter-)glacial European palaeosols and loess sediments (see Zeeden and Hambach, 2021, and references therein). The drop in the susceptibility at ∼ 585 °C likely represents the Curie temperature of magnetite. The further decrease in the χ towards 700 °C is interpreted as a contribution of hematite (Fig. 5f). While for all samples an increase in χ at ∼ 300 °C is present (Fig. 5c–f), samples shown in Fig. 5c and d show this phenomenon most prominently. For the samples from units X and XI (Fig. 5c), this is not surprising as these are from typical loess, which will easily form magnetic minerals when heated. The much higher susceptibility during cooling for some samples (Fig. 5c) implies that non- or weakly magnetic iron phases are prominently present in the sediment. The susceptibilities that are not much higher during cooling for samples from Unit VIIa (merged PSU) and Unit IXe (lower PSU; Fig. 5d) are interpreted as originating from mature, likely interglacial soils. The absence of strong ferrimagnetism in the lower PSU can be explained by the removal of the very fine fraction during slope wash that led to the reworking of a previously present interglacial soil. The upper PSU in KÖN-B corresponds stratigraphically to the upper part of the merged PSU in profile KÖN-C. Yet, our data show that Unit IV has different properties in both profiles. For KÖN-C, please note the presence of a humic palaeosol with incipient clay illuviation cut sharply by overlying loess. In KÖN-B there is a clear subdivision into a brown, weakly aggregated part and a darker, moderately aggregated part, grading into overlying loess. It is likely that units IVe–f correspond to brown pedosediment which was overprinted by a humic palaeosol and successively buried by loess. The presence of carbonate in the pedosediment indicates that decalcification, allowing for clay illuviation (as in KÖN-C), was not reached in this part of the LPS, but micromorphological studies are necessary to support or neglect this hypothesis (cf. Sprafke et al., 2014). Units IVb–d instead are decalcified and have high χ values, indicating that pedogenesis was stronger. The hematite contribution, seen best in samples from the base of the upper PSU (units IVc, d; see Fig. 5f), implies that the upper PSU contains material from a mature, likely interglacial soil. As for the lower PSU, this phenomenon may be related to the incorporation of older pre-weathered material, which is typical of early glacial palaeosols in Central Europe (Frechen et al., 2007; Sprafke et al., 2014).

Overall, our colour, granulometry, magnetic susceptibility, and LOI data considerably support the subdivision and interpretation of the studied LPS (Fig. 4), although we note that the interpretation appears partly ambiguous in the absence of detailed macro- and micromorphological studies (cf. Sprafke et al., 2014; Sprafke, 2016). As the focus of this study was the testing of new methods, specifically luminescence screening and advanced dating protocols, we note a shortcoming in (micro-)structural information to precisely reconstruct the formation of this complex LPS.

5.2 Chronostratigraphy

Sections KÖN-A and KÖN-C comprise the oldest stratigraphic units (XI and X) for which consistent ages of 533 ± 48 ka (KÖN-A-20), 475 ± 60 (KÖN-A-60), and 505 ± 43 ka (KÖN-C-20) have been determined. Assuming the two units (XI and X) are quasi-synchronous allows a mean age of 505 ± 71 ka (CAM) to be calculated for the basal part of the investigated sequence. The large uncertainty does not allow an unambiguous correlation with MIS stratigraphy (Lisiecki and Raymo, 2005), but assuming the loess was deposited during a glacial period makes MIS 14 (563–533 ka) and MIS 12 (478–424 ka) the most likely candidates. However, it is at present not known if the pIR-200 ages are affected by systematic underestimation due to, for example, a low level of fading or the onset of signal saturation. The question of potential underestimation can only be answered by comparison with independent age control, which is so far not available for the region. In the absence of any evidence pointing towards age underestimation, the pIR-200 ages are considered reliable for the time being.

In Profile KÖN-A, unit X with massive loess dolls is overlain by pedosediments corresponding to the lowermost part of the lower PSU (Unit IX). The age of 426 ± 43 ka (KÖN-A-220) corresponds to late MIS 12 or early MIS 11. In section KÖN-B, Unit IX contains five superimposed pIR-200 ages overlapping within uncertainties (Table 1, Fig. 5), which represent a mean (CAM) age of 458 ± 21 ka and hence relate to MIS 12 (478–424 ka). In the Alpine region, Middle Pleistocene stratigraphies vary regionally and are fragmentary, but in northern and western Europe MIS 12 correlates with the large glaciation of the Elsterian (Cohen and Gibbard, 2019). According to our interpretation, Unit IX likely comprises soil material reworked by slope wash. Based on the susceptibility data it likely contains components of a well-developed interglacial soil, which would be pre-Elsterian (possibly Cromerian). The age of 413 ± 36 ka (KÖN-B-250) for Unit VIII on top of Unit IX may represent the MISs 12–11 boundary, as ongoing sedimentation and rather weak pedogenesis appear less likely for an interglacial (MIS 11). Based on geochronology and palaeosol morphology, there is no evidence for an MIS 11 palaeosol in the studied part of the Köndringen outcrop; it may have been eroded subsequent to its formation.

In Unit VII (profile KÖN-B), two consistent pIR-200 ages of 310 ± 25 ka (KÖN-C-130) and 306 ± 28 ka (KÖN-C-70) point towards deposition during MIS 9 (337–300 ka). Both ages are from a well-developed Bt horizon, most likely formed during interglacial conditions; therefore some rejuvenation by bioturbation or a slight age underestimation can be assumed. The highly calcareous loess of Unit VI has an age of 242 ± 18 ka (KÖN-B-340) and hence correlates with MIS 8 (300–243 ka). The age determined for the well-developed Bt horizon Unit V (160 ± 12 ka, KÖN-C-210) likely reflects the age of the parent material deposited during MIS 6 (191–130 ka), whereas soil formation presumably occurred during MIS 5e (130–115 ka), the Last Interglacial period (Eemian). Two pIR-200 ages determined for the upper PSU (Unit IV) of 119 ± 9 ka (KÖN-B-390) and 105 ± 8 ka (KÖN-C-290) fall into earlier phases of MIS 5 and likely correspond to the beginning of the last glacial period during MIS 5d (115–102 ka). The two topmost samples taken from loess above (Unit III) have ages of 94 ± 7 ka (KÖN-B-470) and 93 ± 7 ka (KÖN-C-370), indicating deposition during MIS 5c (102–92 ka) to MIS 5b (92–85 ka).

Ln / Tn values from IRSL screening determined for the lower part of section KÖN-C do not reflect the hiatus between units X and VII that is clearly observed by the pIR-200 ages (505 ± 43 ka versus 310 ± 25 ka and 306 ± 28 ka). In this context, it has to be noted that Ln / Tn values have been determined using IRSL stimulated at 50 °C, hence with a signal that will be affected by fading. In the presence of fading, the latent IRSL signal will rise to an equilibrium point at which the amount of newly produced latent signal equals the decay of the latent signal. This equilibrium point will be defined by the number of electron traps that host the latent signal, the fading rate, and the signal production rate, i.e. dose rate. The latter effect is reflected by the observation that the Ln / Tn values for the basal loess (units XI and X) are lower than those observed for the rest of the sequence. In fact, the dose rate in this part is lower (ca. 2.8 Gy kyr^{-1}) compared to other parts of the sequence (ca. 3.7–3.8 Gy kyr^{-1}), which appear to be in equilibrium. In the present setting, the IRSL screening values carry age information only up to ca. 300 ka.

In the upper part of section KÖN-B, additional chronological information is derived from IRSL screening values that is not provided by the dating itself. First, Unit VI is clearly subdivided into a lower and upper subunit, as indicated by the offset in Ln / Tn values (7.59 ± 0.46 versus 6.20 ± 0.35). Such a significant offset may represent a time of several hundreds of thousands of years; hence, the lower part may correspond to MIS 10 (374–337 ka) and the upper part to MIS 8 (300–243 ka), the latter age being confirmed by a pIR-200 age. The continuation of Ln / Tn values just above and in Unit IV reveals that this part of the sequence was likely also deposited during MIS 8 but overprinted by later soil development. The gradual decrease in values from 8.14 ± 0.41 (160–180 cm) to 6.16 ± 0.16 (230 cm) implies quasi-continuous accumulation in the upper part of the investigated sequence. Apparently, continuous deposition is also observed for the upper part of Unit V in section KÖN-C, and it is shown that the lower part of this unit developed on older material (of Unit VII?). Unit IV and its subunits in this section apparently represent episodic deposition reflected by the different mean Ln / Tn values (Unit IVd: 6.01 ± 0.26; Unit IVc: 5.72 ± 0.24; Unit IVb and lower Unit IVa: 5.61 ± 0.10; Unit IVa: 5.43 ± 0.14). However, since dosimetric effects cannot be ruled out, this statement has to be treated with caution and would require proof by full dating.

From a magnetostratigraphic perspective, we note that the magnetic signatures of the Bt horizons related to MIS 9 and MIS 5 are not as high as those typically are for full interglacial conditions, but URG loess seems to have overall lower χ values than other Central European LPSs. As noted previously (e.g. Necula et al., 2015; Marković et al., 2015), χ values of interglacial soils vary considerably in Europe. Furthermore, the type of pedogenesis and the position in the soil profile apparently influence this proxy. More geographically distributed χ data are necessary to understand the spatial pattern of the proxy intensities.

5.3 Stratigraphic context

During the past decades, research on LPSs in Central Europe has mainly focused on last glacial records, occasionally with obtained ages below Eemian palaeosols (e.g. Kadereit et al., 2013; Moine et al., 2017; Fischer et al., 2021; Lehmkuhl et al., 2016; Zens et al., 2018; Krauss et al., 2018; Rahimzadeh et al., 2021). Many Middle Pleistocene LPSs still lack state-of-the-art chronologies for individual loess and soil units, although palaeomagnetism and tephra stratigraphy are being applied where time intervals and material are present (e.g. Jordanova et al., 2022; Laag et al., 2021; Marković et al., 2015). TL ages from pre-Eemian (MIS 6 and older) loess elaborated during the 1980s to 1990s provide first approximations to the Middle Pleistocene loess chronology, though with large uncertainties (Zöller et al., 1988; Frechen et al., 1992; Frechen, 1994). IRSL ages from the late 1990s to early 2010s provide more robust estimates back to 200–250 ka (e.g. Preusser and Fiebig, 2009) at the LPS Wels-Aschet, Upper Austria. Further methodological advances are related to the application of thermally transferred (TT) OSL (Moska and Bluszcz, 2013) and pIR protocols (Schmidt et al., 2011a, b; Thiel et al., 2011a, b). Post-IR IRSL$_{290}$ dating, for example, extended the numerical age range in loess from Lower Austria (Paudorf, Göttweig-Furth and Aigen, Krems shooting range) and Hungary (Paks brickyard) to 300–350 ka (Thiel et al., 2011b, 2014; Sprafke et al., 2014; Sprafke, 2016). The MET-pIR ages determined at Köndringen reach back to 500 ka and are among the oldest luminescence ages obtained from loess in Central Europe. The opportunity to date back to pre-Holsteinian (MIS 11) times is promising from a geochronological point of view; however, pedostratigraphic relations at Köndringen are rather complicated and provide limited support to assess the reliability of our data in the absence of independent numerical age control.

A central controversy in loess research of Central Europe surrounds the questions of if Luvisols are strictly limited to full interglacial conditions and if these recurred every ca. 100 000 years, as proposed by Bibus (2002) for SW Germany and adopted by Terhorst et al. (2007, 2015) for Upper Austria. This hypothesis is apparently supported by LPSs in NW France, where Antoine et al. (2021) report seven interglacial Bt horizons between the surface soil and the Matuyama–Brunhes boundary (MBB) around 780 ka. However, at the LPS Weilbach (Hesse) it appears that MIS 7 is only represented by two humic horizons (Weilbacher Humuszonen), and the next Bt horizon below the Eemian palaeosol may rather correspond to MIS 9 (Schmidt et al., 2011b). At Harmignies in Belgium, MIS 7 may be represented by two Bt horizons of Luvisols (Haesaerts et al., 2019), similar to findings from Červený kopec (Kukla, 1977) and other localities in Central Europe (e.g. Necula et al., 2015, and references therein). At Wels-Aschet, luminescence ages point to more than one Bt horizon being equivalent to MIS 7, consistent with two prominent global warm phases separated by a cooler phase encompassing MIS 7 (Preusser and Fiebig, 2009). At Koblenz-Metternich a formation of Luvisols reportedly occurred during pronounced interstadial conditions of the early Wurmian (Boenigk and Frechen, 2001). All the mentioned LPSs lack numerical age control by state-of-the-art methods, and there are further prominent LPSs in Central Europe that contain several fossil Bt horizons but lack a robust chronological framework for the Middle Pleistocene parts, for example Kärlich (Boenigk and Frechen, 1998), Bad Soden (Semmel and Fromm, 1976), Kirchheim (Rösner, 1990), Hagelstadt (Strunk, 1990), and Achenheim (Junkmanns, 1995). In summary, considering the discrepancies in Middle Pleistocene loess stratigraphy of Central Europe, it appears mandatory to date several geographically distributed LPSs with state-of-the-art luminescence dating approaches and precisely determine pathways of palaeopedogenesis to understand the regional imprint of spatially distinct palaeoclimates to the pedosphere (Sprafke, 2016).

At Köndringen, there are too many discontinuities to support or disprove available stratigraphic models. The two well-developed Bt horizons correspond to MISs 5e and 9, which suggests that these Luvisol subsoils represent full interglacial conditions. This is in agreement with earlier assumptions of Bronger (1966) and Guenther (1987), who suggest that regional interglacials are typically represented by Luvisols yet without being backed up by numeric age control. Some clay translocation in early glacial pedosediments of Unit IV in KÖN-C is likely related to a remobilisation of illuvial clay after post-Eemian colluviation in the absence of carbonate, as reported for the LPS Schatthausen near Heidelberg (Frechen et al., 2007). Interestingly in KÖN-B, there are no signs of clay translocation in the brown early glacial pedosediments, which may relate to some admixture of carbonate during colluviation, which hampers posterior clay translocation, as suggested for the MIS 5 pedocomplex of the LPS Paudorf, Lower Austria (Sprafke et al., 2014). This underlines that palaeoclimatic inferences from polygenetic and partly reworked palaeosols are difficult and require detailed (chrono-)stratigraphic, sedimentological, and also micromorphological studies. The lack of (micro-)morphological data is obvious with respect to the lower PSU at Köndringen, which is most likely an Elsterian pedosediment (see Sect. 5.2), with incipient interstadial pedogenesis in the lowermost and upper part. Advanced interglacial pedogenesis has most likely occurred before soil reworking, which would be pre-Elsterian (MIS 12), i.e. Cromerian. Thus, a Holsteinian palaeosol in other parts of the outcrop and/or in other sites of the region may be expected. The well-developed carbonate nodules likely represent one or more Cromerian interglacials and are possibly the result of a merged soil developed during MISs 15–13, as interpreted for Central Europe (Terhorst, 2007; Bronger, 2003; Marković et al., 2015; Necula et al., 2015, and references therein).

The loess package between the upper and lower PSUs corresponds to MIS 8, which is known for rather little global ice volume compared to MISs 6, 10, and 12 (Lisiecki and Raymo, 2005). If loess volume is taken as an indicator for upstream glacier activity, the presence of a distinct MIS 8 loess package would imply a major phase of glaciation at this time. However, this period is usually not considered to represent full glacial conditions in the Alps (e.g. van Husen and Reitner, 2011), although it represents the phase of coldest sea surface temperatures of the last 1 million years at the Iberian Margin (Rodrigues et al., 2017, and references therein). Even in northern Switzerland, where one of the most complex glaciation histories has been reconstructed, there is still no unequivocal evidence for a major glaciation during MIS 8 (Preusser et al., 2011). Investigating further LPSs from the southern part of the URG, which is located downstream of the formerly glaciated areas of northern Switzerland, could give insight into aeolian sediment flux that is usually interpreted as a glacial signal in this region.

6 Conclusions

The studied section of the LPS Köndringen consists of loess sediments intercalated by two prominent pedosedimentary units (PSUs), of which the upper one is inclined to the west, cutting into the underlying loess and merging with the lower PSU. The applied high-resolution multi-method approach leads to detailed stratigraphic information and supports the reconstruction of the main phases of dust deposition, pedogenesis, and reworking of those units which were not lost by erosion. MET-pIR ages reach back to more than 500 ka and thus are among the oldest numerical ages obtained from loess in Central Europe. Massive carbonate concretions in the loess below the lower PSU point to advanced (interglacial) pedogenesis, apparently supported by the brownish colour, lack of carbonates, and higher clay contents in the lower PSU. However, the partly layered appearance, a weak pedogenic structure, and low χ values suggest at most interstadial pedogenesis. Temperature-dependent χ results support the assumption that the lower PSU contains reworked interglacial palaeosol material. Soil formation likely occurred during MIS 13 (and/or MIS 15?) and reworking during MIS 12 (Elsterian). The merged PSU in the western part of the studied outcrop comprises two well-developed interglacial Luvisol remnants (Bt horizons) dating to MIS 9 and MIS 5e (Eemian). Superimposed is a humic palaeosol with incipient clay coatings and the highest χ values likely formed during MIS 5c. As the LPS Köndringen contains several hiatuses and polygenetic units, the contribution towards refining the Central European Middle Pleistocene loess stratigraphy remains limited for the time being. However, our study motivates future studies in the region using the applied multi-method approach in combination with MET-pIR state-of-the-art dating. Future studies on loess stratigraphy and chronology in the southern URG will contribute towards a better understanding of the chronology and impact of Alpine glaciations.

Data availability. Relevant data are given either in the main text or in the Supplement.

Supplement. The supplement related to this article is available online at: https://doi.org/10.5194/egqsj-72-1-2023-supplement.

Author contributions. FP, ToS, and AF conceptualised this study. Fieldwork and most laboratory analyses were carried out by TaS and LS, under the supervision of FP, ToS, and AF. Luminescence dating was carried out by AF and magnetic susceptibility measurements by CZ. The original draft was prepared by ToS and FP, based on the master of science thesis written by LS. All authors contributed by additional writing, reviewing, and editing.

Competing interests. At least one of the (co-)authors is a member of the editorial board of *E&G Quaternary Science Journal* and co-editor of the special issue “Quaternary research from and inspired by the first virtual DEUQUA conference”. The peer-review process was guided by an independent editor, and the authors also have no other competing interests to declare.

Special issue statement. This article is part of the special issue “Quaternary research from and inspired by the first virtual DEUQUA conference”. It is a result of the vDEUQUA2021 online conference in September/October 2021.

Acknowledgements. We thank Robert Petizcka (University of Vienna) for providing the spectrophotometer.

Financial support. This open-access publication was funded by the University of Freiburg.

Review statement. This paper was edited by Julia Meister and reviewed by two anonymous referees.

References

Abdulkarim, M., Grema, H. M., Adamu, I. H., Mueller, D., Schulz, M., Ulbrich, M., Miocic, J. M., and Preusser, F.: Effect of using different chemical dispersing agents in grain size analyses of fluvial sediments via laser diffraction spectrometry, Methods Protoc., 4, 44, https://doi.org/10.3390/mps4030044, 2021.

Andres, W., Bos, J. A. A., Houben, P., Kalis, A. J., Nolte, S., Rittweger, H., and Wunderlich, J.: Environmental change and fluvial activity during the Younger Dryas in central Germany, Quatern. Int., 79, 89–100, https://doi.org/10.1016/S1040-6182(00)00125-7, 2001.

Antoine, P., Rousseau, D.-D., Moine, O., Kunesch, S., Hatte, C., Lang, A., Tissoux, H., and Zöller, L.: Rapid and cyclic aeolian deposition during the Last Glacial in European loess: a high-resolution record from Nussloch, Germany, Quaternary Sci. Rev., 28, 2955–2973, https://doi.org/10.1016/j.quascirev.2009.08.001, 2009.

Antoine, P., Coutard, S., Bahain, J. J., Locht, J. L., Hérisson, D., and Goval, E.: The last 750 ka in loess–palaeosol sequences from northern France: environmental background and dating of the western European Palaeolithic, J. Quaternary Sci., 36, 1293–1310, https://doi.org/10.1002/jqs.3281, 2021.

Bibus, E.: Abtragungs- und Bodenbildungsphasen im Rißlöß, E&G Quaternary Sci. J., 25, 166–182, https://doi.org/10.3285/eg.25.1.14, 1974.

Bibus, E.: Zum Quartär im mittleren Neckarraum – Reliefentwicklung, Löß/Paläobodensequenzen, Paläoklima, Tübinger Geowissenschaftliche Arbeiten, D8, 236 pp., ISBN 3-88121-055-5, 2002.

Boenigk, W. and Frechen, M.: Zur Geologie der Deckschichten von Kärlich/Mittelrhein, E&G Quaternary Sci. J., 48, 38–49, https://doi.org/10.3285/eg.48.1.04, 1998.

Boenigk, W. and Frechen, M.: The loess record in sections at Koblenz–Metternich and Tönchesberg in the Middle Rhine Area, Quatern. Int., 76, 201–209, https://doi.org/10.1016/S1040-6182(00)00103-8, 2001.

Bronger, A.: Lösse, ihre Verbraunungszonen und fossilen Böden. Ein Beitrag zur Stratigraphie des oberen Pleistozäns in Südbaden, Schriften des Geographischen Instituts der Universität Kiel 24/2, Geographisches Institut der Universität Kiel, Kiel, 113 pp., 1966.

Bronger, A.: Zur Klimageschichte des Quartärs von Südbaden auf bodengeographischer Grundlage, Petermann. Geogr. Mitt., 113, 112–124, 1969.

Bronger, A.: Zur Mikromorphogenese und zum Tonmineralbestand quartärer Lössböden in Südbaden, Geoderma, 3, 281–320, https://doi.org/10.1016/0016-7061(70)90011-X, 1970.

Bronger, A.: Correlation of loess-paleosol sequences in East and Central Asia with SE Central Europe: towards a continental Quaternary pedostratigraphy and paleoclimatic history, Quatern. Int., 106, 11–31, https://doi.org/10.1016/S1040-6182(02)00159-3, 2003.

Buylaert, J. P., Murray, A. S., Thomsen, K. J., and Jain, M.: Testing the potential of an elevated temperature IRSL signal from K-feldspar, Radiat. Meas., 44, 560–565, https://doi.org/10.1016/j.radmeas.2009.02.007, 2009.

Cohen, K. M. and Gibbard, P. L.: Global chronostratigraphical correlation table for the last 2.7 million years, version 2019 QI-500, Quatern. Int., 500, 20–31, https://doi.org/10.1016/j.quaint.2019.03.009, 2019.

Degering, D. and Degering, A.: Change is the only constant – Time-dependent dose rates in luminescence dating, Quat. Geochronol., 58, 101074, https://doi.org/10.1016/j.quageo.2020.101074, 2020.

EEA (European Environment Agency): European Digital Elevation Model (EU-DEM), version 1.1, Copernicus Land Monitoring Service 2016, European Union, https://land.copernicus.eu/imagery-in-situ/eu-dem/eu-dem-v1.1?tab=download (last access: 20 July 2022), 2016.

Ehlers, J., Gibbard, P. L., and Hughes, P. D. (Eds.): Quaternary Glaciations – Extent and Chronology A Closer Look, Developments in Quaternary Sciences, 15, Elsevier, 1108 pp., ISBN 978-0-444-53447-7, 2011.

Erkens, G., Dambeck, R., Volleberg, K. P., Bouman, M. T. I. J., Bos, J. A. A., Cohen, K. M., Wallinga, J., and Hoek, W. Z.: Fluvial terrace formation in the northern Upper Rhine Graben during the last 20 000 years as a result of allogenic controls and autogenic evolution, Geomorphology, 103, 476–495, https://doi.org/10.1016/j.geomorph.2008.07.021, 2009.

Faershtein, G., Porat, N., and Matmon, A.: Natural saturation of OSL and TT-OSL signals of quartz grains from Nilotic origin, Quat. Geochronol., 49, 146–152, https://doi.org/10.1016/j.quageo.2018.04.002, 2019.

FAO (Food and Agriculture Organization of the United Nations): Guidelines for soil description. Food and Agriculture Organization of the United Nations, 4th edn., Roma, Italy, ISBN 92-5-105521-1, 2006.

Fischer, P., Jöris, O., Fitzsimmons, K., Vinnepand, M., Prud'homme, C., Schulte, P., Hatté, C., Hambach, U., Lindauer, S., Zeeden, C., Peric, Z., Lehmkuhl, F., Wunderlich, T., Wilken, D., Schirmer, W., and Vött, A.: Millennial-scale terrestrial ecosystem responses to Upper Pleistocene climatic changes: 4D-reconstruction of the Schwalbenberg Loess-Palaeosol- Sequence (Middle Rhine Valley, Germany), Catena, 196, 104913, https://doi.org/10.1016/j.catena.2020.104913, 2021.

Frechen, M.: Systematic Thermoluminescence Dating of 2 Loess Profiles from the Middle Rhine Area (F.R.G.), Quaternary Sci. Rev., 11, 93–101, https://doi.org/10.1016/0277-3791(92)90048-D, 1992.

Frechen, M.: Thermolumineszens-Datierungen an Lössen des Tönchesberges aus der Osteifel, E&G Quaternary Sci. J., 44, 79–93, https://doi.org/10.3285/eg.44.1.08, 1994.

Frechen, M., Brückner, H., and Radtke, U.: A comparison of different TL-techniques on loess samples from Rheindahlen (FRG), Quaternary Sci. Rev., 11, 109–113, https://doi.org/10.1016/0277-3791(92)90050-I, 1992.

Frechen, M., Terhorst, B., and Rähle, W.: The Upper Pleistocene loess/palaeosol sequence from Schatthausen in North Baden-Württemberg, E&G Quaternary Sci. J., 56, 212–227, https://doi.org/10.3285/eg.56.3.05, 2007.

Gabriel, G., Ellwanger, D., Hoselmann, C., Weidenfeller, M., Wielandt-Schuster, U., and The Heidelberg Basin Project Team: The Heidelberg Basin, Upper Rhine Graben (Germany): a unique archive of Quaternary sediments in Central Europe, Quatern. Int., 292,43–58, https://doi.org/10.1016/j.quaint.2012.10.044, 2013.

Galbraith, R. F., Roberts, R. G., Laslett, G. M., Yoshida, H., and Olley, J. M.: Optical Dating of single and multiple Grains of

Quartz from Jinmium Rock Shelter, Northern Australia: Part I, Experimental Design and Statistical Models, Archaeometry, 41, 2, 339–364, 1999.

Guenther, E. W.: Sedimentpetrographische Untersuchung von Lössen-Zur Gliederung des Eiszeitalters und zur Einordnung paläolithischer Kulturen, Teil 1 Methodische Grundlagen mit Erläuterung an Profilen, Böhlau Verlag Köln Graz, p. 10, 1961.

Guenther, E. W.: Zur Gliederung der Lösse des südlichen Oberrheintals, E&G Quaternary Sci. J., 37, 67–78, https://doi.org/10.3285/eg.37.1.07, 1987.

Hädrich, F.: Die Böden der Emmendinger Vorbergzone (Südliches Oberrheingebiet), Berichte der Naturforschenden Gesellschaft Freiburg i. Br., 56, 23–76, 1965.

Hädrich, F.: Zur Methodik der Lößdifferenzierung auf der Grundlage der Carbonatverteilung, E&G Quaternary Sci. J., 26, 95–117, https://doi.org/10.3285/eg.26.1.06, 1975.

Hädrich, F.: Paläoböden im südlichen Oberrhein Gebiet, Berichte der Naturforschenden Gesellschaft Freiburg i. Br., 70, 29–48, 1980.

Hädrich, F. and Lamparski, F.: Ein rißzeitlicher Eiskeil im Lößaufschluß von Buggingen (Südbaden) mit einem Beitrag zur Lößkindelgenese, Berichte der Naturforschenden Gesellschaft Freiburg i. Br., 74, 25–47, 1984.

Hädrich, F. and Stahr, K.: Die Böden des Breisgaus und angrenzender Gebiete, Berichte der Naturforschenden Gesellschaft Freiburg i. Br., 91., 148 pp., 2001.

Haesaerts, P., Dupuis, C., Spagna, P., Damblon, F., Balescu, S., Jadin, I., Lavachery, P., Pirson, S., and Bosquet, D.: Révision du cadre chronostratigraphique des assemblages Levallois issus des nappes alluviales du Pléistocène moyen dans le bassin de la Haine (Belgique), in: Actes du XXVIIIe Congrès Préhistorique de France, Amiens, France, 30 May–4 June 2016, Société préhistorique de France, Paris, France, 179–199, 2019.

Heiri, O., Lotter, A. F., and Lemcke, G.: Loss on ignition as a method for estimating organic and carbonate content in sediments: reproducibility and comparability of results, J. Paleolimnol., 25, 101–110, https://doi.org/10.1023/A:1008119611481, 2001.

Heiri, O., Koinig, K. A., Spötl, C., Barrett, S., Brauer, A., Drescher-Schneider, R., Gaar, D., Ivy-Ochs, S., Kerschner, H., Luetscher, M., Moran, A., Nicolussi, K., Preusser, F., Schmidt, R., Schoeneich, P., Schwörer, C., Sprafke, T., Terhorst, B., and Tinner, W.: Palaeoclimate records 60–8 ka in the Austrian and Swiss Alps and their forelands, Quaternary Sci. Rev., 106, 186–205, https://doi.org/10.1016/j.quascirev.2014.05.021, 2014.

Hofmann, F. M., Rauscher, F., McCreary, W., Bischoff, J.-P., and Preusser, F.: Revisiting Late Pleistocene glacier dynamics northwest of the Feldberg, southern Black Forest, Germany, E&G Quaternary Sci. J., 69, 61–87, https://doi.org/10.5194/egqsj-69-61-2020, 2020.

Houben, P.: Spatio-temporally variable response of fluvial systems to Late Pleistocene climate change: a case study from central Germany, Quaternary Sci. Rev., 22, 2125–2140, https://doi.org/10.1016/S0277-3791(03)00181-1, 2003.

Huntley, D. J. and Baril, M. R.: The K content of the K-feldspars being measured in optical dating or in thermoluminescence dating, Ancient TL, 15, 11–13, 1997.

Jordanova, D., Laag, C., Jordanova, N., Lagroix, F., Georgieva, B., Ishlyamski, D., and Guyodo, Y.: A detailed magnetic record of Pleistocene climate and distal ash dispersal during the last 800 kyrs – The Suhia Kladenetz quarry loess-paleosol sequence near Pleven (Bulgaria), Glob. Planet. Change, 214, 103840, https://doi.org/10.1016/j.gloplacha.2022.103840, 2022.

Junkmanns, J.: Les ensembles lithiques d'Achenheim d'apres la collection de Paul Wernert, Bull. Soc. Préhist. Fr., 92, 26–36, 1995.

Kadereit, A., Kind, C.-J., and Wagner, G. A.: The chronological position of the Lohne Soil in the Nussloch loess section – re-evaluation for a European loess-marker horizon, Quaternary Sci. Rev., 59, 67–86, https://doi.org/10.1016/j.quascirev.2012.10.026, 2013.

Kars, R. H., Reimann, T., Ankjærgaard, C., and Wallinga, J.: Bleaching of the post-IR IRSL signal: new insights for feldspar luminescence dating, Boreas, 43, 780–791, https://doi.org/10.1111/bor.12082, 2014.

Keßler, G. and Laiber, J.: Erläuterungen zu Blatt 7813 Emmendingen, Geologisches Landesamt Baden-Württemberg, Landesvermessungsamt Baden-Württemberg, Stuttgart, 1991.

Kleinmann, A., Müller, H., Lepper, J., and Waas, D.: Nachtigall: A continental sediment and pollen sequence of the Saalian Complex in NW-Germany and its relationship to the MIS-framework, Quatern. Int., 241, 97–110, https://doi.org/10.1016/j.quaint.2010.10.005, 2011.

Knipping, M.: Early and Middle Pleistocene pollen assemblages of deep core drillings in the northern Upper Rhine Graben, Germany, Neth. J. Geosci., 87, 51–65, https://doi.org/10.1017/S0016774600024045, 2008.

Kock, S., Huggenberger, P., Preusser, F., Rentzel., P., and Wetzel, A.: Formation and evolution of the Lower Terrace of the Rhine River in the area of Basel, Swiss J. Geosci. 102, 307–321, https://doi.org/10.1007/s00015-009-1325-1, 2009.

Konert, M. and Vandenberghe, J.: Comparison of laser grain size analysis with pipette and sieve analysis: a solution for the underestimation of the clay fraction, Sedimentology, 44, 523–535, https://doi.org/10.1046/j.1365-3091.1997.d01-38.x, 1997.

Krauss, L., Kappenberg, A., Zens, J., Kehl, M., Schulte, P., Zeeden, C., Eckmeier, E., and Lehmkuhl, F.: Reconstruction of Late Pleistocene paleoenvironments in southern Germany using two high-resolution loess-paleosol records, Palaeogeogr. Palaeocl., 509, 58–76, https://doi.org/10.1016/j.palaeo.2017.11.043, 2018.

Kukla G. J.: Pleistocene land-sea correlations. 1: Europe. Earth-Sci. Rev., 13, 307–374, https://doi.org/10.1016/0012-8252(77)90125-8, 1977.

Laag C., Hambach U., Zeeden C., Lagroix F., Guyodo Y., Veres V., Jovanović M., and Marković S. B.: A Detailed Paleoclimate Proxy Record for the Middle Danube Basin Over the Last 430 kyr: A Rock Magnetic and Colorimetric Study of the Zemun Loess-Paleosol Sequence, Front. Earth Sci., 9, 600086, https://doi.org/10.3389/feart.2021.600086, 2021.

Lehmkuhl, F., Zens, J., Krauß, L., Schulte, P., and Kels, H.: Loess-palaeosol sequences at the northern European loess belt in Germany: Distribution, geomorphology and stratigraphy, Quaternary Sci. Rev., 153, 11–30, https://doi.org/10.1016/j.quascirev.2016.10.008, 2016.

Lehmkuhl, F., Nett, J. J., Pötter, S., Schulte, P., Sprafke, T., Jary, Z., Antoine, P., Wacha, L., Wolf, D., Zerboni, A., Hošek, J., Marković, S. B., Obreht, I., Sümergi, P., Veres, D., Zeeden, C., Boemke, B., Schaubert, V., Viehweger, J., and Hambach, U.: Loess landscapes of Europe – Mapping, geomorphology, and zonal differentiation, Earth-Sci. Rev., 215, 103496, https://doi.org/10.1016/j.earscirev.2020.103496, 2021.

Li, B. and Li, S.-H.: Luminescence dating of K-feldspar from sediments: A protocol without anomalous fading correction, Quat. Geochronol, 6, 468–479, https://doi.org/10.1016/j.quageo.2011.05.001, 2011.

Li, Y., Tsukamoto, S., Frechen, M., and Gabriel, G.: Timing of fluvial sedimentation in the Upper Rhine Graben since the Middle Pleistocene: constraints from quartz and feldspar luminescence dating, Boreas, 47, 256–270, https://doi.org/10.1111/bor.12266, 2018.

Lisiecki, L. E. and Raymo, M. E.: A Pliocene-Pleistocene stack of 57 globally distributed benthic δ^{18}O records, Paleoceanography, 20, PA1003, https://doi.org/10.1029/2004PA001071, 2005.

Lowick, S. E., Trauerstein, M., and Preusser, F.: Testing the application of post IR-IRSL dating to fine grain waterlain sediments, Quat. Geochronol., 8, 33–40, https://doi.org/10.1016/j.quageo.2011.12.003, 2012.

Marković, S. B., Stevens, T., Kukla, G. J., Hambach, U., Fitzsimmons, K. E., Gibbard, P., Buggle, B., Zech, M., Guo, Z., Hao, Q., Wu, H., O'Hara Dhand, K., Smalley, I. J., Újvári, G., Sümegi, P., Timar-Gabor, A., Veres, D., Sirocko, F., Vasiljević, D. A., Jary, Z., Svensson, A., Jović, V., Lehmkuhl, F., Kovács, J., and Svirčev, Z.: Danube loess stratigraphy – Towards a pan-European loess stratigraphic model, Earth-Sci. Rev., 148, 228–258, https://doi.org/10.1016/j.earscirev.2015.06.005, 2015.

May, J.-H., Marx, S. K., Reynolds, W., Clark-Balzan, L., Jacobsen, G. E., and Preusser, F.: Establishing a chronological framework for a late Quaternary seasonal swamp in the Australian "Top End", Quat. Geochronol., 47, 81–92, https://doi.org/10.1016/j.quageo.2018.05.010, 2018.

Mercier, J.-L. and Jeser, N.: The glacial history of the Vosges Mountains, Developments in Quaternary Science, 2,113–118, https://doi.org/10.1016/S1571-0866(04)80061-7, 2004.

Meszner, S., Kreutzer, S., Fuchs, M., and Faust, D.: Late Pleistocene landscape dynamics in Saxony, Germany: Paleoenvironmental reconstruction using loess-paleosol sequences, Quatern. Int., 296, 94–107, https://doi.org/10.1016/j.quaint.2012.12.040, 2013.

Meyers, P. A. and Lallier-Verges, E.: Lacustrine sedimentary organic matter records of Late Quaternary paleoclimates, J. Paleolimnol., 21, 345–372, https://doi.org/10.1023/A:1008073732192, 1999.

Moine, O., Antoine, P., Hatté, C., Landais, A., Mathieu, J., Prud'homme, C., and Rousseau, D.-D.: The impact of Last Glacial climate variability in west-European loess revealed by radiocarbon dating of fossil earthworm granules, P. Natl. Acad. Sci. USA, 114, 6209–6214, https://doi.org/10.1073/pnas.1614751114, 2017.

Moska, P. and Bluszcz, A.: Luminescence dating of loess profiles in Poland, Quatern. Int., 296, 51–60, https://doi.org/10.1016/j.quaint.2012.09.004, 2013.

Necula, C., Dimofte, D., and Panaiotu, C.: Rock magnetism of a loess-palaeosol sequence from the western Black Sea shore (Romania), Geophys. J. Int., 202, 1733–1748, https://doi.org/10.1093/gji/ggv250, 2015.

Pécsi, M. and Richter, G.: Löss: Herkunft – Gliederung – Landschaften, Z. Geomorphol., N.F., Supplementband 98, Bornträger, Berlin & Stuttgart, 391 pp., ISBN 3-443-21098-8, 1996.

Prescott, J. R. and Hutton, J. T.: Cosmic ray contributions to dose rates for luminescence and ESR dating: Large depths and long-term time variations, Radiat. Meas., 23, 497–500, https://doi.org/10.1016/1350-4487(94)90086-8, 1994.

Preusser, F.: Towards a chronology of the Late Pleistocene in the northern Alpine Foreland, Boreas, 33, 195–210, https://doi.org/10.1111/j.1502-3885.2004.tb01141.x, 2004.

Preusser F. and Fiebig M.: European Middle Pleistocene loess chronostratigraphy: Some considerations based on evidence from the Wels site, Austria, Quatern. Int., 198, 37–45, https://doi.org/10.1016/j.quaint.2008.07.006, 2009.

Preusser, F., Drescher-Schneider, R., Fiebig, M., and Schlüchter, C.: Re-interpretation of the Meikirch pollen record, Swiss Alpine Foreland, and implications for Middle Pleistocene chronostratigraphy, J. Quaternary Sci., 20, 607–620, https://doi.org/10.1002/jqs.930, 2005.

Preusser, F., Graf, H. R., Keller, O., Krayss, E., and Schlüchter, C.: Quaternary glaciation history of northern Switzerland, E&G Quaternary Sci. J., 60, 21, https://doi.org/10.3285/eg.60.2-3.06, 2011.

Preusser, F., Büschelberger, M., Kemna, H. A., Miocic, J., Mueller, D., and May, J.-H.: Quaternary aggradation in the Upper Rhine Graben linked to the glaciation history of northern Switzerland, Int. J. Earth Sci., 110, 1827–1846, https://doi.org/10.1007/s00531-021-02043-7, 2021.

Qin, J., Chen, J., Li, Y., and Zhou, L.: Initial sensitivity change of K-feldspar pIRIR signals due to uncompensated decrease in electron trapping probability: evidence from radiofluorescence measurements, Radiat. Meas., 120, 131–136, https://doi.org/10.1016/j.radmeas.2018.06.017, 2018.

Rahimzadeh, N., Sprafke, T., Thiel, C., Terhorst, B., and Frechen, M.: A comparison of polymineral and K-feldspar post-infrared infrared stimulated luminescence ages of loess from Franconia, southern Germany, E&G Quaternary Sci. J., 70, 53–71, https://doi.org/10.5194/egqsj-70-53-2021, 2021.

Rees-Jones, J.: Optical Dating Of Young Sediments Using Fine-Grain Quartz, Ancient TL, 13, 9–14, 1995.

Richter, D., Richter, A., and Dornich, K.: Lexsyg smart – a luminescence detection system for dosimetry, material research and dating application, Geochronometria, 42, 202–209, https://doi.org/10.1515/geochr-2015-0022, 2015.

Roberts, H. M., Durcan, J. A., and Duller, G. A. T.: Exploring procedures for the rapid assessment of optically stimulated luminescence range-finder ages, Radiat. Meas., 44, 582–587, https://doi.org/10.1016/j.radmeas.2009.02.006, 2009.

Rodrigues, T., Alonso-García, M., Hodell, D. A., Rufino, M., Naughton, F., Grimalt, J. O., Voelker, A. H. L., and Abrantes, F.: A 1-Ma record of sea surface temperature and extreme cooling events in the North Atlantic: A perspective from the Iberian Margin, Quaternary Sci. Rev., 172, 118–130, https://doi.org/10.1016/j.quascirev.2017.07.004, 2017.

Rösner, U.: Die Mainfränkische Lößprovinz. Sedimentologische, pedologische und morphodynamische Prozesse der Lößbildung währenddes Pleistozäns in Mainfranken, Erlanger Geographische Arbeiten, 301 pp., 1990.

Schmidt, E. D., Frechen, M., Murray, A. S., Tsukamoto, S., and Bittmann, F.: Luminescence chronology of the loess record from the Tönchesberg section: A comparison of using quartz and feldspar as dosimeter to extend the age range beyond the Eemian, Quatern. Int., 234, 10–22, https://doi.org/10.1016/j.quaint.2010.07.012, 2011a.

Schmidt, E. D., Semmel, A., and Frechen, M.: Luminescence dating of the loess/palaeosol sequence at the gravel quarry Gaul/Weilbach, Southern Hesse (Germany), E&G Quaternary Sci. J., 60, 9, https://doi.org/10.3285/eg.60.1.08, 2011b.

Scholger, R. and Terhorst, B.: Magnetic excursions recorded in the Middle to Upper Pleistocene loess/palaeosol sequence Wels-Aschet (Austria), E&G Quaternary Sci. J., 62, 14–21, https://doi.org/10.3285/eg.62.1.02, 2013.

Schulte, P. and Lehmkuhl, F.: The difference of two laser diffraction patterns as an indicator for post-depositional grain size reduction in loess-paleosol sequences, Palaeogeogr. Palaeocl., 509, 126–136, https://doi.org/10.1016/j.palaeo.2017.02.022, 2018.

Schulte, P., Sprafke, T., Rodrigues, L., and Fitzsimmons, K. E.: Are fixed grain size ratios useful proxies for loess sedimentation dynamics? Experiences from Remizovka, Kazakhstan, Aeolian Res., 31, 131–140, https://doi.org/10.1016/j.aeolia.2017.09.002, 2018.

Schulze, T., Schwahn, L., Fülling, A., Zeeden, C., Preusser, F., and Sprafke, T.: Investigating the loess–palaeosol sequence of Bahlingen-Schönenberg (Kaiserstuhl), southwestern Germany, using a multi-methodological approach, E&G Quaternary Sci. J., 71, 145–162, https://doi.org/10.5194/egqsj-71-145-2022, 2022.

Semmel, A.: Studien über den Verlauf jungpleistozäner Formung in Hessen, Frankfurter geographische Hefte, 44, 1–133, 1968.

Semmel, A. and Fromm, K.: Ergebnisse paläomagnetischer Untersuchungen an quartären Sedimenten des Rhein-Main-Gebiets, E&G Quaternary Sci. J., 27, 18–25, https://doi.org/10.3285/eg.27.1.02, 1976.

Smedley, R. K., Duller, G. A. T., and Roberts, H. M.: Bleaching of the post-IR IRSL signal from individual grains of K-feldspar: Implications for single-grain dating, Radiat. Meas., 79, 33–42, https://doi.org/10.1016/j.radmeas.2015.06.003, 2015.

Sprafke, T.: Löss in Niederösterreich – Archiv quartärer Klima- und Landschaftsveränderungen, Würzburg University Press, https://doi.org/10.25972/WUP-978-3-95826-039-9, 2016.

Sprafke, T. and Obreht, I.: Loess: Rock, sediment or soil – What is missing for its definition?, Quatern. Int., 399, 198–207, https://doi.org/10.1016/j.quaint.2015.03.033, 2016.

Sprafke, T., Thiel, C., and Terhorst, B.: From micromorphology to palaeoenvironment: The MIS 10 to MIS 5 record in Paudorf (Lower Austria), Catena, 117, 60–72, https://doi.org/10.1016/j.catena.2013.06.024, 2014.

Sprafke, T., Schulte, P., Meyer-Heintze, S., Händel, M., Einwögerer, T., Simon, U., Peticka, R., Schäfer, C., Lehmkuhl, F., and Terhorst, B.: Paleoenvironments from robust loess stratigraphy using high-resolution color and grain-size data of the last glacial Krems-Wachtberg record (NE Austria), Quaternary Sci. Rev., 248, 106602, https://doi.org/10.1016/j.quascirev.2020.106602, 2020.

Stebich, M., Höfer, D., Mingram, J., Nowaczyk, N., Rohrmüller, J., Mrlina, J., and Kämpf, H.: A contribution towards the palynostratigraphical classification of the Middle Pleistocene in Central Europe: The pollen record of the Neualbenreuth Maar, north-eastern Bavaria (Germany), Quaternary Sci. Rev., 250, 106681, https://doi.org/10.1016/j.quascirev.2020.106681, 2020.

Stephan, H.-J.: Climato-stratigraphic subdivision of the Pleistocene in Schleswig-Holstein, Germany and adjoining areas: status and problems, E&G Quaternary Sci. J., 63, 3–18, https://doi.org/10.3285/eg.63.1.01, 2014.

Stojakowits P., Mayr C., Ivy-Ochs S., Preusser F., Reitner J., and Spötl C.: Environments at the MIS 3/2 transition in the northern Alps and their foreland, Quatern. Int., 581/582, 99–113, https://doi.org/10.1016/j.quaint.2020.08.003, 2021.

Strunk, H.: Das Quartärprofil von Hagelstadt im Bayerischen Tertiärhügelland, E&G Quaternary Sci. J., 40, 85–96, https://doi.org/10.3285/eg.40.1.06, 1990.

Terhorst, B.: Korrelation von mittelpleistozänen Löss-/Paläobodensequenzen in Oberösterreich mit einer marinen Sauerstoffisotopenkurve, E&G Quaternary Sci. J., 56, 172–185, https://doi.org/10.3285/eg.56.3.03, 2007.

Terhorst, B.: A stratigraphic concept for Middle Pleistocene Quaternary sequences in Upper Austria , E&G Quaternary Sci. J., 62, 4–13, https://doi.org/10.3285/eg.62.1.01, 2013.

Terhorst, B., Frechen, M., and Reitner, J.: Chronostratigraphische Ergebnisse aus Lößprofilen der Inn-und Traun-Hochterrassen in Oberösterreich, Z. Geomorphol., Supplementband, 127, 213–232, 2002.

Terhorst, B., Sedov, S., Sprafke, T., Peticzka, R., Meyer-Heintze, S., Kühn, P., and Solleiro Rebolledo, E.: Austrian MIS 3/2 loess–palaeosol records – Key sites along a west–east transect, Palaeogeogr. Palaeocl., 418, 43–56, https://doi.org/10.1016/j.palaeo.2014.10.020, 2015.

Thiel, C., Buylaert, J.-P., Murray, A. S., Terhorst, B., Hofer, I., Tsukamoto, S., and Frechen, M.: Luminescence dating of the Stratzing loess profile (Austria) – testing the potential of an elevated temperature post-IR IRSL protocol, Quatern. Int., 234, 23–31, https://doi.org/10.1016/j.quaint.2010.05.018, 2011a.

Thiel, C., Buylaert, J.-P., Murray, A. S., Terhorst, B., Tsukamoto, S., Frechen, M., and Sprafke, T.: Investigating the chronostratigraphy of prominent palaeosols in Lower Austria using post-IR IRSL dating, E&G Quaternary Sci. J., 60, 11, https://doi.org/10.3285/eg.60.1.10, 2011b.

Thiel, C., Terhorst, B., Jaburová, I., Buylaert, J. P., Murray, A. S., Fladerer, F. A., Damm, B., Frechen, M., and Ottner, F.: Sedimentation and erosion processes in Middle to Late Pleistocene sequences exposed in the brickyard of Langenlois/Lower Austria, Geomorphology, 135, 295–307, https://doi.org/10.1016/j.geomorph.2011.02.011, 2011c.

Thiel, C., Horvaìth, E., and Frechen, M.: Revisiting the loess/-palaeosol sequence in Paks, Hungary: A post-IR IRSL based chronology for the "Young Loess Series", Quatern. Int., 319, 88–98, https://doi.org/10.1016/j.quaint.2013.05.045, 2014.

Tucci, M., Krahn, K.J., Richter, D., van Kolfschoten, T., Rodríguez Álvarez, B., Verheijen, I., Serangeli, J., Lehmann, J., Degering, D., Schwalb, A., and Urban, B.: Evidence for the age and timing of environmental change associated with a Lower Palaeolithic site within the Middle Pleistocene Reinsdorf sequence of the Schöningen coal mine, Germany, Palaeogeogr. Palaeocl., 569, 110309, https://doi.org/10.1016/j.palaeo.2021.110309, 2021.

Vandenberghe, J.: Grain size of fine-grained windblown sediment: A powerful proxy for process identification, Earth-Sci. Rev., 121, 18–30, https://doi.org/10.1016/j.earscirev.2013.03.001, 2013.

Van Husen, D. and Reitner, J. M.: An Outline of the Quaternary Stratigraphy of Austria, E&G Quaternary Sci. J., 60, 24, https://doi.org/10.3285/eg.60.2-3.09, 2011.

Viscarra Rossel, R. A., Walvoort, D. J. J., McBratney, A. B., Janik, L.J., and Skjemstad, J. O.: Visible, near infrared, mid infrared or combined diffuse reflectance spectroscopy for simultaneous assessment of various soil properties, Geoderma, 131, 59–75, https://doi.org/10.1016/j.geoderma.2005.03.007, 2006.

Weidenfeller, M. and Knipping, M.: Correlation of Pleistocene sediments from boreholes in the Ludwigshafen area, western Heidelberg Basin, E&G Quaternary Sci. J., 57, 270–285, https://doi.org/10.3285/eg.57.3-4.1, 2009.

Wintle, A. G. and Murray, A. S.: A review of quartz optically stimulated luminescence characteristics and their relevance in single-aliquot regeneration dating protocols, Radiat. Meas., 41, 369–391, https://doi.org/10.1016/j.radmeas.2005.11.001, 2006.

Zander, A. and Hilgers, A.: Potential and limits of OSL, TT-OSL, IRSL and pIRIR$_{290}$ dating methods applied on a Middle Pleistocene sediment record of Lake El'gygytgyn, Russia, Clim. Past, 9, 719–733, https://doi.org/10.5194/cp-9-719-2013, 2013.

Zeeden, C. and Hambach, U.: Magnetic susceptibility properties of loess from the Willendorf archaeological site: Implications for the syn/post-depositional interpretation of magnetic fabric, Front. Earth Sci., 8, 599491, https://doi.org/10.3389/feart.2020.599491, 2021.

Zeeden, C., Kels, H., Hambach, U., Schulte, P., Protze, J., Eckmeier, E., Markovic, S. B., Klasen, N., and Lehmkuhl, F.: Three climatic cycles recorded in a loess-palaeosol sequence at Semlac (Romania) – Implications for dust accumulation in south-eastern Europe, Quaternary Sci. Rev., 154, 130–142, https://doi.org/10.1016/j.quascirev.2016.11.002, 2016.

Zeeden, C., Mir, J. A., Vinnepand, M., Laag, C., Rolf, C., and Dar, R. A.: Local mineral dust transported by varying wind intensities forms the main substrate for loess in Kashmir, E&G Quaternary Sci. J., 70, 191–195, https://doi.org/10.5194/egqsj-70-191-2021, 2021.

Zens, J., Schulte, P., Klasen, N., Krauß, L., Pirson, S., Burow, C., Brill, D., Eckmeier, E., Kels, H., Zeeden, C., Spagna, P., and Lehmkuhl, F.: OSL chronologies of paleoenvironmental dynamics recorded by loess-paleosol sequences from Europe: Case studies from the Rhine-Meuse area and the Neckar Basin, Palaeogeogr. Palaeocl, 509, 105–125, https://doi.org/10.1016/j.palaeo.2017.07.019, 2018.

Zhang, J.: Behavior of the electron trapping probability change in IRSL dating of K-feldspar: A dose recovery study, Quat. Geochronol., 44, 38–46, https://doi.org/10.1016/j.quageo.2017.12.001, 2018.

Zhang, J. and Li, S.-H.: Review of the Post-IR IRSL Dating Protocols of K-Feldspar, Methods Protoc., 3, 7, https://doi.org/10.3390/mps3010007, 2020.

Zöller, L., Stremme, H., and Wagner, G.A.: Thermolumineszenz-Datierung an Löss-Paläoboden-Sequenzen von Nieder-, Mittel- und Oberrhein/Bundesrepublik Deutschland, Chem. Geol., 73, 39–62, https://doi.org/10.1016/0168-9622(88)90020-6, 1988.

Zöller, L., Fischer, M., Jary, Z., Antoine, P., and Krawczyk, M.: Chronostratigraphic and geomorphologic challenges of last glacial loess in Poland in the light of new luminescence ages, E&G Quaternary Sci. J., 71, 59–81, https://doi.org/10.5194/egqsj-71-59-2022, 2022.

E&G Quaternary Sci. J., 71, 243–247, 2022
https://doi.org/10.5194/egqsj-71-243-2022

Open Access E&G Quaternary Science Journal

Express report

A new Google Earth Engine tool for spaceborne detection of buried palaeogeographical features – examples from the Nile Delta (Egypt)

Tobias Ullmann[1,2], **Eric Möller**[2], **Roland Baumhauer**[2], **Eva Lange-Athinodorou**[3], **and Julia Meister**[2]

[1]Remote Sensing, Institute of Geography and Geology, University of Würzburg, 97074 Würzburg, Germany
[2]Physical Geography, Institute of Geography and Geology, University of Würzburg, 97074 Würzburg, Germany
[3]Institute of Egyptology, University of Würzburg, 97070 Würzburg, Germany

Correspondence: Tobias Ullmann (tobias.ullmann@uni-wuerzburg.de)
and Julia Meister (julia.meister@uni-wuerzburg.de)

Relevant dates: Received: 27 July 2022 – Revised: 12 October 2022 – Accepted: 27 October 2022 –
Published: 18 November 2022

How to cite: Ullmann, T., Möller, E., Baumhauer, R., Lange-Athinodorou, E., and Meister, J.: A new Google Earth Engine tool for spaceborne detection of buried palaeogeographical features – examples from the Nile Delta (Egypt), E&G Quaternary Sci. J., 71, 243–247, https://doi.org/10.5194/egqsj-71-243-2022, 2022.

1 Introduction

With the opening of the Landsat archive in 2002, the largest remote sensing archive became available to the public (Wulder et al., 2012). This record presents the most comprehensive civil database on the Earth's surface, and it has stimulated research across the globe for many disciplines (Wulder et al., 2016). Several spaceborne remote sensing missions have since then been launched (Belward and Skøien, 2015), some of them operating now for more than 20 years, such as the highly successful missions carrying the MODIS instrument. Furthermore, recent spaceborne earth observation missions not only continue the building of global remote sensing archives using various sensors but also significantly increased the temporal and spatial resolution (e.g. the Sentinel-2 mission), allowing the dynamics of the Earth to be studied at so far unprecedented spatio-temporal resolution on a global scale. These datasets have also contributed to the field of geomorphology and geoarchaeology. Exemplarily, Brandolini et al. (2021) and Orengo and Petrie (2017) used time series of the Sentinel-2 or Landsat mission to infer and map differences in soil and moisture properties related to historic or palaeogeographical features. Further, Ullmann et al. (2020) have investigated long-term differences in the normalized difference water index (NDWI) in the Nile Delta to map buried palaeogeographical features, i.e. related to former river branches of the Nile, or buried Pleistocene sand hills ("geziras") often used as settlement mounts. While these archives and datasets certainly offer new opportunities, the handling and analyses come with challenges, most strikingly arising from the enormous data load and the high computing effort. Fortunately, some of these limitations can be overcome by recently available cloud-computing capacities, exemplary offered by the Google Earth Engine (GEE) (Gorelick et al., 2017). These capacities allow processing and analysing large stacks of earth observation data in a cloud environment in a very fast and efficient manner without the need of downloading and processing the raw data. To make these new developments applicable for users with less experience in remote sensing, we present here a freely available GEE tool that allows the processing of remote sensing archive data from Landsat, MODIS, and Sentinel-2 in a user-friendly way. The tool is based on the GEE efforts of previous research (Ullmann et al., 2020) but provides an improved and ready-to-use browser-based application that is suitable for users who are less familiar with GEE. In this contribution, we exemplarily show the processing results of the tool for the entire Nile Delta for Landsat, MODIS, and Sentinel-2 and continue mapping buried palaeogeographical features using the long-term differences in NDWI (see Ullmann et al., 2020).

2 Study area

The Egyptian Nile Delta covers about 24 000 km^2 and is the largest delta of the Mediterranean Sea. Historic textual sources witness up to seven major Nile branches that flowed through the delta, while today only the Rosetta and Damietta branches exist (Fig. 1; Bietak, 1975). In antiquity, these waterways were of high significance for intra-Egyptian trade and traffic, and major ancient Egyptian cities are exclusively found in their immediate surroundings. Hence, the reconstruction of the Holocene delta environments is also crucial for studying the human–environment interactions of ancient Egypt (Butzer, 1976; Pennington et al., 2017; Bietak, 1975). For protection against the seasonal Nile floods, settlements were either built on Pleistocene sand mounds (“geziras”) or on the embankments of the river branches. However, due to the long-term dynamics of the riverine system, the landscape of the Nile Delta has constantly changed. Water courses have been silted up and are no longer visible in the modern landscape. Knowing about the importance of localizing the route of former Nile branches, several geophysical and geoarchaeological investigations were carried out in the past, of which some also rely on remotely sensed imagery, e.g. Ginau et al. (2017) and El-Fadaly et al. (2019).

3 Material and methods

In continuation of these efforts, the processing of remote sensing time series of Landsat (including Landsat 9 and Collection 2 data), Sentinel-2 and MODIS was conducted using the cloud-based processing capacities of the GEE. For this purpose, we developed a script which allows the generation of cloud-free surface reflectance products and various spectral indices for a user-defined period, region of interest, and for the earth observation data of the respective sensors. The source code of this tool is freely available on GitHub (https://github.com/EricMoeller96/master_thesis, last access: 9 November 2022) and comes with documentation on the most important settings. The tool requires a minimum of user inputs for the execution and can be executed for a user-defined region. Exemplarily, the datasets, specified in Table 1, were processed to generate median RBG composites for the entire Nile Delta (Fig. 1). In addition, multispectral indices, such as the normalized difference vegetation index (NDVI), NDWI (Gao, 1996), and normalized difference snow index (NDSI), are calculated and processed by default. Following the approach presented in a preceding work (Ullmann et al., 2020), in this study we exemplarily focus on two median NDWI images which were calculated from the time series: one for the winter (January/February) and one for the summer (July/August) seasons and for each sensor. These NDWI images were then differenced (summer minus winter) to draw the long-term seasonal difference (ΔNDWI; Fig. 2).

4 First results and discussion

The GEE script allows cloud-free summer and winter mosaics to be processed for the entire Nile Delta in a fast manner and for all sensors (Fig. 1) using analysis-ready products (i.e. surface reflectance). Processing time in the GEE was about 10 to 30 min, which would not be achievable using standard computing facilities given the high number of scenes (e.g. more than 1900 scenes for Landsat).

Thus, the analyses are not limited to the spectral indices, but the multispectral information can also be utilized, which opens possibilities for further investigations apart from the differentiation of spectral indices, e.g time series analysis or land cover classification. The ΔNDWI images of all three sensors show corresponding positive and negative anomalies on the broadest scale (Fig. 2), which follow the general systematic outlined in Ullmann et al. (2020). As such, the largest and strongest anomalies likely display distinctive features of the general (palaeo-)environmental setting as sketched by Butzer (1976). For instance, strong negative anomalies of the ΔNDWI somewhat match the proposed location of sands at or near the surface at several locations between the modern course of the Rosetta and the Damietta branches and between Tanta and Cairo. In all datasets negative ΔNDWI values are found in the western Nile Delta (south of Alexandria and west of Damanhur), the central Nile Delta (south of Tanta towards Cairo), and in the northern Nile Delta (in the vicinity of Lake Burullus). Positive ΔNDWI values are less frequent, and the largest patches are found near Lake Burullus (north) and Lake Manzala (east). Obviously, the higher spatial resolution of Landsat and Sentinel-2 allows a more detailed picture to be depicted; in both datasets spatially varying positive and negative anomalies are found in the delta west of the Rosetta branch. Overall, Sentinel-2 data deliver a better geometric resolution revealing more details (e.g. as exemplified for Geziret Sineita in Fig. 2d–f); however, due to the rather short time series of 4 years (compared to 36 years offered by Landsat), anomalies are less clear, and the ΔNDWI image shows more heterogeneities compared to the results of Landsat. This is also displayed by the higher deviation used to scale the ΔNDWI images (Fig. 2). It is likely that this issue is linked to the short time series as seasonal differences in NDWI become best visible when long timescales are analysed (Ullmann et al., 2020). As such, a long observation

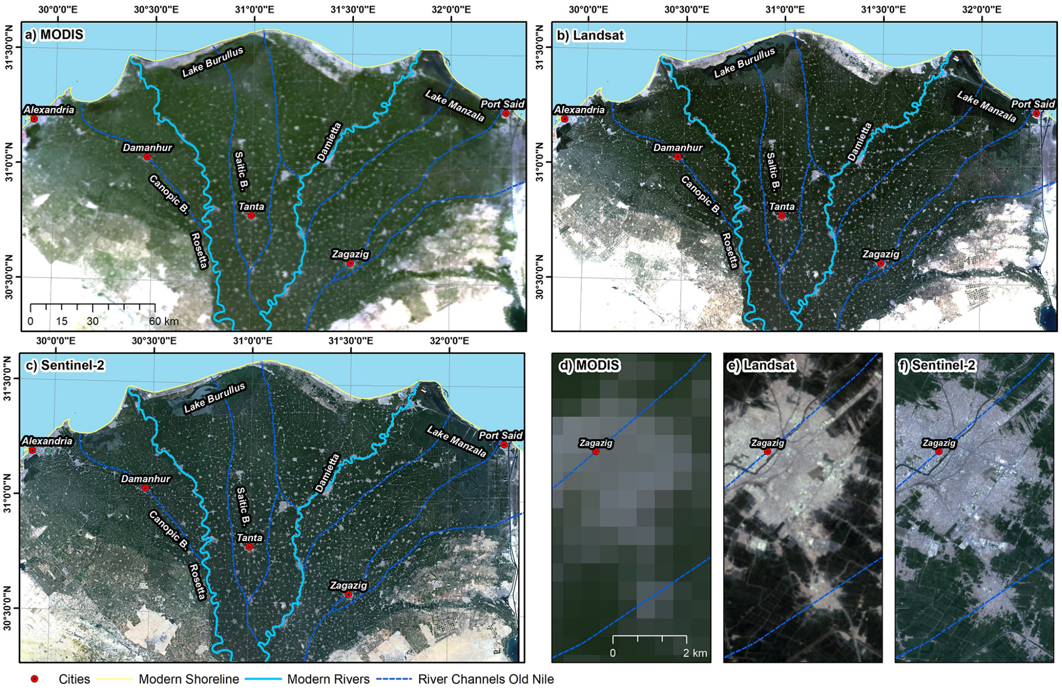

Figure 1. Comparison of cloud-free summer (July/August) median RGB composites of the Nile Delta: **(a)** MODIS (2001–2021), **(b)** Landsat (1985–2021), **(c)** Sentinel-2 (2017–2021), and **(d–f)** detailed views of the city of Zagazig. Ancient river channels of the Nile are drawn according to Pennington et al. (2017).

Table 1. Overview of investigated remote sensing datasets which were processed using the Google Earth Engine. Bands refer to B = blue, G = green, R = red, NIR = near infrared, and SWIR = short-wave infrared. Multispectral indices and products are as follows: NDVI = normalized difference vegetation index, NDWI = normalized difference water index, NDSI = normalized difference snow index, NBR = normalized burn ratio, and LST = land surface temperature. Composites of each band, index, and product were generated using the median operator; as such, a pixel shows the median value over the entire stack of all cloud-free acquisitions within the period of investigation.

Mission	Resampled geometric resolution (m)	Bands	Multispectral indices and products	Period of investigation	Number of images
MODIS	500	B, G, R, NIR1, NIR2, SWIR1, SWIR2	NDVI, NDWI, NBR, NDSI, LST	January/February 2001 to 2021	1240
MODIS	500	B, G, R, NIR1, NIR2, SWIR1, SWIR2	NDVI, NDWI, NBR, NDSI, LST	July/August 2001 to 2021	1363
Landsat	30	B, G, R, NIR, SWIR1, SWIR2	NDVI, NDWI, NBR, NDSI	January/February 1985 to 2021	620
Landsat	30	B, G, R, NIR, SWIR1, SWIR2	NDVI, NDWI, NBR, NDSI	July/August 1985 to 2021	1310
Sentinel-2	20	B, G, R, Red Edge 1, Red Edge 2, Red Edge 3, NIR, Red Edge 4, SWIR1, SWIR2	NDVI, NDWI, NBR, NDSI	January/February 2017 to 2021	412
Sentinel-2	20	B, G, R, Red Edge 1, Red Edge 2, Red Edge 3, NIR, Red Edge 4, SWIR1, SWIR2	NDVI, NDWI, NBR, NDSI	July/August 2017 to 2021	814

period is important to identify rather weak anomalies in the ΔNDWI. Thus for now, the Landsat archive appears to be the most useful and promising record for identifying ΔNDWI anomalies associated with surface and near-surface discontinuities in soil properties. Taking this further, Fig. 3 shows preliminary results from the continued mapping efforts. The visual analysis of the Landsat ΔNDWI revealed several additional linear and meandering anomalies, especially between Damanhur and Tanta and in the surroundings of Zagazig. Some of them correspond remarkably well with the general

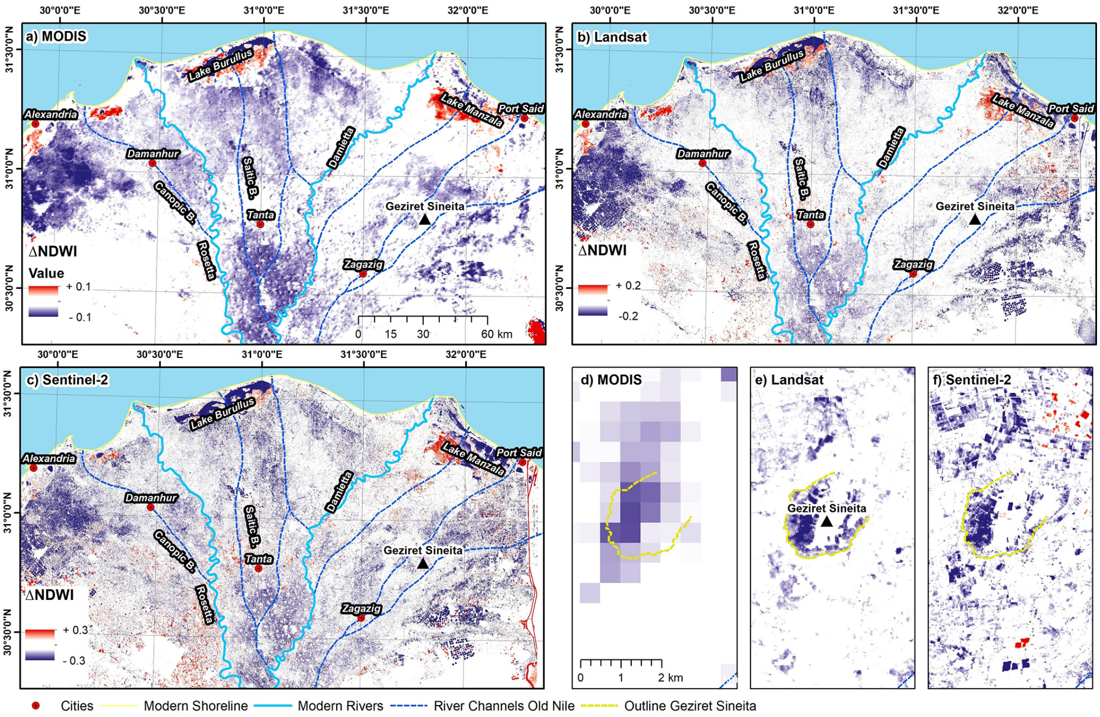

Figure 2. Comparison of ΔNDWI anomalies of the Nile Delta: **(a)** MODIS (2001–2021), **(b)** Landsat (1985–2021), **(c)** Sentinel-2 (2017–2021), and **(d–f)** detailed views of Geziret Sineita (Tell es-Sunayta) (see van den Brink, 1987). Ancient river channels of the Nile are drawn according to Pennington et al. (2017).

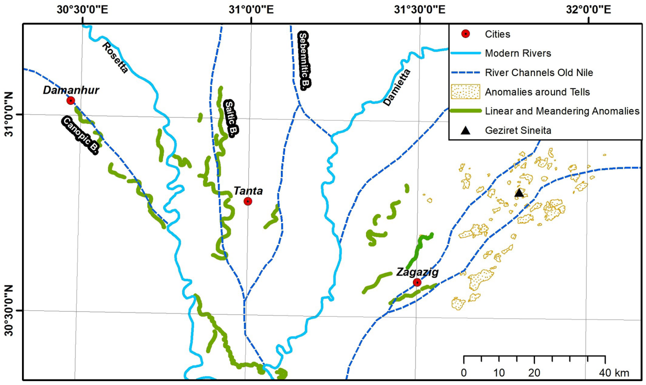

Figure 3. Preliminary mapping results of ΔNDWI anomalies in the central Nile Delta based on Landsat imagery (1985–2021). Ancient river channels of the Nile are drawn according to Pennington et al. (2017).

flow directions and river routes indicated by Pennington et al. (2017). These anomalies could therefore indicate former courses of the Canopic Branch and Saitic Branch.

5 Conclusion

The increased number and availability of spaceborne remote sensing records, their enhanced spatio-temporal resolution, and latest cloud-based processing capacities open new opportunities to study the nature and dynamics of the land surface on a local to global scale. This opens opportunities in the field of geomorphology and geoarchaeology, e.g. in the context of landscape archaeology. In the present contribution, we highlight as an example the application of a freely available Google Earth Engine (GEE) tool to process cloud-free composites for the Nile Delta using the archives of MODIS, Landsat, and Sentinel-2. Following a preliminary approach, seasonal differences in the NDWI were investigated and interpreted in the context of buried palaeogeographical features. Among the investigated data, the Landsat archive offers the most promising record to identify spectral anomalies related to surface and surficial discontinuities of soil and land properties. Given the global availability of remote sensing data from Sentinel-2, Landsat, and MODIS, as well as the capacities that arise from the Google Earth Engine, a transfer to other sites with similar environmental conditions (e.g. continuous rather that homogeneous land cover) seems certainly feasible and of interest for future investigations.

Code and data availability. Data relating to this paper are available from the corresponding authors upon reasonable request. The Google Earth Engine code is available at https://doi.org/10.5281/zenodo.7313130 (EricMoeller96, 2022).

Author contributions. The methodology was developed by TU and EM. The formal analysis was conducted by TU and EM. TU, EM, RB, ELA and JM interpreted the results jointly. Funding was acquired by TU and JM. The manuscript was prepared by TU and JM with contributions from all authors.

Competing interests. At least one of the (co-)authors is a member of the editorial board of *E&G Quaternary Science Journal*. The peer-review process was guided by an independent editor, and the authors also have no other competing interests to declare.

Special issue statement. This article is part of the special issue "Quaternary research from and inspired by the first virtual DEUQUA conference". It is a result of the vDEUQUA2021 online conference in September/October 2021.

Acknowledgements. We are grateful to Janek Walk for providing valuable feedback.

Financial support. This research has been supported by the Deutsche Forschungsgemeinschaft (DFG, German Research Foundation; grant no. 507687060).

This open-access publication was funded by
Julius-Maximilians-Universität Würzburg.

Review statement. This paper was edited by Christian Zeeden and reviewed by Janek Walk.

References

Belward, A. S. and Skøien, J. O.: Who launched what, when and why; trends in global land-cover observation capacity from civilian earth observation satellites, ISPRS J. Photogramm., 103, 115–128, https://doi.org/10.1016/j.isprsjprs.2014.03.009, 2015.

Bietak, M.: Tell El-Dab'a II: Der Fundort im Rahmen einer archäologisch-geographischen Untersuchung über das ägyptische Ostdelta, in: Untersuchungen der Zweigstelle Kairo des Österreichischen Archäologischen Instituts, Verlag der Österreichischen Akademie der Wissenaschaften, Wien, 236 pp., ISBN 978-3-7001-0136-9, 1975.

Brandolini, F., Domingo-Ribas, G., Zerboni, A., and Turner, S.: A Google Earth Engine-enabled Python approach for the identification of anthropogenic palaeo-landscape features, Open Res Europe, 1, 22, https://doi.org/10.12688/openreseurope.13135.2, 2021.

Butzer, K. W.: Early hydraulic civilization in Egypt: a study in cultural ecology, University of Chicago Press, Chicago, 134 pp., ISBN: 0-226-08634-8, 1976.

El-Fadaly, A., Abouarab, M. A. R., El Shabrawy, R. R. M., Mostafa, W., Wilson, P., Morhange, C., Silverstein, J., and Lasaponara, R.: Discovering Potential Settlement Areas around Archaeological Tells Using the Integration between Historic Topographic Maps, Optical, and Radar Data in the Northern Nile Delta, Egypt, Remote Sens., 11, 3039, https://doi.org/10.3390/rs11243039, 2019.

EricMoeller96: EricMoeller96/master_thesis: Script_by_Eric_Moeller_v6, Version V6, Zenodo [code], https://doi.org/10.5281/zenodo.7313130, 2022.

Gao, B.: NDWI–A normalized difference water index for remote sensing of vegetation liquid water from space, Remote Sens. Environ., 58, 257–266, https://doi.org/10.1016/S0034-4257(96)00067-3, 1996.

Ginau, A., Schiestl, R., Kern, F., and Wunderlich, J.: Identification of historic landscape features and settlement mounds in the Western Nile Delta by means of remote sensing time series analysis and the evaluation of vegetation characteristics, Journal of Archaeological Science: Reports, 16, 170–184, https://doi.org/10.1016/j.jasrep.2017.09.034, 2017.

Gorelick, N., Hancher, M., Dixon, M., Ilyushchenko, S., Thau, D., and Moore, R.: Google Earth Engine: Planetary-scale geospatial analysis for everyone, Remote Sens. Environ., 202, 18–27, https://doi.org/10.1016/j.rse.2017.06.031, 2017.

Orengo, H. and Petrie, C.: Large-Scale, Multi-Temporal Remote Sensing of Palaeo-River Networks: A Case Study from Northwest India and its Implications for the Indus Civilisation, Remote Sens., 9, 735, https://doi.org/10.3390/rs9070735, 2017.

Pennington, B. T., Sturt, F., Wilson, P., Rowland, J., and Brown, A. G.: The fluvial evolution of the Holocene Nile Delta, Quaternary Sci. Rev., 170, 212–231, https://doi.org/10.1016/j.quascirev.2017.06.017, 2017.

Ullmann, T., Nill, L., Schiestl, R., Trappe, J., Lange-Athinodorou, E., Baumhauer, R., and Meister, J.: Mapping buried paleogeographical features of the Nile Delta (Egypt) using the Landsat archive, E&G Quaternary Sci. J., 69, 225–245, https://doi.org/10.5194/egqsj-69-225-2020, 2020.

van den Brink, E. C. M.: A Geo-Archaeological Survey in the North-Eastern Nile Delta, Egypt; the First Two Seasons, a Preliminary Report, Mitteilungen des Deutschen Archäologischen Instituts, Abteilung Kairo, 43, 7–31, 1987.

Wulder, M. A., Masek, J. G., Cohen, W. B., Loveland, T. R., and Woodcock, C. E.: Opening the archive: How free data has enabled the science and monitoring promise of Landsat, Remote Sens. Environ., 122, 2–10, https://doi.org/10.1016/j.rse.2012.01.010, 2012.

Wulder, M. A., White, J. C., Loveland, T. R., Woodcock, C. E., Belward, A. S., Cohen, W. B., Fosnight, E. A., Shaw, J., Masek, J. G., and Roy, D. P.: The global Landsat archive: Status, consolidation, and direction, Remote Sens. Environ., 185, 271–283, https://doi.org/10.1016/j.rse.2015.11.032, 2016.

E&G Quaternary Sci. J., 71, 227–241, 2022
https://doi.org/10.5194/egqsj-71-227-2022

Open Access E&G Quaternary Science Journal

Research article

Comparison of bulk and sequential sampling methodologies on mammoth tooth enamel and their implications in paleoenvironmental reconstructions

Zuorui Liu[1], **Amy Prendergast**[1], **Russell Drysdale**[1], **and Jan-Hendrik May**[1,2]

[1]School of Geography, Earth and Atmospheric Sciences (SGEAS), University of Melbourne, Melbourne, VIC, Australia
[2]GeoQuest Research Centre, School of Earth, Atmospheric and Life Sciences, University of Wollongong, Wollongong, NSW, Australia

Correspondence: Zuorui Liu (zuoruil@student.unimelb.edu.au), Amy Prendergast (amy.prendergast@unimelb.edu.au), and Jan-Hendrik May (janhendrikmay@unimelb.edu.au)

Relevant dates: Received: 29 March 2022 – Revised: 18 August 2022 – Accepted: 30 August 2022 – Published: 30 September 2022

How to cite: Liu, Z., Prendergast, A., Drysdale, R., and May, J.-H.: Comparison of bulk and sequential sampling methodologies on mammoth tooth enamel and their implications in paleoenvironmental reconstructions, E&G Quaternary Sci. J., 71, 227–241, https://doi.org/10.5194/egqsj-71-227-2022, 2022.

Abstract: Mammoth teeth have been widely investigated using stable-isotopic analysis for paleoenvironmental and paleoecological reconstructions due to their large size and frequent discoveries. Many past investigations sampled the tooth enamel with the “bulk” method, which involves drilling one sample from the occlusal surface to the root for each tooth. Some of the more recent studies applied the “sequential” method, with a sequence of samples drilled following the dominant enamel growth direction to produce a time series of isotopic oscillations that reflects high-resolution environmental changes, as well as changes in mammoth dietary behavior. Although both the bulk and mean sequential $\delta^{18}O$ values are expected to represent the averaged signal over the time of tooth formation, it is uncertain whether their paleoenvironmental records were formed during similar periods of time. In this study, we applied both sampling methods (sequential drilling first followed by a thin layer of bulk drilling) on the same enamel ridges of multiple mammoth teeth and compared their respective $\delta^{18}O$ values. The results indicated that, in most enamel ridges, the bulk samples have more negative $\delta^{18}O$ values compared to the average sequential values, and some of the bulk values even fall outside the range of sequential values. The most likely explanation for the differences is the structure and formation stages of enamel that caused uneven distributions of different seasons recorded in the samples. This finding provides insights into current limitations of the two sampling methods and the applicability of cross-method data comparison from past studies.

Kurzfassung: Aufgrund ihrer relativen Fundhäufigkeit und Grösse werden Mammuthmolare vielfach für paläoökologische Zwecke und Umweltrekonstruktionen mit Hilfe von stabilen Isotopen herangezogen. Bei vielen der bislang publizierten Arbeiten wurde dabei Zahnschmelz mit der “Bulk”-Methode beprobt, bei der für jeden Zahn eine einzelne Probe von der Kaufläche bis zur Wurzel gebohrt wird. Neuere Studien wenden nun die “sequenzielle” Methode an, bei der eine Reihe von Proben entlang der Hauptwachstumsrichtung des Zahnschmelzes gebohrt wird, um die Variation der Isotopenwerte über die Zeit zu bestimmen, welche sowohl hochauflösende Umweltveränderungen als auch Veränderungen im Ernährungsverhalten der Mammuts widerspiegeln kann. Obwohl sowohl “Bulk”- als auch die gemittelten sequenziellen δ^{18}O-Werte ein zeitlich gemitteltes Signal der Zahnbildung repräsentieren sollten, ist bislang nicht klar, inwieweit diese Werte tatsächlich den selben, direkt vergleichbaren Zeitraum wiederspiegeln. In dieser Studie haben wir beide Methoden der Probenahme (zuerst sequenzielle Proben, dann eine dünne Schicht von “Bulk”-Proben) an denselben Schmelzkämmen mehrerer Mammutzähne angewandt und ihre jeweiligen δ^{18}O-Werte verglichen. Die Ergebnisse zeigen, dass in den meisten Schmelzkämmen die “Bulk”-Proben im Vergleich zu den mittleren sequenziellen Werten negativere δ^{18}O-Werte aufweisen, und einige der “Bulk”-Werte sogar außerhalb der Variationsbreite der sequenziellen Werte liegen. Die wahrscheinlichste Erklärung für diese Unterschiede liegt in der Struktur sowie den Bildungsraten und -stadien des Zahnschmelzes, welche eine ungleichmäßige Verteilung der verschiedenen in den Proben erfassten Jahreszeiten verursachen. Die Ergebnisse geben Einblick in die derzeitigen Grenzen der beiden Probenahmeverfahren und ermöglichen damit einen kritischeren und verbesserten methoden-übergreifenden Datenvergleich.

1 Introduction

Stable-isotopic analysis on mineralized tissues of animals has added great knowledge to our understanding of past environments and climates. Among all the animal tissues, Pleistocene mammoth teeth and tusks are of special interest for paleoenvironmental and paleoclimatic reconstructions over the past decades due to their large size and frequent discoveries. Oxygen-isotope ratios in mammoths can represent their surrounding environmental properties because they are directly related to the isotopic ratios of their ingested environmental water, which in turn primarily reflects regional temperature and water balance (Dansgaard, 1964; Longinelli, 1984; Luz et al., 1984). Previous studies of oxygen isotopes in mammoth remains have provided paleoenvironmental records in Europe and North America from Marine Isotope Stage (MIS) 5 to MIS 2 (130–22 ka cal BP). In most previous studies, the sampling method has been drilling one “bulk” sample from each tooth from the occlusal surface to the root (Genoni et al., 1998; Tütken et al., 2007; Ukkonen et al., 2007; Iacumin et al., 2010; Kovács et al., 2012; Pryor et al., 2013). The purpose of bulk sampling is to try to cover the longest possible period of time of tooth formation (Pryor et al., 2013), as the sample should represent an averaged isotopic signal across the tooth formation time (Fricke and O’Neil, 1996; Sharp and Cerling, 1998; Hoppe, 2004). Although this method can effectively reconstruct the averaged paleoclimatic conditions over several years, the temporal resolution of reconstruction is limited to decadal scale, and consequently, a very small amount of data exist on sub-annual environmental conditions and climatic variations during the Quaternary from these regions. Such data, however, are crucial in understanding how the highly variable climate of the Late Pleistocene translated into regional- to local-scale environmental conditions, ultimately affecting a range of animal–environmental and human–environmental interactions (Denton et al., 2005; Bradtmöller et al., 2012; Prendergast and Schöne, 2017; Prendergast et al., 2018).

To address this issue, a “sequential” approach has also been applied to mammoth and isotope research in some studies (Koch et al., 1989; Fisher and Fox, 2007; Metcalfe and Longstaffe, 2012; Widga et al., 2021; Wooller et al., 2021). Like most mammal species, mammoth tooth enamel has a dominant growth direction from the occlusal surface to the roots at a relatively constant rate (Metcalfe and Longstaffe, 2012). Therefore, it has the potential to yield highly resolved time series of paleoenvironmental information over the course of tooth formation. In several recent studies, multiple sequential samples were drilled from the same mammoth tooth following its growth direction with a resolution up to 1mm per sample, forming a time series of isotopic oscillations that likely reflects paleoenvironmental changes at sub-annual scales (Metcalfe and Longstaffe, 2012; Wooller et al., 2021; Miller et al., 2022). The mean value of the sequential samples should therefore reflect the averaged isotopic signal during the period of time of tooth growth, which is also what the bulk sample is expected to represent. However, this remains untested, and it is unknown whether the mean sequential value and the bulk value obtained from the same mammoth tooth yield similar isotopic compositions, as well as whether they have recorded the environmental properties during approximately the same period of time. Due to this limitation, it is still uncertain whether isotopic results obtained from bulk and sequential sampling methods can be directly compared, interpreted, and used for paleoenvironmental reconstruction.

In this study, we explored the potential differences between the sequential and the traditional bulk sampling methods. We obtained four mammoth teeth of MIS 3 age from southwestern Germany and applied both sampling methods on each tooth. The bulk and average sequential δ^{18}O values from the same tooth were then compared.

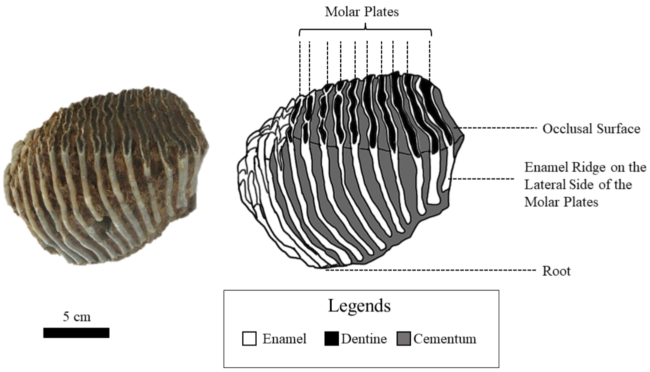

Figure 1. A photograph and its corresponding schematic diagram of a mammoth molar tooth used in this study (UW-1).

2 Background

2.1 Mammoth tooth growth

Similar to modern elephants, the woolly mammoths (*Mammuthus primigenius*) had six sets of teeth and a total number of 24 molar teeth throughout their lifespan. At any one time only one tooth was fully in operation in each of the four jaws (Maschenko, 2002; Lister and Bahn, 2007). Each molar tooth of *M. primigenius* is a combination of 22–24 molar plates (Lister and Bahn, 2007), which are flat thin sections of dentine folded in enamel. Each molar plate is adhered by cementum (Ferretti, 2003). The apex of these molar plates forms the occlusal surface for grinding food, and their lateral outer surface is exposed, forming separate enamel ridges (Fig. 1).

Within each molar plate, mammoth tooth enamel has primary and secondary stages of formation (Smith, 1998; Smith and Tafforeau, 2008). During the secretory (primary) stage, daily incremental features grow from the enamel-dentine junction (EDJ) to the outermost surface, and these incremental lines are parallel to the EDJ under microscopic view (Metcalfe and Longstaffe, 2012). Tooth increments formed during the primary stage take up only about 20 %–30 % of the entire enamel weight (Passey and Cerling, 2002; Passey et al., 2005). The maturation (secondary) stage starts after the secretory stage ends, and it takes up most enamel weight and formation time (approximately two-thirds of total formation time) (Smith, 1998). During this stage, enamel formation starts at the apex (occlusal surface) near the EDJ side, growing dominantly along the tooth height to the root while extending to the outermost surface simultaneously. Secondary daily incremental features captured by microscopic analysis indicated that enamel growth direction is inclined at an angle of 55–60° to the EDJ (Metcalfe and Longstaffe, 2012).

2.2 Oxygen isotopes and mammoth water source

Oxygen isotopic composition in animal bioapatite can be used as an indicator of past climates and environmental conditions. For large-sized homeothermic animals (animals which can keep a constant body temperature) such as the mammoths, the δ^{18}O values in their enamel carbonate are solely determined by the δ^{18}O values in their body water (Longinelli, 1984; Luz et al., 1984). Mammoths were obligate drinkers, with more than two-thirds of their body water being obtained from direct consumption of environmental water (Koch et al., 1989; Ayliffe et al., 1992). Therefore, their body water δ^{18}O values directly reflect those in their ingested environmental water, which are in turn primarily controlled by local- to regional-scale environmental factors such as discharge, precipitation, and air temperature (Dansgaard, 1964). A cyclicity of oxygen isotopic variations is expected from the sequentially drilled mammoth enamel samples, since they should reflect regional surface water δ^{18}O values, and nearly all natural water bodies, including streams, estuaries, and lakes, experience seasonal oscillations of δ^{18}O values due to seasonally differing water balances (Rozanski et al., 2001; Theakstone, 2003). The surface water isotopic content of any given water body is determined by the isotopic composition and amount of its water sources (input), as well as those of the water output (Rozanski et al., 2001; Benson and Paillet, 2002). In the context of the late Pleistocene Rhine River catchment (Fig. 2), the main input water sources for the catchment would have included groundwater, precipitation sourced from the Atlantic ocean, and snow and glacier melt, and output is primarily runoff and evaporation. These input water sources have different effects on the δ^{18}O values in surface water. Glacier and snow meltwater usually have the most depleted ^{18}O/^{16}O ratio (Theakstone, 2003), and the ^{18}O/^{16}O ratio in precipitation and groundwater is usually more enriched than surface water (Theakstone, 2003; Yeh and Lee, 2018; Bedaso and Wu, 2021). We also analyzed modern hydrological data of the Rhine River (for the period 2005–2010 at Lobith, Netherlands) to better constrain the mechanism of isotopic oscillations. In the modern Rhine River, δ^{18}O values show seasonal variations, with δ^{18}O values being approximately 1 ‰ more negative during summer than in winter months (Rozanski et al., 2001). Under interglacial (Holocene) climatic conditions, the summer ^{18}O/^{16}O depletion is caused by increased contributions of meltwater from alpine glaciers (Rozanski et al., 2001). Therefore, in the sequential δ^{18}O records from the mammoth teeth, local troughs (minima) in a curve are expected to correspond to the summer months when glacier melt is highest, and local peaks (maxima) are the coldest winter month. A cycle of isotopic variation should thus closely approximate the range of climatic variability throughout a year, with the distance between two neighboring maxima (or minima) corresponding to one "hydrological year" of tooth growth (Metcalfe and Longstaffe, 2012; Prendergast and Schöne, 2017).

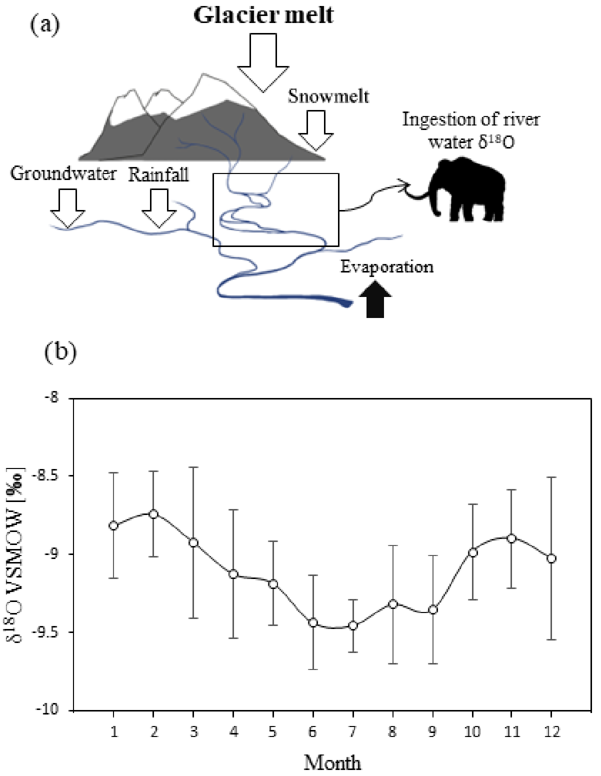

Figure 2. (a) A schematic diagram of mammoth water source model during the Late Pleistocene; **(b)** average modern monthly water $\delta^{18}O$ values of the Rhine River (Lobith, Netherlands, 2005–2010). Error bars represent standard deviation. Data collected from local IAEA stations and retrieved from https://nucleus.iaea.org/wiser/index.aspx (last access: 24 March 2022).

3 Methodology

3.1 Study location and materials

Three complete molar teeth (one M1 and two M3 molars) and one fragmentary molar of woolly mammoths (*Mammuthus primigenius*) were recovered from a gravel quarry called Hardtsee, which is located in Ubstadt-Weiher, Upper Rhine Graben, southwestern Germany (49.17694° N, 8.622163° E; Fig. 3). The quarry lake where the teeth were discovered is approximately 2 km east of the Rhine River, and gravel mining occurs underwater via dredging at controlled depths. The teeth were recovered from various depths between 5 and 15 m, and they stem from fluvial sediments that were predominantly transported to the Upper Rhine Graben by meltwater discharge from an upstream alpine glacier advance (Preusser et al., 2021). The enamel on the outermost surface was preserved with no indication of erosion, which suggests they were not likely transported over long distances. Therefore, we essentially interpret the Hardtsee location as the death location of the mammoths and the Rhine catchment as their primary water source. The teeth were radiocarbon dated, and the resulting ages fit into four different time windows during Marine Isotope Stage 3, approximately 43–34 ka cal BP (Table 1).

3.2 Analytical methods

A 1 mm cylindrical diamond-coated drill bit attached to a low speed hand drill and a state drill model were used to drill the enamel and collect its powder. Two sampling methods were applied. The first method was bulk drilling, which involves taking one sample from one enamel ridge by scraping down the entire enamel length, and only a thin layer (< 1 mm) of powder was collected. The second method is sequential sampling. For this, we drilled each enamel ridge by taking successive samples along a horizontal line perpendicular to the tooth height at a resolution between 1.5 and 2 mm, starting from the occlusal surface and moving downward (Fig. 4). Both methods were applied to all available enamel ridges of the four samples. We first used the drill bit to remove the outermost surface of all enamel ridges, followed by sequentially sampling the enamel, and finally we took one bulk sample from each enamel ridge in the same trench as the sequential sampling. The mass of each sample was approximately 15 mg.

We then conducted chemical pretreatment, following the protocol developed by Snoeck and Pellegrini (2015), which involves soaking the samples in acetic acid (1 M, buffered with sodium acetate, pH = 4.5) for 30 min and rinsing in distilled water before drying overnight at 40°C. Pretreated samples were analyzed using an Analytical Precision AP2003 continuous-flow stable-isotope ratio mass spectrometer at the SGEAS, University of Melbourne. Containers were first placed on a hot plate set to 70 °C. Then they were purged with ultrapure helium gas, followed by injection of 0.5–1 mL of 104 % orthophosphoric acid with syringes. Samples were left to react with the acid for 30 min, and the headspace CO_2 gas produced was introduced to the mass spectrometer for analysis. Results are presented in delta (δ) notation and in units of per mil (‰) in relation to the Vienna Pee Dee Belemnite (VPDB) standard. The AP2003 mass spectrometer analyzed both $\delta^{18}O$ and $\delta^{13}C$ values for each sample; however, our main focus is only the oxygen isotopic values in this study. Three inorganic standards, NEW1, NEW12, and NBS 18, were used to set the calibration scale. The analytical precision was approximately 0.12 ‰ for $\delta^{18}O$ and 0.08 ‰ for $\delta^{13}C$, which was the standard deviation calculated based on the replicate analysis of in-house standards.

3.3 Statistical analysis

The similarity of bulk and mean sequential values was first assessed by their offset. If the offset is less than the analytical precision of the mass spectrometer (0.12 ‰), the two values are considered the same, and *t* tests were also performed to examine the statistical differences between the bulk and mean sequential values in each tooth.

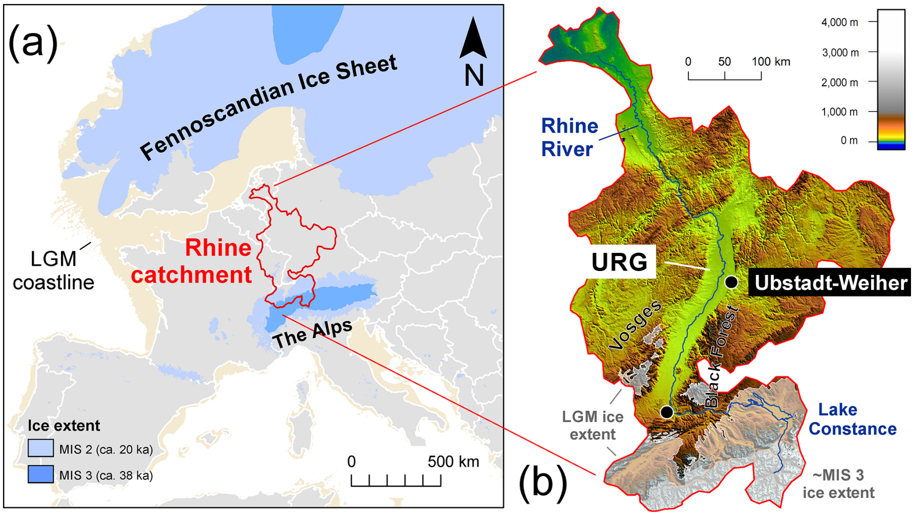

Figure 3. **(a)** Geographic context of the Rhine catchment during MIS 3 and MIS 2 (Ehlers et al., 2011; Hughes et al., 2015; Seguinot et al., 2018). **(b)** Topographic map of the Rhine catchment highlighting of study location site at Ubstadt-Weiher at a resolution of 15 arcsec (Tozer et al., 2019).

Table 1. Information on the mammoth teeth used in this study. Radiocarbon dating was undertaken at the Research School of Earth Science, Australian National University, and calibrated with Calib (http://calib.org/calib/calib.html, last access: 27 August 2020). Samples were dated to stadial/interstadial phases by comparing their ages with Greenland ice-core records (GISP2) (Grootes and Stuiver, 1999).

Sample name	Depth (m)	Radiocarbon dates (ka cal BP, median)	Radiocarbon dates (ka cal BP, 95 % CI)	Phase in MIS 3	No. of enamel ridges assessed
UW-1	5	33.7	34.6–32.7	Stadial	6
UW-2	10	36.4	38.0–34.7	Interstadial	10
UW-3	15	39.7	40.8–38.2	Interstadial	7
UW-3b	15	42.3	45.1–40.2	Uncertain	1

In addition to offsets, we also used a “modified seasonal method” to analyze where the bulk value sits in relation to the range of values from the sequential samples. This method is based on the season of mollusk collection method from Prendergast et al. (2016), in which four seasons can be differentiated from the sequential records by generating quartiles in the range of δ^{18}O values. However, in this study we applied this method not for reconstructing seasons; instead it is being adapted as a way of comparing the data distributions of bulk and sequential values. We differentiated the sequential δ^{18}O values from each enamel ridge into four quartiles with equal data distributions. Based on the Late Pleistocene hydrological model we built in Fig. 2a and by reference to seasonal variations in δ^{18}O values in the current Rhine River, we defined the lower quartile ($<$ 25th percentile) in the sequential results to reflect the warmest summer months when an increased amount of glacier meltwater was mixed in the river discharge; consequently, the upper quartile ($>$ 75th percentile) reflects the coldest winter months, and the middle quartiles (25–75th percentile) reflect intermediate environmental conditions during autumn or spring. Although this method can effectively analyze various paleoenvironmental aspects (e.g., seasonality and season of death) in the sequential records (Koch et al., 1989; Fisher and Fox, 2007; Prendergast and Schöne, 2017), it may be inappropriate for the comparison between bulk and sequential values due to two arguments. First, the bulk value is not from the same dataset as the sequential results, and consequently it has the possibility of falling outside the sequential data distribution. Also, the four seasons interpreted from the quartiles are based on the sequential δ^{18}O values within 1 year of records. One enamel ridge of a mammoth tooth may hold several either complete or incomplete years of records. The median and quartile values may skew when an incomplete year was recorded. For instance, if the enamel ridge contains 2.5 years of records, there are unequal numbers of warming and cooling seasons, which may skew the data distribution to one direction.

To address the two issues, this seasonal method was further modified, and we decided to calculate a “relative percentile” of bulk values compared to sequential data distribu-

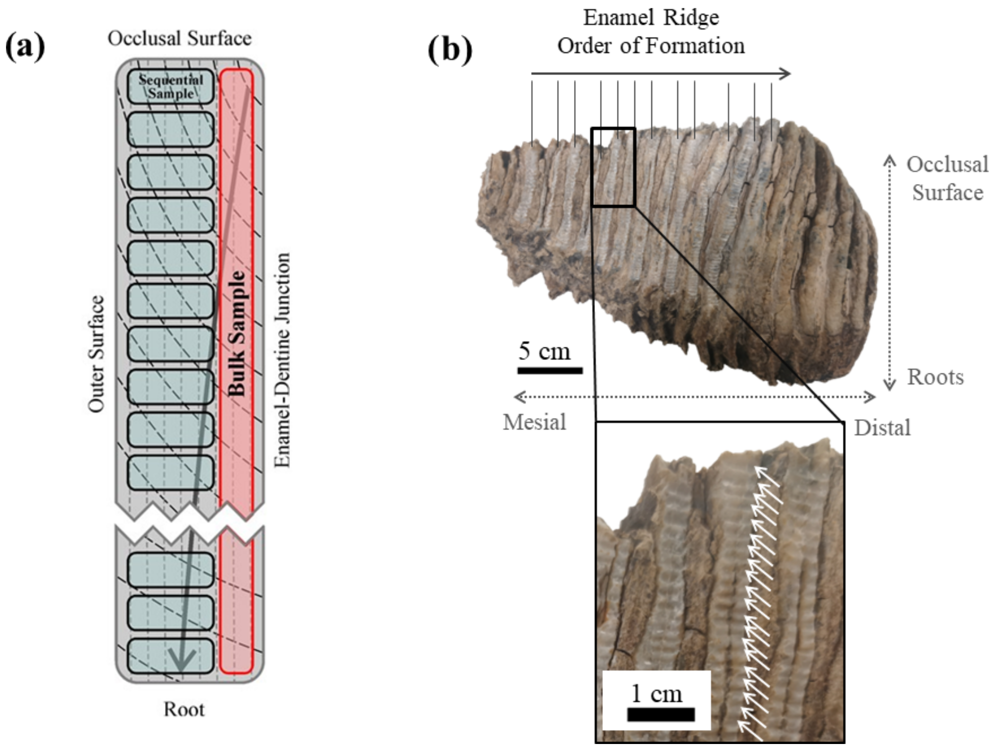

Figure 4. **(a)** A schematic diagram of an enamel section showing the difference between bulk and sequential sampling methods. Vertical dashed lines represent primary incremental lines of enamel, and black curves represent secondary incremental lines of enamel, with the arrow indicating the growth direction. **(b)** Photograph of sampled tooth UW-2 as an illustration of the sequential sampling technique. White arrows highlight the drilling spots.

tions with the following equation:

$$\text{Relative Percentile } (\%) = \frac{\text{Bulk Value} - \text{Min (Seq. Value)}}{\text{Max (Seq. Value)} - \text{Min (Seq. Value)}} \times 100 .$$

In this equation, we defined the minimum and maximum sequential values along one enamel ridge to be between 0 % and 100 %, respectively, and this range was equally divided into 100 units. Within this range, we still divided the data into four quartiles. The bulk value is expected to fall within the middle quartiles, as the averaged signal over several years is unlikely to reflect environmental conditions during extreme summer or winter months.

4 Results

4.1 Data distribution

In total, 24 bulk and 1114 sequential samples were drilled out of 24 enamel ridges. The results for each enamel ridge are summarized in Table 2 and plotted in Fig. 5. In the sequential results, we removed the outliers with boxplots. The data distributions of each tooth were box-plotted separately, and values that are smaller than the 25th percentile minus 1.5 interquartile ranges and greater than the 75th percentile plus 1.5 interquartile ranges were considered as outliers and removed ($n = 16$). After removing outliers, the bulk δ^{18}O values range from −10.4 ‰ to −7.6 ‰, and sequential values are between −11.3 ‰ and −5.7 ‰. Both the bulk and sequential values for all teeth are significantly different to each other based on t tests ($p < 0.05$). The fragmentary molar UW-3b is excluded from bulk comparison since there is only one value.

For both bulk and average sequential values, more positive δ^{18}O values were found in teeth UW-2 and UW-3, which are dated to interstadials, compared to tooth UW-1, which is dated to a stadial period (Fig. 4a). Tooth UW-1 is also the youngest sample; therefore, the three complete molar teeth show progressively more negative mean δ^{18}O values from the oldest to the youngest between 39 and 33 ka cal BP. The bulk δ^{18}O value of UW-3b is more positive than the younger UW-1 and UW-2, and it is intermediate to those of UW-3. The mean sequential δ^{18}O value of UW-3b, however, is the most negative value among all four teeth.

4.2 Intra-enamel isotopic variations

The cyclicity of all enamel ridges was assessed to identify features of seasonal environmental changes. For UW-1, UW-2, and UW-3, the intra-tooth sequential δ^{18}O exhibits mul-

Table 2. The list of results of the study, including the length, number of identifiable years, and the bulk and sequential δ^{18}O values of all sampled enamel ridges (outliers removed).

	Enamel ridge	Length (mm)	No. of years identified	Bulk value (‰)	Seq. value mean (‰)	Offset (bulk seq. mean) (‰)	Seq. value min (‰)	Seq. value max (‰)	Relative percentile (%)
UW-1	1	136	5	−9.90	−9.27	−0.64	−10.46	−8.3	25.78
	2	150	6.5	−10.41	−9.39	−1.02	−10.55	−8.1	5.93
	3	150	8	−9.72	−9.25	−0.47	−10.44	−8.51	37.41
	4	160	8	−10.03	−9.23	−0.81	−10.12	−8.17	4.51
	5	152	9.5	−9.49	−9.46	−0.03	−10.29	−8.52	45.10
	6	146	7.5	−9.66	−9.35	−0.31	−10.32	−8.38	34.09
UW-2	1	32	2	−8.54	−7.88	−0.66	−8.9	−7.45	24.93
	2	42	1.5	−8.77	−8.09	−0.68	−8.67	−7.68	−10.06
	3	54	3	−8.64	−8.1	−0.54	−8.76	−7.43	9.01
	4	54	4	−8.70	−8.43	−0.28	−8.96	−7.9	24.23
	5	72	5	−8.50	−8.38	−0.12	−9.11	−7.54	39.01
	6	74	6	−8.36	−8.49	0.13	−8.98	−7.92	58.41
	7	80	6	−8.63	−8.24	−0.39	−9.22	−7.48	34.21
	8	84	6.5	−8.44	−8.29	−0.15	−9.14	−7.52	43.07
	9	92	8	−8.57	−8.33	−0.24	−9.12	−7.63	37.19
	10	100	8	−8.41	−8.61	0.20	−9.35	−7.88	63.88
UW-3	1	60	2.5	−8.31	−6.93	−1.38	−7.9	−6.03	−21.80
	2	78	3.5	−8.19	−6.98	−1.21	−7.63	−6.07	−36.28
	3	78	3.5	−8.50	−7.12	−1.38	−8.06	−6.03	−21.77
	4	82	3.5	−8.54	−7.28	−1.26	−8.4	−6.49	−7.20
	5	90	3.5	−7.86	−7.15	−0.71	−8.15	−6.1	14.17
	9	112	5	−8.19	−7.1693	−1.02	−8.17	−6	−1.06
	10	108	5	−7.63	−7.13	−0.50	−7.98	−6.31	20.56
UW-3b	1	37.5	NA	−8.25	−9.6	1.35	−11.29	−8.14	96.63

NA: not available.

tiple local maxima and minima along the entire ca. 100–150 mm of enamel length, and examples are plotted in Fig. 6. The data resemble cyclic oscillations, with the δ^{18}O values of maxima being approximately 0.8 ‰ to 1.1 ‰ higher than those of the minima. Among these three teeth, the sequential values of UW-3 show the clearest oscillations, with five complete cycles of similar incremental lengths identified. In teeth UW-1 and UW-2, however, the cyclicity is more difficult to identify, as both selected enamel ridges have a reduced amplitude of isotopic variation in the middle of the enamel ridge. The enamel ridge of the fragmentary molar UW-3b has the most difficult isotopic variation to interpret. Although we can identify one maximum and minimum (and potentially a second maximum), it is uncertain whether these data cover a full year of records considering the incremental length is only 37.5 mm. The number of cycles in each enamel ridge ranges from one to eight, and they are correlated to the incremental length of enamel ridges ($r^2 = 0.60$, $n = 23$), with longer enamel ridges generally containing more interpreted hydrological years.

4.3 Comparison of bulk and sequential values

Significant differences ($p < 0.05$) were detected between bulk and mean sequential δ^{18}O values in all complete teeth based on t tests (i.e., UW-1, UW-2, UW-3), with the difference varying from 0.03 ‰ to 1.35 ‰. One enamel ridge from UW-1 has a difference of less than 0.12 ‰. The differences of three enamel ridges from UW-2 are between 0.1 ‰ and 0.15 ‰. All other samples have differences greater than 0.2 ‰ (Table 2). Overall, the mean differences in the younger teeth UW-1 (0.54 ‰) and UW-2 (0.34 ‰) are smaller compared to the older UW-3 (1.06 ‰) and UW-3b (1.35 ‰). For all enamel ridges of teeth UW-1 and UW-3, the bulk values are more negative than the mean sequential values. The bulk values of most enamel ridges (8 out of 10) of UW-2 are more negative, and the other two are slightly more positive. The bulk value of UW-3b is 1.35 ‰ more positive than the sequential value, which is the greatest among all enamel ridges.

The relative percentile values were also analyzed and shown in Table 2 and Fig. 7. The bulk values of most enamel ridges of teeth UW-1 (4 out of 6) and UW-2 (6 out of 10) are located between the 25th and 75th percentiles within the mid-

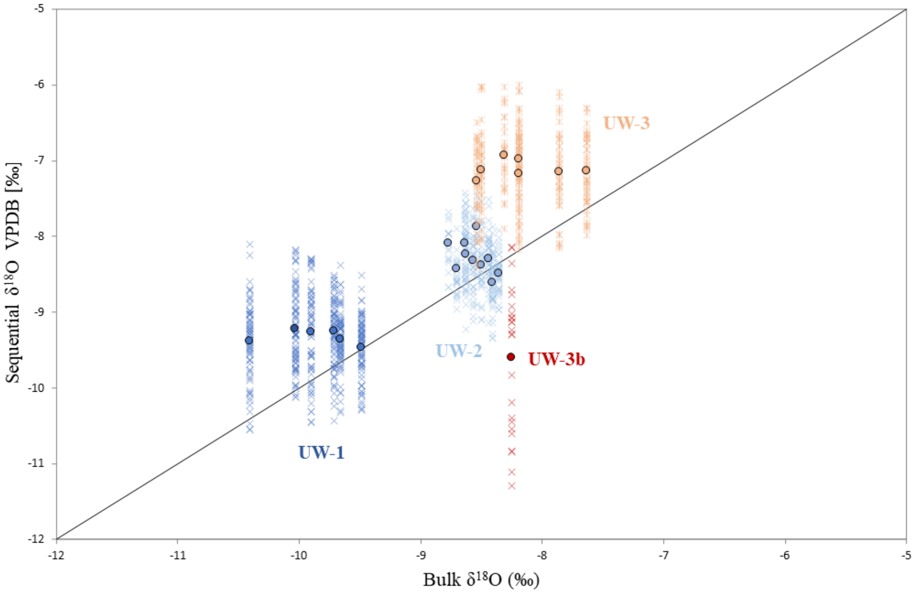

Figure 5. Data distribution of the four teeth and comparison between bulk and sequential results. Each cross represents the δ^{18}O value of one sequential spot, and dots are bulk (x axis) and averaged sequential (y axis) δ^{18}O values of different enamel ridges. The diagonal line represents data points for which bulk and sequential means are equal; if a dot is located above this line, the mean sequential δ^{18}O value of this enamel ridge is more positive than the bulk value, and vice versa.

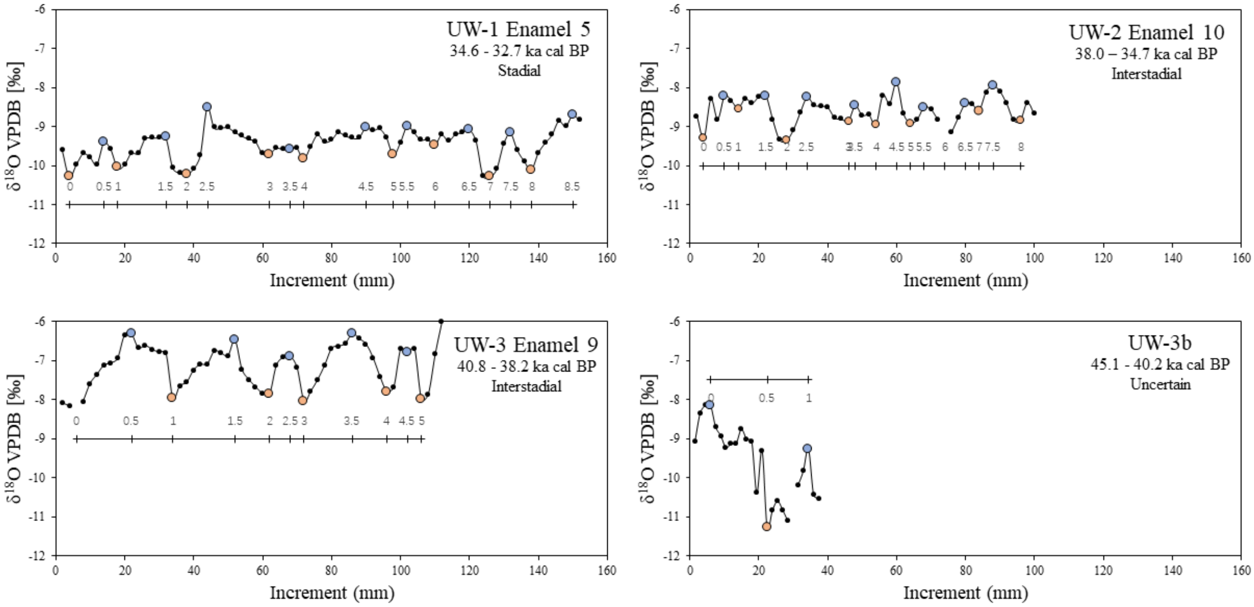

Figure 6. Examples of δ^{18}O variations along one enamel from each tooth with expected years. Local maxima (winter) and minima (summer) are highlighted with blue and orange dots, respectively.

dle quartile with the remaining values falling below the 25th percentile including one value for UW-2 being more negative than the minimal sequential value. The bulk values of all enamel ridges of tooth UW-3 are below the 25th percentile, with the majority (5 out if 7) being more negative than the minimal sequential value. The relative percentile of UW-3b is 96.3 %, the only data point above the 75th percentile.

5 Discussion

5.1 Sample preservation

It is essential to evaluate whether physical and chemical transformations of sample materials may lead to isotopic exchange and loss of primary isotopic signal (Keenan, 2016;

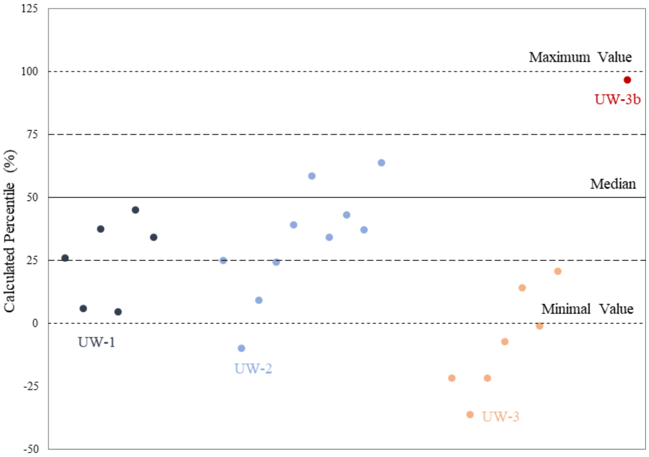

Figure 7. The plot of relative percentiles of bulk values from all the enamel ridges of the four teeth.

Goedert et al., 2016). The preservation condition of our mammoth teeth was assessed, and based on three pieces of evidence, at least part of their original materials seems to have been preserved. The first piece of evidence is the sequential δ^{18}O values which show variations that mimic seasonal patterns. The δ^{18}O values of all sequential samples would likely be homogenized if all material had been completely recrystallized (Metcalfe and Longstaffe, 2012; Goedert et al., 2016); therefore, this supports the point that at least some of the primary enamel material is preserved and still holds records of paleoenvironmental changes, but it is not a full proof. The carbon isotopic compositions, although not analyzed in detail in this study, provide additional evidence of primary material preservation. Carbon isotopes of herbivorous animals are incorporated from the vegetation they consumed (Arppe and Karhu, 2006; Kovács et al., 2012; Prendergast and Schöne, 2017), with the δ^{13}C values of animals which forage upon C_3 and C_4 plants to be -20 ‰ to -8 ‰ and from 0 ‰ to $+5$ ‰, respectively (Kohn and Cerling, 2002). The δ^{13}C values of the four teeth range between -13.13 ‰ and -11.21 ‰ (Liu, 2020), which falls within the C_3 foraging range, and this agrees with mammoth dietary behavior observed from their fecal remains (Kirillova et al., 2016). Therefore, both oxygen and carbon isotopic results suggest that at least some primary isotopic signal is preserved. In addition, we drilled additional enamel powder from each tooth, and the powder was sub-divided into pretreated and non-pretreated groups. The isotopic values of both groups were tested, and no statistically significant differences were detected between the δ^{18}O values of these two groups.

Although there is still a possibility of diagenetic alteration, all samples were pretreated with acetic acid to remove any secondary carbonates. Additionally, due to its low porosity and low organic contents, tooth enamel is one of the most resistant materials to diagenetic alteration and is capable of preserving primary isotopic signals for millions of years. Based on all the above considerations, we assume our mammoth teeth have at least partially preserved their original isotopic signals, and the acquired δ^{18}O values reflect their living environmental properties.

5.2 Comparison between bulk and mean sequential values

Differences between bulk and sequential results are present in all four mammoth teeth, with the bulk values being generally more negative than the mean sequential values. There is only one exception, which is the enamel ridge of UW-3b, with the bulk value being 1.35 ‰ more positive. This may be caused by the absence of a complete annual cycle, as only 37.5 mm of material was sampled. The incomplete hydrological year in the records of UW-3b could also cause the data distribution of sequential samples to taper. Older tooth samples also have generally greater offsets. Only one enamel ridge from UW-1 has a difference less than 0.12 ‰, which is within the precision of the mass spectrometer. Therefore, the bulk and sequential values for this sample can be considered as equal. Three enamel ridges from UW-2 show slightly greater offsets between 0.12 ‰ and 0.15 ‰, which may still be considered as similar. Most other enamel ridges in teeth UW-1 and UW-2 ($n = 11$) have offsets between 0.2 ‰ and 0.81 ‰, with only one enamel ridge from UW-1 having a difference value over 1 ‰. All enamel ridges from teeth UW-3 and UW-3b have difference values of at least 0.5 ‰, and most of them (6 out of 8) are greater than 1 ‰. The relative percentiles for all UW-3b enamel ridges are located in the lower quartile, while most enamel ridges from teeth UW-1 and UW-2 are within the middle quartile. However, even if some samples are located within the middle quartile, most of them in UW-2 and all samples in UW-1 are more negative than the median. The uneven distributions suggest that bulk and sequential samples reflect different environmental conditions in these two teeth.

One explanation for the difference is the geometry of incremental lines. Our two sampling methods each predominantly cover one growth direction: a bulk sample covering the entire enamel height with only a thin layer of enamel collected, whereas each sequential sample includes a deeper sampling pit covering the majority of the enamel thickness but with only a small proportion of the enamel height. Neither of the two methods followed the exact enamel growth direction: the incremental lines of mammoth secondary enamel material are inclined at an angle of 55–60° to the enamel-dentine junction (EDJ). The inconsistency between drilling orientation and enamel growth direction can cause “damping” of the isotopic signal due to time averaging (Passey et al., 2005; Metcalfe and Longstaffe, 2012). A simplified model is presented in Fig. 8 to illustrate how the angle of incremental lines can cause potential isotopic damping. In this model, although we assumed the four seasons in a year have the same incremental distance in a section of the enamel ridge, the seasonal distribution in the bulk sample is uneven with an incomplete representation of increments formed during the last summer and autumn. The sequential samples have the same issue, with the first autumn incompletely represented in our model. Therefore, this may result in bulk results more similar to the isotopic signals near the occlusal surface and mean sequential values more similar to those near the root. However, the seasonal distribution of the combination of all sequential samples is slightly more even as they occupy more enamel thickness (and much more enamel material overall). If only one method is applied and it covers the entire enamel thickness, then the obtained samples would theoretically have even distributions of the four seasons.

This problem may be more significant in enamel ridges of shorter lengths. In Fig. 9, we plotted the difference values against the incremental lengths of each enamel ridge. Teeth UW-2 and UW-3 have enamel ridges of different lengths, varying from 32 to 112 mm, and both of them show strong negative relationships between enamel length and difference value. No correlation was detected from the enamel ridges of UW-1. This could be due to their similar lengths (136–160 mm). Inter-tooth comparison also indicates that enamel ridges with longer lengths generally have smaller differences between bulk and mean sequential values: greater difference values (> 1 ‰) predominantly occurred in enamel ridges less than 100 mm in length. When the bulk sample recorded uneven distributions of seasons, it mainly occurred at the apex and root of the enamel (Fig. 8); therefore, a longer enamel ridge with more annual records in the middle would theoretically reduce this impact. However, despite the correlation between the offsets and incremental lengths, the primary deciding factor of the offsets is still inter-tooth difference given that (1) the inter-tooth difference of values is greater than intra-tooth variations especially between UW-2 and UW-3 and (2) the offset values of UW-1 have a variation of nearly 1 ‰, although all of its enamel ridges are more than 100 mm.

The geometry of incremental lines may have another consequence, which is reduced seasonal amplitude in sequential isotopic records (Passey et al., 2005). In Fig. 8, one sequential sample may contain increments formed during more than one season, especially those formed during seasonal transitions. In fact, oxygen and carbon isotopic cyclicity has been detected from the EDJ to the outer surface, indicating that there was tooth growth through the enamel thickness, although the growth rate was much slower compared to the growth along tooth height. Therefore, each sequential sample obtained in this study may hold an averaged isotopic signal of one or multiple seasons, and the isotopic variation in environmental water would have potentially greater amplitude.

Another possible explanation for the difference between bulk and sequential results is that the two methods collect enamel formed during different times. Reade et al. (2015) sampled the tooth enamel of Barbary sheep (*Ammotragus lervia*) with both bulk and sequential sampling strategies. They also found different bulk and mean sequential δ^{18}O values. The main difference between the two studies is that the locations of the two sampling methods are the opposite: their bulk samples were taken before the sequential samples and therefore are closer to the outer surface. They proposed an explanation, which is that the bulk samples in their study contain a greater proportion of enamel mineralized later because the enamel mineralization process at their sampling locations (outer surface) is slower than the sequential samples obtained near the EDJ (Suga, 1979, 1982). In our case, the bulk samples are then expected to contain more enamel mineralized earlier, and this argument agrees with the impact caused by the angle of incremental lines (Fig. 8). Therefore, there could be an offset in the formation time of the material collected by the two methods, and in turn this caused differences in isotopic compositions due to different time averaging in the samples.

A third explanation is the mixture of primary and secondary enamel increments in the samples. We primarily sampled the secondary incremental lines in the teeth. However, there was also a primary mineralization phase in mammoth tooth formation, although it only took up 20 %–30 % of the total enamel mass (Passey and Cerling, 2002; Passey et al., 2005). Primary mineralization forms vertical incremental lines under microscopic view, indicating the material grows from the EDJ to the outer surface (Metcalfe and Longstaffe, 2012). Therefore, the thin layer of enamel powder collected by the bulk sampling method may also contain primary mineralized material formed during a short period of time. This period of time could be during any season; consequently, if the collected primary increments were formed during extreme summer or winter months, the mixture of primary and secondary enamel material might skew the isotopic signal to one direction. This could be the cause of the bulk values of several enamel ridges falling outside the data distribution of sequential values, since primary increments were formed during a different time to the secondary increments. If the collected primary increments were formed during spring or autumn months with the isotopic signal in environmental water closer to the annual average, there is less impact from primary material, and the bulk and mean sequential values would be more similar. The sequential samples again are less influenced by the primary mineralization, as more enamel thickness is sampled, covering primary increments formed during a longer period of time and maybe including multiple seasons.

5.3 Comparison of sampling methods

The bulk and mean sequential results obtained in this study show both similar and different values. Here we discuss how these differences may help us decide the optimal sampling methods for future research. The bulk samples, at least those obtained through the method applied in this study, do not always reflect an averaged isotopic signal at decadal scales.

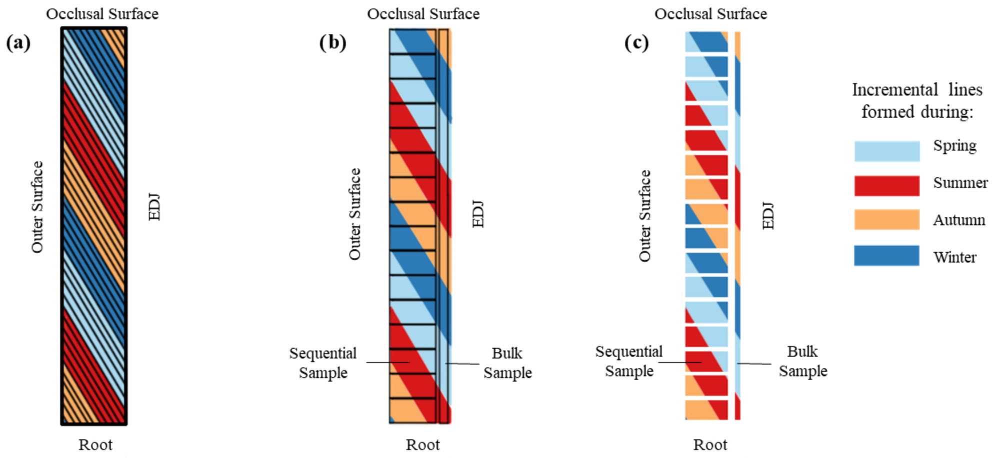

Figure 8. A simplified model showing secondary incremental lines formed during different seasons and the sampling spots. **(a)** A schematic diagram of an enamel section with the assumption of the four seasons having equal incremental lengths, **(b)** sampling spots for both bulk and sequential sampling methods, and **(c)** the duration and distribution of different seasons included in each sample.

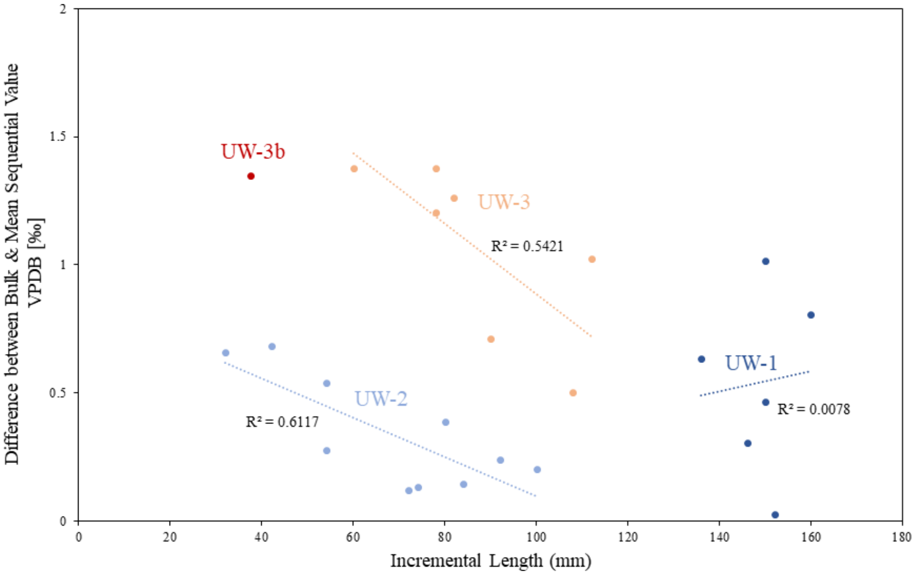

Figure 9. Plot of difference values against incremental lengths of all enamel ridges.

Instead, it is more likely a reflection of either extreme summer/winter environmental conditions or spring/autumn isotopic compositions which are close to the annual mean value. In comparison, the sequential method is less influenced by the primary increments and the geometry of secondary incremental lines. We do not suggest the sequential sampling method itself can more accurately reflect paleoenvironmental conditions. The main reason it does in this study is that with our drilling method, the combination of all sequential samples covers the entire enamel length and the majority of enamel thickness, which included increments formed during a longer period of time than the thin layer of the bulk sample. Reade et al. (2015) suggested sampling the entire tooth height, as well as the enamel thickness, to reduce isotopic damping caused by the enamel growth pattern. We also recommend that future studies which involve surface sampling on mammoth teeth drill all available enamel material in both directions, regardless of which sampling method will be applied.

However, this means we can only apply one method to each enamel ridge. We suggest the sequential sampling method is more optimal because it provides not only an averaged multi-annual-scale isotopic composition (mean sequential value) but more importantly a time series of high-resolution paleoenvironmental records. Such records are crucial for understanding the highly variable climatic conditions of the Late Pleistocene and deciphering human–environmental interactions (Denton et al., 2005; Bradtmöller et al., 2012; Prendergast et al., 2018). In addition, the sequential δ^{18}O variations that reflect seasonal environmental changes can also indicate whether there is a complete annual cycle, and if so, how many of them are recorded in each enamel ridge. A fragmentary enamel ridge without one annual cycle may not provide an accurate annual mean δ^{18}O value, so the temporal duration of the record is unsuitable for the bulk sampling method. This also indicates that the completeness and size of mammoth teeth should be important criteria considered during sample selection. Mammoth teeth with complete and long enamel ridges should have the highest priority because long enamel ridges generally contain more annual cycles of δ^{18}O oscillations. Although offsets between bulk and mean sequential values may still be detected in long ridges, the difference value is likely smaller than those of short enamel ridges, as the long sequence of isotopic records reduces the impact of uneven seasonal distributions in both bulk and sequential samples.

Although we recommend using complete and large-sized mammoth molar teeth as the preferred study material, we are aware that such samples are not always available at certain sites. Mammoth teeth may have been weathered and transported by surrounding environments, and consequently they may break into fragments and lose enamel thickness through erosion. Due to this limitation, it is unclear which part of the enamel and how much enamel thickness and tooth height were sampled in many past stable-isotope studies on mammoth teeth, especially those which employed bulk sampling methods. Given that the bulk values in some of our samples fall outside the range of sequential values, we recommend only comparing results obtained from sequential sampling methods with other sequential sampling studies. If results obtained from two different methods are compared directly, the potential isotopic offset between bulk and sequential samples may be falsely concluded to reflect different environmental conditions.

5.4 Limitations and future research

The main limitation of this study is the different locations of the two sampling methods. Although the sampling spots are from the same trenches, bulk and sequential samples are powder from different parts of the enamel ridge. A possible improvement in further studies is to use only part of the powder in each sequential sample and combine all the remaining powder along one enamel ridge to form the bulk sample. In this case, enamel powder taken from the two methods would have covered roughly the same incremental length of enamel thickness and tooth height. Another possible improvement is applying the two methods on the enamel ridges at two sides of the same molar plate. However, this method assumes that enamel ridges on both sides grow simultaneously. Nonetheless, this study has provided insights into the degree to which we can compare past studies, as it is likely that different parts of enamel ridges were sampled in different studies, and some studies might have only sampled a thin layer of enamel material as the bulk samples.

Another limitation is that we considered primary enamel mineralization as a factor that caused differences in bulk and sequential results, but we are uncertain about the proportion of primary mineralization collected in each sample and its degree of impact. These questions require further investigations into mammoth dental morphology and separate isotopic analysis of primary and secondary incremental materials.

In addition, although the sequential samples provide high-resolution records of likely seasonal environmental changes, they are not perfect reflections of paleoenvironments. The geometry of secondary incremental lines potentially caused several different seasons recorded in one sequential sample, averaging the isotopic signal and in turn reducing the amplitude of isotopic oscillations. In future sequential sampling of mammoth teeth, we may section the teeth to expose the enamel thickness, identify incremental features under microscopic views so that we can perform spot-drilling on each incremental line to avoid seasonal averaging.

6 Conclusion

We applied both bulk and sequential sampling methods to mammoth enamel and compared the results. Both similar and different δ^{18}O values between bulk and mean sequential results were discovered, and in most samples, they are different, with the bulk samples having more negative δ^{18}O values. Multiple potential factors might have jointly caused the offsets, including the geometry of secondary incremental lines, the mixture of primary increments, and different periods of time formation near the EDJ and outer surface. In this study, the mean sequential values may be more accurate reflections of decadal-scale paleoenvironmental conditions because their samples include most material in both tooth height and enamel thickness direction. A thin layer of enamel material collected by the bulk sampling method may have uneven distributions of different seasons, and consequently the δ^{18}O values may reflect either an annual average or conditions in only a certain season. Choosing long enamel ridges that contain more annual cycles as study materials may reduce the impact of uneven seasonal distribution caused by incremental line geometry. Therefore, we recommend that future isotopic analysis on mammoth teeth selects complete and large-sized samples and drills the entire tooth height and enamel thickness if possible. Considering that the sampling locations are unknown in many past studies, a cross-method data comparison is not recommended.

We also effectively obtained high-resolution paleoenvironmental records of sub-seasonal resolution. These records hold the potential of reconstructing paleo-climate and paleo-hydrology for various aspects, such as seasonality and inter-annual differences, in future studies. However, we must be aware that the amplitude of isotopic signal obtained from this sequential sampling method might be reduced, since the drilling direction has an angle against the incremental lines so that enamel materials formed during more than one season could be mixed in each sample. This issue may be improved by combining the sequential sampling method with microscopic analysis on mammoth dental morphology to achieve spot-drilling on each incremental line in future research.

Data availability. The data that support the findings of this study will be uploaded to the PANGAEA database and be open to other researchers in the near future.

Author contributions. The research idea was conceived by JHM and AP; sample acquisition was carried out by JHM; experiment planning was carried out by ZL, AP, and JHM; laboratory work was carried out by ZL; isotopic data processing was carried out by RD; data analysis and interpretation were carried out by ZL, AP, and JHM; ZL drafted the manuscript. All co-authors reviewed and made inputs to the manuscript.

Competing interests. At least one of the (co-)authors is a member of the editorial board of *E&G Quaternary Science Journal*. The peer-review process was guided by an independent editor, and the authors also have no other competing interests to declare.

Disclaimer.

Special issue statement. This article is part of the special issue "Quaternary research from and inspired by the first virtual DEUQUA conference". It is a result of the vDEUQUA2021 online conference in September/October 2021.

Acknowledgements. We would like to thank Frank Kiesewetter from the Ubstadt-Weiher gravel quarry for collecting and providing the mammoth teeth for this research, and we thank Rachel Wood from Australian National University for undertaking the radiocarbon dating of the samples. We are also grateful for Niels de Winter and another anonymous reviewer for providing valuable feedback.

Review statement. This paper was edited by Christian Zeeden and reviewed by Niels de Winter and one anonymous referee.

References

Arppe, L. M. and Karhu, J. A.: Implications for the Late Pleistocene climate in Finland and adjacent areas from the isotopic composition of mammoth skeletal remains, Palaeogeogr. Palaeocl., 231, 322–330, https://doi.org/10.1016/j.palaeo.2005.08.007, 2006.

Ayliffe, L. K., Lister, A. M., and Chivas, A. R.: The preservation of glacial-interglacial climatic signatures in the oxygen isotopes of elephant skeletal phosphate, Palaeogeogr. Palaeocl., 99, 179–191, https://doi.org/10.1016/0031-0182(92)90014-V, 1992.

Bedaso, Z. and Wu, S.-Y.: Linking precipitation and groundwater isotopes in Ethiopia – Implications from local meteoric water lines and isoscapes, J. Hydrol., 596, 126074, https://doi.org/10.1016/j.jhydrol.2021.126074, 2021.

Benson, L. V. and Paillet, F.: HIBAL: A hydrologic-isotopic-balance model for application to paleolake systems, Quaternary Sci. Rev., 21, 1521–1539, https://doi.org/10.1016/S0277-3791(01)00094-4, 2002.

Bradtmöller, M., Pastoors, A., Weninger, B., and Weniger, G.-C.: The repeated replacement model – Rapid climate change and population dynamics in Late Pleistocene Europe, Quatern. Int., 247, 38–49, https://doi.org/10.1016/j.quaint.2010.10.015, 2012.

Dansgaard, W.: Stable isotopes in precipitation, Tellus, 16, 436–468, https://doi.org/10.3402/tellusa.v16i4.8993, 1964.

Denton, G., Alley, R., Comer, G., and Broecker, W.: The role of seasonality in abrupt climate change, Quaternary Sci. Rev., 24, 1159–1182, https://doi.org/10.1016/j.quascirev.2004.12.002, 2005.

Ehlers, J., Gibbard, P. L., and Hughes, P. D. (Eds): Quaternary Glaciations – Extent and Chronology: A Closer Look, Elsevier, ISBN: 9780444534477, 2011.

Ferretti, M. P.: Structure and evolution of mammoth molar enamel, Acta Palaeontol. Pol., 48, 383–396, 2003.

Fisher, D. C. and Fox, D. L.: Season of death of the Dent mammoths distinguishing single from multiple mortality events, in: Frontiers in Colorado Paleoindian Archaeology: From the Dent Site to the Rocky Mountains, University Press of Colorado, 123–153, ISBN: 9781607323549, 2007.

Fricke, H. C. and O'Neil, J. R.: Inter- and intra-tooth variation in the oxygen isotope composition of mammalian tooth enamel phosphate: implications for palaeoclimatological and palaeobiological research, Palaeogeogr. Palaeocl., 126, 91–99, https://doi.org/10.1016/S0031-0182(96)00072-7, 1996.

Genoni, L., Iacumin, P., Nikolaev, V., Gribchenko, Yu., and Longinelli, A.: Oxygen isotope measurements of mammoth and reindeer skeletal remains: an archive of Late Pleistocene environmental conditions in Eurasian Arctic, Earth Planet. Sc. Lett., 160, 587–592, https://doi.org/10.1016/S0012-821X(98)00113-7, 1998.

Goedert, J., Amiot, R., Boudad, L., Buffetaut, E., Fourel, F., Godefroit, P., Kusuhashi, N., Suteethorn, V., Tong, H., Watabe, M., and Lécuyer, C.: Preliminary investigation of seasonal patterns recorded in the oxygen isotope compositions of theropod dinosaur tooth enamel, PALAIOS, 31, 10–19, https://doi.org/10.2110/palo.2015.018, 2016.

Grootes, P. M. and Stuiver, M.: GISP2 Oxygen Isotope Data, PANGAEA [dataset], https://doi.org/10.1594/PANGAEA.56094, 1999.

Hoppe, K. A.: Late Pleistocene mammoth herd structure, migration patterns, and Clovis hunting strategies inferred from isotopic analyses of multiple death assemblages, Paleobiology, 30, 129–145, https://doi.org/10.1666/0094-8373(2004)030<0129:LPMHSM>2.0.CO;2, 2004.

Hughes, A. L., Gyllencreutz, R., Lohne, Ø. S., Mangerud, J., and Svendsen, J. I.: DATED-1: compilation of dates and time-slice reconstruction of the build-up and retreat of the last Eurasian (British-Irish, Scandinavian, Svalbard-Barents-Kara Seas) Ice Sheets 40-10 ka, PANGAEA [dataset], https://doi.org/10.1594/PANGAEA.848117, 2015.

Iacumin, P., Di Matteo, A., Nikolaev, V., and Kuznetsova, T. V.: Climate information from C, N and O stable isotope analyses of mammoth bones from northern Siberia, Quatern. Int., 212, 206–212, https://doi.org/10.1016/j.quaint.2009.10.009, 2010.

Keenan, S. W.: From bone to fossil: A review of the diagenesis of bioapatite, Am. Mineral., 101, 1943–1951, https://doi.org/10.2138/am-2016-5737, 2016.

Kirillova, I. V., Argant, J., Lapteva, E. G., Korona, O. M., van der Plicht, J., Zinovyev, E. V., Kotov, A. A., Chernova, O. F., Fadeeva, E. O., Baturina, O. A., Kabilov, M. R., Shidlovskiy, F. K., and Zanina, O. G.: The diet and environment of mammoths in North-East Russia reconstructed from the contents of their feces, Quatern. Int., 406, 147–161, https://doi.org/10.1016/j.quaint.2015.11.002, 2016.

Koch, P. L., Fisher, D. C., and Dettman, D.: Oxygen isotope variation in the tusks of extinct proboscideans: A measure of season of death and seasonality, Geology, 17, 515–519, https://doi.org/10.1130/0091-7613(1989)017<0515:OIVITT>2.3.CO;2, 1989.

Kohn, M. J. and Cerling, T. E.: Stable Isotope Compositions of Biological Apatite, Rev. Mineral. Geochem., 48, 455–488, https://doi.org/10.2138/rmg.2002.48.12, 2002.

Kovács, J., Moravcová, M., Újvári, G., and Pintér, A. G.: Reconstructing the paleoenvironment of East Central Europe in the Late Pleistocene using the oxygen and carbon isotopic signal of tooth in large mammal remains, Quatern. Int., 276–277, 145–154, https://doi.org/10.1016/j.quaint.2012.04.009, 2012.

Lister, A. and Bahn, P.: Mammoths: Giants of the Ice Age Hardcover – 15 November 2007, University of California Press, ISBN: 0520253191, 2007.

Liu, Z.: Reconstruction of Paleo-Environments in Southern Germany during the Last Glacial Maximum with Mammoth Teeth, Honors thesis, School of Geography, Earth and Atmospheric Sciences, University of Melbourne, Australia, https://doi.org/10.13140/RG.2.2.32020.63361, 147 pp., 2020.

Longinelli, A.: Oxygen isotopes in mammal bone phosphate: A new tool for paleohydrological and paleoclimatological research?, Geochim. Cosmochim. Ac., 48, 385–390, https://doi.org/10.1016/0016-7037(84)90259-X, 1984.

Luz, B., Kolodny, Y., and Horowitz, M.: Fractionation of oxygen isotopes between mammalian bone-phosphate and environmental drinking water, Geochim. Cosmochim. Ac., 48, 1689–1693, https://doi.org/10.1016/0016-7037(84)90338-7, 1984.

Maschenko, E. N.: Individual development, biology and evolution of the woolly mammoth, Cranium, 19, 4–120, 2002.

Metcalfe, J. Z. and Longstaffe, F. J.: Mammoth tooth enamel growth rates inferred from stable isotope analysis and histology, Quaternary Res., 77, 424–432, https://doi.org/10.1016/j.yqres.2012.02.002, 2012.

Miller, J. H., Fisher, D. C., Crowley, B. E., Secord, R., and Konomi, B. A.: Male mastodon landscape use changed with maturation (late Pleistocene, North America), P. Natl. Acad. Sci. USA, 119, e2118329119, https://doi.org/10.1073/pnas.2118329119, 2022.

Passey, B. H. and Cerling, T. E.: Tooth enamel mineralization in ungulates: Implications for recovering a primary isotopic time-series, Geochim. Cosmochim. Ac., 66, 3225–3234, https://doi.org/10.1016/S0016-7037(02)00933-X, 2002.

Passey, B. H., Cerling, T. E., Schuster, G. T., Robinson, T. F., Roeder, B. L., and Krueger, S. K.: Inverse methods for estimating primary input signals from time-averaged isotope profiles, Geochim. Cosmochim. Ac., 69, 4101–4116, https://doi.org/10.1016/j.gca.2004.12.002, 2005.

Prendergast, A. L. and Schöne, B. R.: Oxygen isotopes from limpet shells: Implications for palaeothermometry and seasonal shellfish foraging studies in the Mediterranean, Palaeogeogr. Palaeocl., 484, 33–47, https://doi.org/10.1016/j.palaeo.2017.03.007, 2017.

Prendergast, A. L., Stevens, R. E., O'Connell, T. C., Fadlalak, A., Touati, M., al-Mzeine, A., Schöne, B. R., Hunt, C. O., and Barker, G.: Changing patterns of eastern Mediterranean shellfish exploitation in the Late Glacial and Early Holocene: Oxygen isotope evidence from gastropod in Epipaleolithic to Neolithic human occupation layers at the Haua Fteah cave, Libya, Quatern. Int., 407, 80–93, https://doi.org/10.1016/j.quaint.2015.09.035, 2016.

Prendergast, A. L., Pryor, A. J. E., Reade, H., and Stevens, R. E.: Seasonal records of palaeoenvironmental change and resource use from archaeological assemblages, J. Archaeol. Sci. Rep., 21, 1191–1197, https://doi.org/10.1016/j.jasrep.2018.08.006, 2018.

Preusser, F., Büschelberger, M., Kemna, H. A., Miocic, J., Mueller, D., and May, J.-H.: Exploring possible links between Quaternary aggradation in the Upper Rhine Graben and the glaciation history of northern Switzerland, Int. J. Earth Sci., 110, 1827–1846, https://doi.org/10.1007/s00531-021-02043-7, 2021.

Pryor, A. J. E., O'Connell, T. C., Wojtal, P., Krzemińska, A., and Stevens, R. E.: Investigating climate at the Upper Palaeolithic site of Kraków Spadzista Street (B), Poland, using oxygen isotopes, Quatern. Int., 294, 108–119, https://doi.org/10.1016/j.quaint.2011.09.027, 2013.

Reade, H., Stevens, R. E., Barker, G., and O'Connell, T. C.: Tooth enamel sampling strategies for stable isotope analysis: Potential problems in cross-method data comparisons, Chem. Geol., 404, 126–135, https://doi.org/10.1016/j.chemgeo.2015.03.026, 2015.

Rozanski, K., Froehlich, K., and Mook, W. G.: Environmental isotopes in the hydrological cycle: principles and applications, IHP-V, Technical Documents in Hydrology, No. 39, vol. III: Surface water, UNESCO, Paris, 2001.

Seguinot, J., Ivy-Ochs, S., Jouvet, G., Huss, M., Funk, M., and Preusser, F.: Modelling last glacial cycle ice dynamics in the Alps, The Cryosphere, 12, 3265–3285, https://doi.org/10.5194/tc-12-3265-2018, 2018.

Sharp, Z. D. and Cerling, T. E.: Fossil isotope records of seasonal climate and ecology: Straight from the horse's mouth, Geology, 26, 219–222, https://doi.org/10.1130/0091-7613(1998)026<0219:FIROSC>2.3.CO;2, 1998.

Smith, C. E.: Cellular and Chemical Events During Enamel Maturation, Crit. Rev. Oral Biol. M., 9, 128–161, https://doi.org/10.1177/10454411980090020101, 1998.

Smith, T. M. and Tafforeau, P.: New visions of dental tissue research: tooth development, chemistry, and structure, Evol. Anthropol., 17, 213–226, https://doi.org/10.1002/evan.20176, 2008.

Snoeck, C. and Pellegrini, M.: Comparing bioapatite carbonate pretreatments for isotopic measurements: Part 1–Impact on structure and chemical composition, Chem. Geol., 417, 394–403, https://doi.org/10.1016/j.chemgeo.2015.10.004, 2015.

Suga, S.: Comparative Histology of Progressive Mineralization Pattern of Developing Incisor Enamel of Rodents, J. Dent. Res., 58, 1025–1026, https://doi.org/10.1177/00220345790580021401l, 1979.

Suga, S.: Progressive mineralization pattern of developing enamel during the maturation stage, J. Dent. Res., 61, 1532–1542, 1982.

Theakstone, W. H.: Oxygen isotopes in glacier-river water, Austre Okstindbreen, Okstindan, Norway, J. Glaciol., 49, 282–298, https://doi.org/10.3189/172756503781830700, 2003.

Tozer, B., Sandwell, D. T., Smith, W. H. F., Olson, C., Beale, R., and Wessel, P.: Global Bathymetry and Topography at 15 Arc Sec: SRTM15+, OpenTopography [data set], https://doi.org/10.5069/G92R3PT9, 2019.

Tütken, T., Furrer, H., and Vennemann, T. W.: Stable isotope compositions of mammoth teeth from Niederweningen, Switzerland: Implications for the Late Pleistocene climate, environment, and diet, Quatern. Int., 164–165, 139–150, https://doi.org/10.1016/j.quaint.2006.09.004, 2007.

Ukkonen, P., Arppe, L., Houmark-Nielsen, M., Kjær, K. H., and Karhu, J. A.: MIS 3 mammoth remains from Sweden–implications for faunal history, palaeoclimate and glaciation chronology, Quaternary Sci. Rev., 26, 3081–3098, https://doi.org/10.1016/j.quascirev.2007.06.021, 2007.

Widga, C., Hodgins, G., Kolis, K., Lengyel, S., Saunders, J., Walker, J. D., and Wanamaker, A. D.: Life histories and niche dynamics in late Quaternary proboscideans from midwestern North America, Quaternary Res., 100, 224–239, https://doi.org/10.1017/qua.2020.85, 2021.

Wooller, M. J., Bataille, C., Druckenmiller, P., Erickson, G. M., Groves, P., Haubenstock, N., Howe, T., Irrgeher, J., Mann, D., Moon, K., Potter, B. A., Prohaska, T., Rasic, J., Reuther, J., Shapiro, B., Spaleta, K. J., and Willis, A. D.: Lifetime mobility of an Arctic woolly mammoth, Science, 373, 806–808, https://doi.org/10.1126/science.abg1134, 2021.

Yeh, H.-F. and Lee, J.-W.: Stable Hydrogen and Oxygen Isotopes for Groundwater Sources of Penghu Islands, Taiwan, Geosciences, 8, 84, https://doi.org/10.3390/geosciences8030084, 2018.

E&G Quaternary Sci. J., 71, 213–226, 2022
https://doi.org/10.5194/egqsj-71-213-2022

Open Access E&G Quaternary Science Journal

Research article

Fluvial activity of the late-glacial to Holocene "Bergstraßenneckar" in the Upper Rhine Graben near Heidelberg, Germany – first results

Max Engel[1], **Felix Henselowsky**[1,2], **Fabian Roth**[1], **Annette Kadereit**[1], **Manuel Herzog**[1], **Stefan Hecht**[1],
Susanne Lindauer[3], **Olaf Bubenzer**[1], **and Gerd Schukraft**[1,✝]

[1]Institute of Geography, Heidelberg University, Im Neuenheimer Feld 348, 69120 Heidelberg, Germany
[2]Institute of Geography, Johannes Gutenberg University Mainz, Johann-Joachim-Becher-Weg 21, 55099 Mainz, Germany
[3]Curt-Engelhorn-Centre Archaeometry, D6, 3, 68159 Mannheim, Germany
✝deceased, April 2020

Correspondence: Max Engel (max.engel@uni-heidelberg.de) and Felix Henselowsky (felix.henselowsky@uni-mainz.de)

Relevant dates: Received: 9 February 2022 – Revised: 13 July 2022 – Accepted: 20 July 2022 – Published: 8 September 2022

How to cite: Engel, M., Henselowsky, F., Roth, F., Kadereit, A., Herzog, M., Hecht, S., Lindauer, S., Bubenzer, O., and Schukraft, G.: Fluvial activity of the late-glacial to Holocene "Bergstraßenneckar" in the Upper Rhine Graben near Heidelberg, Germany – first results, E&G Quaternary Sci. J., 71, 213–226, https://doi.org/10.5194/egqsj-71-213-2022, 2022.

Abstract: The term "Bergstraßenneckar" (BSN) refers to an abandoned course of the river Neckar. It flowed in a northern direction east of the river Rhine in the eastern part of the northern Upper Rhine Graben in southwestern Germany. The former meandering course merged with the Rhine ca. 50 km further north of the site of the present-day confluence near Mannheim. The palaeo-channels are still traceable by their depressional topography, in satellite images and by the curved boundaries of adjacent settlements and land parcels. In the plan view, satellite and aerial images reveal a succession of meander bends, with older bends being cut off from younger channels. Based on stratigraphic investigations of the channel infill in the northern part of the BSN, fluvial activity is assumed from ca. 14 500 years ago until the onset of the Holocene. We present results of the first stratigraphic investigations at two sites in the southern part of the BSN near Heidelberg (Rindlache, Schäffertwiesen), together with results from granulometric, carbonate and organic content analyses, as well as electrical resistivity tomography (ERT) measurements. The data clearly show a change from high-energy fluvial bedload (sand, gravel) to low-energy fluvio-limnic suspended load (organoclastic and calcareous mud) and to peat formation. Radiocarbon dating indicates a time lag of ca. 1500 years between the cut-off meander site (Schäffertwiesen) and the younger site (Rindlache) that was possibly still active until the present-day confluence near Mannheim was established and the BSN eventually became abandoned. Our preliminary data conform with the pedo-sedimentary evidence from the northern BSN, but slight differences in the stratigraphic pattern of the youngest channels are identified: whilst for the younger channel sections of the northern BSN the channel-bottom facies (sand, gravel) is directly overlain by peat, the channel at Rindlache shows substantial intervening mud deposition, which is interpreted as suspension load from flooding by the new Neckar channel nearby. The study shows that more chronostratigraphic data from channel sections of the southern BSN are needed to better constrain the timing of the fluvial activity and to decipher the reasons for the abandonment of the BSN. These data are also necessary to better understand the pattern of temporary reactivation of the BSN channels across the Holocene and their usage by humans, which can be deduced from historical sources and archaeological data.

Kurzfassung: Mit dem Begriff Bergstraßenneckar (BSN) wird der heute inaktive mäandrierende Lauf des Neckars bezeichnet, der im Spätglazial dem östlichen Rand des nördlichen Oberrheingrabens folgte. Von dort floss der BSN dem Rhein bei Trebur zu, bevor er sein Mündungsgebiet um ca. 50 km nach Süden in den Raum Mannheim verlegte. Die morphologischen Strukturen der verlandeten Neckarbetten sind in Satellitenbildern, im Mikrorelief und am Verlauf von Flurgrenzen erkennbar. Auf Basis von stratigraphischen Untersuchungen an Rinnenfüllungen des nördlichen BSN wird die Aktivität dieses Flusslaufs von ca. 14 500 Jahren vor heute bis zum Beginn des Holozäns angenommen. Hier präsentieren wir die ersten stratigraphischen Untersuchungen zweier Lokalitäten im südlichen Bereich des BSN (Rindlache, Schäffertwiesen) gemeinsam mit granulometrischen, Organik-, Karbonat- und widerstandsgeoelektrischen Daten. Die Ergebnisse reflektieren deutlich den Übergang von einer aktiv durchflossenen Rinne (Sand- und Kiesfazies) hin zu Verlandung unter fluvio-limnischen Bedingungen (organoklastische und kalkreiche Feinkornablagerungen) mit abschließendem Torfwachstum. Die bislang verfügbaren ^{14}C-Daten deuten auf einen zeitlichen Versatz der Aktivität von ca. 1500 Jahren zwischen der morphologisch älteren Mäanderschlinge (Schäffertwiesen) und der jüngeren Lokalität (Rindlache) hin, die möglicherweise noch zu der Zeit die Hauptrinne bildete, als die Mündung nach Süden in den Raum Mannheim verlagert wurde. Die hier präsentierten vorläufigen Daten sind mit der bestehenden Chronologie am nördlichen BSN vereinbar, wenngleich auch Unterschiede in der stratigraphischen Abfolge der Verlandungssedimente in den zuletzt aktiven Rinnen identifiziert werden: Während im Norden die fluviale Sand- und Kiesfazies unmittelbar von Niedermoortorf überlagert wird, sind in den jüngeren Rinnen im Süden Feinkornablagerungen zwischengeschaltet, die als Suspensionsfracht periodischer Überflutungen möglicherweise ausgehend vom nur wenige Kilometer entfernten neuen Neckarlauf interpretiert werden. Die Ergebnisse verdeutlichen, dass weitere chrono-stratigraphische Untersuchungen an Rinnenstandorten des südlichen BSN erforderlich sind, um den Zeitrahmen und die Abfolge der fluvialen Aktivität besser eingrenzen und die Ursachen für die Laufverlagerung besser definieren zu können. Zudem ergäben sich so detailliertere Hinweise auf die temporäre Reaktivierung bestimmter Abschnitte des BSN über das gesamte Holozän hinweg sowie auf deren Nutzung durch den Menschen, die in historischen Quellen und durch archäologische Daten belegt ist.

1 Introduction

The term “Bergstraßenneckar” (BSN) refers to an abandoned course of the river Neckar in the eastern part of the northern Upper Rhine Graben in southwestern Germany. Whilst the modern river Neckar flows in a western direction to connect with the river Rhine at Mannheim after leaving the Odenwald Mountains at Heidelberg, the BSN flowed from Heidelberg almost 50 km in a northern direction to join the river Rhine near Trebur (Fig. 1a). The palaeo-meanders of the BSN run parallel to the foothill zone (“Bergstraße”) connecting the Odenwald Mountains and the Upper Rhine Graben (Mangold, 1892; Bernhard and Hickethier, 1966; Dambeck, 2005; Dambeck and Bos, 2002; Dambeck and Thiemeyer, 2002; Beckenbach, 2016). The palaeo-meanders can be identified by their sinuous courses, lowered surface and the typically curved boundaries of adjacent settlements and roads, as well as cadastral boundaries. Satellite and aerial images reveal a relative chronology of younger and older meander bends, with younger bends truncating the older bends and older bends being cut off from younger channel sections. Since early modern times, it has been contentious whether natural or anthropogenic processes caused the Neckar to abandon the BSN riverbed. The hypothesis of a man-made diversion of the lower Neckar from a northern flow direction (i.e., the BSN) to a western direction towards Mannheim (i.e., the modern Neckar) in the late Middle Ages (after 1354 CE) as a flood protection measure (e.g. Saur, 1593; Winkelmann, 1697; Mone, 1826) was later rejected (Mangold, 1892; Barsch and Mäusbacher, 1979, 1988). Some palaeo-channel sections of the BSN may have still served as waterways in historical times, particularly in the Roman period (Eckoldt, 1985; Wirth, 2011). Systematic chronological and sedimentological investigations from the northern Upper Rhine Graben indicate drainage of the lower Neckar catchment through the BSN during a short period between ca. 14 500 years ago and the onset of the Holocene (see Große-Brauckmann et al., 1990; Dambeck, 2005; Dambeck and Thiemeyer, 2002; Bos et al., 2008, 2012). This phase of fluvial activity encompasses the formation and abandonment of different meanders, a relative chronology of which has been established by Dambeck (2005). Here, we aim to generate an initial chronostratigraphy of palaeo-meanders in the southern part of the BSN near Heidelberg (hereafter: southern BSN). We compare our results to meander activity phases as identified for the northern BSN by Dambeck (2005), Dambeck and Bos (2002), and Dambeck and Thiemeyer (2002) to establish working hypotheses for detailed investigations on the southern BSN in the future.

2 Regional setting

Two palaeo-meanders were investigated at the field sites Rindlache (RL) and Schäffertwiesen (SW). The sites are located 1 km apart, ca. 15 km northwest of Heidelberg and ca. 10 km northeast of Mannheim, at the border between the German federal states of Baden-Württemberg and Hesse near Viernheim (Fig. 1b). The study area is part of the eastern Upper Rhine Graben and located between the river Rhine and the eastern graben shoulder, formed by the southern Odenwald with a Palaeozoic basement covered by (among others) Triassic Buntsandstein sandstone (Barsch and Mäusbacher, 1979, 1988; Nickel and Fettel, 1979; Eisbacher and Fielitz, 2010). Quaternary subsidence rates of the eastern Upper Rhine Graben near Heidelberg of $\sim 0.2\,\mathrm{mm\,yr^{-1}}$ are an order of magnitude higher compared to other parts of the graben and lead to high sedimentation rates and a thick late Quaternary infill (Peters and van Balen, 2007; Buness et al., 2009; Gabriel et al., 2013).

The study sites are located north of the alluvial fan of the Neckar, which forms where the river leaves the Odenwald and enters the surface of the last-glacial Lower Terrace inside the Upper Rhine Graben (Fig. 1b) (Barsch and Mäusbacher, 1979, 1988). In the northernmost part of the Upper Rhine Graben, the Lower Terrace is categorised into an upper Lower Terrace (t6, early to middle Würm) underlying the fluvial landscape of the northern BSN and a lower Lower Terrace (t7, late Würm) underlying the Rhine and its floodplain (Scheer, 1978; Dambeck, 2005; Erkens et al., 2009). In the area of the southern BSN no such distinction is made (Schottler, 1906; Kupfahl et al., 1972; Holzhauer, 2013). The Lower Terrace around the study sites shows varying ratios of sand and gravel, has an irregular surface, is cut by BSN channels, and is overlain by up to several metres of BSN-related sand- and silt-dominated flood deposits (Barsch and Mäusbacher, 1979; Löscher, 2007). During the late Pleistocene–Holocene transition, dunes formed on top of the silt- and sand-covered Lower Terrace (Löscher, 2007; Löscher et al., 1989) as elements of a larger regional dune system covering substantial parts of the northern Upper Rhine Graben (Dambeck, 2005; Holzhauer, 2013; Holzhauer et al., 2017; Pflanz et al., 2022).

The meandering course of the former BSN is reflected in the spatial distribution of peat deposits in Fig. 1a corresponding to morphological depressions of a depth of ∼ 2–4 m (Fig. 1b) (Barsch and Mäusbacher, 1979). The two study sites are situated in the most prominent palaeochannels of the southern BSN (Fig. 1b) with distinct channel morphologies of inwardly convex and outwardly concave banks, and with diameters (half-meander path lengths sensu Howard and Hemberger, 1991) of 800–900 m. The two sites have been chosen as representative examples of (1) the presumably youngest course of the BSN (meander Rindlache) and (2) an earlier fluvial phase (cut-off meander Schäffertwiesen) (see maps in Mangold, 1892; Barsch and Mäusbacher, 1979) (Fig. 1b). The historical field names indicate that the sites were formerly used for pasture (*Rind* = cattle; *Wiese* = meadow) likely due to waterlogging (*Lache* = marsh/swamp) caused by a high groundwater table. The formerly high groundwater table in the Upper Rhine Graben has lowered significantly due to major regulation measures on the Neckar and Rhine since the early 19th century and subsequent river incision. More recently, the intensified exploitation of drinking and irrigation water added to groundwater level fall (see Barsch and Mäusbacher, 1979; Dister et al., 1990).

3 Methods

The stratigraphy at both sites was studied using 2-D electrical resistivity tomography (ERT) and sediment cores. ERT profiles were measured using a GeoTom MK1E100 device with Schlumberger configuration, 100 electrodes and 1 m spacing, as in Kneisel (2003). The composite ERT profile 6–7–8–11 at Rindlache consists of four separate profiles integrated with an overlap of 25 m (profiles 6–8) and 66 m (profiles 8 and 11), respectively. ERT profile 1–2 (112.5 m long) at Schäffertwiesen combines two separate profiles overlapping for 37.5 m. Post-processing of ERT data comprises the calculation of standard inversions without filtering using Res2Dinv software. Erroneous data points, e.g. resulting from disconnected electrodes during the measurement, were removed from the raw data prior to data modelling.

Along the ERT profiles, sediment cores were taken using a vibracorer and two different stainless-steel sampling tubes (Table S1 in the Supplement): (1) open percussion gouges (ø 6 cm) (Figs. S1, S2) and (2) closed percussion gouges equipped with PVC liner tubes (ø 5 cm) (Figs. S3–S7). Sediment cores taken in the open gouges were documented and sampled in the field according to Ad-hoc-AG Boden (2005) and the Munsell Soil Color Charts (Munsell Color Labo-

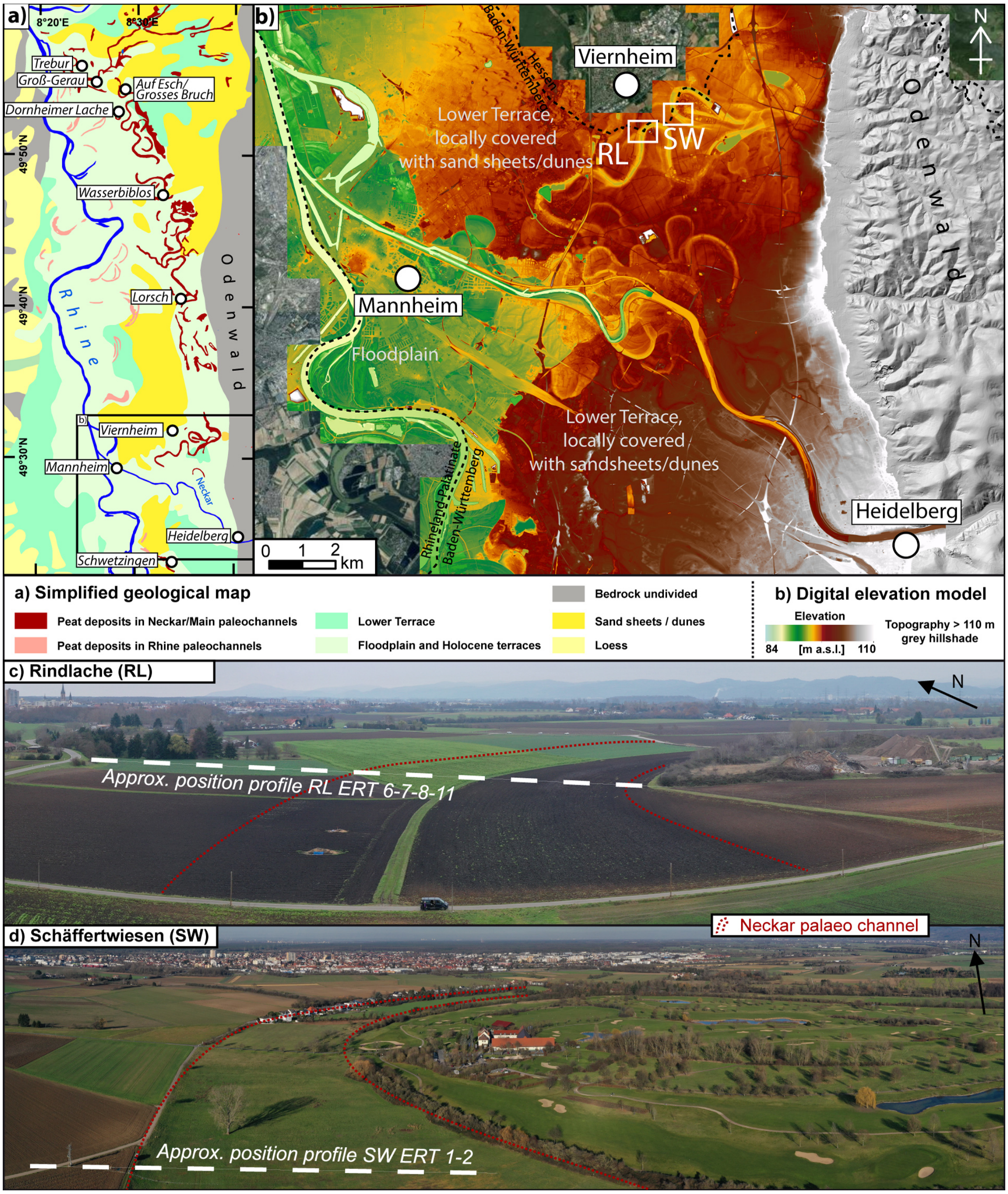

Figure 1. Overview of the study area. **(a)** Simplified geological map of the northern Upper Rhine Graben based on the Geological Map of Germany 1 : 1 000 000 (GK1000) and, for the peat deposits, the General Geological Map of Germany 1 : 200 000 (GUEK200), sheets CC 6310 Frankfurt/Main – West and CC 7110 Mannheim. Data source: Bundesanstalt für Geowissenschaften und Rohstoffe (BGR). **(b)** High-resolution digital elevation model emphasising relief variation at 84–110 m NHN to highlight the active and abandoned fluvial channels of the BSN between Heidelberg and Mannheim. RL = Rindlache; SW = Schäffertwiesen. Data source: DGM1 of the Federal State of Baden-Württemberg provided by Landesamt für Geologie, Rohstoffe und Bergbau (LGBR) and established in 2000–2005. **(c)** Drone-based photograph of the Rindlache site (9 November 2020). **(d)** Drone-based photograph of the Schäffertwiesen site (17 January 2020).

ratory, 2000) (Table S2). The upper part of each core segment is prone to disturbances from material collapsing inside the borehole or from the recovery process. These disturbances were identified based on comparison with the lowermost part of the overlying core segment and removed from the record. The PVC liners were opened and the sediment documented (Munsell Color Laboratory, 2000; Ad-hoc-AG Boden, 2005) and sampled in the Laboratory for Geomorphology and Geoecology, Institute of Geography, Heidelberg University (Table S3). One additional core (RL01) was taken using an Edelman-type corer. At each site one core was analysed in more detail in the laboratory to support facies interpretation. All depths reported in the result section follow the original documentation and correspond to the core photographs in Figs. S1–S7. Additionally, adjusted depths of unit boundaries of the uppermost compressed metre are given in Tables S2 and S3. Samples were dried, carefully pestled by hand and sieved for the < 2 mm fraction. Grain-size distributions of the < 2 mm fraction were measured using a laser particle sizer (Fritsch Analysette P22) with a measurable range of 0.8–2000 µm at the Laboratory of Sedimentology, Institute of Geosciences, Heidelberg University. All samples were pre-treated with 10 mL H_2O_2 (30 %) to remove organic carbon and $Na_4P_2O_7$ (55.7 g L^{-1}) for aggregate dispersion. Univariate statistical measures were calculated using the Excel sheet GRADISTAT v9.1 (Blott and Pye, 2001). Organic matter was determined by loss-on-ignition (LOI) following a protocol slightly modified from Heiri et al. (2001). Samples of 3–5 g were combusted at 550 °C for 4 h in a muffle furnace. The carbonate content was measured using the Scheibler method according to DIN ISO 10693.

Four samples of autochthonous peat were dated by ^{14}C accelerator mass spectrometry (AMS) at the Curt-Engelhorn-Centre Archaeometry in Mannheim, Germany. The absence of allochthonous root material was verified under a binocular microscope prior to sample submission to the dating laboratory. All samples were pre-treated with HCl, NaOH and HCl according to the acid–base–acid (ABA) method, during which the "base" step eliminates ex situ humic acids (Wild et al., 2013). The non-dissolved residual was then used for dating. The analysis was carried out on a MICADAS type AMS system (Kromer et al., 2013). Results were calibrated using CALIB 8.2 (Stuiver et al., 2022) and the IntCal20 dataset (Reimer et al., 2020). For age interpretation, the 2σ error was considered (Table S4). The reference date for all calibrated ^{14}C data is 1950 CE.

The positions of all sediment cores and ERT electrodes, as well as topographic corrections, were determined using a Leica GS16 differential global navigation satellite system (DGNSS) and the satellite positioning service of the Federal State of Baden-Württemberg (SAPOS BW) in real-time kinematic (RTK) mode (lateral error: 1–2 cm; vertical error: 2–3 cm). Elevations are given in metres above NHN (*Normalhöhen-Null*: official vertical datum used in Germany signifying mean sea level in reference to *Normaal Amsterdams Peil* or Amsterdam Ordnance Datum) within the DHHN2016 (*Deutsches Haupthöhennetz*: official German height reference system, newly levelled and introduced in 2016–2017; AdV, 2018).

4 Results

4.1 The Rindlache site

4.1.1 Stratigraphic record

Sediment core RL09 represents the stratigraphy of the BSN at Rindlache and was taken on a harvested crop field in the central part of the assumed palaeo-channel (Fig. 1b). The bottom unit of 5.45–5.20 m b.s. (below surface) is dominated by sand of changing colour and shows only minor amounts of silt and fine gravel (Figs. 2, S2). Between 5.20 and 4.50 m b.s., it is grain-supported, and coarser components of up to 5 cm (long axis) contribute up to > 50 %. The sorting varies. The LOI values are very low, and the carbonate content is around 8 %. The section 4.50–2.30 m b.s. shows medium to coarse sand with lower amounts of coarser components and with improved sorting. The organic content is equally low, and the carbonate content decreases to 5 %–7 %. This unit is overlain by light greyish brown mud with upward-increasing carbonate content, culminating in a high value of > 90 % in the uppermost part at 1.50 m b.s. Sand or coarser components are absent, whereas reddish brown vertical root casts are visible. Unfortunately, the lower boundary could not be identified due to core loss (2.30–2.00 m b.s.); however, it is abrupt in parallel core Gerd 1b (Fig. S3). The LOI values up to 1.36 m b.s. increase slightly to levels of 3 %–4 %. Above a sharp contact, black peat was found, most of which was lost during the core recovery (core loss: 1.30–1.00 m b.s.). The LOI values reach up to > 40 %. In the parallel core Gerd 1b, peat from this unit at 1.05 m b.s. was dated to 6539–6402 cal yr BP (MAMS 43 986). The peat is overlain by dark grey, well-sorted organic-rich mud (0.92–0.80 m b.s.) showing LOI values of 13 %, a very low carbonate content and many fine roots. From 0.80 to 0.57 m b.s., the grey mud contains a few terrestrial gastropod shells and shell fragments, as well as some fine vertical roots. The carbonate content is slightly increased, whereas the LOI value is lower. Above this unit, the clayey silt has a light yellowish-brown colour, still containing gastropod shell fragments exhibited as higher carbonate content. The uppermost unit (0.46–0.15 m b.s.; for decompacted values see Table S3) is silt-dominated with increased LOI values representing the anthropogenically turbated plough horizon.

4.1.2 Electrical resistivity tomography (ERT)

The ERT profile 6–7–8–11 runs perpendicular to the BSN channel, indicated by a surface depression (Fig. 2a, c). It includes the flanks on both sides and intersects with core RL09 at 183 m horizontal distance (h.d.). In the northwest, the ERT profile starts at the foot of a late Pleistocene dune (Bettenberg, Fig. 2c; mapped in Barsch and Mäusbacher, 1979) at ca. 102 m NHN, running down a slightly concave slope with a small terrace bordering the outer bank at approximately 75–95 m h.d. It reaches the lowest elevations of the palaeo-

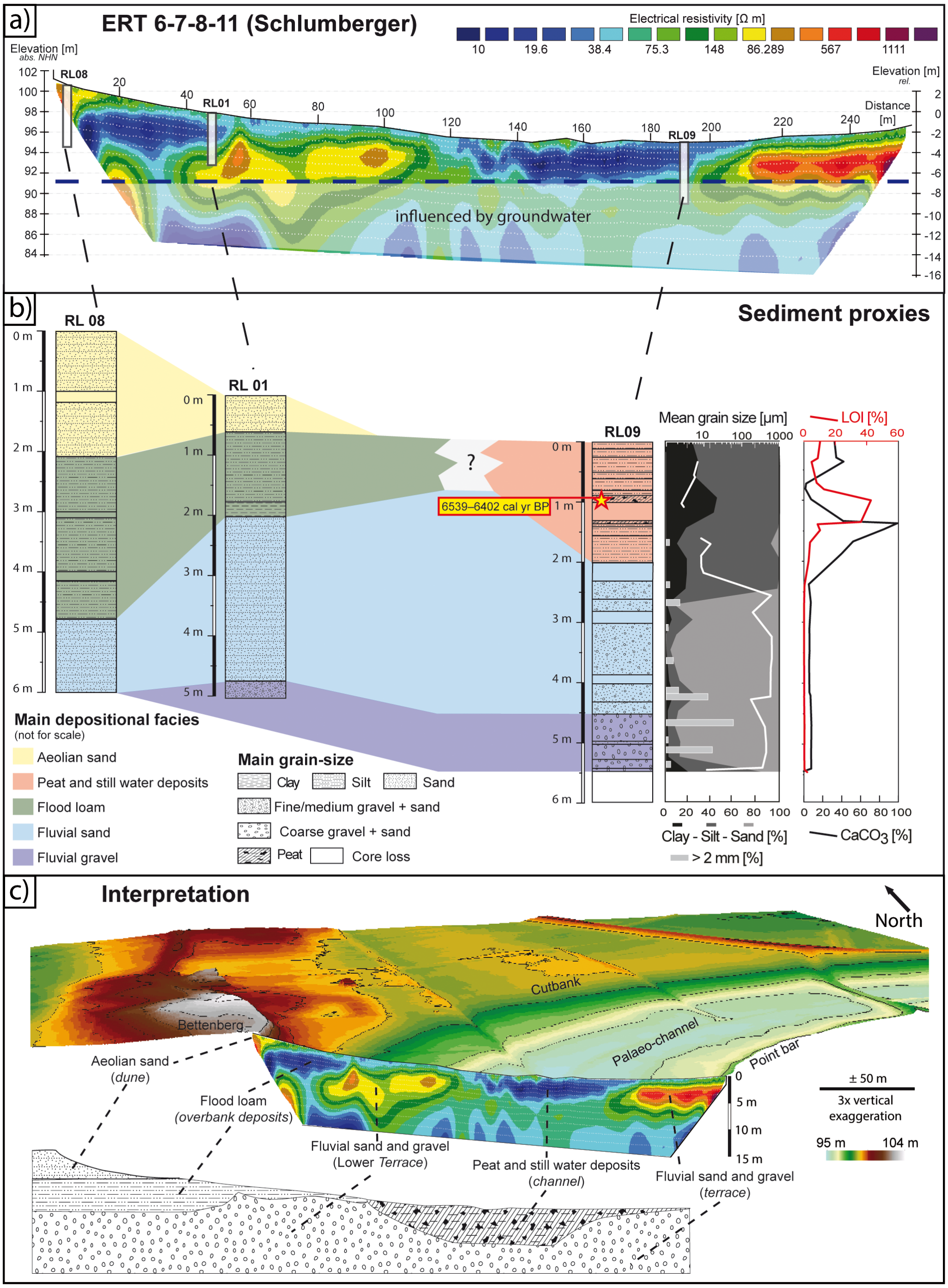

Figure 2. BSN meander at Rindlache. **(a)** Transect ERT 6–7–8–11 crossing the palaeo-river channel and showing the distribution of fine-grained deposits in blue (low resistivity values) and coarse-grained deposits in green, yellow, brown and red (intermediate to high resistivity values). **(b)** Synopsis of sediment cores RL08, RL01 and RL09 with tentative facies interpretation. For RL09, grain-size distributions, mean grain size, LOI values and $CaCO_3$ content are displayed. **(c)** Oblique view of the BSN meander in combination with the transect ERT 6–7–8–11 and tentative facies interpretation. A legend for the bottom drawing is provided in panel **(b)**. Data source: DGM1 of the Federal State of Baden-Württemberg provided by LGBR and established in 2000–2005.

meander channel at ca. 95 m NHN (ca. 125 to 210 m h.d.) and terminates at the inner bank of the palaeo-meander. The root mean square error (RMSE) is 4.1 % after three iterations of data modelling. The maximum difference in elevation across the entire profile is 6.5 m. The measured resistivity ranges between ∼ 10 and ∼ 1100 Ωm, and a depth of ca. 20 m b.s. was reached (Fig. 2a). The central channel between 125 and 210 m h.d. shows the lowest resistivity in the uppermost 4–6 m. This is in strong contrast to values which are an order of a magnitude higher at the southeastern end of the ERT profile between 210 and 260 m h.d. The slope at the foot of the Bettenberg dune also shows higher resistivities of 200–500 Ωm with a slightly thicker wedge of low-resistivity materials on top. Between 10 and 55 m h.d. this pattern is reversed, with ca. 1 m of medium resistivities (50–100 Ωm) at the top above very low resistivities, similar to the palaeo-meander channel infill.

4.2 The Schäffertwiesen site

4.2.1 Stratigraphic record

The sediment cores from Schäffertwiesen were taken along an ERT profile oriented perpendicular to the meander channel including the outer bank and a part of the channel (Figs. 1b, 3b, c). Sediment core SW01 was taken on the slope of the outer bank and reaches a depth of 4 m b.s. (Fig. S4). The lower part from 4.00 m to 1.74 m b.s. is characterised by a medium to coarse sand matrix and varying amounts of well-rounded gravel components, the latter mostly below 2.68 m b.s. This lowermost section is clast-supported between 3.45 m and 3.00 m b.s. (mostly limestone of Middle Triassic Muschelkalk, Upper Jurassic Weißjurakalk and red sandstone of Lower to Middle Triassic Buntsandstein, as well as other limestone and quartzite varieties). It shows increased carbonate content of up to 10 % and very low LOI values (< 0.3 %). Between 2.75 m and 2.40 m b.s. some finer and darker laminae occur. From 2.40 m to 2.00 m b.s., the core is disturbed by collapsed material. A sharp boundary separates the sand to gravel deposits from sandy to clayey mud (1.74–0.84 m b.s.), where LOI values increase to up to 6 %, and carbonate content reaches up to 25 %. A thin sand layer resembling the bottom facies is intercalated at 1.61–1.57 m b.s. Plant remains from a depth of 1.67 m b.s. were dated to 11 258–11 195 cal yr BP (MAMS 46037). The carbonate-rich mud is overlain by peat (0.84–0.59 m b.s.) with LOI values of up to 57 % and a very low carbonate content of < 1 %. Peat-derived ^{14}C data range from 11 079–10 722 cal yr BP (0.80 m b.s., MAMS 46036) to 7920–7701 cal yr BP (0.60 m b.s., MAMS 46035). This peat section is separated from the organic-rich topsoil (0.28–0.11 m b.s.; LOI values up to 24 %) by a brownish grey sandy mud section.

The coarse sand and gravel unit was found in the basal parts of all cores from Schäffertwiesen, where it varies in thickness (Fig. 3b). Its sharp upper boundary rises from 93.11 m NHN in the west (SW03) to 93.72 m b.s. (SW01), 94.22 m b.s. (SW04) and 96.17 m b.s. (SW02) in the east. The overlying poorly sorted sandy mud from SW01 (1.74–0.84 m b.s.) was not found in SW02 and SW04 but can be correlated with a much thicker occurrence in the western part of the profile (SW03; 4.45–0.55 m b.s.). The peat, however, is only present in SW04, close to the top of the sequence, in similar thickness as observed in SW01.

4.2.2 Electrical resistivity tomography (ERT)

The stratigraphic correlations between the cores are reflected by the ERT profile 1–2 at Schäffertwiesen (Fig. 3a). It has a length of 112.5 m and an RMS error of 3.9 % after three iterations of data modelling. Resistivity values are in the same range as in ERT profile 6–7–8–11 at Rindlache. From its southwestern end, the profile traverses over a flat terrace for ca. 30 m at ca. 98 m NHN before following a concave slope down to ca. 95.5 m NHN in the lowest part of the profile, which is also where core SW01 was taken. Between 45 m h.d. and the northeastern end, the profile gradually rises in the form of a slightly convex slope to ca. 96.5 m NHN. The flat part of the profile in the southwest, represented by core SW03, shows very low resistivity values (10–40 Ωm) correlating with the sandy mud facies. Here, resistivity only increases below ca. 5 m b.s., where the sand and gravel deposits were encountered in SW03. Likewise, in the topographically lowest part of the profile, corresponding to SW01, the basal sand and gravel deposits are reflected by medium resistivity values of around 80 Ωm, compared to 20–50 Ωm in the sandy mud and peat of the uppermost 1.70 m of the sequence. In the northeastern part of the profile, medium to high resistivity values reach close to the surface, following the rising boundary between the sand and gravel unit and the peat.

5 Discussion

5.1 Fluvial activity as reconstructed from facies patterns

The sand and gravel deposits found in the basal part of all cores from both palaeo-meander sites consist of varying ratios of predominantly medium to coarse sand and rounded to well-rounded gravel components. They represent the bedload of the BSN deposited at the bottom of the formerly active meander channel. Primary deposition of the material in pre-late-glacial times, perhaps in a braided system in Pleniglacial times of the last-glacial period, and subsequent reworking of these deposits in late-glacial times by a single meandering channel is plausible. As the channels are incised into the Lower Terrace of the Rhine, it is possible that Rhine deposits were reactivated by the BSN. Although a quantitative petrographic analysis to discriminate between Rhine and Neckar deposits is still pending, the visual inspection of basal gravel components in both master cores RL09 and SW01 already shows a dominance of Muschelkalk, Weißjura and other

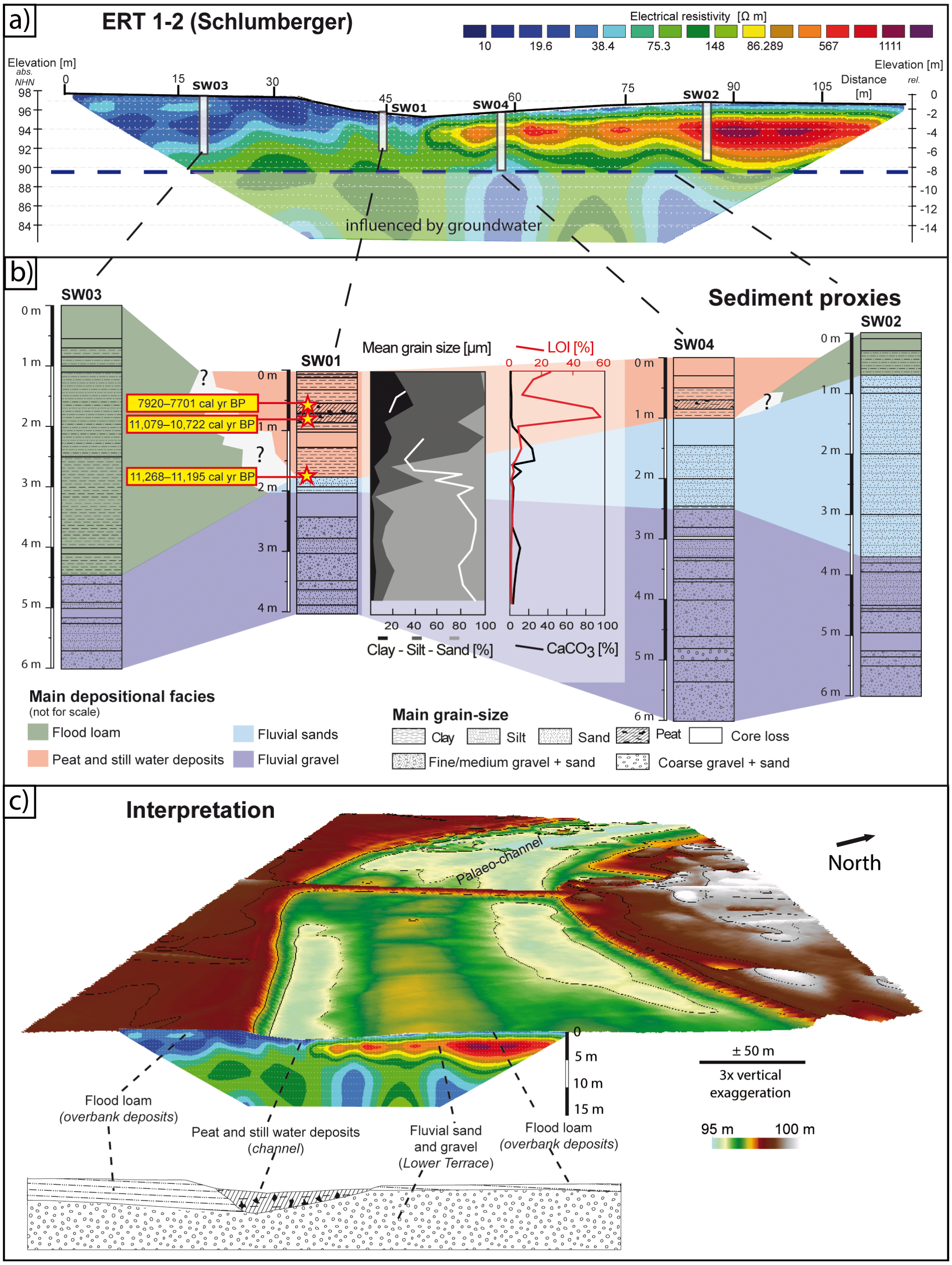

Figure 3. BSN meander at Schäffertwiesen. **(a)** Transect ERT 1–2 crossing the palaeo-river channel and showing the distribution of fine-grained deposits in blue (low resistivity values) and coarse-grained deposits in green, yellow, brown and red (intermediate to high resistivity values). **(b)** Synopsis of sediment cores SW03, SW01, SW04 and SW02 with tentative facies interpretation. For SW04, grain-size distributions, mean grain size, LOI values and CaCO$_3$ content are displayed. **(c)** Oblique view of the BSN meander in combination with the transect ERT 6–7–8–11 and tentative facies interpretation. A legend for the bottom drawing is provided in panel **(b)**. Data source: DGM1 of the Federal State of Baden-Württemberg provided by LGBR and established in 2000–2005.

limestones, as well as Buntsandstein sandstone, collectively representing the main erosional products of the Neckar catchment (Barsch and Mäusbacher, 1979; Fezer, 1997; Bibus and Rähle, 2003; Löscher, 2007; LGBR, 2021). These deposits shape the youngest part of the wide alluvial fan of the Neckar (Löscher et al., 1980; Barsch and Mäusbacher, 1988), which belongs to the Mannheim Formation (LGBR, 2021) and, at its northern boundary, almost reaches the study area (Fezer, 1997; Beckenbach, 2016).

The typical sediment sequence of palaeo-meander channels of the northern BSN (e.g. site of "Wasserbiblos" in Dambeck, 2005; Dambeck and Bos, 2002) also starts with fluvial sands and few pebbles. The general fining-up gradient from a sand and gravel mixture (in the southern BSN with some clast-supported sections) to matrix-supported units and pure fluvial sands indicates a decrease in fluvial transport capacity at the end of the phase of fluvial activity of the BSN. This decrease is either related to lower discharge or a thalweg shifting away from the coring site. However, it cannot be excluded that the increasing medium sand component in the upper part of the fining-up sequence is partially related to reactivated aeolian processes and input during the Younger Dryas (Löscher et al., 1989; Dambeck and Thiemeyer, 2002; Pflanz et al., 2022). The poorly sorted greyish-brown sandy mud overlying the in-channel fluvial sands in RL09 (boundary at 2.30 m b.s.) and SW01 (boundary at 1.74 m b.s.) reflects a distinct shift from a fluvial channel carrying bedload – until then presumably the main active channel of the BSN – to a cut-off channel restricted to suspension-load settling during stages of overbank flow by an adjacent active channel (Barsch and Mäusbacher, 1979). At Schäffertwiesen, this adjacent channel was the Rindlache channel. After the BSN was entirely abandoned, the Rindlache site was subject to flooding and received suspension load from a new Neckar course close by. This might have been the current channel heading straight to the Rhine near Mannheim, although this assumption requires verification with future research. Along the northern BSN this type of fluvio-limnic deposition is observed for the older meander generation before peat formation commenced, whereas at the younger meander sites peat deposits immediately overlie the coarse-grained channel-bottom deposits (Dambeck, 2005; Dambeck and Bos, 2002). Thus, the sedimentary sequences at Rindlache and Schäffertwiesen both resemble the infill of the older meander sites along the northern BSN. At some palaeo-channel sites of the northern BSN (e.g. "Auf Esch", "Großes Bruch"), as well as at Rindlache, peat formation is interrupted by organic-rich black clays that may represent a reactivation of overbank deposition and indicate increased input of fine-grained material into the inactive fluvial system (Dambeck, 2005; Dambeck and Thiemeyer, 2002).

Dambeck and Bos (2002) and Dambeck and Thiemeyer (2002) refer to the sandy mud overlying the fluvial channel-bottom facies at the older meander sites as clays, silts, loam or gyttja with occasional fine sandy laminae, depending on the site. The very high carbonate content in the uppermost part of this fine-grained unit (> 90 % in RL09) right below the overlying peat, also referred to as calcareous gyttja along the northern BSN (Dambeck and Bos, 2002; Bos et al., 2008), was identified as secondary carbonate precipitation. At present, two models for the formation of this carbonate precipitation are considered.

- The first is precipitation within the sediment body at distinct substrate boundaries in the groundwater fluctuation zone, along the capillary fringe, as described for the so-called *Rheinweiß* in similar contexts (Dambeck, 2005; Holzhauer, 2013; Holzhauer et al., 2017). Being this close to the present-day land surface, the *Rheinweiß* represents a relict feature. It predates the river regulation measures in the Upper Rhine Graben from 1817 CE on that led to rapid linear incision of the Rhine and to lowering of groundwater levels by several metres in the entire graben area (Barsch and Mäusbacher, 1979; Dister et al., 1990).

- The second is precipitation in the fluvio-limnic environment of the cut-off meander by photosynthesising Charophyceae and aquatic plants, aided by the uptake of CO_2 from bicarbonate (HCO_3^-) dissolved in the water (e.g. Bohnke and Hoek, 2007). The general model, according to which carbonate ions (CO_3^{2-}) are released and attract Ca^{2+} ions to form Ca_2CO_3 in the immediate vicinity of the photosynthesising organisms, is described in, for example, Merz (1992).

Whilst in both the southern and the northern (site "Wasserbiblos" in Dambeck and Bos, 2002) parts of the BSN these calcareous muds mostly date into the Preboreal (11.7–10.3 kyr ago) (Fig. 4), they are also well recognised to have formed earlier during the Alleröd (13.4–12.7 kyr ago) elsewhere in Central Europe (e.g. Bohncke and Hoek, 2007; Pawłowski et al., 2016). They may in general be associated with warmer phases of the late-glacial to Holocene transition with more abundant (aquatic) vegetation, shifting the carbonate balance and leading to increased carbonate precipitation (Waldmann, 1989; Dambeck, 2005).

5.2 Timing of fluvial activity of the southern BSN

There are diverging assumptions regarding the timing of the fluvial activity of the BSN. Its relatively short existence has been associated with the late-glacial formation of the north–south-directed dune belt between Schwetzingen and Lorsch (Fig. 1a) (e.g. Dambeck, 2005), which is assumed to have blocked the direct connection with the Rhine between Heidelberg and Mannheim. Yet, none of the palaeo-channels of the northern BSN are covered by any significant drift sands, the formation of which terminated mostly before the Older Dryas (13.6–13.4 kyr ago). Instead, drift sands were eroded by the BSN in some places, indicating that fluvial activ-

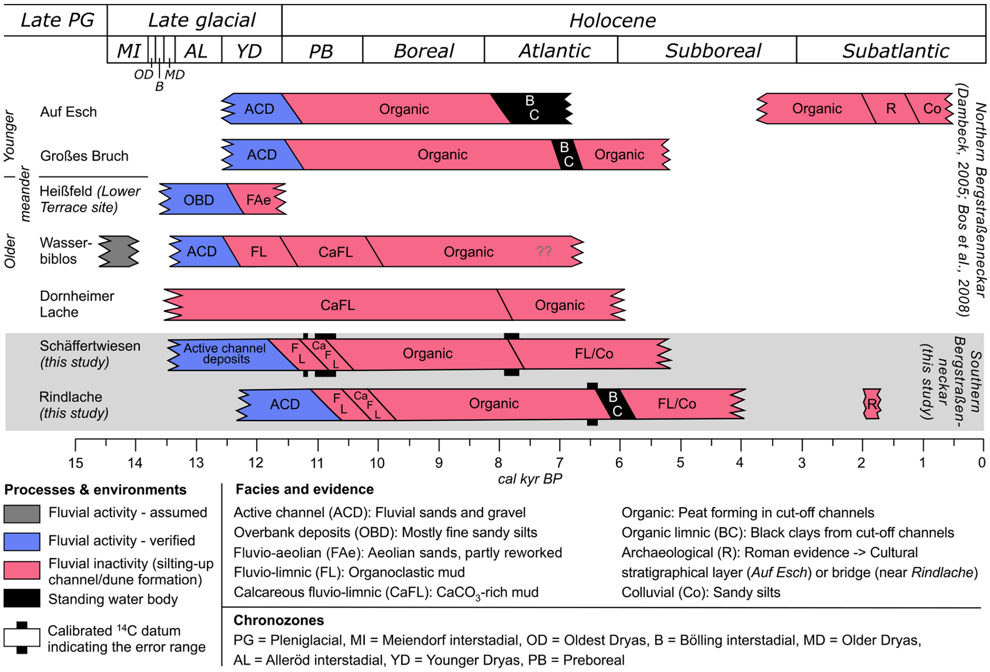

Figure 4. Assumed timeline of fluvial activity and inactivity of the Bergstraßenneckar (BSN). All sites refer to profiles from palaeo-channels, apart from Heißfeld (profile on the Lower Terrace adjacent to a BSN palaeo-channel). Results from the northern BSN (upper part) were taken from Dambeck (2005) and Bos et al. (2008). Preliminary data and interpretation from the southern BSN (this study) are shown in the lower part on the grey background. Wetland or temporary standing-water conditions at Rindlache during Roman times are inferred from the partially excavated wooden bridge across the same BSN channel ca. 1 km to the south (Wirth, 2011).

ity postdates the period of main aeolian activity. Initial activity of the BSN is tentatively dated to ca. 14 500 years ago (Dambeck, 2005). At the site “Fasanerie” near Groß-Gerau (Dambeck, 2005) and near Schwanheim (Hoffmann and Kzyzanowski, 1984) (Fig. 1a), Laacher See tephra, now dated to 13 006 ± 9 cal yr BP (Reinig et al., 2021), was identified in overbank deposits of the northern BSN. The detailed stratigraphic investigations in the northern part of the BSN indicate a dune breach of the Neckar towards the Rhine at approximately 12 800 to 11 500 years ago during the Younger Dryas (12.7–11.7 kyr ago) and an end to fluvial activity of the BSN channels at some point between ca. 11 600 and 10 120 years ago (Haupt, 1928; Wagner, 1981; Große-Brauckmann et al., 1990; Dambeck, 2005; Dambeck and Bos, 2002; Bos et al., 2008, 2012). However, there are several historical accounts and archaeological data pointing to the reactivation of certain sections of the BSN by smaller tributaries draining the western Odenwald Mountains and their use as waterways for the transport of goods, in particular during Roman times (Eckoldt, 1985; Wirth, 2011).

For the northern BSN, two palaeo-meander generations have been classified. Whilst the relatively younger meander generation forms a more or less continuous course to the former mouth west of Trebur, the relatively older meanders are morphologically detached (Kupfahl et al., 1972; Dambeck, 2005). Based on palynostratigraphical evidence and radiocarbon data, mud deposition in cut-off meanders of the older generation started in Alleröd times (site “Dornheimer Lache” in Bos et al., 2008) or by the end of the Younger Dryas (site “Wasserbiblos” in Dambeck, 2005; Dambeck and Bos, 2002; Bos et al., 2012). Elsewhere, it is assumed that sands were blown out from the inactive point bars of cut-off meanders to form proximal dunes on the Lower Terrace (HLfB, 1990), e.g. at the site “Heißfeld” (Dambeck, 2005; Dambeck and Thiemeyer, 2002) at a time, during the Younger Dryas, when aeolian dunes and drift sands of the northern Upper Rhine Graben were reactivated to a limited extent (Löscher et al., 1989; Dambeck and Bos, 2002; Pflanz et al., 2022). The younger meander sites show a distinct shift from fluvial sands to peat growth roughly at the beginning of the Preboreal (Fig. 4), possibly reflecting the abandonment of the BSN and confluence of the Neckar with the Rhine further to the south near Mannheim (Dambeck, 2005).

The basic stratigraphic patterns of the northern and southern BSN show striking similarities, but presently, very few radiocarbon ages are available for the southern BSN. However, if these are used as chronometric tie points as illustrated in Fig. 4 (lower part), the similarities become even more obvious. As the clastic mud deposits at the site Schäffertwiesen may date to the Younger Dryas to Preboreal period, we assume that the coarse-grained channel-bottom deposits underneath date to late-glacial times. The shift from mud sedimentation to peat growth may have been induced by a denser vegetation cover at the onset of the Preboreal (Dambeck and Bos, 2002; Bos et al., 2008) leading to reduced suspension load during flood events and termination of the silting-up process. At the site "Wasserbiblos", northern BSN, sedimentation of similar silty and calcareous mud, reflecting a change in fluvial conditions from in-channel bedload transport and accumulation at the channel bottom to fluvio-limnic conditions inside a cut-off meander, is also dated to the end of the late-glacial period. A temporal overlap of changing fluvial dynamics at the Schäffertwiesen meander (between 12 000 and 11 500 cal yr BP) at the southern BSN and the older meander generation at the northern BSN, represented by the site "Wasserbiblos" (Dambeck, 2005; Dambeck and Bos, 2002; Bos et al., 2012), is likely. Yet peat formation at the northern BSN started earlier, during Preboreal times, and lasted until the end of the Boreal or beginning of the Atlantic period (ca. 8000–7500 cal yr BP). The peat at Rindlache continued to form until ca. 1500 years later (ca. 6500–6000 cal yr BP) (Fig. 4). The deposition of organic-rich black clays inside the channels and as overbank fines during the Atlantic period may represent an initial signal of anthropogenic soil erosion by Middle Neolithic communities (Große-Brauckmann et al., 1990; Dambeck and Thiemeyer, 2002). This interpretation is supported by the first occurrence of *Cerealia* in pollen spectra of northern BSN sites as an indicator of the introduction of agriculture and a decrease of *Ulmus*, which is related to the Neolithic Linear Pottery and Rössen cultures using this type of wood for fire and construction (Bos et al., 2012). In the area of the southern BSN people of the Late Neolithic Michelsberg (ca. 4400–3500 BCE; Lang, 1996) and/or the end Neolithic Corded Ware ceramic cultures (ca. 2900–2350 BCE; König, 2015) may have intensified soil erosion resulting in a subsequent increase in suspension load and the formation of the black clays.

Assuming that the Rindlache site – in contrast to the cut-off meander of Schäffertwiesen – represented the active channel until the modern Neckar channel was established and the BSN finally abandoned, the entire chronostratigraphy may be offset by ca. 1500 years. Thus, it would overlap with the chronostratigraphy of northern BSN sites representing the younger meander generation, sensu Dambeck (2005), even though the Rindlache site shows an interim sequence of fluvio-limnic sandy mud, which in the north is characteristic of only older meander sites (Fig. 4).

6 Conclusions and outlook

Palaeo-meanders of the southern BSN are an understudied geomorphological archive. This is all the more surprising as studies along the northern BSN in Hesse proved to reveal detailed aspects of the late-glacial to Holocene history of the Upper Rhine Graben riverscape (e.g. Dambeck, 2005; Dambeck and Thiemeyer, 2002; Bos et al., 2008). The palaeo-meander channels of the southern BSN can still be morphologically identified in the field, as well as from satellite imagery and digital elevation models (Beckenbach, 2016), representing a sequence of relatively older meanders which have been cut off from younger channels. Our pilot study at the relatively older Schäffertwiesen meander and the younger Rindlache meander shows a stratigraphic sequence reaching from partially clast-supported sand and gravel in-channel facies to muds and peat representing the phase after which the meanders were cut off, and the Neckar shifted its course entirely. The ^{14}C data of the upper boundaries of the peat deposits at both sites, Schäffertwiesen (cut-off meander) and Rindlache (part of the latest course), are offset by ca. 1500 years, reflecting the overall older age of the Schäffertwiesen sequence. In comparison with the abandoned riverscape of the northern BSN (Dambeck, 2005), both sites studied here resemble the stratigraphic pattern of the older meander phase with fluvio-limnic mud deposition which is vertically confined by coarse-grained in-channel facies (below) and peat and black clays (above). The chronology of the Schäffertwiesen site tentatively correlates with the older meander generation, while the Rindlache site has more of a chronological overlap with the younger meander generation of the northern BSN, where, however, the intermittent mud is absent. Therefore, the presence of fluvio-limnic sediments in the abandoned river channel may be a function of flooding frequency and proximity to a still active channel. Whilst this was the case for both of the southern sites after the final abandonment of the BSN as they were still close to the new Neckar course, the northern BSN channel sites were cut off from a regular flooding regime.

Evidently, more palaeo-channel stratigraphies of the southern BSN need to be investigated and correlated, in combination with an extended chronological dataset of ^{14}C ages for the organic-rich sediments and optically stimulated luminescence ages for the sand-dominated in-channel facies, for which no data are available to date. In particular, the palaeoenvironments of the fluvio-limnic muds, along with any potential anthropogenic impact, require further attention and need to be reconstructed in more detail. Deciphering a chronology of fluvial activity in the southern BSN domain will provide the basis for investigating the reactivation of some reaches of and human interaction with the BSN across the Holocene, in particular during Roman times and later historical periods, for which only fragmented historical and archaeological information is available so far (e.g. Eckoldt, 1985).

Data availability. All data from this study can be found in the Supplement.

Supplement. The supplement related to this article is available online at: https://doi.org/10.5194/egqsj-71-213-2022-supplement.

Author contributions. The concept of the study was jointly developed by all authors at the Institute of Geography, Heidelberg University, in the context of field courses held at the two study sites. All these authors were involved in the fieldwork. Sedimentary laboratory analyses were carried out by FR, GS and ME. FR contributed results from his master of science thesis. Processing and analysis of ERT data were carried out by MH, FH and SH. The GIS for this project was set up by FH. SL performed the ^{14}C dating. A first draft of the manuscript was written by ME, FH and AK. ME, FH, FR, AK, MH, SH, SL and OB commented on and approved the manuscript.

Competing interests. The contact author has declared that none of the authors has any competing interests.

Special issue statement. This article is part of the special issue "Quaternary research from and inspired by the first virtual DEUQUA conference".

Acknowledgements. We thank Peter Müller (Mannheim-Straßenheim) and the Bach family (Heddesheim) for permission to conduct fieldwork on their properties. Undergraduate students of the geography programmes at Heidelberg University are thanked for their engagement during field courses. Nicola Manke kindly provided support during one field course and during the laboratory analyses. Support and permission to use the laser particle sizer of the Sedimentology and Marine Paleoenvironmental Dynamics research group at the Institute of Geosciences at Heidelberg University by Andre Bahr are greatly appreciated. Finally, we would like to thank the Landesamt für Geologie, Rohstoffe und Bergbau (LGBR) for providing the digital elevation model DGM1 of the state of Baden-Württemberg. We are thankful for the helpful reviews of one anonymous person and of Rainer Dambeck, who provided highly detailed comments, plenty of ideas and improved the manuscript by sharing his great regional expertise.

Gerd Schukraft was a driving force of the research on the southern Bergstraßenneckar and one of the initiators back in 2019. He sadly passed away in April 2020.

Financial support. This research was supported by funds of Heidelberg University. For the publication fee we acknowledge financial support by Deutsche Forschungsgemeinschaft within the funding programme "Open Access Publikationskosten", as well as by Heidelberg University.

Review statement. This paper was edited by Julia Meister and reviewed by Rainer Dambeck and one anonymous referee.

References

Ad-hoc-AG Boden: Bodenkundliche Kartieranleitung, 5th edn., Schweizerbart, Hannover, 438 pp., 2005.

AdV (Arbeitsgemeinschaft der Vermessungsverwaltungen der Länder der Bundesrepublik Deutschland): DHHN2016 – Die Erneuerung des Deutschen Haupthöhennetzes und der einheitliche integrierte geodätische Raumbezug 2016, Landesamt für Digitalisierung, Breitband und Vermessung Bayern, München, 2018.

Barsch, D. and Mäusbacher, R.: Erläuterungen zur Geomorphologischen Karte 1:25 000 der Bundesrepublik Deutschland – GMK 25 Blatt 3, 6417 Mannheim-Nordost, in: GMK Schwerpunktprogramm, Geomorphologische Detailkartierung in der Bundesrepublik Deutschland, edited by: Barsch, D., Fränzle, O., Leser, H., Liedtke, H., and Stäblein, G., Berlin, 1–56, 1979.

Barsch, D. and Mäusbacher, R.: Zur fluvialen Dynamik beim Aufbau des Neckarschwemmfächers, Berlin. Geogr. Abh., 47, 119–128, https://doi.org/10.23689/fidgeo-3194, 1988.

Beckenbach, E.: Geologische Interpretation des hochauflösenden digitalen Geländemodells von Baden-Württemberg, PhD thesis, University of Stuttgart, Germany, https://doi.org/10.18419/opus-8846, 2016.

Bernhard, H. and Hickethier, H.: Beitrag zur Kenntnis des alten Neckarlaufs am Westrand des Odenwalds bei Bensheim, Notizbl. Hess. L.-Amt Bodenforsch., 94, 385–389, 1966.

Bibus, E., and Rähle, W.: Stratigraphische Untersuchungen an molluskenführenden Terrassensedimenten und ihren Deckschichten im mittleren Neckarbecken (Württemberg), E&G Quaternary Sci. J., 53, 94–113, https://doi.org/10.3285/eg.53.1.06, 2003.

Blott, S. J., and Pye, K.: GRADISTAT: a grain size distribution and statistics package for the analysis of unconsolidated sediments, Earth Surf. Proc. Landf., 26, 1237–1248, https://doi.org/10.1002/esp.261, 2001.

Bohncke, S. J. P. and Hoek, W. Z.: Multiple oscillations during the Preboreal as recorded in a calcareous gyttja, Kingbeekdal, The Netherlands, Quaternary Sci. Rev., 26, 1965–1974, https://doi.org/10.1016/j.quascirev.2007.02.017, 2007.

Bos, J. A. A., Dambeck, R., Kalis, A. J., Schweizer, A., and Thiemeyer, H.: Palaeoenvironmental changes and vegetation history of the northern Upper Rhine Graben (southwestern Germany) since the Lateglacial, Neth. J. Geosci., 87, 67–90, https://doi.org/10.1017/S0016774600024057, 2008.

Bos, J. A. A., Dambeck, R., and Bouman, M. I. T. J.: Paläoökologische Untersuchungen im nördlichen Oberrheingraben vom Spätglazial bis Atlantikum; Vegetationsgeschichte und anthropogene Einflüsse, Frankfurt. Archäol. Schr., 18, 59–90, 2012.

Buness, H., Gabriel, G., and Ellwanger, D.: The Heidelberg Basin drilling project: Geophysical pre-site surveys, E&G Quaternary Sci. J., 57, 338–366, https://doi.org/10.3285/eg.57.3-4.4, 2009.

Dambeck, R.: Beiträge zur spät- und postglazialen Fluss- und Landschaftsgeschichte im nördlichen Oberrheingraben, PhD thesis, University of Frankfurt/Main, Germany, 438 pp., 2005.

Dambeck, R. and Bos, J. A. A.: Lateglacial and Early Holocene landscape evolution of the northern Upper Rhine River valley, south-western Germany, Z. Geomorph. Suppl., 128, 101–127, 2002.

Dambeck, R., and Thiemeyer, H.: Fluvial history of the northern Upper Rhine River (southwestern Germany) during the

Lateglacial and Holocene times, Quaternary Int., 93, 53–63, https://doi.org/10.1016/S1040-6182(02)00006-X, 2002.

Dister, E., Gomer, D., Obrdlik, P., Petermann, P., and Schneider, E.: Water management and ecological perspectives of the upper Rhine's floodplains, Regul. River., 5, 1–15, https://doi.org/10.1002/rrr.3450050102, 1990.

Eckoldt, M.: Schiffahrt auf kleinen Flüssen. T. 2, Gewässer im Bereich des "Odenwaldneckars" im ersten Jahrtausend n. Chr., Deutsch. Schiffahrtsarch., 8, 101–116, 1985.

Eisbacher, G. H. and Fielitz, W.: Karlsruhe und seine Region. Nordschwarzwald, Kraichgau, Neckartal, südlicher Odenwald, Oberrhein-Graben, Pfälzerwald und westliche Schwäbische Alb. Sammlung Geologischer Führer Vol. 103, Bornträger, Stuttgart, 2010.

Erkens, G., Dambeck, R., Volleberg, K. P., Bouman, M. T., Bos, J. A., Cohen, K. M., Wallinga, J., and Hoek, W. Z.: Fluvial terrace formation in the northern Upper Rhine Graben during the last 20 000 years as a result of allogenic controls and autogenic evolution, Geomorphology, 103, 476–495, https://doi.org/10.1016/j.geomorph.2008.07.021, 2009.

Fezer, F.: 220 m Altpleistozän im "Heidelberger Loch", E&G Quaternary Sci. J., 47, 145–153, https://doi.org/10.3285/eg.47.1.10, 1997.

Gabriel, G., Ellwanger, D., Hoselmann, C., Weidenfeller, M., Wielandt-Schuster, U., and The Heidelberg Basin Project Team: The Heidelberg Basin, Upper Rhine Graben (Germany): A unique archive of Quaternary sediments in Central Europe, Quaternary Int., 292, 43–58, https://doi.org/10.1016/j.quaint.2012.10.044, 2013.

Große-Brauckmann, G., Malchow, G., and Streitz, B.: Makrofossil- und pollenanalytische Befunde vom Altneckarbett bei Riedstadt-Goddelau, in: Die Holzbrücken bei Riedstadt-Goddelau, Kreis Groß-Gerau, edited by: Wagner, P., Mater. Vor- u. Frühgesch. Hessen, 5, 111–132, 1990.

Haupt, O.: Die Pfahlbausiedlung am Phillipshospital bei Goddelau im hessischen Ried sowie das Alter der Neckarbetten und des Modauschuttkegels an der Bergstraße, Notizbl. Ver. Erdk. Hess. Geol. L.-Anst., V(10), 239–245, 1928.

Heiri, O., Lotter, A. F., and Lemcke, G.: Loss on ignition as a method for estimating organic and carbonate content in sediments: reproducibility and comparability of results, J. Paleolimnol., 25, 101–110, https://doi.org/10.1023/A:1008119611481, 2001.

HLfB (Hessisches Landesamt für Bodenforschung): Bodenkarte der nördlichen Oberrheinebene 1:50000, Wiesbaden, 1990.

Hoffmann, J. and Krzyzanowski, J.: Laacher-Bimstuff-Vorkommen im Bereich des ehemaligen Neckarlaufs bei Zwingenberg (Bergstraße), Geol. Jb. Hessen, 112, 77–81, 1984.

Holzhauer, I.: Landschaftsgeschichte und menschlicher Einfluss im Umfeld der Schwetzinger Hardt seit dem Würm-Hochglazial, PhD thesis, Heidelberg University, Germany, https://doi.org/10.11588/heidok.00015714, 2013.

Holzhauer, I., Kadereit, A., Schukraft, G., Kromer, B., and Bubenzer, O.: Spatially heterogeneous relief changes, soil formation and floodplain aggradation under human impact – geomorphological results from the Upper Rhine Graben (SW Germany), Z. Geomorph., 61 (Suppl. 1), 121–158, https://doi.org/10.1127/zfg_suppl/2017/0357, 2017.

Howard, A. D. and Hemberger, A. T.: Multivariate characterization of meandering, Geomorphology, 4, 161–186, https://doi.org/10.1016/0169-555X(91)90002-R, 1991.

Kneisel, C.: Electrical resistivity tomography as a tool for geomorphological investigations – some case studies, Z. Geomorph. Suppl., 132, 37–49, 2003.

König, P.: Eine vorgeschichtliche und frühmittelalterliche Siedlung von Heddesheim, Rhein-Neckar-Kreis, Fundber. Baden-Württemb., 35, 141–204, https://doi.org/10.11588/fbbw.2015.0.44523, 2015.

Kromer, B., Lindauer, S., Synal, H. A., and Wacker, L.: MAMS – a new AMS facility at the Curt-Engelhorn-Centre for Achaeometry, Mannheim, Germany, Nucl. Instr. Meth., 294, 11–13, https://doi.org/10.1016/j.nimb.2012.01.015, 2013.

Kupfahl, H.-G., Meisl, S., and Kümmerle, E.: Erläuterungen zur geologischen Karte von Hessen 1:25000, Blatt 6217 Zwingenberg an der Bergstraße, Hessisches Landesamt für Bodenforschung, Wiesbaden, 276 pp., 1972.

Lang, A.: Die Infrarot-Stimulierte-Lumineszenz als Datierungsmethode für holozäne Lössderivate. Ein Beitrag zur Chronometrie kolluvialer, alluvialer und limnischer Sedimente in Südwestdeutschland, Heidelb. Geogr. Arb., 103, 1–137, 1996.

LGBR (Landesamt für Geologie, Bergbau und Rohstoffe): Kiese und Sande des Neckars im Oberrheingraben, https://lgrbwissen.lgrb-bw.de/rohstoffgeologie/rohstoffe-des-landes/kiese-sandig/kiese-sande-des-neckars-im-oberrheingraben, last access: 27 August 2021.

Löscher, M.: Die quartären Ablagerungen auf der Mannheimer Gemarkung, in: Mannheim vor der Stadtgründung. Teil 1 Band 1, edited by: Probst, H., Friedrich Pustet Verlag, Regensburg, 28–47, 2007.

Löscher, M., Haag, T., and Münzing, K.: Zum Alter der Dünen im nördlichen Oberrheingraben bei Heidelberg und zur Genese ihrer Bänderparabraunerden, E&G Quaternary Sci. J., 39, 98–108, https://doi.org/10.3285/eg.39.1.10, 1989.

Löscher, M., Becker, B., Bruns, M., Hieronymus, U., Mäusbacher, R., Münnich, M., Münzing, K., and Schedler, J.: Neue Ergebnisse über das Jungquartär im Neckarschwemmfächer bei Heidelberg, E&G Quaternary Sci. J., 30, 89–100, https://doi.org/10.3285/eg.30.1.07, 1980.

Mangold, A.: Die alten Neckarbetten in der Rheinebene, Abh. Großherzogl. Hess. Geol. Landesanst. Darmstadt, 2, 75–114, 1892.

Merz, M. U. E.: The biology of carbonate precipitation by cyanobacteria, Facies, 26, 81–102, https://doi.org/10.1007/BF02539795, 1992.

Mone, F. J.: Ueber den alten Flußlauf im Oberrheintal, Badisch. Arch. z. Vaterlandsk. in allseit. Hinsicht, 1, 1–47, 1826.

Munsell Color Laboratory: Munsell Soil Color Chart, New Windsor, 2000.

Nickel, E. and Fettel, M.: Odenwald – Vorderer Odenwald zwischen Darmstadt und Heidelberg, Sammlung Geologischer Führer Vol. 65, Bornträger, Stuttgart, 1979.

Pawłowski, D., Borówka, R. K., Kowalewski, G. A., Luoto, T. P., Milecka, K., Nevalainen, L., Okupny, D., Tomkowiak, J., and Zieliński, T.: Late Weichselian and Holocene record of the paleoenvironmental changes in a small river valley in Central Poland, Quaternary Sci. Rev., 135, 24–40, https://doi.org/10.1016/j.quascirev.2016.01.005, 2016.

Peters, G. and van Balen, R. T.: Tectonic geomorphology of the northern Upper Rhine Graben, Germany, Global Planet. Change, 58, 310–334, https://doi.org/10.1016/j.gloplacha.2006.11.041, 2007.

Pflanz, D., Kunz, A., Hornung, J., and Hinderer, M.: New insights into the age of aeolian sand deposition in the northern Upper Rhine Graben (Germany), Quaternary Int., 625, 1–13, https://doi.org/10.1016/j.quaint.2022.03.019, 2022.

Reimer, P. J., Austin, W. E., Bard, E., Bayliss, A., Blackwell, P. G., Ramsey, C. B., and Grootes, P. M.: The IntCal20 northern hemisphere radiocarbon age calibration curve (0–55 cal kBP), Radiocarbon, 62, 725–757, https://doi.org/10.1017/RDC.2020.41, 2020.

Reinig, F., Wacker, L., Jöris, O., Oppenheimer, C., Guidobaldi, G., Nievergelt, D., Adolphi, F., Cherubini, P., Engels, S., Esper, J., Land, A., Lane, C., Pfanz, H., Remmele, S., Sigl, M., Sookdeo, A., and Büntgen, U.: Precise date for the Laacher See eruption synchronizes the Younger Dryas, Nature, 595, 66–69, https://doi.org/10.1038/s41586-021-03608-x, 2021.

Saur, A.: Parvum theatrum urbium, Frankfurt, 1593.

Scheer, H.-D.: Gliederung und Aufbau der Niederterrassen von Rhein und Main im nördlichen Oberrheintalgraben, Geol. Jb. Hessen, 106, 273–289, 1978.

Schottler, W.: Erläuterungen zur geologischen Karte des Grossherzogtums Hessen im Maßstabe 1:25000, Hessischer Staatsverlag, 1906.

Stuiver, M., Reimer, P. J., and Reimer, R. W.: CALIB 8.2 (WWW program), http://calib.org, last access: 19 January 2022.

Wagner, P.: Riedstadt-Goddelau, Kreis Groß-Gerau. Holzbrücken im alten Neckarbett, Ausgrabungen im Hessischen Ried 1976–1977, Archäol. Denkm. Hessen, 20, 1–12, 1981.

Waldmann, F.: Beziehungen zwischen Stratigraphie und Bodenbildungen aus spätglazialen und holozänen Sedimenten in der nördlichen Oberrheinebene, PhD thesis, University of Freiburg, Germany, 1989.

Wild, E. M., Steier, P., Fischer, P., and Höflmayer, F.: ^{14}C dating of humic acids from Bronze and Iron Age plant remains from the eastern Mediterranean, Radiocarbon, 55, 599–607, https://doi.org/10.1017/S003382220005774X, 2013.

Winkelmann, J. J.: Gründliche Beschreibung der Fürstenthümer Hessen und Hersfeld, Brauer, Bremen, 1697.

Wirth, K.: Ein Bohlenweg oder eine Sumpfbrücke aus römischer Zeit in Mannheim-Straßenheim, in: Archäologie der Brücken, Vorgeschichte, Antike, Mittelalter, Neuzeit, edited by: Pflederer, T. and Sommer, C., Friedrich Pustet Verlag, Regensburg, 102–105, 2011.

E&G Quaternary Sci. J., 71, 191–212, 2022
https://doi.org/10.5194/egqsj-71-191-2022

Open Access E&G Quaternary Science Journal

Research article

Morpho-sedimentary characteristics of Holocene paleochannels in the Upper Rhine alluvial plain, France

Mubarak Abdulkarim[1,2], **Stoil Chapkanski**[3], **Damien Ertlen**[4], **Haider Mahmood**[1], **Edward Obioha**[1], **Frank Preusser**[1], **Claire Rambeau**[4], **Ferréol Salomon**[4], **Marco Schiemann**[1], and **Laurent Schmitt**[4]

[1]Institute of Earth and Environmental Science, University of Freiburg, Freiburg, Germany
[2]Department of Geology, Federal University Birnin Kebbi, Kebbi, Nigeria
[3]Laboratoire de Géographie Physique (UMR-8591), CNRS/Université Paris 1, Meudon, France
[4]Laboratoire Image, Ville, Environnement (LIVE UMR 7362), CNRS/Université de Strasbourg/ENGEES, Strasbourg, France

Correspondence: Mubarak Abdulkarim (mubarak.abdulkarim@geologie.uni-freiburg.de)

Relevant dates: Received: 23 May 2022 – Revised: 26 July 2022 – Accepted: 9 August 2022 – Published: 8 September 2022

How to cite: Abdulkarim, M., Chapkanski, S., Ertlen, D., Mahmood, H., Obioha, E., Preusser, F., Rambeau, C., Salomon, F., Schiemann, M., and Schmitt, L.: Morpho-sedimentary characteristics of Holocene paleochannels in the Upper Rhine alluvial plain, France, E&G Quaternary Sci. J., 71, 191–212, https://doi.org/10.5194/egqsj-71-191-2022, 2022.

Abstract: The French Upper Rhine alluvial plain is characterized by a complex system of paleochannels inherited from Late Glacial to Holocene fluvial dynamics of the Rhine and Ill river systems, among other smaller rivers. These paleochannels represent valuable archives for understanding and reconstructing the fluvial and landscape evolution of the area. However, the Holocene temporal trajectories of the paleochannels, in response to a range of environmental changes, remain poorly understood. This study presents a detailed and systematic mapping and characterization of an extensive network of paleochannels spanning the entire width (19 km) of a reach of the central French Rhine plain. Based on qualitative and quantitative lidar analysis, field investigations, and provenance investigations of paleochannel infill sequences, five distinct paleochannel groups (PG 1 to PG 5) were identified in the study area. These paleochannel groups differ considerably regarding their channel patterns, morphological characteristics, and sedimentary sources of the infilling sediments. The interpretation of the different datasets indicates that the development of these different paleomorphologies is attributed to significant changes in hydro-geomorphodynamic processes in the area during the Holocene, especially lateral migrations of the Rhine and Ill rivers. The findings reported here are promising and will have significant implications for reconstructing the long-term (Late Glacial to Holocene) evolution of the Upper Rhine fluvial hydrosystem in response to various controlling factors.

Kurzfassung: Die französische Oberrheinebene ist durch ein komplexes System von ehemaligen Fließrinnen gekennzeichnet, die aus der spätglazialen bis holozänen fluvialen Dynamik des Rhein- und Ill-Systems sowie einiger anderer kleinerer Flüsse stammen. Diese Fließrinnen stellen wertvolle Archive dar, die für das Verständnis und die Rekonstruktion der fluvialen und landschaftlichen Entwicklung des Gebietes von zentraler Bedeutung sind. Die zeitliche Entwicklung der Fließrinnen im Holozän, als Reaktion auf die Veränderung einer Reihe von Umweltbedingungen, ist jedoch nach wie vor nur unzureichend bekannt. Diese Studie präsentiert eine detaillierte und systematische Kartierung und Charakterisierung eines ausgedehnten Netzwerks von ehemaligen Fließrinnen, das sich über die gesamte Breite (19 km) eines Abschnitts der zentralen französischen Rheinebene erstreckt. Auf Grundlage von qualitativen und quantitativen lidar-Analysen, sowie durch Feld- und Provenienzuntersuchungen von Sedimentfüllungen wurden im Untersuchungsgebiet fünf verschiedene Rinnengruppen (PG 1 bis PG 5) identifiziert. Diese Gruppen unterscheiden sich erheblich in Bezug auf ihre Rinnenmuster, morphologischen Merkmale und Sedimentherkunft. Die Interpretation der verschiedenen Datensätze deutet darauf hin, dass die Entwicklung dieser unterschiedlichen Paläo-Morphologien auf signifikante Veränderungen der hydro-geomorphodynamischen Prozesse in diesem Gebiet während des Holozäns zurückzuführen ist, insbesondere auf die seitlichen Verlagerungen von Rhein und Ill. Die hier vorgestellten Ergebnisse sind vielversprechend und bilden die Basis für eine Rekonstruktion der langfristigen (spätglazialen bis holozänen) Entwicklung des fluvialen Oberrhein-Hydrosystems in Abhängigkeit von verschiedenen Einflussfaktoren.

1 Introduction

The French Upper Rhine alluvial plain (eastern France) is characterized by a complex pattern of paleochannels inherited from the Late Glacial to Holocene fluvial dynamics of the Rhine and Ill rivers, as well as some other tributaries or sub-tributaries of the Rhine (Hirth, 1971; Carbiener, 1983a; Striedter, 1988). From Colmar to Sélestat, which is a part of the so-called “Ried central d’Alsace” (Carbiener, 1983a), the formation and evolution of the paleochannel network is attributed to significant landscape changes throughout the Holocene, as exemplified by the narrowing and eastward lateral migration of the Rhine fluvial hydrosystem and a westward displacement for its main tributary, the Ill River (Schmitt et al., 2016). Consequently, these paleochannels inherited from these lateral displacements preserve a comprehensive record of Holocene environmental changes, which is invaluable for understanding past landscape evolution and fluvial processes, as well as providing insights into the factors that controlled these changes (Bowler, 1978; Page et al., 1996; Dambeck and Thiemeyer, 2002; Sylvia and Galloway, 2006; Kemp and Spooner, 2007; Bisson et al., 2011; Nandini et al., 2013; Resmi et al., 2017). However, both the internal structure and organization of the extensive and well-preserved network of paleochannels, as well as the temporal development of trajectories in response to environmental change during the Holocene remain poorly understood.

Around the world, paleochannels have been extensively studied using a variety of methodological approaches in order to reconstruct the evolution of fluvial hydrosystems and associated landscapes in the geological and historical past (e.g., Page et al., 1996; Dambeck and Thiemeyer, 2002; Bos et al., 2008; Rossetti and Góes, 2008; Erkens et al., 2011; Plotzki et al., 2015; Jotheri et al., 2016; Resmi et al., 2017; Scorpio et al., 2018; Candel et al., 2020; Khosravichenar et al., 2020; von Suchodoletz et al., 2022). Likewise, in the Ried central d’Alsace, pioneering studies (e.g., Carbiener, 1969, 1983a; Hirth, 1971; Al Siddik, 1986; Boës et al., 2007; Schmitt et al., 2016) have investigated paleochannels and paleoenvironments with the aim to reconstruct the Holocene evolution of the landscape and/or study past human–river interactions. However, these research efforts lacked precision (e.g., no location of the sampling sites, no provenance study of fine sediments) or were, in many cases, concentrated around some archeological sites located close the village of Mussig (Boës et al., 2007) and focused on a rather limited number of paleochannels between the Rhine and Ill rivers. No study has yet extensively mapped and characterized systematically the paleochannel network over the entire width of the large and complex alluvial plain.

Against this backdrop, the present study aims at providing new insights into the formation and evolution of the paleochannels. The study specifically aims to (1) map the paleochannels and measure their morphometric properties using remote sensing data, (2) characterize paleochannel geometry and stratigraphic infillings of selected paleochannels using hand-augured core data, and (3) determine the provenance of paleochannel infillings through mid-infrared spectroscopic analysis. In addition, as the chosen research tools have barely been used, this study may also provide some methodological outputs.

2 Geological and geomorphological setting

The study area is located in the French Rhine alluvial plain, within the Upper Rhine Graben (URG). The URG is a 30–40 km wide rift valley extending 300 km from the Jura Mountains to the southern border of the Rhenish Massif (Fig. 1). The valley is bounded to the west by the Vosges and Pfälzerwald (Palatinate Forest) mountains and to the east by the Black Forest and Odenwald mountains. This rift structure ensued from the formation of the Alps starting during the middle Eocene, with the main phase of its rifting occurring during the Oligocene and Miocene, as well as extending into the Pleistocene and Holocene (Przyrowski and Schäfer, 2015). Today, it forms a down-faulted trough through which the Rhine has flown continuously since the start of the Pleistocene (Preusser, 2008). During this time period, the URG was an important sink for sediments from the Rhine River and its tributaries, mostly unconsolidated fluvial sediments of up to several hundreds of meters thickness (e.g., Haimberger et al., 2005; Gabriel et al., 2013). In the French Rhine alluvial plain, the Pleistocene sediments, primarily gravel and sand deposited during glacial periods, intercalate with fine-grain layers (sand, silt, and clay) attributed to warm periods. Hence, the superficial Holocene deposits generally have finer textures than the Pleistocene sediments (Simler et al., 1979), except on the historical Rhine braided belt (Schmitt, 2001; Schmitt et al., 2016).

Following the Older Dryas (13.9 ka cal BP; van Raden et al., 2013), the longitudinal profile of the Rhine readjusted in response to several controlling factors: (i) a decrease in water and sediment fluxes due to Holocene climate warming (Hirth, 1971); (ii) trapping of sediment in Swiss lakes (e.g., Lake Constance) for 60 % of the Rhine basin area upstream of Basel after their formation by the retreat of Alpine glaciers, which decreased the sediment load and intensity of floods (Walser, 1959; Hirth, 1971); and (iii) positive tectonic movements (uplift) upstream and downstream of Mulhouse (Nivière et al., 2006; Kock et al., 2009) and negative (downward) tectonic movements around Marckolsheim (Jung and Schlumberger, 1936; Illies and Greiner, 1978) or even over the entire Marckolsheim–Strasbourg sector and north of Strasbourg (Jung and Schlumberger, 1936; Illies and Greiner, 1978; Vogt, 1992).

Consequently, the longitudinal profile of the Rhine became more incised between the Basel–Neuf-Brisach and Strasbourg–Lauterbourg sections during the Holocene and remained unchanged or even rose slightly in the Neuf-Brisach–Strasbourg section (Carbiener, 1969, 1983a). Thus, the Holocene Upper Rhine and its alluvial plain are classified into four major longitudinal sections based on geomorphological characteristics and dynamics (Carbiener, 1969, 1983a; Schmitt et al., 2016; Fig. 2). The upstream sector (from Basel to Neuf-Brisach) is characterized by a braided channel pattern, while a braided-anastomosing channel pattern characterizes the middle sector, from Neuf-Brisach to Strasbourg. The downstream sector (from Strasbourg to Karlsruhe–Maxau) is distinguished by a combination of anastomoses and incipient meanders, whereas further north, beyond the French Rhine Plain, the Rhine River is characterized by an almost pure meandering style. It has to be noted that the natural channel pattern and dynamics have been completely destroyed by human regulation works (correction, regularization, and canalization) since the 19th century (e.g., Eschbach et al., 2018).

The central study area of our research, within the French Rhine alluvial plain, corresponds roughly to a large transect (14 km) from Houssen to Baltzenheim along which paleochannels were cored (Fig. 1b). To gain insight into the channel pattern of these paleochannels, we studied the surface topography using a light detection and ranging (lidar) digital elevation model (DEM) over a larger spatial scale, which corresponds to an extended studied area (Fig. 1b). The area stretches between the villages of Neuf-Brisach and Sainte-Croix-en-Plaine in the south and Illhaeusern and Marckolsheim in the north, covering an area of approximately 572 km^2 (Fig. 1b). This area corresponds mainly to the braided-anastomosing sector and is delimited by the Rhine River in the west and the Ill River in the east. It corresponds also to the southern part of the so-called “Grand Ried central d’Alsace”, which extends up to south of Strasbourg and corresponds to a large, wet alluvial area whose biodiversity is extremely rich (Carbiener, 1983a). The Fecht River represents a major western tributary of the Ill River in this area, which joins the Ill at Illhaeusern. Until the end of the Pleistocene, the Ill River did not exist as the Rhine fluvial hydrosystem (with mostly braided channel pattern) occupied almost the entire width of the plain (Schmitt et al., 2016). At the start of the Holocene, a change in the dynamics and narrowing of the Rhine fluvial hydrosystem resulted in the formation of the Ill River (Schmitt et al., 2016).

The Rhine and Ill rivers then continuously moved laterally across the plain until human interference, with fine sediments deposited on the alluvial plain with an average thickness of 0.5–1 m but reaching several meters in channel structures (Schmitt et al., 2016). As a consequence, the current floodplain features a complex network of paleochannels. These paleochannels are generally embedded into the Rhine gravels, incompletely filled, and are therefore visible as geomorphological features (depressions and levees) in the surface topography. The former channels have been filled with clastic and organic sediments and are mainly bereft of flowing water, although some remain active today due to perennial or intermittent upstream hydrological connection to the Ill or Rhine rivers or to groundwater (Carbiener, 1983a, b; Trémolières et al., 1993; Schmitt, 2001; Schmitt et al., 2016), forming phreatic and semi-phreatic rivers (Carbiener, 1983a, b; Schmitt et al., 2007). These streams support an abundance of biodiversity, in particular aquatic macrophytes (Carbiener, 1983b; Trémolières et al., 1993).

The alluvial plain is generally categorized into two main geomorphological units based on geomorphological, hydrological, pedological, and ecological properties: the “Hardt” and the “Ried” (Carbiener, 1969; Hirth, 1971; Ollive et al., 2006, Fig. 3). The “Hardt” is an area with gravelly islands associated with the Late Pleistocene alluvial fan of the Rhine, primarily located in the central part of the alluvial plain. The “Ried” comprises low-lying, swampy areas primarily consisting of fine sand, silt, clay, and organic matter, which may be mixed together (Hirth, 1971; Kremer et al., 1978; Al Siddik, 1986; Ollive et al., 2006). These two zones are further subdivided into six subunits: “Hardt Rouge”, “Hardt Grise”, “Ried Blond”, “Ried Brun”, “Ried Noir”, and “Ried Gris” (Hirth, 1971; Kremer et al., 1978, Fig. 3).

The Hardt Rouge represents the intact Pleistocene alluvial fan, whereas the Hardt Grise has been remobilized at the surface. The Ried Blond is the sub-modern floodplain of the

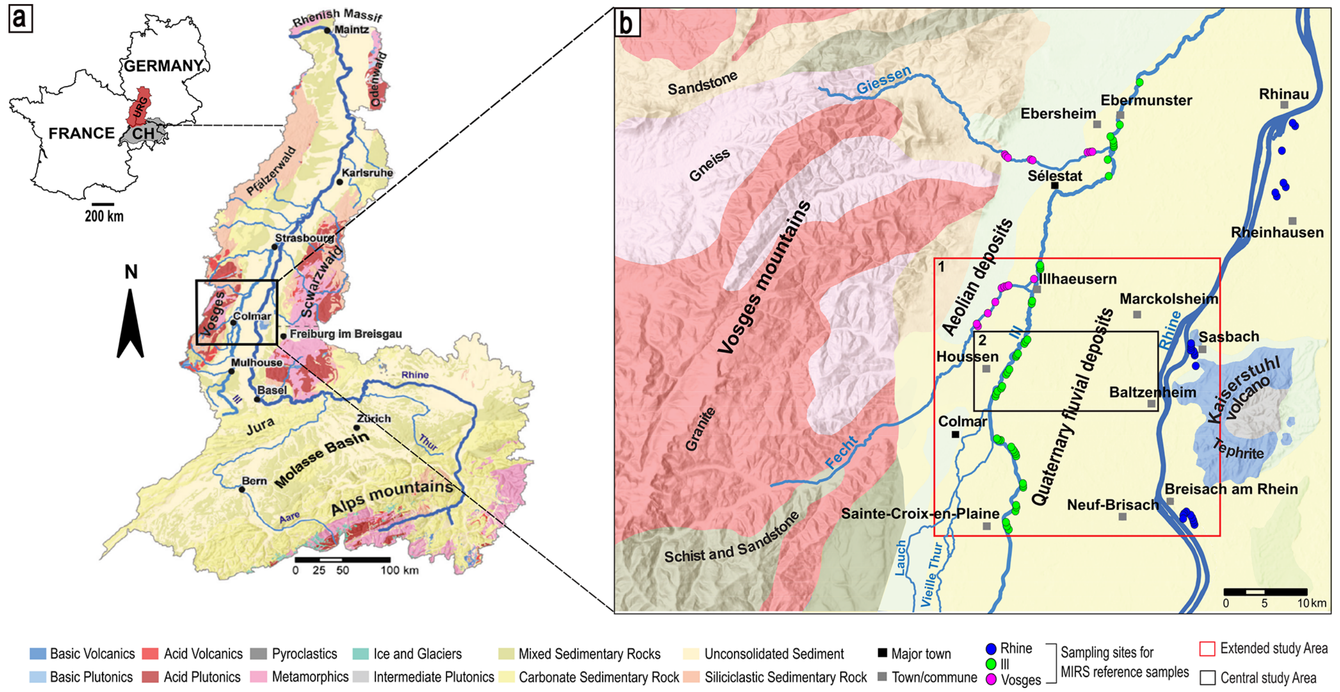

Figure 1. **(a)** Geological setting and location of the Upper Rhine Graben (URG). **(b)** Location of the two spatial scales of the study area within the French Rhine alluvial plain: (1) the extended study area (red) on which the lidar DEM was studied and (2) the central study area (black) on which the paleochannels were bored by hand auger. The figure also shows the sampling sites for MIRS reference samples. Modified from Chapkanski et al. (2020). Source of data: ESRI, BRGM.

Rhine prior to the correction works (width of about 5–7 km), composed of sandy/silty and calcareous alluvium and in some places overlapped by young soils (Kremer et al., 1978). Ried Brun corresponds to a series of moderately overhanging post-Roman Rhine levees and terraces located within the sub-modern floodplain of the Rhine, with limestone-rich soils and highly mineralized organic matter. The Ried Noir, situated further to the west of the plain, corresponds to marshy depressions with permanent or semi-permanent contact to groundwater. It is composed of black hydromorphic soils rich in organic matter and locally peat (Carbiener, 1969, 1983a; Hirth, 1971). The westernmost component, the Ried Gris, represents the area regularly flooded by the Ill River, consisting of fine floodplain sediments, mainly fine sand, silt, and clay (Carbiener, 1969, 1983a; Hirth, 1971; Al Siddik, 1986).

3 Methods

3.1 Remote sensing

Paleochannels within the study area were identified and comprehensively mapped through the combined use of a lidar-derived DEM, a photogrammetric digital terrain model (DTM), aerial photos, and historical maps from the 18th and 19th centuries. The elevation data, aerial photos, and historical maps are found in the Supplement. The primary data used are a lidar-generated DEM with a resolution of 50 cm and pixel values ranging from 132.47 to 556.82 m. However, a portion of the research area (approximately 65 km^2) currently lacks lidar coverage (Fig. 4); it is covered by a photogrammetric DTM with a 1 m resolution. The photogrammetric DTM was developed in 2018 and obtained from the RGE ALTI® database of the National Institute of Geographic and Forestry Information, France (IGN-F). In addition to the elevation data, aerial photographs, and historical maps dating from 1702 CE to 1838 CE were geo-referenced and digitized to complement the identification and mapping of paleochannels. Prior to mapping, the datasets were processed, and enhancement techniques (e.g., contrast stretching, hill shading, and slope maps) were applied to improve visualization and enhance the appearance of the microtopography and detectability of the geomorphologic features of interest (paleochannels).

After their mapping, the paleochannels were further characterized in relation to their surface topographic properties, including channel width, channel depth, width / depth ratio, sinuosity, and orientation (paleochannel direction). For the determination of these geometrical properties, four transect lines were drawn across the study area, perpendicular to the orientation of the main valley (Fig. S3 in the Supplement). Based on the surface topography, paleochannel width and depth were measured at points where they intersect with these profile lines using the *Measure* tool and *3D Analyst*

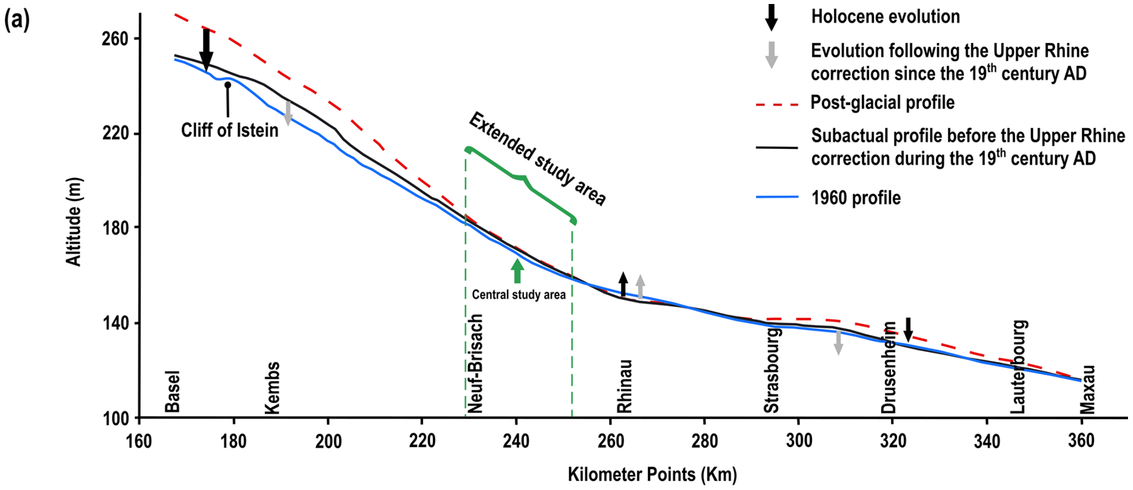

(b)

Variable / Sector	Braided	Braided and anastomosing	Anastomosing and meandering	Meandering
Width of the hydrosystem	2.9 Km	5.9 Km	4.9 Km	5.5 Km
Slope	0.93 %	0.66 %	0.46 %	0.31 %
Specific stream power	45 W.m^{-2}	33 W.m^{-2}	26 W.m^{-2}	22 W.m^{-2}
Number of braided channels	7.1	7.4	5.6	–
Number of anasto. channels	2.6	4.6	2.8	–
Sinuosity	1.11	1.22	1.33	1.45

Figure 2. **(a)** Post-glacial and Holocene Upper Rhine longitudinal profiles. **(b)** Some hydromorphological characteristics according to the Upper Rhine sectorization (adapted from Commission Internationale de l'Hydrologie du Bassin du Rhin, 1977; Carbiener and Dillmann, 1992; Schmitt, 2001; and Schmitt et al., 2019).

tool in ArcMap 10.4. The sinuosity index (P) of the paleochannels was also estimated using the *Measure* tool in ArcMap 10.4, following the method of Fuller et al. (2013). All morphometric parameters were determined three times, with the average values reported. Except for the measurements of paleochannel orientations, which were performed using the open-source GIS program QGIS V10.3, all dataset processing, paleochannel mapping, and planform measurements were carried out using ESRI ArcGIS 10.4.1.

3.2 Paleochannel coring

A total of 16 paleochannels within the alluvial plain were originally chosen for this study. The selection strategy was designed to include all paleochannels from the Rhine to the left (western) side of the Ill River (Figs. 4a; 5a). Furthermore, the paleochannels were chosen based on a number of criteria, including the absence of significant anthropogenic disturbances and whether or not they had been previously investigated. Only 12 of the 16 paleochannels could be investigated (Fig. 4) due to inaccessibility or the lack of authorization by landowners. The paleochannels with current activity were given names based on their present streams, while others that are completely abandoned and filled were assigned names reflecting their geographical location. Borings with an Edelman hand auger were used to characterize the subsurface geometry and sedimentary infillings of the selected paleochannels. The cores were placed at irregular (3–5 m) intervals along transects that spanned the entire width of the paleochannels, while the thickness of fine sediment infill determined the depth of the cores. Almost every coring penetrated fine sediment (clay, silt, and sand) and terminated in underlying gravel beds. The gravel deposits were encountered at depths ranging from less than 0.5 m near the channel margins to depths up to 5 m at the deepest portions of some paleochannels. Sediment samples were collected at 20 cm depth intervals and described in terms of dominant grain size, color, and organic matter content (qualitatively). These data were compiled to delineate stratigraphic units filling the paleochannels.

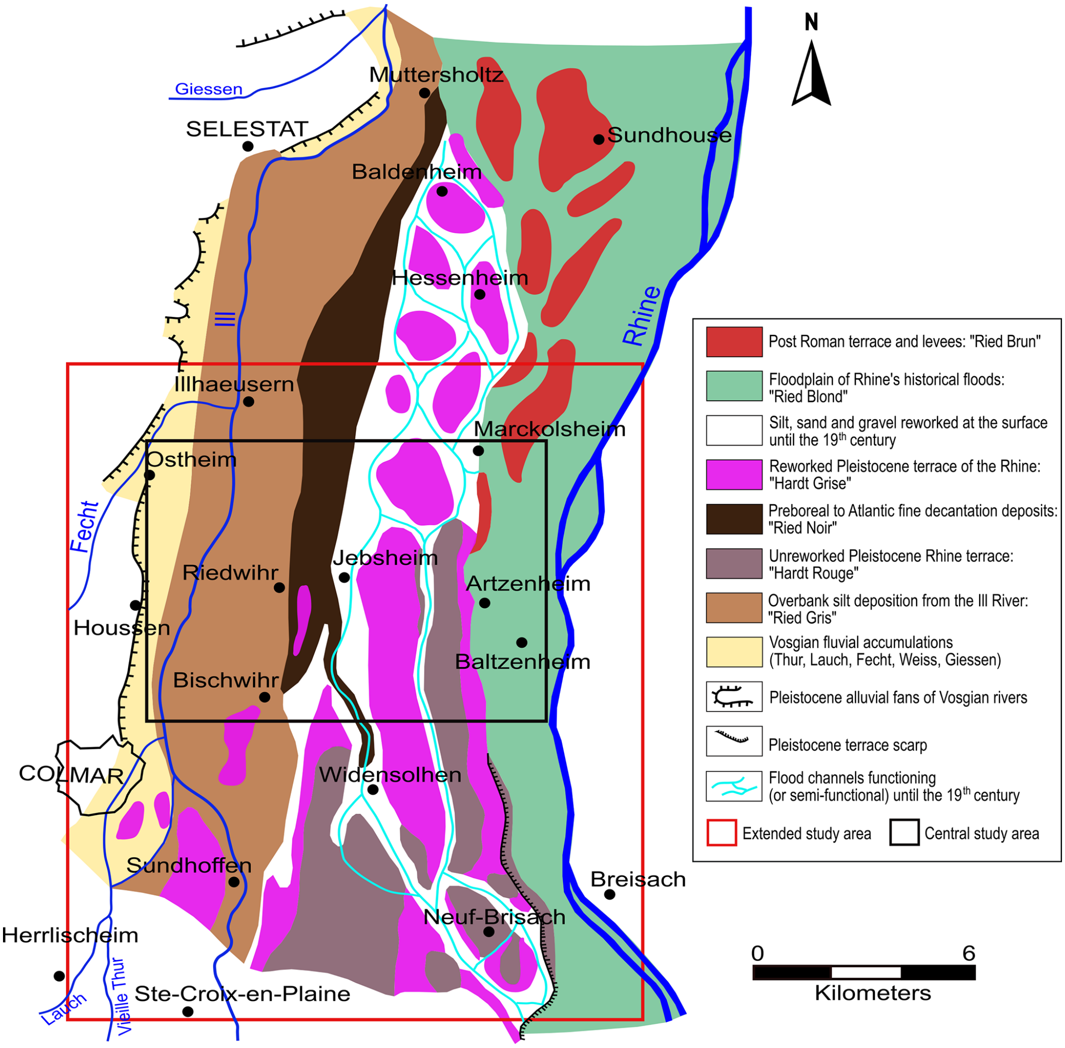

Figure 3. Geomorphological map of a part of the French Rhine alluvial plain whose southern part corresponds to our extended study area (Colmar-Sélestat; Hirth, 1971, modified by Schmitt, 2001, and Schmitt et al., 2016). Figure modified from Schmitt et al. (2016).

3.3 Provenance analysis

The source region of sediments and the contributions from different drainage basins within the same sedimentary basin can be determined by performing provenance studies (Haughton et al., 1991). The data from these analyses will facilitate a better understanding of fluvial paleodynamics at large spatiotemporal scales (Chapkanski et al., 2020). Following Chapkanski et al. (2020), the provenance of paleochannel infills and basal gravel deposits was determined by combining mid-infrared spectroscopy (MIRS) measurements and discriminant analyses (DAs). MIRS is a molecular-based, non-destructive and rapid method permitting the characterization of both mineralogical and bio-chemical properties of sediments (Bertaux et al., 1998). Therefore, using mid-infrared spectra to feed discriminant analysis allows mineralogical similarities to be established between samples from a sedimentary reference dataset and samples from paleochannel infills (Chapkanski et al., 2020). The reference dataset used in this study contains 196 (sub-)surface samples covering the main potential sedimentary sources in the study area (i.e., Rhine River, Ill River, and Vosges tributaries; Chapkanski et al., 2020; see also Fig. 1b). A total of 46 additional reference samples were collected and incorporated into the original reference dataset. A total of 73 samples from the paleochannel infills (referred to as target samples) were collected in the 12 paleochannels from different stratigraphic units.

Both the reference and target samples were dried for 7 d at 30 °C before sieving through a 2 mm sieve. The samples were then ground for 3 min using a vibratory disc mill equipped with an agate grinding set to obtain a fine, homogenous powder. Spectroscopic measurements were performed on a Fourier-transform infrared spectroscopy (FT-IR) frontier spectrometer (PerkinElmer, USA) with KBr beam split-

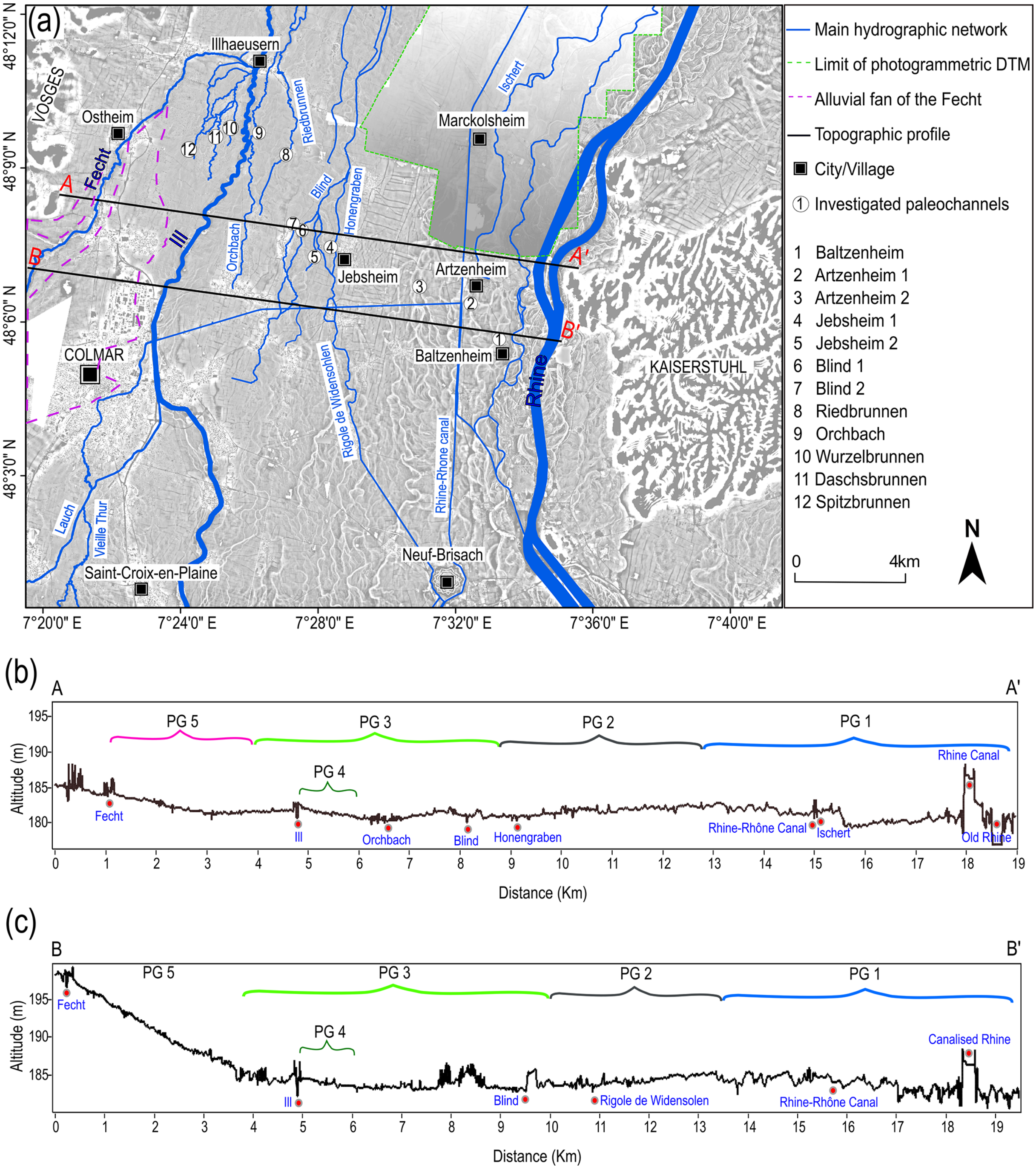

Figure 4. **(a)** Lidar DEM and photogrammetric DTM of the study area, with the main river network and coring sites of the investigated paleochannels. **(b)** Topographic profile along line A–A′. **(c)** Topographic profile along line B–B′. Data sources: lidar DEM: Regional Council of Grand Est and the European Collectivity of Alsace; photogrammetric DTM: IGN France.

ter equipped with a diffuse reflectance sampling accessory. The powdered samples were scanned from 4000 to 450 cm^{-1} with a 2 cm^{-1} resolution. Each spectrum is the average of 20 scans of each sample. Following Chapkanski et al. (2020), spectra resolution was averaged over a 16 cm^{-1} interval to improve spectra pattern recognition. Standard normal variates, baseline, and second derivate pre-treatments were performed to reduce scatter effects and improve the spectral alignment. Moreover, only the fingerprint mid-infrared spectral region (from 1500 to 450 cm^{-1}) was selected prior to statistical treatments in order to reduce misleading results due to organic matter absorbing in the regions between

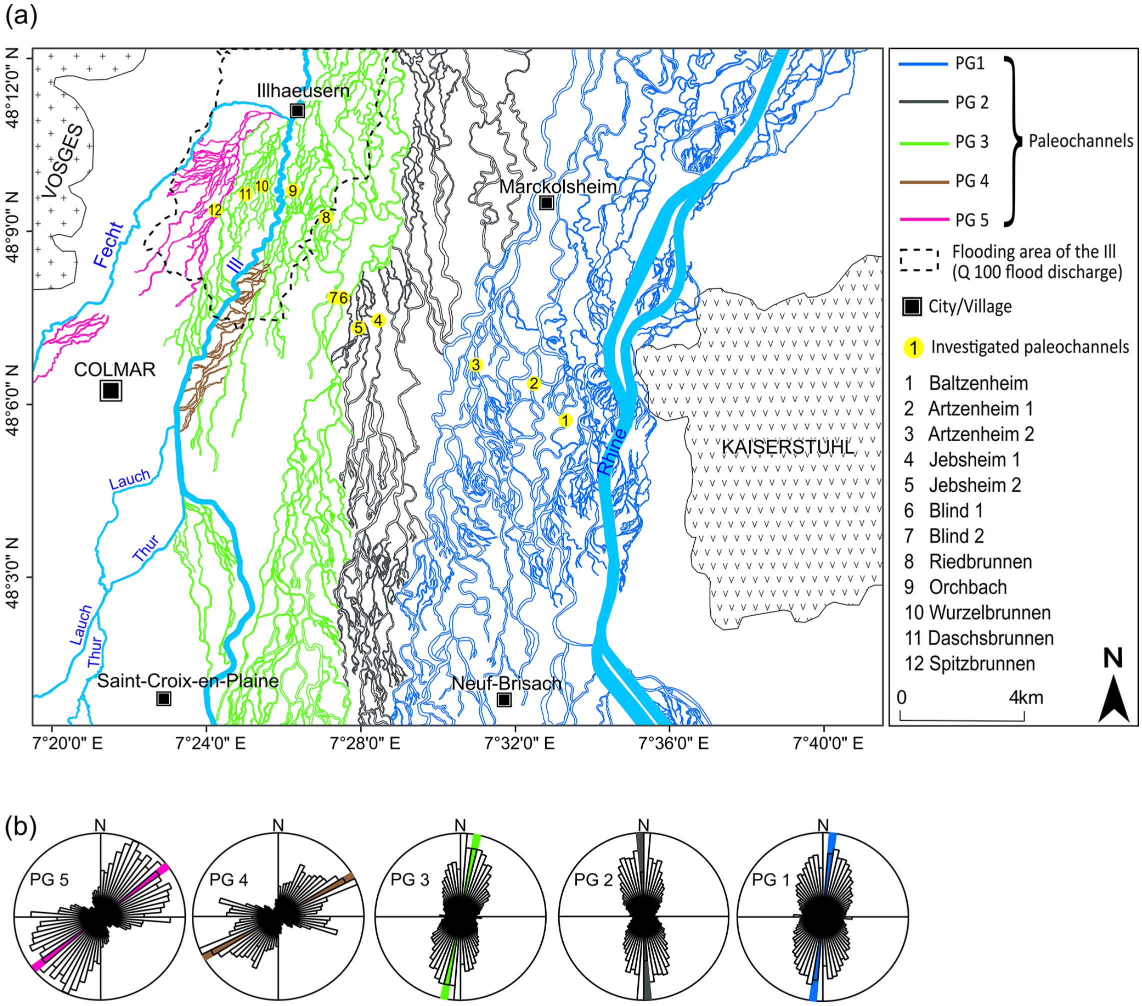

Figure 5. **(a)** Map showing the paleochannel network in the extended study area based on the surface topography, as well as the spatial delineation of five paleochannel groups (PG 1 to PG 5). **(b)** Distribution of the directions of the five paleochannel groups.

3750–3450 cm^{-1} (Bertaux et al., 1998) and 2950–2850 cm^{-1} (Kaufhold et al., 2012). A stepwise discriminant analysis was applied using the Mahalanobis distance to assess the spectral resemblances between the reference and the target samples. The sedimentary provenance of target samples was deduced as the function of the nearest barycenter of reference groups. Detailed statistical treatments are described by Ertlen et al. (2010) and Chapkanski et al. (2020).

In order to evaluate the effect of organic matter on spectra and thus misleading provenance prediction, samples collected in paleochannels (target samples) were analyzed before and after organic matter removal by hydrogen peroxide (H_2O_2). The deviation of the Mahalanobis distance of samples before and after organic matter removal was used to assess the effects of organic matter on provenance determination.

4 Results

4.1 Remote-sensing-based mapping and analysis

We were able to map a detailed and extensive network of paleochannels (about 19 km wide) covering the entire study area by integrating elevation data and aerial images. A map of the area was created (Fig. 5), revealing far more information about the paleochannels than the lidar data provided. The area was divided into five paleochannel groups (PG 1 to PG 5) based on the expected genesis of the paleochannels by showing where the channels are coming from, their location within the alluvial plain, direction, and general channel pattern. Quantitative (lidar) analyses revealed further differences in the surface topographical properties (channel width, depth, sinuosity, and orientation) of these paleochannel groups (Figs. 5 and 6, Table 1).

PG 1. The paleochannels span a 7 km wide corridor in the eastern section of the study area, close to the current Rhine

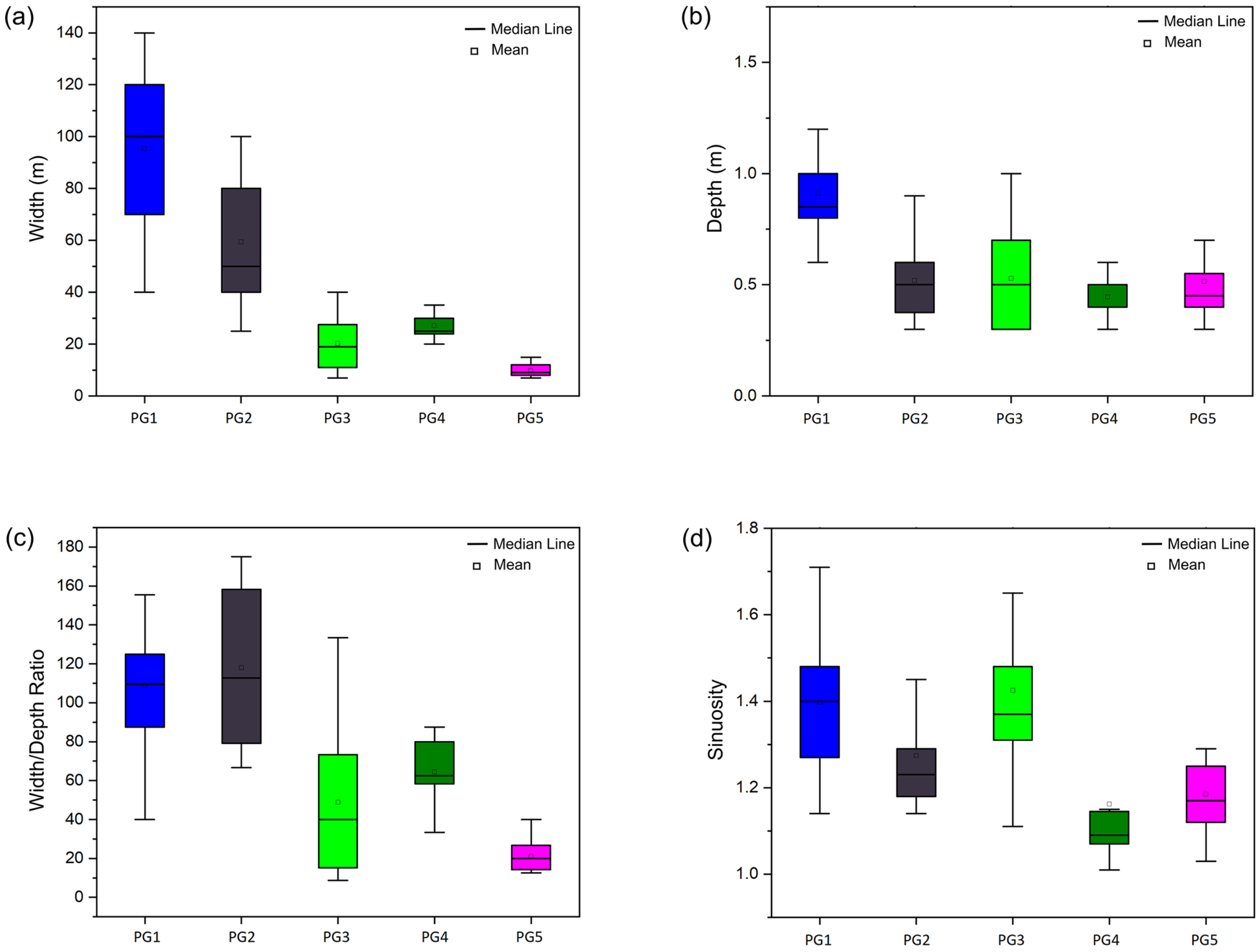

Figure 6. Box plot diagrams of four morphometric parameters for the five paleochannel groups. **(a)** Channel width, **(b)** channel depth, **(c)** width / depth ratio, and **(d)** sinuosity.

Table 1. Summary data of four morphometric parameters for the surface topography of the paleochannel groups (PG 1 to PG 5). The values of each morphometric parameter are arithmetic means and variation coefficients (in brackets).

	Paleochannel groups				
	PG 1	PG 2	PG 3	PG 4	PG 5
Mean channel width	95.38 (27.66)	59.38 (40.89)	20.16 (53.5)	27.11 (21.06)	9.81 (29.3)
Mean channel depth	0.91 (26.37)	0.52 (34.61)	0.53 (43.39)	0.44 (25.00)	0.50 (44.46)
Mean width / depth ratio	108.88 (28.14)	117.88 (33.09)	48.83 (72.30)	64.44 (29.38)	20.93 (35.9)
Sinuosity	1.40 (11.42)	1.27 (11.81)	1.42 (12.67)	1.16 (15.52)	1.18 (8.47)

fluvial hydrosystem. This group comprises multi-threaded channel networks with a high degree of sinuosity (average 1.40). The paleochannels follow a south-southwest–north-northeast trend and are on average 95 m wide and 1 m deep (surface topography). The majority of these paleochannels are located on the lowest topographical level of the alluvial plain, but there is a general increase in surface elevation moving east to west, with a sharp elevation increase in the center of the group (Fig. 4b).

PG 2. This paleochannel group is located in the central sector of the study area and is generally south-southeast–north-northwest trending. Similar to PG 1, the paleochannels exhibit a multi-threaded channel pattern but are less sinuous (average 1.27) than the paleochannels of PG 1. The paleochannel surface topography exhibits an average width of 60 m and an average depth of 0.5 m. The trace of these paleochannels becomes less visible downstream around the village of Jebsheim due to agricultural activity in the area, which has smoothed the microtopography over time. The PG 2 paleochannels are situated on the same topographical level as the western portion of the PG 1 paleochannels, but the elevation decreases progressively from east to west (Fig. 4b and c).

PG 3. These paleochannels extend approximately 6 km from the central portion of the study area, where they appear to intersect the paleochannels of PG 2, to the western side of the Ill River. The paleochannels exhibit both single- and multi-threaded channel patterns, as well as a high degree of sinuosity (average 1.43). They run south-southwest–north-northeast and are significantly smaller than PG 1 and PG 2 paleochannels, with the channel size decreasing from east to west. Their widths range from less than 10 to 45 m, with an average width of 20 m and a depth of 0.5 m. The PG 3 paleochannels are on a similar topographic level as PG 2, but the elevation increases towards the current channel of the Ill River.

PG 4. The paleochannels are localized very close to the current channel of the Ill River and are associated with the paleochannels of PG 3. Although these paleochannels are associated with the PG 3 paleochannels, they all originate on the Ill River's eastern bank, where they cut into the Ill levee before connecting to the PG 3 paleochannels. In comparison to PG 3 paleochannels, these are low sinuosity (average 1.16), single-thread channels that average 27 m in width and 0.4 m in depth. The PG 4 paleochannels are at a relatively high elevation, which corresponds to the levee of the Ill River. However, there is a progressive decrease in elevation from west to east (Fig. 4b and c). These channels are only visible with lidar. They are barely noticeable in the field or in aerial photos, as they are hidden by dense grassland or in some sectors by the dike of the Ill River.

PG 5. These paleochannels are limited to the northwestern sector of the study area, covering an area of about 2.5 km width. The paleochannels originate on the Fecht River's western bank, from where they flow northeast towards the current channel of the Fecht around Illhaeusern, where they coalesce and gradually taper out (Fig. 5). The paleochannels are mainly multi-threaded to meandering channels (average sinuosity of 1.18) and are much smaller compared to the paleochannels of the other groups. They have an average width of 10 m and a depth of 0.5 m. These paleochannels are located on the highest topographical level of the alluvial plain, which corresponds to the downstream extremity of the alluvial fan of the Fecht River (Fig. 4b and c).

4.2 Paleochannels cross sections, infill sedimentary characteristics, and provenance

The geometry and internal architecture of the investigated paleochannels vary significantly across the study area. The paleochannels range from shallow and narrow channels less than 30 m wide to deep (ca. 5 m) and wide channels with lateral extents exceeding 80 m. The paleochannel infills (sequences) vary across the channels as well, but generally sequences fining upward are observed regardless of channel geometry. For nearly all paleochannels, sandy deposits at the basal parts are overlain by a heterogeneous succession of fine materials (silt, clay), interrupted by peat and organic mud units at some locations (Fig. 7).

4.2.1 PG 1: Channel 1: Baltzenheim (48°05′53.6″ N, 7°33′1.9″ E)

The paleochannel of Baltzenheim is located 2 km west of the current Rhine channel. It is the most eastern of the paleochannels investigated, located within the historical floodplain of the Rhine ("Ried Blond"), and is part of PG 1. This paleochannel has a width of about 80 m and a maximum depth of 2.8 m. The base of the channel infill is composed of 1.5 m thick beige medium sand that extends the entire width of the channel. This unit gradually changes into a subsequent thin layer of beige silty sand. The sandy deposits (medium sand and silty sand) are overlain by brown clayey silt, capped by dark brown silt with some sand that covers the entire width of the channel. MIRS provenance studies indicate that the sedimentary infills of this paleochannel are primarily attributed to the Rhine catchment (Figs. 7a and 8b).

4.2.2 PG 1: Channel 2: Artzenheim 1 (48°06′28.8″ N, 7°32′15.2″ E)

This paleochannel is located 2.5 km west of the present-day Rhine channel within the historical floodplain of the Rhine River and is part of PG 1. However, it exhibits a more complex morphologic and stratigraphic character than the Baltzenheim paleochannel. The paleochannel reaches a maximum depth of around 5 m and a maximum width of 60 m. The lowermost section of the channel is formed of beige-colored fine to medium sand that extends the channel's entire width. Peat and organic mud which range in color from dark brown to black and are approximately 1.5 m thick overlie the sand unit but are restricted to the western and deepest portion of the channel. This peat unit contains abundant plant macrorests and is interbedded with thin, laterally discontinuous clay and carbonate layers (carbonate concretions and shell fragments). The peat/organic mud is topped by a dark gray clayey silt unit marked by shell fragments, pebbles, and thin layers of bright orange coarse sand. On the eastern side of the channel, adjacent to the clayey silt unit, is a layer of beige silty sand with a maximum thickness of 0.8 m. The succession of medium sand, peat, clay, and silty sand is overlain by dark brown clayey silt that spans the entire width of the paleochannel. All units are capped by a 0.5 m thick dark brown organic-rich silt and sand, replete with pebbles, plant macrorests, and traces of plowing. Similar to the sediments

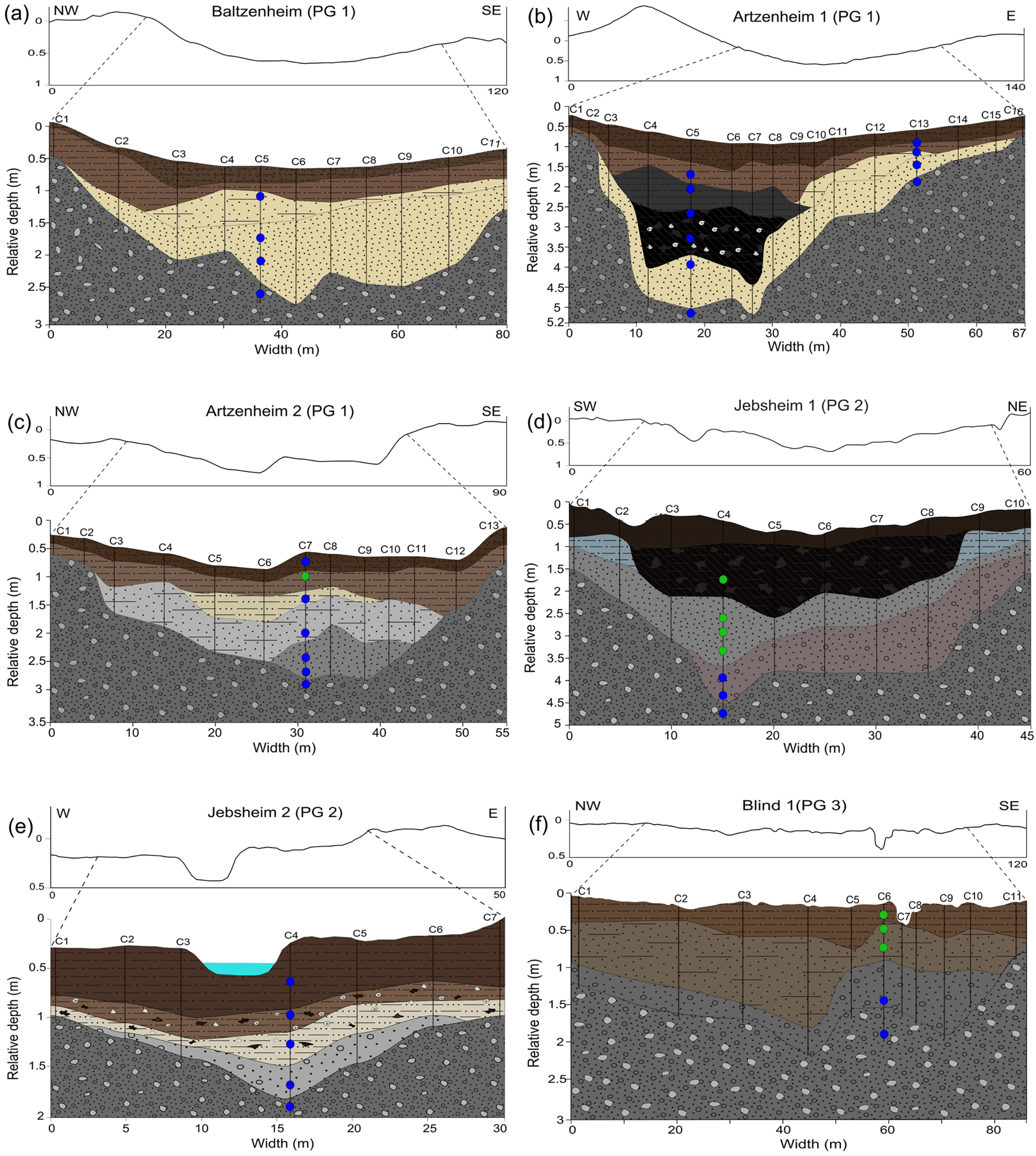

Figure 7.

of the Baltzenheim paleochannel, all the stratigraphic units of this paleochannel also show a complete Rhine provenance affinity (Figs. 7b and 8b).

4.2.3 PG 1: Channel 3: Artzenheim 2 (48°06′50.3″ N, 7°30′46.3″ E)

This paleochannel is located about 5 km west of the present-day Rhine channel and is associated with PG 1. The pale-

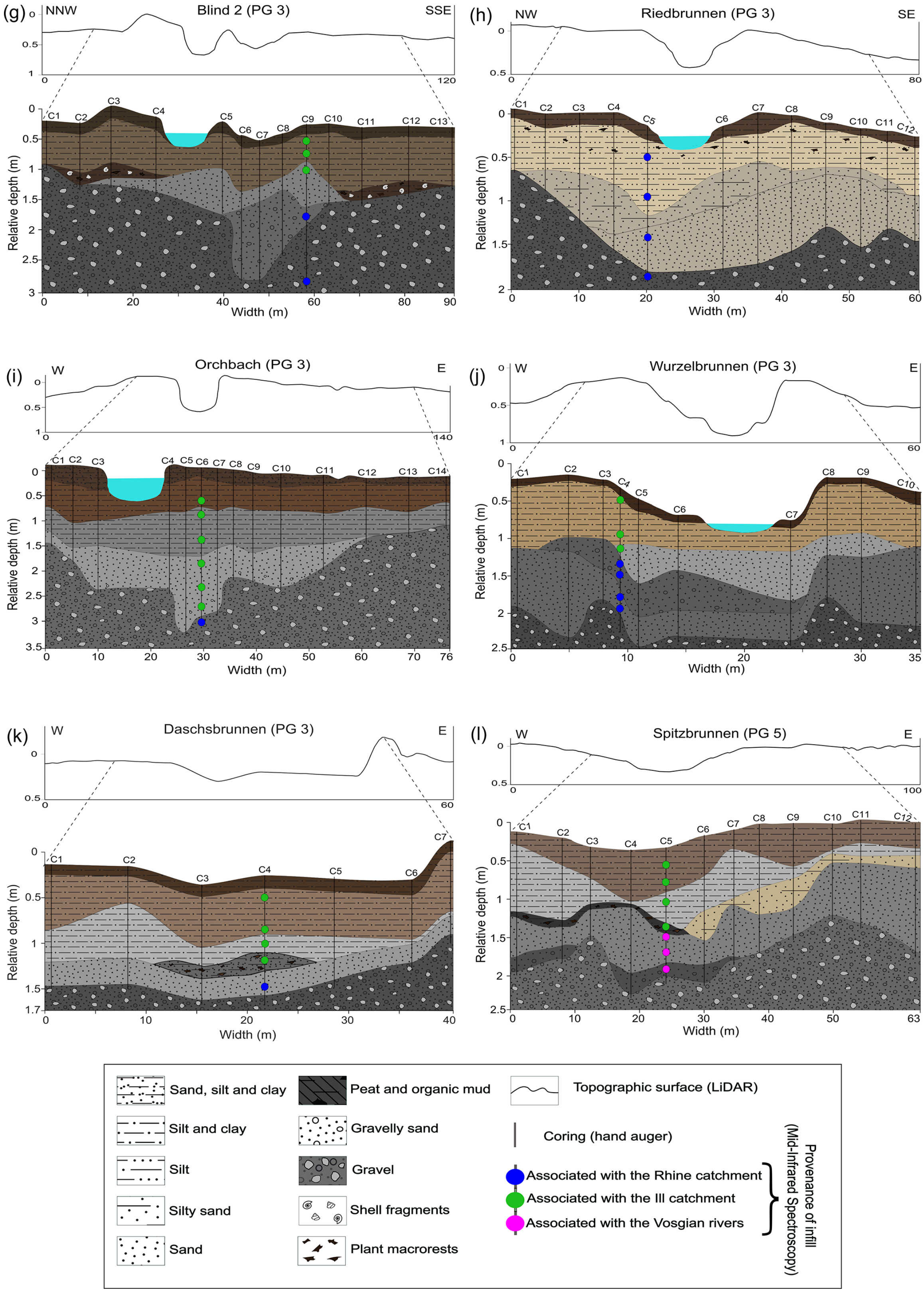

Figure 7. Cross-sections of investigated paleochannels showing internal architecture and stratigraphy based on augured boreholes, as well as description and interpretation of the stratigraphical units. Using lidar data, surface topographical profiles were drawn beyond the limit of the corings to show the full extent of the banks and levees. The figure also shows the provenance of the sediments based on mid-infrared spectroscopy analysis (MIRS) (see also Fig. 8).

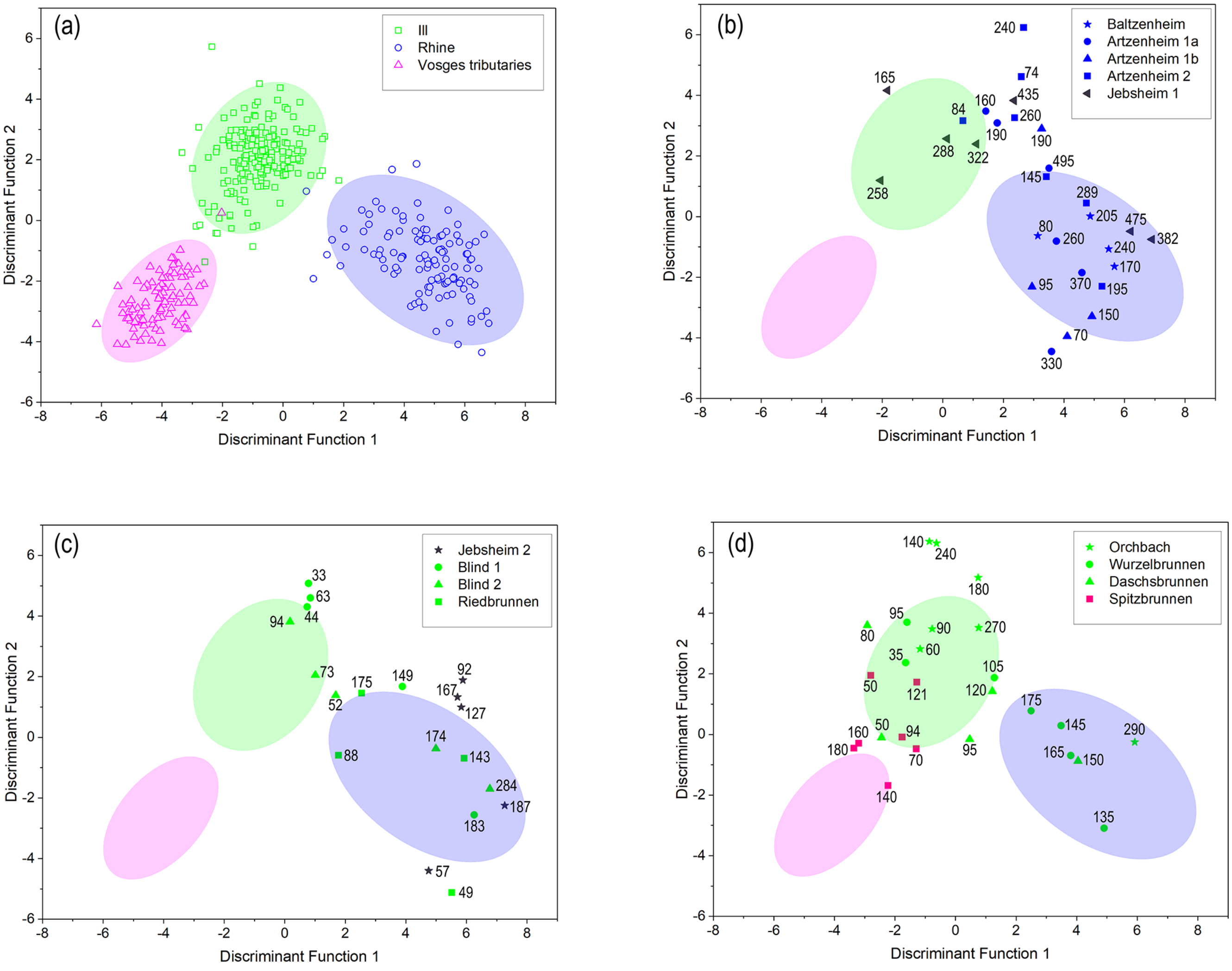

Figure 8. **(a)** Two-dimensional scatter plots showing the MIRS reference samples classified into three distinct source groups based on discriminant analysis (DA). Panels **(b)**, **(c)**, and **(d)** show the DA scores of the paleochannel (target) samples compared to reference samples. The ellipses show the area where 90 % of the different reference samples are concentrated, while the numbers indicate the depths (in cm) at which the target samples were taken.

ochannel has a maximum recorded depth of 2.8 m and is approximately 50 m wide. The sequence of units consists of gray medium sand with intermittent pebbles at the lowermost part of the channel, which is confined to the eastern portion of the channel. The unit gradually changes to gray silty-fine sand with a maximum thickness of ca. 1 m which extends almost the full width of the channel. A thin (ca. 0.5 m thick) beige silt unit follows but is confined only to the center of the channel. This silt is completely covered by a greyish-brown clayey silt unit that spans the channel's width. A dark brown sandy clayey silt with pebbles and plant macrorests completes the sequence. MIRS investigations indicate a Rhine origin for all the stratigraphic units, except for the silt unit, which shows an Ill provenance affinity (Figs. 7c and 8c).

4.2.4 PG 2: Channel 4: Jebsheim 1 (48°07′33.3″ N, 7°28′06.1″ E)

This paleochannel is located in a forested area and belongs to PG 2. The paleochannel is approximately 4.5 m deep but relatively narrow (ca. 40 m wide). The basal channel fills are composed of reddish-gray gravelly sand at the lowest level, which gradually changes to an overlying unit of gray medium sand with occasional gravel lenses. The sandy deposits are overlain by a 1 m thick layer of dark brown to black peat with intermittent layers of organic mud and clay. Numerous plant macrorests and shell fragments are found in the peat layer. Laterally adjacent to the peat on both sides is a bluish-gray clayey silt unit with a maximum thickness of 0.5 m. The peat and clayey silt layers are topped with a dark brown organic-rich clayey silt. The unit contains roots, partially decomposed organic debris, and shell fragments. MIRS data indicate that the gravelly sand unit at the base of this paleochannel is Rhine-sourced. In contrast, the overlying medium sand and peat units are in good correspondence with an Ill provenance source (Figs. 7d and 8b).

4.2.5 PG 2: Channel 5: Jebsheim 2 (48°07′23.7″ N, 7°27′42.1″ E)

This paleochannel is located 600 m southwest of the Jebsheim 1 paleochannel and is also classified as PG 2. This paleochannel, which serves as the course of an unnamed stream, is relatively narrow (about 25 m wide) and shallow, with a maximum recorded depth of 1.7 m. The infill succession of the paleochannel begins with coarse gravelly sand at its lowermost section, followed by beige silt with abundant plant fragments, and eventually a transition to brown organic-rich clayey silt. This clayey unit contains abundant shell fragments and plant macrorests, capped by a dark brown clayey silt with some pebbles. In contrast to the Jebsheim 1 paleochannel, which contains sediments from both the Rhine and Ill systems, Jebsheim 2 shows only Rhine-derived infill sediments (Figs. 7e and 8c).

4.2.6 PG 3: Channels 6 and 7: Blind River (Blind 1 and Blind 2)

This location comprises two paleochannels: one that serves as the course for an inactive tributary of the Blind River (Blind 1: 48°07′52.9″ N, 7°27′13.4″ E), colloquially named "Old Blind", and another that serves as the current course for the Blind River (Blind 2: 48°07′55.7″ N, 7°27′08.3″ E). Both paleochannels are classified as PG 3 and are located within the "Ried Gris".

The "Old Blind" paleochannel (Blind 1) is relatively wide (about 80 m) but shallow, reaching a maximum depth of 1.8 m. The infill sediment sequence shows a basal gravelly sand unit (maximum thickness 0.7 m) overlain by a 1 m thick brownish-gray silty sand unit which gradually transitions to a brown clayey silt unit that caps the sequence. The gravelly sand at the base of the paleochannel has a Rhine origin, while the overlying units are composed of Ill-derived sediments (Figs. 7f and 8c).

The paleochannel of Blind 2 is also relatively wide (approximately 80 m) and has a depth of 2.8 m. The Blind River does not flow through the deepest section of the paleochannel but rather around 10 m to the west. The flowing channel of Blind 2 appears to be artificial, with a regular trapezoidal shape and an artificial right bank levee. Furthermore, at the top of the deepest part of the paleochannel, the surface topography preserves a former channel that likely corresponds to the natural channel (Fig. 7g). At Blind 2, the paleochannel infill sequence consists of, from bottom to top, a 1 m thick gravelly sand unit concentrated in the middle of the paleochannel, overlain by gray fine to medium sand that reaches a maximum thickness of 0.6 m. Overlying the medium sand on both the eastern and western channel margins is a layer of dark brown organic clay with shell fragments and some pebbles. A brown clayey silt unit (0.8 m thick) lies above the organic clay, followed by an organic-rich silty-clay unit. MIRS results show an origin from the Rhine for the gravelly sand unit, while the overlying fine sand and clayey silt units have an Ill origin (Figs. 7g and 8c).

4.2.7 PG 3: Channel 8: Riedbrunnen (48°09′19.4″ N, 7°26′46.2″ E)

The Riedbrunnen paleochannel is classed as PG 3 and contains the current course of the Riedbrunnen River, which flows near the deepest section of the paleochannel. The paleochannel is relatively shallow and narrow, reaching a maximum depth of 1.9 m and a width of about 60 m. At the channel's base, a greige color, fine to medium sand unit (maximum thickness 0.8 m) is overlain by a greige silty sand unit (maximum thickness 0.5 m). Following this unit is a succession of beige to light gray sandy silt with abundant plant detritus in its upper part. The upper 0.2 m of the channel infill is formed of dark brown organic-rich silty clay with partially decomposed plant macrorests. Sediment provenance analyses indicate that all the infill sediments of the Riedbrunnen paleochannel originate from the Rhine catchment (Figs. 7h and 8c).

4.2.8 PG 3: Channel 9: Orchbach (48°09′45.7″ N, 7°25′54.7″ E)

The Orchbach is another PG 3 paleochannel within the floodplain of the Ill ("Ried Gris"). This paleochannel is located about 350 m east of the Ill River and contains the current course of the Orchbach River. The paleochannel has a maximum depth of 3.2 m and a width of approximately 65 m. The Orchbach River's current channel is about 10 m west of the center of the paleochannel. The lowest section of the paleochannel comprises gray medium to coarse sand with a maximum recorded thickness of 1.5 m. A 1 m thick gray clayey silt unit covering the entire channel width overlies the sand, followed progressively by a brown clayey silt (0.7 m thick) unit with shell fragments and plant macrorests. Dark brown clayey silt with some sand caps the infill succession. Unlike the sediments of the nearby Riedbrunnen paleochannel, which have a Rhine origin, all of the infill sediments of the Orchbach paleochannel are of Ill provenance (Figs. 7i and 8d).

4.2.9 PG 3: Channel 10: Wurzelbrunnen (48°09′51.6″ N, 7°25′07.9″ E)

Wurzelbrunnen is the first of three paleochannels that have been investigated west of the Ill River. It is also of PG 3 and located around 450 m west of the Ill River in the "Ried Gris". The paleochannel is currently active and serves as the course of the shallow Wurzelbrunnen stream. The paleochannel is roughly 35 m wide and reaches a maximum depth of 2.4 m. The infill of the paleochannel begins with a gray medium sand unit with a maximum thickness of 1.2 m, which is overlain by gray gravelly sand concentrated in the western and central sections of the paleochannel. The gravelly sand is overlain by another unit of gray medium sand (maximum thickness 1.2 m) that runs the channel's central and eastern sections. The medium sand is covered by a beige-brown clayey silt unit that extends the full width of the paleochannel and is topped by dark brown clayey silt with root fragments and traces of plowing. MIRS analysis indicates that the first two sandy units at the base of the paleochannel are composed of sediments derived from the Rhine provenance area. In contrast, the upper sand unit is primarily associated with the Ill, albeit with a little Rhine influence. The clayey silt has a pure Ill origin (Figs. 7j and 8d).

4.2.10 PG 3: Channel 11: Daschsbrunnen (48°09′44.8″ N, 7°24′43.0″ E)

The Daschsbrunnen paleochannel is located 450 m west of Wurzelbrunnen and is also a part of PG 3 on the western side of the Ill River. The paleochannel is approximately 40 m wide and 1.6 m deep. The basal 0.5 m are gray fine to medium sand with scattered pebbles, followed by 0.2 m of dark brown to gray silty sand with abundant plant fragments. This silty sand unit is restricted to the mid-section of the paleochannel. The overlying unit consists of gray 1.2 m thick clayey silt, which gradually changes to greyish brown in the upper 0.5 m. The topmost 0.2 m of the paleochannel is built up of dark brown clayey silt. MIRS data reflect a Rhine origin for the basal sand infill, while the overlying silty sand is Ill-derived with some Rhine influence. In contrast, the clayey silt units bear a pure Ill signature (Figs. 7k and 8d).

4.2.11 PG 5: Channel 12: Spitzbrunnen (48°09′25.5″ N, 7°24′0.8″ E)

Spitzbrunnen is the westernmost of the studied paleochannels, located about 1.9 km west of the Ill River and 2.2 km east of the Fecht River. It is the only paleochannel of PG 5 that has been investigated. The paleochannel reaches a maximum depth of 2.2 m and is approximately 65 m wide. At its base, the paleochannel is filled with dark gray gravelly sand localized in the middle of the channel. A gravel bank separates this gravelly sand from an identical unit on the western side of the channel. The unit directly overlying the gravelly sand is made of gray medium to coarse sand that reaches a thickness of about 1 m. Above the medium sand is a layer of beige silty sand that extends from the center of the channel to the eastern bank. This layer is flanked by a dark gray, organic-rich silty sand that gradually changes to gray clayey silt that stretches the entire channel width. All the units are then topped by brownish-gray clayey silt with a maximum thickness of 0.6 m. Provenance analysis (MIRS) shows that the basal sand units (gravelly sand and medium to coarse sand) of the Spitzbrunnen paleochannel originated primarily from the Vosges source area. In contrast, the overlying silty units are composed of Ill-derived sediments (Figs. 7l and 8d).

5 Discussion

5.1 Consolidation of the MIRS method to identify sediment provenance

Chapkanski et al. (2020) pioneered the use of MIRS and discriminant analysis (DA) to identify the provenance of paleochannel infills within the Upper Rhine alluvial plain. However, since the methodology was only tested on one paleochannel, it remained unknown whether the MIRS–DA technique could be widely applied to determine the provenance of paleochannel infillings across a large part of the alluvial plain. As a result, we employed the MIRS–DA approach to determine the provenance of several paleochannel infillings over the whole width of the French Upper Rhine plain. Our findings clearly demonstrate the robustness of this method in identifying the sources of paleochannel infilling, which may have changed during the filling for some paleochannels. The Baltzenheim 1 and Baltzenheim 2 paleochannels, for example, are entirely filled with Rhine sediments, whereas the Orchbach paleochannel is filled with Ill sediments. In contrast, the filling of paleochannels such as Blind, Wurzelbrunnen, and Daschsbrunnen began with Rhine sediments and subsequently transitioned to Ill deposits (Figs. 7 and 8).

While the MIRS–DA technique has demonstrated great potential for determining the provenance of sediments, Chapkanski et al. (2020) suggested that high organic matter (more than 5 % to 10 %) in sediment samples might affect the mid-infrared spectra, resulting in less accurate measurements. To address this potential constraint, we pre-treated target samples with an organic matter content of more than 5 % (see Sect. 3.3). The results (Table 2) show that the deviations of the samples from their initial position before OM removal remain within a reasonable range of < 1.5 (Mahalanobis distance). However, those samples containing more than 10 % of organic matter recorded deviations ranging from 1.5 to 5, which could induce modification of provenance attribution. However, the results here showed no significant inconsistencies in the attribution of sediment provenance except for two samples (Az1_260 and Az1_330) from peaty deposits and two other samples (NB_73 and L'O_90) from organic-rich units. Therefore, these confirm suggestions provided by Chapkanski et al. (2020), and we recommend systematically pre-treating samples containing more than 10 % of organic matter.

Overall, our findings confirm that the MIRS–DA technique is capable of determining the provenance of paleochannel infills within the French Rhine alluvial plain with high specificity. Moreover, the method is a low-cost and ef-

Table 2. Provenance attribution of target samples containing more than 5 % organic matter (OM) before and after organic matter treatment. The table also shows the deviation of each sample after organic matter removal. F1: discriminant function 1; F2: discriminant function 2.

Sample ID	Depth (cm)	Paleochannel	OM before treatment (%)	Deviation from F1 after treatment	Deviation from F2 after treatment	Provenance before organic matter treatment	Provenance after organic matter treatment
Bz_80	80	Baltzenheim	15.38	1.71	1.58	Rhine	Rhine
Az1_260	260	Artzenheim 1	16.86	3.60	3.11	Ill	Rhine
Az1_330	330	Artzenheim 1	14.91	3.44	4.58	Ill	Rhine
Az2_145	145	Artzenheim 2	5.79	0.02	1.43	Rhine	Rhine
Jebs1_165	165	Jebsheim 1	6.89	0.09	0.17	Ill	Ill
Jebs2_57	57	Jebsheim 2	11.77	0.07	2.79	Rhine	Rhine
OB_44	44	Blind 1	8.25	1.96	1.13	Rhine	Rhine
NB_73	73	Blind 2	12.21	5.14	4.79	Vosges	Ill
NB_94	94	Blind 2	6.62	0.63	0.44	Ill	Ill
Ried_88	88	Riedbrunnen	6.73	1.22	1.19	Rhine	Rhine
L'O_60	60	Orchbach	12.24	1.96	0.81	Ill	Ill
L'O_90	90	Orchbach	11.85	3.14	0.34	Rhine	Ill
Wz_35	35	Wurzelbrunnen	11.34	1.53	2.58	Ill	Ill
Spt_94	94	Spitzbrunnen	9.93	0.92	0.88	Ill	Ill
Spt_121	121	Spitzbrunnen	10.47	0.58	2.30	Ill	Ill

ficient alternative for provenance investigations of deposits in large and complex fluvial systems. The MIRS–DA technique, however, has so far only been applied in the Upper Rhine Valley, and it remains to be tested in other large river floodplains.

5.2 Establishment of sedimentary facies

The subsurface morphology of the investigated paleochannels exhibits a range of geometric forms, as well as varied sedimentary infill (Fig. 7). Several other paleochannels within the French Rhine alluvial plain have shown a similar pattern of varying subsurface morphology and infill stratigraphy (e.g., Schmitt et al., 2016; Chapkanski et al., 2020). These differences in internal sedimentary infills across the plain indicate infilling by rivers with varying dynamics, reflecting lateral dynamics of the Rhine, Ill, and Fecht rivers. To better understand the various dynamics and channel activity over time, we classified the stratigraphic units of our investigated paleochannels into four genetic groups ("Gravel", "Active", "Infill", and "Surficial" facies). These classifications are based on the characterization and interpretations of various Late Pleistocene and Holocene fluvial deposits from the Upper Rhine Valley (Dambeck and Thiemeyer, 2002; Schirmer et al., 2005; Erkens et al., 2009, 2011; Schmitt et al., 2016). By deciphering the different stages of channel activity and assigning a provenance of filling dynamics to the stages, we determined the river system(s) that contributed to the infilling of the investigated paleochannels.

The gravelly sediments at the very bottom of the paleochannels are categorized as "Gravel" deposits. These sediments form the base and lateral limits of the paleochannels and are easily differentiated from the overlying fill sediments by their significantly larger grain sizes, with gravel dominating. This facies is interpreted to have formed by high-energy depositional conditions via non-selective bedload transport (Chardon et al., 2021). Moreover, Gravel is ubiquitously present throughout the study area, and MIRS spectroscopy reveals an unambiguous Rhine origin for these deposits (Figs. 7 and 8). The ubiquity of these gravels, as well as their sedimentary characteristics and provenance, indicates that they are deposits of the Rhine braided belt, which covered nearly the entire plain of the URG during the Late Pleistocene (Lang et al., 2003; Kock et al., 2009). It is worth noting that these sediments do not directly constitute the infilling sequences of the paleochannels. However, some fluvial reworking of the sediments and their deposition within the stratigraphic infills may occur, thus forming essential components for understanding channel dynamics.

The "Active" facies constitute the sand-rich stratigraphic units (gravelly sands, sands, and silty sands) at the basal parts of the paleochannels and overlying the Pleistocene gravel (Gravel). These sandy strata are interpreted as channel deposits, comprising gravelly channel lags (bedload) and sandy channel fills (bedload and graduated suspension; Plotzki et al., 2015; Delile et al., 2016). The deposits indicate deposition during moderate- to high-energy periods of flow at the beginning of infill. So this facies reveals deposition during a permanent or intermittent connection to a basin-fed river. Bank accretion may also have occurred during such periods. Thus, by identifying the Active deposits and their provenance, we were able to discern which rivers were active in infilling of each paleochannel. In contrast to the gravel deposits, which are exclusively Rhine-sourced, the sandy channel deposits (Active) show Rhine, Ill, and Vosges signatures as revealed by MIRS (Figs. 7 and 8). This disparity in provenance sources indicates that the infilling sources changed over time in some cases, highlighting active past lateral dynamics of the main rivers within the alluvial plain.

The succession of silty and clayey layers, interspersed with peat and organic mud, are classified as "Infill" facies. Unlike the Active channel deposits, which are generally restricted to the paleochannels' deepest and central sections, the Infill sediments mostly form a blanket of fine-grained materials that covers the whole width of the paleochannels (Fig. 7). Furthermore, these units are characterized by an abundance of plant macrorests and shell fragments. Accordingly, these units' stratigraphic position and sedimentary characteristics represent low- (silt) to very low-energy (clay, organic mud, peat) depositional environments. Silt and clay transport (and deposition) also indicates a homogeneous suspension (Delile et al., 2016). In such a context, channels have no (or a weak) upstream connection to a basin-fed river. The peat and organic mud, which can be considered a sub-class of the Infill facies (given the close association in the successions), indicate autochthonous sedimentation and starvation or minimal input of clastic sediments in the channels (Hoffmann et al., 2008; Toonen et al., 2012).

Consequently, the Infill sediments serve as key stratigraphic markers for determining an important filling phase associated with reduced fluvial activity and a partial or total disconnection from feeding rivers. Such depositions occurred mostly during floods which extended to the channels. Furthermore, establishing the provenance of these sediments was critical for determining which river(s) contributed to the paleochannel filling phase (after their abandonment). Provenance (MIRS) investigations reveal a mixture of Rhine, Ill, and Vosges signatures for the Infill sediments (Figs. 7 and 8), confirming the lateral movements of the basin-fed rivers across the alluvial plain.

The uppermost sequences of the paleochannels are classed as "Surficial" facies and are typically formed of clays and silts (and in some places, reworked floodplain sands and gravel). Additionally, this facies contains biogenic materials and some anthropogenic materials locally. Typically, the uppermost portion of these floodplain surface deposits shows organic soils and traces of agricultural activity (plowing). The pedogenesis indicates (quasi-)total channel abandonment and a very weak sedimentation rate for centuries. In the cases where a current stream runs in the paleochannels, the presence of this surface facies indicates that the current channel is in a (quasi-)steady state (which may be linked in some cases to some human dredging activities; Schmitt, 2001; Schmitt et al., 2007, 2011). Considering the Upper Rhine valley is highly anthropized (Lang et al., 2003; Wantzen et al., 2021), these units are considered to be affected by direct human alteration. Hence, they are only used to develop an understanding of soil formation processes and agricultural practices in the immediate environment. They are not used to make direct inferences regarding the fluvial processes within the alluvial plain.

5.3 Reconstructing the temporal trajectories of the five paleochannel groups

Remote sensing combined with qualitative and quantitative morphometric analysis of the surface topography provided a basis for classifying five paleochannel groups within our study area. Additional datasets from the fieldwork and provenance analysis provide information into further complexities amongst these paleochannel groups. In the following section, we combine all of the datasets, as well as information from earlier studies, to provide insights into the origins and the temporal trajectories of these paleochannel groups and speculate on the various basin-fed rivers with which they may be associated.

5.3.1 PG 1

The PG 1 paleochannels in the easternmost sector of the study area are clearly visible in the landscape, with the highest values of width and depth of all the paleochannel groups (Fig. 6; Table 1). These paleochannels exhibit a relatively high degree of sinuosity (average 1.4), as well as a multi-threaded channel pattern, and are almost entirely composed of Rhine-sourced infill sediments, as shown by the paleochannels Baltzenheim, Artzenheim 1, and Artzenheim 2 (Fig. 7a–c). The topographic surfaces and lidar analysis indicate a braided channel pattern. However, the remaining streams in this part of the alluvial plain exhibit an anastomosing channel pattern (Schmitt et al., 2007, 2011). Furthermore, as depicted on historical maps, the sub-modern Rhine system in this region was characterized by a similar anastomosing channel pattern (see Supplement). Thus, we consider the PG 1 paleochannels to consist of two main generations of paleochannels: an initial system with a braided channel pattern, which metamorphosed (fluvial metamorphosis) to the current anastomosing (and paleo-anastomosing, i.e., disconnected upstream) system. Accordingly, the PG 1 paleochannel group can be described as a palimpsest, consisting of the current and paleo-anastomosing patterns, with a low level of flow energy, superimposed on – and controlled by – the former braided channel pattern of the highly dynamic (with a high level of energy) Late Glacial Rhine fluvial hydrosystem (Schmitt, 2010).

5.3.2 PG 2

The south-southeast–north-northwest-oriented PG 2 paleochannels exhibit a similar multi-threaded pattern to PG 1. They are, however, less sinuous (average 1.27) than the PG 1 paleochannels. The surface channel pattern of these paleochannels is obscured by agricultural activity in the area, which has smoothed much of the microtopography. However, visual inspection of the elevation data and aerial photographs reveals traces of some features that appear to reflect a braided channel pattern. This is reinforced by high values of the width / depth ratio (Schmitt et al., 2007). Furthermore, the PG 1 and PG 3 paleochannels to the east and west respectively appear to cross and intersect the PG 2 paleochannels, which may indicate an older age for the PG 2 paleochannels. Based on these observations, it can thus be suggested that the PG 2 paleochannels are relicts of the Late Glacial braided Rhine system, with a more south–north flow direction. This fluvial style was the dominant character of the Rhine system during the Late Pleistocene, occupying almost the entirety of the alluvial plain (Lang et al., 2003; Schmitt et al., 2016). At the start of the Holocene, the individualization of the Rhine and Ill rivers resulted in the abandonment and partial filling up of the PG 2 paleochannels.

In comparison to the PG 1 paleochannels, which contain only Rhine-sourced sediments, it is worth noting that the Active facies of the Jebsheim 1 paleochannel show both Rhine and Ill sediments. Gravelly sand at the basal part of paleochannel is Rhine-sourced, while the overlying medium sand has an ill origin (Fig. 7). In contrast, all the stratigraphic units of the Jebsheim 2 paleochannel are Rhine-sourced (Figs. 7 and 8). A similar mixed Rhine–Ill sediment infilling pattern was observed in a northwest-trending paleochannel about 3 km north (downstream) of the Jebsheim 1 paleochannel (Chapkanski et al., 2020). Thus, the presence of Ill-derived sediments in the braided Rhine paleochannels can be explained by branches of the ensuing Holocene anastomosing Ill system re-occupying parts of the paleochannels before it migrated westward as well (Schmitt et al., 2016). Following the lateral migrations of the Rhine and Ill systems and the abandonment of the PG 2 paleochannels, the central area of the alluvial plain most likely remained dry except for periodic large floods.

The channel pattern is relatively more anastomosing in the downstream part of this group (north of Colmar), which is likely due to a general slope decrease.

5.3.3 PG 3

The PG 3 paleochannels are generally south-southwest–north-northeast trending and correspond to paleochannels of the main course of the Ill River, as well as former main and flood channels of this river at the eastern and western banks of the Ill. The surface topography shows these paleochannels to be narrower (average 20.13) than those of the PG 1 and PG 2 groups. The channel pattern shows a relatively high sinuosity, with a general multi-threaded channel pattern (Fig. 5). These paleochannels correspond to Ill-inherited geomorphic features. However, there are significant differences in their internal stratigraphy and sediment provenance. The Blind paleochannels, for example, are first filled by Rhine sediments and afterward by Ill sediments (Fig. 7f and g). The Riedbrunnen paleochannel is entirely filled by Rhine deposits, whereas the nearby Orchbach paleochannel is completely filled with Ill sediments (Figs. 7 and 8). On the western side of the Ill River, a similar Rhine sequence, followed by an Ill infilling sequence, is also recorded for the smaller Wurzelbrunnen and Daschsbrunnen paleochannels. Based on these findings, we propose that the PG 3 paleochannels are actually a mixture of Rhine and Ill paleochannels. The Rhine not only transported and deposited gravelly Active sediments, but Rhine discharge also shaped some of the paleochannels. However, there is no prior record of coeval activity of the Rhine and Ill systems in this area. Following the individualization of the Rhine and Ill, the Rhine shifted westwards progressively, and the channels were abandoned after some of them were more or less filled by Rhine sediments. The ensuing Ill system then reoccupied and modified several of these ancient Rhine paleochannels, depositing Ill sediments.

The investigated PG 3 paleochannels provide an excellent illustration of these dynamics. The Blind paleochannels, for instance, are defined by a meandering/anastomosing channel pattern in the lidar DEM, suggestive of the Ill system. However, the fill stratigraphy reveals "a wide paleochannel" with coarse-grained Active deposits from the Rhine, overlain by Active and Infill sediments bearing an Ill signature. Thus, we presume that the Blind paleochannel was created and used by the Rhine. Following its abandonment, the Ill re-occupied and modified the channel, depositing Ill sediments. This conjecture is consistent with the findings of Carbiener (1969), Hirth (1971), and Schmitt et al. (2016), the latter suggesting that the current Blind River is flowing in a former main channel of the Ill River.

In comparison, the Riedbrunnen paleochannel, located close to the contemporary Ill River, is completely filled with Rhine-derived sediments. This atypical sediment provenance can be explained by a former Rhine channel that was abandoned and completely filled by the Rhine, probably before it moved far further east. As a result, this paleochannel was not re-occupied by the Ill system. Interestingly, the Orchbach paleochannel, 1.5 km east of the Riedbrunnen, contains only Ill-derived sediments. Looking at the spatial position, planform morphology, and infilling of the Orchbach paleochannel, it appears that the Orchbach paleochannel was a former main channel of the Ill River that was created and used solely by the Ill River.

Other paleochannels documented in this section of the alluvial plain (Al Siddik, 1986; Schmitt et al., 2016) show paleochannels of mixed origin, as well as those of pure Rhine and pure Ill origin. Some with a pure Ill provenance were also recorded further downstream of our study area. Based on these findings, we can conclude that the PG 3 paleochannels are best described as a mixture of older Rhine and younger Ill paleochannels. This distribution pattern is also the result of the Ill being relatively smaller than the Rhine, and it did not wholly occupy large areas of the Holocene alluvial plain. This explains why a small part of the Rhine "Hardt Grise" exists close to the Ill River, southwest of the village of Bischwihr (Fig. 3; Hirth, 1971).

5.3.4 PG 4

The PG 4 paleochannels constitute distinctively southwest–northeast-trending paleochannels that originate from the eastern bank of the current Ill River channel. Although field investigations and provenance analysis remain to be undertaken for these paleochannels, analysis of their surface topography and spatial distribution indicates that they are most likely natural flood channels cutting the eastern bank of the Ill River. They were most likely only active during high floods, diverting floodwaters away from the Ill River towards the floodplain. Owing to the lack of a temporal context for these paleochannels, it is unknown if they are contemporaneous with some PG 3 paleochannels or if they were periodically active during historical times. These paleochannels are predominantly concentrated along the regulated reach of the Ill River (where no floods occur anymore), upstream of the Ill River floodplain ($Q100$ flood discharge; Fig. 5). Therefore, these paleochannels are not currently active, but they were probably active prior to the mid-19th century regulation of the Ill River.

5.3.5 PG 5

The PG 5 paleochannels, the westernmost component, are the narrowest (average 10 m), primarily single-threaded channels with low sinuosity (average 1.18). These paleochannels have a southwest–northeast orientation and a fluvial style different from those of the Rhine and Ill, which may reflect a link with the Fecht River fluvial hydrosystem. Moreover, the infilling of the Spitzbrunnen paleochannel shows an Active facies with Vosges signature, overlain by Infill sediments of Ill provenance (Fig. 7l). This filling pattern indicates that the Spitzbrunnen paleochannel was carved by a Vosgian river and later filled with overbank sediments from the Ill following its abandonment. A detailed examination of the Spitzbrunnen's surface topography indicates parallels to the modern Fecht River. As a result, it can be argued that the Spitzbrunnen paleochannel was most likely a former bed of the Fecht River. Considering the morphology and infill of the Spitzbrunnen, as well as the character and placement of the other PG 5 paleochannels, we propose that the PG 5 paleochannels are very likely to be the former channels and side channels of the Fecht River. Accordingly, we assume that the Fecht River was located farther east within the alluvial plain, and it moved westwards towards its current position over the course of its evolution, naturally and/or by human activities (Schmitt, 2001).

This delineation of a putative Fecht paleochannel cluster and the absence of true Ill paleochannels beyond the Spitzbrunnen imply that the Ill River did not extend beyond the Spitzbrunnen paleochannel in its western lateral migration. This observation is consistent with the suggestion of Schmitt et al. (2016) that the Ill River's western migration during the Holocene was limited to somewhere near the Wurzelbrunnen paleochannel. However, our findings show that the Ill did migrate slightly westward, up to the Daschsbrunnen paleochannel. As a result, we assume that the Ill River's Holocene displacement limit was somewhere between the Daschsbrunnen and Spitzbrunnen paleochannels. This boundary corresponds to an area near the eastern limit of the Fecht's alluvial fan.

6 Conclusions

Using remote sensing data, we identified and mapped a detailed and extensive network of paleochannels spanning a 19 km wide corridor within the French Upper Rhine alluvial plain. The mapped paleochannels exhibit a range of surface morphological characteristics, including planform character, geometry, and paleo-flow orientations. Additional data from field investigations and provenance analysis revealed considerable differences in the sedimentary characteristics and provenance of the infillings of the paleochannels, indicating significant changes in hydro-geomorphodynamic processes, especially lateral displacements of the main rivers.

Five paleochannel groups (PG 1 to PG 5) were delineated in the study area based on assessments and interpretations of the remotely sensed data, hand-augured core data, and mid-infrared spectroscopic analysis. The PG 1 paleochannels correspond to remnants of the Holocene braided Rhine hydrosystem which is currently predominantly an anastomosing system, while the PG 2 paleochannels represent relicts of the Late Pleistocene braided Rhine. The PG 3 paleochannels, on the other hand, are a complex mixture of paleochannels from the Ill hydrosystem superimposed on the Rhine braided channels. The PG 4 paleochannels are ancient Ill flood channels, while the Fecht river system formed the PG 5 paleochannels.

While our findings unequivocally establish the presence of at least five paleochannel groups in the area, their temporal trajectory remains vague. Age assignments for the paleochannel systems, as well as additional sedimentological analyses, need to be established. Accordingly, further studies on these paleochannels will be carried out to develop these datasets, which will provide new insights into the chronology of paleochannel development, the paleoenvironments in which they formed, and the processes that controlled their formation, all mainly linked to the Holocene lateral dynamics of the Rhine, Ill, and Fecht rivers.

Data availability. All data relevant for this study are either presented in the main text or the Supplement.

Supplement. The supplement related to this article is available online at: https://doi.org/10.5194/egqsj-71-191-2022-supplement.

Author contributions. FP and LS designed and supervised the study. Funding was acquired by FP and MA. Fieldwork was carried out by MA, HM, EO, MS, CR, and FS. MA, CR, FS, SC, and DE were responsible for methodology and formal analysis under the supervision of LS. EO, HM, and MS assisted with methodology. MA wrote the original draft with input from SC. The manuscript was reviewed and edited by LS and FP. All authors commented on and approved the final version of the manuscript.

Competing interests. The contact author has declared that none of the authors has any competing interests.

Special issue statement. This article is part of the special issue "Quaternary research from and inspired by the first virtual DEUQUA conference". It is a result of the vDEUQUA2021 online conference in September/October 2021.

Acknowledgements. Special thanks to Alexander Fülling, Elijah Fon, Armelle Ballian, and Amir Bangash for their assistance in the field. Thanks go to Grégoire Skupinski and Jérome Houssier for processing and treating the raw lidar data. We thank the local administrators of the various communes for giving us permission to conduct the fieldwork. We also express our gratitude to the landowners who permitted us to drill on their property. The Regional Council of Grand Est and the European Collectivity of Alsace are also acknowledged for providing the lidar data.

Financial support. This research has been supported by the Landesgraduiertenförderung Baden-Württemberg (state graduate funding) through a PhD scholarship to Mubarak Abdulkarim.

This open-access publication was funded
by the University of Freiburg.

Review statement. This paper was edited by Christian Zeeden and reviewed by Dominik Faust and one anonymous referee.

References

Al Siddik, A. M.: Contribution à l'étude de la dynamique de l'humification des sols hydromorphes du Ried Ello-Rhénan (Région d'Illhaeusern, Haut-Rhin), PhD thesis, Nancy 1 University, France, 95 pp., unpublished, 1986.

Bertaux, J., Frohlich, F., and Ildefonse, P.: Multicomponent analysis of FTIR spectra; quantification of amorphous and crystallized mineral phases in synthetic and natural sediments, J. Sediment. Res., 68, 440–447, https://doi.org/10.2110/jsr.68.440, 1998.

Bisson, M., Piccinini, S., and Zanchetta, G.: A multidisciplinary GIS-Based approach for mapping paleoriver migration: A case study of the Serchio River (Lucca Alluvial Plain, Tuscany), GIsci Remote Sens., 48, 566–582, https://doi.org/10.2747/1548-1603.48.4.566, 2011.

Boës, E., Schmitt, L., Schwartz, D., Gebhardt, A., Goepp, S., and Lasserre, M.: L'anthropisation des zones humides de la plaine d'Alsace au cours de la Protohistoire: problématiques d'études à partir des fouilles récentes menées sur les tumulus de Mussig Plaetze (Bas-Rhin), in: L'âge du Fer dans l'arc jurassien et ses marges. Dépôts, lieux sacrés et territorialité à l'âge du Fer. Annales Littéraires, Série "Environnement, sociétés et archéologie", edited by: Barral, P., Daubigney, A., Dunning, C., Kaenel, G., and Roulière-Lambert, M. J., Presses Universitaires de Franche-Comté, 113–118, ISBN 978-2848672014, 2007.

Bos, J. A. A., Dambeck, R., Kalis, A. J., Schweizer, A., and Thiemeyer, H.: Palaeoenvironmental changes and vegetation history of the northern Upper Rhine graben (southwestern Germany) since the Lateglacial, Neth. J. Geosci., 87, 67–90, https://doi.org/10.1017/S0016774600024057, 2008.

Bowler, J. M.: Quaternary climate and tectonics in the evolution of the Riverine Plain, southeastern Australia, in: Landform evolution in Australasia, edited by: Davies, J. L., and Williams, M. A. J., Australian National University Press, Canberra, 70–112, ISBN 978-0-7081-1194-9, 1978.

Candel, J. H., Makaske, B., Kijm, N., Kleinhans, M. G., Storms, J. E., and Wallinga, J.: Self-constraining of low-energy rivers explains low channel mobility and tortuous planforms, Depos. Rec., 6, 648–669, https://doi.org/10.1002/dep2.112, 2020.

Carbiener, R.: Le Grand Ried d'Alsace, Ecologie d'un paysage, Bull. Soc. Ind. Mulhouse, 1, 15–44, 1969.

Carbiener, R.: Le grand Ried central d'Alsace: ecologie et évolution d'une zone humide d'origine fluviale rhénane, Bull. Écol., 14, 249–277, 1983a.

Carbiener, R.: Brunnenwasser, Encyclopedie de l'Alsace, 2, Publitotal, Strasbourg, 891–900, 1983b.

Carbiener R. and Dillmann E.: Cas type de Rhinau-Daubensand: l'évolution du paysage rhénan dans la région de Rhinau, au coeur du secteur des Giessen, des Muhlbach et Brunnenwasser, in: Die Auen am Oberrhein/Les Zones alluviales du Rhin Supérieur, edited by: Gallusser, W. A., and Schencker, A, Birkhäuser, Switzerland, 113–136, https://doi.org/10.1007/978-3-0348-6237-0_13, 1992.

Chapkanski, S., Ertlen, D., Rambeau, C., and Schmitt, L.: Provenance discrimination of fine sediments by mid-infrared spectroscopy: Calibration and application to fluvial palaeoenvironmental reconstruction, Sedimentology, 67, 1114–1134, https://doi.org/10.1111/sed.12678, 2020.

Chardon, V., Schmitt, L., Arnaud, F., Piégay, H., and Clutier A.: Efficiency and sustainability of gravel augmentation to restore large regulated rivers: insights from three experiments on the Rhine River (France/Germany), Geomorphology, 380, 107639, https://doi.org/10.1016/j.geomorph.2021.107639, 2021.

Commission Internationale de l'Hydrologie du Bassin du Rhin: Le bassin du Rhin: monographie hydrologique, ISBN 978-90-12-01775-6, 1977.

Dambeck, R. and Thiemeyer, H.: Fluvial History of the northern Upper Rhine river (south-western Germany) during the Lateglacial and Holocene times, Quatern. Int., 93–94, 53–63, https://doi.org/10.1016/S1040-6182(02)00006-X, 2002.

Delile, H., Schmitt, L., Jacob-Rousseau, N., Grospretre, L., Privolt, G., and Preusser, F.: Headwater valley response to climate and land use changes during the Little Ice Age in the Massif Central (Yzeron basin, France), Geomorphology, 257, 179–197, https://doi.org/10.1016/j.geomorph.2016.01.010, 2016.

Erkens, G., Dambeck, R., Volleberg, K. P., Bouman, M. T. I. J., Bos, J. A. A., Cohen, K. M., Wallinga, J., and Hoek, W. Z.: Fluvial terrace formation in the northern Upper Rhine Graben during the last 20 000 years as a result of allogenic controls and autogenic evolution, Geomorphology, 103, 476–495, https://doi.org/10.1016/j.geomorph.2008.07.021, 2009.

Erkens, G., Hoffmann, T., Gerlach, R., and Klostermann J.: Complex fluvial response to Lateglacial and Holocene allogenic forcing in the Lower Rhine Valley (Germany), Quaternary Sci. Rev. 30, 611–627, https://doi.org/10.1016/j.quascirev.2010.11.019, 2011.

Ertlen, D., Schwartz, D., Trautmann, M., Webster, R., and Brunet, D.: Discriminating between organic matter in soil from grass and forest by near-infrared spectroscopy, Eur. J. Soil Sci., 61, 207–216, https://doi.org/10.1111/j.1365-2389.2009.01219.x, 2010.

Eschbach, D., Schmitt, L., Imfeld, G., May, J.-H., Payraudeau, S., Preusser, F., Trauerstein, M., and Skupinski, G.: Long-term temporal trajectories to enhance restoration efficiency and sustainability on large rivers: an interdisciplinary study, Hydrol. Earth Syst. Sci., 22, 2717–2737, https://doi.org/10.5194/hess-22-2717-2018, 2018.

Fuller, I. C., Reid, H. E., and Brierley, G. J.: Methods in geomorphology: investigating river channel form, in: Treatise on geomorphology, edited by: Shroder, J. F., Academic Press, San Diego, 73–91, https://doi.org/10.1016/B978-0-12-374739-6.00374-2, 2013.

Gabriel, G., Ellwanger, D., Hoselmann, C., Weidenfeller, M., and Wielandt-Schuster, U.: The Heidelberg basin, Upper Rhine Graben (Germany): A unique archive of Quaternary sediments in Central Europe, Quatern. Int., 292, 43–58, https://doi.org/10.1016/j.quaint.2012.10.044, 2013.

Haimberger, R., Hoppe, A., and Schäfer, A.: High-resolution seismic survey on the Rhine River in the northern Upper Rhine Graben, Int. J. Earth Sci. (Geol. Rundsch.), 94, 657–668, https://doi.org/10.1007/s00531-005-0514-z, 2005.

Haughton, P. D. W., Todd, S. P., and Morton, A.C.: Sedimentary provenance studies, Geol. Soc. London. Spec. Publ., 57, 1–11, https://doi.org/10.1144/GSL.SP.1991.057.01.01, 1991.

Hirth, C.: Eléments d'explication à la formation des Rieds ellorhénans au nord de Colmar du début du Post-glaciaire à la canalisation du Rhin au XIXè siècle, Bull. Soc. Hist. nat. Colmar, 54, 21–44, 1971.

Hoffmann, T., Lang, A., and Dikau, R.: Holocene river activity: analysing 14C-dated fluvial and colluvial sediments from Germany, Quaternary Sci. Rev., 27, 2031–2040, https://doi.org/10.1016/j.quascirev.2008.06.014, 2008.

Illies, J. H. and Greiner, G.: Rhinegraben and the Alpine system, Geol. Soc. Am. Bull., 89, 770–782, https://doi.org/10.1130/0016-7606(1978)89<770:RATAS>2.0.CO;2, 1978.

Jotheri, J., Allen, M. B., and Wilkinson, T. J.: Holocene avulsions of the Euphrates River in the Najaf area of western Mesopotamia: Impacts on human settlement patterns, Geoarchaeology, 31, 175–193, https://doi.org/10.1002/gea.21548, 2016.

Jung, J. and Schlumberger, C.: Soulèvement des alluvions du Rhin par des intrusions salines diapires de Haute-Alsace: déformation de la surface de la basse terrasse du Rhin et tectonique du bassin salifère de Haute-Alsace, Bull. du Service de la Carte géologique d'Alsace et de Lorraine, 3, 77–86, 1936.

Kaufhold, S., Hein, M., Dohrmann, R., and Ufer, K.: Quantification of the mineralogical composition of clays using FTIR spectroscopy, Vib. Spectrosc., 59, 29–39, https://doi.org/10.1016/j.vibspec.2011.12.012, 2012.

Kemp, J. and Spooner, N. A.: Evidence for regionally wet conditions before the LGM in southeast Australia: OSL ages from a large palaeochannel in the Lachlan Valley, J. Quaternary Sci., 22, 423–427, https://doi.org/10.1002/jqs.1125, 2007.

Khosravichenar, A., Fattahi, M., Amini, H., and von Suchodoletz, H.: The potential of small mountain river systems for paleoenvironmental reconstructions in drylands – An example from the Binaloud Mountains in Northeastern Iran, Geosci., 10, 448, https://doi.org/10.3390/geosciences10110448, 2020.

Kock, S., Huggenberger, P., Preusser, F., Rentzel, P., and Wetzel, A.: Formation and evolution of the Lower Terrace of the Rhine River in the area of Basel, Swiss J. Geosci., 102, 307–321, https://doi.org/10.1007/s00015-009-1325-1, 2009.

Kremer, M., Rieb, J.-P., Rebholtz, C., and Delecolle, J.-C.: Écologie des Cératopogonidés de la plaine d'Alsace – I. – Le genre Culicoides des sols humides du Ried, Ann. Parasitol. Hum. Comp., 53, 101–115, https://doi.org/10.1051/parasite/1978531101, 1978.

Lang, A., Bork, H. R., Mäckel, R., Preston, N., Wunderlich, J., and Dikau, R.: Changes in sediment flux and storage within a fluvial system: some examples from the Rhine catchment, Hydrol. Process., 17, 3321–3334, https://doi.org/10.1002/hyp.1389, 2003.

Nandini, C. V., Sanjeevi, S., and Bhaskar, A. S.: An integrated approach to map certain palaeochannels of South India using remote sensing, geophysics, and sedimentological techniques, Int. J. Remote Sens., 34, 6507–6528, https://doi.org/10.1080/01431161.2013.803629, 2013.

Nivière, B., Giamboni, M., Innocent, C., and Winter, T.: Kinematic evolution of a tectonic wedge above a flat-lying décollement: The Alpine foreland at the interface between the Jura Mountains (Northern Alps) and the Upper Rhine graben, Geology, 34, 469–472, https://doi.org/10.1130/G22334.1, 2006.

Ollive, V., Petit, C., Garcia, J. P., and Reddé, M.: Rhine flood deposits recorded in the Gallo-Roman site of Oedenburg (Haut-Rhin, France), Quatern. Int., 150, 28–40, https://doi.org/10.1016/j.quaint.2006.01.006, 2006.

Page, K., Nanson, G., and Price, D.: Chronology of Murrumbidgee River palaeochannels on the Riverine Plain, southeastern Australia, J. Quaternary Sci., 11, 311–326, https://doi.org/10.1002/(SICI)1099-1417(199607/08)11:4<311::AID-JQS256>3.0.CO;2-1, 1996.

Plotzki, A., May, J. H., Preusser, F., Roesti, B., Denier, S., Lombardo, U., and Veit, H.: Geomorphology and evolution of the late Pleistocene to Holocene fluvial system in the south-eastern Llanos de Moxos, Bolivian Amazon, Catena, 127, 102–115, https://doi.org/10.1016/j.catena.2014.12.019, 2015.

Preusser, F.: Characterisation and evolution of the River Rhine system, Neth. J. Geosci., 87, 7–19, https://doi.org/10.1017/s0016774600024008, 2008.

Przyrowski, R. and Schäfer, A.: Quaternary fluvial basin of northern Upper Rhine Graben, Z. Dtsch. Ges. Geowiss., 166, 71–98, https://doi.org/10.1127/1860-1804/2014/0080, 2015.

Resmi, M. R., Achyuthan, H., and Jaiswal, M. K.: Middle to late Holocene paleochannels and migration of the Palar River, Tamil Nadu: Implications of neotectonic activity, Quatern. Int., 443, 211–222, https://doi.org/10.1016/j.quaint.2016.05.002, 2017.

Rossetti, D. F. and Góes, A. M.: Late Quaternary drainage dynamics in northern Brazil based on the study of a large paleochannel from southwestern Marajó Island, An. Acad. Bras. Cienc., 80, 579–593, https://doi.org/10.1590/s0001-37652008000300017, 2008.

Schirmer, W., Bos, J. A., Dambeck, R., Hinderer, M., Preston, N., Schulte, A., Schwalb, A., and Wessels, M.: Holocene fluviatile processes and valley history in the River Rhine catchment, Erdkunde, 59, 199–215, https://doi.org/10.3112/erdkunde.2005.03.03, 2005.

Schmitt, L.: Typologie hydro-géomorphologique fonctionnelle de cours d'eau: recherche méthodologique appliquée aux systèmes fluviaux d'Alsace, PhD thesis, University of Strasbourg, France, 348 pp., unpublished, 2001.

Schmitt, L.: Dynamiques fluviales et gestion environnementale durable des hydrosystèmes. Application à une grande plaine alluviale (Rhin-Ill, Alsace) et à hydrosystème périurbain (Yzeron, Ouest Lyonnais), Habilitation thesis, Lumière University Lyon 2, France, 296 pp., unpublished, 2010.

Schmitt, L., Tremolieres, M., Nobelis, P., and Maire, G.: Complémentarité entre typologies hydro-géomorphologique et biologique de rivières dans l'hydrosystème fluvial ello-rhénan français, in: Protéger, restaurer et gérer les zones alluviales. Pourquoi et comment?/Floodplain protection, restoration, management. Why and How?, edited by: Tremolieres, M., Schnitzler, A., and Silan, P, Editions TEC & DOC, Lavoisier, Paris, 123–136, ISBN 978-2-7430-1011-9, 2007.

Schmitt, L., Lafont, M., Tremolieres, M., Jezequel, C., Vivier, A., Breil, P., Namour, P., Valin, K., and Valette, L.: Using hydrogeomorphological typologies in functional ecology: preliminary results in contrasted hydrosystems, Phys. Chem. Earth, 36, 539–548, https://doi.org/10.1016/j.pce.2009.11.011, 2011.

Schmitt, L., Houssier, J., Martin, B., Beiner, M., Skupinski, G., Boës, E., Schwartz, D., Ertlen, D., Argant, J., Gebhardt, A., Schneider, N., Lasserre, M., Trintafillidis, G., and Ollive, V.: Paléo-dynamique fluviale holocène dans le compartiment sud-occidental du fossé rhénan (France), Rev. Archéologique l'Est, 42, 15–33, 2016.

Schmitt, L., Beisel, J. N., Preusser, F., de Jong, C., Wantzen, K. M., Chardon, V., Staentzel, C., Eschbach, D., Damm, C., Rixhon, G., Salomon, F., Glaser, R., Himmelsbach, I., Meinard, Y., Dumont, S., Hardion, L., Jérôme, H., Rambeau, C., Chapkanski, S., and Brackhane, S.: Sustainable management of the Upper Rhine River and its alluvial plain: Lessons from interdisciplinary research in France and Germany, in: Sustainability research in the Upper Rhine region, concepts and case studies, edited by: Hamman, P. and Vuilleumier, S., Presses Universitaires de Strasbourg, Strasbourg, 201–226, ISBN 978-2-86820-549-0, 2019.

Scorpio, V., Surian, N., Cucato, M., Dai Prá, E., Zolezzi, G., and Comiti, F.: Channel changes of the Adige River (Eastern Italian Alps) over the last 1000 years and identification of the historical fluvial corridor, J. Maps, 14, 680–691, https://doi.org/10.1080/17445647.2018.1531074, 2018.

Simler, L., Valentin, L., and Duprat A.: La nappe phréatique de la plaine du Rhin en Alsace, Sci. Geol., 60, 1–266, 1979.

Striedter, K.: Holozäne Talgeschichte im Unterelsass, PhD thesis, University of Düsseldorf, Germany, 235 pp., unpublished, 1988.

Sylvia, D. A. and Galloway, W. E.: Morphology and stratigraphy of the late Quaternary lower Brazos valley: Implications for paleoclimate, discharge and sediment delivery, Sediment. Geol., 190, 159–175, https://doi.org/10.1016/j.sedgeo.2006.05.023, 2006.

Toonen, W. H., Kleinhans, M. G., and Cohen, K. M.: Sedimentary architecture of abandoned channel fills, Earth Surf. Proc. Land., 37, 459–472, https://doi.org/10.1002/esp.3189, 2012.

Trémolières, M., Eglin, I., Roeck, U., and Carbiener, R.: The exchange process between river and groundwater on the Central Alsace floodplain (Eastern France), Hydrobiologia, 254, 133–148, https://doi.org/10.1007/bf00014108, 1993.

Van Raden, U. J., Colombaroli, D., Gillia, A., Schwander, J., Bernasconi, S.M., van Leeuwen, J., Leuenberger, M., and Eicher, U.: High-resolution late-glacial chronology for the Gerzensee lake record (Switzerland): δ^{18}O correlation between a Gerzensee-stack and NGRIP, Palaeogeogr. Palaeoclimatol. Palaeoecol, 391, 13–24, https://doi.org/10.1016/j.palaeo.2012.05.017, 2013.

Vogt, H.: Le relief en Alsace. Etude géomorphologique du rebord sud-occidental du fossé rhénan, Oberlin, Strasbourg, 239 pp., ISBN 9782853691284, 1992.

von Suchodoletz, H., Pohle, M., Khosravichenar, A., Ulrich, M., Hein, M., Tinapp, C., Schultz, J., Ballasus, H., Veit, U., Ettel, P., Werther, L., Zielhofer, C., and Werban, U.: The fluvial architecture of buried floodplain sediments of the Weiße Elster River (Germany) revealed by a novel method combination of drill cores with two-dimensional and spatially resolved geophysical measurements, Earth Surf. Proc. Land., 47, 955–976, https://doi.org/10.1002/esp.5296, 2022.

Walser, E.: Le bassin du Rhin à l'amont de Bâle et l'influence des lacs sur le régime du fleuve, Houille Blanche, 45, 115–124, https://doi.org/10.1051/lhb/1959028, 1959.

Wantzen, K. M., Uehlinger, U., Van der Velde, G., Leuven, R. S. E. W., Schmitt, L., and Beisel, J. N.: The Rhine River basin, in: Rivers of Europe, 2nd edn., edited by: Tockner, K., Zarfl, C., and Robinson, C. T., Academic Press, London, 331–389, ISBN 9780081026137, 2021.

E&G Quaternary Sci. J., 71, 145–162, 2022
https://doi.org/10.5194/egqsj-71-145-2022

Open Access E&G Quaternary Science Journal

Research article

Investigating the loess–palaeosol sequence of Bahlingen-Schönenberg (Kaiserstuhl), southwestern Germany, using a multi-methodological approach

Tabea Schulze[1], **Lea Schwahn**[1], **Alexander Fülling**[1], **Christian Zeeden**[2], **Frank Preusser**[1], **and Tobias Sprafke**[3,4]

[1]Institute of Earth and Environmental Sciences, University of Freiburg, Freiburg, Germany
[2]Rock Physics and Borehole Geophysics, Leibniz Institute for Applied Geophysics, Hanover, Germany
[3]Center of Competence for Soils, BFH-HAFL, Zollikofen, Switzerland
[4]Institute of Geography, University of Bern, Bern, Switzerland

Correspondence: Frank Preusser (frank.preusser@geologie.uni-freiburg.de)

Relevant dates: Received: 14 May 2022 – Revised: 6 July 2022 – Accepted: 20 July 2022 –
Published: 23 August 2022

How to cite: Schulze, T., Schwahn, L., Fülling, A., Zeeden, C., Preusser, F., and Sprafke, T.: Investigating the loess–palaeosol sequence of Bahlingen-Schönenberg (Kaiserstuhl), southwestern Germany, using a multi-methodological approach, E&G Quaternary Sci. J., 71, 145–162, https://doi.org/10.5194/egqsj-71-145-2022, 2022.

Abstract: Loess–palaeosol sequences (LPSs) are key archives for the reconstruction of Quaternary environmental conditions, but there is a lack of investigated records from the southern Upper Rhine Graben (southwestern Germany). To close this gap, a LPS at Bahlingen-Schönenberg was investigated at high resolution using a multi-method approach. Infrared stimulated luminescence screening reveals a major hiatus in the lower part of the LPS that according to luminescence dating is older than marine isotope stage (MIS) 4. The section above the hiatus formed by quasi-continuous loess sedimentation between ca. 34 and 27 ka, interrupted by phases of weak reductive pedogenesis. The fact that this pedogenesis is much weaker compared to corresponding horizons in the more northerly part of the Upper Rhine Graben could be due to regionally drier conditions caused by a different atmospheric circulation pattern at the time of deposition. Our results reinforce earlier notions that the major environmental shifts leading into the Last Glacial Maximum (LGM) of southern Central Europe significantly predate the transition of MIS 3 to 2 (ca. 29 ka). In particular, the last massive phase of loess accumulation started several thousand years prior to the arrival of glaciers in the foreland of the Alps, which raises questions regarding the source and transport paths of the dust. It is also noted that no loess dating to the LGM or the time thereafter was observed due to either a lack of deposition or later erosion.

Kurzfassung: Löss-Paläoboden Sequenzen (LPS) sind Schlüsselarchive für die Rekonstruktion von quartären Umweltbedingungen, aber es mangelt an der Untersuchung solcher Abfolgen aus dem südlichen Oberrheingraben. Um diese Lücke zu schließen, wurde eine LPS bei Bahlingen-Schönenberg mit einem multimethodischen Ansatz hochauflösend untersucht. Die Untersuchung mit Infrarot Stimulierter Lumineszenz Screening zeigt einen Hiatus im unteren Teil der LPS, der laut Lumineszenzdatierungen älter ist als das Marine Isotopenstadium (MIS) 4. Der Abschnitt oberhalb des Hiatus bildete sich durch quasi-kontinuierliche Lössablagerung zwischen ca. 34 und 27 ka, unterbrochen von Phasen

Published by Copernicus Publications on behalf of the Deutsche Quartärvereinigung (DEUQUA) e.V.

schwacher reduktiver Pedogenese. Da die Pedogenese im Vergleich zu entsprechenden Horizonten im nördlicheren Teil des Oberrheingrabens viel schwächer ausgeprägt ist, könnte dies auf regional trockenere Bedingungen zurückzuführen sein, verursacht durch ein anderes atmosphärisches Zirkulationsmuster zur Zeit der Ablagerung. Unsere Ergebnisse bestätigen frühere Annahmen, dass die großen Umweltveränderungen, die zum letzten glazialen Maximum (LGM) im südlichen Mitteleuropa führten, deutlich vor dem Übergang von MIS 3 zu 2 (ca. 29 ka) lagen. Insbesondere begann die letzte massive Phase der Lössakkumulation mehrere tausend Jahre vor der Ankunft der Gletscher im Alpenvorland, was Fragen zu den Quellen und Transportwegen des Staubs aufwirft. Es ist auch festzustellen, dass kein Löss aus dem LGM oder der Zeit danach gefunden wurde, entweder aufgrund fehlender Ablagerung oder späterer Erosion.

1 Introduction

Loess is among the most abundant Pleistocene sediments in Central Europe, and thick loess–palaeosol sequences (LPSs) are key archives to reconstruct Quaternary palaeoenvironments (e.g. Lehmkuhl et al., 2016; Sprafke, 2016). On the one hand, a warm to moderately temperate humid climate leads to the formation of different types of soils (depending on the nature and timing of climate conditions). On the other hand, a cool to cold dry climate is often characterised by the accumulation of loess but requires at least a grassland vegetation cover (mammoth steppe) to trap the dust. Furthermore, the subaerially deposited dust undergoes quasi-pedogenic or quasi-diagenetic processes, known as loessification, that result in the typical aggregation of loess (cf. Sprafke and Obreht, 2016; Smalley and Obreht, 2018). Another relevant question regards the source of the dust and its transport paths, which appear rather complex (e.g. Pye, 1995; Smalley, 1995; Wright, 2001; Smalley et al., 2009). For loess deposits found in proximity to formerly glaciated areas, it is usually assumed that dust formation is caused by different forms of grinding related directly to ice contact and meltwater streams, producing fine-grained debris also known as glacier milk. However, fine-grained sediment production is likely also related to different types of periglacial processes including frost shattering and abrasion during slope processes.

Another feature that is common in many LPS, but that has seen very limited attention in loess research, is the presence of hiatuses in the records (e.g. Huayu et al., 2006; Steup and Fuchs, 2017). In fact, most kinds of soil formation will form a break or massive reduction in sediment accumulation. Furthermore, LPSs feature unconformities, i.e. erosional boundaries, when parts of pre-existing loess and palaeosols have been removed (Meszner et al., 2013; Sprafke, 2016; Lehmkuhl et al., 2016; Zöller et al., 2022). In theory, this can be induced by three different processes, soil creep, sheet erosion (by water), and deflation, all of which are related to different climatic conditions.

In Central Europe, the Rhine represents the main drainage of the northwestern Alps with frequent occurrences of LPSs on both sides of the river (Lehmkuhl et al., 2016, 2021). Due to its direct connection to the Alps, the onset of the last phase of loess accumulation along the river Rhine should be directly related to the advance of glaciers towards their last maximum extent (Last Glacial Maximum, LGM). For the Swiss Alps, the chronology of the last advance is rather well constrained, and glaciers did reach the foreland likely shortly after 30 ka (reviewed by Stojakowits et al., 2021). The maximum of the last glaciation was reached around 24–25 ka, followed by rapid decay of ice within a few thousand years (e.g. Gaar et al., 2019). Interestingly, it has been demonstrated that the last massive phase of loess accumulation already started soon after 35 ka, as shown at the sites of Schwalbenberg (Fischer et al., 2021), Nussloch (Antoine et al., 2001, 2009; Moine et al., 2017), and Möhlin (Gaar and Preusser, 2017). A substantial increase in sediment accumulation rate peaking around 32 ka is also observed at Bergsee, a macro-fossil radiocarbon-dated lake record that is only a few kilometres' distance from the Möhlin site in the Rhine Valley (Duprat-Oualid et al., 2017). In summary, there is a clear offset between the onset and likely even the peak in dust flux, as well as theoretical assumptions regarding dust availability in the context of the last glaciation in this part of Central Europe.

A suitable area to further investigate the above issues would be the southern part of the Upper Rhine Graben, an area located directly downstream of the formerly glaciated areas of the Swiss Alps and the Black Forest (Preusser et al., 2011; Hofmann et al., 2020). In particular the Kaiserstuhl area, an extinct volcanic complex formed during the Miocene (Rotsein and Schaming, 2011), is well-known for its wide-spread loess deposits, mainly on its northern and eastern flanks (Smalley et al., 1973; Guenther, 1961, 1987). However, the most recent studies of the loess deposits in the Kaiserstuhl area were published more than 30 years ago (Guenther, 1987; Zöller et al., 1988; Zöller and Wagner, 1990) and do not represent the present stage of methodology. In particular, there have been substantial improvements in luminescence dating since the late 1980s, which allow for robust age control as a prerequisite to investigate the regional connection between mountain glaciations, glaciofluvial response, regional dust dynamics, palaeovegetation, and soil formation.

The LPS Bahlingen-Schönenberg (coordinates: 48.124312° N, 7.731780° E) is located on a small plateau west of the village Bahlingen at the northeastern Kaiserstuhl (Fig. 1), where up to 20 m deep, largely vegetated hollow ways are present. Where the road reaches its highest point, a 7 m high loess cliff without obvious palaeosols is present. The section investigated here is a 5 m thick profile starting 1.5 m below the disturbed top of the loess cliff. In order to develop a robust stratigraphy from this weakly differentiated LPS, we analyse colour (spectrophotometer), granulometry (laser diffraction), magnetic susceptibility, and organic matter and carbonate content (loss on ignition – LOI 550 and 950 °C, respectively) of samples taken at 5 cm resolution. Infrared stimulated luminescence (IRSL) screening at 10 cm resolution is applied to evaluate the chronostratigraphic continuity of the LPS, whereas numerical ages are derived from quartz optically stimulated luminescence (OSL) and feldspar multi-elevated-temperature (MET) post-IR IRSL (pIR). Besides establishing the chronology of the site investigated, this is also a test to check the performance of the applied proxy data and dating approaches and estimate their potential for future studies in the region.

2 Materials and methods

2.1 Profile preparation and sampling

In order to minimise impact to the loess cliff, which is located next to a road, we carefully prepared a 60 cm wide and 30 cm deep trench with spades and scratchers. A general profile description was carried out based on observed colour and structural differences. For sedimentary analyses, including determination of organic and carbonate content, grain size analysis, and colour measurements, samples at 5 cm resolution were taken as continuous column (Antoine et al., 2009; Fig. 2). For luminescence dating, 11 samples were collected using metal tubes with a length of 10–15 cm and a diameter of ca. 7 cm. These were hammered into the profile every 50 cm. These samples were also used for the determination of water absorption capacity. About 51 samples were taken for IRSL screening using small and opaque plastic tubes hammered about 3 cm into the profile every 10 cm (Fig. 2c).

2.2 Colour measurements

For colour measurements at the University of Bern, a ColorLite sph850 spectrophotometer was used on air-dried fine earth (Sprafke, 2016). The measuring diameter is 3.5 mm, the observer angle 10°, and the light source corresponds to D65, emitted from six LEDs. With this spectrophotometer wave lengths from 400 to 700 nm can be measured with a spectral resolution of 3.5 nm. The measuring head was gently pushed into the loose sample material until it was completely sealed from daylight. Between two triplicate measurements at different sample positions, the sample material was stirred. After every 10th measurement the spectrophotometer was calibrated using a white standard disc. All data (various colour variables, remission spectra) were exported to Microsoft Excel© tables with the spectrophotometer software ColorDaTra 1.0.181.5912. After checking for outliers, mean values for each sample were calculated and visualised as real colours based on RGB variables. RGB tuning in three steps was done according to Sprafke et al. (2020) to determine subtle colour variations in the weakly differentiated profile. Variations between oxidative and reductive colours are indicated by the warm–cold value (WCV) according to Sprafke et al. (2013) as the ratio between the spectral reflectance values of 600–700 nm divided by the values of 400–500 nm. Variations in lightness are represented by the L^* value of the CIELAB colour space (Viscarra Rossel et al., 2006).

2.3 Grain size analysis

Grain sizes were determined with laser diffraction spectrometry (LDS), using a Malvern Mastersizer 3000 at the University of Freiburg. The Mastersizer 3000 determines the particle size indirectly by irradiating a suspension with a laser and evaluating the generated angles and intensities of scattered light. For measurements the samples were dried at 105 °C for at least 12 h and sieved through a mesh size of 1 mm. 1–2 g of the subsample < 1 mm was dispersed for 12 h with 50 ml liquid consisting of 33 g $Na_6O_{18}P_6$ and 7 g Na_2CO_3 dissolved in 1 L of distilled water (Abdulkarim et al., 2021). The standard operating procedure for every sample comprised five measurements for each sample and the calculation of grain sizes after the Mie theory of light scattering. After measurements, the data were exported to a Microsoft Excel© worksheet, and average values for each sample were calculated out of the five measurements using MATLAB R2021a. Clay contents determined by LDS strongly underestimate clay contents determined by classical pipette methods; therefore, we use the boundary of 6.3 µm as equivalent to pipette clay measurements (cf. Makó et al., 2017). To interpret changes in wind intensity and dynamics, the grain size index (GSI: [percent between 20 and 63 µm] / [percent < 20 µm]) was calculated (Antoine et al., 2009).

2.4 Determination of organic carbon and carbonate content

After removing the pore water by drying at 105 °C, the samples were pestled with a mortar and sieved through a 2 mm sieve. About 1 g, referred to as dry weight DW_{105}, was weighed out and put in a crucible with known weight. For the determination of organic carbon content, the material was burned in a first cycle at 550 °C for 5 h in a Nabertherm muffle (Heiri et al., 2001). Afterwards the crucible was weighed. The LOI is calculated in weight percentage (wt %) out of the

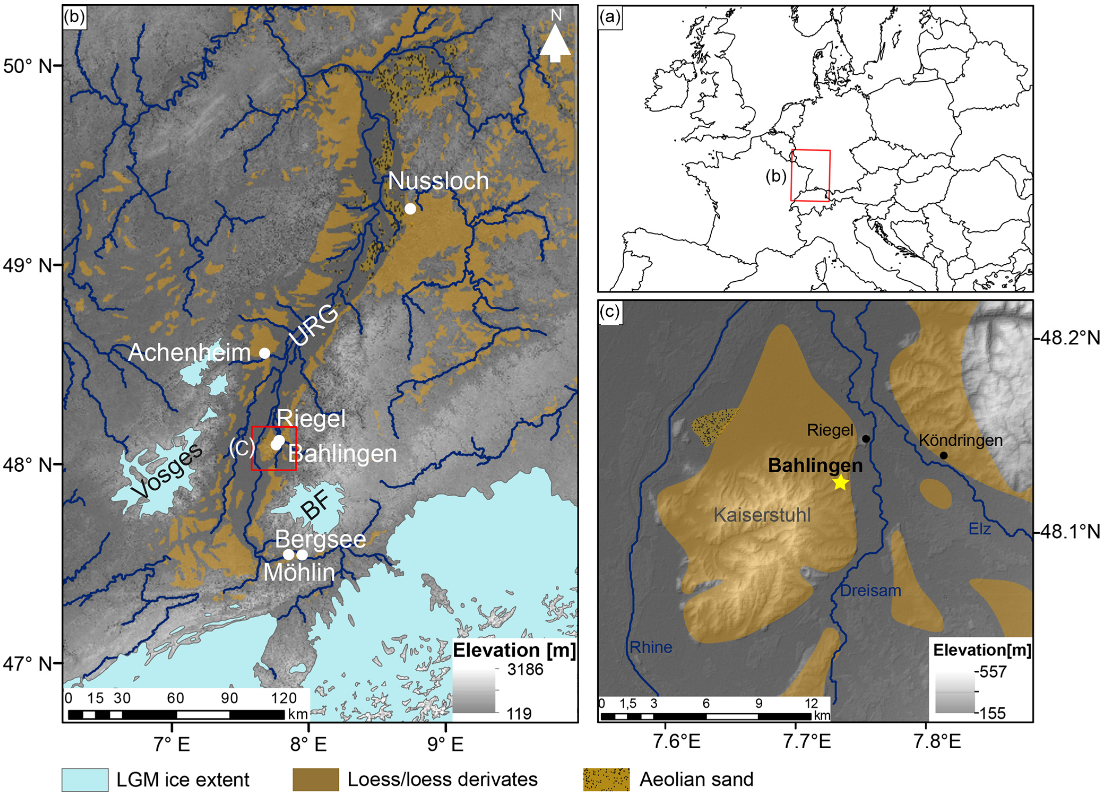

Figure 1. **(a)** Location of the study region in Europe and **(b)** a digital elevation model (DEM) of the Upper Rhine Graben (URG) and its surroundings. The URG is bordered by the Vosges in the west and the Black Forest (BF) in the east. The river Rhine flows along the centre of the graben, and the Kaiserstuhl volcanic range of hills is located in its eastern part. Displayed are also the extent of glaciers during the maximum of the last glaciation (ca. 24 ka) and the aeolian deposits. **(c)** The investigated profile is situated in the northeastern part of the Kaiserstuhl on a plateau (Schönenberg) to the west of the village of Bahlingen (yellow star) (map of Germany from https://www.landkartenindex.de/, last access: 1 April 2022; DEM based on Shuttle Radar Topography Mission (SRTM) data, provided by USGS and processed with ArcMap 10.6.1; distribution of aeolian sediments following Lehmkuhl et al., 2021, and ice extent following Ehlers et al., 2011).

dry weight and the weight measured after the 550 °C burning cycle (Heiri et al., 2001). As per Meyers and Lallier-Verges (1999), the calculated LOI after the 550 °C burning cycle is twice the real organic carbon content. Therefore, the calculated data are bisected to obtain the organic carbon content in a last step. The carbonate content was determined in a second burning cycle, which comprised burning for a further 3 h at 950 °C (Heiri et al., 2001). The LOI after 950 °C can be calculated similarly to the LOI after 550 °C, out of the dry weight, the weight measured after the 550 °C burning cycle, and the weight measured after the 950 °C burning cycle (Heiri et al., 2001). Since carbon dioxide has a molar mass of $\sim 44\,\mathrm{g\,mol^{-1}}$ and carbonate ($CO_3{}^{-2}$) has a mass of $60\,\mathrm{g\,mol^{-1}}$, the LOI_{950} has to be multiplied by the ratio of these two masses (1.36) to obtain the carbonate content in the sample (Bengtsson and Enell, 1986; Heiri et al., 2001).

2.5 Magnetic susceptibility

For magnetic susceptibility (weight normalised; χ) measurements, carried out at the Leibniz Institute for Applied Geophysics in Grubenhagen, samples were dried, homogenised, and placed in non-magnetic plastic boxes of $6.4\,\mathrm{cm^3}$ in a way that material is fixed and cannot move. The χ was measured in alternating fields of 505 and 5050 Hz with $400\,\mathrm{A\,m^{-1}}$ using a MAGNON VFSM (variable field susceptibility metre), providing both low-field χ and frequency dependency of the χ. χ is given weight-normalised, taking weights of samples and boxes into account. Temperature-dependent χ was measured following Zeeden et al. (2021) in an Argon atmosphere for five samples (depths: 1.00, 2.60, 2.65, 3.20, 3.95 m) using an AGICO CS3 high-temperature furnace.

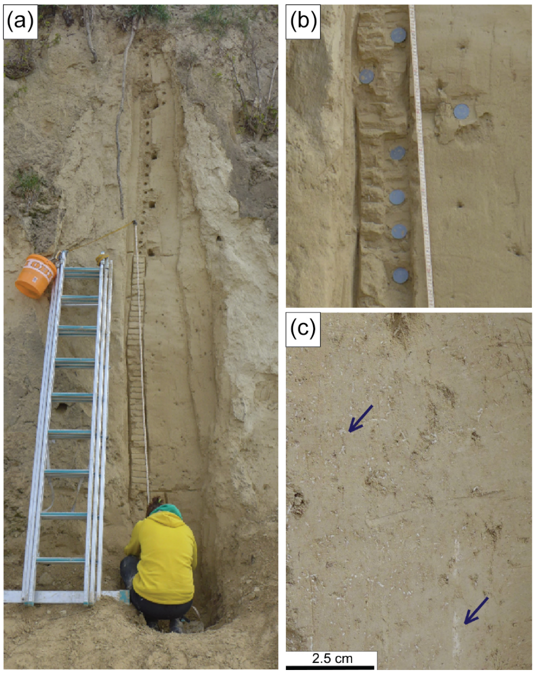

Figure 2. **(a)** The 5 m high loess profile Bahlingen-Schönenberg situated below 1.5 m thick loess disturbed by roots, pedogenesis, and agricultural activity. Note that macroscopically only a few colour changes are visible, mainly related to varying moisture. Small holes at around 1 m height and from 1.8 to 2.6 m were caused by carbonate concretions that fell out. **(b)** Plastic tubes hammered into the loess profile every 10 cm for IRSL screening. **(c)** Examples of pseudomycelia (secondary carbonate of former grass root channels).

2.6 Luminescence screening and dating

2.6.1 Methodological background

During the past decades, luminescence dating has established as key method for constraining the age of LPS (e.g. Roberts, 2008). The advantage of the method is that it allows us to directly determine the age of dust deposition, uses the omnipresent quartz and feldspar minerals, and has a dating range potentially reaching back several hundreds of thousands of years. However, luminescence dating is quite laborious and is affected by several methodological challenges (e.g. Preusser et al., 2008; Rittenour, 2018). While quartz and feldspar overall share the underlying physics, the two minerals have some important differences in luminescence properties. Quartz is known to have an OSL signal that is quickly reset by daylight and to be stable over geological periods (e.g. Preusser et al., 2009). It is hence usually preferred in dating applications. However, depending on provenance, the quartz OSL signal can have problematic properties (e.g. Preusser et al., 2006; Steffen et al., 2009), it may have limited age range due to low saturation dose (e.g. Faershtein et al., 2019), and yet a poorly understood underestimation of quartz has been observed on some occasions (e.g. Lowick et al., 2010; Anechitei-Deacu et al., 2018). Since feldspar usually shows both bright signals and a much higher saturation level, this mineral has attracted a lot of attention over the last 15 years. However, feldspar IRSL is known to contain signal components that are not stable with time. This phenomenon, known as anomalous fading (Wintle, 1973), is explained by the tunnelling of electrons within the crystal structure and will cause underestimation of IRSL ages. While several procedures have been suggested to correct for fading (e.g. Huntely and Lamothe, 2001; Kars et al., 2008), these are all based on measuring signal loss (i.e. the fading rate) over short periods of time (hours to months). The signal loss is then extrapolated to geological time periods (thousand to hundred thousand of years), assuming fading is constant with time and independent of environmental condition such as temperature.

To overcome the need of fading correction, it has been suggested to remove the unstable IRSL component by a first measurement and collect a more stable signal during subsequent stimulations at elevated temperature (Thomsen et al., 2008; Buylaert et al., 2009). This procedure is known as post-IR IRSL and has seen increasingly frequent application since its original development (see review by Zhang and Li, 2020). A modification of the original approach was introduced by Li and Li (2011), who introduced a protocol during which IRSL is subsequently stimulated at increasingly higher temperatures at 50°C increments. The advantage of this MET approach is that it delivers additional information as the degree of stability at higher temperatures is usually at the cost of bleachability of the signal (Kars et al., 2014). Furthermore, higher stimulation temperatures may be affected by changes of sensitivity that may lead to incorrect estimates (e.g. Zhang, 2018). As a consequence, despite the huge potential to expand the dating range, application of the MET post-IR IRSL approach is not always straightforward.

Due to the time and costs required for producing luminescence ages, portable luminescence readers have been used in particular to identify potential breaks in sedimentary sequences in the field (see review by Munyikwa et al., 2021). A similar approach is to take samples to the laboratory but reduce the amount of preparation and simplify the measurement procedures to speed up the required time for receiving preliminary age information (e.g. Roberts et al., 2009; May et al., 2018). This approach is referred to as screening.

2.6.2 IRSL screening

In the red-light laboratory, the outer ca. 1 cm of the sample material from the light-contaminated ends of the sampling tubes was discarded. Samples were then dried at 50 °C for at least 24 h and gently pestled in a mortar. Part of the material gained this way was fixed on small steel sample discs that were previously coated with a thin layer of silicon oil (6 mm stamp) so that the sample material would stick to the surface during measurement. For each sample, three subsamples were generated. Measurements were done on a Lexsyg Smart device (Freiberg Instruments; Richter et al., 2015) with the detection window centred at 410 nm. The measurement protocol comprised IRSL stimulation (850 nm, 130 mW cm^{-3}) of the natural signal (Ln) and that induced by laboratory irradiation (Tn, ca. 22 Gy, source dose rate ca. 0.1 Gy s^{-1}), both after heating to 250 °C (preheat) and using a stimulation at 50 °C (Table S1 in the Supplement). The ratio Ln/Tn was calculated based on the IRSL emission recorded during the first 20 s of stimulation, after subtracting the last 20 s as background.

2.6.3 Luminescence dating

Under red-light laboratory illumination, 5 cm sample material from the light-contaminated ends of the metal tubes was removed and used for gamma spectrometry and determination of water absorption capacity. From the inner sample material, due to the shortage of sand, the fraction 63–250 µm was gained by wet sieving, first being treated with hydrochloric acid (ca. 20 %) to remove carbonates, followed by treatment with hydrogen peroxide (30 %) to remove organic components. After each chemical treatment the material was washed with distilled water. A feldspar ($\delta < 2.58$ g cm^{-3}) and quartz fraction ($\delta > 2.58$, $\delta < 2.70$ g cm^{-3}) was subsequently isolated by density separation (LST Fastfloat©). The quartz fraction was etched with 40 % hydrofluoric acid for 60 min to dissolve any feldspar contamination and remove the outer layer of the grains. For measurements, grains were mounted on metal discs with a 2 mm stamped spot of silicon oil (ca. 100 grains).

All equivalent dose (D_e) measurements were done on a Lexsyg Standard device (Freiberg Instruments; Richter et al., 2013). Overall, the amount of sand-size grains was quite low which limited the number of replicate measurements. Quartz OSL was measured using a slightly modified version of the single aliquot regenerative dose (SAR) protocol originally developed by Murray and Wintle (2000, 2003; Table S2). Stimulation was done by green LEDs (525 nm, 90 mW cm^{-2}) with application of a detection window centred at 365 nm (Schott BG39 3 mm plus Delta BP 365/50 EX Interference 5 mm). For feldspar, the MET post-IR IRSL following Li and Li (2011) was used (Table S3), with stimulation centred at 850 nm (300 mW cm^{-2}) and detection peak at 410 nm (Schott BG39 3 mm plus AHF BrightLine 414/46 interference filter). For all samples, mean D_e was calculated using the central age model (Galbraith et al., 1999) as individual D_e values are normally distributed and show overdispersion values < 20 % (most between 10 % and 15 %), which is considered to indicate well-bleached samples. The only exceptions apply to quartz OSL of the lower two samples, which is discussed below.

Material for water absorption capacity tests and measurement of dose-rate-relevant elements was dried at 105 °C for at least 12 h, ground, and sieved < 2 mm. Water absorption capacity was determined after DIN 18132 using an Enslin–Neff apparatus. This resulted in an average value of 38 ± 2 %. The present-day water content was measured to 6 ± 3 %, with the highest value of 10 % determined for the lower part of the sequence that was better protected from drying out. While water uptake capability gives the maximum value of the unconsolidated material, present-day water content likely represents a minimum estimate due to drying of sediment close to the surface of the exposure. Hence, an average water content of 20 ± 5 % was used in the calculations.

High-resolution gamma spectrometry was carried out using a high-purity germanium (HPGe) detector (ORTEC GMX30P4-PLB-S, n-type coaxial, 30 % efficiency, 1.9 keV FWHM (full width at half maximum) at 1.33 MeV, detector diameter 54.8 mm, end cap diameter 70 mm, liquid nitrogen cooling). Plastic containers with a volume of ca. 130 cm^3 were completely filled with homogenised sediment, sealed with adhesive tape, and stored for at least a month to build up equilibrium between radon and its daughters. After storage, the sample containers were measured for several days to determine the activities of primordial radionuclides ^{40}K, ^{232}Th, and ^{238}U. The detector is installed in a lead shielding to minimise the influence of the environmental radioactivity. Additionally, a blank sample (empty container) was measured to account for background radiation. The ^{238}U content was determined by analysing the peaks of the ^{226}Ra daughters ^{214}Pb (295.2 and 351.9 keV) and ^{214}Bi (609.3, 1120.3, 1764.5 keV). The ^{234}Th line at 63.3 keV was used to quantify a possible radioactive disequilibrium in the ^{238}U decay chain. The ^{232}Th content was determined by analysing the peaks of the ^{228}Ra daughter ^{228}Ac (338.3, 911.1, 969.1 keV) and the ^{228}Th daughters ^{212}Pb (238.6 keV) and ^{208}Tl (583.2 keV). ^{40}K was measured directly at 1460.8 keV. The weighted mean of all selected peaks was then calculated to determine the activities of the parent radionuclides ^{238}U and ^{232}Th.

Dose rates (Table S4) and ages were calculated using the software ADELE v2017 (Degering and Degering, 2020; https://www.add-ideas.de/, last access: 1 April 2022), which uses the dose rate conversion factors of Guérin et al. (2011). Cosmic-ray dose rates were corrected for geographic position and burial depth following Prescott and Hutton (1994). All ages are given at 1σ level with reference to the year of sampling (2021 CE).

2.6.4 Age–depth modelling

Age–depth models of both OSL and pIR-200 dates were constructed using the model of Zeeden et al. (2018). This method establishes an age–depth model from luminescence ages without making assumptions regarding sedimentation rate or the sedimentation process itself. It involves an inverse model and uses a conservative measure for the random part of the overall uncertainty. In this case, uncertainty is dominantly of random nature because the mean luminescence ages show several inversions which we assign to random uncertainty.

3 Results

3.1 Profile description

The investigated profile consists of silt-dominated loess with only subtle colour differences, notably a slightly darker tone in the lowermost metre (Fig. 3). Throughout the section, there are concretions of iron and/or manganese of 1–3 mm in size, pseudomycelia (secondary carbonate of former grass root channels; Fig. 2c), and snail shells and shell fragments. Sieving to < 250 µm for luminescence dating confirmed that larger components in this profile are mainly calcified root cells, carbonate cemented silty pore walls, and shell fragments. From 1 to 1.35 m several loess dolls were observed with a diameter of ~ 3 cm, and from 2.1 to 2.8 m their diameter was 1–2 cm. The occurrences of snail shells, manganese concretions, and loess dolls in the profile stratigraphy are shown in Fig. 3. The stratigraphic subdivision into four main units (I–IV), each with four to nine subunits, was finally defined based on quantitative colour and grain size data (cf. Sprafke et al., 2020).

3.2 Colour and stratigraphy

Field and untuned RGB colours indicate a weak stratigraphic differentiation of the profile, which becomes clearer by enhanced RGB colours (Fig. 3). The WCV (range: 1.8–2.1) and the L^* value (range: 64–67) differentiate the main colour components. The inversely plotted WCV and the L^* value show largely similar variations, indicating that major deviations from loess colour are pale blue and slightly darker brownish horizons. Unit VI at the bottom of the sequence has the highest WCV of the profile (> 1.95) due to an overall light brown colour. L^* values from < 65 to 66 indicate a gradient from brown to pale brown colours from bottom to top, leading to the classification of Bw and BC or CB horizons, respectively. Unit III has the highest L^* values (> 66) of the whole profile in its lower part; the WCV differentiates greyish (C[r]) from brownish (CA and CB) horizons. Units II and I have a comparable colour pattern with different C(r) and CA or CB horizons.

3.3 Grain size composition

The granulometry reveals the predominance of coarse silt (20–63 µm; 45 %–60 %) and a mode of 20–25 µm throughout the profile (Fig. 3). Little sand (< 1.6 %) is present, mainly in Units I and IIIe to VI. The mean grain size of the profile is coarse silt, and only in Unit IVd is it partly medium–fine silt (20–6.3 µm). The GSI ranges approximately between 1 and 2.5 and has more or less the same pattern as the mean grain size, with maxima in Units I and III and minima in Units II and IV (Fig. 3). Clay content (LDS particles < 6.3 µm) varies largely parallel to the GSI between 6 % and 12 % in Units I–III and has its maximum (ca. 14 %) in Unit IV. Sand contents vary largely parallel to the GSI. However, in Unit III the GSI has much more pronounced variability compared to sand contents.

3.4 Organic carbon, carbonate content, and magnetic susceptibility

In general, the organic carbon content (C_{org}) varies relatively constant around 1 wt % along the profile, with no clear relation to stratigraphy (Fig. 3). A distinct peak at 3.5 m, along with comparably low carbonate contents, was confirmed by repeated measurement establishing that this is a real sample property. These unusual values may relate to a crotovine with soil material (low carbonate, high C_{org}) not recognised during sampling. Carbonate contents vary between 19 % and 24 %, with the highest values in Unit IV and minima in Units IIIa–c. Small oscillations are usually parallel to the inversely plotted contents of C_{org}, indicating these parameters are rather antagonists. Overall carbonate contents appear largely opposite to the GSI, which means that finer loess has higher carbonate contents. This trend is not confirmed in Unit I, where carbonate contents remain constant, despite the highest sand contents.

Mass-specific χ values oscillate around 12–$14 \times 10^{-8}\,\mathrm{m^3\,kg^{-1}}$. The (inversely plotted) χ shows contrasting trends to variations in carbonate content and is opposite to variations of the GSI (Fig. 3). The three χ maxima in Unit III and a distinct peak in Unit IIe, all corresponding to CA horizons, do not follow this general pattern. In these horizons, the carbonate contents are also the lowest. The thin or less pronounced CA horizon IIb and IIg do not show χ maxima and carbonate minima. Generally, χ is low compared to other loess localities in Eurasia but comparable to loess of similar age from Nussloch (Taylor and Lagroix, 2015). The temperature-dependent magnetic susceptibility properties are similar to loess in Willendorf, Austria (Zeeden and Hambach 2021). The susceptibility stays rather constant until 250 °C, increases towards 300 °C, then decreases until ~ 420 °C, and increases towards ~ 550 °C. From this maximum during heating, the susceptibility decreases sharply towards ~ 600 °C and continues to decrease from ~ 600 to 700 °C (Fig. 4). This pattern is observed for all samples; therefore, only one is shown in Fig. 4.

3.5 IRSL screening

The IRSL screening results show two distinct groups of Ln/Tn values (Fig. 3). The first group comprises Unit IV and is characterised by Ln/Tn values between 5.4 and 6.1. In comparison to the second group the distribution is partly scattered and shows some increase in Ln/Tn values with increasing height. This indicates either a change in dose rate or the presence of partial bleaching of the IRSL signal prior to deposition in some of the samples. The second group comprises Units I to III and is characterised by Ln/Tn values between 1.7 and 2.2, with a single outlier of 2.6 at a height of

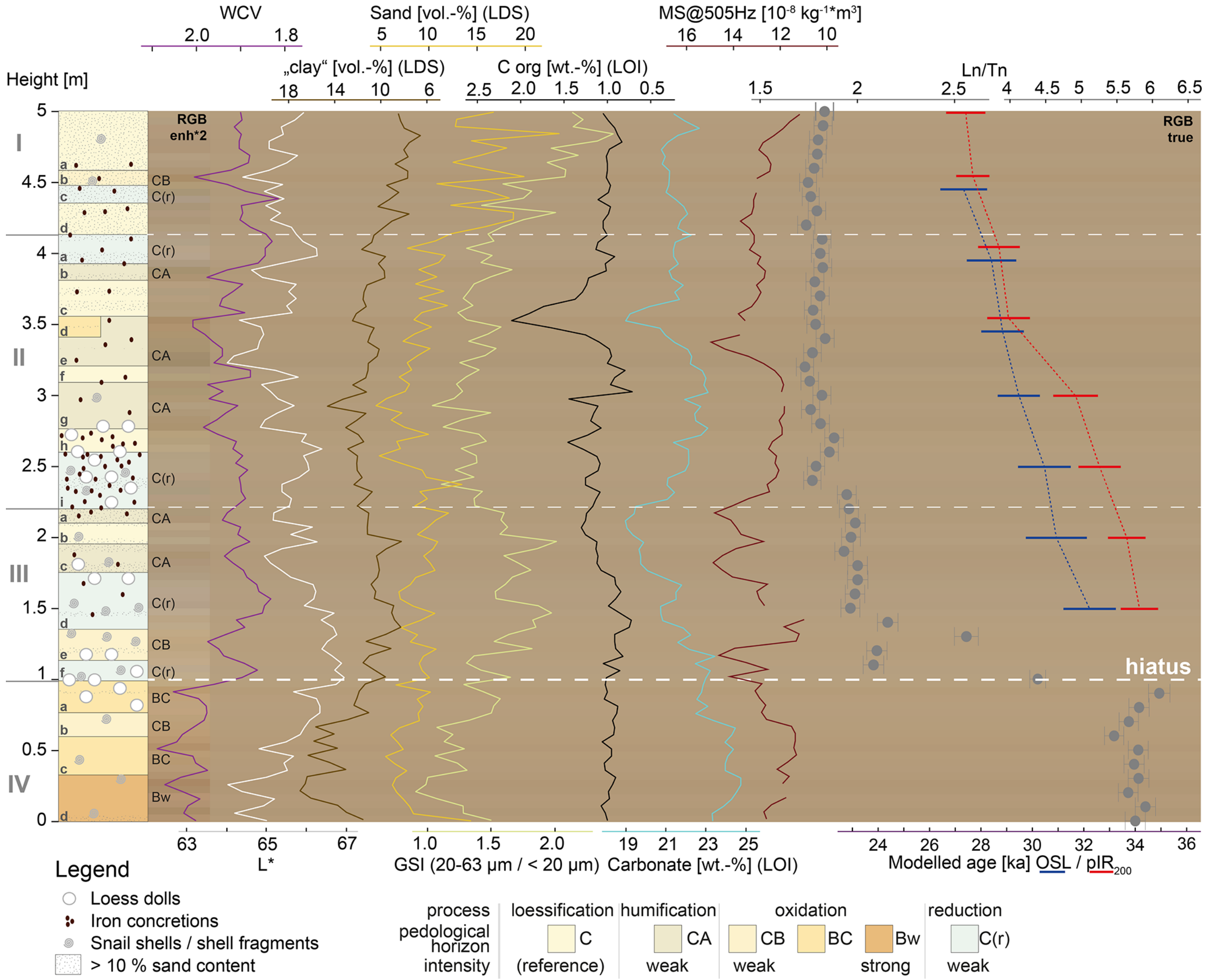

Figure 3. Stratigraphy and main laboratory data with two times enhanced RGB colours behind pedological horizons and true RGB colours behind the data plots. Data peaks oriented to the left indicate enhanced oxidative soil formation, and peaks to the right indicate more aeolian activity and reductive pedogenesis. "Clay" refers to the LDS fractions < 6.3 µm (see "Materials and methods" section). Note the change in scale of the luminescence screening results (Ln/Tn).

1.3 m. The values are not perfectly aligned and show smaller offsets, namely at a height of 1.45, 1.85, 2.35, 2.55, 2.75, 2.95, 3.35, and 4.05 m. However, the second group of values appears overall quite homogeneous with limited variability in the Ln/Tn values. The most likely explanation for the observed two groups of Ln/Tn values appears to be a large hiatus in between Units III and IV. The sample taken across the expected hiatus between Units III and IV, which was not obvious in the field, has a Ln/Tn value of 4.4, which represents the average of the Ln/Tn values directly above and below.

3.6 Luminescence dating

Originally, 11 samples were taken for luminescence dating at intervals of 50 cm along the profile. Due to the likely hiatus within the profile at a height of 1 m, the sample taken at this height (across the hiatus) was discarded. For all investigated samples, the quartz OSL signals are moderately bright and show a rather rapid decay, reaching background within ca. 2 s of stimulation (note that green stimulated OSL decays much slower than blue stimulated OSL). The shape of the OSL decay curves of the natural and artificially irradiated sample is similar, and OSL growth curves fit well when using the sum of exponential saturating functions (Fig. 5a). Unfortunately, the amount of quartz remaining after sample preparation was low for several samples, which limited the number of replicate measurements (Table S5). The feldspar signals are also only moderately bright but much brighter than quartz OSL. Interestingly, the growth curves of IRSL

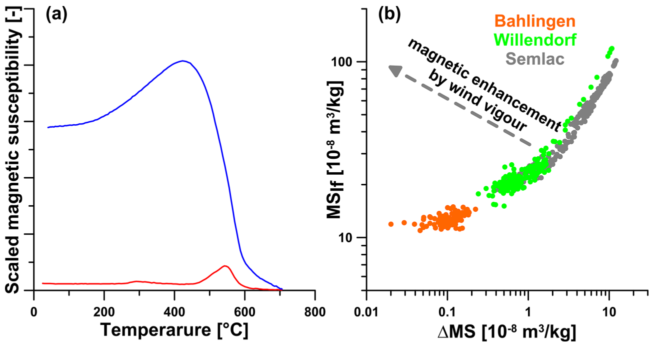

Figure 4. **(a)** Temperature-dependent susceptibility heating (red) and cooling curve (blue). Note that during heating the main decrease in susceptibility occurs around 600 °C, indicative of magnetite. **(b)** Comparison of the magnetic susceptibility and its frequency dependence to the loess sections of Willendorf and Semlac (Zeeden et al., 2016; Zeeden and Hambach, 2021). This shows both the low susceptibility and also the low-frequency dependence. Because the frequency dependence is lower than also pure loess at Semlac, water logging and the associated decrease in at least the frequency-dependent susceptibility are assumed. No strong indication for wind vigour is present.

and the different post-IR IRSL signals show pronounced differences in shape (Fig. 5b). While IRSL and pIR-100 have a quite similar behaviour, pIR-150 shows a much steeper shape of the growth curve. Both the pIR-200 and pIR-250 show a much flatter shape of dose response.

All luminescence ages are presented in Table 1. The determined ages confirm the hiatus between the lower (Unit IV) and upper part (Units I to III) of the profile (Fig. 3). The samples from above the hiatus are internally consistent but show significant differences between the different approaches (Fig. 6). The average ratios in relation to OSL (excluding the top and two bottom samples) are 0.53 ± 0.03 (IRSL), 0.76±0.05 (pIR-100), 0.93±0.05 (pIR-150), 1.04± 0.06 (pIR-200), and 1.16 ± 0.08 (pIR-250). The differences are likely explained by signal instability, as well as the effect of partial bleaching and/or thermal transfer, as discussed later in the paper.

For the samples from below the hiatus at 1 m, sample BL-0 has an OSL age of 101.9±13.9 ka and sample BL-50 an OSL age of 96.0 ± 16.1 ka. However, these ages are only based on 3 and 10 replicate measurements, respectively, which calls for caution with regard to the chronological interpretation. The corresponding pIR ages show a significant offset and are internally not consistent; sample BL-50 (pIR-200: 205.7 ± 8.4 ka) shows a clearly older age than the underlying samples BL-0 (pIR-200: 149.8±8.3 ka), as is discussed further below.

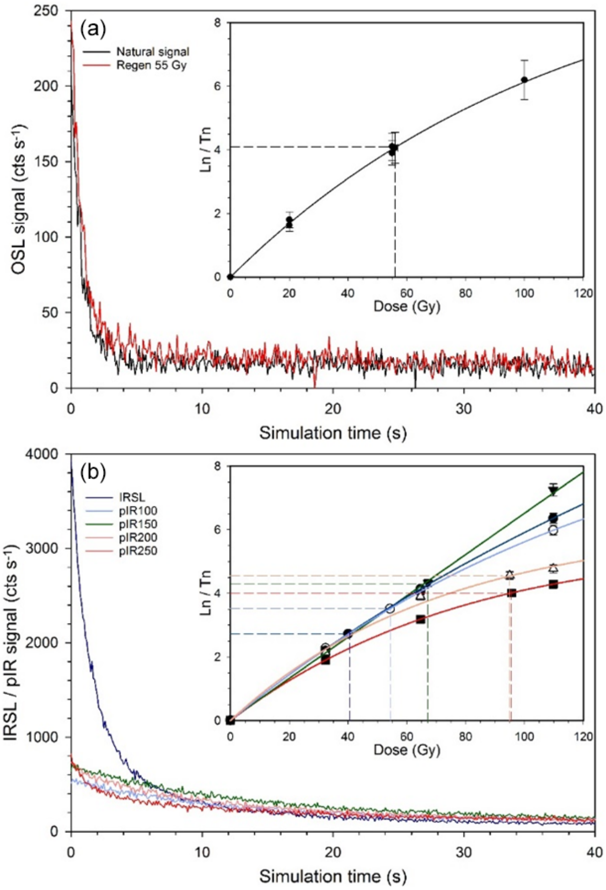

Figure 5. Example of luminescence characteristics. **(a)** Quartz extracted from sample BAL-200 reveals rather weak OSL emissions but a similar decay shape for both the natural and laboratory-induced signal. Dose response curves are well described by a single-exponential saturating function. **(b)** IRSL decay curves are several times brighter than for pIR. The shape of the IRSL and pIR growth curves is significantly different for the different approaches. Both pIR-200 and pIR-250 show a less steep increase compared to lower stimulation temperatures, implying an earlier saturation level.

4 Discussion

4.1 Variations in proxy data

In the field, the LPS Bahlingen gives the impression of weakly differentiated loess with some loess-specific features such as loess dolls, snails shells, and iron/manganese concretions. Luminescence screening, confirmed by the dating results, indicates a major hiatus between Units IV and III. There is no indication of major erosional phases within Units I–III; therefore, this part of the profile will likely have recorded subtle palaeoenvironmental variations during a quasi-constant build-up. While granulometry of weakly differentiated LPSs largely reflects changes in sedimentation dynamics (Antoine et al., 2009; Schulte et al., 2018), changes in colour, χ, C_{org}, and possibly clay content are sensitive to

Table 1. Ages determined at 50 (IRSL), 100, 150, 200, and 250 °C using the MET pIR protocol are shown for the different profile heights, as well as the ages determined using quartz and a SAR protocol (OSL). Ages are given in kiloyears before the year of sampling (2021).

Height (cm)	OSL (ka)	IRSL (ka)	pIR-100 (ka)	pIR-150 (ka)	pIR-200 (ka)	pIR-250 (ka)
500	23.1 ± 2.0	15.6 ± 0.5	19.2 ± 0.7	24.1 ± 1.0	27.6 ± 1.1	30.9 ± 1.3
450	27.0 ± 1.2	14.7 ± 0.5	19.5 ± 0.7	23.6 ± 0.7	27.4 ± 0.9	29.6 ± 1.0
400	29.3 ± 1.4	14.6 ± 0.5	21.7 ± 0.9	25.9 ± 0.9	29.2 ± 1.0	32.0 ± 1.2
350	28.4 ± 1.2	14.9 ± 0.5	20.3 ± 0.7	25.1 ± 0.9	27.5 ± 1.1	30.7 ± 1.0
300	29.4 ± 1.2	15.4 ± 0.5	20.9 ± 0.9	27.4 ± 0.9	31.7 ± 1.2	36.0 ± 1.3
250	31.0 ± 1.4	16.6 ± 0.7	24.7 ± 1.2	29.2 ± 1.3	32.6 ± 1.2	36.9 ± 2.0
200	29.6 ± 1.7	17.3 ± 0.6	25.0 ± 1.1	30.3 ± 1.0	33.7 ± 1.1	37.8 ± 1.8
150	32.7 ± 1.3	17.3 ± 0.6	25.8 ± 0.9	30.8 ± 1.0	34.2 ± 1.1	38.4 ± 1.3
50	96.0 ± 16.1	99.6 ± 5.5	146.8 ± 9.3	185.3 ± 7.1	205.7 ± 8.4	210.3 ± 11.4
0	101.9 ± 13.9	68.4 ± 3.6	110.4 ± 6.7	133.4 ± 6.0	149.8 ± 8.3	157.8 ± 9.6

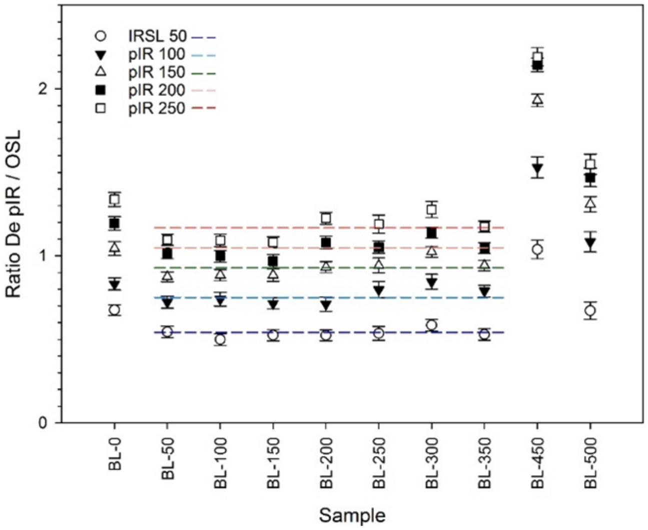

Figure 6. Comparison of IRSL/pIR versus OSL ratios calculated for all samples investigated in this study. Most samples (BL-50 to BL-350) reveal rather similar ratios. The ratio for the two samples from below the lower discontinuity show higher ratios, which reflects either an underestimation of OSL or, more likely, overestimation of IRSL and pIR due to incomplete bleaching of the signal. Furthermore, the top sample (BL-50) also reveals a consistently higher ratio, which is interpreted to reflect an underestimation of the OSL age in this case.

post-sedimentary alteration, i.e. pedogenesis (Sprafke et al., 2020).

Initial soils from loess are usually characterised by enhanced amounts of organic matter, although in palaeosols this is usually lower than in surface soils due to decomposition, while dark colours may persist. Buried dark steppe soils of the LPS Dolní Věstonice have much lower organic carbon contents (0.9 %–1.4 %) than surface steppe soils (ca. 5 %) (Antoine et al., 2013). Advanced development of pedogenesis under warm and humid climate leads to decalcification, oxidation, and clay formation by hydrolysis (Sprafke, 2016); this usually goes along with increasing χ in the course of soil formation (e.g. Heller et al., 1993; Bradak et al., 2021, and references therein). In the presence of permafrost and in the absence of dust deposition, reduced soils form if sufficient soil moisture is present. This will lead to greyish colours, commonly the formation of iron/manganese concretions (Antoine et al., 2009; Terhorst et al., 2015), and possibly the leaching of iron and a reduction of magnetic susceptibility (e.g. Baumgart et al., 2013, and references therein).

Located on a plateau position, the presence of reworked soils and sediments can largely be excluded for the LPS Bahlingen-Schönenberg, and the applied multi-parameter approach is expected to reveal phases of initial pedogenesis (Schulte et al., 2018; Sprafke et al., 2020; Vlaminck et al., 2018). Unit IV appears to be a moderately pigmented pedocomplex with enhanced clay content, but at the same time it contains the highest amount of carbonate throughout the profile and exhibits no increase in χ. This is contrary to common models of pedogenesis on loess, in which oxidation (increase in brownish pigments, higher χ) and clay formation (by hydrolysis) most efficiently take place after decalcification (Stahr et al., 2020). At the LPS Krems-Wachtberg East, loess and brownish (BC) horizons contain 27 % and 18 % of carbonate, respectively, indicating that in the presence of easy weatherable iron-bearing silicates (there: biotite) no complete decalcification is required for brunification (Meyer-Heintze et al., 2018). Yet, at Bahlingen-Schönenberg even higher carbonate values in brownish loess compared to unaltered loess can only be explained by secondary enrichment. We hypothesise that Unit IV was enriched in carbonate during leaching of a formerly superimposed but now eroded and well-developed palaeosol. This does not exclude brunification and changes in magnetic susceptibility in the presence of carbonate. Low magnetic susceptibility may be related to leaching of iron due to high precipitation during pedogenesis (e.g. Ma et al., 2013).

Rather weak colour variations indicate the absence of well-developed palaeosols in Units I–III. It is challenging to link the colour-supported stratigraphy to the other parameter variations as there is no unidirectional pathway of pedogenic alteration, and changes in original sedimentary properties cannot be excluded. It is surprising that Units IIe and IIg share the same colour tone but have distinct differences in C_{org} and carbonate contents, as well as χ. This deviation is independent of some contamination (IId) likely due to a crotovine.

Coarse silt and fine sand content, as well as the GSI, show a rather similar pattern, contrasting with the variations observed for clay to medium silt content. In the absence of significant weathering and reworking, changes in wind speed as represented by the GSI likely explain most variations in granulometry (Antoine et al., 2009). Another explanation could be changing sediment sources or changes in source granulometry and vegetation cover (Sun et al., 2004; Schulte et al., 2016). Units I and III have a higher content of coarse silt to fine sand, possibly indicating more frequent dust storms during their formation (Antoine et al., 2009).

In Units II to III, carbonate contents vary in opposite pattern to the GSI, indicating that coarser grain sizes contain a smaller contribution of carbonate. CA horizons found in Units IIe, IIIa, and IIc do not only have darker pigments but are characterised by higher χ and lower carbonate contents, possibly indicating initial soil formation. Besides these initial terrestrial palaeosols, there are several pale horizons that likely correspond to very weak tundra gley soils that formed under waterlogged conditions (semi-terrestrial) above permafrost (Antoine et al., 2009, Sprafke et al., 2020). Yet, granulometry and magnetic susceptibility show little sensitivity for these initial palaeosols.

The χ values at Bahlingen-Schönenberg are rather low compared to other Central European loess sections, and it has been shown that χ is influenced by a suite of processes (e.g. Baumgart et al., 2013). The low χ is likely partly caused by a high proportion of quartz and other coarse diamagnetic materials diluting the magnetic signal. Yet, χ oscillates in the same range as χ at the LPS Nussloch and also has a close relation to GSI variations. At Nussloch, enhancement of χ, together with a higher GSI, is explained by a higher proportion of relatively dense (i.e. heavier) magnetite minerals delivered from the Rhine floodplain (Antoine et al., 2009). This wind-vigour model of magnetic enhancement in glacial loess is known from Alaska (Begét and Hawkins, 1989) and Siberia (Chlachula et al., 1998), and it likely also explains the present observations. Here, the effect of dissolution of fine magnetic particles most likely contributes to the feature of the low-frequency dependency of χ. Coarse magnetic particles are too large to be completely dissolved during water logging conditions.

We interpret the temperature-dependent susceptibility properties (Fig. 4) as indicative for contributions of both magnetite and hematite. Here, the decrease in the susceptibility at $\sim 580\,^{\circ}\mathrm{C}$ is interpreted to represent the Curie temperature of magnetite. The further decrease in χ towards $700\,^{\circ}\mathrm{C}$ is interpreted as a contribution of hematite; whether this is an original signal or an effect of heating is at this point uncertain, but sediment colour does not speak for a major contribution of hematite. These properties imply that more or less typical loess is present; a large quantity of the iron is originally not in a strongly magnetic phase.

4.2 Luminescence screening and dating

IRSL screening has proven here as a fast (measurements required only ca. 48 h machine time) and low-cost method to identify qualitative variations in the stored luminescence signal. This helped to quickly identify the substantial hiatus between Units III and IV that was not obvious in the field and to discard the sample that was taken exactly on the hiatus. The age from this sampling tube contains grains from above and below the hiatus, which would have produced a mixed age without much value. Nevertheless, in comparison to actual dating the method only provides semi-quantitative results, and small variations in the measured luminescence signal should not be overinterpreted.

For the upper part of the sequence (Units I to III), the OSL ages are within the time range usually considered to yield reliable results. Hence, the OSL ages are considered as reference. Whereas the lower IRSL, pIR-100, and pIR-150 ages are likely underestimated due to fading (Li and Li, 2011), the higher pIR-250 ages possibly relate to hard-to-bleach components or thermal transfer (Preusser et al., 2014) and may thus overestimate the real age of deposition. As a consequence, it appears that the pIR-200 ages should be regarded as the most reliable, and these indeed fit mainly well with the OSL ages. One exception is the topmost sample BL-500, which shows much higher ratios of IRSL and pIR versus OSL age (Fig. 6). In fact, the OSL age of this sample is some 4000 years younger than those determined for the rest of the sequence above the hiatus. However, neither the IRSL and pIR ages nor the IRSL screening data nor the stratigraphy point towards a major hiatus in this part of the sequence. Hence, it appears appropriate to rather favour the pIR-200 age (27.6 ± 1.1 ka) as being more reliable than the OSL of this sample. While there is no obvious explanation supporting the apparent underestimation of this particular OSL age, it should be noted that it is based on only 10 replicate measurements (due to material shortage), compared to 20 to 30 carried out for most other samples.

Two semi-independent age–depth models were constructed for both OSL and pIR-200 (Fig. 3). We excluded the lower part of the sequence from the age–depth model as, first, including only two samples appears to be too few, second, the number of quartz replicate measurements is very low, and, third, the feldspar ages are inconsistent. While underestimation of quartz has been reported from loess (e.g. Anechitei-Deacu et al., 2018), this is usually for higher D_e

values than those observed here. The higher apparent pIR ages could rather be explained by partial bleaching of the signal prior to deposition, which could be due to short distance reworking of sediment (Yi et al., 2016) in a potentially different geomorphological setting than at present (plateau situation). Due to the limited number of ages and the inconsistency with pIR, we only attribute a minimum age of ca. 100 ka for this part of the sequence. It must be the target of future studies to investigate the nature of the hiatus (soil micromorphology) and its spatial appearance (palaeotopography), as well as to address the chronological position in more detail.

4.3 Upper Pleniglacial chronostratigraphy

The OSL age–depth model indicates quasi-constant loess accumulation from ca. 33 to 27 ka. The pIR-200 age model is largely similar for the sequence above 3 m, whereas below, the mean ages are systematically ca. 2000 years older. According to this age model, loess accumulation may have started around 35 ka and continued until ca. 27 but was interrupted (hiatus) at around 30 ka (Figs. 3 and 7). There is no independent numerical or relative stratigraphic age control in support of either the OSL or the pIR-200 age model. Tundra gley soils and other palaeosols are very weakly developed at the LPS Bahlingen-Schönenberg, challenging pedostratigraphic inferences. The variations in the GSI at Bahlingen largely differ for the GSI of the contemporary part of the LPS Nussloch. At Nussloch the GSI is low before 30 ka and during later interstadials is represented by tundra gley soils, whereas at Bahlingen, the sequence older than 30 ka has distinct GSI peaks and lacks a GSI peak corresponding to the first major Nussloch loess event around 30 ka (Fig. 7). As we did not observe evidence for loess reworking, this pattern is likely related to a distinct aeolian deposition regime at Bahlingen.

Despite the uncertainties related to different age models and the lack of information from the disturbed upper 1.5 m of the outcrop, the available age information from the LPS Bahlingen-Schönenberg clearly shows that the major period of dust deposition predates the Alpine LGM (25–24 ka). Linearly extrapolating the age models to the top of the sequence results in ages of not more than 25 ka. Hypothetically, several metres of previously deposited loess could have been removed by erosion, but our local survey along the hollow lanes did not reveal thick packages of reworked loess. Assuming that the apparent lack of deposition during and after the LGM is real, this is in a way in disagreement with the classical notion that glaciations in the upper reaches of river systems enhance silt production, fluvial and eventually aeolian transport, and deposition (Smalley et al., 2009). A possible scenario would be that during the LGM the local climate at the topographically exposed loess plateau west of Bahlingen was too cold and/or dry (polar-desert-like ecosystem) to support vegetation cover capable of capturing relevant quantities of windblown dust (Sirocko et al., 2016; Sprafke et al., 2020). The hiatus around 30 ka suggested by the pIR-200 age model may be explained in a similar way (Fig. 7), as during the time of Heinrich Event 3 very harsh environmental conditions prevailed from western to Central Europe (Starnberger et al., 2011; Fuhrmann et al., 2021). While the LPS Nussloch likely had sufficient vegetation cover during the Heinrich events and the LGM to collect thick amounts of mineral dust, recorded as loess events (Antoine et al., 2009), the LPS Krems-Wachtberg (Lower Austria) records phases of erosion and reworking attributed to polar-desert-like ecosystems (Sprafke et al., 2020). The lack of loess deposition at Bahlingen-Schönenberg during Heinrich Event 3 and the LGM may equally be explained by the local presence of polar-desert-like ecosystems during these periods.

The OSL age model suggests continuous dust deposition starting around 33 ka, without a clear effect of Heinrich Event 3 (Fig. 7). A slightly earlier onset of loess accumulation around 34–35 ka, as suggested by the pIR-200 model, is in agreement with results from the LPS Nussloch, where loess above the Lohne soil is robustly dated to ca. 35 ka (Gocke et al., 2014; Moine et al., 2017). This represents the transition from the Middle Pleniglacial to the Upper Pleniglacial of the last glacial period, corresponding to the end of Greenland Interstadial 7 (Antoine et al., 2009; Moine et al., 2017). It is possible that at Bahlingen-Schönenberg a Lohne soil equivalent has overprinted the upper part of Unit IV, below the major hiatus, but there are no data to support this assumption. The weak tundra gley soils at 1.0 to 3.5 m height could stratigraphically correspond to the G1 and G2 tundra gley soils at Nussloch that formed before 30 ka, correlative to the Erbenheim soil E0 (Lehmkuhl et al., 2016). These early Upper Pleniglacial tundra gley soils likely correspond to Greenland Interstadials 5 and 6. Taking the OSL age model into account, also the CA horizon at 3 m height may still be part of this suite of weak palaeosols; in this case we can tentatively attribute it to the very weak Greenland Interstadial 5.1 (Fig. 7).

Considerable mineral dust accumulation peaking around 34–29 ka is also reported from the LPS Möhlin (Gaar and Preusser, 2017), ca. 100 km upstream of the Rhine and the nearby Bergsee lacustrine record (Duprat-Oualid et al., 2017). There is no evidence for contemporary major glacier advances into the upstream Swiss Alpine forelands, but Alpine palaeoglacier dynamics and regional palaeoenvironments were likely favourable to contribute to downstream aeolian silt deposition. It appears that Alpine glaciers only advanced into the forelands around 30 ka (Gaar et al., 2019), apparently coinciding with Heinrich Event 3 (Starnberger et al., 2011). Interestingly, none of the dust records in the region (Bahlingen, Bergsee, Möhlin) recorded an increased dust accumulation during and after the LGM, calling for more data to unravel the regional response to the large-scale palaeoclimatic and palaeoenvironmental evolution. Yet, our results strongly support the notion that the Middle to Up-

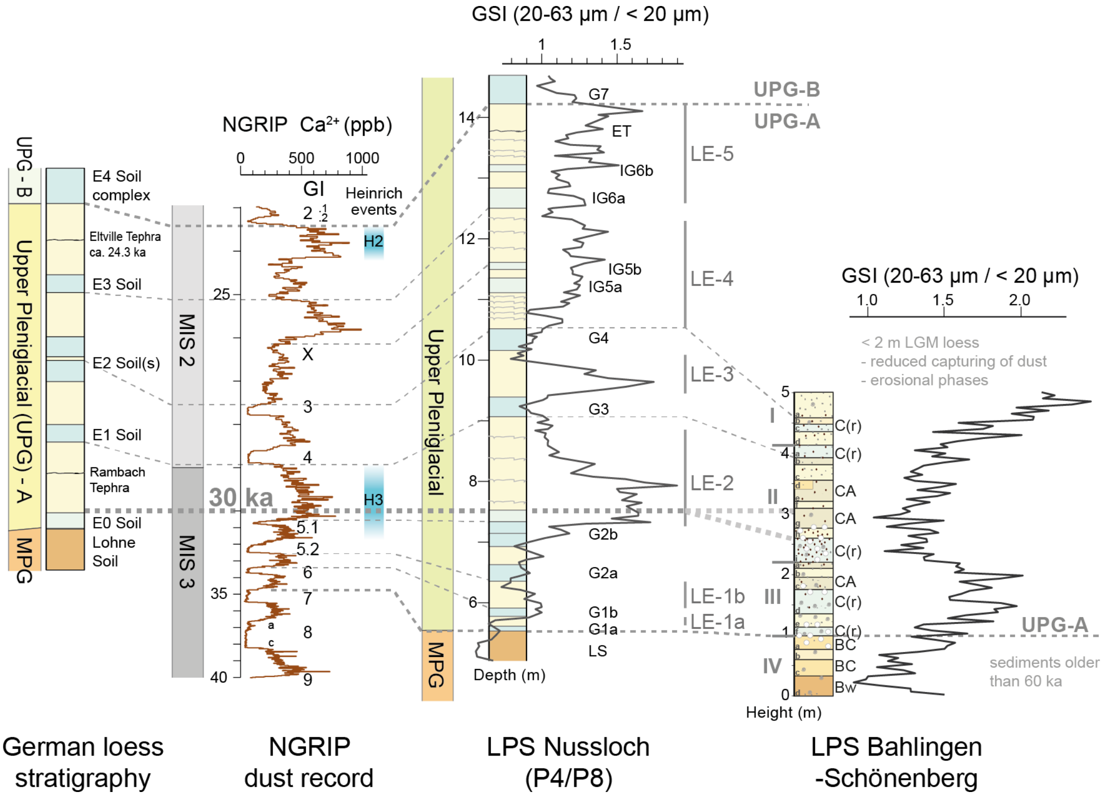

Figure 7. LPS Bahlingen-Schönenberg stratigraphy and GSI record in comparison to the LPS Nussloch (Antoine et al., 2009; Moine et al., 2017), correlated to the North Greenland Ice Core Project (NGRIP) dust record from 40 to 23 ka (Rasmussen et al., 2014), and German loess stratigraphy (Lehmkuhl et al., 2016). UPG = Upper Pleniglacial; MPG = Middle Pleniglacial.

per Pleniglacial transition, as recorded in Central European loess, predates the marine isotope stage (MIS) 3–2 transition (29 ka; Lisiecki and Raymo, 2005) by ca. 5000 years, as also recognised in other LPSs (Antoine et al., 2009, Terhorst et al., 2015, Lehmkuhl et al., 2016, Sprafke et al., 2020).

4.4 Upper Pleniglacial palaeoenvironments

In the classical German loess stratigraphy, originally developed in the northern part of the Upper Rhine Graben (URG; Schönhals et al., 1964; Semmel, 1967), the Upper Pleniglacial often comprises up to five well-developed tundra gleys, named Erbenheim soils after the type locality in southwestern Hesse. The Upper Pleniglacial loess record of Nussloch contains even nine tundra gley complexes of varying intensity. The absence of well-developed tundra gleys at the LPS Bahlingen-Schönenberg is striking but possibly represents a regional phenomenon as such palaeosols have so far not been reported from the southern URG (Guenther, 1987). Krauss et al. (2016) explain weakly developed tundra gleys in LPSs of the northern Harz foreland by drier palaeoclimatic conditions. At present, this region receives less than 600 mm of mean annual precipitation, compared to 600–700 mm in the northern URG and > 800 mm at Nussloch (Institut für Länderkunde, 2003). Bahlingen receives > 800 mm precipitation; therefore, present-day climatic conditions are no adequate reference to explain the absence of tundra gleys in the studied LPS. High dust accumulation rates equally do not explain the absence of palaeosols as the contemporary part of the LPS Nussloch is even thicker, and accumulation rates at Nussloch (1.1 mm yr^{-1}) and Bahlingen-Schönenberg (0.8 mm yr^{-1}) are very similar. Carbonate contents and magnetic susceptibility of the LPS Bahlingen-Schönenberg are also similar to those of the LPS Nussloch; therefore, we can largely exclude an influence of parent material differences on palaeopedogenesis. The absence of tundra gleys in the Pannonian Basin has been related to the lack of continuous permafrost in this region (Terhorst et al. 2015). However, during the Upper Pleniglacial, the Vosges (Mercier and Jeser, 2004), Black Forest (Hofmann et al., 2020), Jura (Buoncristiani and Campy, 2004), and Alps (Preusser et al., 2011) surrounding the southern URG were covered by considerable ice masses; therefore, the absence of permafrost in the area between appears rather unlikely. Yet, this specific topographic and palaeoenvironmental framework likely caused a specific regional palaeoclimate. A possible scenario to explain the absence of tundra gley soils in the Upper Pleniglacial loess of the study region could be a distinct pattern of precipitation during this period. While the missing presence of tundra gleys in the southern URG has to be confirmed, a possible explanation would be the southern advection of precipitation during the LGM, first suggested by Florineth and Schlüchter (2000) and later promoted by several other authors (e.g. Kuhlemann et al., 2008; Monegato et al., 2017; Gribenski et al., 2021). The underlying precipitation pattern would place the southern URG in a rain shadow position north of the Alps that could have been less pronounced further north. However, a robust palaeoenvironmental interpretation of pale horizons in the southern URG requires more detailed studies on this and other regionally distributed loess profiles. For the URG, a reliable pedo- and chronostratigraphic scheme of the Late Pleistocene remains to be established. For the LPS Nussloch, a clear connection of Upper Pleniglacial tundra gley soils to Greenland interstadials was possible only through a very robust age–depth model, based on radiocarbon dating of calcified earthworm casts (Moine et al., 2017).

5 Conclusions

The loess profile of Bahlingen-Schönenberg is the first LPS from the southern Upper Rhine Graben that has been investigated using a multi-method approach. While the site shows little stratigraphic differentiation and no typical response of palaeoenvironmental proxies, it covers a relatively short period of time (ca. 7000 years) at high resolution, covering the onset of the Upper Pleniglacial and the MIS 3–2 transition. IRSL screening has shown its potential as a tool that may help to quickly and cost-efficiently identify gaps in sedimentation and could be used in the future to position samples for luminescence dating more efficiently. Identifying the nature of and possible causes producing the hiatus observed in the lower part of Bahlingen-Schönenberg requires more detailed work in the surroundings. The sequence above the hiatus is characterised by weakly developed tundra gleys that are less intensely developed as tundra gleys found in the same stratigraphic position in the middle and northern part of the Upper Rhine Graben. It is here hypothesised that this could be due to drier regional climate during the time of their formation, possibly caused by the different circulation pattern over the North Atlantic and Europe that has already been deduced from the analyses of glacial features. Another interesting fact is the lack of loess dating to the LGM and the time thereafter. This could be explained either by lack of loess deposition during that time due to wind speed that is too high and/or a lack of vegetation required to fix the dust or by substantial erosion during the late glacial period and early Holocene before the area was occupied by dense vegetation. More regional palaeoenvironmental records are required to further address the above research questions in the future.

Data availability. Relevant data are given either in the main text or in the supplement.

Supplement. The supplement related to this article is available online at: https://doi.org/10.5194/egqsj-71-145-2022-supplement.

Author contributions. FP, ToS, and AF conceptualised this study. Fieldwork and most laboratory analyses were carried out by TaS and LS, under the supervision of FP, ToS, and AF. Luminescence dating was carried out by AF and magnetic susceptibility measurements by CZ. CZ calculated the age models. The original draft was prepared by ToS and FP, based on the MSc thesis written by TaS. All authors contributed by additional writing, reviewing, and editing.

Competing interests. At least one of the (co-)authors is a member of the editorial board of *E&G Quaternary Science Journal*. The peer-review process was guided by an independent editor, and the authors also have no other competing interests to declare.

Special issue statement. This article is part of the special issue “Quaternary research from and inspired by the first virtual DEUQUA conference”. It is a result of the vDEUQUA2021 online conference in September/October 2021.

Acknowledgements. The authors thank Jan-Hendrik May, University of Melbourne, for inspiring discussions regarding the concepts of landscape dynamics and sediment flux in the Upper Rhine Graben. Many thanks to Robert Peticzka, University of Vienna, for providing the spectrophotometer.

Financial support. This open-access publication was funded by the University of Freiburg.

Review statement. This paper was edited by Hans von Suchodoletz and reviewed by Markus Fuchs and Ludwig Zoeller.

References

Abdulkarim, M., Grema, H. M., Adamu, I. H., Mueller, D., Schulz, M., Ulbrich, M., Miocic, J. M., and Preusser, F.: Effect of using different chemical dispersing agents in grain size analyses of fluvial sediments via laser diffraction spectrometry, Methods and Protocols, 4, 44, https://doi.org/10.3390/mps4030044, 2021.

Anechitei-Deacu, V., Timar-Gabor, A., Constantin, D., Trandafir-Antohi, O., Valle, L. D., Fornós, J. J., Gómez-Pujol, L., and Wintle, A. G.: Assessing the maximum limit of SAR-OSL dating using quartz of different grain sizes, Geochronometria, 45, 146–159, https://doi.org/10.1515/geochr-2015-0092, 2018.

Antoine, P., Rousseau, D.-D., Zöller, L., Lang, A., Munaut, A.-V., Hatte, C., and Fontugne, M.: High-resolution record of the last Interglacial-glacial cycle in the Nussloch loess-palaeosol sequences, Upper Rhine Area, Germany, Quatern. Int., 76/77, 211–229, https://doi.org/10.1016/S1040-6182(00)00104-X, 2001.

Antoine, P., Rousseau, D.-D., Moine, O., Kunesch, S., Hatte, C., Lang, A., Tissoux, H., and Zöller, L.: Rapid and cyclic aeolian deposition during the Last Glacial in European loess: a high-resolution record from Nussloch, Germany, Quaternary Sci. Rev., 28, 2955–2973, https://doi.org/10.1016/j.quascirev.2009.08.001, 2009.

Antoine, P., Rousseau, D.-D., Degeai, J.-P., Moine, O., Lagroix, F., Kreutzer, S., Fuchs, M., Hatte, C., Gauthier, C., Svoboda, J., and Lisa, L.: High-resolution record of the environmental response to climatic variations during the Last Interglacial-Glacial cycle in Central Europe: the loess-palaeosol sequence of Dolní Vestonice (Czech Republic), Quaternary Sci. Rev., 67, 17–38, https://doi.org/10.1016/j.quascirev.2013.01.014, 2013.

Baumgart, P., Hambach, U., Meszner, S., and Faust, D.: An environmental magnetic fingerprint of periglacial loess: records of Late Pleistocene loess–palaeosol sequences from Eastern Germany, Quatern. Int., 296, 82–93, https://doi.org/10.1016/j.quaint.2012.12.021, 2013.

Begét, J. and Hawkins, D.: Influence of orbital parameters on Pleistocene loess deposition in central Alaska, Nature, 337, 151–153, https://doi.org/10.1038/337151a0, 1989.

Bengtsson, L. and Enell, M.: Chemical analysis, in: Handbook of Holocene Palaeoecology and Palaeohydrology, edited by: Berglund, B. E., John Wiley & Sons Ldt., Chichester, 423–451, ISBN 978-1-930665-80-4, 1986.

Bradák, B., Seto, Y., Stevens, T., Újvári, G., Fehér, K., and Költringer, C.: Magnetic susceptibility in the European Loess Belt: New and existing models of magnetic enhancement in loess, Palaeogeogr. Palaeoclimatol. Palaeoecol., 569, 110329, https://doi.org/10.1016/j.palaeo.2021.110329, 2021

Buoncristiani, J. F. and Campy, M.: Expansion and retreat of the Jura Ice sheet (France) during the last glacial maximum, Sediment. Geol., 165, 253–264, https://doi.org/10.1016/j.sedgeo.2003.11.007, 2004.

Buylaert, J. P., Murray, A. S., Thomsen, K. J., and Jain, M.: Testing the potential of an elevated temperature IRSL signal from K-feldspar, Radiat. Meas., 44, 560–565, https://doi.org/10.1016/j.radmeas.2009.02.007, 2009.

Chlachula, J., Evans, M. E., and Rutter, N. W.: A magnetic investigation of a Late Quaternary loess/palaeosol record in Siberia, Geophys. J. Int., 132, 128–132, https://doi.org/10.1046/j.1365-246x.1998.00399.x, 1998.

Degering, D. and Degering, A.: Change is the only constant – Time-dependent dose rates in luminescence dating, Quat. Geochronol., 58, 101074, https://doi.org/10.1016/j.quageo.2020.101074, 2020.

European Standards: DIN 18132:1995-12, Soil, testing procedures and testing equipment – Determination of water absorption, https://www.en-standard.eu/din-18132-soil-testing, last access: 1 April 2022.

Duprat-Oualid, F., Rius, D., Bégeot, C., Magny, M., Millet, L., Wulf, S., and Appelt, O.: Vegetation response to abrupt climate changes in Western Europe from 45 to 14.7k cal a BP: the Bergsee lacustrine record (Black Forest, Germany), J. Quaternary Sci., 32, 1008–1021, https://doi.org/10.1002/jqs.2972, 2017.

Ehlers, J., Gibbard, P. L., and Hughes, P. D. (Eds.): Quaternary Glaciations – Extent and Chronology – A Closer Look, in: Developments in Quaternary Sciences, Elsevier, 15, 1108 pp., ISBN 9780444534477, 2011.

Faershtein, G., Porat, N., and Matmon, A.: Natural saturation of OSL and TT-OSL signals of quartz grains from Nilotic origin, Quat. Geochronol., 49, 146–152, https://doi.org/10.1016/j.quageo.2018.04.002, 2019.

Fischer, P., Jöris, O., Fitzsimmons, K., Vinnepand, M., Prud'homme, C., Schulte, P., Hatté, C., Hambach, U., Lindauer, S., Zeeden, C., Peric, Z., Lehmkuhl, F., Wunderlich, T., Wilken, D., Schirmer, W., and Vött, A.: Millennial-scale terrestrial ecosystem responses to Upper Pleistocene climatic changes: 4D-reconstruction of the Schwalbenberg Loess-Palaeosol- Sequence (Middle Rhine Valley, Germany), Catena, 196, 104913, https://doi.org/10.1016/j.catena.2020.104913, 2021.

Florineth, D. and Schlüchter, C.: Alpine Evidence for Atmospheric Circulation Patterns in Europe during the Last Glacial Maximum, Quaternary Res., 54, 295–308, https://doi.org/10.1006/qres.2000.2169, 2000.

Fuhrmann, F., Seelos, K., and Sirocko, F.: Eolian sedimentation in central European Auel dry maar from 60 to 13 ka, Quaternary Res., 101, 4–12, https://doi.org/10.1017/qua.2020.81, 2021.

Gaar, D. and Preusser, F.: Age of the Most Extensive Glaciation of Northern Switzerland: Evidence from the scientific drilling at Möhliner Feld, E&G Quaternary Sci. J., 66, 1–5, https://doi.org/10.3285/eg.66.1.er1, 2017.

Gaar, D., Graf, H. R., and Preusser, F.: New chronological constraints on the timing of Late Pleistocene glacier advances in northern Switzerland, E&G Quaternary Sci. J., 68, 53–73, https://doi.org/10.5194/egqsj-68-53-2019, 2019.

Galbraith, R. F., Roberts, R. G., Laslett, G. M., Yoshida, H., and Olley, J. M.: Optical Dating of single and multiple Grains of Quartz from Jinmium Rock Shelter, Northern Australia: Part I, Experimental Design and Statistical Models, Archaeometry, 41, 339–364, https://doi.org/10.1111/j.1475-4754.1999.tb00987.x, 1999.

Gocke, M., Hambach, U., Eckmeier, E., Schwark, L., Zöller, L., Fuchs, M., Löscher, M., and Wiesenberg, G. L. B.: Introducing an improved multi-proxy approach for paleoenvironmental reconstruction of loess–paleosol archives applied on the Late Pleistocene Nussloch sequence (SW Germany), Palaeogeogr. Palaeocl., 410, 300–315, https://doi.org/10.1016/j.palaeo.2014.06.006, 2014.

Gribenski, N., Valla, P., Preusser, F., Roattino, T., Crouzet, C., and Buoncristiani J.-F.: Out-of-phase Late Pleistocene glacier advances in the western Alps reflect past changes in North Atlantic atmospheric circulation, Geology, 49, 1096–1101, https://doi.org/10.1130/G48688.1, 2021.

Guenther, E. W.: Sedimentpetrographische Untersuchung von Lössen – Zur Gliederung des Eiszeitalters und zur Einordnung paläolithischer Kulturen – Teil 1 Methodische Grundlagen mit Erläuterung an Profilen, Böhlau Verlag, Köln, Graz, p. 10, Reihe B, Bd. 1, 1961.

Guenther, E. W.: Zur Gliederung der Lösse des südlichen Oberrheintals, E&G Quaternary Sci. J., 37, 67–78, https://doi.org/10.3285/eg.37.1.07, 1987.

Guérin, G., Mercier, N., and Adamiec, G.: Dose-rate conversion factors: Update, Ancient TL, 29, 5–8, 2011.

Heiri, O., Lotter, A. F., and Lemcke, G.: Loss on ignition as a method for estimating organic and carbonate content in sediments: reproducibility and comparability of results, J. Paleolimnol., 25, 101–110, https://doi.org/10.1023/A:1008119611481, 2001.

Heller, F., Shen, C. D., Beer, J., Liu, X. M., Liu, T. S., Bronger, A., Suter, M., and Bonani, G.: Quantitative estimates of pedogenic ferromagnetic mineral formation in Chinese loess and palaeoclimatic implications, Earth Planet. Sc. Lett., 114, 385–390, https://doi.org/10.1016/0012-821X(93)90038-B, 1993.

Hofmann, F. M., Rauscher, F., McCreary, W., Bischoff, J.-P., and Preusser, F.: Revisiting Late Pleistocene glacier dynamics northwest of the Feldberg, southern Black Forest, Germany, E&G Quaternary Sci. J., 69, 61–87, https://doi.org/10.5194/egqsj-69-61-2020, 2020.

Huayu, L., Stevens, S., Shuangwen, Y., and Xuefeng, S.; An erosional hiatus in Chinese loess sequences revealed by closely spaced optical dating, Chinese Sci. Bull., 51, 2253–2259, https://doi.org/10.1007/s11434-006-2097-x, 2006.

Huntley, D. J. and Lamothe, M.: Ubiquity of anomalous fading in K-feldspars and the measurement and correction for it in optical dating, Can. J. Earth Sci., 38, 1093–1106, https://doi.org/10.1139/e01-013, 2001.

Institut für Länderkunde: Nationalatlas der Bundesrepublik Deutschland, Band 3 – Natur und Umwelt II: Klima, Pflanzen und Tierwelt, ISBN 978-3827409560, 2003.

Kars, R. H., Wallinga, J., and Cohen, K. M.: A new approach towards anomalous fading correction for feldspar IRSL dating – tests on samples in field saturation, Radiat. Meas., 43, 786–790, https://doi.org/10.1016/j.radmeas.2008.01.021, 2008.

Kars, R. H., Reimann, T., Ankjærgaard, C., and Wallinga, J.: Bleaching of the post-IR IRSL signal: new insights for feldspar luminescence dating, Boreas, 43, 780–791, https://doi.org/10.1111/bor.12082, 2014.

Krauss, L., Zens, J., Zeeden, C., Schulte, P., Eckmeier, E., and Lehmkuhl, F.: A Multi-Proxy Analysis of two Loess-Palaeosol Sequences in the Northern Harz Foreland, Germany, Palaeogeogr. Palaeocl., 461, 401–417, https://doi.org/10.1016/j.palaeo.2016.09.001, 2016.

Kuhlemann, J., Rohling, E. J., Krumrei, I., Kubik, P., Ivy-Ochs, S., and Kucera, M.: Regional synthesis of Mediterranean atmospheric circulation during the last glacial maximum, Science, 321, 1338–1340, https://doi.org/10.1126/science.1157638, 2008.

Lehmkuhl, F., Zens, J., Krauß, L., Schulte, P., and Kels, H.: Loess-palaeosol sequences at the northern European loess belt in Germany: Distribution, geomorphology and stratigraphy, Quaternary Sci. Rev., 153, 11–30, https://doi.org/10.1016/j.quascirev.2016.10.008, 2016.

Lehmkuhl, F., Nett, J. J., Pötter, S., Schulte, P., Sprafke, T., Jary, Z., Antoine, P., Wacha, L., Wolf, D., Zerboni, A., Hošek, J., Marković, S. B., Obreht, I., Sümergi, P., Veres, D., Zeeden, C., Boemke, B., Schaubert, V., Viehweger, J., and Hambach, U.: Loess landscapes of Europe – Mapping, geomorphology, and zonal differentiation, Earth Sci. Rev., 215, 103496, https://doi.org/10.1016/j.earscirev.2020.103496, 2021.

Li, B. and Li, S.-H.: Luminescence dating of K-feldspar from sediments: A protocol without anomalous fading correction, Quat. Geochronol., 6, 468–479, https://doi.org/10.1016/j.quageo.2011.05.001, 2011.

Lisiecki, L. E. and Raymo, M. E.: A Pliocene-Pleistocene stack of 57 globally distributed benthic d18O records, Paleoceanography, 20, PA10032005, https://doi.org/10.1029/2004PA001071, 2005.

Lowick, S. E., Preusser, F., Pini, R., and Ravazzi, C.: Underestimation of quartz OSL dating towards the Eemian: comparison with palynostratigraphy from Azzano Decimo, northeastern Italy, Quat. Geochronol., 5, 583–590, https://doi.org/10.1016/j.quageo.2009.12.003, 2010.

Ma, M., Liu, X., Pillans, B. J., Hu, S., Lü, B., and Liu, H.: Magnetic properties of Dashing Rocks loess at Timaru, South Island, New Zealand, Geophys. J. Int., 195, 75–85, doi.org/10.1093/gji/ggt206, 2013.

Makó, A., Tóth, G., Weynants, M., Rajkai, K., Hermann, T., and Tóth, B.: Pedotransfer functions for converting laser diffraction particle-size data to conventional values, Eur. J. Soil Sci., 68, 769–782, https://doi.org/10.1111/ejss.12456, 2017.

May, J.-H., Marx, S. K., Reynolds, W., Clark-Balzan, L., Jacobsen, G. E., and Preusser, F.: Establishing a chronological framework for a late Quaternary seasonal swamp in the Australian "Top End", Quat. Geochronol., 47, 81–92, https://doi.org/10.1016/j.quageo.2018.05.010, 2018.

Mercier, J.-L. and Jeser, N.: The glacial history of the Vosges Mountains, Developments in Quaternary Science, 2, 113–118, https://doi.org/10.1016/S1571-0866(04)80061-7, 2004.

Meszner, S., Kreutzer, S., Fuchs, M., and Faust, D.: Late Pleistocene landscape dynamics in Saxony, Germany: Paleoenvironmental reconstruction using loess-palaeosol sequences, Quatern. Int., 296, 94–107, https://doi.org/10.1016/j.quaint.2012.12.040, 2013.

Meyer-Heintze, S., Sprafke, T., Schulte, P., Terhorst, B., Lomax, J., Fuchs, M., Lehmkuhl, F., Neugebauer-Maresch, C., Einwögerer, T., Händel, M., Simon, U., and Solís Castillo, B.: The MIS 3/2 transition in a new loess profile at Krems-Wachtberg East – A multi-methodological approach, Quatern. Int., 464, 370–385, https://doi.org/10.1016/j.quaint.2017.11.048, 2018.

Meyers, P. A. and Lallier-Verges, E.: Lacustrine sedimentary organic matter records of Late Quaternary paleoclimates, J. Paleolimnol., 21, 345–372, https://doi.org/10.1023/A:1008073732192, 1999.

Moine, O., Antoine, P., Hatté, C., Landais, A., Mathieu, J., Prud'homme, C., and Rousseau, D.-D.: The impact of Last Glacial climate variability in west-European loess revealed by radiocarbon dating of fossil earthworm granules, PNAS, 114, 6209–6214, https://doi.org/10.1073/pnas.1614751114, 2017.

Monegato, G., Scardia, G., Hajdas, I., Rizzini, F., and Piccin, A.: The Alpine LGM in the boreal ice-sheets game, Sci. Rep., 7, 2078, https://doi.org/10.1038/s41598-017-02148-7, 2017.

Munyikwa, K., Kinnaird, T. C., and Sanderson, D. C. W.: The potential of portable luminescence readers in geomorphological investigations: a review, Earth Surf. Proc. Land., 46, 131–150, https://doi.org/10.1002/esp.4975, 2021.

Murray, A. S. and Wintle, A. G.: Luminescence dating of quartz using an improved single-aliquot regenerative-dose protocol, Radiat. Meas., 32, 57–73, https://doi.org/10.1016/S1350-4487(99)00253-X, 2000.

Murray, A. S. and Wintle, A. G.: The single aliquot regenerative dose protocol: potential for improvements in reliability, Radiat. Meas., 37, 377–381, https://doi.org/10.1016/S1350-4487(03)00053-2, 2003.

Prescott, J. R. and Hutton, J. T.: Cosmic ray contributions to dose rates for luminescence and ESR dating: Large depths and long-term time variations, Radiat. Meas., 23, 497–500, https://doi.org/10.1016/1350-4487(94)90086-8, 1994.

Preusser, F., Ramseyer, K., and Schlüchter, C.: Characterisation of low luminescence intensity quartz from Westland, New Zealand, Radiat. Meas., 41, 871–877, https://doi.org/10.1016/j.radmeas.2006.04.019, 2006.

Preusser, F., Degering, D., Fuchs, M., Hilgers, A., Kadereit, A., Klasen, N., Krbetschek, M., Richter, D., and Spencer, J. Q. G.: Luminescence dating: basics, methods and applications, E&G Quaternary Sci. J., 57, 95–149, https://doi.org/10.3285/eg.57.1-2.5, 2008.

Preusser, F., Chithambo, M. L., Götte, T., Martini, M., Ramseyer, K., Sendezera, E. J., Susino, G. J., and Wintle A. G.: Quartz as a natural luminescence dosimeter, Earth-Sci. Rev., 97, 196–226, https://doi.org/10.1016/j.earscirev.2009.09.006, 2009.

Preusser, F., Graf, H. R., Keller, O., Krayss, E., and Schlüchter, C.: Quaternary glaciation history of northern Switzerland, E&G Quaternary Sci. J., 60, 21, https://doi.org/10.3285/eg.60.2-3.06, 2011.

Preusser, F., Muru, M., and Rosentau, A.: Comparing different post-IR IRSL approaches for the dating of Holocene foredunes from Ruhnu Island, Estonia, Geochronometria, 41, 342–351, https://doi.org/10.2478/s13386-013-0169-7, 2014.

Pye, K.: The nature, origin and accumulation of loess, Quaternary Sci. Rev., 14, 653–667, https://doi.org/10.1016/0277-3791(95)00047-X, 1995.

Rasmussen, S. O., Bigler, M., Blockley, S. P., Blunier, T., Buchardt, S. L., Clausen, H. B., Cvijanovic, I., Dahl-Jensen, D., Johnsen, S. J., Fischer, H., Gkinis, V., Guillevic, M., Hoek, W. Z., Lowe, J. J., Pedro, J B., Popp, T., Seierstadt, I. K., Steffensen, J. P., Svensson, A. M., Vallelonga, P., Vinther, B. M., Walker, M. J. C., Wheatley, J. J., and Winstrup, M.: A stratigraphic framework for abrupt climatic changes during the Last Glacial period based on three synchronized Greenland ice-core records: refining and extending the INTIMATE event stratigraphy, Quaternary Sci. Rev., 106, 14–28, https://doi.org/10.1016/j.quascirev.2014.09.007, 2014.

Richter, D., Richter, A., and Dornich, K.: Lexsyg – A new system for luminescence research, Geochronometria, 40, 220–228, https://doi.org/10.2478/s13386-013-0110-0, 2013.

Richter, D., Richter, A., and Dornich, K.: Lexsyg smart – a luminescence detection system for dosimetry, material research and dating application, Geochronometria, 42, 202–209, https://doi.org/10.1515/geochr-2015-0022, 2015.

Rittenour, T. M.: Dates and rates of earth-surface processes revealed using luminescence dating, Elements, 14, 21–26, https://doi.org/10.2138/gselements.14.1.21, 2018.

Roberts, H.: The development and application of luminescence dating to loess deposits: a perspective on the past, present and future, Boreas, 37, 483–507, https://doi.org/10.1111/j.1502-3885.2008.00057.x, 2008.

Roberts, H. M., Julie A Durcan, J. A., and Duller, G. A. T.: Exploring procedures for the rapid assessment of optically stimulated luminescence range-finder ages, Radiat. Meas., 44, 582–587, https://doi.org/10.1016/j.radmeas.2009.02.006, 2009.

Rotstein, Y. and Schaming, M.: The Upper Rhine Graben (URG) revisited: Miocene transtension and transpression account for the observed first-order structures, Tectonics, 30, TC3007, https://doi.org/10.1029/2010TC002767, 2011.

Schönhals, E., Rohdenburg, H., and Semmel, A.: Ergebnisse neuerer Untersuchungen zur Würmlöß-Gliederung in Hessen, E&G Quaternary Sci. J., 15, 199–206, https://doi.org/10.3285/eg.15.1.15, 1964.

Schulte, P., Lehmkuhl, F., Steininger, F., Loibl, D., Lockot, G., Protze, J., Fischer, P., and Stauch, G.: Influence of HCl pretreatment and organo-mineral complexes on laser diffraction measurement of loess–palaeosol-sequences, Catena, 137, 392–405, https://doi.org/10.1016/j.catena.2015.10.015, 2016.

Schulte, P., Sprafke, T., Rodrigues, L., and Fitzsimmons, K. E.: Are fixed grain size ratios useful proxies for loess sedimentation dynamics? Experiences from Remizovka, Kazakhstan, Aeolian Res., 31, 131–140, https://doi.org/10.1016/j.aeolia.2017.09.002, 2018.

Semmel, A.: Neue Fundstellen von vulkanischem Material in hessischen Lössen, Notizblatt hessisches Landesamt für Bodenforschung, 95, 10–108, 1967.

Sirocko, F., Knapp, H., Dreher, F., Förster, M. W., Albert, J., Brunck, H., Veres, D., Dietrich, S., Zech, M., Hambach, U., Röhner, M., Rudert, S., Schwibus, K., Adams, C., and Sigl, P.: The ELSA-Vegetation-Stack: Reconstruction of Landscape Evolution Zones (LEZ) from laminated Eifel maar sediments of the last 60 000 years, Global Planet. Change, 142, 108–135, https://doi.org/10.1016/j.gloplacha.2016.03.005, 2016.

Smalley, I.: Making the material: The formation of silt sized primary mineral particles for loess deposits, Quaternary Sci. Rev., 14, 645–651, https://doi.org/10.1016/0277-3791(95)00046-1, 1995.

Smalley, I. and Obreht I.: The formation of loess ground by the process of loessification: a history of the concept, Geologos, 24, 163–170, https://doi.org/10.2478/logos-2018-0015, 2018.

Smalley, I., O'Hara-Dhand, K., Wint, J., Machalett, B., Jary, Z., and Jefferson, I.: Rivers and loess: the significance of long river transportation in the complex event-sequence approach to loess deposit formation, Quatern. Int., 198, 7–18, https://doi.org/10.1016/j.quaint.2008.06.009, 2009.

Smalley, I. J., Krinsley, D. H., and Vita-Finzi C.: Observations on the Kaiserstuhl loess, Geol. Mag., 110, 29–36, https://doi.org/10.1017/S0016756800047269, 1973.

Sprafke, T.: Löss in Niederösterreich – Archiv quartärer Klima- und Landschaftsveränderungen, Würzburg University Press, 42–47, ISBN 978-3827409560, 2016.

Sprafke, T. and Obreht, I.: Loess: Rock, sediment or soil – What is missing for its definition?, Quatern. Int., 399, 198–207, https://doi.org/10.1016/j.quaint.2015.03.033, 2016.

Sprafke, T., Terhorst, B., Peticzka, R., and Thiel, C.: Paudorf locus typicus (Lower Austria) revisited: The potential of the classic loess outcrop for Middle to Late Pleistocene landscape reconstructions, E&G Quaternary Sci. J., 62, 59–72, https://doi.org/10.3285/eg.62.1.06, 2013.

Sprafke, T., Schulte, P., Meyer-Heintze, S., Händel, M., Einwögerer, T., Simon, U., Peticka, R., Schäfer, C., Lehmkuhl, F., and Terhorst, B.: Paleoenvironments from robust loess stratigraphy using high-resolution color and grain-size data of the last glacial Krems-Wachtberg record (NE Austria), Quaternary Sci. Rev., 248, 106602, https://doi.org/10.1016/j.quascirev.2020.106602, 2020.

Stahr, K., Kandeler, E., Herrmann, L. and Streck, T.: Bodenkunde und Standortlehre, 4th edn., Utb. Ulmer, Stuttgart, 327 pp., https://doi.org/10.36198/9783838553450, 2020.

Starnberger, R., Rodnight, H., and Spötl, C.: Chronology of the Last Glacial Maximum in the Salzach Palaeoglacier Area (Eastern Alps), J. Quaternary Sci., 26, 502–510, https://doi.org/10.1002/jqs.1477, 2011.

Steffen, D., Preusser, F., and Schlunegger, F.: OSL quartz age underestimation due to unstable signal components. Quat. Geochronol., 4, 353–362, https://doi.org/10.1016/j.quageo.2009.05.015, 2009.

Steup, R. and Fuchs, M.: The loess sequence at Münzenberg (Wetterau/Germany): A reinterpretation based on new luminescence dating results, Z. Geomorphol. Supp., 61, 101–120, https://doi.org/10.1127/zfg_suppl/2016/0408, 2017.

Stojakowits, P., Mayr, C., Ivy-Ochs, S., Preusser, F., Reitner, J., and Spötl, C.: Environments at the MIS 3/2 transition in the northern Alps and their foreland, Quatern. Int., 581/582, 99–113, https://doi.org/10.1016/j.quaint.2020.08.003, 2021.

Sun, D., Bloemendal, J., Rea, D.K., An, Z., Vandenberghe, J., Lu, H., Su, R., and Liu, T.: Bimodal grain-size distribution of Chinese loess, and its paleoclimatic implications, Catena, 55, 325–340. https://doi.org/10.1016/S0341-8162(03)00109-7, 2004.

Taylor, S. N. and Lagroix, F.: Magnetic anisotropy reveals the depositional and postdepositional history of a loess-paleosol sequence at Nussloch (Germany), J. Geophys. Res.-Sol. Ea., 120, 2859–2876, https://doi.org/10.1002/2014JB011803, 2015.

Terhorst, B., Sedov, S., Sprafke, T., Peticzka, R., Meyer-Heintze, S., Kühn, P., and Solleiro Rebolledo, E.: Austrian MIS 3/2 loess–palaeosol records – Key sites along a west–east transect, Palaeogeogr. Palaeocl., 418, 43–56, https://doi.org/10.1016/j.palaeo.2014.10.020, 2015.

Thomsen, K. J., Murray, A. S., Jain, M., and Bøtter-Jensen, L.: Laboratory fading rates of various luminescence signals from feldspar-rich sediment extracts, Radiat. Meas., 43, 1474–1486, https://doi.org/10.1016/j.radmeas.2008.06.002, 2008.

Viscarra Rossel, R. A., Walvoort, D. J. J., McBratney, A. B., Janik, L. J., and Skjemstad, J. O.: Visible, near infrared, mid infrared or combined diffuse reflectance spectroscopy for simultaneous assessment of various soil properties, Geoderma, 131, 59–75, https://doi.org/10.1016/j.geoderma.2005.03.007, 2006.

Vlaminck, S., Kehl, M., Rolf, C., Franz, S. O., Lauer, T., Lehndorff, E., Frechen, M., and Khormali, F.: Late Pleistocene dust dynamics and pedogenesis in Southern Eurasia - Detailed insights from the loess profile Toshan (NE Iran), Quaternary Sci. Rev., 180, 75–95, https://doi.org/10.1016/j.quascirev.2017.11.010, 2018.

Wintle, A. G.: Anomalous fading of thermoluminescence in mineral samples, Nature, 245, 143–144, https://doi.org/10.1038/245143a0, 1973.

Wright, J. S.: "Desert" loess versus "glacial" loess: quartz silt formation, source areas and sediment pathways in the formation of loess deposits, Geomorphology, 36, 231–256, https://doi.org/10.1016/S0169-555X(00)00060-X, 2001.

Yi, S., Buylaert, J-P., Murray, A. S., Lu, H., Thiel, C., and Zeng, L.: A detailed post-IR IRSL dating study of the Niuyangzigou loess site in northeastern China, Boreas, 45, 644–657, https://doi.org/10.1111/bor.12185, 2016.

Zeeden, C. and Hambach, U.: Magnetic susceptibility properties of loess from the Willendorf archaeological site: Implications for the syn/post-depositional interpretation of magnetic fabric, Front. Earth Sci., 8, 599491, https://doi.org/10.3389/feart.2020.599491, 2021.

Zeeden, C., Kels, H., Hambach, U., Schulte, P., Protze, J., Eckmeier, E., Markovic, S. B., Klasen, N., and Lehmkuhl, F.: Three climatic cycles recorded in a loess-palaeosol sequence at Semlac (Romania) – Implications for dust accumulation in south-eastern Europe, Quaternary Sci. Rev., 154, 130–142, https://doi.org/10.1016/j.quascirev.2016.11.002, 2016.

Zeeden, C., Dietze, M., and Kreutzer, S.: Discriminating luminescence age uncertainty composition for a robust Bayesian modelling, Quat. Geochronol., 43, 30–39, https://doi.org/10.1016/j.quageo.2017.10.001, 2018.

Zeeden, C., Mir, J. A., Vinnepand, M., Laag, C., Rolf, C., and Dar, R. A.: Local mineral dust transported by varying wind intensities forms the main substrate for loess in Kashmir, E&G Quaternary Sci. J., 70, 191–195, https://doi.org/10.5194/egqsj-70-191-2021, 2021.

Zhang, J.: Behavior of the electron trapping probability change in IRSL dating of K-feldspar: A dose recovery study, Quat. Geochronol., 44, 38–46, https://doi.org/10.1016/j.quageo.2017.12.001, 2018.

Zhang, J. and Li, S.-H.: Review of the Post-IR IRSL Dating Protocols of K-Feldspar, Methods and Protocols, 3, 7, https://doi.org/10.3390/mps3010007, 2020.

Zöller, L. and Wagner, G. A.: Thermoluminescence Dating of Loess – Recent Developments, Quatern. Int., 7/8, 119–128, https://doi.org/10.1016/1040-6182(90)90046-7, 1990.

Zöller, L., Stremme, H., and Wagner, G. A.: Thermolumineszenz-Datierung an Löss-Paläoboden-Sequenzen von Nieder-, Mittel- und Oberrhein/Bundesrepublik Deutschland, Chem. Geol., 73, 39–62, https://doi.org/10.1016/0168-9622(88)90020-6, 1988.

Zöller, L., Fischer, M., Jary, Z., Antoine, P., and Krawczyk, M.: Chronostratigraphic and geomorphologic challenges of last glacial loess in Poland in the light of new luminescence ages, E&G Quaternary Sci. J., 71, 59–81, https://doi.org/10.5194/egqsj-71-59-2022, 2022.

E&G Quaternary Sci. J., 71, 123–143, 2022
https://doi.org/10.5194/egqsj-71-123-2022

Open Access E&G Quaternary Science Journal

Research article

A pedo-geomorphological view on land use and its potential in the surroundings of the ancient Hispano-Roman city Munigua (Seville, SW Spain)

André Kirchner[1], Nico Herrmann[2], Paul Matras[1], Iris Müller[3], Julia Meister[3], and Thomas G. Schattner[4]

[1]Department of Geography, University of Hildesheim, Universitätsplatz 1, 31141, Hildesheim, Germany
[2]Department of Soil Protection and Soil Survey, State Authority for Mining, Energy and Geology of Lower Saxony (LBEG), Stilleweg 2, 30655, Hanover, Germany
[3]Institute of Geography and Geology, University of Würzburg, Am Hubland, 97074, Würzburg, Germany
[4]Madrid Department, German Archaeological Institute (DAI), C. Serrano 159, 28002, Madrid, Spain

Correspondence: André Kirchner (andre.kirchner@uni-hildesheim.de), Julia Meister (julia.meister@uni-wuerzburg.de)

Relevant dates: Received: 23 March 2022 – Revised: 6 July 2022 – Accepted: 7 July 2022 –
Published: 3 August 2022

How to cite: Kirchner, A., Herrmann, N., Matras, P., Müller, I., Meister, J., and Schattner, T. G.: A pedo-geomorphological view on land use and its potential in the surroundings of the ancient Hispano-Roman city Munigua (Seville, SW Spain), E&G Quaternary Sci. J., 71, 123–143, https://doi.org/10.5194/egqsj-71-123-2022, 2022.

Abstract: This study investigates the surroundings of Munigua (municipium Flavium Muniguense), a small Roman town in the ancient province of Hispania Baetica (SW Spain). The city's economy was based primarily on copper and iron mining, which brought financial prosperity to its citizens. Local production of agricultural goods is thought to have been of little importance, as the regional soil conditions do not seem to be suitable for extensive agriculture.

To evaluate the recent soil agro-potential and to find evidence for prehistoric and historic land use in the surroundings of Munigua, we applied a pedo-geomorphological approach based on the physicochemical analysis of 14 representative soil and sediment exposures. Selected samples were analyzed for bulk chemistry, texture and phytoliths. The chronostratigraphy of the sequences was based on radiocarbon dating of charcoal samples. The site evaluation of the present-day soil agro-potential was carried out according to standard procedures and included evaluation of potential rootability, available water-storage capacity and nutrient budget within the uppermost 1 m.

The results show that moderate to very good soil agro-potential prevails in the granitic and floodplain areas surrounding Munigua. Clearly, recent soil agro-potential in these areas allows the production of basic agricultural goods, and similar limited agricultural use should also have been possible in ancient times. In contrast, weak to very weak present-day soil agro-potential prevails in the metamorphic landscape due to the occurrence of shallow and sandy to stony soils.

In addition, the study provides pedo-geomorphological evidence for prehistoric and historic land use in pre-Roman, Roman and post-Roman times. Catenary soil mapping in the vicinity of a Roman house complex reveals multi-layered colluvial deposits. They document phases of hillslope erosion mainly triggered by human land use between 4063 ± 82 and 3796 ± 76 cal BP, around

2601 ± 115 cal BP, and between 1424 ± 96 and 421 ± 88 cal BP. Moreover, geochemical and phytolith analyses of a Roman hortic Anthrosol indicate the local cultivation of agricultural products that contributed to the food supply of Munigua.

Overall, the evidence of Roman agricultural use in the Munigua area indicates that the city's economy was by no means focused solely on mining. The production of basic agricultural products was also part of Munigua's economic portfolio. Our geoarcheological study thus supports the archeological concept of economically diversified Roman cities in the province of Baetica and in Hispania.

Kurzfassung:

Diese Studie untersucht die Umgebung von Munigua (municipium Flavium Muniguense), einer kleinen römischen Stadt in der antiken Provinz Hispania Baetica (Südwestspanien). Die Wirtschaft der Stadt basierte in erster Linie auf dem Kupfer- und Eisenbergbau, der den Bürgern finanziellen Wohlstand bescherte. Es wird angenommen, dass die lokale Produktion von landwirtschaftlichen Gütern von geringer Bedeutung war, da insbesondere die regionalen Bodenbedingungen für eine extensive Landwirtschaft nicht geeignet zu sein scheinen.

Um das rezente landwirtschaftliche Potenzial der Böden zu bewerten und mögliche Hinweise für prähistorische und historische Landnutzung in der Umgebung von Munigua zu finden, wurden geoarchäologische Untersuchungen durchgeführt, im Zuge derer 14 repräsentative Boden- und Sedimentaufschlüsse bearbeitet wurden. Ausgewählte Proben wurden auf ihre physikalisch-chemischen Eigenschaften sowie Phytholiten untersucht. Die chronostratigraphische Einordnung erfolgte auf der Grundlage von Radiokohlenstoffdatierungen. Die Standortbewertung des heutigen landwirtschaftlichen Potenzials der Böden wurde nach Standardverfahren durchgeführt und umfasste die Bewertung der potenziellen Durchwurzelbarkeit, der verfügbaren Wasserspeicherkapazität und des Nährstoffhaushalts.

Die Ergebnisse zum landwirtschaftlichen Potenzial der Böden zeigen, dass in Granit- und Auengebieten rund um Munigua ein mäßiges bis sehr gutes Ertragspotenzial vorherrscht, dass die begrenzte Produktion von landwirtschaftlichen Erzeugnissen erlauben würde. Eine vergleichbar begrenzte landwirtschaftliche Nutzung dürfte auch in der Antike möglich gewesen sein. Die Böden in der umgebenden Metamorphitlandschaft besitzen im Gegensatz dazu ein nur schwaches bis sehr schwaches Agrarpotenzial und Hinweise auf eine antike Agrarnutzung sind nicht vorhanden. Darüber hinaus liefert die Studie weitere Hinweise auf prähistorische und historische Landnutzung in vorrömischer, römischer und nachrömischer Zeit. So zeigt eine Catena, die in der Nähe eines römischen Hauskomplexes angelegt wurde, eine reliefabhängige Bodenabfolge mit mehrgliedrigen Hangkolluvien, die anthropogene Bodenerosion zwischen 4063 ± 82 und 3796 ± 76 cal BP, um 2601 ± 115 cal BP, und zwischen 1424 ± 96 und 421 ± 88 cal BP dokumentieren. Darüber hinaus weisen geochemische und Phytolithen-Analysen eines untersuchten römischen Gartenbodens (Hortic Anthrosol) auf den lokalen Anbau landwirtschaftlicher Produkte hin, die zur Nahrungsmittelversorgung von Munigua beitrugen.

Die im Rahmen dieser Untersuchung erzielten Belege für eine landwirtschaftliche Nutzung im Gebiet von Munigua zeigen, dass die Wirtschaft der Stadt keineswegs nur auf den Bergbau ausgerichtet war. Auch die Produktion von landwirtschaftlichen Grunderzeugnissen gehörte zum wirtschaftlichen Portfolio Muniguas. Die Hypothese, dass die lokale Produktion von landwirtschaftlichen Gütern aufgrund eines unzureichenden Ertragspotentials der Böden unbedeutend war, kann somit nicht bestätigt werden. Vielmehr unterstützt diese Studie das archäologische Konzept einer wirtschaftlich diversifizierten römischen Stadt.

1 Introduction

During the imperial period, the economy of small Roman cities in the Roman Empire and particularly in the Roman province of Baetica is assumed to have been very diverse and, depending on the city, typically specialized around a certain economic good (Bowman and Wilson, 2009, 2011). In addition to archeological evidence, abundant historical sources provide a vivid and rich picture of ancient agriculture, fishing and mineral resources, basic foodstuffs, and luxury products (e.g., Blázquez Martinez, 1967; Remesal Rodríguez, 2020).

This study was carried out in the surroundings of the Hispano-Roman municipium Flavium Muniguense, in modern times known as Castillo de Mulva or Munigua (Schattner, 2003), a small urban center in the ancient province of Hispania Baetica. From a historiographic perspective, Munigua is a key site for understanding Roman urbanization on the Iberian Peninsula (Schattner, 2005) since it is one of the few places in Spain that has been systematically excavated for the past 65 years. The local economy was particularly based on copper and iron mining in the surroundings of the town, and Munigua was the largest iron-producer in the Sierra Morena in the 1st and 2nd centuries CE (Schattner, 2019b). Income from the mining activities provided financial prosperity for the citizens and an architectural climax, which culminated in the construction of the impressive terrace sanctuary situated on the highest point in the west of the city (Schattner, 2019a, 2021). In addition to the mining industry, olive oil presses and an oil cellar (*cella olearia*) were located inside the city, indicating the processing of agricultural by-products within the urban area (Schattner, 2003; Peña Cervantes, 2010; Teichner and Peña Cervantes, 2012). Furthermore, wine production and quarrying contributed to economic output even though they were much less significant than the mining operations (Hanel, 1989; Schattner, 2019b).

Current opinion on the food supply strategy of Munigua is based on the assumption that food was obtained in particular from the fertile lower Guadalquivir valley, which was and still is the agricultural center of the region, located just 10 km south of Munigua. Additionally, fish bones and oyster shells indicate connections to the sea (Boessneck and von den Driesch, 1980). In contrast, the local production of agricultural goods is thought to have been of minor relevance (Schattner, 2019b). In this context, it has been suggested that regional soil conditions are currently unsuitable for extensive agriculture and therefore seem to suggest that an ancient agrarian use of the region was also unlikely (Schattner, 2019b). However, so far there has been a lack of evidence-based studies on the agricultural suitability and potential agricultural use of the surroundings of Munigua, and it is only recently that an archeological study has challenged the idea of food imports having been dominant (Krug, 2018). Based on the investigation of small finds, the study stated that tools such as shovels, spades, sickles and billhooks suggest the existence of gardens, meadows for smaller animals and trees which had to be tended and harvested in the wider surroundings of the town (Krug, 2018).

In this paper, we present initial findings from a geoarcheological pilot project and provide new insights into the regional land use history of the Munigua site. Firstly, physicochemical analysis of 14 representative soil and sediment exposures provides a first evidence-based evaluation of present-day agro-potential. Secondly, we present site-specific evidence of prehistoric and historic land use in the surroundings of the city and thus improve understanding of its food supply strategy. In this way we, thirdly, aim to contribute a pedo-geomorphological view to the archeological debate on the diversification of the urban economy in the Roman province of Baetica (e.g., Bowman and Wilson 2009, 2011), a topic that has not yet been developed for this region of the Roman Empire.

2 Study area

2.1 Environmental setting

Munigua is located in the southern part of the Sierra Morena about 50 km northeast of the Andalusian capital Seville (Fig. 1a). To the south the region is bordered by the wide valley of the lower Guadalquivir River, which drains large parts of Andalusia and today flows into the Atlantic Ocean southwest of Seville. The region experiences a dry, subhumid, semi-oceanic Mediterranean climate, with arid summers and winter rains due to low-pressure systems from the Atlantic Ocean (Zazo et al., 2008). Average rainfall is around 580 mm yr^{-1}, and the annual average temperature is 18.0 °C (Gómez-Zotano et al., 2015), leading to species-rich Mediterranean vegetation cover with evergreen woody plants such as *Quercus faginea*, *Quercus suber, Quercus rotundifolia, Olea europaea L.* and *Chamaerops humilis* (Frey and Lösch, 2010). In steeper areas, the taller trees are replaced by maquis shrubland, mainly composed of hardwood bushes (e.g., *Cistus* spp.). However, as in the entire Sierra Morena, vegetation has been greatly altered by centuries of agrosilvopastoral farming, in Spanish known as *dehesa* farming (Joffre et al., 1988), resulting in scattered forest cover accompanied by grassland (Fig. 1c and d).

Geologically, the region belongs to the Ossa-Morena Zone (OMZ), a geotectonic unit of the Iberian Massif (Strauss and Madel, 1974; Tornos et al., 2004; Ribeiro et al., 2010). Granite dominates the petrography in the region (Sanz et al., 1973; Schattner et al., 2005). Geomorphologically, the granite area is mainly characterized by flat to slightly undulating landforms with moderately steep slopes, small depressions and ridges (Fig. 1b). They frequently show linear erosion channels (gullies) and are mostly located close to animal pathways. Steep gully flanks and exposed roots of the existing vegetation crossing the gullies indicate modern gully formation (Fig. 1d).

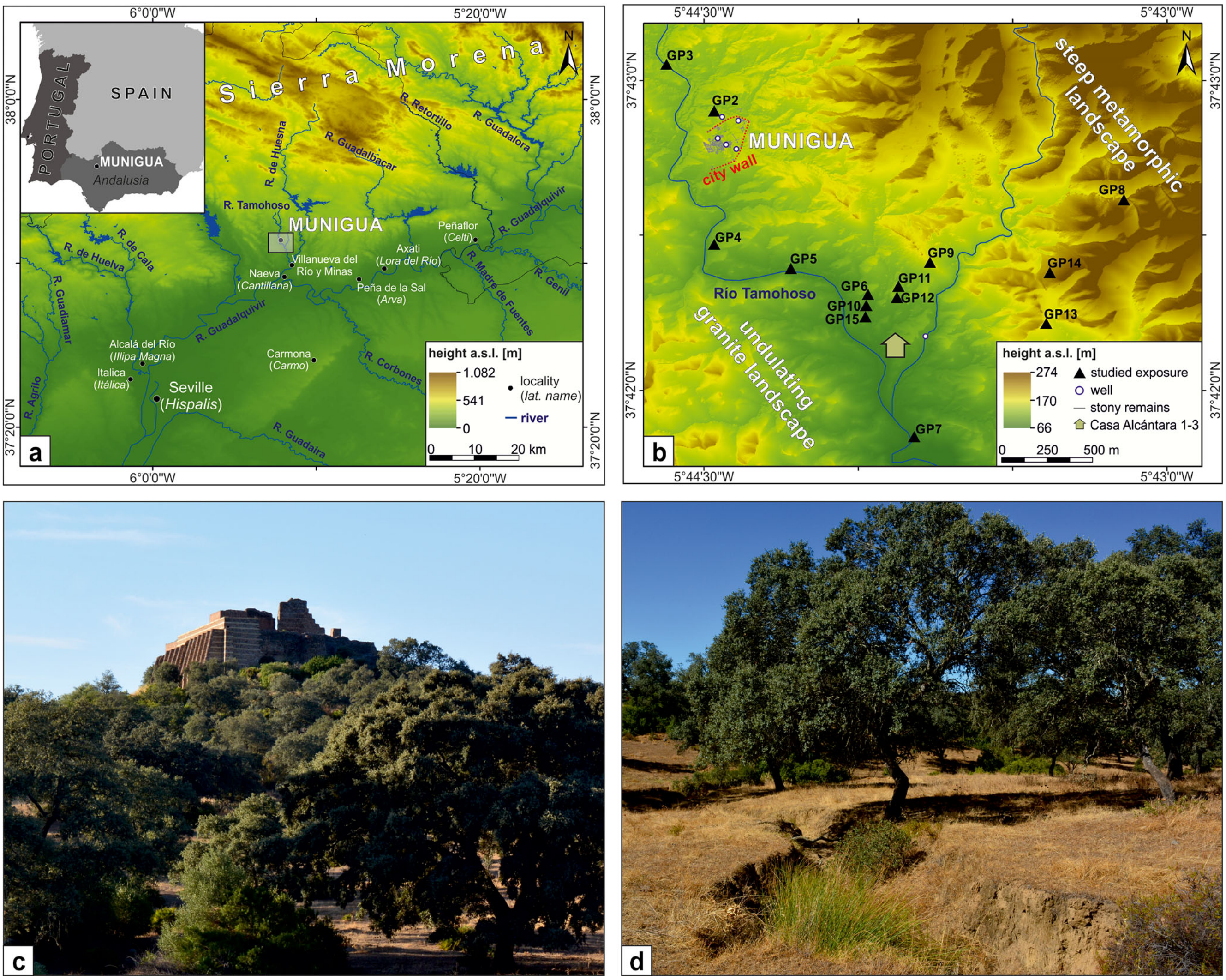

Figure 1. **(a)** Location of Munigua (grey box) in modern SW Spain. **(b)** Investigated soil and sediment exposures within the surroundings of Munigua. GP8, GP13 and GP14 are located in a metamorphic landscape southeast of the city. GP2, GP4, GP6, GP9, GP10, GP11, GP12 and GP15 are in granite areas, and GP3, GP5 and GP7 are within the floodplain of the Tamohoso River. **(c)** South view of Munigua's terrace sanctuary surrounded by scattered forests and grassland. **(d)** Undulated granite landscape with loose holm oak (*Quercus rotundifolia*) and grass understory, typical for the Munigua region. The surface is dissected by a gully about 1.3 m in depth, indicating modern linear soil erosion processes.

The granite landscape is surrounded by mountains consisting of metamorphic Paleozoic rocks, mainly shale, metagreywacke and quartzite (Sanz et al., 1973). This landscape is located in the east of the city and is characterized by much steeper relief, exceeding the altitude of the granite landscape by up to 100 m (Fig. 1b). The main settlement of Munigua with its residential houses and monumental buildings is situated on a morphologically very resistant rhyolite dike (Sanz et al., 1973; Schattner et al., 2005), forming a gently inclined hill that is up to 30 m higher than the adjacent granite landscape (Fig. 1c). Along the Tamohoso River, flowing through the west of Munigua and draining into the Guadalquivir River via the Huesna River (Fig. 1a), a flat alluvial plain has developed in wider valley sections, covering the denudated granite basement (Sanz et al., 1973).

Regional soil investigations in the western sector of the Sierra Morena show poorly developed Regosols, Leptosols and Cambisols. There are frequent erosional features which are often associated with increases in land use over the past two millennia. In consequence, more advanced soil development, leading to the formation of Luvisols or Acrisols, is restricted to small areas (e.g., Paneque and Bellinfante, 1964; Nuñez and Recio, 2002; Recio et al., 2002).

2.2 Archeological background

Munigua is located on the edge of the Iberian Pyrite Belt (IPB), one of the largest and most important volcanogenic polymetallic sulfide districts worldwide, which has been exploited since late prehistoric times (Nocete et al., 2011). The mining importance of Munigua is based in particular on the copper- and iron-bearing ores (e.g., pyrite, chalcopyrite) found near the town (Schattner et al., 2005; Schattner, 2019a).

The oldest archeological finds indicate the presence of humans since the Epipaleolithic period. Especially for the Early (approx. 1750–1550 BCE) and Middle Bronze Age (approx. 1550–1150 BCE), several fortified settlements have been identified and linked to copper mining and the processing and export of mining products to the Guadalquivir valley, a region with limited mineral resources that was highly dependent on continuous supplies from the Sierra Morena mines (Schattner, 2019b). In the 4th century BCE (approx. 360–330 BCE), a small pre-Roman (Turdetan) settlement was founded on the top of the aforementioned rhyolite dike. Traces of urban structure are noticeable from the first half of the 1st century BCE, for instance documented by the construction of thermae (Chic García, 1997; Gutiérrez-Rodríguez et al., 2019; Schattner, 2019b). In 74 CE the settlement was awarded the rank of a municipium after Emperor Vespasian's edict and experienced its heyday. This is revealed by comprehensive urban development and the construction of imposing religious and public buildings like, for example, the terrace sanctuary and the forum. Thus, Munigua possessed a large variety of the typical structural features of a Roman city, although the total size of the settlement was only about 3.8 ha (Ullrich et al., 2007; Schattner, 2019b). Some villas and smaller settlements were established in the surroundings of the city in this period, for example the Roman house complex Casa de Alcántara 1, 2 and 3 located about 1 km southeast of the city (Fig. 1b; Meyer et al., 2007; Schattner, 2019b). At this time, Munigua was part of a dense urban network consisting of some 195 towns and nucleated settlements established in central and western Baetica between approx. 500 BCE and 200 CE (Keay and Earl, 2011).

In the late and post-Roman period (3rd century CE), urban development reached an inflection point expressed by massive depopulation and drastic changes in urban structure. This is thought to be related to seismic activities that caused structural damage to the city, and similar occurrences are also recorded in other Roman cities of the Baetica province (e.g., Rodríguez-Pascua et al., 2011; Giner-Robles et al., 2016; Ruiz-Bueno, 2017). Smaller population groups retreated to the hills in the surroundings where there are traces of a human presence until the end of the 4th century CE (Grünhagen, 1959). The existence of a settlement is documented for Munigua until at least the 7th century CE, even though it is uncertain if ore mining and smelting were still practiced at that time (Eger, 2016). An Arab coin, typical Islamic vessels, oil lamps made of terracotta and burials of Muslim individuals indicate an Islamic settlement on the hill of Munigua from approximately the 8th to the 12th century CE (Teichner, 1998; Eger, 2016). Probably due to its exposed location, Munigua was not reoccupied until its rediscovery in the 16th to 17th century CE (Schattner, 2005). With the industrial expansion of carboniferous coal extraction in the nearby city of Villanueva del Río y Minas (Fig. 1a), regional population density and land use intensity (especially grazing) massively increased during the 19th and 20th centuries CE (Tomás García, 1991).

3 Methods

3.1 Field methods

A total of 14 representative exposures were selected for field investigations: three sites with metamorphic lithology (GP8, GP13 and GP14), eight sites in granite areas (GP2, GP4, GP6, GP9, GP10, GP11, GP12 and GP15) and three floodplain sites (GP3, GP5 and GP7; Fig. 1b). Taking the local relief conditions into account, the soil profiles were arranged in a catenary manner along hillslopes (Semmel, 1977; Evans and Hartemink, 2014; Borden et al., 2020).

Macroscale features were subsequently described by following the German soil mapping instructions (Ad-hoc-AG Boden, 2005). Identified soil horizons were designated according to Jahn et al. (2006) and Zádorová and Penížek (2018). Soil classifications were conducted according to the IUSS Working Group WRB (2015). An exception was made only for colluvium or colluvial deposits, which were used as geoarchives documenting human-induced soil erosion (Dotterweich, 2008; Kittel, 2014), following the definition by Leopold and Völkel (2007, p. 134). Accordingly, colluvium and colluvial deposits are defined as "sediments deposited due to anthropogenic-induced soil erosion, caused by settling, clearing, mining, grazing, and/or farming." According to Zádorová and Penížek (2018) the soil horizon symbol "M" (*migrare* [lat.]; Ad-hoc-AG Boden, 2005) was added, and multiple layers of colluvial deposits within a profile were separated by using suffix numbers, in which the number 1 was always given to the uppermost colluvium. If the overall thickness of colluvial deposits exceeded 50 cm, the soil type was classified as Colluvisol. Otherwise, the term "colluvic" was used as a prefixed qualifier.

In contrast, slope sediments that were mainly mobilized and relocated by natural erosion were classified as slope deposits. Field diagnostic properties have been used to separate colluvial and slope deposits. Slope deposits dominated by properties from the geological subsurface show a denser packing and do not contain anthropogenic remains. In contrast colluvial deposits frequently show a comparable loose packing and anthropogenic remains like pottery shards, slag fragments and bricks.

3.2 Laboratory methods

A total of 57 samples were taken from 10 of the 14 profiles studied in the field and were subjected to further laboratory treatment (Table S1 in the Supplement). Prior to physico-chemical analyses, samples were air dried and the fine-earth fraction (≤ 2.0 mm) was sieved. Grain size analyses utilized a combination of the Köhn pipette method (silt and clay fractions) and wet sieving (sand fractions) (DIN ISO 11277, 2002). Samples were pre-treated with 0.4 M sodium pyrophosphate ($Na_4P_2O_7$) overnight and afterwards shaken for 6 h. When soil organic matter (SOM) exceeded 2.0 %, the samples were additionally pre-treated with 17.5 % hydrogen peroxide (H_2O_2). The sand fraction was divided into coarse (2000–630 µm), medium (630–200 µm) and fine (200–63 µm) sand by wet sieving using the vibratory sieve shaker AS 200 (Retsch). Coarse silt (63–20 µm), medium silt (20–6.3 µm), fine silt (6.3–2.0 µm) and clay (< 2.0 µm) were identified by the Köhn pipette method using the SEDIMAT 4–12 (UGT).

Total carbon (C_t) and total nitrogen (N_t) were measured on milled samples using the CN analyzer vario EL cube (Elementar). Due to the absence of inorganic carbon, as proven in pretests using hydrochloric acid (10 %), the C_t is equal to the amount of total organic carbon (TOC). TOC values were multiplied by 1.724 (Amelung et al., 2018) in order to obtain contents of soil organic matter (SOM). C / N ratio was calculated by dividing TOC by N_t (Blume et al., 2011).

The plant-available macronutrients magnesium (Mg), calcium (Ca), sodium (Na) and potassium (K) were extracted with 1 M NH_4NO_3 and quantified by an atomic absorption spectrophotometer (Perkin Elmer PinAAcle 900T). Additionally, K_2O and P_2O_5 were measured according to the calcium–acetate–lactate method (Schüller, 1969) using a Spectronic C301 spectrophotometer (Milton Roy). The pH value was measured in a 1 : 2.5 suspension in 0.01 M $CaCl_2$ (Jahn et al., 2006).

The content of total phosphorus (P_t), used in archeology as an important indicator for human activity in agricultural and pre-agricultural societies (e.g., Holliday and Gartner, 2007; Weihrauch, 2018), was determined by colorimetry with the spectrophotometer C21 (Milton Roy) following ignition and then acid extraction based on Bleck (1965).

The soil agro-potential of the site was evaluated according to standard procedures (Blume et al., 2011; Amelung et al., 2018), including assessment of potential rootability, the available water-storage capacity and the nutrient budget within the uppermost 1 m. All evaluations consider the total particle-size fractions (coarse and fine-earth fractions) and further take account of the field-estimated bulk density (Ad-hoc-AG Boden, 2005). For stony soils and sediments, deductions have to be made from the available soil volume, which influences the nutrient budget and the water-storage capacity accordingly (Blume et al., 2011). The evaluation was based on a five-step classification including the following classes: (1) very favorable/very good, (2) favorable/good, (3) moderate, (4) unfavorable/weak and (5) very unfavorable/very weak. Blume et al. (2011) suggested the following values for the classification of potential rootability: (1) > 120 cm, (2) 70 to 120 cm, (3) 30 to < 70 cm, (4) 15 to < 30 cm and (5) < 15 cm. The available water-storage capacity was assessed according to the following values: (1) $> 200\,\mathrm{L\,m^{-2}}$, (2) 140 to $200\,\mathrm{L\,m^{-2}}$, (3) 90 to $< 140\,\mathrm{L\,m^{-2}}$, (4) 50 to $< 90\,\mathrm{L\,m^{-2}}$ and (5) $< 50\,\mathrm{L\,m^{-2}}$. The classification of the nutrient budget was mainly derived from the contents of macronutrients (Mg, Ca, Na and K), grain size distribution, SOM content and pH values, which primarily determine the base saturation and effective cation exchange capacity (Ad-hoc-AG Boden, 2005; Blume et al., 2011). Possible deficiencies in nitrogen and calcium-lactate-soluble phosphorus (P_2O_5) and potassium (K_2O) contents were additionally checked and included in the assessment of the nutrient budget. For GP5, GP9, GP10 and GP14, the evaluation is based on field assessments and conclusions drawn by analogy, considering comparable nearby profiles from this study.

Phytolith extraction followed the procedures outlined by Albert et al. (1999). Approximately 1 g of air-dried sample (< 2 mm) was treated with 3 N HCl, 3 N HNO_3 and H_2O_2 to remove carbonates, phosphates and organic material. The mineral components of the samples were separated according to their densities using $\sim 2.4\,\mathrm{g\,mL^{-1}}$ sodium polytungstate solution [$Na_6(H_2W_{12}O_{40})H_2O$]. Slides were prepared by weighing out about 1 mg of sample onto a microscope slide and mounting with Entellan new (Merck). Counting was performed using a KERN OBE-114 microscope at 400× magnification. A total of 200 phytoliths were identified and counted in each sample wherever possible. Unidentifiable phytoliths were counted and recorded as weathered morphotypes. Images of selected phytoliths were recorded using a KERN ODC 825 microscope camera. The numbers of phytoliths per gram of sample were estimated by relating the phytolith amounts and weights of the processed sample material to the initial sample weights. The morphological identification of phytoliths was based on standard literature (Twiss et al., 1969; Brown, 1984; Mulholland and Rapp, 1992; Piperno, 2006), as well as on modern plant reference collections from the Mediterranean area (Albert, 2000; Albert and Weiner, 2001; Tsartsidou et al., 2007; Portillo et al., 2014; Meister et al., 2017). The International Code for Phytolith Nomenclature was followed where possible (Madella et al., 2005; Neumann et al., 2019).

Radiocarbon dating was carried out on 17 charcoal samples at the Curt-Engelhorn-Centre of Archaeometry (MAMS) and at Beta Analytic (BETA) using the accelerator mass spectrometer (AMS) technique (e.g., Hajdas, 2008). Charcoal samples were pretreated using the acid–alkali–acid method to remove contamination by carbonates and humic acids (de Vries and Barendsen, 1954). Conventional ^{14}C ages (BP) were calibrated using the IntCal 13 calibration set (Reimer et al., 2013).

4 Results

4.1 Granite landscape

4.1.1 Casa de Alcántara house complex

A granite area southeast of urban Munigua was chosen for a detailed survey (Fig. 1b) since a Roman rural house complex known as Casa de Alcántara 1–3 and a nearby ancient well document the presence of Roman settlers who may have worked as farmers in ancient times (Meyer et al., 2007; Schattner, 2019b). The schematic catena (Fig. 2) shows shallow Leptosols (GP11) and moderately deep Cambisols (GP15) in upper slope positions and flatter ridge areas. Soil erosion has led to a shallowing of these profiles and frequently to the deposition of a thin colluvial cover (Fig. 2). Here, potential rootability, water-storage capacity and nutrient budget is very weak to weak (Fig. 3, Table S1).

At the transition from upper to middle slopes Cambisols (GP9) and Colluvisols (GP12, GP6, GP10 and GP4) were mapped. They are deeper, favoring potential rootability and improving water-storage capacity (Fig. 3). Essential nutrients (Mg, Ca, Na, K, P_2O_5 and K_2O) are available (Table S1) although with relatively low values of P_2O_5 (median = 5.8 mg kg^{-1}, SD = 10.1, $n = 18$). The pH values range from 4.5 to 6.1 (median = 5.5, SD = 0.5, $n = 18$) and can accordingly be predominantly classified as slightly acidic (Table S1). The SOM (median = 0.5 %, SD = 1.4, $n = 18$) and N_t contents (median = 0.04 %, SD = 0.06, $n = 18$) decrease with depth and are generally low. In sum the nutrient budget of Cambisols and Colluvisols in the surroundings of the Roman house complex Casa de Alcántara 1–3 is moderate (Fig. 3).

For the temporal reconstruction of soil erosion processes around the Casa de Alcántara house complex, seven charcoal samples from three colluvial sequences (GP4, GP10 and GP12) were ^{14}C-dated (Fig. 2, Table 1). The results indicate prehistoric soil erosion phases between around 4063 ± 82 and 3796 ± 76 cal BP (Copper Age to Early Bronze Age), as well as around 2601 ± 115 cal BP (Early Iron Age). Four additional ^{14}C datings from GP10 and GP4 provided ages of 1424 ± 96, 1094 ± 155, 606 ± 51 and 421 ± 88 cal BP.

4.1.2 Profile GP2

Profile GP2 is located less than 100 m north of the fortified urban area of the Muniguan granite landscape (Fig. 1b) in the immediate surroundings of a small, temporary stream and an ancient well (Fig. 4a).

The profile was excavated down to granite-derived slope sediments (3BC horizon) present below approximately 64 cm. The uppermost 23 cm are formed by loosely deposited yellow-brown fluvial sediments (Fig. 4b). Missing pedogenic features and an oral report of a recent flood of the above-mentioned adjacent stream suggest that the sediments were deposited relatively recently. The texture is sandy (sand contents between 61 % and 93 %, Fig. 4), and the fluvial deposits mainly show moderate gravel contents (Table S1). Sharply defined, finer-grained substrate follows below 23 cm. This can be further subdivided into an upper (2MAhub, 23–46 cm) and a lower (2Mub, 46–64 cm) horizon by grain size and minor differences in color (10YR 3/3 vs. 2.5YR 3/3). Both horizons contain numerous pottery shards, slag fragments and bricks, all of which can be assigned to the Roman inventory and thus allow these horizons to be archeologically dated to the Roman period (terminus post quem). A ^{14}C-dated charcoal taken at a depth of 56 cm revealed a Roman age of 2147 ± 147 cal BP (Fig. 4b, Table 1). A second piece of charcoal from a depth of 38 cm could not be dated due to its young age (after 1950). The lowermost profile section (64–70 cm) is formed by yellow-brown slope deposits (3BC horizon) showing a loamy texture and does not contain archeological remains.

Measured pH values are moderately acidic and vary slightly from 5.8 to 5.4 (Fig. 4, Table S1). SOM values are between 0.4 % and 2.3 %, and, interestingly, increased SOM content (1.7 %) is found in the lower section of the Roman horizon (2Mub horizon; 46–64 cm). C / N ratios vary between 10.75 (MAhb2 horizon) and 12.63 (2Mub horizon). Calcium-lactate-soluble phosphorus (P_2O_5) and total phosphorus (P_t) show a first maximum of 108 mg kg^{-1} and 1.895 mg kg^{-1}, respectively, in the uppermost sample (MAh horizon; 0–7 cm), decreasing downwards. However, this trend reverses, and, especially within the lower section of the Roman horizon (2Mub horizon; 46–64 cm), a second maximum is noticeable (123 and 2786 mg kg^{-1}). The same holds true for the macro-nutrient elements Mg, Ca, Na, K and K_2O, which are generally increased in the lower part of the Roman horizon and the lowermost slope deposits (Fig. 4, Table S1). Based on diagnostic criteria (color, determine base saturation, SOM, P_2O_5, thickness) the Roman horizon was classified as a hortic horizon (IUSS Working Group WRB, 2015). In terms of soil agro-potential this site is categorized as good to moderate (Fig. 3).

The amounts of phytoliths in the samples vary considerably, ranging from 6483 phytoliths per gram of sediment to 323 253 phytoliths per gram of sediment, while the highest concentrations were reached in the Roman hortic horizons (Fig. 6a; Table S2.2). A total of 33 different phytolith morphotypes were identified in the six samples studied (Fig. 5, Table S2.1). Overall, the samples are similar in their morphotype assemblages (Fig. 6b, Table S2.2). While about 26.8 % (SD = 3.8, $n = 6$) of the phytoliths were not morphologically identifiable, grass phytoliths, occurring at an average rate of 50.8 % (SD = 4.6, $n = 6$), were the most common group. The amounts of dicotyledonous leaf, wood and bark phytoliths are relatively low, with an average value of 17.1 % (SD = 4.8, $n = 6$). *Parallelepipedal blocky* phytoliths, one of the most common wood/bark morphotypes, for instance, were observed at an average concentration of 10.2 % (SD = 5.9, $n = 6$). *Spheroid echinate* phytoliths, commonly

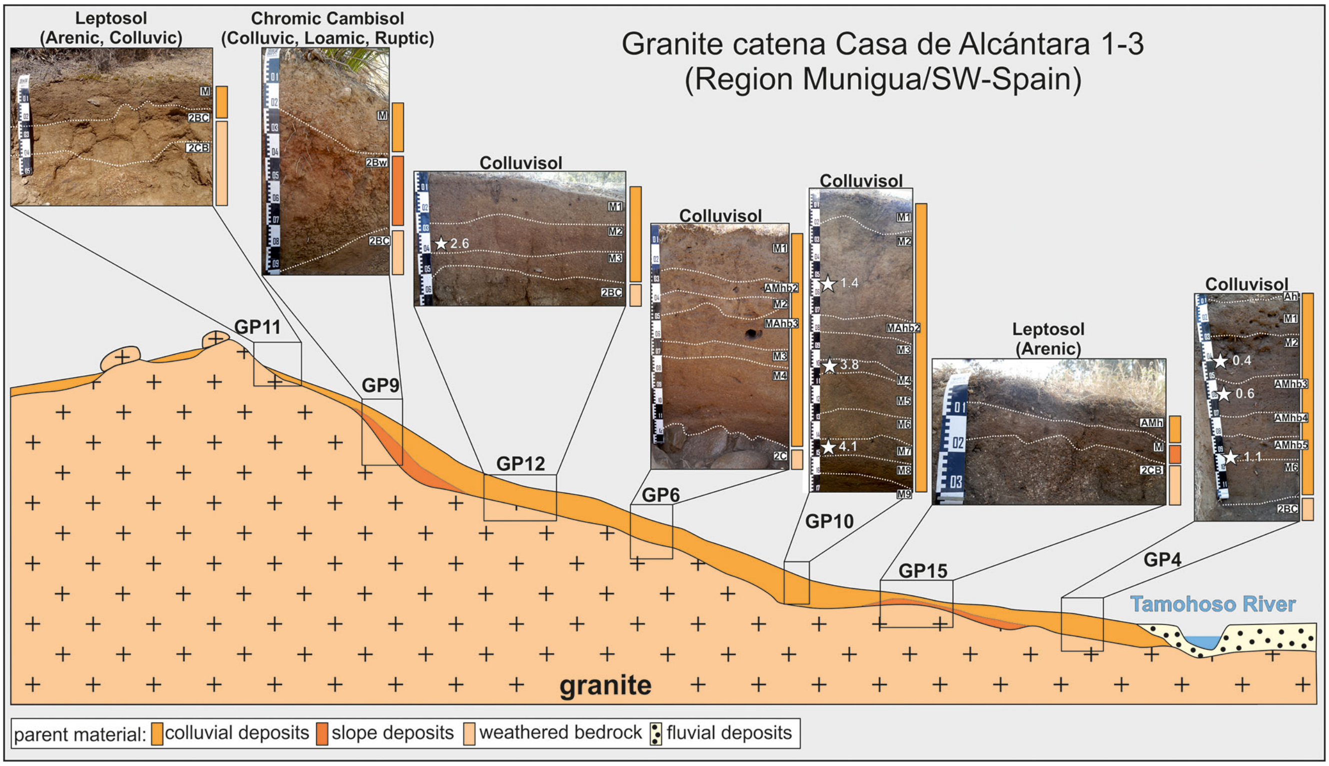

Figure 2. Schematic soil catena for a granite landscape in the surroundings of the Roman house complex Casa de Alcántara 1–3. Soil horizon designations are shown in white boxes. Physico-chemical results are summarized in Table S1. White stars within the photographs indicate the positions of ^{14}C-dated charcoal samples (the calibrated ages are given in ka). The shown catena is exaggerated for illustration purposes.

Table 1. Results of radiocarbon dating in the Munigua region.

Site	Depth (cm)	Facies	Lab. no.	Dated material	^{14}C age BP	Calibrated ^{14}C age BP (2σ range)	δ^{13}C (‰)
GP2	38	hortic	MAMS 43603	charcoal	modern	modern	−31.2
GP2	56	hortic	BETA 551526	charcoal	2120 ± 30	2147 ± 147	−26.0
GP3	44	fluvic	MAMS 43604	charcoal	165 ± 21	196 ± 89	−25.7
GP3	84	fluvic	MAMS 43605	charcoal	121 ± 20	141 ± 128	−19.0
GP3	112	fluvic	MAMS 43606	charcoal	126 ± 21	140 ± 130	−22.8
GP4	40	colluvic	MAMS 43607	charcoal	396 ± 21	421 ± 88	−28.2
GP4	58	colluvic	MAMS 43608	charcoal	622 ± 19	606 ± 51	−25.1
GP4	98	colluvic	MAMS 43609	charcoal	1175 ± 22	1094 ± 84	−32.4
GP7	50	fluvic	MAMS 43610	charcoal	163 ± 18	159 ± 159	−19.4
GP7	115	fluvic	MAMS 43611	charcoal	243 ± 20	157 ± 156	−29.3
GP7	140	fluvic	MAMS 43612	charcoal	172 ± 18	155 ± 155	−24.6
GP7	169	fluvic	MAMS 43613	charcoal	264 ± 20	290 ± 134	−29.6
GP7	190	fluvic	MAMS 43614	charcoal	206 ± 18	157 ± 157	−18.8
GP10	53	colluvic	BETA 562782	charcoal	1510 ± 30	1424 ± 96	−24.3
GP10	100	colluvic	MAMS 43615	charcoal	3525 ± 21	3796 ± 76	−26.8
GP10	145	colluvic	MAMS 43616	charcoal	3710 ± 22	4063 ± 82	−25.8
GP12	39	colluvic	MAMS 43617	charcoal	2481 ± 20	2601 ± 115	−26.4

Geomorphological unit	Geomorphic position	Site	Site evaluation		
			available water-storage capacity	nutrient budget	potential rootability
Granite landscape	Upper slope	GP11	--	-	-
		GP9	+	o	+
	Middle slope	GP12	-	o	o
		GP6	+	o	++
	Lower slope	GP15	--	-	--
		GP10	+	o	++
		GP4	+	o	++
	Plain	GP2	+	o	+
Metamorphic landscape	Upper slope	GP13	--	--	--
	Middle slope	GP14	-	-	-
	Lower slope	GP8	-	-	o
Floodplain	Plain	GP3	++	o	++
		GP5	o	-	+
		GP7	++	o	++

very good	good	moderate	weak	very weak
++	+	o	-	--
very favorable	favorable	moderate	unfavorable	very unfavorable

Figure 3. Site evaluation of investigated soil and sediment exposures in the Munigua area, subdivided according to the studied geological and geomorphological units.

associated with palms (Arecaceae), reached an average concentration of 5.3 % (SD = 4.2, $n = 6$).

The short cell morphologies of the grass phytoliths reveal them to belong mostly to the C3 Pooid subfamily, with *rondel and trapezoid short cells* commonly produced in the leaves, stems and inflorescences of Pooids. Concentrations between 59.1 % in the uppermost sample and 32.7 % in the upper part of the Roman hortic horizon were found (mean = 45.6 %, SD = 9.3, $n = 6$; Fig. 6c; Table S2.2). The proportion of inflorescence phytoliths varies slightly around an average concentration of 15.2 % (SD = 6.2, $n = 6$). The concentrations of phytoliths from grass stems and leaves are higher in the lower profile section (23–70 cm), reaching a maximum of 50.8 % in the upper part of the Roman hortic horizon (mean = 39.2 %, SD = 10.1, $n = 6$). Due to the absence of multicellular phytoliths in the samples, however, it was not possible to identify the type of grasses.

4.2 Metamorphic landscape

The pedo-morphological conditions were also investigated for three sites (GP8, GP14 and GP13) within the metamorphic landscape, located in the southeast of Munigua (Fig. 1b). Here, the lithology is formed by quartzitic metagreywacke, and the soils were classified as Leptosols or Cambisols (Fig. 7). All observed soils in this metamorphic landscape unit are conspicuously shallow and stony (Table S1). Potential rootability, available water-storage capacity and nutrient budget are weak to very weak (Fig. 3). No geomorphological or pedological evidence of prehistoric or historic land use (e.g., colluvial deposits) is preserved in the observed metamorphic landscape so far.

4.3 Tamohoso River floodplain

The investigated fluvial sequence GP3 is located about 500 m upstream of Munigua's urban infrastructure, whereas GP7 is located about 600 m downstream of the Casa de Alcántara

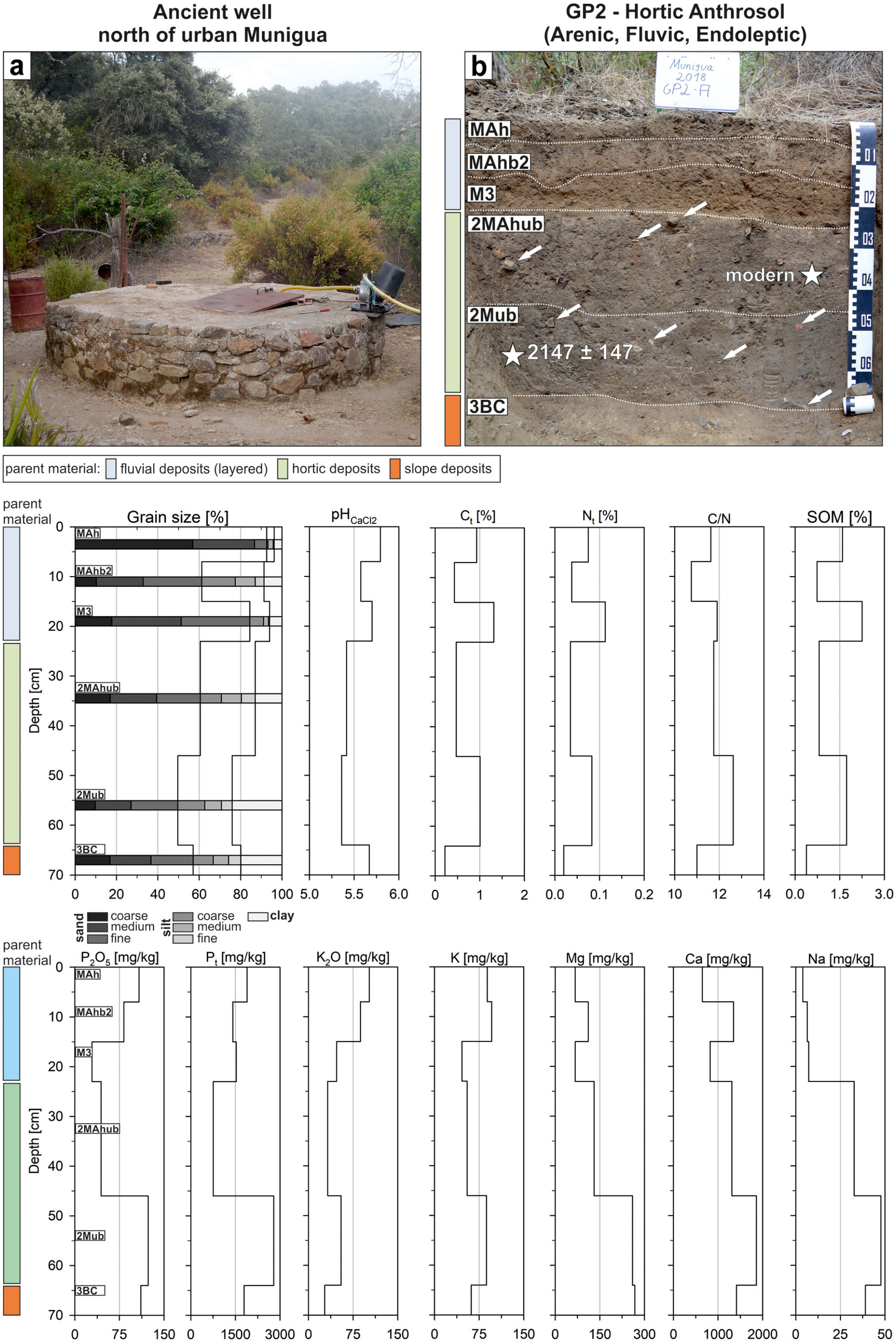

Figure 4. **(a)** Ancient well located outside of Munigua's city wall (Fig. 1b). **(b)** Excavated hortic Anthrosol (arenic, fluvic, endoleptic). Identified parent material is marked on the left of the profile photo. Soil horizon designations are shown in white boxes. White arrows indicate some larger Roman artifacts (e.g., ceramics, brick). Sampling positions and calibrated ^{14}C ages (cal BP) are marked with white stars. Lower section: laboratory results for the hortic Anthrosol (arenic, fluvic, endoleptic).

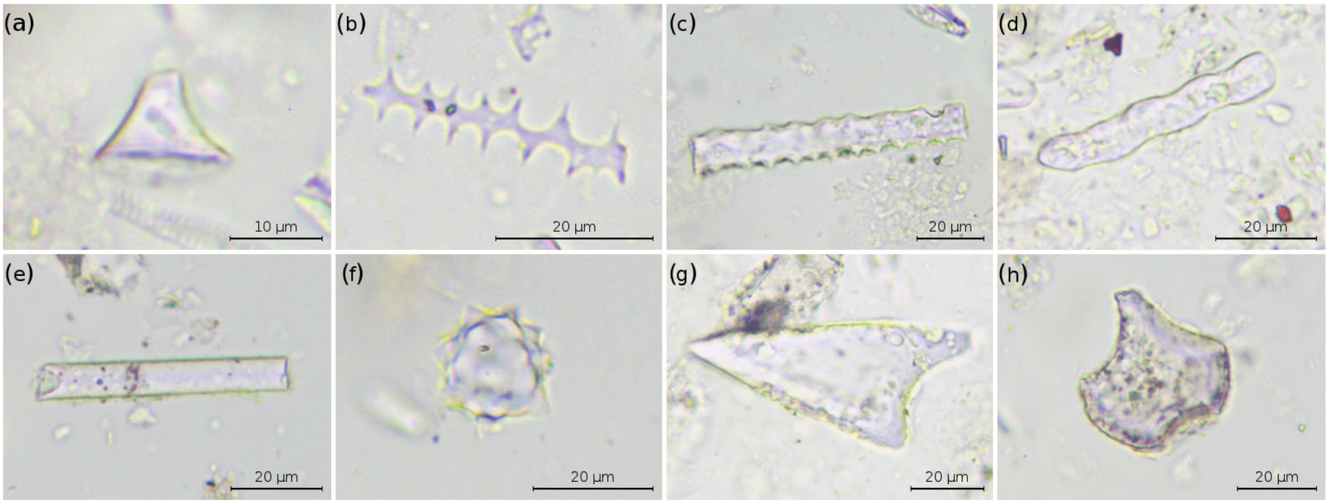

Figure 5. Photomicrographs of selected phytolith morphotypes identified in the GP2 samples. The photographs were taken at 400× magnification. **(a)** Short cell rondel; **(b)** elongate dendritic; **(c)** elongate dentate; **(d)** elongate wavy; **(e)** elongate entire; **(f)** spheroid echinate; **(g)** prickle; **(h)** bulliform.

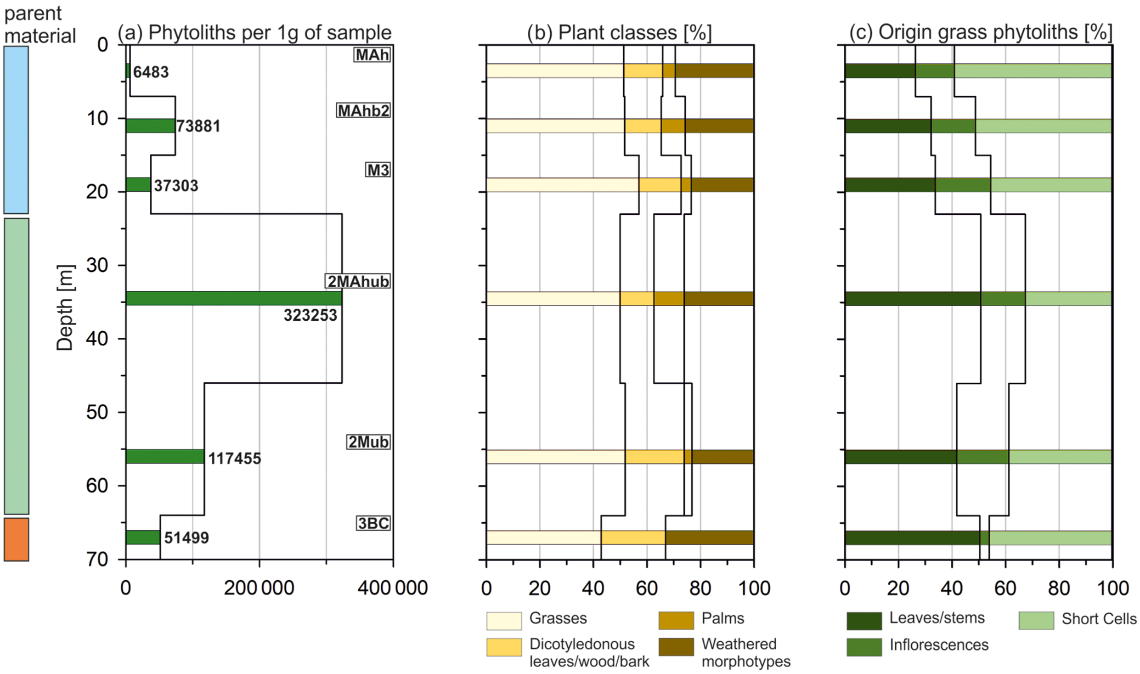

Figure 6. Results of phytolith analyses conducted at site GP2. Identified parent material is marked to the left of the graph according to Fig. 4b. Soil horizon designations are shown in white boxes. **(a)** Phytolith concentrations, **(b)** relative abundances of phytoliths from different plant classes and **(c)** anatomical origin of grass phytoliths.

house complex (Fig. 1b). GP5 is situated between these two sites.

GP3 was excavated to a depth of 145 cm below the surface (Fig. 8). The base of the profile shows coarse-clastic riverbed deposits, classified as moderately rounded gravels or moderately rounded blocks. Upwards, this is followed by alternately deposited, predominantly cross-bedded sands (74 %–84 % sand), which are occasionally interstratified by finer-grained and in particular silty deposits (Figs. 8 and 9). The profile contains charcoal pieces of different sizes in almost all sections, which could indicate the former presence of activities involving fire in the catchment area.

GP7 was excavated to a depth of 250 cm (Fig. 8). Below 220 cm, weakly weathered granite is present and forms

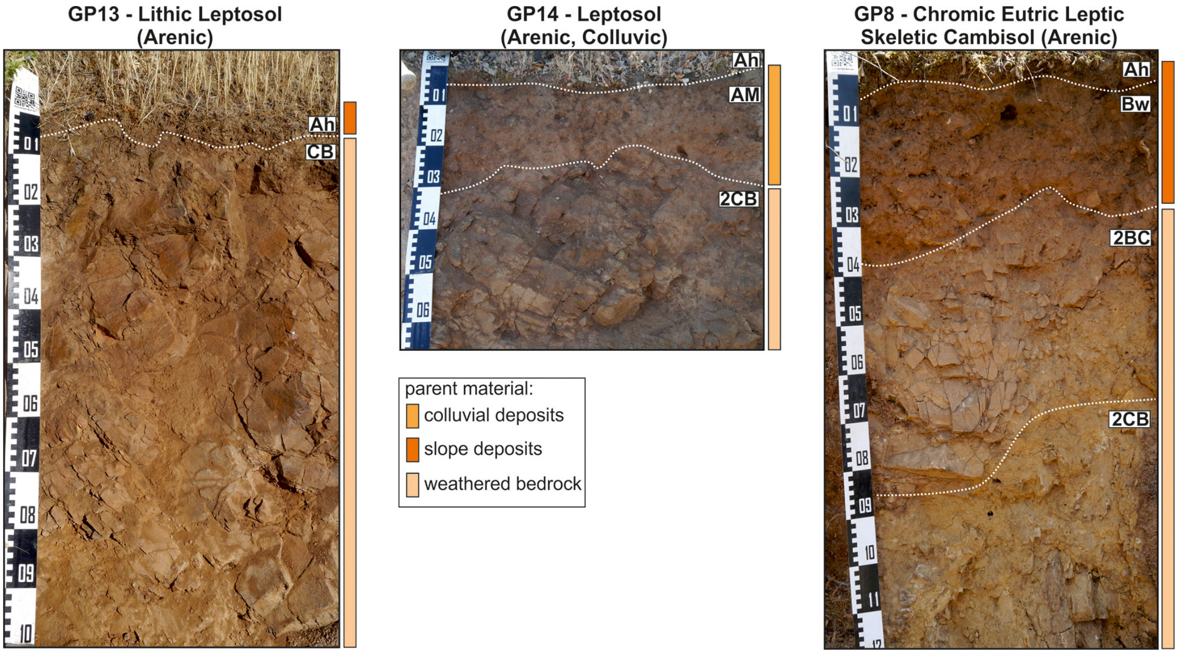

Figure 7. Investigated soil sequences in a metamorphic landscape southeast of Munigua. Soil horizon designations are shown in white boxes. Physico-chemical laboratory results are summarized in Table S1.

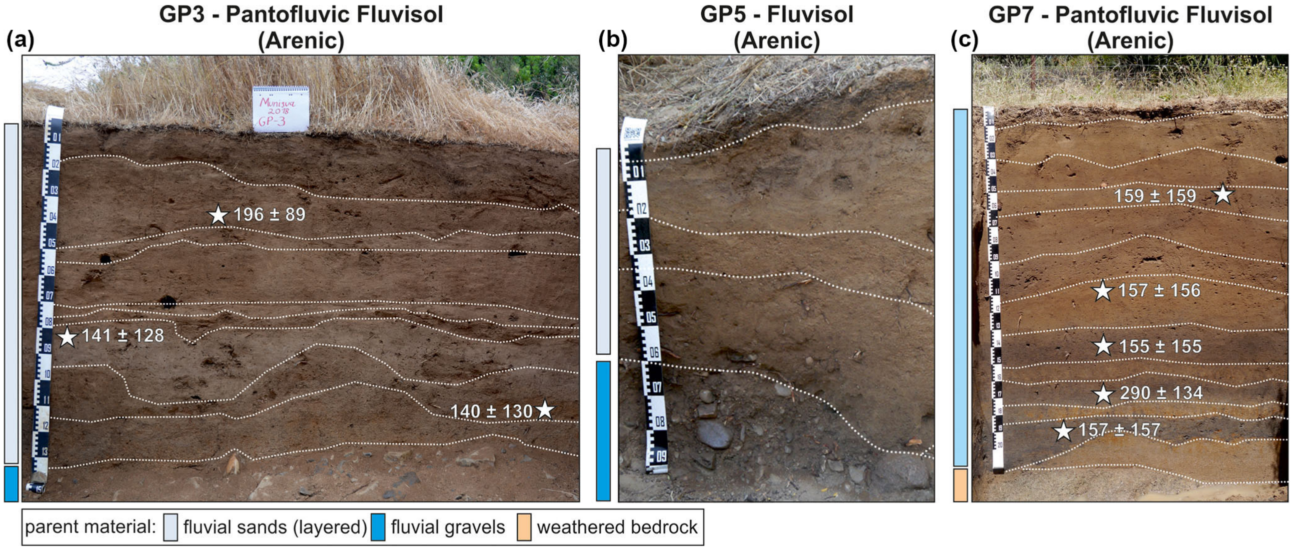

Figure 8. Profile photos of fluvial sequences GP3 **(a)**, GP5 **(b)** and GP7 **(c)**. Identified parent material is marked on the left of the profile photos. Sampling positions for dated charcoal samples and calibrated ^{14}C ages (cal BP) are marked with white stars.

the basis of the profile. Similar to profile GP3, predominantly charcoal-bearing, sand-dominated sediments (59 %–96 % sand) were deposited above 220 cm. Humic sections (Ahb horizons) are preserved at depths of 135–150, 160–175 and 185–200 cm below the surface (Figs. 8 and 10, Table S1).

GP5 is rather shallow and less than 90 cm deep (Fig. 8). Similar to GP3 and GP7, the stratigraphy shows charcoal-bearing brown sands (10YR 3/2 to 4/3) in its upper section. They are relatively loose and overlie rounded gravels and blocks exposed below 60 cm. Due to its stratigraphical similarity to GP3 and GP7, as well as comparably low depth, GP5 was only investigated in the field and not sampled for further laboratory analysis.

Due to the thickness of the fluvial deposits (Fluvisols), potential rootability for plants and available water-storage capacity are very good at sites GP3 and GP7 and are respectively moderate to good at site GP5 (Fig. 3). The nutrient situation of GP3 and GP7 is evaluated as moderate (Ta-

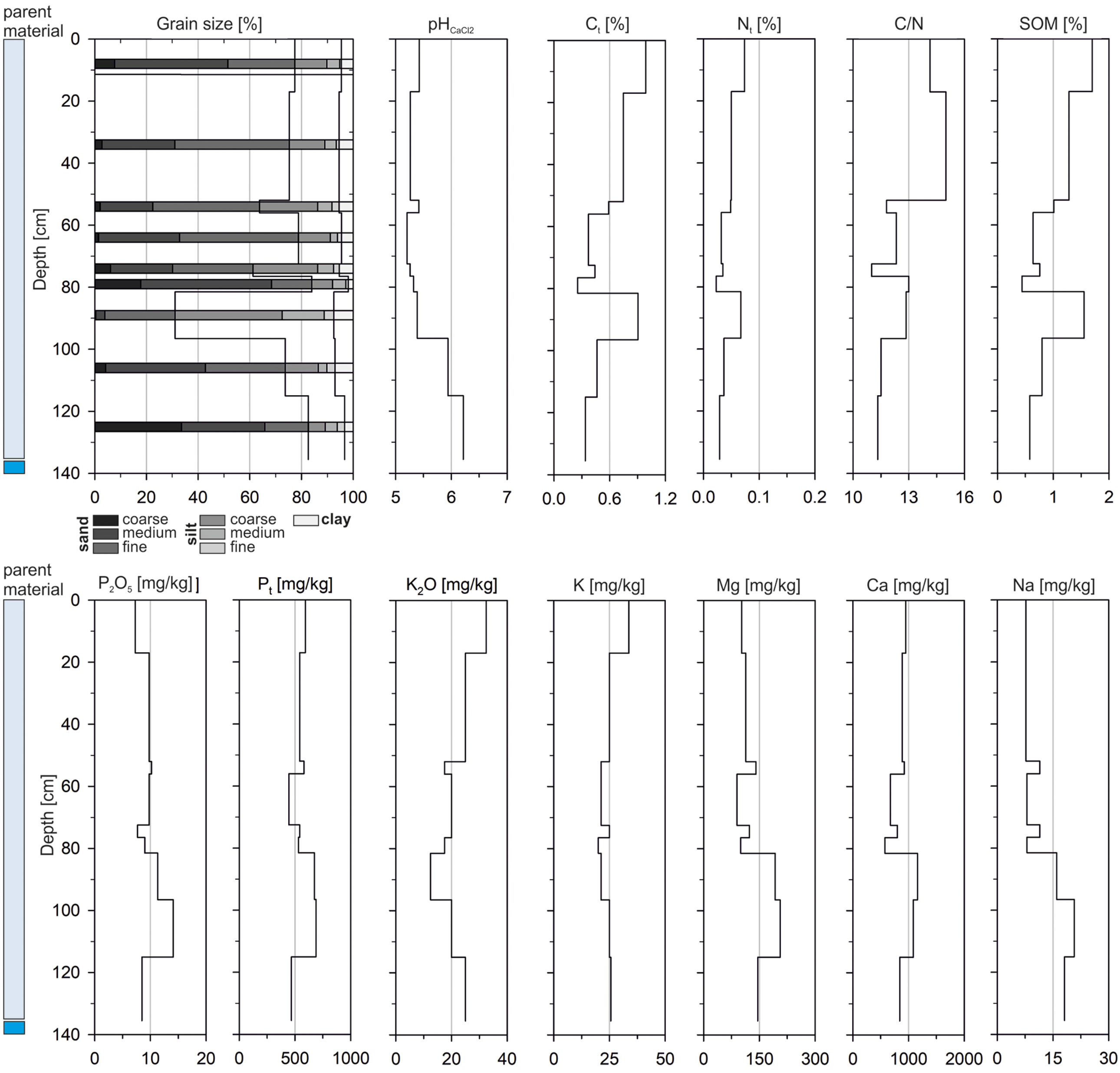

Figure 9. Laboratory results for the pantofluvic Fluvisols (Arenic) at floodplain site GP3. Identified parent material is marked according to Fig. 8.

ble S1, Figs. 9 and 10), and once more only P_2O_5 shows relatively low values (median = 7.5 mg kg^{-1}, SD = 9.4, $n = 22$). The pH values range between 4.9 and 6.5 (median = 5.5, SD = 0.5, $n = 22$). N_t content is low again (median = 0.05 %, SD = 0.13, $n = 22$), and SOM shows average values of 0.83 % (SD = 1.1, $n = 22$).

The ^{14}C dating results from GP3 and GP7 show modern ages for all eight charcoal samples with an oldest age of 290 ± 134 cal BP (Fig. 8, Table 1).

5 Discussion

5.1 Land use and its potential in granite landscape of the Munigua region

Catenary soil mapping in the surroundings of the Roman house complex Casa de Alcántara 1–3 indicates a heterogeneous soil pattern, with soil types clearly depending on geomorphological position (Fig. 2). Most likely this is due to modifications by past soil erosion and related colluviation, leading to profile shallowing in upper slope sites and the deposition of a colluvial cover in middle to lower slope

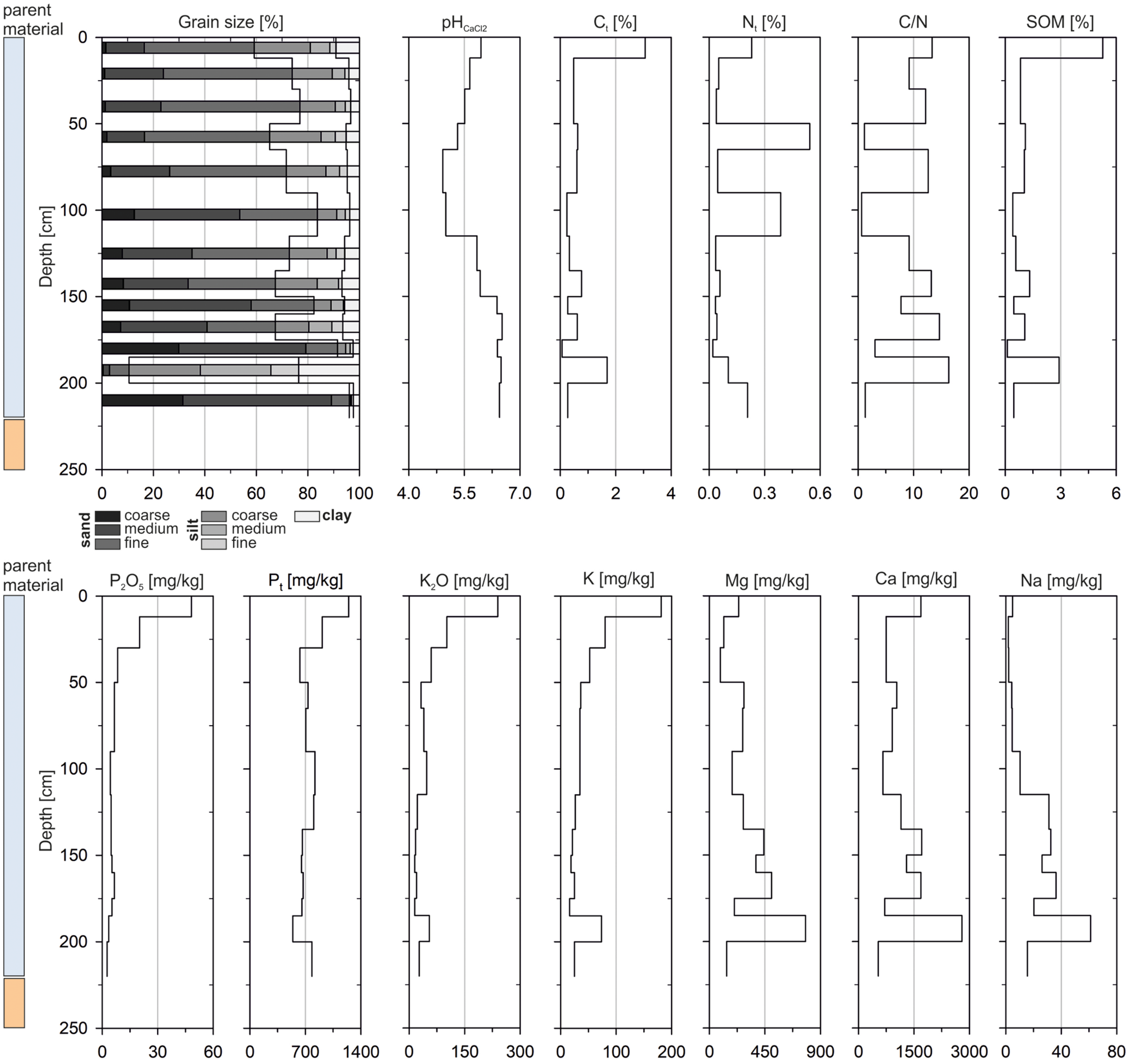

Figure 10. Laboratory results for the pantofluvic Fluvisols (Arenic) at floodplain site GP7. Identified parent material is marked according to Fig. 8.

positions and depressions. Frequent occurrences of embedded bricks, shards and charcoal indicate that mobilization and translocation processes were mainly triggered by anthropogenic factors like settling, clearing and/or local agriculture (Leopold and Völkel, 2007). This is in agreement with other investigations in the western Sierra Morena that highlight erosive processes triggered by accelerated human impact (e.g., Recio Espejo et al., 2002). The ^{14}C dating results of this pilot study (Fig. 2, Table 1) provide evidence for past soil erosion phases in pre-Roman, late Roman and post-Roman times and therefore strongly suggest that farming has recurred within the investigated granite landscape and has been a typical land use strategy over very long periods. This observation chronologically reasonably matches with recent investigations in Spanish river catchments. May et al. (2021) reported on increased fluvial and alluvial deposition during Roman or post-Roman times (after approx. 2100 cal BP) and suggest that this is related to a high anthropogenic impact on the local landscape. Similarly, Faust and Wolf (2017) describe a supply of top soil material to many western Mediterranean floodplains that started about 2.2 kyr ago and seems to be related to anthropogenic influences (e.g., agriculture) especially in the lowest-order catchments. The achieved results of this study support this assumption and therefore refer to larger-scale erosion patterns in the entire region. Along with the in situ evidence for soil erosion triggered by anthropogenic land use activities, this finding furthermore indicates the basic suitability of the granite-derived soils for agricultural purposes. The unexpected fact that no colluvia from Munigua's heyday have been found so far might be related to the limited number of age datings, the applied dating technique and the number of locations investigated in this pilot project. In our opinion it does not necessarily mean that there was no colluviation during this period, and further research is needed for a conclusive assessment on soil erosion and colluviation in the region.

The heterogeneous soil inventory revealed variations in present-day soil agro-potential in the surroundings of Casa de Alcántara 1–3. Truncated Leptosols to moderately deep Cambisols in upper slope positions and flatter ridge areas (Fig. 2) show unfavorable to very unfavorable conditions today (Fig. 3). In particular, the low soil depths of these sites and the sandy soil texture (Table S1) have an unfavorable effect on potential rootability, available water-storage capacity and the nutrient budget. The overall soil agro-potential of these sites can be evaluated as unfavorable to very unfavorable (Fig. 3, Table S1).

In contrast, currently moderate to good soil potential exists in middle to lower slope positions, where multi-layered colluvial deposits almost ubiquitously cover the weathered granite (Fig. 3). Here the potential rootability for cultivated plants ranges from moderate to very good due to increased soil depths at these sites. This also favors available water-storage capacity, which can be evaluated as moderate to good. The nutrient situation is mostly reasonable and would certainly allow the cultivation of agricultural crops. Consequently, the cultivation of cereals, such as emmer, barley or millet, which were part of the Roman diet (Flach, 1990; Gerlach, 2001), as well as vegetables, should definitely be possible at many sites within the regional granite landscape. This assumption is supported by the fact that even today, wild oats grow in this landscape and could also have been cultivated as green fodder or hay in Roman times, if not necessarily for human consumption.

Our observations in the surroundings of the Roman house complex Casa de Alcántara 1–3 therefore do not confirm the aforementioned assumptions that the regional soil conditions (i) are currently unsuitable for extensive agriculture and (ii) generally speak against ancient agricultural use in the region (Schattner, 2019b). Instead, the multiphase deposition of colluvium over longer periods and the moderate to good soil agro-potential rather support archeological assumptions concerning agricultural production (Peña Cervantes, 2010; Teichner and Peña Cervantes, 2012; Krug, 2018) involving fields and gardens, as well as pastures for small animals and trees in the wider surroundings of the town.

However, a challenging question in this context is the extent to which the characteristics of current soils provide information on past soil potential. Extensive studies from the Mediterranean supply clear evidence for soil degradation and decreased soil productivity due to the long-term history of land use (e.g., Redman, 1999; García-Ruiz, 2010; Bellin et al., 2013; García-Ruiz et al., 2013; Dotterweich, 2013). It follows that various areas may have been more productive during Roman times, especially sites in erosion-prone hillslope positions (GP11, GP15) that were evaluated as unfavorable to very unfavorable for the present day. The actual status assigned to the sites thus underestimates the ancient soil agro-potential. Vice versa, it can be assumed that the soil potential in aggradational locations, like flat hillslope positions or slope depressions, has improved. Here, colluviation has led to increased soil thickness, which generally favors potential rootability and available water-storage capacity. However, the ^{14}C-derived chronology provides evidence that colluviation had already taken place, at least in part, before the Roman period (Fig. 2, Table 1), which is why the ancient soil agro-potential in these locations was probably not significantly different to that of the present day. We therefore argue that the prevailing moderate to good soil potential of the granite landscape around Munigua today probably also pertained for antiquity.

Further robust evidence for Roman agriculture was gained in a granite area close to the urban center of Munigua (Fig. 1b). Since this area is located outside the fortified urban area, the withdrawal of water for possible irrigation or livestock seems likely. Less than 5 m away from a Roman well, an enrichment of SOM, P_2O_5, $P_{t,}$ K_2O and other nutrients (Mg, Ca, Na and K) was detected, especially in the lowermost section of a Roman-dated hortic horizon (Fig. 4, Table S1). We interpret these results as indicating intentional humus or compost fertilization intended to further improve the site and secure yields. In this context, it is assumed that organic, nutrient-enriched waste, settlement residues (e.g., pottery, slag fragments or bricks) and possibly also animal excrements were frequently distributed across the surface after harvesting and mixed into the granitoid slope deposits, leading to the gradual development of the Roman hortic horizon. The lower SOM, phosphate and nutrient contents in the upper part of the hortic horizon (23–46 cm) could be due to multiple causes. On the one hand, the abandonment of the site and the associated lack of phosphate and organically enriched fertilizers could have led to an increased decomposition of SOM and increased phosphate and nutrient consumption by vegetation. On the other hand, it is well-known that larger mammals (e.g., wild boars) and soil organisms impact the physical and chemical properties of soil (e.g., Mohr et al., 2005; Risch et al., 2010; Wirthner et al., 2011). This could have led to a mixing of the substrate in post-Roman times and ultimately to a relative depletion of SOM, phosphate and nutrient concentrations in the upper part of the Roman horizon. Additionally, this mixing process would plausibly explain the incorporation of the modern charcoal at 38 cm (Fig. 4b, Table 1) when this profile section formed the terrain surface.

The greatly enhanced phytolith concentrations within the Roman-dated hortic horizon (Fig. 6a) generally indicate increased plant input and can be plausibly explained by phytolith enrichment through agricultural activities (e.g., Cabanes et al., 2011; Madella and Lancelotti, 2012; Meister et al., 2017). This supports the geochemical interpretation of a Roman hortic soil at site GP2. The observed phytolith assemblages are dominated by Pooids containing some of the major Mediterranean crops, such as barley, wheat or rye (Schiemann, 1948), which could indicate the cultivation of cereals. This is supported by the fact that leaf and stem grass phytoliths within the lower profile section dominate over grass phytoliths formed in the inflorescences or in other plant organs (Fig. 6c). The accumulation of the former could be a consequence of harvesting activities, when only the ears (inflorescences) are collected and the stems and leaves are left on the fields (Flach, 1990; Dietrich et al., 2019; Scherer et al., 2021). It is also conceivable that food crops other than cereals might have been cultivated in this area since, for example, the consumption of vegetables is well documented for the Roman period (Bockisch, 1988; Demandt, 2008). Moreover, in their works on agricultural and horticultural practices, the famous ancient authors Columella (*De re rustica*) and Palladius (*Opus agriculturae*) described a crop rotation system in which different cereals and vegetables were grown in successive years on the same fields (Flach, 1990). However, although phytoliths have been documented, for instance, for numerous specimens from the Fabaceae (Leguminosae) family, phytolith production varies substantially among different subfamilies (Cummings, 1992), while other important vegetable plants (e.g., root vegetables) produce no or only small amounts of phytoliths (Piperno, 2006). Phytolith analysis thus provides no indication of whether the area was used exclusively for cereals or whether vegetables were also cultivated.

Summing up, it can be asserted that both geochemical and phytolith analyses suggest an ancient agrarian use of site GP2. The exclusive use of the site for pasturing or feeding seems rather unlikely since the large number of Roman artifacts incorporated into the Roman hortic horizon clearly document invasive soil cultivation in the sense of digging or hoeing. Since water supply is guaranteed by the nearby well, the site offers suitable conditions for irrigated agriculture almost all year round.

5.2 Land use and its potential in the metamorphic landscape of the Munigua region

A contrasting land use evaluation has to be made for soils within metamorphic landscape, Here, mostly shallow and sandy to stony soils occur (Fig. 7, Table S1), strongly limiting potential rootability and resulting in unfavorable to very unfavorable water-storage capacity and nutrient budget (Fig. 3). Thus the present-day soil agro-potential is evaluated as unfavorable to very unfavorable at these metamorphic sites.

In addition to the pedological limitations, geomorphological circumstances render agriculture rather unprofitable in these areas. The slopes in the metamorphic landscape are generally steeper, and cultivation would be more exhausting in this landscape unit (Fig. 1b). Furthermore, limits on water availability prevent the all-season agricultural use of these sites since streams are commonly deeply incised and natural springs are rare here, rendering irrigation of agricultural areas difficult. These pedological and geomorphological characteristics make it unlikely that the metamorphic landscape was used for agriculture even in Roman times. Lastly, this assumption is supported by the fact that thick colluvial deposits clearly indicate land use in the granitic landscape but are absent in the observed metamorphic landscape. If there had been historical agricultural use, such deposits should have been preserved at least in places.

5.3 Land use and its potential in the Tamohoso floodplain

Floodplains are usually known to be fertile areas and have therefore been used for agriculture around the globe for thousands of years (Brown, 1997). The nearby lower Guadalquivir valley, for example, is a settlement chamber that has been continuously used for agriculture since the Copper Age at the latest and remains a preferred area for agricultural production (Nocete et al., 2008; García Sanjuán et al., 2013). It therefore seems likely that the alluvial deposits of the nearby Tamohoso River could also have been a favored area for agriculture during Roman times, contributing to the food supply of Munigua.

The analyses of the floodplain sites mostly show moderate to good soil agro-potential (Fig. 3). In particular, thicknesses > 1 m (Fig. 8, Table S1) favor potential rootability and available water-storage capacity. Additionally, the nutrient budget is moderate, resulting in the floodplain soils having overall moderate to good agrarian potential from today's perspective. Moreover, in addition to the physico-chemical properties, the flat terrain of the alluvial plain and the easy access to water favor the agricultural use of the floodplain sites.

Nevertheless, so far we have no information on the appearance of the Tamohoso floodplain in Roman times. Eight ^{14}C ages from fluvial sequences indicate deposition within an active meander belt in modern times (Fig. 8, Table 1). This might have been caused by intensified modern land use activities in the 19th and 20th centuries CE (Tomás García, 1991), as also seen in the widespread juvenile gully systems within the area (Fig. 1d). Regarding the ancient situation, it seems likely that comparable conditions existed in the Tamohoso floodplain at least locally during the heyday of Munigua since past soil erosion should already have led to sediment transfer into the streams. However, associated sediments were probably eroded and relocated due to contemporary active meander dynamics.

5.4 A pedo-geomorphological perspective on the Roman economy

The economy of small cities in the Roman province of Baetica was enormously diverse but commonly specialized around a certain economic activity (e.g., Blázquez Martinez, 1967; Chic García, 1997; Bowman and Wilson, 2009, 2011; Remesal Rodríguez, 2020). In the case of Munigua, metallurgy was without doubt the main and most profitable economic activity and led to considerable wealth in the region (Schattner, 2019b). However, multi-layered colluvial deposits in the surroundings of Munigua (Sect. 4.1.1) and a preserved Roman hortic Anthrosol (Sect. 4.1.2) provide proper pedo-geomorphological evidence of prehistoric and historic agrarian land use in granite areas around Munigua. This indicates that there was at least a second economic activity. It can thus rather be assumed that Roman cities were economically diversified rather than being dedicated to a single economic activity. Using a pedo-morphological approach, the present study therefore generally confirms the concept of an economic diversification of Roman towns in the province of Baetica and Hispania.

6 Conclusions

Using a pedo-geomorphological approach, the investigation underlines that the soils around Munigua currently have the potential for at least limited agricultural use in larger areas. The granite landscape and the floodplain areas of the Tamohoso River show conditions that would certainly allow the production of basic agricultural goods, not only today but most likely also in Roman times.

Whereas the existence of tilled floodplain soils during Roman times cannot be proven by this study, clear evidence of agrarian use is detectable in granite areas. Here, profile truncation and multi-layered colluvial deposits indicate multiple soil erosion phases in the surroundings of a Roman rural house complex southeast of the urban center of Munigua. Based on our initial ^{14}C-results, anthropogenic soil erosion and colluviation occurred in pre-Roman, late Roman and post-Roman times, which strongly suggests the long-term agrarian utilization of the area. For a granite area close to Munigua, phytolith and geochemical analyses provide evidence of the existence of a Roman garden, where cereals and vegetables might have been cultivated at least on a small scale. The site was most likely fertilized by humus or compost to improve and secure crop yields, confirming the Roman population's extensive knowledge of agricultural practices, already described by ancient authors like, for instance, Columella or Palladius. Hence, the results of investigations in the granite landscape surrounding Munigua indicate a local cultivation of agricultural products that made an active contribution to the food supply of the area. This seems even more likely if the variety of agricultural equipment (Krug, 2018) and olive oil presses (Peña Cervantes, 2010; Teichner and Peña Cervantes, 2012) excavated in the town are also taken into account. This study thus could not confirm the hypothesis that deficient pedological conditions in the surroundings of Munigua generally prevented the agricultural use of the area during Roman times and that therefore the population was mainly dependent on food imports from the lower Guadalquivir valley (Schattner, 2019b). However, there remain many open questions for future research in the coming years, i.e., concerning the extent and production rates of agricultural activities, the cultivated products, or the adaptation techniques applied to cope with seasonal water deficiencies.

In addition to the site-specific information, the study also provides geoarcheological evidence supporting the concept of an economic diversification of Roman cities in Baetica province and Hispania. Even though metallurgy was without doubt the main and most profitable activity in the Munigua region, the economy was certainly not only dedicated to mining activities. Whereas specialty goods were imported, basic agrarian products (e.g., crops, olive oil, wine) were also part of Munigua's economic portfolio and exemplify the economic diversity of urban settlements in the Roman Baetica province.

Data availability. Data relating to this paper can be found in the Supplement or are available from the corresponding author upon reasonable request.

Supplement. The supplement related to this article is available online at: https://doi.org/10.5194/egqsj-71-123-2022-supplement.

Author contributions. AK, NH and TGS organized the project. AK, NH and PM carried out the fieldwork. The concept and structure of the paper were organized by AK and NH. The laboratory work was mainly done by PM, IM and JM. AK took the lead in writing the manuscript, with input from NH, JM and TGS. All authors discussed the results and contributed to the final manuscript.

Competing interests. At least one of the (co-)authors is a member of the editorial board of *E&G Quaternary Science Journal*. The peer-review process was guided by an independent editor, and the authors also have no other competing interests to declare.

Special issue statement. This article is part of the special issue “Quaternary research from and inspired by the first virtual DEUQUA conference”. It is a result of the vDEUQUA2021 online conference in September/October 2021.

Acknowledgements. The authors are very grateful to Heinrich Thiemeyer, Doris Bergmann-Dörr and Dagmar Schneider (all Goethe University Frankfurt) for the conscientious implementation of selected soil analyses. Furthermore, Katharine Thomas is acknowledged for improving the language of the manuscript.

Financial support. This research was financially supported by the Madrid Department of the German Archaeological Institute. This publication was supported by the open-access publication fund of the University of Wuerzburg.

Review statement. This paper was edited by Tobias Sprafke and reviewed by two anonymous referees.

References

Ad-hoc-AG Boden: Bodenkundliche Kartieranleitung, 5th edn., Schweizerbart, Stuttgart, 438 pp., ISBN 9783510959204, 2005.

Albert, R. M.: Study of ash layers through phytolith analyses from the Middle Paleolithic levels of Kebara and Tabun caves, Universitat de Barcelona, Barcelona, ISBN 9788459244265, 2000.

Albert, R. M. and Weiner, S.: Study of phytoliths in prehistoric ash layers using a quantitative approach, in: Phytoliths, Applications in Earth Sciences and Human History, edited by: Meunier, J. D. and Colin, F., A.A. Balkema Publishers, Lisse, 251–266, ISBN 9789058093455, 2001.

Albert, R. M., Lavi, O., Estroff, L., Weiner, S., Tsatskin, A., Ronen, A., and Lev-Yadun, S.: Mode of occupation of Tabun Cave, Mt Carmel, Israel during the Mousterian Period: a study of the sediments and phytoliths, J. Archaeol. Sci., 26, 1249–1260, https://doi.org/10.1006/jasc.1999.0355, 1999.

Amelung, W., Blume, H.-P., Fleige, H., Horn, R., Kandeler, E., Kögel-Knabner, I., Kretzschmar, R., Stahr, K., and Wilke, B.-M.: Scheffer/Schachtschabel: Lehrbuch der Bodenkunde, 17th edn., Springer Spektrum, Berlin, Heidelberg, 750 pp., https://doi.org/10.1007/978-3-662-55871-3, 2018.

Bellin, N., Vanacker, V., and De Baets, S.: Anthropogenic and climatic impact on Holocene sediment dynamics in SE Spain: A review, Quatern. Int., 308, 112–129, https://doi.org/10.1016/j.quaint.2013.03.015, 2013.

Blázquez Martínez, J. M.: Estructura económica de la Bética al final de la República romana y a comienzos del Imperio (años 72 a.C.–100 d.C.), Hispania, 27, 7–62, 1967.

Bleck, R.-D.: Zur Durchführung der Phosphatmethode, Ausgrabungen und Funde, 10, 213–218, 1965.

Blume, H.-P., Stahr, K., and Leinweber, P.: Bodenkundliches Praktikum, 3rd edn., Springer Spektrum, Berlin, Heidelberg 255 pp., https://doi.org/10.1007/978-3-8274-2733-5, 2011.

Bockisch, G.: Essen und Trinken im alten Rom, Das Altertum, 34, 87–95, 1988.

Boessneck, J. and von den Driesch, A.: Knochenfunde aus dem römischen Munigua (Mulva), Sierra Morena. Studien über frühe Knochenfunde von der Iberischen Halbinsel, München Uni-Druck, 160–193, 1980.

Borden, W. R., Baillie, I. C., and Hallett, I. C.: The East African contribution to the formalisation of the soil catena concept, Catena, 185, 104291, https://doi.org/10.1016/j.catena.2019.104291, 2020.

Bowman, A. and Wilson, A.: Quantifying the Roman Economy: Methods and Approaches (Oxford Studies on the Roman Economy 1), Oxford University Press, Oxford, 376 pp., https://doi.org/10.1093/acprof:oso/9780199562596.001.0001, 2009.

Bowman, A. and Wilson, A.: Settlement, Urbanization, and Population, Oxford University Press, Oxford, 362 pp., https://doi.org/10.1093/acprof:oso/9780199602353.001.0001, 2011.

Brown, A. G.: Alluvial Geoarchaeology. Floodplain Archaeology and Environmental Change, Cambridge University Press, Cambridge, 377 pp., https://doi.org/10.1017/CBO9780511607820, 1997.

Brown, D. A.: Prospects and limits of a phytolith key for grasses in the central United States, J. Archaeol. Sci., 11, 345–368, https://doi.org/10.1016/0305-4403(84)90016-5, 1984.

Cabanes, D., Weiner, S., and Shahack-Gross, R.: Stability of phytoliths in the archaeological record: a dissolution study of modern and fossil phytoliths, J. Archaeol. Sci., 38, 2480–2490, https://doi.org/10.1016/j.jas.2011.05.020, 2011.

Chic García, G.: Historia económica de la. Bética en la época de Augusto, Padilla Libros, Sevilla, ISBN 84-89769-18-4, 1997.

Cummings, L. S.: Illustrated phytoliths from assorted food plants, in: Phytolith Systematics: Emerging Issues, Advances in Archaeological and Museum Science, edited by: Rapp Jr., G. and Mulholland, S. C., Springer Science & Business Media, 175–192, ISBN 978-1489911575, 1992.

Demandt, A.: Geschichte der Spätantike: Das Römische Reich von Diocletian bis Justinian 284–565 n. Chr., 2nd edn., C. H. Beck, München, 604 pp., ISBN 978-3-406-70032-3, 2008.

de Vries, H. and Barendsen, G. W.: Measurements of age by the carbon-14 technique, Nature, 174, 1138–1141, 1954.

Dietrich, L., Meister, J., Dietrich, O., Notroff, J., Kiep, J., Heeb, J., Beuger, A., and Schütt, B.: Cereal processing at Early Neolithic Göbekli Tepe, southeastern Turkey, PLOS ONE, 14, e0215214, https://doi.org/10.1371/journal.pone.0215214, 2019.

DIN ISO 11277: Soil Quality – Determination of particle size distribution in mineral soil material – method by sieving and sedimentation, Beuth, Berlin, 2002.

Dotterweich, M.: The history of soil erosion and fluvial deposits in small catchments of Central Europe: deciphering the long-term interaction between humans and the environment – a review, Geomorphology, 101, 192–208, https://doi.org/10.1016/j.geomorph.2008.05.023, 2008.

Dotterweich, M.: The history of human-induced soil erosion: Geomorphic legacies, early descriptions and research, and the development of soil conservation – A global synopsis, Geomorphology, 201, 1–34, https://doi.org/10.1016/j.geomorph.2013.07.021, 2013.

Eger, C.: Frühislamische Bestattungen in Munigua (Prov. Sevilla/E), Archäologisches Korrespondenzblatt, 46, 255–269, 2016.

Evans, D. M. and Hartemink, A. E.: Terra Rossa catenas in Wisconsin, USA, Catena, 123, 148–152, https://doi.org/10.1016/j.catena.2014.07.007, 2014.

Faust, D. and Wolf, D.: Interpreting drivers of change in fluvial archives of the Western Mediterranean

– A critical view, Earth-Sci. Rev., 174, 53–83, https://doi.org/10.1016/j.earscirev.2017.09.011, 2017.

Flach, D.: Römische Agrargeschichte, C. H. Beck, München, 347 pp., ISBN 978-3-406-33989-9, 1990.

Frey, W. and Lösch, R.: Geobotanik. Pflanze und Vegetation in Raum und Zeit, 3rd edn., Springer Spektrum, Berlin, Heidelberg, 638 pp., https://doi.org/10.1007/978-3-8274-2336-8, 2010.

García-Ruiz, J. M.: The effects of land use on soil erosion in Spain. A review, Catena, 81, 1–11, https://doi.org/10.1016/j.catena.2010.01.001, 2010.

García-Ruiz, J. M., Nadal-Romero, E., Lana-Renault, N., and Beguería, S.: Erosion in Mediterranean landscapes. Changes and future challenges, Geomorphology, 198, 20–36, https://doi.org/10.1016/j.geomorph.2013.05.023, 2013.

García Sanjuán, L., Luciañez Triviño, M., Schuhmacher, T., Wheatley, D., and Banerjee, A.: Ivory Craftsmanship, Trade and Social Significance in the Southern Iberian Copper Age: The Evidence from the PP4-Montelirio Sector of Valencina de la Concepción (Seville, Spain), Eur. J. Archaeol., 16, 610–635, https://doi.org/10.1179/1461957113Y.0000000037, 2013.

Gerlach, G.: Zu Tisch bei den alten Römern: Eine Kulturgeschichte des Essens und Trinkens, Konrad Theiss, Stuttgart, 112 pp., ISBN 978-3806213539, 2001.

Giner-Robles, J. L., Bardají, T., Rodríguez-Pascua, M. A., Silva, P. G., Roquero, E., Elez, J., Perucha, M. A., Baena, R., Guerrero, I., Fernández-Caro, J. J., Pérez-López, R., and Rodríguez-Escudero, E: Análisis arqueosismológico del conjunto arqueológico romano de Mulva- Munigua (Sevilla, España), Geotemas, 16, 605–608, 2016.

Gómez-Zotano, J., Alcántara-Manzanares, J., Olmedo-Cobo, J.-A., and Martínez-Ibarra, E.: La sistematiza-cíon del clima mediterráneo: identificacíon. Clasificacíon y caracterizacíon climática de Andalucía (España), Rev. Geogr. Norte Gd., 61, 161–180, https://doi.org/10.4067/S0718-34022015000200009, 2015.

Grünhagen, W.: Die Ausgrabungen des Terrassenheiligtums von Munigua, in: Neue deutsche Ausgrabungen im Mittelmeergebiet und im Vorderen Orient, edited by: Boehringer, E., 329–343, 1959.

Gutiérrez-Rodríguez, M., Goldberg, P., Martín Peinado, F. J., Schattner, T. G., Martini, W., Orfila, M., and Bashore Acero, C.: Melting, bathing and melting again. Urban transformation processes of the Roman city of Munigua: the public thermae, Archaeol. Anthropol. Sci., 11, 51–67, https://doi.org/10.1007/s12520-017-0527-0, 2019.

Hajdas, I.: Radiocarbon dating and its applications in Quaternary studies, E&G Quaternary Sci. J., 57, 2–24, https://doi.org/10.3285/eg.57.1-2.1, 2008.

Hanel, N.: Römische Öl- und Weinproduktion auf der Iberischen Halbinsel am Beispiel von Munigua und Milreu, Madrider Mitteilungen, 30, 205–238, 1989.

Holliday, V. T. and Gartner, W. G.: Methods of soil P analysis in archaeology, J. Archaeol. Sci., 34, 301–333, https://doi.org/10.1016/j.jas.2006.05.004, 2007.

IUSS Working Group WRB: World Reference Base for Soil Resources 2014, update 2015. International soil classification system for naming soils and creating legends for soil maps, World Soil Resources Reports No. 106, FAO, Rome, ISBN 978-92-5-108369-7, 2015.

Jahn, R., Blume, H.-P., Asio, V. B., Spaargaren, O., and Schad, P.: Guidelines for soil description, FAO, Rome, 97 pp., ISBN 92-5-105521-1, 2006.

Joffre, R., Vacher, J., del los Llanos, C., and Long, G.: The Dehesa: an agrosilvopastoral system of the Mediterranean region with special reference to the Sierra Morena area of Spain, Agrofor-est Syst., 6, 71–96, https://doi.org/10.1007/BF02220110, 1988.

Keay, S. and Earl, G.: Towns and Territories in Roman Baetica, in: Settlement, Urbanization, and Population, edited by: Bowman, A., and Wilson, A., Oxford University Press, 276–316, https://doi.org/10.1093/acprof:oso/9780199602353.001.0001, 2011.

Kittel, P.: Slope deposits as an indicator of anthropopressure in the light of research in Central Poland, Quatern. Int., 324, 34–55, https://doi.org/10.1016/j.quaint.2013.07.021, 2014.

Krug, A.: Mulva VI: Die Kleinfunde/ Los hallazgos menores, Madrider Beiträge, 36, 436 pp., ISBN 978-3954902378, 2018.

Leopold, M. and Völkel, J.: Colluvium: definition, differentiation, and possible suitability for reconstructing Holocene climate data, Quatern. Int., 162–163, 133–140, https://doi.org/10.1016/j.quaint.2006.10.030, 2007.

Madella, M. and Lancelotti, C.: Taphonomy and phytoliths: A user manual, Quatern. Int., 275, 76–83, doi10.1016/j.quaint.2011.09.008, 2012.

Madella, M., Alexandre, A., and Ball, T.: International Code for Phytolith Nomenclature 1.0, Ann. Bot., 96, 253–260, https://doi.org/10.1093/aob/mci172, 2005.

May, S. M., Norpoth, M., Pint, A. Shumilovskikh, L., Raith, K., Brill, D., Rixhon, G., Moret, P. Jiménez-Vialás, H., Grau-Mira, I., García-Jiménez, I., Marzoli, D., León-Martín, C., Reicherter, K., and Brückner, H.: Mid- to late Holocene environmental changes and human-environment interactions in the surroundings of La Silla del Papa, SW Spain, Geoarchaeology, 36, 573–600, https://doi.org/10.1002/gea.21846, 2021.

Meister, J., Krause, J., Müller-Neuhof, B., Portillo, M., Reimann, T., and Schütt, B.: Desert agricultural systems at EBA Jawa (Jordan): Integrating archaeological and paleoenvironmental records, Quatern. Int., 434, 33–50, https://doi.org/10.1016/j.quaint.2015.12.086, 2017.

Meyer, C., Ullrich, B., and Barlieb C. D. M.: Archaeological Questions and Geophysical Solutions: Ground-Penetrating Radar and Induced Polarization Investigations in Munigua, Spain, Archaeol. Prospect., 14, 202–212, https://doi.org/10.1002/arp.314, 2007.

Mohr, D., Cohnstaedt, L. D., and Topp, W.: Wild boar and red deer affect soil nutrients and soil biota in steep oak stands of the Eifel, Soil Biol. Biochem., 37, 693–700, https://doi.org/10.1016/j.soilbio.2004.10.002, 2005.

Mulholland, S. C. and Rapp Jr., G.: A morphological classification of grass silica-bodies, in: Phytolith Systematics: Emerging Issues, Advances in Archaeological and Museum Science, edited by: Rapp Jr., G. and Mulholland, S. C., Springer Science & Business Media, 65–89, ISBN 978-1489911575, 1992.

Neumann, K., Strömberg, C. A. E., Ball, T., Albert, R. M., Vrydaghs, L., and Cummings, L. S.: International code for phytolith nomenclature (ICPN) 2.0, Ann. Bot., 124, 189–199, https://doi.org/10.1093/aob/mcz064, 2019.

Nocete, F., Queipo, G., Sáez, R., Nieto, J. M., Inácio, N., Bayona, M. R., Peramo, A., Vargas, J. M., Cruz-Auñón, R., Gil-Ibarguchi,

J. I., and Santos, J. F.: The Smelting Quarter of Valencina de la Concepción (Seville, Spain): The Specialised Copper Industry in a Political Centre of the Guadalquivir Valley During the Third Millennium BC (2750–2500 BC), J. Archaeol. Sci., 35, 717–732, https://doi.org/10.1016/j.jas.2007.05.019, 2008.

Nocete, F., Sáez, R., Bayona, M. R., Peramo, A., Inacio, N., and Abril, D.: Direct chronometry (14C AMS) of the earliest copper metallurgy in the Guadalquivir Basin (Spain) during the third millennium BC: first regional database, J. Archaeol. Sci., 38, 3278–3295, https://doi.org/10.1016/j.jas.2011.07.008, 2011.

Nuñez, M. A. and Recio, J. M.: Holocene pedoenvironmental situations in the eastern Sierra Morena region (Andújar, Spain), Quatern. Int., 93–94, 191–195, https://doi.org/10.1016/S1040-6182(02)00017-4, 2002.

Paneque, G. and Bellinfante, N.: Mediterranean brown forest soils of the Sierra Morena (Spain), their micromorphology and petrography, in: Soil Micromorphology, edited by: Jongerius, A., 189–200, ISBN 978-0444403254, 1964.

Peña Cervantes, Y.: Torcularia: la producción de vino y aceite en Hispania, Tarragona: ICAC, Institut Català d'Arqueologia Clàssica, 284 pp., ISBN 978-84-937734-1-0, 2010.

Piperno, D. R.: Phytoliths: A Comprehensive Guide for Archaeologists and Paleoecologists, Rowman Altamira, Lanham, New York, Toronto, Oxford, 238 pp., https://doi.org/10.1017/S0016756807003159, 2006.

Portillo, M., Kadowaki, S., Nishiaki, Y., and Albert, R. M.: Early Neolithic household behavior at Tell Seker al-Aheimar (Upper Khabur, Syria): a comparison to ethnoarchaeological study of phytoliths and dung spherulites, J. Archaeol. Sci., 42, 107–118, https://doi.org/10.1016/j.jas.2013.10.038, 2014.

Recio Espejo, J. M., Faust, D., and Nuñez Granados, M. A.: The origin of the Sierra de Aracena Hollows in the Sierra Morena, Huelva, Andalucia, Spain, Geomorphology, 45, 197–209, https://doi.org/10.1016/S0169-555X(01)00154-4, 2002.

Redman C. L.: Human impact on ancient environments, University of Arizona Press, Tucson, 256 pp., ISBN 978-0816519637, 1999.

Reimer, P., Bard, E., Bayliss, A., Beck, J. W., Blackwell, P. G., Ramsey, C. B., Buck, C. E., Cheng, H., Edwards, R. L., Friedrich, M., Grootes, P. M., Guilderson, T. P., Haflidason H., Hajdas, I., Hatte, C., Heaton, T. J., Hoffmann, D. L., Hogg, A. G., Hughen, K. A., Kaiser, K. F., Kromer, B., Manning, S. W., Niu, M., Reimer, R. W., Richards, D. A., Scott, E. M., Southon, J. R., Staff, R. A., Turney, C. S. M., and van der Plicht, J.: IntCal13 and Marine13 radiocarbon age calibration curves 0–50 000 years cal BP, Radiocarbon, 55, 1869–1887, https://doi.org/10.2458/azu_js_rc.55.16947, 2013.

Remesal Rodríguez, J.: Die politische und wirtschaftliche Entwicklung der Baetica in der Kaiserzeit, Madrider Mitteilungen, 61, 115–132, 2020.

Ribeiro, A., Munhá, J., Fonseca, P. E., Araújo, A., Pedro, J.C., Mateus, A., Tassinari, C., Machado, G., and Jesus, A.: Variscan ophiolite belts in the Ossa-Morena Zone (Southwest Iberia): Geological characterization and geodynamic significance, Gondwana Res., 17, 408–421, https://doi.org/10.1016/j.gr.2009.09.005, 2010.

Risch, A. C., Wirthner, S., Busse M. D., Page-Dumroese, D. S., and Schütz M.: Grubbing by wild boars (Sus scrofa) and its impact on hardwood forest soil carbon dioxide emissions in Switzerland, Oecologia, 164, 773–784, https://doi.org/10.1007/s00442-010-1665-6, 2010.

Rodríguez-Pascua, M. A., Pérez-López, R., Silva, P. G., Giner-Robles, J. L., Garduño-Monroy, V. H., and Reicherter, K.: A comprehensive classification of Earthquake Archaeological Effects (EAE) for archaeoseismology: application to ancient remains of Roman and Mesoamerican cultures, Quatern. Int., 242, 20–30, https://doi.org/10.1016/j.quaint.2011.04.044, 2011.

Ruiz-Bueno, M. D.: Actividad sísmica en el mediodía ibérico durante el siglo III d.C. La incidencia arqueológica en Corduba (Córdoba), Pyrenae, 48, 29–51, https://doi.org/10.1344/Pyrenae2017.vol48num2.2, 2017.

Sanz, T., Sampelayo, H., and Ledesma Garcia, F.: Mapa Geológica de España. Escala 1 : 50.000, edited by: Instituto geológico y minero de España (IGME), 941, 13–38, 1973.

Schattner, T. G.: Munigua: Cuarenta años de investigaciones, Sevilla: Junta de Andalucía, Instituto Arqueológico Alemán, 335 pp., ISBN 84-8266-364-X, 2003.

Schattner, T. G.: Die Wiederentdeckung von Munigua: Abriss der Forschungsgeschichte, Madrider Mitteilungen, 46, 267–288, 2005.

Schattner, T. G.: Antike "Mondlandschaften", Archäologie Weltweit, 7, 26–31, 2019a.

Schattner, T. G.: Munigua: Un recorrido por la arqueología del Municipium Flavium Muniguense, Editorial Universidad de Sevilla-Secretariado de Publicaciones, Sevilla, 225 pp., ISBN 978-8447219179, 2019b.

Schattner, T. G., Ovejero Zappino, G., and Pérez Macías, J. A.: Avances sobre la producción metalúrgica en Munigua, Habis, 36, 253–276, 2005.

Scherer, S., Höpfer, B., Deckers, K., Fischer, E., Fuchs, M., Kandeler, E., Lechterbeck, J., Lehndorff, E., Lomax, J., Marhan, S., Marinova, E., Meister, J., Poll, C., Rahimova, H., Rösch, M., Wroth, K., Zastrow, J., Knopf, T., Scholten, T., and Kühn, P.: Middle Bronze Age land use practices in the northwestern Alpine foreland – a multi-proxy study of colluvial deposits, archaeological features and peat bogs, SOIL, 7, 269–304, https://doi.org/10.5194/soil-7-269-2021, 2021.

Schiemann, E.: Weizen, Roggen, Gerste. Systematik, Geschichte und Verwendung, Gustav Fischer Verlag, Jena, 102 pp., 1948.

Schüller, H.: Die CAL-Methode, eine neue Methode zur Bestimmung des pflanzenverfügbaren Phosphates in Böden, Zeitschrift für Pflanzenernährung, Düngung und Bodenkunde, 123, 48–63, 1969.

Semmel, A.: Grundzüge der Bodengeographie, Teubner, Stuttgart, 101 pp., ISBN 978-3519134084, 1977.

Strauss, G. K. and Madel, J.: Geology of massive sulphide deposits in the Spanish-Portuguese Pyrite Belt, Geol. Rundsch., 63, 191–211, 1974.

Teichner, F.: Spuren islamischer Besiedlung auf dem Castillo de Mulva (Villanueva del Río y Minas, prov. Sevilla)?, Madrider Mitteilungen, 39, 336–355, 1998.

Teichner, F. and Peña Cervantes, Y.: Archäologisches zur Herstellung von Olivenöl und Wein im römischen Hispanien, Bonner Jahrbücher, 210/211, 375–458, 2012.

Tomás García, L. J.: La Minería sevillana del carbón. Minas de La Reunión y la Compañía de los Ferrocarriles de M.Z.A, Diputación Provincial de Sevilla, Sevilla, ISBN 84-7798-059-4, 1991.

Tornos, F., Inverno, C. M. C., Casquet, C., Mateus, A., Ortiz, G., and Olivera, V.: The metallogenic evolution of the Ossa-Morena Zone, J. Iber. Geol., 30, 143–181, 2004.

Tsartsidou, G., Lev-Yadun, S., Albert, R.-M., Miller-Rosen, A., Efstratiou, N., and Weiner, S.: The phytolith archaeological record: strengths and weaknesses evaluated based on a quantitative modern reference collection from Greece, J. Archaeol. Sci., 34, 1262–1275, https://doi.org/10.1016/j.jas.2006.10.017, 2007.

Twiss, P. C., Suess, E., and Smith, R. M.: Morphological classification of grass phytoliths, Soil Sci. Soc. Am. Pro., 33, 109–115, https://doi.org/10.2136/sssaj1969.03615995003300010030x, 1969.

Ullrich, B., Meyer, C., and Weller, A.: Geoelektrik und Georadar in der archäologischen Forschung: geophysikalische 3D-Untersuchungen in Munigua (Spanien), in: Einführung in die Archäometrie, edited by: Wagner, G. A., Springer, 76–93, https://doi.org/10.1007/978-3-540-71937-3, 2007.

Weihrauch, C.: Phosphor-Dynamiken in Böden. Grundlagen, Konzepte und Untersuchungen zur räumlichen Verteilung des Nährstoffs, Springer Spektrum, Wiesbaden, 369 pp., https://doi.org/10.1007/978-3-658-22348-9, 2018.

Wirthner, S., Frey, B., Busse, M. D., Schütz M., and Risch A. C.: Effects of wild boar (Sus scrofa) rooting on the bacterial community structure in mixed-hardwood forest soils in Switzerland, Eur. J. Soil Biol., 47, 296–302, https://doi.org/10.1016/j.ejsobi.2011.07.003, 2011.

Zádorová, T. and Penížek, V.: Formation, morphology and classification of colluvial soils: A review, Eur. J. Soil Sci., 69, 577–591, https://doi.org/10.1111/ejss.12673 2018.

Zazo, C., Dabrio, C. J., Goy, J. L., Lario, J., Cabero, A., Silva, P. G., Bardají, T., Mercier, N., Borja, F., and Roquero, E.: The coastal archives of the last 15ka in the Atlantic–Mediterranean Spanish linkage area: Sea level and climate changes, Quatern. Int., 181, 72–87, https://doi.org/10.1016/j.quaint.2007.05.021, 2008.

E&G Quaternary Sci. J., 71, 83–90, 2022
https://doi.org/10.5194/egqsj-71-83-2022

Open Access E&G Quaternary Science Journal

Research article

^{18}O analyses of bulk lipids as novel paleoclimate tool in loess research – a pilot study

Jakob Labahn[1], Lucas Bittner[1], Philip Hirschmann[1], Christopher-Bastian Roettig[1], Diana Burghardt[2], Bruno Glaser[3], Slobodan B. Marković[4], and Michael Zech[1]

[1]Heisenberg Chair of Physical Geography with Focus on Paleoenvironmental Research, Technische Universität Dresden, Helmholtzstraße 10, 01069 Dresden, Germany
[2]Institute of Groundwater Management, Department of Hydro Sciences, Technische Universität Dresden, Bergstraße 66, 01069 Dresden, Germany
[3]Soil Biogeochemistry, Institute of Agronomy and Nutritional Sciences, Martin Luther University Halle-Wittenberg, Von-Seckendorff-Platz 3, 06120 Halle (Saale), Germany
[4]Chair of Physical Geography, Faculty of Sciences, University of Novi Sad, Trg D. Obradovića 3, 21000 Novi Sad, Serbia

Correspondence: Jakob Labahn (jakob.labahn@tu-dresden.de) and Michael Zech (michael.zech@tu-dresden.de)

Relevant dates: Received: 2 November 2021 – Revised: 25 February 2022 – Accepted: 28 February 2022 – Published: 13 April 2022

How to cite: Labahn, J., Bittner, L., Hirschmann, P., Roettig, C.-B., Burghardt, D., Glaser, B., Marković, S. B., and Zech, M.: ^{18}O analyses of bulk lipids as novel paleoclimate tool in loess research – a pilot study, E&G Quaternary Sci. J., 71, 83–90, https://doi.org/10.5194/egqsj-71-83-2022, 2022.

Abstract: The analysis of the stable oxygen isotopes ^{18}O and ^{16}O has revolutionized paleoclimate research since the middle of the last century. Particularly, δ^{18}O of ice cores from Greenland and Antarctica is used as a paleotemperature proxy, and δ^{18}O of deep-sea sediments is used as a proxy for global ice volume. Important terrestrial archives to which δ^{18}O as a paleoclimate proxy is successfully applied are speleothems, lake sediments, or tree rings. By contrast, δ^{18}O applications to loess–paleosol sequences (LPSs) are scarce. Here we present a first continuous δ^{18}O record ($n = 50$) for the LPS Crvenka in Serbia, southeastern Europe, spanning the last glacial–interglacial cycle (since 145 ka). From a methodological point of view, we took advantage of a recently proposed paleoclimate/paleohydrological proxy based on bulk δ^{18}O analyses of plant-derived lipids. The Crvenka $\delta^{18}O_{\text{bulk lipid}}$ values range between -10.2 ‰ and $+23.0$ ‰ and are systematically more positive in the interglacial and interstadial (paleo-)soils corresponding to marine oxygen-isotope stage (MIS) 1, 3, and 5, compared to the loess layers (MIS 2, 4, and 6). Our Crvenka $\delta^{18}O_{\text{bulk lipid}}$ record provides no evidence for the occurrence of interstadials and stadials comparable to the Dansgaard–Oeschger events known from the Greenland $\delta^{18}O_{\text{ice core}}$ records. Concerning the interpretation of our Crvenka $\delta^{18}O_{\text{bulk lipid}}$ record, plant-derived lipids such as fatty acids and alcohols are certainly strongly influenced by climatic factors such as temperature (via $\delta^{18}O_{\text{precipitation}}$) and relative air humidity (via ^{18}O enrichment of leaf water due to evapotranspiration). However, pool effects in the form of non-water-correlated lipids such as sterols or the input of root-derived lipids need to be considered, too. Similarly, the input of soil-microbial lipids and oxygen exchange reactions represent uncertainties challenging quantitative paleoclimate/paleohydrological reconstructions based on $\delta^{18}O_{\text{bulk lipid}}$ analyses from LPSs.

Published by Copernicus Publications on behalf of the Deutsche Quartärvereinigung (DEUQUA) e.V.

Kurzfassung: Die Analyse der stabilen Sauerstoffisotope ^{18}O und ^{16}O hat die Paläoklimaforschung seit Mitte des letzten Jahrhunderts revolutioniert. Insbesondere wird δ^{18}O von Eisbohrkernen aus Grönland und der Antarktis als Paläo-Temperaturproxy sowie δ^{18}O von Tiefseesedimenten als Proxy für das globale Eisvolumen verwendet. Wenngleich sich in terrestrischen Archiven, wie Speläothemen, Seesedimenten oder Baumringen, paläoklimatische Rekonstruktionen unter der Anwendung von δ^{18}O als Proxy bewährt haben, wurden solche Analysen bislang in Löß-Paläobodensequenzen (LPS) selten durchgeführt. In dieser Studie präsentieren wir einen ersten kontinuierlichen δ^{18}O Datensatz ($n = 50$) für die LPS Crvenka in Serbien, der den letzten Glazial-Interglazial-Zyklus (~ 145 ka) abdeckt. Die δ^{18}O-Werte basieren auf der Analyse von pflanzlichen Lipiden, deren Anwendung als paläoklimatischer/hydrologischer Proxy vor Kurzem vorgeschlagen wurde.

Die $\delta^{18}\text{O}_{\text{bulk-lipid}}$-Werte von Crvenka liegen zwischen −10.2 ‰ und +23.0 ‰ und sind in den interglazialen und interstadialen (Paläo-)Böden, die den marinen Sauerstoff-Isotopenstufen (MIS) 1, 3 und 5 entsprechen, systematisch positiver als in den Lößlagen (MIS 2, 4 und 6). Sie liefern keine Hinweise für das Auftreten von Interstadialen und Stadialen, die mit den aus den grönländischen $\delta^{18}\text{O}_{\text{ice-core}}$ bekannten Dansgaard-Oeschger-Ereignissen vergleichbar wären. In Bezug auf die Interpretation der $\delta^{18}\text{O}_{\text{bulk-lipid}}$-Werte gilt es zu berücksichtigen, dass die Isotopie pflanzlicher Lipide, wie z.B. von Fettsäuren und Alkoholen, stark durch die Klimafaktoren Temperatur (über δ^{18}O-Niederschlag) und relativer Luftfeuchtigkeit (über die ^{18}O-Anreicherung des Blattwassers aufgrund von Evapotranspiration) beeinflusst werden. Weiter zu beachtende Faktoren stellen Einträge von Sterolen sowie von generell wurzel-bürtigen Lipiden dar (Pool-Effekte). In ähnlicher Weise bergen der Einfluss von bodenmikrobiellen Lipiden und Sauerstoffaustauschreaktionen Unsicherheiten, die quantitative paläoklimatische/hydrologische Rekonstruktionen auf der Grundlage von $\delta^{18}\text{O}_{\text{bulk-lipid}}$-Analysen aus LPS erschweren können.

1 Introduction

The analysis of the stable oxygen isotopes ^{18}O and ^{16}O has revolutionized paleoclimate research since the middle of the last century. Particularly, the oxygen isotopic composition δ^{18}O of ice cores from Greenland and Antarctica is used as a paleotemperature proxy (e.g., NGRIP members, 2004), and δ^{18}O of deep-sea sediments is used as a proxy for global ice volume (e.g., Lisiecki and Raymo, 2005). Important terrestrial archives to which δ^{18}O as a paleoclimate proxy is currently successfully applied are speleothems (e.g., Spötl et al., 2006), lake sediments (e.g., Bittner et al., 2021), or tree rings (e.g., Roden et al., 2000). In all these archives, the δ^{18}O signal of paleoprecipitation ($\delta^{18}\text{O}_{\text{precipitation}}$) plays a major role, for which four effects can be highlighted. (1) The "temperature effect" describes that the colder the temperature is, the more negative $\delta^{18}\text{O}_{\text{precipitation}}$ becomes. (2) The "amount effect" describes that $\delta^{18}\text{O}_{\text{precipitation}}$ becomes more negative with increasing precipitation amount. (3) The "altitude effect" describes that $\delta^{18}\text{O}_{\text{precipitation}}$ becomes more negative with increasing altitude. (4) The "source effect" explains that air masses derived from different moisture sources can have distinct and variable $\delta^{18}\text{O}_{\text{precipitation}}$ values (e.g., Dansgaard, 1964; Lachniet, 2009; Lemma et al., 2021).

In contrast to the aforementioned terrestrial archives, δ^{18}O applications to loess–paleosol sequences (LPSs) are still scarce, although these represent unique and widespread occurring paleoenvironmental archives. For instance, Pustovoytov and Terhorst (2004) examined calcified root cells in an LPS using δ^{13}C and δ^{18}O analyses to determine climatic conditions based on the signal obtained during post-sedimentary Holocene soil formation, and Prud'homme et al. (2016) used δ^{18}O of earthworm calcite granules from an LPS to reconstruct paleotemperatures. Other approaches with respect to isotope analyses in loess archives have lately focused on the study of biomarkers (e.g., R. Zech et al., 2013; Schäfer et al., 2016; Häggi et al., 2019). These biomarkers are primarily compounds derived from plants, such as lipids or sugars (monosaccharides). For example, M. Zech et al. (2013) applied compound-specific δ^{18}O analysis of plant-derived sugar biomarkers to a permafrost LPS from Siberia. Similar to compound-specific δ^{2}H analyses of leaf-wax-derived n-alkane biomarkers (R. Zech et al., 2013), δ^{18}O of sugar biomarkers has a great potential to serve as a paleoclimate proxy in sedimentary archives (Zech et al., 2014). However, this latter approach could not be adopted so far due to the considerable carbonate amounts in classical LPSs. To sum up, no continuous δ^{18}O records could be established for classical LPSs up to now.

Recently, Silva et al. (2015) and Maxwell et al. (2018) proposed δ^{18}O of plant-derived bulk lipids ($\delta^{18}\text{O}_{\text{bulk lipids}}$) as a proxy for reconstructing ecosystem water balances. Lipids are important constituents of cuticular waxes and comprise, e.g., non-oxygen-bearing long-chain n alkanes as well as oxygen-bearing molecules such as long-chain alkanols and

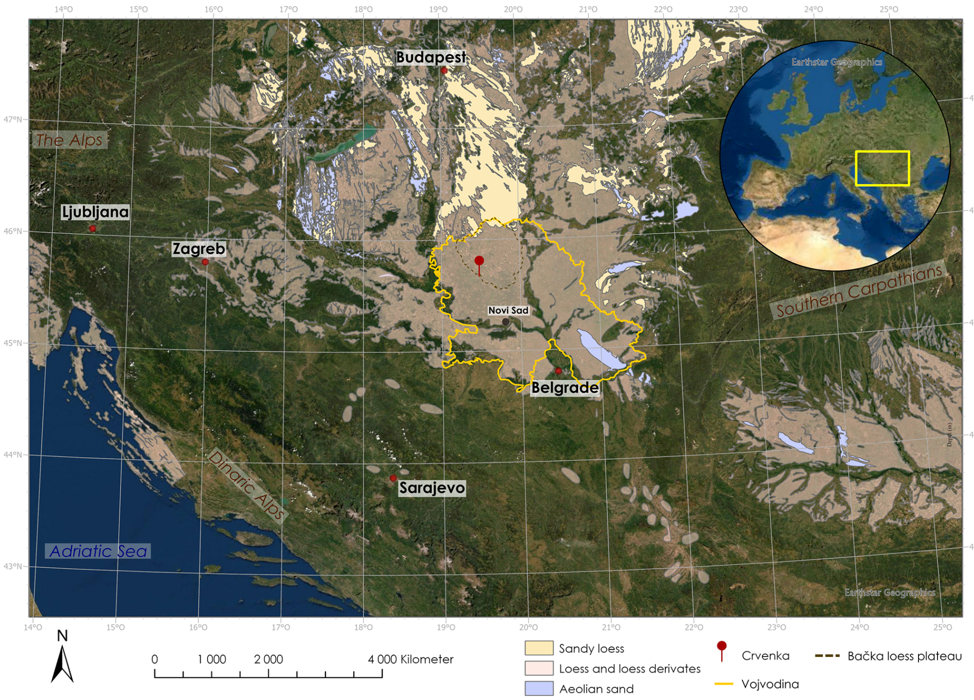

Figure 1. Map of the Carpathian basin with loess deposits according to Lehmkuhl et al. (2021) and location of the Crvenka study area (created with ArcGIS Pro).

alkanoic acids. From an analytical point of view, total lipid extraction from plants, soils, or sediments for yielding bulk lipids is relatively simple and can be achieved, e.g., by Soxhlet, ultrasonic, or microwave extraction. Lipids are generally hydrophobic and thus not specifically prone to translocation by percolating water in soils. Moreover, they are relatively persistent against biodegradation and can thus be studied even over geological timescales in paleosols and sediments. According to our knowledge, $\delta^{18}O_{\text{bulk lipid}}$ analyses have hitherto not been applied to paleoenvironmental archives such as LPSs.

The aim of our pilot study presented here was therefore to test the applicability of $\delta^{18}O_{\text{bulk lipid}}$ analyses to LPSs. Given that abundant research, including numerical dating, has already been conducted there, we chose the late Middle Pleistocene–Holocene LPS Crvenka in Serbia (Marković et al., 2015; Stevens et al., 2011; R. Zech et al., 2013) and followed the following specific research questions and objectives:

- How high are the bulk lipid contents in the LPS Crvenka, and are the extractable amounts sufficient for $\delta^{18}O_{\text{bulk lipid}}$ analyses?
- In the case that a $\delta^{18}O_{\text{bulk lipid}}$ record can be established for the LPS Crvenka, does it show variations coinciding with the marine oxygen-isotope stage (MIS) or with interstadials known from Greenland $\delta^{18}O_{\text{ice core}}$ records?
- Which factors need to be considered when interpreting $\delta^{18}O_{\text{bulk lipid}}$ records?

2 Material and methods

2.1 Study site and sampling

The LPS Crvenka (45°39.750′ N, 19°28.774′ E; 108 m a.s.l.) is located in the center of the Carpathian basin, southeastern Europe, in a brickyard exposure on the southwestern edge of the Bačka loess plateau in the Vojvodina region (see Fig. 1). According to the effective classification of Köppen, the current climate in the Carpathian basin is mainly classified as Cfb (i.e., C – temperate, f – without dry season, b – warm summers), but the regional climate can vary greatly due to its location in the border area between the Atlantic, continental, and Mediterranean climate zones. In January the average temperature is −0.1 °C, and in July it is 21.9 °C, while mean annual precipitation is 612 mm with a maximum in spring (Peel et al., 2007). We chose the LPS Crvenka (spanning about the last 145 kyr) for our $\delta^{18}O_{\text{bulk lipid}}$ pilot study due to previous detailed stratigraphic and pedologic descriptions, geochemical analyses, and numerical dating (Marković et al., 2015; Stevens et al., 2011; R. Zech et al., 2013). The chronostratigraphy can be summarized as follows: vertically, the profile extends over a depth of approximately 10 m (Fig. 2).

The oldest pale-yellow loess unit ("L2") of the Crvenka LPS consists mainly of penultimate glacial silts and extends only over the lowest 100 cm of the profile. The over-

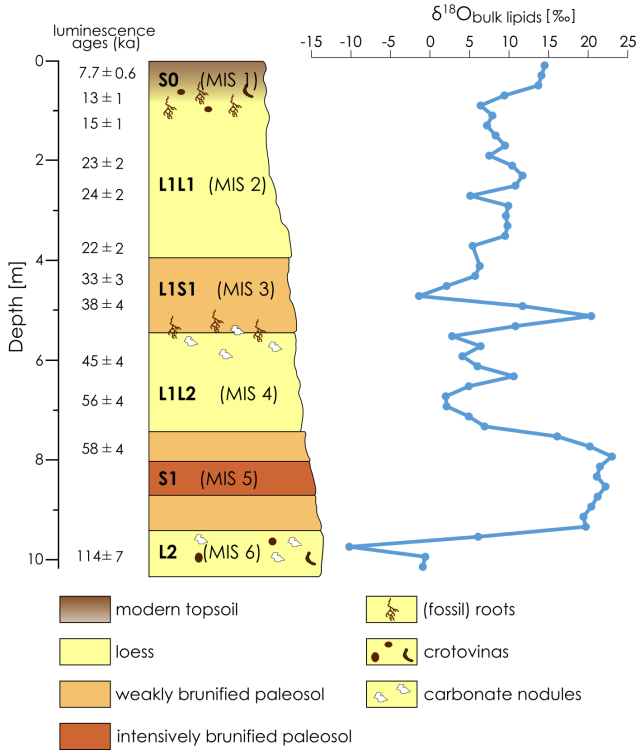

Figure 2. Stratigraphy of the LPS Crvenka after R. Zech et al. (2013) and the $\delta^{18}O_{\text{bulk lipid}}$ record. Note that the luminescence ages of Stevens et al. (2011) are "preferred" ages and that a numerical age model could only be constructed for the last 50 to 60 kyr. Lower luminescence ages than expected for older sediments probably indicate post-depositional effects on the luminescence signal (Stevens et al., 2011).

lying reddish-brown, clay-rich, and strongly brunified paleosol complex, with a thickness between 215–235 cm ("S1"), is correlated with MIS 5 and thus formed during the last interglacial. Above there is a loess package (L1) up to 8 m thick, which was deposited over the last glacial period. It is composed of two loess layers L1L1 (top) and L1L2 (bottom) separated by a weakly developed paleosol complex ("L1S1"). The lower light-yellow-grey L1L2 layer correlates with MIS 4 and is coarser-grained than the very porous L1L1 loess layer assigned to MIS 2. The interstadial, weakly developed paleosol complex ("L1S1") corresponds roughly to MIS 3. The uppermost part of the profile consists of a black-to-reddish-brown Holocene soil ("S0") that ranges in thickness from 50 to 80 cm and can be associated with MIS 1.

For our $\delta^{18}O_{\text{bulk lipid}}$ pilot study, we used 50 loess and paleosol samples that were taken by continuous sampling in ∼ 20 cm intervals by Zech et al. (2013) in 2009.

2.2 Total lipid extraction and $\delta^{18}O_{\text{bulk lipid}}$ measurement

Total lipid extraction from about 20 g of sample material was performed using an ultrasonic bath for 15 min and 30 mL of DCM : MeOH (9 : 1) as a solvent. In preceding tests, we found that bulk lipid yields from loess–paleosol samples are much lower when, e.g., hexane is used as a solvent instead of DCM : MeOH (9 : 1) and that the $\delta^{18}O_{\text{bulk lipid}}$ results are less reproducible. The total lipid extracts were centrifuged at 2000 rpm for 15 min and were subsequently passed over pipette columns filled with glass fiber. The extraction and purification procedures were repeated two more times with 20 mL of solvent for each sample. After solvent reduction using rotary evaporation, the total lipid extracts were transferred into silver capsules with DCM. Bulk lipid yields were quantified by weighing the silver capsules before and after the transfer and solvent evaporation. The bulk $\delta^{18}O$ measurements of the lipids were performed at the Institute of Groundwater Management of the Technische Universität (TU) Dresden using an EA IsoLink elemental analyzer coupled to a Delta V Plus IRMS (isotope ratio mass spectrometer; Thermo Fisher Scientific GmbH, Bremen, Germany). For calibration, the reference materials NBS 127, GISP, VSMOW2 (Vienna Standard Mean Ocean Water), CH3, and CH6 (all from the International Atomic Energy Agency, IAEA) were used. The standard deviation for replication measurements of these reference materials was on average 0.5 ‰ and never exceeded 1.2 ‰. All results are reported in the usual δ notation versus the Vienna Standard Mean Ocean Water (VSMOW).

3 Results and discussion

3.1 Bulk lipid contents and comparison of the Crvenka $\delta^{18}O_{\text{bulk lipid}}$ record with marine oxygen-isotope stages and Greenland $\delta^{18}O$ records

The bulk lipid contents of the LPS Crvenka range from 0.023 to 0.140 mg g^{-1}, and the absolute amounts range between 0.5 and 2.9 mg. These amounts allowed us to perform $\delta^{18}O_{\text{bulk lipid}}$ measurements for all samples: the $\delta^{18}O_{\text{bulk lipid}}$ values range between −10.2 ‰ and +23.0 ‰ and are systematically more positive in the interglacial (paleo-)soils compared to the loess layers (see Figs. 2 and 3). The modern Holocene soil, roughly corresponding with MIS 1, is characterized by $\delta^{18}O_{\text{bulk lipid}}$ values around +14 ‰, and the intensively brunified last interglacial paleosol complex V S1 coinciding with MIS 5 is characterized by $\delta^{18}O_{\text{bulk lipid}}$ values > +20 ‰. MIS 5 substages a–e are generally not differentiated by pedogenetic or analytical features in the Serbian LPSs (Marković et al., 2015; R. Zech et al., 2013). It is therefore not surprising that our $\delta^{18}O_{\text{bulk lipid}}$ record does not indicate these substages either. The weakly developed interstadial paleosol complex L1S1, coinciding with MIS 3, shows a striking large fluctuation with a minimum $\delta^{18}O_{\text{bulk lipid}}$ value of −1.4 ‰ in the middle and a maximum $\delta^{18}O_{\text{bulk lipid}}$ value of +20.4 ‰ in the lower part. The $\delta^{18}O_{\text{bulk lipid}}$ values of the last glacial loess layers L1L1 and L1L2 (coinciding with MIS 2 and 4, respectively) range between +2.0 ‰

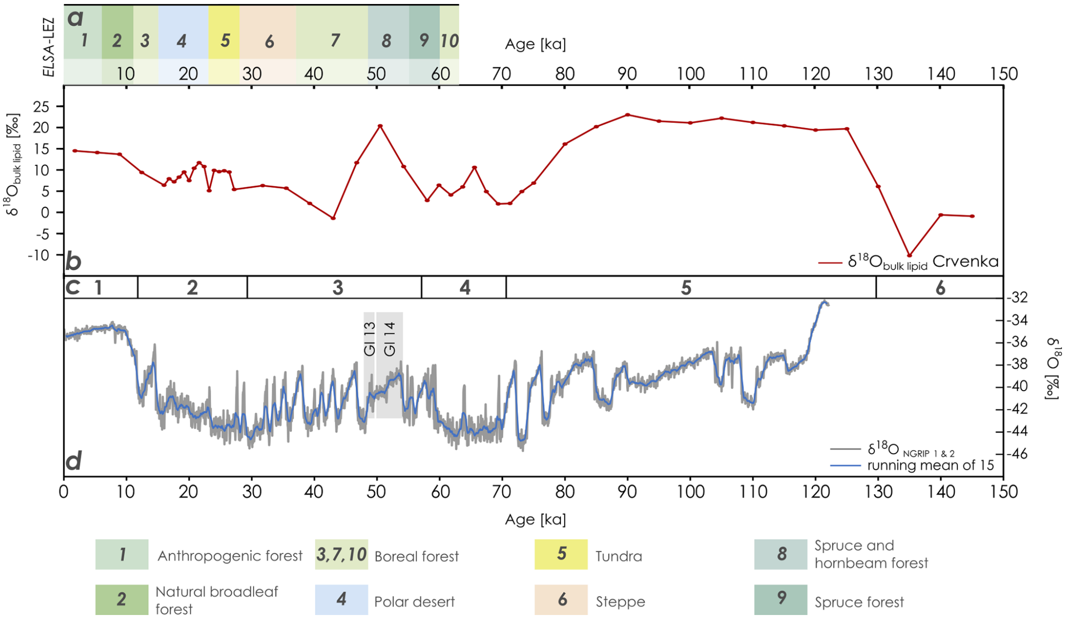

Figure 3. Comparison of **(a)** the landscape evolution zones after Sirocko et al. (2016), **(b)** the Crvenka $\delta^{18}\mathrm{O}_{\text{bulk lipid}}$ record (based on the MIS-based age–depth model of R. Zech et al., 2013), **(c)** the marine isotope stages after Lisiecki and Raymo (2005), and **(d)** the Greenland $\delta^{18}\mathrm{O}$ records (based on data of NGRIP members, 2004). GI 13 and 14 represent Greenland Interstadial 13 and 14, respectively. ELSA-LEZ: landscape evolution zones (LEZs) reconstructed from the Eifel Laminated Sediment Archive (ELSA). NGRIP: North Greenland Ice Core Project.

and +11.7 ‰. Loess layer L2, representing the penultimate glacial and coinciding with MIS 6, is characterized by the most negative $\delta^{18}\mathrm{O}_{\text{bulk lipid}}$ values of up to −10.2 ‰.

In order to enable the comparison of our Crvenka $\delta^{18}\mathrm{O}_{\text{bulk lipid}}$ record with Greenland $\delta^{18}\mathrm{O}_{\text{ice core}}$ records, we adopted the MIS-scale age–depth model of R. Zech et al. (2013). Although the LPS Crvenka is one of the best luminescence-dated LPSs in the Carpathian basin (Stevens et al., 2011), we refrain from applying a luminescence-based age–depth model (see Fig. 2 for preferred ages according to Stevens et al., 2011) due to likely age underestimations. Figure 3 shows that the Crvenka $\delta^{18}\mathrm{O}_{\text{bulk lipid}}$ record only partly resembles the Greenland $\delta^{18}\mathrm{O}_{\text{NGRIP}}$ record. Particularly the Holocene and the time period from around 80 to 130 ka, including the Eemian interglacial, are characterized by more positive $\delta^{18}\mathrm{O}_{\text{bulk lipid}}$ values. While one striking $\delta^{18}\mathrm{O}_{\text{bulk lipid}}$ maximum occurs around 50 ka, our Crvenka $\delta^{18}\mathrm{O}_{\text{bulk lipid}}$ record does not reflect the succession of stadials and interstadials known from the Greenland ice core records, i.e., the famous Dansgaard–Oeschger events. When comparing our southeastern European $\delta^{18}\mathrm{O}_{\text{bulk lipid}}$ record with the mid-European landscape evolution zones (LEZs) identified by Sirocko et al. (2016) based on pollen and total carbon analyses from laminated Eifel maar sediments, LEZ 8 ranging from 49 to 55 ka is characterized by the unexpected dominance of thermophilous tree taxa (see Fig. 3a). This suggests that Greenland Interstadial 13 and 14 (see Fig. 3d; the latter is often referred to as the Glinde interstadial) were the warmest periods of MIS 3. However, the chronological resolution of MIS 3 in the LPS Crvenka is quite limited. Thus, similar to unresolved MIS 5 substages a–e, the absence of stadial–interstadial successions in our $\delta^{18}\mathrm{O}_{\text{bulk lipid}}$ record in the LPS Crvenka does not necessarily mean that these climate variations did not occur in southeastern Europe. However, interestingly around this period very high $\delta^{18}\mathrm{O}_{\text{bulk lipid}}$ values are found in our LPS as well.

The last glacial maximum (around 25 to 20 ka) is not characterized, as one might expect, by particularly negative $\delta^{18}\mathrm{O}_{\text{bulk lipid}}$ values. Last but not least, the amplitude of the Crvenka $\delta^{18}\mathrm{O}_{\text{bulk lipid}}$ values cover around double the amplitude compared to the $\delta^{18}\mathrm{O}_{\text{NGRIP}}$ amplitude (Fig. 3). Possible explanations for these two findings, as well as all factors needing consideration when interpreting $\delta^{18}\mathrm{O}_{\text{bulk lipid}}$ records from LPSs, are discussed in the following section.

3.2 Paleoclimatic interpretation of the Crvenka $\delta^{18}\mathrm{O}_{\text{bulk lipid}}$ record

$\delta^{18}\mathrm{O}$ analyses of cellulose are a widely applied tool in paleoclimate research. Yet, its application to classical LPSs is still hampered by analytical challenges mainly associated with low cellulose and high carbonate contents, hindering the acid-hydrolytic extraction of (hemi-)cellulose-derived sugar biomarkers. In their groundbreaking study "Beyond the cellulose: Oxygen isotope composition of plant lipids as a proxy for terrestrial water balance", Silva et al. (2015) ob-

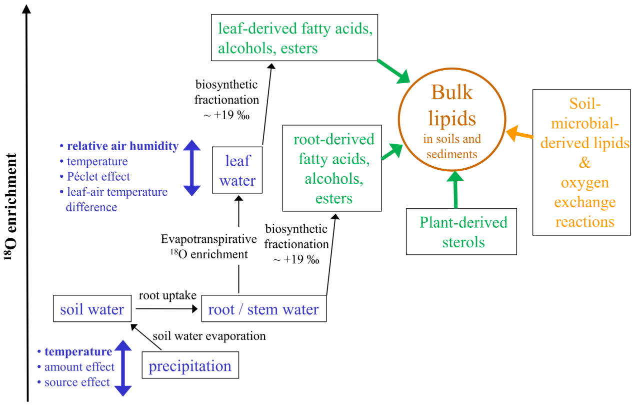

Figure 4. Conceptual diagram illustrating the major factors influencing the oxygen isotopic composition of bulk lipids ($\delta^{18}O_{\text{bulk lipid}}$) in soils and sediments (modified after Zech et al., 2014). Apart from climatic factors (blue colors) with, e.g., relative air humidity controlling the isotopic enrichment of leaf water by evapotranspiration, "pool effects" (green colors) particularly by the admixture of sterols and root-derived lipids need consideration. Last but not least, the buildup of soil-microbial-derived lipids is also a kind of a pool effect introducing uncertainty, too, and a part of the oxygen bound in lipids is prone to exchange reactions with soil water.

served a strong linear relationship between $\delta^{18}O_{\text{bulk lipid}}$ and $\delta^{18}O_{\text{cellulose}}$. This corroborates that $\delta^{18}O$ values of many plant-derived lipids such as organic acids, carbonyls, alcohols, and esters are water-correlated, although this does not hold true for plant-derived sterols that contain atmospheric-derived oxygen (Schmidt et al., 2001). Accordingly, oxygen from fatty acids or acyl-derived alcohols is about +19 ‰ more positive compared to water. Such systematic offsets are usually described as biosynthetic fractionation factors and are certainly one important factor needing consideration when interpreting $\delta^{18}O_{\text{bulk lipid}}$ records from LPSs (Fig. 4).

Concerning plant water in which the lipids are biosynthesized, it is generally accepted that the uptake of soil water by plants is not associated with discernible isotopic fractionation. Thus, in cases where significant evaporative enrichment of soil water can be excluded, $\delta^{18}O$ of root and stem water reflects the mean isotopic composition of local precipitation. In high latitudes $\delta^{18}O_{\text{precipitation}}$ is primarily temperature-controlled. Hence, it is likely that the temperature effect on $\delta^{18}O_{\text{precipitation}}$ is one important factor controlling the glacial–interglacial variability of our Crvenka $\delta^{18}O_{\text{bulk lipid}}$ record, with more positive/negative values during the warm interglacials/cold glacials (Figs. 2, 3, and 4). However, on the one hand, apart from the temperature effect neither the amount effect nor the source effect can be excluded as possible factors that had influenced $\delta^{18}O_{\text{precipitation}}$ in the Crvenka study area during the past. Unfortunately, their quantitative assessment has been rather challenging so far. On the other hand, $\delta^{18}O_{\text{precipitation}}$ changes alone can certainly not explain the $\delta^{18}O_{\text{bulk lipid}}$ amplitude of our Crvenka record, ranging between −10.2 ‰ and +23.0 ‰. Indeed, leaf-(wax-)derived lipids do not reflect the isotopic composition directly of precipitation but instead of isotopically enriched leaf water (Fig. 4). This is well known for $\delta^{2}H$ of leaf-wax-derived *n* alkanes, where due to evaporation leaf water can be isotopically enriched by up to ∼ 50 ‰ compared to xylem water (e.g., Zech et al., 2015). In the case of $\delta^{18}O$, leaf water enrichment of up to ∼ 25 ‰ was for instance reported by Zech et al. (2014). The main controlling factor for this enrichment is relative air humidity (RH), with lower RH values resulting in stronger ^{2}H and ^{18}O enrichment of leaf water. Further minor influencing factors are temperature, leaf–air temperature differences, and the so-called Péclet effect. The latter describes, in simplified terms, the mixing of water from the xylem and from evaporation sites within plant leaves. Water that flows to evaporation sites by transpiration is enriched in $H_2^{18}O$ at the evaporation sites by back diffusion of the enriched water (cf. Farquhar and Lloyd, 1993; Ferrio et al., 2012).

Next to the climatic factors temperature and relative air humidity, also "pool effects" need to be considered when interpreting $\delta^{18}O_{\text{bulk lipid}}$ values in plants and soils. This is comparable to bulk $\delta^{2}H$ results of soils and sediments, where pool effects exert influence, too (cf. Zech et al., 2015). On the one hand, as mentioned above $\delta^{18}O$ of plant-derived sterols is not water-correlated, and thus sterols dilute the climate signal of the leaf-derived fatty acids and alcohols (Fig. 4). On the other hand, root and stem input of fatty acids and alcohols likely introduces a $\delta^{18}O$ signal that does not carry the ^{18}O enrichment of leaf water (Fig. 4). For instance, in the MIS 2 part of our Crvenka $\delta^{18}O_{\text{bulk lipid}}$ record, one might have expected more negative values in the case of a mere climate control (Figs. 2 and 3). Hence, postsedimentary Holocene root input of oxygen-bearing lipids into the L1L1 layer could possibly explain the absence of a more pronounced $\delta^{18}O_{\text{bulk lipid}}$ minimum. Moreover, bulk lipids extracted from soils and sediments not only are plant-derived but also contain soil-microbial-derived lipids. Variable and unknown contributions of such soil-microbial-derived lipids introduce another source of uncertainty that is difficult to quantify based on the current state of knowledge. In addition, a part of the oxygen bound in lipids is prone to exchange reactions with soil water (Fig. 4). For instance, using laboratory incubation studies with isotopically enriched water, Maxwell et al. (2018) found that 22 % of oxygen from bulk soil lipid extracts is exchangeable.

4 Conclusions and outlook

Our pilot study suggests that $\delta^{18}O$ analyses of bulk lipids ($\delta^{18}O_{\text{bulk lipid}}$) can successfully be applied to loess–paleosol sequences, since absolute bulk lipid yields for the LPS Crvenka ranged between 0.5 and 2.9 mg per 20 g of sample material. Our Crvenka $\delta^{18}O_{\text{bulk lipid}}$ record reflects the alternation between loess layers and (paleo-)soils (more negative and more positive $\delta^{18}O_{\text{bulk lipid}}$ values, respectively) and thus marine oxygen-isotope stage (MIS) 1 to 6. Yet, this does not involve MIS 5 substages a–e, which are not differentiated in the LPS Crvenka. Similarly, our Crvenka $\delta^{18}O_{\text{bulk lipid}}$ record does not provide evidence for the occurrence of interstadials and stadials comparable to the Dansgaard–Oeschger events known from the Greenland $\delta^{18}O_{\text{ice core}}$ records. This will require further and higher-resolution data in combination with more robust age models in the future.

Concerning the interpretation of our Crvenka $\delta^{18}O_{\text{bulk lipid}}$ record, plant-derived lipids such as fatty acids and alcohols are certainly strongly influenced by climatic factors such as temperature (via $\delta^{18}O_{\text{precipitation}}$) and relative air humidity (via ^{18}O enrichment of leaf water due to evapotranspiration). However, also pool effects in the form of non-water-correlated lipids such as sterols or the input of root-derived lipids should not be overlooked. Furthermore, also the input of soil-microbial lipids and oxygen exchange reactions represent uncertainties that are challenging quantitative paleoclimate/paleohydrological reconstructions based on $\delta^{18}O_{\text{bulk lipid}}$ analyses.

Data availability. Underlying data can be found in the Supplement.

Supplement. The supplement related to this article is available online at: https://doi.org/10.5194/egqsj-71-83-2022-supplement.

Author contributions. MZ developed the project idea in consultation with LB, CBR, and JL. The analyzed samples were taken during the fieldwork by RZ in cooperation with MZ. The laboratory work was mainly done by PH and DB with the participation of JL, who prepared the manuscript. SBM and BG, as well as all other co-authors, participated in the interpretation of the results and contributed to the completion of the manuscript.

Competing interests. The contact author has declared that neither they nor their co-authors have any competing interests.

Special issue statement. This article is part of the special issue “Quaternary research from and inspired by the first virtual DEUQUA conference”. It is a result of the vDEUQUA2021 online conference in September/October 2021.

Acknowledgements. We kindly thank Gerhard Gebauer and his team from the Laboratory of Isotope Biogeochemistry of the BayCEER at the University of Bayreuth as well as Tobias Krause (Institute of Soil Science and Site Ecology, TU Dresden), Erik Michalowski and Amelie Demmer (both Institute of Geography, TU Dresden), Doreen Degenhardt and Patricia Stock (both Institute of Groundwater Management, TU Dresden), and Marianne Zech for their support of laboratory work and isotope analyses. Special thanks go to Hans von Suchodoletz for his editorial handling, as well as to two anonymous reviewers for the valuable suggestions and their constructive reviews.

This paper is dedicated to Ludwig Zöller and Dominik Faust. Ludwig Zöller was born in 1953 and held the Chair of Geomorphology at the University of Bayreuth from 2002 until his retirement in 2018. Dominik Faust was born in 1954 and held the Chair of Physical Geography at the Technische Universität Dresden from 2000 until his retirement in 2020. Ludwig Zöller supervised the dissertation and habilitation of Michael Zech. Both Ludwig Zöller and Dominik Faust were important mentors of Michael Zech and opened the door towards loess research for Michael Zech and his team with their methodological expertise on biomarkers and stable isotopes.

Financial support. This research has been supported by the Deutsche Forschungsgemeinschaft (grant nos. DFG ZE 844/14-1 and DFG FA 239/26-1).

This open-access publication was funded
by the Technische Universität Dresden (TUD).

Review statement. This paper was edited by Hans von Suchodoletz and reviewed by two anonymous referees.

References

Bittner, L., Gil-Romera, G., Grady, D., Lamb, H., Lorenz, E., Weiner, M., Meyer, H., Bromm, T., Glaser, B., and Zech, M.: The Holocene lake-evaporation history of the afro-alpine Lake Garba Guracha in the Bale Mountains, Ethiopia, based on δ^{18}O records of sugar biomarker and diatoms, Quaternary Res., 105, 23–36, https://doi.org/10.1017/qua.2021.26, 2021.

Dansgaard, W.: Stable isotopes in precipitation, Tellus, 16, 436–468, https://doi.org/10.1111/j.2153-3490.1964.tb00181.x, 1964.

Farquhar, G. D. and Lloyd, J.: 5 – Carbon and Oxygen Isotope Effects in the Exchange of Carbon Dioxide between Terrestrial Plants and the Atmosphere, in: Stable Isotopes and Plant Carbon-water Relations, edited by: Ehleringer, J. R., Hall, A. E., and Farquhar, G. D., Academic Press, San Diego, 47–70, https://doi.org/10.1016/B978-0-08-091801-3.50011-8, 1993.

Ferrio, J. P., Pou, A., Florez-Sarasa, I., Gessler, A., Kodama, N., Flexas, J., and Ribas-Carbo, M.: The Péclet effect on leaf water enrichment correlates with leaf hydraulic conductance and mesophyll conductance for CO_2, Plant, Cell Environ., 35, 611–625, https://doi.org/10.1111/j.1365-3040.2011.02440.x, 2012.

Häggi, C., Eglinton, T. I., Zech, W., Sosin, P., and Zech, R.: A 250 ka leaf-wax δD record from a loess section in Darai

Kalon, Southern Tajikistan, Quaternary Sci. Rev., 208, 118–128, https://doi.org/10.1016/j.quascirev.2019.01.019, 2019.

Lachniet, M. S.: Climatic and environmental controls on speleothem oxygen-isotope values, Quaternary Sci. Rev., 28, 412–432, https://doi.org/10.1016/j.quascirev.2008.10.021, 2009.

Lehmkuhl, F., Nett, J. J., Pötter, S., Schulte, P., Sprafke, T., Jary, Z., Antoine, P., Wacha, L., Wolf, D., Zerboni, A., Hošek, J., Marković, S. B., Obreht, I., Sümegi, P., Veres, D., Zeeden, C., Boemke, B., Schaubert, V., Viehweger, J., and Hambach, U.: Loess landscapes of Europe – Mapping, geomorphology, and zonal differentiation, Earth-Sci. Rev., 215, 103496, https://doi.org/10.1016/j.earscirev.2020.103496, 2021.

Lemma, B., Bittner, L., Glaser, B., Kebede, S., Nemomissa, S., Zech, W., and Zech, M.: $\delta^2H_{n-alkane}$ and $\delta^{18}O_{sugar}$ biomarker proxies from leaves and topsoils of the Bale Mountains, Ethiopia, and implications for paleoclimate reconstructions, Biogeochem., 153, https://doi.org/10.1007/s10533-021-00773-z, 2021.

Lisiecki, L. E. and Raymo, M. E.: A Pliocene-Pleistocene stack of 57 globally distributed benthic δ^{18}O records, Paleoceanography, 20, https://doi.org/10.1029/2004PA001071, 2005.

Marković, S., Stevens, T., Kukla, G., Hambach, U., Fitzsimmons, K., Gibbard, P., Buggle, B., Zech, M., Guo, Z., Hao, Q., Wu, H., O'Hara-Dhand, K., Smalley, I., Újvári, G., Sümegi, P., Timar-Gabor, A., Veres, D., Sirocko, F., Vasiljevic, D., Vidojko, J., Zdzislaw, J., Anderss, S., Lehmkuhl, F., Kovács, J., and Svirčev, Z.: Danube loess stratigraphy – Towards a pan-European loess stratigraphic model, Earth-Sci. Rev., 148, 228–258, https://doi.org/10.1016/j.earscirev.2015.06.005, 2015.

Maxwell, T. M., Silva, L. C. R., and Horwath, W. R.: Predictable Oxygen Isotope Exchange Between Plant Lipids and Environmental Water: Implications for Ecosystem Water Balance Reconstruction, J. Geophys. Res.-Biogeosc., 123, 2941–2954, https://doi.org/10.1029/2018JG004553, 2018.

NGRIP members: High-resolution record of Northern Hemisphere climate extending into the last interglacial period, Nature, 431, 147–151, https://doi.org/10.1038/nature02805, 2004.

Peel, M. C., Finlayson, B. L., and McMahon, T. A.: Updated world map of the Köppen-Geiger climate classification, Hydrol. Earth Syst. Sci., 11, 1633–1644, https://doi.org/10.5194/hess-11-1633-2007, 2007.

Prud'homme, C., Lécuyer, C., Antoine, P., Moine, O., Hatté, C., Fourel, F., Martineau, F., and Rousseau, D.-D.: Palaeotemperature reconstruction during the Last Glacial from δ^{18}O of earthworm calcite granules from Nussloch loess sequence, Germany, Earth Planet. Sci. Lett., 442, 13–20, https://doi.org/10.1016/j.epsl.2016.02.045, 2016.

Pustovoytov, K. and Terhorst, B.: An isotopic study of a late Quaternary loess-paleosol sequence in SW Germany, Revista mexicana de ciencias geológicas, ISSN 1026-8774, Vol. 21, No. 1, 2004 (Ejemplar dedicado a: VI International Symposium and Field Workshop on Paleopedology), 21, 88–93 pp., 2004.

Roden, J. S., Lin, G., and Ehleringer, J. R.: A mechanistic model for interpretation of hydrogen and oxygen isotope ratios in tree-ring cellulose, Geochim. Cosmochim. Acta, 64, 21–35, https://doi.org/10.1016/S0016-7037(99)00195-7, 2000.

Schäfer, I., Bliedtner, M., Wolf, D., Faust, D., and Zech, R.: Evidence for humid conditions during the last glacial from leaf wax patterns in the loess–paleosol sequence El Paraíso, Central Spain, Quaternary Int., 407, 64–73, https://doi.org/10.1016/j.quaint.2016.01.061, 2016.

Schmidt, H. L., Werner, R. A., and Rossmann, A.: ^{18}O pattern and biosynthesis of natural plant products, Phytochemistry, 58, 9–32, https://doi.org/10.1016/s0031-9422(01)00017-6, 2001.

Silva, L. C. R., Pedroso, G., Doane, T. A., Mukome, F. N. D., and Horwath, W. R.: Beyond the cellulose: Oxygen isotope composition of plant lipids as a proxy for terrestrial water balance, Geochem. Perspect. Lett., 33–42, https://doi.org/10.7185/geochemlet.1504, 2015.

Sirocko, F., Knapp, H., Dreher, F., Foerster, M., Albert, J., Brunck, H., Veres, D., Dietrich, S., Zech, M., Hambach, U., Röhner, M., Rudert, S., Schwibus, K., Adams, C., and Sigl, P.: The ELSA-Vegetation-Stack: Reconstruction of Landscape Evolution Zones (LEZ) from laminated Eifel maar sediments of the last 60,000 years, Global Planet. Change, 148, 108–135, https://doi.org/10.1016/j.gloplacha.2016.03.005, 2016.

Spötl, C., Mangini, A., and Richards, D. A.: Chronology and paleoenvironment of Marine Isotope Stage 3 from two high-elevation speleothems, Austrian Alps, Quaternary Sci. Rev., 25, 1127–1136, https://doi.org/10.1016/j.quascirev.2005.10.006, 2006.

Stevens, T., Marković, S. B., Zech, M., Hambach, U., and Sümegi, P.: Dust deposition and climate in the Carpathian Basin over an independently dated last glacial–interglacial cycle, Quaternary Sci. Rev., 30, 662–681, https://doi.org/10.1016/j.quascirev.2010.12.011, 2011.

Zech, M., Tuthorn, M., Detsch, F., Rozanski, K., Zech, R., Zöller, L., Zech, W., and Glaser, B.: A 220ka terrestrial δ^{18}O and deuterium excess biomarker record from an eolian permafrost paleosol sequence, NE-Siberia, Complete, 220–230, https://doi.org/10.1016/j.chemgeo.2013.10.023, 2013.

Zech, M., Mayr, C., Tuthorn, M., Leiber-Sauheitl, K., and Glaser, B.: Oxygen isotope ratios (^{18}O/^{16}O) of hemicellulose-derived sugar biomarkers in plants, soils and sediments as paleoclimate proxy I: Insight from a climate chamber experiment, Geochim. Cosmochim. Acta, 126, 614–623, https://doi.org/10.1016/j.gca.2013.10.048, 2014.

Zech, M., Zech, R., Rozanski, K., Gleixner, G., and Zech, W.: Do n-alkane biomarkers in soils/sediments reflect the δ^2H isotopic composition of precipitation? A case study from Mt. Kilimanjaro and implications for paleoaltimetry and paleoclimate research, Isotop. Environ. Health Stud., 51, 508–524, https://doi.org/10.1080/10256016.2015.1058790, 2015.

Zech, R., Zech, M., Marković, S., Hambach, U., and Huang, Y.: Humid glacials, arid interglacials? Critical thoughts on pedogenesis and paleoclimate based on multi-proxy analyses of the loess–paleosol sequence Crvenka, Northern Serbia, Palaeogeogr. Palaeoclim. Palaeoecol., 387, 165–175, https://doi.org/10.1016/j.palaeo.2013.07.023, 2013.

Quaternary research from and inspired by the first virtual DEUQUA conference

https://www.eg-quaternary-science-journal.net/ ISSN 0424-7116